Lagrangian Modeling in the vicinity of the Eastfrisian Islands

Von der Fakultät für Mathematik und Naturwissenschaften der Carl von Ossietzky Universität Oldenburg zur Erlangung des Grades und Titels eines

Doctor rerum naturalium (Dr. rer. nat.)

angenommene Dissertation

von Herrn **Florian Hahner**

geboren am 29.01.1986 in Oldenburg

Eigenständigkeitserklärung

Hiermit versichere ich, dass ich diese Arbeit selbständig verfasst und keine anderen als die angegebenen Quellen und Hilfsmittel benutzt habe. Außerdem versichere ich, dass ich die allgemeinen Prinzipien wissenschaftlicher Arbeit und Veröffentlichung, wie sie in den Leitlinien guter wissenschaftlicher Praxis der Carl von Ossietzky Universität Oldenburg festgelegt sind, befolgt habe.

Abstract

An interdisciplinary consortium, tackling scientific descriptions and solutions for macroplastics pollution in the North Sea, was funded by the Lower Saxony Ministry for Science and Culture (MWK) and established by the ICBM at the Carl-von-Ossietzky University Oldenburg. As part of the reasearch-project *Macroplastics North Sea*, development and operation of a multi-scale, nested hydrodynamic model of the North Sea, using the COAWST [Warner et al., 2008b, 2010] framework, is described. Development of a MatLab toolbox, allowing offline computations and evaluation of Lagrangian trajectories based on numerical and measured data for surface currents, winds and waves, is presented. The role of Stokes Drift, wind drag and tidal currents for distribution and potential beaching of surface drifting objects is investigated using Lagrangian modeling and high resolution numerical data near the barrier island Spiekeroog. These physical parameters are found significantly altering advection and distribution of surface drifting objects in this nearshore area. Stokes Drift and numerical handling of landmasks in Lagrangian and hydrodynamic modeling are found significantly influencing floating periods and beaching locations of Lagrangian particles. Theoretical wind drag estimates by Niiler and Paduan [1995] for GPS-drifters, developed by Meyerjürgens et al. [2019] and Breitbach [2018], are compared to numerical estimates based on modeled hydrodynamic and wave data resp. winds provided by the DWD. Derived drag parameters significantly differ from theoretical values and vary for three different drag models: *a* using Lagrangian currents and parameters for wind drag and wind deflection, *b* using Eulerian currents and wind drag parameters and *c* using Lagrangian currents based on drag parameters for Stoke Drift resp. wind drag. Parametrization of Stokes Drift is found not satisfyingly representable by wind drag in nearshore areas. Results agree with findings by Callies et al. [2011], Allen and Plourde [1999], Anderson et al. [1998], recommending individual drag parameter estimations for different models, datasets and regions. The developed modeling framework is qualitatively representing measured drifter paths and beaching locations in nearshore areas on short time scales. Due to highly dynamical features of winds, Stokes Drift and bottom topography at the Eastfrisian islands, quantitative forecasts on mid to long time scales are concluded impossible.

Contents

Contents

List of Figures

List of Figures

List of Figures

List of Tables

List of Symbols

A Area. For meaning of subscripts, see *Index abbreviations*.
  In subsubsection 2.3.1: Wave amplitude.

A_z Vertical eddy viscosity.

$abs\,(...)$ Absolute value of ..., e.g. $abs(\vec{X}) = \sqrt{x^2 + y^2 + z^2}$ is the length of the cartesian vector $\vec{x})\,(x, y, z)$.

BfG German Federal Institute of Hydrology.

BSH Federal Maritime and Hydrographic Agency of Germany.

BSHcmod Hydrodynamic operational model of the BSH .

C Drag coefficient. For meaning of subscripts, see *Index abbreviations*.

C_u, C_v Courant numbers for u- and v-velocities.

c Wave celerity.

$C(\varsigma)$ Stretching function for vertical coordinates in equation (41).

COAWST Coupled Ocean-Atmosphere Wave-Sediment Transport Model, see section 4.

$Clst_i(N, t, r_{max})$ Particle cluster with minimal cardinal number N of particles, maximum particle distance r_{max} at time t, defined by equation (45).

$D(l)$ Numerical horizontal eddy diffusion for data of discrete velocities of spatial resolution l.

$D(l_0)$, l_0 Reference length scales in equation (33).

D_t Material derivative.
  $D_t\Phi := \partial_t\Phi + \vec{v} \cdot \nabla\Phi$, rate of change of a scalar or vector field Φ.

DWD German Weather Service.

E Energy.

$E(k)$ Wave energy spectrum.

$\vec{e}$ Directional vector, e.g. $\vec{e}_x = (1, 0, 0)$.

e Euler's number, $e \approx 2.71828$.

ECMWF European Center for Medium-Range Weather Forecasts.

ERA5 Numerical model for atmospheric and hydrodynamic data, operated by the ECMWF .

(J_*, K_*) Vortex Forces. See equation (28), details are given in Hahner [2016].

$\vec{F}$ Forces. A superscript denotes type of force, e.g. $\vec{F}^{sext}$ = external force.

f Coriolis Parameter, $f = 2\Omega \sin \phi$. Measure of strength of Coriolis forces at Latitude ϕ. $\Omega = 7.3 \times 10^{-5} \mathrm{s}^{-1}$ is the earth's rotation frequency.

g Gravitational acceleration. $g \approx 9.81 \, \mathrm{m\,s}^{-1}$.

H Wave height. H_{sig} is the significant wave height. $H = 2A$ for waves of amplitude A.

h Local water depth respective to $z = 0$, positive downward. In general $h = h(x, y)$ describes bathymetry.

$\mathcal{H}$ Scaled total water depth in equation (28).

Index abbreviations As not mentioned otherwise, the following subscript letters denote: l = *Lagrangian*, e = *Eulerian*, St= *Stokes*, o= *Ocean* i.e. *Water*, w= *Wind*, wav= *Waves*, p= *Particle*, i, k, l = running index as denoted in the text, superscript ext = *external*, superscript t = discrete time step, superscript primes = fluctuations, subscript $\vec{x}$ = discrete space coordinate (x, y, z)

k Wave number, $k = \frac{2\pi}{L}$, where L is wavelength.

$\vec{k}$ Wave vector, $\vec{k} = (k_x, k_y)$, $\left| \vec{k} \right| = k$.

$\hat{k}$ Wave directional vector, $\hat{k} = \frac{\vec{k}}{k}$.

$\mathcal{K}_*$ Bernoulli-Head, used in equation (28).

L Wave length.

$\vec{L}$ Leeway, $\vec{L} = \vec{L}_C + \vec{L}_D$. Velocity of a drifting object due to wind drag. $\vec{L}_D$ is the *downwind* and $\vec{L}_C$ the *crosswind* velocity.

List of Symbols

m Mass, e.g. m_p is the mass of particle p, m_o is water mass etc. See also *Index abbreviations*.

MCT Model Coupling Toolbox, see section 4.

$Mod(t)$ Vectorial Mode, $Mod(t) = (x(t)_{i,max}, y(t)_{i,max})$.

N Total number. Usually upper index of summation and/or total number of particles.
$N(\omega, \theta) = \frac{E}{\omega}$ is the ratio of wave energy $E(\omega, \theta)$ and frequency ω.

NaN Not a Number. Numerical term for describing fill values of discrete variables in numerical code. Calculation rules are $NaN + x = NaN$ and $NaN \cdot x = NaN$ for all $x \in \mathbb{R}$.

Nil Fill values of zero for discrete variables in numerical code, ie.e. $x = 0$ for a numerical variable x.

NLWKN Lower Saxony Water Management, Coastal Defense and Nature Conservation Agency.

$\mathcal{O}(...)$ Order of ...

P Probability.

PSU Practical Salinity Unit. Unit for measuring salt concentrations of water in physical oceanography.

$\vec{R}$ Noise term for describing particle diffusion in equation (32), $\vec{R}(t) = (R_x(t), R_y(t))$.

r (Radial) distance.

ROMS Regional Ocean Modeling System, hydrodynamic model, see section 4.

S Salinity.
Generalized terrain-following vertical coordinate in equation (41).

$S(t)$ Time dependent center-coordinate of particle clusters, defined by equation (46).

SD Vectorial standard deviations, $SD(t) = \sqrt{\frac{1}{N-1} \sum_{i=1}^{N} \left(x_i'^2 + y_i'^2 \right)}$.

SWAN Simulating Waves Nearshore, numerical wave model, see section 4.

T Temporal period.

T_{inert} Inertial period, $T_{inert} = \frac{2\pi}{f}$.

T_p Wave peak period.

t Time.

dt, Δt Temporal intervals and time stepping length.

$\vec{u}$ Horizontal velocities of ambient currents, Stokes Drift and winds, in general $\vec{u}(x, y, z, t) = (u(x, y, z, t), v(x, y, z, t), 0)$. Continuous space-time coordinates are omitted for clarity, sub- and superscripts indicate types of velocities (l, e, St, etc.) and discrete coordinates, as described by *Index abbreviations*.

$\vec{u}_{int}$ Depth integrated horizontal velocities.
$\vec{u}_{int} = (u_{int}, v_{int})$

$\vec{u}'$ Turbulent component of velocities $\vec{u}$.

$\bar{u}$, $\bar{v}$ Ambient (mean) velocities, e.g. geostrophic currents in equation (5).

$u*$ Friction velocity, $u* = \sqrt{\frac{\tau}{\rho_o}}$. τ is the absolute wind stress and ρ_o water density.

$\mathcal{U}$ Correlations of wave vector $\vec{k}$ with current and long wave velocities $\vec{u}^c$ and $\vec{u}^{lw}$. $\mathcal{U} = \vec{k} \cdot (\vec{u}^{lw} + \vec{u}^c)$

V Constant of integration in equation (12).

$\vec{v}_p$ Time dependent velocity of particle p, in general:

$$\vec{v}(x, y, z, t) = (u(x, y, z, t), v(x, y, z, t), w(x, y, z, t))$$

at position $\vec{x} = (x, y, z)$ and time t. Without loss of generality, horizontal velocities are used throughout this thesis, i.e. $w(t) = 0 \forall t$. Superscripts indicate time indices, e.g. $\vec{v}^{t+\Delta t}$ is the velocity at discrete time step $t + \Delta$, continuous space-time indices are omitted for clarity. Subscripts denote particle indices p and spatial coordinates $\vec{x}$.

WSV German Federal Waterways and Shipping Administration.

$\vec{x}$ Position vector. $\vec{x}(t) = (x(t), y(t), z(t))$ is the time dependent trajectory.

List of Symbols

(x, y, z) Spatial coordinates.

$\hat{x}, \hat{y}, \hat{z}$ Unit vectors.

(x_0, y_0) Reference coordinates.

$\mathcal{Z}$ Scaled vertical coordinate in equation (28).

$ZM_k(t)$ k'th vectorial central moment, $ZM_k(t) = \left(x_i'^k, y_i'^k\right) = \frac{1}{N} \sum_{i=1}^{N} \left(\vec{x}_i - S(t)\right)^k$

$\boldsymbol{\alpha}$ Rotation matrix, describing wind deflection ba an angle α.

$$\boldsymbol{\alpha} = \begin{pmatrix} \cos(\alpha) & -\sin(\alpha) \\ \sin(\alpha) & \cos(\alpha) \end{pmatrix}$$

α_s Speed factor, describing the ration of wind driven surface currents velocities u_{surf} and wind speed u_w, $\alpha_s = \frac{u_{surf}}{u_w}$.

δ_e Ekman-depth.

Ω Rotational frequency of the earth, $\Omega = 7.3 \times 10^{-5} \text{s}^{-1}$.

ω (Wave) angular frequency.

ϕ Latitude.

Φ Velocity potential.
$\quad \nabla \Phi = \vec{v}$

π Archimedes' constant, $\pi \approx 3.14149$.

ψ Wave phase.
$\quad \psi = (\omega t - \vec{k}\vec{x})$

ρ Density.

ς Terrain-following vertical sigma-coordinate.

$\vec{\tau}$ Horizontal wind stress vector, $\vec{\tau} = (\tau_x, \tau_y)$.

$D_{\xi\mu\varsigma}$ Substantielle Ableitung in krummlinigen Sigma"=Koordinaten.
$\quad D_{\xi\mu\varsigma}\Phi := \partial_t \left(\frac{H_z \Phi}{mn}\right) + \vec{v} \cdot \nabla_{\xi\eta\varsigma}\Phi$, für eine skalare oder vektorielle Größe Φ.

∇_x Horizontaler Gradient:
$$\nabla_x := (\partial_x, \partial_y)^T$$

$\nabla_{\xi\mu\varsigma}$ Nabla-Operator in krummlinigen Sigma"=Koordinaten.
$$\nabla_{\xi\mu\varsigma} := \left(\frac{H_z}{n}\partial_\xi + \frac{H_z}{m}\partial_\eta + \frac{H_z}{mn}\partial_\varsigma \right), \text{ hierbei ist } H_z = \partial_\varsigma z.$$

ζ Sea surface elevation (SSE).

$\vec{\xi}$ Relative Vorticity.
$$\vec{\xi} = \nabla \times \vec{v}$$

$\angle \left(\vec{a}, \vec{b} \right)$ Angle between vectors $\vec{a}$ and $\vec{b}$.

∂_t Partial derivative for t.
$$\partial_t a := \frac{\partial a}{\partial t}, \text{ defined for arbitrary } a(t, ...) \in \mathbb{R} \text{ and } t \in \mathbb{R}.$$

$\overline{(...)}$ Phase average.
$$\overline{(...)} := \frac{1}{2\pi} \int_0^{2\pi} ... \, d\psi, \text{ i.e. averaging over wave phase } \psi. \text{ Used e.g. in}$$
equation (24).

$\langle ... \rangle$ Phase average for long waves.
$$\langle ... \rangle := \frac{1}{2\pi} \int_0^{2\pi} ... \, d\psi^{lw}, \text{ Average over phse of long waves } \psi^{lw}, \text{ used in}$$
equation (28). Details are given in Hahner [2016].

1. Introduction

This work is written in LaTeX using the font size, line spacing and page margins as prescribed by the University of Oldenburg. Graphs and pictures have been made using MATLAB and LIBREOFFICE DRAW. MATLAB was used for data evaluation and presentation. References are cited and managed using the BibTex package *natbib* and the style *plainnat*. Most Figures shown in this thesis are plotted using *Matlab* and the *M_Map* package (version 1.4) [Pawlowicz, 2020]. Coastlines were plotted using the *Global Self-consistent, Hierarchical, High-resolution Geography Database (GSHHG)* [Wessel and Smith, 1996] (version 2.3.7, provided by the *National Oceanic and Atmospheric Administration, NOAA*) or derived from landmasks of the hydrodynamic models.

1.1. Plastic Pollution in the Ocean

Plastic pollution in the oceans is a serious problem gaining growing attention during the last ten or twenty years. Today it is a common threat for sea life which might mistakenly eat it (e.g van Franeker [1985]) or become entangled in it and is negatively impacting tourism due to accumulation of debris at beach sides. It is even harming humans as toxins, attached to microplastics, might be indirectly ingested within the food chain [Thompson et al., 2009, Goldstein and Goodwin, 2013]. Additionally, plastics debris can even serve as floats, transporting microorganisms and hence cause damage by invasive species [Viršek et al., 2017]. Although numerous publications are dealing with of micro- and macroplastics in the oceanic environment, given numbers of total mass in the oceans vary due to different approaches on in situ measurements and countings[1]. Additionally, most estimates are based on sparse publicly available datasets. The following section focuses on on a limited amount of papers due to the huge amount of publications in recent years.

Plastics account for about 10% of total debris mass in 58% of countries with available data on waste management [Kaza et al., 2018]. Jambeck et al. [2015] estimate a total mass of 275×10^6 t plastic debris, produced

---

[1]There is currently no consistency in the literature about quantifying amounts of sampled plastics, as usage of absolute mass and item numbers are changing depending on different authors. Even particle density is defined differently as some are using *mass per volume*, *mass per area* or *number of items per transect length*, [e.g. Gutow et al., 2018, Jambeck et al., 2015, Benton, 1995, Carson et al., 2013].

1. Introduction

in 192 coastal states in 2010, of which about $(4.8...12.7) \times 10^6$t end up in the ocean by winds, tides, rivers and tourism. This "landborn plastics" might account for about 80% of the total ocean plastics input per year (i.e. shipping and offshore dumping are accounting for $\approx 20\%$ of yearly plastics input). Germany is estimated to account for $(0.01...0.25) \times 10^6$t of plastic debris ending up in the marine environment [see Fig. 1 in Jambeck et al., 2015]. Projection of these numbers lead to $(100...250) \times 10^6$t of global ocean plastics until 2025[2].

Once entering the sea, plastic debris is advected by surface currents, winds and waves[3], creating numerous possible paths, as physical properties alter due to changing buoyancy[4] and size of objects[5]. Also, "plastics" just serves as proxy for numerous kinds of chemical compounds with different properties in the marine environment. "The Great Pacific Garbage Patch" has now become a buzzword in public media, describing the fate of marine plastics.

Based on 41 surveys of net samplings[6] over the period of 2001 to 2010, Law et al. [2014] estimate increasing amounts of marine debris in the North Pacific Gyre by two orders since the 1970s and 80s when compared to previous datasets. Although publications, for e.g. the Atlantic gyre, do not show such significant increase during the last decades, accumulation of debris in oceanic gyre systems is well known and stated throughout the scientific literature[7]. Even though large scale distribution is governed by a combination of Ekman- and geostrophic currents, hence accumulation in all oceanic gyres might occur [Maximenko et al., 2012], nearshore measurements and beach cleanup data indicate fronts, tides, waves and wind drag as driving factors for small scale distribution and beaching of debris. Composition and shape of beaches is influencing distribution patterns, as sandy beaches are classified as possible sinks by burying particles, whereas rocky shores might

---

[2]Figure 2 of Jambeck et al. [2015] shows the cumulated sum from 2010 to 2025, assuming a constant world wide production of the 2010's value in three scenarios (15%, 25% and 45% of global plastics entering the oceans).

[3]Transport by waves occurs due to Stokes Drift and transfer of wave energy, of which the latter is negligible in most applications, see subsection 2.3.

[4]E.g. due to biofouling [Benton, 1995] or water intrusion, e.g. water entering inside a plastic bottle.

[5]Due to UV-radiation, physical work by waves and chemical degradation

[6]A common approach is surface sampling with plancton nets on transects of certain length and counting litter items by eye. Multiplying diameter of the net and transect length leads to estimates of debris in units of $\frac{items}{km^2}$.

[7]Law et al. [2014] explain differences for each gyre system by different data binning and temporal scales of measurements. Although clusters of debris are stable over long periods, exact locations of cluster centers vary on short time scales.

2

act as "mills" for larger particles [Eriksson and Burton, 2003], thus serving as secondary sources of microplastics. Thiel et al. [2013][8] conclude that large amounts of beached litter are originating from nearby local sources like tourism, industries and rivers. Experiments by Carson et al. [2013] support this finding: Pathways of surface drifting litter were investigated via wooden plates with unique ID, deployed at predefined locations of Hawaii, and were then reported by foremost local residents after beaching.

Whereas various publications deal with distribution and composition of microplastics in the Southern North Sea [e.g. Gerdts et al., 2017, Dibke et al., 2021] measurements of macroplastics in this region are sparse. Gutow et al. [2018] combined in situ measurements of net trawls of the top and bottom water layer with a numerical model for Lagrangian floats in the northeastern part of the North Sea. Therein floating litter was found in almost 95% of surface trawls, of which plastics accounted for 65%[9]. Seafloor litter was found on 60% of sampled transects and was dominated by plastic fibers from fisheries[10]. While surface and bottom samples were dominated by plastics, overall compositions differed significantly, leading to the assumption of different transport mechanisms at the surface and bottom of the water column. Simulations with a hydrodynamic model in combination with Lagrangian trajectories showed strong correlation of beaching with a chosen wind drag value[11]. Residence times of particles within the modeling domain varied between 16 and 23 days. A large amount of particles was estimated to deposit at the Danish coast or leave at the northern border of the domain. Backward simulations indicated nearshore clusters to originate from nearby sources at the German and Dutch coast as well from the main rivers Ems, Weser and Elbe. This corroborates findings for other regions [Carson et al., 2013, Thiel et al., 2013] mentioned above. In summary, Gutow et al. [2018] conclude higher average litter densities at bottom layers and traces of fishing gear as dominant items. Differences in litter composition at the top and bottom

---

[8]Thiel et al. [2013] compared composition of sampled litter at shores and nearshore waterlines from the Coastal System of Coquimbo (Chile): Data from different sampling sites showed almost identical composition whereas indicators for foreign debris, like e.g. labels, were mostly absent.

[9]Gutow et al. [2018] use $\frac{items}{km^2}$ to quantify the amount and composition of marine debris.

[10]Gutow et al. [2018] mention dolly ropes as abundant litter items. These plastic fibers are used as scoring protectors for bottom nets.

[11]Gutow et al. [2018] used a numerical hydrodynamic model with about $9\,km \times 9\,km$ spatial resolution and Lagrangian simulations with a 2nd order Runge-Kutha integration scheme. Beaching occured as numerical artifact due to normal wind components on coastlines.

layer hint to differing physical distribution mechanisms in both layers and negligible vertical transport of plastics.

Backward simulations of Lagrangian ensembles over a 90 days period, performed by Neumann et al. [2014], showed litter following the well known mean anticlockwise residual circulation of the North Sea, if wind drag on particles is disregarded. However, regarding wind drag fastened particle advection and lead to a dispersed distribution in these simulations, mitigating clusters of floating debris in offshore regions. Wind drag also seemed to hinder influences of bathymetrical features on currents and hence can be determined as important driver for litter distribution in the North Sea.

1.2. The Macroplastics North Sea Research Project

As mentioned above, research regarding distribution and possible sources of macroplastics in the North Sea region is sparse. Therefore the interdisciplinary research project *Macroplastics North Sea* of the Institute of Chemistry and Biology of the Marine Environment (ICBM) and the Carl-von-Ossietzky University Oldenburg was funded by the government of Lower Saxony to investigate possible sources, pathways and accumulation areas of marine debris. Goal was the development of enhanced abatement strategies in cooperation with stackholders from local industries and administrations.

Focus was set to coastlines of Lower Saxony, the main North Sea rivers Elbe, Weser and Ems and shipping lanes within the German Bight. In total, 14 researches with backgrounds in geography, biology, physics and oceanography contributed to 5 Working Packages, each dealing with specialized research topics: *Nearshore hydrodynamic modeling (WP1), litter monitoring (WP2), basin-scale hydrodynamic modeling (WP3), information technology (drifter report) and public relations (WP4)* and *marine sensoring (WP5)*. Cooperating institutions and external researchers were associated and public communities were closely involved (Figure 1). Details about each working package and an overview of results are given by Schöneich-Argent et al. [2016], Schöneich-Argent et al. [2017] and Meyerjürgens et al. [2021].

1.2.1. Working Package 1: Nearshore Hydrodynamic Modeling

Main task of WP1 was setting up and running a high resolution numerical modeling system for the region of the German Bight to complement large scale data from WP3. Main goal was investigating the importance of wind,
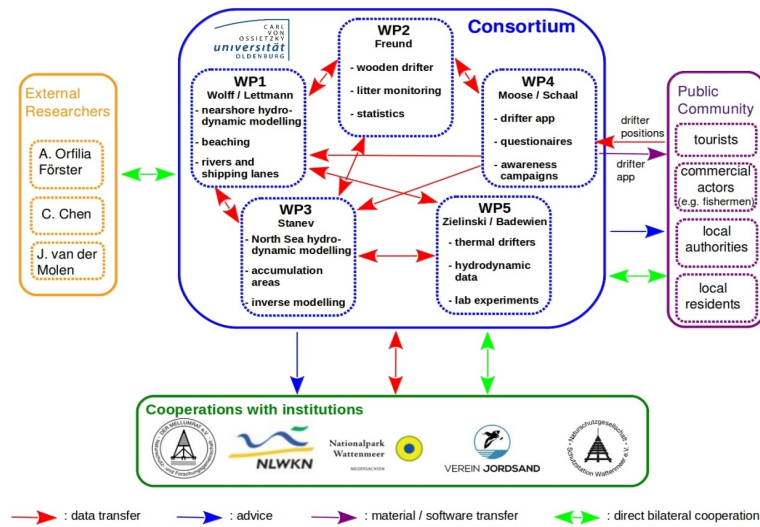
Figure 1: Synopsis of the Macroplastics North Sea research project: A consortium of 14 researchers from the ICBM and University of Oldenburg in association with external researchers, cooperating institutions and public communities. (Taken from [Macroplastics North Sea])

waves and bathymetrical features on particle advection and small scale distribution of surface floating particles.

This thesis serves as assessment report and operational guideline for this modeling framework and shows data validation as well as first results on the importance of waves and winds on particle advection in the region of barrier islands.

Fundamentals of describing particle advection in numerical models are given in section 2, where important physical processes and basics of Lagrangian trajectories are described. Section 3 gives a short introduction to hydrodynamics of the North Sea with main focus on the German Bight and the Eastfrisian Islands. A description of meteorological and hydrodynamic datasets used for forcing the hydrodynamic model is also shown. The modeling framework is described and validated in sections 4 and 5. Section 6 reviews the influence of wind and waves in the case of a basic numerical parametrization of particle beaching. This academical test is extended by an real world example based on in-situ GPS-drifter data in section 7. In section 8, a short description of additional work with cooperating working groups at the ICBM is given. Results of associated master theses and sug-

gestions for future research using the developed framework is given therein.

The thesis at hand is complemented by four master's theses, which were set as integral part of WP1: Heinrich [2018] estimated wind drag using modeled surface currents of the German Bight[12] and GPS-data of prototype drifters developed by WP5. Wüllner [2018] supported setting up and validating the modeling framework by contributing a small scale model for hydrodynamics and waves, operated in offline-nesting applications[13]. Different numerical approaches for describing Stokes Drift were also compared by Wüllner [2018]. Schönung [2018] estimated dispersion of macroplastics within the Weser river using Lagrangian particle tracking and data from the unstructured hydrodynamic model FVCOM in combination with drifter data from WP2. A detailed overview of wave effects, Stokes Drift and current-wave interactions, briefly described in section 2, is given in Hahner [2016].

---

[12]Heinrich [2018] used data from a prototype-setup of the GB-Model, described in section 4.

[13]See section 4.

2. Theory

Particle motion at the sea surface is caused by external forces $\vec{F}_i^{ext}$ acting on the particle's body. Following Newtons second law[14], one obtains [Breivik and Allen, 2008]

$$(m_p + m_o)\frac{d\vec{v}_p}{dt} = \sum_i \vec{F}_i^{ext} \tag{1}$$

$d\vec{v}_p/dt$ is the particle's acceleration, m_p its mass and m_o are the accelerated water masses along the particle's hull. As small objects tend to accelerate rapidly[15], an infinite acceleration and thus constant velocity can be assumed for finite time steps dt, leading to $\frac{d\vec{v}_p}{dt} = 0$. The force balance equation (1) can then be simplified as[16]

$$\sum_i \vec{F}_i^{ext} = 0 \tag{2}$$

External forces acting on surface drifting particles are caused by ocean currents[17], waves acting on the particle's body[18] and wind stress[19]. These effects are described in the following subsections.

2.1. Particle Motion due to Ambient Currents

The water drag $\vec{F}_o$ on a moving particle of velocity $\vec{v}_p$ in an ambient current $\vec{u}_l$[20] is determined by its effective area A_o, i.e. the water exposed cross-sectional area, water density ρ_o and the velocity of the moving particle rel-

---

[14]Netwon's second law in it's original form is formulated via the momentum p as $F = \frac{dp}{dt}$, which in case of a constant mass m with velocity v is simplified to $F = m \cdot a$, where $a = \frac{dv}{dt}$ is acceleration.

[15]Hodgins and Hodgins [1995, 1998] observed life rafts to reach a terminal velocity after approximately $20\,\text{s}$ under the influence of strong winds in the range of $20\,\text{m}\,\text{s}^{-1}$.

[16]This assumption follows the common approach of search and rescue and oil spill models and is valid in most cases, as hydrodynamic and atmospheric data is usually in the range of several minutes to hours, see e.g. [Breivik and Allen, 2008] and [Shchekinova et al., 2016].

[17]And also subgrid scale diffusion of momentum, which is not resolved by ocean models or measured data as described in subsection 2.4.

[18]*Active* Forces due to waves with wavelengths in the range of the object's size and *passive* forces, which influence the ocean currents and thus are influencing the particle's motion. These passive forces are described via *Vortex Forces* or *Radiation Stresses*. These as well as Stokes Drift are termed *passive* here, as they are represented by the Lagrangian velocity of the ocean currents, although they are indeed affecting the particle's motion. See subsection 2.3.

[19]Again acting *actively* on the wind exposed surface area of the particles and *passively* by accelerating water masses due to the surface wind stress.

[20]$\vec{u}_l$ is the Lagrangian current velocity.

ative to ambient currents $\vec{u}_l - \vec{v}_p$ [Röhrs et al., 2012]

$$\vec{F}_o = \underbrace{\frac{1}{2}\rho_o \left|\vec{u}_l - \vec{v}_p\right| \left(\vec{u}_l - \vec{v}_p\right)}_{\text{kin. energy}} A_o C_o \tag{3}$$

The drag coefficient C_o is determined by the particle's shape. Kinetic energy per volume is transferred to the particle by moving water masses and is highlighted in (3). Neglecting wave effects on currents, one can simplify $\vec{u}_l \approx \vec{u}_e$ [Röhrs et al., 2012][21]. Substitution of (3) into (2) as the sole external force then leads to[22]

$$0 = \frac{1}{2}\rho_o A_o C_o \left|\vec{u}_l - \vec{v}_p\right|\left(\vec{u}_l - \vec{v}_p\right) \quad |\text{def. } \vec{e}_\xi, |\vec{e}_\xi| = 1$$

$$\vec{e}_\xi \parallel \left(\vec{u}_l - \vec{v}_p\right)$$

$$0 = \frac{1}{2}\rho_o A_o C_o \left|\vec{u}_l - \vec{v}_p\right|^2 \vec{e}_\xi \qquad |\sqrt{}$$

$$0 = \sqrt{\frac{1}{2}\rho_o A_o C_o} \left|\vec{u}_l - \vec{v}_p\right| \vec{e}_\xi \qquad |\text{resubst. of } \vec{e}_\xi$$

$$0 = \sqrt{\frac{1}{2}\rho_o A_o C_o} \left(\vec{u}_l - \vec{v}_p\right) \tag{4}$$

Thus particles with negligible inertia travel with the ambient current's speed if no additional forces, e.g. due to wind and waves, are considered.

2.2. Wind Influence on Drifting Objects

As stated above, the wind's influence on drifting particles can be described via *passive* effects, which are part of the ocean currents, and *active* effects, i.e. direct drag on particles. So defined passive effects are important for understanding and interpreting trajectories of drifting objects and will be discussed to some extent. The section is then followed by an description of *Leeway Drift*, i.e. the active effect of wind drag on objects.

2.2.1. Wind Driven Currents

Horizontal winds blowing along a water surface exert accelerating forces due to the wind stress $\vec{\tau} = (\tau_x, \tau_y)$ and thus cause horizontal currents, which

---

[21]Lagrangian velocity is the sum of Eulerian currents $\vec{u}_e$ and the waves' Stokes Drift $\vec{u}_s$, see subsection 2.3 and the cited literature therein.

[22]A directional vector $\vec{e}_\xi \parallel (\vec{u}_l - \vec{v}_p)$ is defined in the first step, thus leading to the substitution $(\vec{u}_l - \vec{v}_p) = |\vec{u}_l - \vec{v}_p| \vec{e}_\xi$ in the second line. Due to this "trick", usage of the square root is allowed to obtain (4).

are deflected from the downwind direction due to the Coriolis Force. This phenomenon was first described mathematically by Ekman [1905][23] for an idealized ocean of infinite depth with homogeneous water masses of constant density and eddy viscosity in the absence of horizontal boundaries. Following these assumptions, the horizontal momentum equations are [Cushman-Roisin and Beckers, 2011]

$$
\begin{aligned}
-f(v - \bar{v}) &= A_z \frac{\partial^2 u}{\partial z^2} \\
f(u - \bar{u}) &= A_z \frac{\partial^2 v}{\partial z^2}
\end{aligned}
\tag{5}
$$

Here $(\bar{u}, \bar{v})$ is an ambient geostrophic current, A_z is the vertical eddy viscosity and $f = 2\Omega \sin \phi$ is the latitude depending *Coriolis Parameter*[24]. Assuming wind stress as driving factor at the surface, i.e. at $z = 0$, and a solely geostrophic current $(\bar{u}, \bar{v})$ in the interior of the fluid, i.e. $z \to -\infty$, defines the boundary conditions [Cushman-Roisin and Beckers, 2011]

$$
\begin{aligned}
\tau_x &= \rho_0 A_z \frac{\partial u}{\partial z} & \text{at } z = 0 \\
\tau_y &= \rho_0 A_z \frac{\partial v}{\partial z} & \text{at } z = 0 \\
u &= \bar{u} & \text{for } z \to -\infty \\
v &= \bar{v} & \text{for } z \to -\infty
\end{aligned}
\tag{6}
$$

Solving equation (5) using (6) yields

$$
\begin{aligned}
u &= \bar{u} + \frac{\sqrt{2}}{\rho_0 f \delta_E} \exp(z/\delta_E) \left(\tau_x \cos\left(\frac{z}{\delta_E} - \frac{\pi}{4} \right) - \tau_y \sin\left(\frac{z}{\delta_E} - \frac{\pi}{4} \right) \right) \\
v &= \bar{v} + \frac{\sqrt{2}}{\rho_0 f \delta_E} \exp(z/\delta_E) \left(\tau_x \sin\left(\frac{z}{\delta_E} - \frac{\pi}{4} \right) + \tau_y \cos\left(\frac{z}{\delta_E} - \frac{\pi}{4} \right) \right)
\end{aligned}
\tag{7}
$$

Wind driven currents are described by the ageostrophic parts in the second term of equation (7), adopting a spiral pattern with decreasing absolute values in incremental depths z. Starting with a clockwise deflection angle $\angle(\vec{\tau}, \vec{u}) = 45°$, these currents adopt an antiparallel direction to wind stress at the Ekman-depth $\delta_E = \sqrt{2A_z)/f}$ with decreased absolute values by a factor e^π. Note the dependence of f in the second term of (7), thus its change

---

[23]Vagn Walfrid Ekman, 1874-1954

[24]$f = 2\Omega \sin \phi$, with latitude ϕ and earth's rotational frequency $\Omega = 7.3 \times 10^{-5} s^{-1}$ [Pedlosky, 1987].

2. Theory

with latitude ϕ. The speed factor[25] $\alpha_s = u_{surf}/u_w$, i.e. the ratio of wind driven surface currents u_{surf}[26] to wind speed u_w[27], can be approximated by [Ekman, 1905]:

$$\alpha_s = 0.0127 \frac{1}{\sqrt{\phi}} \tag{8}$$

However, homogeneous mixed waters are seldom found in real oceans and eddy viscosity A_z depends on the actual wind speed u_w leading to varying deflection angles and speed factors. Huang [1979] found e.g. deflection angles in the range $\angle(\vec{\tau}, \vec{u}) = (1°...47°)$ and speed factors in the range of $\alpha_s = (0.01...0.07)$ for various seas and lakes. Depth of the Ekman-layer also becomes shallower in the case of stratified fluids, leading to an Ekman-depth of [Cushman-Roisin and Beckers, 2011]

$$\delta_E \leq 0.4 \frac{u*}{f} \tag{9}$$

where equality holds for neutral stratification. Furthermore, as density, eddy viscosity and stratification change with seasons, the deflection angle and speed factor, as well as the depth of the Ekman-layer, change. Yoshikawa and Masuda [2009] e.g. found from HF-radar measurements in the Tsushima Straight $\alpha_s \approx (1.0...1.3) \times 10^{-2}$ and $\angle(\vec{\tau}, \vec{u}) \approx (18°...27°)$ during winter months and $\alpha_s \approx (1.3...1.9) \times 10^{-2}$ and $\angle(\vec{\tau}, \vec{u}) \approx (49°...67°)$ respectively in summer. Resolving the upper Ekman-layer in numerical models is important for incorporating realistic deflection of wind driven surface currents.

The horizontal motion of a water parcel for ceasing winds in the absence of additional forces on the rotating earth is solely dictated by the Coriolis force and ambient geostrophic currents $(\bar{u}, \bar{v})$: [e.g. Cushman-Roisin and Beckers, 2011]

$$\begin{aligned} -f(v - \bar{v}) &= \frac{\partial u}{\partial t} \\ f(u - \bar{u}) &= \frac{\partial v}{\partial t} \end{aligned} \tag{10}$$

---

[25] An analogue is the *friction velocity* $u* = \sqrt{(\tau/\rho_o)}$, used in most textbooks, e.g. Cushman-Roisin and Beckers [2011].

[26] u_{surf} is the absolute value of a vector defined by the second terms in equation (7).

[27] u_w is usually taken at $10\,\text{m}$ height.

Solving equation (10) yields

$$
\begin{aligned}
u &= V \sin\left(ft + \varphi\right) + \bar{u} \\
v &= V \cos\left(ft + \varphi\right) + \bar{v}
\end{aligned}
\tag{11}
$$

where the constant of integration $V = \sqrt{(u - \bar{u})^2 + (v - \bar{v})^2}$ is the absolute relative velocity of a water parcel and the geostrophic component and φ is a phase term. Integrating (11) yields the trajectory:

$$
\begin{aligned}
x &= x_0 - \frac{V}{f} \cos\left(ft + \varphi\right) + \bar{u}t \\
y &= y_0 + \frac{V}{f} \sin\left(ft + \varphi\right) + \bar{v}t
\end{aligned}
\tag{12}
$$

Equation (12) describes circular trajectories of radius V and midpoint $(x_0 + \bar{u}t, y_0 + \bar{v}t)$, moving with the background currents $(\bar{u}, \bar{v})$. Hence forming helical trajectories called *inertia currents*, see e.g. Figure 9 on page 29. Radial velocity is $2\pi f$, i.e. the *inertial period* $T_{inert} = 2\pi/f$ is determined by the local Coriolis parameter and thus depends on latitude.

2.2.2. Leeway Drift

Drifting objects are accelerated by atmospheric winds due to wind drag acting on air exposed cross-sectional areas. This aerodynamic force can be decomposed into a drag and lift component, with the latter being balanced by the hydrodynamic lift on the underwater part of the drifting object, if a steady motion is assumed. Figure 2 shows a simplified illustration of drag and lift components after Richardson [1997][28]. Breivik and Allen [2008] define resulting motions due to wind drag as *Leeway* $\vec{L}$, which usually do not coincide with the local wind directions due to the aforementioned lift component[29]. Deviations of the Leeway Drift from local wind velocities $\vec{u}_w$ are dependent on the object's size and the angle at which a relative wind is acting on the object[30]. To account for this deflection, the Leeway can be

---

[28]Richardson [1997] uses the resulting wind velocity, which differs from the local wind velocity u_w as the particle's motion is regarded therein. Because of passively drifting objects are considered throughout this thesis and the object's velocity v_p can be assumed much smaller than wind velocities u_w, i.e. $v_p << u_w$, resulting wind velocities can be replaced by local winds here.

[29]Richardson [1997] describes the balance and resulting Leeway model in detail for a steaming ship.

[30]Note this deflection angle differs from the one defined in the Ekman theory of subsubsection 2.2.1, as it is caused by wind induced lift forces and not the Coriolis force.
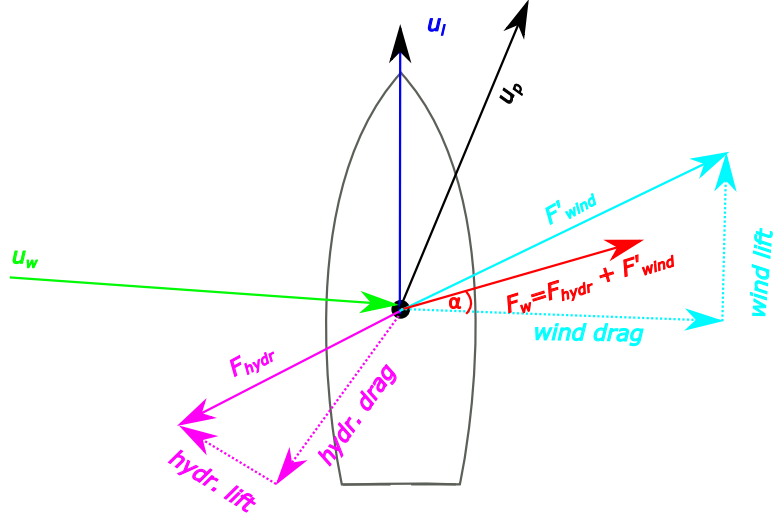
Figure 2: Illustration of the hydrodynamic (magenta) and wind (cyan) lift and drag components on a drifting object after Richardson [1997]. A force F'_{wind} (solid cyan arrow) is exerted by the local wind speed u_w (green arrow), which is the sum of *wind drag* ($\parallel u_w$) and *aerodynamic lift* ($\perp u_w$), indicated by dashed cyan arrows. Equally, a hydrodynamic force F_{hydr} (magenta) is exerted by water masses as sum of *hydrodynamic drag*, antiparallel to u_p, and *hydrodynamic lift* (dashed magenta arrows). In total, the resulting wind drag then is $F_w = F_{hydr} + F'_{wind}$ (red arrow and equation (16)). As a result, wind drag F_w is generally inclined to local winds u_w, defining the deflection angle α. Equation (18) yields the local particle velocity u_p as sum of Lagrangian currents u_l and resulting wind drag velocity.

decomposed into a *downwind* and *crosswind* Leeway component $\vec{L}_D \parallel \vec{u}_w$ and $\vec{L}_C \perp \vec{u}_w$ [Breivik and Allen, 2008]

$$\vec{L} = \vec{L}_C + \vec{L}_D \tag{13}$$

Introducing the rotation matrix

$$\boldsymbol{\alpha} = \left(\begin{array}{cc} \cos(\alpha) & -\sin(\alpha) \\ \sin(\alpha) & \cos(\alpha) \end{array} \right) \tag{14}$$

and deflection angle $\alpha = \angle(\vec{u}_w, \vec{L})$, i.e. the angle between local winds and Leeway direction, equation (13) can be written as

$$\vec{L} = C_w \, \boldsymbol{\alpha} \cdot \vec{u}_w \tag{15}$$

C_w is the wind drag coefficient. Analogues to the water drag equation (3), wind drag on a small object then can be described as [Shchekinova et al., 2016][31]

$$\vec{F}_w = \frac{1}{2} \rho_w A_w C_w \left| \boldsymbol{\alpha} \cdot \vec{u}_w \right| (\boldsymbol{\alpha} \cdot \vec{u}_w) \tag{16}$$

where A_w is the wind exposed cross section of the object and ρ_w is the density of air. Using wind drag (16) and water drag (3) in the force balance equation (2) yields

$$0 = \sqrt{\frac{1}{2} \rho_o A_o C_o} \, (\vec{u}_l - \vec{v}_p) + \sqrt{\frac{1}{2} \rho_w A_w C_w} \, (\boldsymbol{\alpha} \cdot \vec{u}_w) \tag{17}$$

Solving equation (17) for the particle velocity $\vec{v}_p$ yields

$$\vec{v}_p = \vec{u}_l + \sqrt{\frac{\frac{1}{2} \rho_w A_w C_w}{\frac{1}{2} \rho_o A_o C_o}} \, (\boldsymbol{\alpha} \cdot \vec{u}_w) \tag{18}$$

C_w and $\boldsymbol{\alpha}$, hence $\vec{L}_D$ and $\vec{L}_C$, depend on the object's size and initial orientation to the wind $\vec{u}_w$ and have to be evaluated experimentally. Anderson et al. [1998] give an overview of drag coefficients for different shapes and Allen and Plourde [1999] summarize Leeway coefficients for different objects regarding Search and Rescue applications. Usage of $\vec{L}_C$ and $\vec{L}_D$ based on linear regression models is recommended by Breivik and Allen [2008], resulting in

---

[31]Shchekinova et al. [2016] use 10m-wind velocities without rotation in the wind drag equation, introducing cross- and down-wind components in later sections of their paper.

robust estimates which are applicable in a wide range of wind speeds. However, definition via a rotation matrix $\boldsymbol{\alpha}$ with constant deflection angle α for all wind speeds is used throughout this thesis, as such implementation into numerical models can easily be applied. Furthermore, main focus is set on objects[32] with persistent wind drag behavior throughout large ensembles[33].

2.3. Wave Effects

Waves tend to alter current fields due to wave-current interactions[34], arise in Lagrangian currents $\vec{u}_l$ in the form of *Stokes Drift* $\vec{u}_s$ and are "actively" exerting forces to solid and stationary objects [Mei et al., 2005]. In this section, a short description of wave effects, relevant for the movement of surface drifting objects, is given. A detailed description of surface waves physics is given by e.g. Malcherek [2010] and Holthuijsen [2007], a comprehensive overview of wave-current interactions and their implementation into numerical models can be found in Hahner [2016][35].

2.3.1. Stokes Drift

According to linear wave theory[36], waves can be described via the velocity potential Φ [Fredsoe and Deigaard, 1992]:

$$\Phi = \underbrace{-A\frac{g}{\omega}\frac{\cosh\left(k(h+z)\right)}{\cosh(kh)}}_{=:\hat{\Phi}}\sin(\underbrace{\omega t - kx}_{\psi}) \tag{19}$$

Here A, ω and k are wave amplitude, frequency and wave number, g and h are the local gravitational acceleration and water depth. In this framework, water parcels move on closed ellipses underneath surface waves[37], which can

---

[32]Small objects and symmetrical GPS-Drifters.

[33]Although using alternating angles $\pm\alpha$ with 50% probability seems necessary, as initial orientations of objects to wind vectors is unknown.

[34]Described via *Radiation Stresses* [Longuet-Higgins and Stewart, 1964] or *Vortex Forces* [McWilliams et al., 2004], which are outlined in subsubsection 2.3.2.

[35]The following descriptions are based on Hahner [2016].

[36]First described by *George Biddell Airy* (1801-1892) in 1845 [e.g. Svendsen, 2006]: Assuming wave amplitudes A to be much smaller than wave lengths L, i.e. $A << L$.

[37]And so do particles in the water column.

be seen by taking the gradient $\vec{u} = \nabla\Phi$ of the velocity potential (19):

$$
\begin{aligned}
u &= \overbrace{A\omega\frac{\cosh\left(k(h+z)\right)}{\sinh(kh)}}^{\hat{U}}\cos(\omega t - kx)\\
v &= 0\\
w &= \underbrace{-A\omega\frac{\sinh\left(k(h+z)\right)}{\sinh(kh)}\sin(\omega t - kx)}_{\hat{W}}
\end{aligned}
\tag{20}
$$

Integration of equation (20) in the time domain yields the particle paths on these ellipses [Holthuijsen, 2007, p. 121]:

$$
\begin{aligned}
x' &= \overbrace{A\frac{\cosh\left(k(h+z_0)\right)}{\sinh(kh)}}^{H_x}\sin(\omega t - kx_0)\\
z' &= \underbrace{-A\frac{\sinh\left(k(h+z_0)\right)}{\sinh(kh)}}_{H_z}\cos(\omega t - kx_0)
\end{aligned}
\tag{21}
$$

$\hat{U}$, $\hat{W}$, H_x and H_z are the semi-axis of the orbital ellipses. Note equations (20) and (21) are formulated in local Cartesian coordinates (x', z') with origin (x_0, z_0) in the ellipse centers, see Figure 3. Thus, equation (20) is formulated in a Eulerian framework and wave period averages of (21) become nil, i.e. no net movement is applied by the waves. To account for net transport caused by waves, a vanishing mean velocity of equation (20) in the water column, except the interval $[-A, \zeta]$, with ζ denoting the free surface elevation, is assumed. Spatiotemporal averaging[38] of the velocity $u(z = 0)$ of equation (20) leads to [Fredsoe and Deigaard, 1992]:

$$
u_{Drift} = \frac{1}{T}\int_0^T\int_{-A}^{\zeta} u(z=0)\, dz\, dt = \frac{A^2\omega}{\tanh(kh)}
\tag{22}
$$

This Drift velocity is restricted to the region $z \in [-A, \zeta]$ between the wave's crest ζ and trough $-A$ and is vanishing elsewhere.

Following an Lagrangian view, a vertical profile of the Drift velocity can be obtained by Taylor expansion with respect to $\vec{x}(t = 0) = \vec{x}_0 = (x_0, y_0)$

---

[38]Within the non-zero interval $[-A, \zeta]$ and over a wave period T.

2. Theory
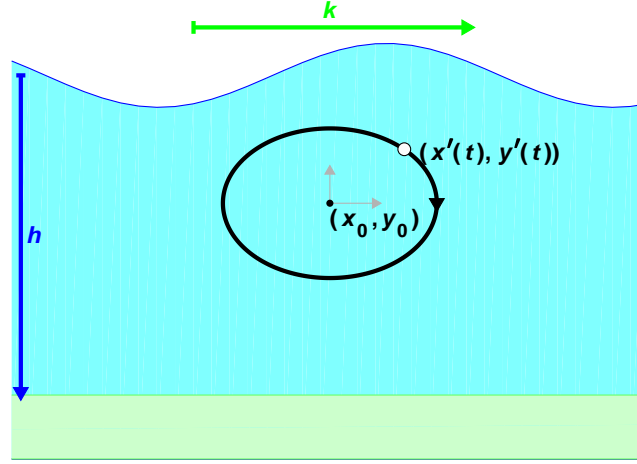
Figure 3: Depiction of the framework according to equation (21). Grey arrows indicate the local coordinate system (x', y'). Assuming a positive wave direction, particles move on closed ellipses.

[Phillips, 1977]:

$$\vec{v}_l(\vec{x}(t), t) = \vec{v}(\vec{x}_0) + \left(\int_0^t \vec{v}_l(\vec{x}, t') \, dt' \cdot \nabla \right) \vec{v}(\vec{x}_0) + \mathcal{O}(\nabla^2 \vec{v})$$

$$\vec{v}_l \approx \vec{v}_e + \left(\int_0^t \vec{v}_l \, dt' \cdot \nabla \right) \vec{v}_e \tag{23}$$

Subscripts l and e denote Lagrangian and Eulerian velocities respectively and the vector gradient $(\vec{v} \cdot \nabla) \cdot \vec{v}$ is used in equation (23)[39]. The Eulerian velocity $\vec{v}(\vec{x}_0) = \vec{v}_e$ is equivalent to the orbital velocity of equation (20). Following Airy's theory, Lagrangian velocities in the integral part are approximated by Eulerian velocities, $\vec{v}_l \to \vec{v}_e$ [Bakhoday-Paskyabi, 2015], and phase averaging of equation (23) yields

$$\bar{u}_l = \frac{A^2 \omega k}{2} \frac{\cosh(2k(z+h))}{2 \sinh^2(kh)}$$

$$\bar{w}_l = 0 \tag{24}$$

Integrating equation (24) within the water column $z \in [h, 0]$ again yields the overall drift u_{drift} of equation (22).

---

[39]Definitions are given in the List of Symbols.

16

The phase average $\bar{u}_l$ is the Stokes Drift[40]

$$u_s = \overline{\left(\left(\int_0^t \vec{v}_l \, dt' \cdot \nabla\right)\vec{v}_e\right)_x} = \frac{A^2 \omega k}{2}\frac{\cosh(2k(z+h))}{2\sinh^2(kh)} \qquad (25)$$

describing lateral drift of water parcels due to surface waves. As u_s solely arises from the integral term in equation (23) it is inherent to Lagrangian velocities u_l and has to be regarded in equation (4) [Bakhoday-Paskyabi, 2015]:

$$\vec{u}_l = \vec{u}_e + \vec{u}_s \qquad (26)$$

Assuming a known wave spectrum $E(\vec{k})$[41], a vertical Stokes-Drift profile can also be calculated as [Kenyon, 1969]:

$$u_s = g \int_{-\infty}^{\infty} E(k)\frac{k}{\omega}\left(\frac{2k\cosh\left(2k\left(z+h\right)\right)}{\sinh(2kh)}\right) dk \qquad (27)$$

In contrast to equation (25), which is formulated for monochromatic waves with constant amplitude A and wave number k, computation of equation (27) accounts for all wave frequencies. Breivik et al. [2014] give an overview of calculated Stokes-Drift profiles via the monochromatic equation (25) and a deep-water approximation of equation (27), concluding that a monochromatic approach using an intermediate wave number[42] underestimates Stokes Drift in deeper water levels[43]. Neglecting the high-frequency-tail in Stokes Drift calculations also can lead to underestimated drift velocities at the surface layer[44]. Wüllner [2018] implemented an algorithm for Stokes Drift calculations based on equation (27) into the SWAN wave model as part of the macroplastics research project, details are given therein.

2.3.2. Wave Generated Currents

Wave generated orbital velocities, described by equation (25), yield a momentum of $\rho_w \vec{u}$. In combination with wave induced pressure gradients, this momentum leads to an effective force acting on the water column, hence currents are accelerated. Wave induced currents were first described in a

---

[40] *George Gabriel Stokes*, 1819-1903

[41] E.g. from a numerical model or reconstructed from measurements.

[42] Using e.g. significant wave height and peak period from a numerical wave model.

[43] Long waves penetrate deeper into the water column.

[44] Even though short waves' influence is restricted to the surface, they contribute significantly in upper water levels. Resolving this influence depends on the cut-off frequency of measurements or wave model data.

2. Theory

two-dimensional approach via *Radiation Stresses* by Longuet-Higgins and Stewart [1964], which were later expanded for three-dimensional applications by Mellor [2003] and implemented into numerical models. Mathematically, the Radiation Stresses act as additional term in the hydrodynamic momentum balance equations. Because of numerical artifacts in Mellor's approach, an alternate description via Vortex Forces was proposed by McWilliams et al. [2004] and implemented into the coupled numerical model COAWST [Kumar et al., 2012], which was used throughout this thesis. These *Vortex Forces* arise by interactions of the waves' Stokes Drift and currents' vorticity and can be obtained by introducing different length scales for short, intermediate and long wavelengths into linear wave theory. Applying calculations of perturbation on each length scale independently preserve higher orders of wave effects in the resulting momentum equations. The Vortex Forces are: [McWilliams et al., 2004][45]

$$
\begin{aligned}
\vec{J}_* &= -\hat{z} \times \langle \vec{u}_s \rangle \left(\xi_z^c + f \right) - \langle w_s \rangle \, \partial_z \vec{u}^c \\
K_* &= -\langle \vec{u_s} \rangle \cdot \partial_z \vec{u} \\
\mathcal{K}_* &= \frac{1}{4} \left\langle \frac{\omega A^2}{k \sinh^2(\mathcal{H})} \int_{-\mu H}^{z} (\partial_z^2 \mathcal{U}) \sinh(2k(z - z')) \, dz' \right\rangle \\
&\quad + \frac{9}{64} \left\langle \frac{A^4 \omega^2 k^2 \cosh(4\mathcal{Z})}{\sinh^8(\mathcal{H})} \right\rangle + \frac{1}{2} \overline{((\vec{u}^{lw})^2)}
\end{aligned}
\tag{28}
$$

Here $\langle \cdot \rangle$ denotes phase-averages as described in the List of Symbols, $\hat{z}$ is the vertical unit-vector, $\vec{u}_s$ and w_s are the horizontal Stokes Drift (25) and the *vertical pseudo-velocity*[46], $\mathcal{Z}$ and $\mathcal{H}$ are a scaled vertical coordinate and water depth and $\mathcal{U} = \vec{k} \cdot (\vec{u}^{lw} + \vec{u}^c)$ describes correlations of the wave-vector $\vec{k}$ with velocities of long waves and currents, denoted by subscripts lw and c. ξ_z^c is the z-component of relative vorticity and $(\vec{J}_*, K_*)$ is the so called Vortex-Force vector, which describes vortex shear between Stokes Drift and ambient currents. The Bernoulli-Head $\mathcal{K}_*$ is a measure for wave energy density. A comprehensive overview of the derivations of the Radiation Stresses and Vortex Forces, their implementation into the numerical models SWAN and ROMS, as well as the (still ongoing) discussion in the scientific community[47] is given in Hahner [2016].

---

[45]For a short summary of the derivation and the meaning of all variables see Hahner [2016].

[46]See e.g. [Hahner, 2016, eq. 71]

[47]See e.g. [Mellor, 2003], [Mellor, 2005], [Mellor, 2008], [Mellor, 2011], [McWilliams et al., 2004], [Ardhuin et al., 2008], [Bennis and Ardhuin, 2011].

2.3.3. Wave Forces on Particles

Additional to Stokes Drift and wave induced currents, which are represented in the Lagrangian current velocity $\vec{u}_l$, waves exert a force on reflecting bodies [Anderson et al., 1998][48]

$$\vec{F}_{wav} = \frac{1}{2}\rho_o g C_{wav} L_p A^2 \hat{\boldsymbol{k}} \tag{29}$$

where L_p is the length scale of the body dimensions, A is the wave amplitude, $\hat{\boldsymbol{k}}$ is the unit wave vector and C_{wav} is a reflections coefficient for incident waves. The maximum value of $C_{wav,max} = 1$ corresponds to total reflection of the incoming wave energy. As in the case of wind drag, the value of C_{wav} has to be determined experimentally. Anderson et al. [1998] show this wave force can exceed wind drag. However, most Lagrangian drift models are neglecting wave forces, as only wavelengths in the order of L_p contribute significantly and L_p is small for a majority of drifting objects. Furthermore, formulation of equation (29) regards stationary objects and direct wave forces are much smaller for drifting objects [Breivik and Allen, 2008]. In most studies, parallel wind and wave directions are assumed and wave forces are taken into account by increasing the wind drag coefficient C_w. In the following, it is assumed that wave forces are sufficiently accounted for by adding Stokes Drift to Lagrangian velocities in equation (18)[49].

To illustrate the roles of water drag, wind drag and wave forces, assume a hypothetical drifter of cubic shape and size of $1\,\text{m} \times 1\,\text{m} \times 1\,\text{m}$, which is exposed to air and water by one half each, i.e. $A_o = A_w = 0.5\,\text{m}$ in equations (3) and (16). This "box" might be drifting in a homogeneous ocean of constant depth $h = 10\,\text{m}$. Water and air densities are assumed to be $\rho_o = 1024\,\text{kg/m}^3$ and $\rho_w = 1.11\,\text{kg/m}^3$ respectively. Calculating the wave force in equation (29) requires a known wave Amplitude A. As wave lengths $L \approx L_p$ of the object's size $L_p = 1\,\text{m}$ are most effective in transferring energy, the maximum Amplitude A_{max} affecting the box can be approximated by

---

[48]Here simplified equations of [Anderson et al., 1998] and [Breivik and Allen, 2008], which are based on detailed derivations of [Mei et al., 2005], are used.

[49]If it seems still necessary, forces due to reflected waves can be achieved by introducing a Stokes Drift drag coefficient $C_s \geq 1$. Using an *effective Stokes Drift* $u_{s,eff} = C_s \vec{u}_s$ might result in a better parametrization than increased wind drag, as directions of wind and waves differ significantly in many coastal areas, which will be shown in section 7.

the Miche criterion [Malcherek, 2010]

$$A_{max} = \frac{0.142}{2} L \tanh\left(\frac{2\pi h}{L}\right) = 7.1\,\text{cm} \tag{30}$$

Figure 4 shows water drag F_o (blue), wind drag F_w (red) and wave force F_{wav} (grey) as calculated by equations (3), (16) and (29) with respect to different Lagrangian velocities and wind speeds for this gedankenexperiment. Water drag for $u_l = 1\,\text{m s}^{-1}$ is exceeding wind drag for $u_w = 10\,\text{m s}^{-1}$ by one order. These forces are of the same order, when wind induced surface currents of about $1-2\%$ of local wind speeds is taken into account[50]. Wave forces are constant for all velocities in this example[51] and surpassed by water drag for $u_l \geq 4\,\text{cm s}^{-1}$. For $u_w = 10\,\text{m s}^{-1}$, wind drag and wave forces become equal. Note the dependence of wave amplitude on wind speeds in real world applications and short to intermediate waves, which are predominantly affecting small objects, are mostly wind generated. However, wave reflection C_{wav} might be much smaller than C_o and C_w, hence wave forces might be overestimated in this example. Wave forces are assumed to be sufficiently described as part of Stokes Drift and thus in Lagrangian velocities throughout this thesis.

2.4. Particle Diffusion

Turbulent processes in surface currents lead to diffusion of particle ensembles, even though individual starting locations and times $\vec{x}_0(t_0)$ coincide. Although subgrid scale processes are parametrized in hydrodynamic models and thus included in modeled data, computed currents are still somewhat deterministic. Hence two particles, starting at the same location and time, will move on identical trajectories in an Lagrangian model based on equation (4). This problem can be tackled by introducing a turbulent component $\vec{u}'$ into the Lagrangian currents $\vec{u}_l$:

$$\vec{u} = \vec{u}_l + \vec{u}' \tag{31}$$

Following Callies et al. [2011][52] the stochastic term $\vec{u}'$ can be calculated

---

[50]See subsubsection 2.2.1.

[51]Of course this is simplified, as surface waves are generated by gradients of air pressure and thus influenced by winds. Also strong currents might deflect wave directions and influence wavelength and frequency due to the Doppler shift.

[52]The following descriptions are based on the PELETS-2D program package from the
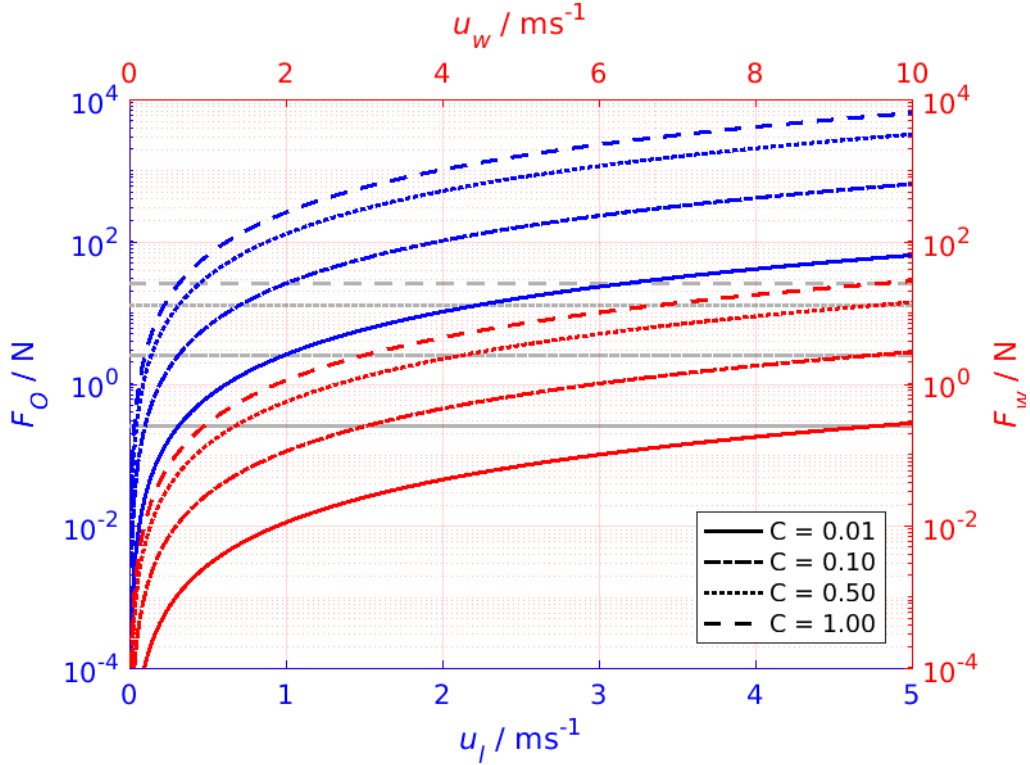
Figure 4: Comparison of forces F_o, exerted by Lagrangian Currents (blue), F_w, exerted by wind drag (red) and F_{wav} exerted by waves (grey) for a cubic shaped drifter with respect to Lagrangian velocity u_l, wind speed u_w and different drag coefficients C. Note the logarithmic scaling and differences in u_l- (bottom) and u_w-axes (top). Details are given in the text.

via a noise term $\vec{R}(t)$:

$$\vec{u}' = \sqrt{\frac{2D(l)}{dt}}\vec{R}(t) \tag{32}$$

This noise term $\vec{R}(t) = (R_x(t), R_y(t))$ can be implemented into numerical models as random number from a distribution with zero mean and variance one, which is derived in every time step dt for every component independently [Callies et al., 2011]. The horizontal eddy diffusion $D(l)$ is dependent on length scale l, i.e. the spatial resolution of used velocity data resp. the model's numerical grid. It can be calculated by [Schönfeld, 1995]

$$D(l) = D(l_0)\left(\frac{l}{l_0}\right)^{4/3} \tag{33}$$

Here $D(l_0)$ and l_0 are reference length scales and can be set to $l_0 = 1\,\mathrm{km}$

Helmholtz-Zenrum Geesthacht [Callies et al., 2011].

and $D(l_0) = 1\,\mathrm{m}^2/\mathrm{s}$ [Callies et al., 2011]. Figure 5 shows a plot of $D(l)$ for values of l representing numerical grids used throughout this thesis. Note that similar stochastic terms might be introduced into the wind velocity in equation (16).

Instead of using the Random Walk approach (32), particle diffusion can also be accounted for by using ensemble simulations with N particles[53] starting at slightly different locations and times around a reference point $\vec{x}_0(t_0)$[54].

Döös et al. [2013] give a short overview on how diffusion is affecting trajectories in their TRACMASS model, references for further reading can also be found therein.
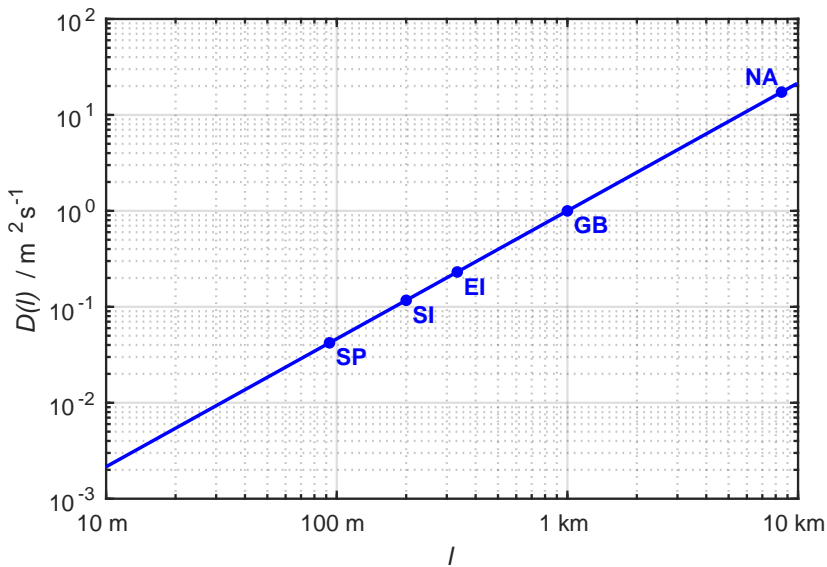
Figure 5: Horizontal eddy diffusion $D(l)$, defined by equation (33), for different length scales l. Values for each numerical grid of section 4 are marked by dots.

2.5. Time Integration

In subsection 2.1 and subsubsection 2.2.2 equations (4) and (18) were derived, which allow for computation of particle velocities $\vec{v}_p(t)$ in a given velocity field. Thus the particle's trajectory can be derived by integrating the equation of motion:

$$\frac{d\vec{x}_p(t)}{dt} = \vec{v}_p(x, y, z, t) \tag{34}$$

---

[53]Here $i = 1, 2, ..., N$ refers to the particle index of an whole ensemble of N particles.

[54]E.q. a spherical shaped starting region with radius R: $\{\vec{x}_{0,i} \text{ with } |\vec{x}_{0,i}| \leq R\}$ and individual starting times $t_{0,i} \in [t_{start}, t_{end}]$ for each particle.

where $\vec{v}_p(x, y, z, t)$ is the particle velocity at position (x, y, z) and time t and is given by e.g. equations (4) or (18).

Assuming a known velocity field, e.g. from a gridded numerical ocean model or wind data with discrete time coordinates, equation (34) must be solved numerically for each time step t^i in an iterative process. Three different numerical schemes are briefly discussed in the following subsections[55].

A short remark on the following notation: $\vec{x}_p(t)$ is used for the trajectory of particle p as a function of time t, whereas notations with sub- and superscripts indicate discrete values of particle positions and velocities at a fixed location and time. E.g. $\vec{x}_p^{t^i}$ indicating the discrete location of particle p at the actual time t^i. The index i denotes time step numbers of size t to $t + \Delta t$, and subscripts $\vec{x}_p^t$ indicate locations where the particle's property[56] is defined[57].

2.5.1. Euler Integration

The Euler[58] Scheme is the simplest approach for calculating particle trajectories $\vec{x}_p(t)$ based on velocities. Assuming a known position $\vec{x}_p^t$ and velocity $\vec{v}_{p,\vec{x}_p^t}^t$ at a given time t, the particle's location $\vec{x}_p^{t+\Delta t}$ at a future time step $t + \Delta t$ can be estimated by assuming a displacement with constant velocity $\vec{v}_{p,\vec{x}_p^t}^t$ during the time interval Δt, hence:

$$\vec{x}_p^{t+\Delta t} = \vec{x}_p^t + \Delta t \vec{v}_{p,\vec{x}_p^t}^t \tag{35}$$

Figure 6 illustrates the Euler Scheme for a particle in a stationary velocity field[59] and a fixed time step of Δt for each iteration: First, the velocity $\vec{v}_p^t$ is calculated[60], then the particle is displaced by the vector $\Delta t \cdot \vec{v}_p^t$ leading to the new location $\vec{x}_p^{t+\Delta t}$. The numerical error of this method is $\mathcal{O}(\Delta t^2)$, as can be shown by comparing equation (35) with the Taylor expansion of (34).

---

[55]See Joy [2007] for a comprehensive overview.

[56]In the following cases velocities: $\vec{v}_{p,\vec{x}_p^t}$ is the velocity of particle p at location $\vec{x}_p^t$.

[57]Note that time index of location where the properties value is defined might differ from the actual time index of the property, as explained in detail for the Runge-Kutta 4 integration scheme in subsubsection 2.5.3

[58]Leonhard Euler, 1707-1783.

[59]For convenience, a massless particle is assumed, which is passively moving with the ambient current, hence $\sqrt{\frac{1}{2}\rho_o A_o C_o} = 1$ in equation (4).

[60]E.g. by interpolating the velocity field to the particle position and then using equation (4) or (18)
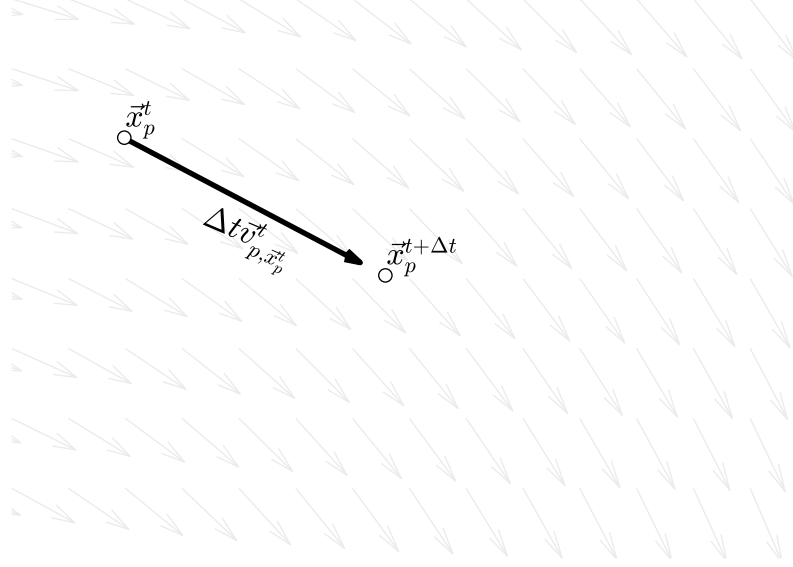
Figure 6: Illustration of the Euler Scheme. At each time step i, the particle is displaced by the vector $\Delta t \vec{v}_p^{t_i}$. Details are given in the text.

2.5.2. Leapfrog Integration

The Leapfrog scheme accounts for variations in an velocity field over the course of a time step Δt. Thus velocity values $\vec{v}_{p,\vec{x}_p^{t+\Delta t/2}}^{t+\Delta t/2}$ at an intermediate time $t + \Delta t/2$ are used as estimates for this variation. Similar to the Euler Scheme, the new particle position at time $t + \Delta t$ is calculated by using this intermediate value:

$$\vec{x}_p^{t+\Delta t} = \vec{x}_p^t + \Delta t \vec{v}_{p,\vec{x}_p^{t+\Delta t/2}}^{t+\Delta t/2} \tag{36}$$

Hence the name: One 'leapfrogs' the intermediate time $t + \Delta t/2$ to jump from t to $t + \Delta t$. As the velocity $\vec{v}_{p,\vec{x}_p^{t+2\Delta t/2}}^{t+\Delta t/2}$ is usually calculated by linear interpolation of discrete velocities $\vec{v}_{p,\vec{x}_p^t}^t$ and $\vec{v}_{p,\vec{x}_p^{t+\Delta t}}^{t+\Delta t}$, equation (36) can also be written as an Euler Scheme with two distinct time steps of length $\Delta t/2$:

$$\vec{x}_p^{t+\Delta t} = \vec{x}_p^t + \underbrace{\frac{\Delta t}{2}\vec{v}_{p,\vec{x}_p^t}^t}_{predictor} + \underbrace{\frac{\Delta t}{2}\vec{v}_{p,\vec{x}_p^{t+\Delta t}}^{t+\Delta t}}_{corrector} \tag{37}$$

Therefore this scheme is sometimes called 'improved Euler' Scheme with a predictor- and an corrector step. Figure 7 illustrates each calculation of the improved Euler Scheme for the same example as shown before:

- **Initial Step:** Start at the particle location $\vec{x}_p^t$ at time t.

- **Predictor Step**: Calculate the velocity $\vec{v}^t_{p,\vec{x}^t_p}$ (red arrow) and then *predict* the new position $\vec{x}^{t+\Delta t}_{p1} = \vec{x}^t_p + \Delta t \vec{v}^t_{p,\vec{x}^t_p}$ (red dot).

- **Corrector Step:** Calculate the velocity $\vec{v}^{t+\Delta t}_{p,\vec{x}^{t+\Delta t}_{p1}}$ (blue arrow) at the *predicted* position $\vec{x}^{t+\Delta t}_{p1}$ (red dot) at time $t + \Delta t$.

- **Final Step:** Calculate the final position $\vec{x}^{t+\Delta t}_p$ via equation (37) using the computed predictor and corrector velocities (black arrows).

This numerical method is symmetrical in time, i.e. backward integration from $\vec{x}^{t+\Delta t}_p$ to $\vec{x}^t_p$ with a negative time step $-\Delta t$ and using inversed velocities will reproduce the same trajectory as forward integration. Accuracy of this scheme is $\mathcal{O}(\Delta t^3)$.
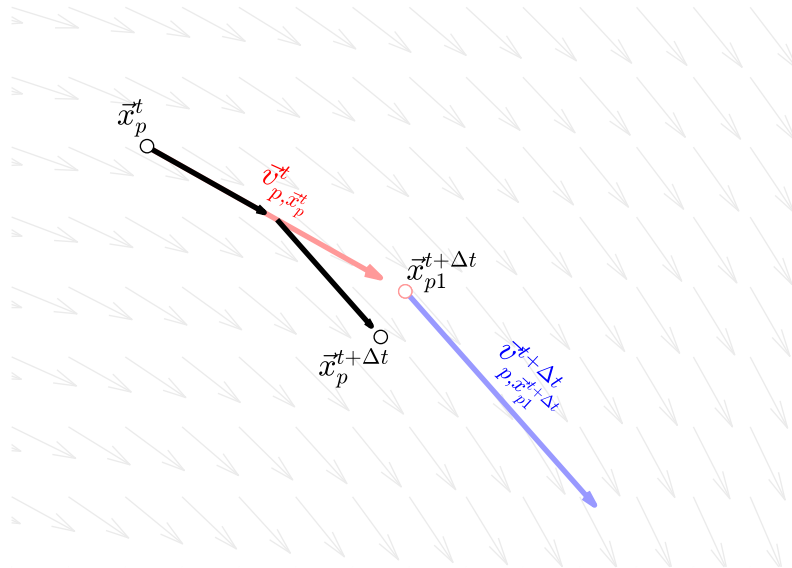
Figure 7: Illustration of the Euler Predictor-Corrector Integration. First, a position is predicted via an Euler Step (red arrow and dot), then a corrector velocity at the predicted location (blue arrow) is computed. The overall displacement is the mean of these predictor- and corrector velocities (black arrows).

2.5.3. Runge-Kutta 4 Integration

Similar to the aforementioned improved Euler Scheme, the 4th-Order Runge-Kutta[61] (RK4) Integration uses three predictor locations and weighted time

---

[61]Carl Runge, 1856-1927 and Wilhelm Kutta, 1867-1944

steps to calculate resulting particle displacements. Starting at location $\vec{x}_p^t$ the new position at time $t + \Delta t$ is:

$$\vec{x}_p^{t+\Delta t} = \vec{x}_p^t + \frac{\Delta t}{6} \vec{v}_{p,\vec{x}_p^t}^t + \frac{\Delta t}{3} \vec{v}_{p,\vec{x}_{p1}^{t+\Delta t/2}}^{t+\Delta t} + \frac{\Delta t}{3} \vec{v}_{p,\vec{x}_{p2}^{t+\Delta t/2}}^{t+\Delta t} + \frac{\Delta t}{6} \vec{v}_{p,\vec{x}_{p3}^{t+\Delta t}}^{t+\Delta t} \qquad (38)$$

Note the difference in time indices for velocities $\vec{v}_{p,\vec{x}_{p_i}^{t_j}}^{t_k}$ and positions $\vec{x}_{p_i}^{t_j}$. Time stepping for predictor *locations* is of length $\Delta t/2$ while *velocities* are calculated for t (first predictor) and $t + \Delta t$. This is illustrated in Figure 8:

- **Initial Step:** Start at the actual particle location $\vec{x}_p^t$ at time t.

- **1st Predictor Step:** Calculate the velocity $\vec{v}_{p,\vec{x}_p^t}^t$ (light red arrow) and then *predict* a new position $\vec{x}_{p1}^{t+\Delta t/2} = \vec{x}_p^t + \frac{\Delta t}{2} \vec{v}_{p,\vec{x}_p^t}^t$ (red arrow and dot).

- **2nd Predictor Step:** Calculate the velocity $\vec{v}_{p,\vec{x}_{p1}^{t+\Delta t/2}}^{t+\Delta t}$ (light blue arrow) at the predicted position $\vec{x}_{p1}^{t+\Delta t/2}$ (red dot) using velocities at time $t + \Delta t$. Then *predict* another position $\vec{x}_{p2}^{t+\Delta t/2} = \vec{x}_p^t + \frac{\Delta t}{2} \vec{v}_{p2,\vec{x}_{p1}^{t+\Delta t/2}}^{t+\Delta t}$ (blue arrow and dot).

- **3rd Predictor Step:** Calculate the velocity $\vec{v}_{p,\vec{x}_{p2}^{t+\Delta t/2}}^{t+\Delta t}$ (light green arrow) at the new predicted position $\vec{x}_{p2}^{t+\Delta t/2}$ (blue dot) using velocities at time $t + \Delta t$. Then *predict* another position $\vec{x}_{p3}^{t+\Delta t} = \vec{x}_p^t + \Delta t \vec{v}_{p3,\vec{x}_{p2}^{t+\Delta t/2}}^{t+\Delta t}$ (green arrow and dot).

- **Corrector Step:** Calculate the velocity $\vec{v}_{p,\vec{x}_{p3}^{t+\Delta t}}^{t+\Delta t}$ (magenta arrow) at the new predicted position $\vec{x}_{p3}^{t+\Delta t}$ (green dot) using velocities at time $t + \Delta t$.

- **Final Step:** Calculate the final position $\vec{x}_p^{t+\Delta t}$ via equation (38) using the previously computed predictor and corrector velocities (black arrows).

As the name suggests, the RK4 scheme has accuracy $\mathcal{O}(\Delta t^4)$, making it the most accurate method at hand. The caveat is its lack of time symmetry.

2.5.4. Comparison

In this section, the aforementioned time integration schemes are compared using inertia currents according to equation (12). As particle paths and
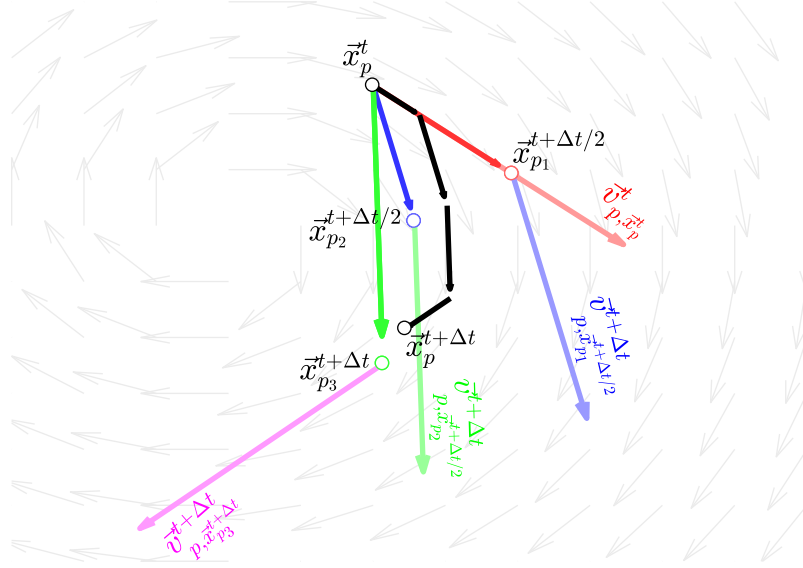
Figure 8: Illustration of the RK4-Integration. It can be interpreted as an predictor-corrector integration using Euler steps with adaptive time stepping length. In total, three predictor locations $\vec{x}_{p_j}^{t^i}$ (red, blue and green dots) and four corresponding velocities $\vec{v}_{\vec{x},p_j}^{t^k}$ (red,blue,green and magenta arrows) are used to compute a resulting displacement (black arrows) for each time step. Details are given in the text.

velocities for this type of currents can be computed analytically, numerical errors due to spatial or temporal interpolation of discrete velocity values are eliminated and deviations of numerical trajectories from analytical paths of equation (12) are solely caused by the error of each integration method. This basic test was advocated by Fabbroni [2009] and also used by Döös et al. [2016] to test the accuracy of their numerical Lagrangian trajectory model TRACMASS. In the following examples, inertia currents with a Coriolis frequency of $f = 2\Omega \sin(54°) \approx 1.17 \times 10^{-4}\text{s}^{-1}$, i.e. an inertial period of 14 h 55 min corresponding to values at the German Bight, and underlying geostrophic component $\bar{u} = 6\,\text{cm}\,\text{s}^{-1}$ in the x-direction[62] are used. The initial velocity is set to $V = 30\,\text{cm}\,\text{s}^{-1}$.

To illustrate differences in forward and backward integration of trajectories, a path is first integrated over a 7 days period with time stepping length $dt = 15\,\text{min}$ in case of all three numerical schemes. Endpoints of these tra-

---

[62]I.e. $\bar{v} = 0$ in equation (12).

jectories are then used as initial location for backwards trajectories. These are calculated using inversed time steps $dt = -15 \, \text{min}$ and inverted currents, which are achieved by multiplying equation (12) with a factor -1. Obtained forward and backward trajectories for each integration scheme, as well as the analytical solution of equation (12), are shown in Figure 9. Even though forward trajectories (red lines) resemble the analytical solution (black lines) quite well for all three cases, accuracy of the simple Euler scheme is obviously inferior when compared to the Improved Euler and Runge-Kutta methods. This is even more evident in backward trajectories (green lines), significantly deviating from the forward trajectory and analytical solution in case of the simple Euler integration. Differences between the Improved Euler and the Runge-Kutta schemes are almost absent in this qualitative review and forward and backward trajectories almost coincide in both cases.

Differences between forward and backward integration for each scheme are quantified in Figure 10. Here absolute differences of forward $\vec{x}_{dt}$ and backward trajectories $\vec{x}_{-dt}$, i.e. $\Delta x = abs\left(\vec{x}_{dt} - \vec{x}_{-dt}\right)$ are shown with respect to integration time. Maximum difference of forward and backward trajectories in the simple Euler (red solid line) and the Runge-Kutta (green dash-dotted line) cases are $425 \, \text{m}$ resp. $25 \, \text{m}$. In case of an improved Euler integration (blue dashed line), forward and backward trajectories coincide as its the only time reversible scheme of these three methods.

Accuracy of each numerical integration is generally improved by decreasing time stepping lengths, hence performance can be adjusted by the choice of dt. Figure 11 shows differences between analytical $\vec{x}_{ana}$ and numerical solutions $\vec{x}_{num}$ in terms of absolute distance $\Delta x = abs\left(\vec{x}_{ana} - \vec{x}_{num}\right)$, when different time stepping lengths are used in each integration scheme. Choosing time steps in the range $dt = 15 \, \text{min}...60 \, \text{min}$ yield the Improved Euler method to show highest accuracy of all schemes. This advantage disappears for choices $dt \geq 120 \, \text{min}$, where accuracy of the Improved Euler and RK4 algorithms coincide. Again, errors are significantly larger when a simple Euler scheme is used, where $dt = 15 \, \text{min}$ yields comparable accuracy to the other schemes for $dt \approx 2 \, \text{h}$.

The worse performance of the Runge-Kutta scheme in comparison to the Improved Euler scheme in this test is caused by the fact, that predictor steps two and three as well the corrector step coincide, as all these steps are taken at time $t + \Delta t$ and hence yield the same velocity value according to
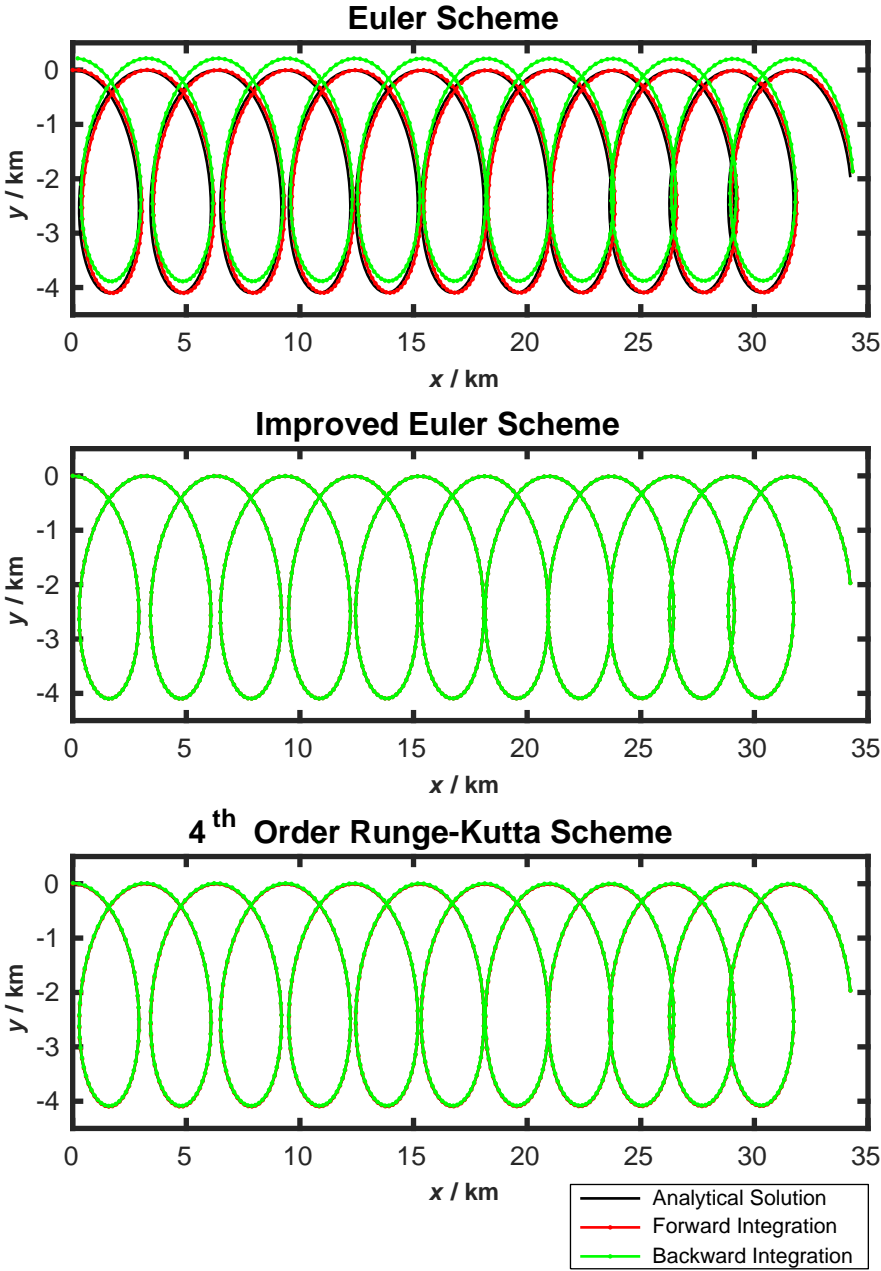
Figure 9: Comparison of calculated trajectories using the numerical integration methods (35), (37) and (38). Black solid lines indicate the analytical solution of equation (12), red lines represent forward time integration with $dt = 15\,\mathrm{min}$ time steps. Green lines depict backward time integration ($dt = -15\,\mathrm{min}$) for initial locations at endpoints of each respective forward trajectory. Parcel positions at each time step are denoted by dots.

equation (12). The Runge-Kutta scheme thus equals sort of an improved
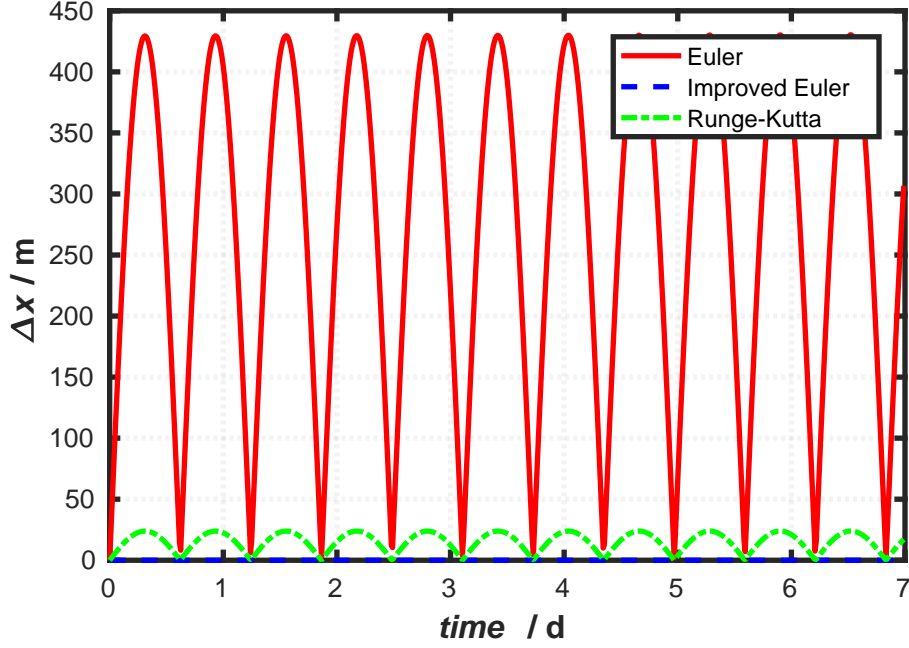
Figure 10: Difference of the Forward and Backward trajectories shown in Figure 9.

Euler scheme with weights $1/6$ for $\vec{v}^{t}_{p,\vec{x}^{t}_{p}}$ and $5/6$ for $\vec{v}^{t+\Delta t}_{p,\vec{x}^{t+\Delta t}_{p}}$ [63].

In most practical applications, no analytical expression for a given velocity field is known and velocities are given on spatial grids at discrete times, e.g. from a numerical model. In this case, the Runge-Kutta scheme indeed gives most accurate estimates as each predictor and corrector velocity is taken at differing locations in space. Deviations of the velocity field are then approximated on four nodes over the course of each time step. Performance of each scheme for gridded data is illustrated by a test using stationary swirl currents of period $T = 15\,\text{h}$ for one cycle[64] and spatial dimensions of $20\,\text{km} \times 20\,\text{km}$. In this case a spatial resolution of $50\,\text{m} \times 50\,\text{m}$ is used. Velocity values are given as function of the radial distance $r = \sqrt{(x - x_0)^2 + (y - y_0)^2}$ from the swirl's center (x_0, y_0):

$$
\begin{aligned}
u &= -\omega(x - x_0) \\
v &= \omega(y - y_0)
\end{aligned}
\tag{39}
$$

Here $\omega = \frac{2\pi}{T}$ is the angular frequency. Parcels and hence particles within this swirl current move on closed circles with a constant radial velocity of

---

[63]Compare equations (37) and (38).

[64]Resembling the inertial period in the German Bight.
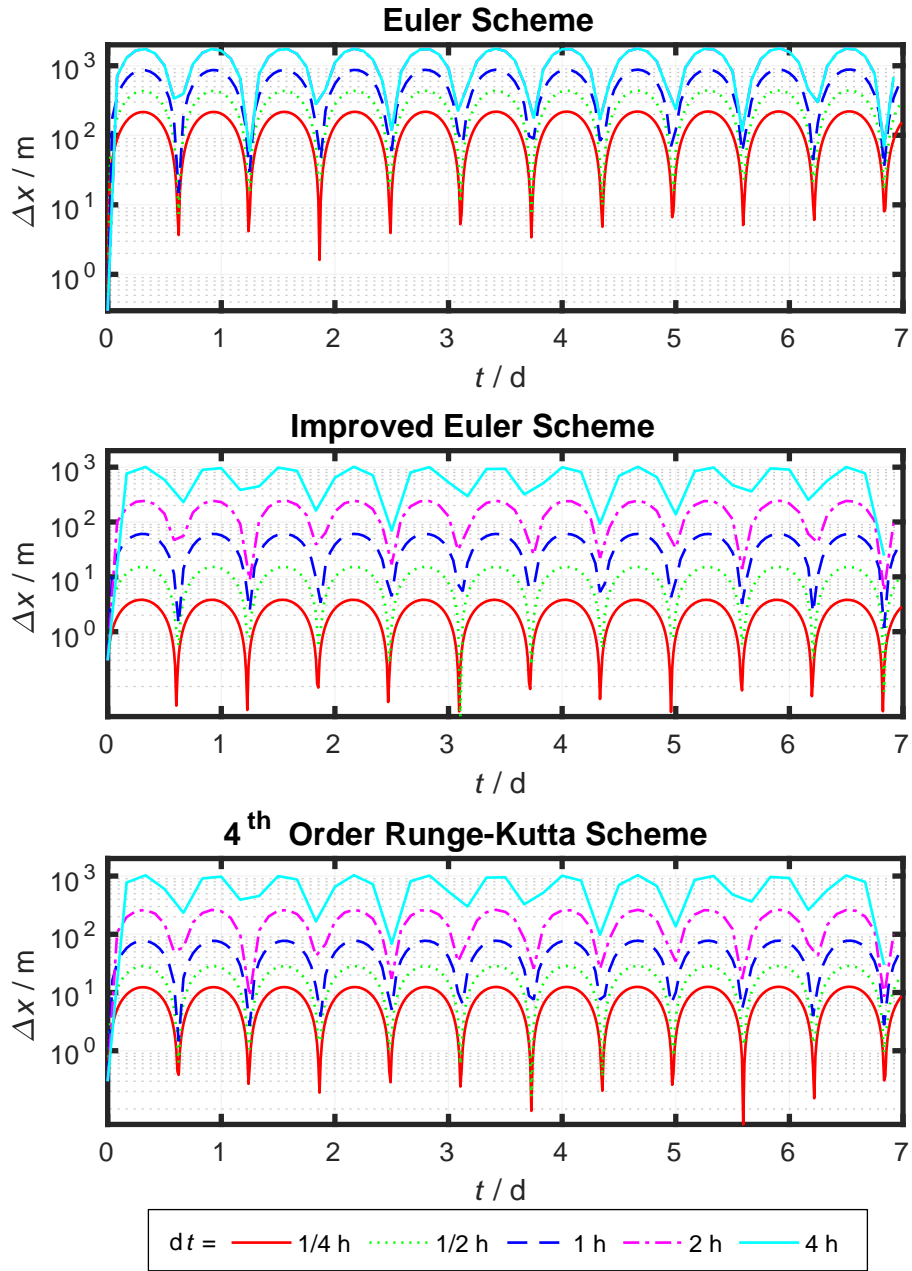
Figure 11: Absolute difference of the numerical solution from the analytical solution of equation (12) for three numerical integration schemes with different time steps dt. Details are given in the text.

$r \cdot \omega$ in counterclockwise direction, performing one loop in $T = 15\,\text{h}$.

Trajectories for this discrete swirl current data have been computed with the FLOPPSY toolbox, described in section 5, using each integration scheme and several time stepping lengths. The initial location was set to $(0\,\text{m}, 5000\,\text{m})$ and trajectories were calculated for integration periods of 30 days. Exactly,

trajectories should perform closed circles of radius $r = 5\,\mathrm{km}$ and constant radial velocity $r \cdot \omega = 58\,\mathrm{cm\,s^{-1}}$.

Resulting trajectories for $dt = 1\,\mathrm{h}$ and $dt = 15\,\mathrm{min}$ are shown in Figure 12. A black cross indicates initial locations, terminal locations after 30 days of integration time are highlighted by an white circle. Discrete locations for each time step are given by small dots. Choosing $dt = 1\,\mathrm{h}$ (top panel) leads Euler trajectories to leave the swirl after just 12 time steps, i.e. not even traversing one full circle. Accuracy is improved by choice of an improved Euler Scheme (blue line), where trajectories almost perform one closed circle, leaving the swirl after 165 iterations. In total 11 rotations are performed. Best results are achieved by using an RK4 method, where trajectories stay on closed circles until the end of integration. Note the difference between start (cross) and end positions (dot). This is a consequence of terminating computations after a period of $30\,\mathrm{d} - dt$, because a future time step is needed for each iteration and hence is absent for $t = 30\,\mathrm{d}$.

Decreasing time stepping lengths to $dt = 15\,\mathrm{min}$ (bottom panel) drastically improves accuracy of trajectories in both Euler cases, even though results are instable[65]. Simple Euler trajectories (red line) are leaving the swirl after 135 iterations (corresponding to 9 rotations) whereas improved Euler integration yields trajectories staying within the swirl but adopting a spiral shape with slowly growing radius r. Runge-Kutta integration results in stable trajectories (green line) as even discrete particle locations on each cycle (dots) coincide.

This test demonstrates a superior accuracy of the Runge-Kutta scheme when compared to the Euler approaches. Major drawbacks of the former is its slower computing time, as discrete velocities have to be interpolated four times per iteration and its time irreversibility. However, longer time steps can be set, lowering the number of iterations. In case of the FLOPPSY toolbox, RK4 integration is in fact the most economic scheme, as a time stepping length of $dt = 1\,\mathrm{h}$ is more accurate than using time steps of $dt = 15\,\mathrm{min}$ in the Improved Euler case. Computation times then still are twice as fast due to a decreased number of total iterations[66]. Setting $dt = 1\,\mathrm{h}$ is approximately the upper limit for achieving stable results using an RK4 Scheme in this particular test. Setting e.g. $dt = 1.5\,\mathrm{h}$ results in "overstable"

---

[65]In the sense of staying on closed circles.
[66]See Figure 31 for an overview of computing times with respect to the number of iterations.
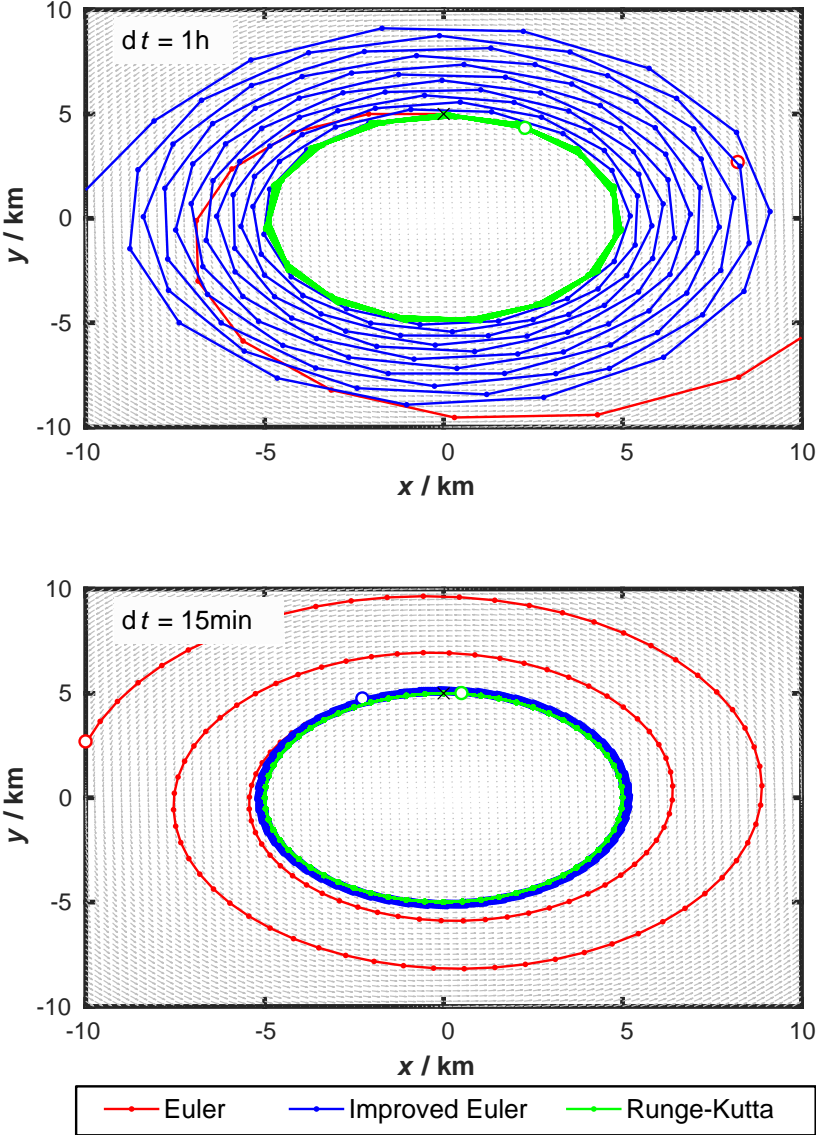
Figure 12: Comparison of trajectories in a rotational current using three integration schemes. A stationary swirl-current with rotational period $T = 15\,\mathrm{h}$ and scale $20\,\mathrm{km} \times 20\,\mathrm{km}$ was used. Trajectories for 30 days time span have been computed using time steps $dt = 1\,\mathrm{h}$ (top) and and $dt = 15\,\mathrm{min}$ (bottom). Grey arrows indicate local current velocities on every fifth grid point. Locations for each discrete time step are indicated by dots, initial and terminal positions of each trajectory are shown by a black cross and white circle respectively.

behavior with trajectories spiraling into the swirl's center[67].

---

[67]Contrary to "unstable" outward spiral patterns. Overstable solutions are not shown here.

In conclusion, a simple Euler scheme should be rejected in most practical applications, as even time stepping lengths of $dt = 2.5\,$s result in trajectories leaving closed circles and missing the exact terminal position by $224\,$m (Figure 13).
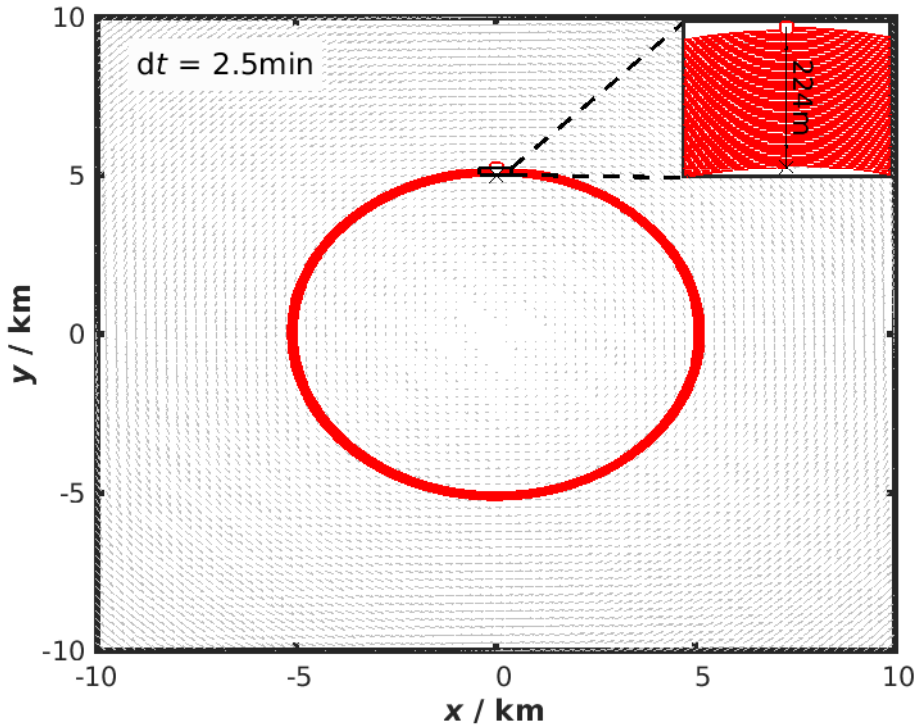
Figure 13: Trajectories in rotational currents, computed ba an Euler Scheme with time steps of $dt = 2.5\,$min. The insert shows a magnification of the starting area. After 30 days integration time, the terminal positions has an error of $224\,$m.

2.6. Beaching Models

In this subsection, a short overview of different types of beaching parametrization in numerical models is given. As in situ observations are sparse, the exact role of physical processes for beaching and resuspension of (litter) particles is still not exactly understood and prospect of ongoing research. There is, however, consensus in scientific literature, that wind [Critchell et al., 2015, Critchell and Lambrechts, 2016, Gutow et al., 2018, Turrell, 2018] and waves [Turrell, 2018] are major drivers of beaching and refloating of debris at shorelines. As these effects are overseen in many numerical models due to a lack of sufficient data, especially for waves, parametrization based on Monte Carlo

methods [e.g. Liubartseva et al., 2018] or beaching as numerical artifact [e.g. Gutow et al., 2018] is used in a majority of studies.

2.6.1. Numerical Beaching

Lagrangian particle tracking is usually based on current data from hydrodynamic models with temporal resolutions in the range of several minutes to hours and spatial scales of hundreds meters or kilometers. As *land* is described via grid points with absent velocities[68], Lagrangian particles can travel onto these landpoints during one time step. This is illustrated in Figure 14: The red particle at location $\vec{x}^t$ is advected by an onshore velocity $\vec{u}$ (blue arrows). The resulting particle velocity $\vec{v}_p = \Delta t \vec{u}$ (red arrow) is penetrating the land-water boundary at a time step $t \rightarrow t + \Delta t$. As velocity values vanish on land, it is then trapped within the yellow land grid and interpreted as *beached*. We will refer to this process as *numerical beaching*, as it is a consequence of numerical discretization and is dependent on spatial resolution of the hydrodynamic data. Handling of numerical grid points[69], boundary conditions[70], integration method[71] and time stepping size Δt are also influencing this type of beaching. As no parametrization is needed, it is a common approach in many studies [e.g. Gutow et al., 2018]. However, it can result in artificial alongcoast movement of Lagrangian particles when data on a staggered grid is used. This will be shown in section 6. It can still be beneficial as refloating of particles by offshore winds can easily be implemented. This approach is discussed further in a later section.

Numerical handling of velocities on land points can affect numerical beaching: As currents are vanishing, velocities are either set to *Nil* or *NaN*[72] in most hydrodynamic models. Particles might be defined as beached in the latter approach due to spatial interpolation of velocities, even though not reaching land points at all. This is illustrated in Figure 15: Using bilinear interpolation of four adjacent velocity values results in $\vec{v}_p = NaN$ for the red particle[73]. However, using a break condition for *NaN* values allows for suppressing resuspension of particles in certain applications.

---

[68]Either by setting $\vec{u} = 0$ or as *Not a Number*. This is explained in further detail below.
[69]As shown in section 6.
[70]Normal velocities onto landpoints are usually vanishing, whereas parallel velocities are allowed or not, depending on a *slip* or *no-slip* conditions in a hydrodynamic model.
[71]Using e.g. RK4 integration generally eliminates this type of beaching.
[72]Not a Number.
[73]By definition, numerical operations consisting of at least one *NaN* are resulting in *NaN*.

2. Theory
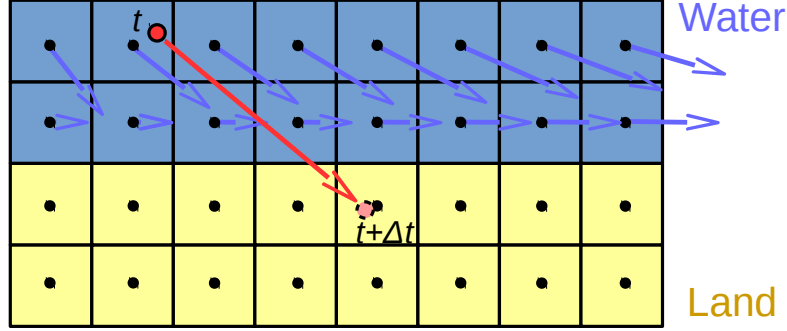
Figure 14: Depiction of numerical beaching: At a time step $t \rightarrow t + \Delta t$ the red Lagrangian particle moves with velocity $\vec{v}^t$ (red arrow) onto a yellow land point. As velocities there are vanishing, it will stay on land until the end of computations. This type of beaching solely occurs due to numerics, hence its name. Gridpoints for land and water are indicated by yellow and blue coloring.

2.6.2. Location Based Beaching

This is a simple parametrization by defining particles as *beached*, when a certain region is reached. This is generally a cell of the hydrodynamic grid adjacent to land points. It is commonly used in global scale advection models [e.g. Maximenko et al., 2012, van Sebille et al., 2015]. Liubartseva et al. [2018] extended this approach by adding a Monte Carlo term for beached particles, which is based on Lagrangian oil spill modeling. Here a particle sticks to a coastline when reached, but has a probability $P_{coast \rightarrow water}$ of resuspension [Liubartseva et al., 2018]:

$$P_{coast \rightarrow water} = \begin{cases} a_{coast} \exp\left(\frac{-t}{T_{coast}}\right) & t < T_{stag} \\ 0 & \text{else} \end{cases} \qquad (40)$$

where a_{coast} is a washing rate and T_{coast} and T_{stag} are mean retention times and mean stagnation periods respectively. Liubartseva et al. [2018] used $a_{coast} = 2\,\mathrm{d}^{-1}$, $T_{coast} = 2\,\mathrm{d}$ and $T_{stag} = 5\,\mathrm{d}$ for the Mediterranean. Equation (40) describes an exponentially declining probability for rewashing of particles, which vanishes after a temporal period of T_{stag}. Resuspension can be applied by e.g. re-releasing particles at a nearest water grid cell.
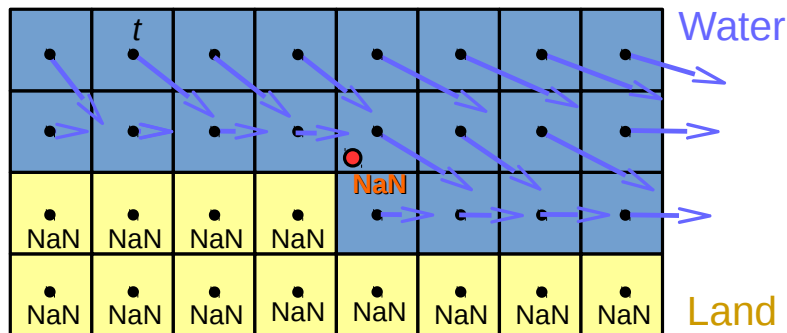
Figure 15: Bilinear interpolating adjacent velocities onto the red particle's location results in a *NaN* velocity value by definition. The particle is then defined as beached without reaching a yellow land cell.

2.6.3. Parametrization

Critchell and Lambrechts [2016] expanded the probabilistic method of Liubartseva et al. [2018] by requiring a normal[74] wind component to "push" particles onto the beach. In their approach, a particle is flushed back if its actual location is exposed to offshore directed normal wind components. Shadowing of winds due to geographical features like headlands is also regarded. In a simplified academical study by Turrell [2018][75], resuspension of particles occurs if normal winds exceed a certain value. These approaches can further be refined by accounting for different types of beaches and coasts, e.g. varying probabilities in equation (40) for rocky, sandy or grassy beaches etc. Unfortunately, these ideas could not be verified within the temporal scope of the macroplastics research project, but some remarks are given throughout this thesis.

---

[74]With respect to the coastline.

[75]Turrell [2018] described a simplified approach based on normal components of currents and winds and even regarding simplified wave effects by adding random sea surface heights.

3. Research Region: The Southern North Sea

A brief description of oceanographic and atmospheric properties of the research region in the southern North Sea is given in this section. An overview about the physical state of the whole North Sea region is given in subsection 3.1, a detailed description can be found e.g. in Howarth [2001] and [Charnock, 1994]. A further look is then given to specific dynamics in the nearshore region of the German Bight in subsection 3.2. Attention is given on the Wadden Sea and Eastfrisian Islands. The section is closed by a short description of atmospheric and oceanographic conditions based on datasets which were used for validation and forcing of the hydrodynamic model, which is presented in section 4.

3.1. North Sea Oceanography

The North Sea is a semi-enclosed shelf sea of about $500\,\mathrm{km} \times 1000\,\mathrm{km}$ size[76], transitioning to the Atlantic Ocean in the north. Eastern and western boundaries are closed by the British Isles and Schleswig-Holstein respectively, with the Dover Strait forming a narrow connection to the English Channel at the former. While fresher waters from the Baltic enter the North Sea through the Skagerrak and Kattegat at the eastern border, the European mainland is a natural closure to the south. Water depths transition smoothly from shallow regions ($\leq 40\,\mathrm{m}$) at the Southern North Sea and the Dogger Bank to depths of about $40\,\mathrm{m}$ to $200\,\mathrm{m}$ northward. Deepest regions are found at the Norwegian Trench, which is contoured by strong bathymetry-gradients. A relief map of the North Sea region is shown in Figure 24.

Circulation is mainly dominated by M_2-tides, yielding semidiurnal periods of $12\,\mathrm{h}\,25\,\mathrm{min}\,16\,\mathrm{s}$[77]. The tidal wave is entering from the Atlantic Ocean at the north-western boundary and progressing as Kelvin wave in anti-clockwise direction[78]. Three amphidromies are present near East Anglia and the Netherlands (approx. $E3.0°, N53.0°$), in the central region (approx. $E5.5°, N55.5°$) and near Stavangar at the Norwegian coast (approx. $E7.5°, N58.0°$). Locating in the northern latitudinal belt of the atmospheric westerlies, the North Sea is generally subject to steady wind stress from westerly winds. In

---

[76]Measured in (W-E $\times$ S-N)-directions.

[77]Derived for a radial frequency $1.40512 \times 10^{-4}\mathrm{s}^{-1}$ [e.g. Malcherek, 2010].

[78]In shallower parts tidal distortions are caused by higher harmonics, which is described in subsection 3.2.

combination with density gradients caused by freshwater input from rivers and the Baltic Sea, a predominately cyclonic residual circulation pattern is formed. Even though it is assumed to be generally stable, annual storms from September to April may alter this circulation pattern. Stanev et al. [2019] even described events of entire reversal into anticyclonic directions.

3.2. Nearshore Dynamics in the German Bight

The German Bight is a shallow, semi-enclosed shelf sea in the Southern North Sea. It is bounded by the coasts of Netherlands, Germany and Denmark in the South and East and the north-western located Dogger Bank. Depth is generally less than 40 m in this region [Charnock, 1994]. Tidal ranges vary regionally from 2.5 m near Borkum and Sylt to 3.5 m at the Elbe river mouth [Staneva et al., 2009] with maximum current velocities[79] reaching 0.4 m s^{-1} at deeper offshore regions to 1 m s^{-1} near the Elbe [Charnock, 1994]. Even though the $M2$-component is prevailing in gauge data, higher harmonics due to non-linear dynamics cause significant distortions in the tidal signal. Waters are generally well mixed, showing bottom-top differences for temperature and salinity in the range of 1 °C resp. 1PSU [Charnock, 1994]. Mean depth averaged annual temperatures are (11 ± 6)°C and mean depth averaged salinities range from $\approx (34 \pm 0.25)$ in offshore regions to $\approx (32 \pm 0.25)$ at the Barriers Islands[80]. However, customarily fronts occur near main freshwater sources, i.e. the river mouths of the three largest rivers *Elbe*, *Weser* and *Ems*. Secondary but important fresh water inlets are generated by runoff from the mainland Staneva et al. [2009].

The Wadden Sea is the main focus of this thesis. It is a shallow area comprised of wide tidal flats and the Eastfrisian Barrier Islands, which form natural borders for waves and seperate backbarrier regions south of the islands from the northern offshore region. In these offshore regions, waves are major drivers of sediment and hydrological dynamics[81]. Offshore and back-barrier regions are connected via tidal channels, which separate the islands. Water masses and suspended particulate matter are exchanged between both regions through these channels with varying characteristics during ebb and flood cycles [Stanev et al., 2003a,b]. These dynamics can drastically change during storm events [Lettmann et al., 2009].

---

[79]Measured for mean spring amplitude.
[80]Values are given as annual mean $\pm$ annual variation [Charnock, 1994].
[81]See e.g. Lettmann et al. [2009] for a study on sediment dynamics and Grashorn et al. [2015] for wave effects on hydrodynamics.

3.3. Description of Datasets

3.3.1. The ECMWF ERA5 Dataset: Atmospheric Data and Ocean Wave Properties

The ERA5 [Bell et al., 2020] dataset combines model and observation data, derived from the fifth generation reanalysis for climate and weather by the European Center for Medium-Range Weather Forecasts (ECMWF). Data is given on a regular global grid of $0.25° \times 0.25°$ (atmosphere) resp. $0.5° \times 0.5°$ (ocean waves) spatial resolution and temporal spacing on 1 h-intervals. Datasets are provided via the Climate Data Store [CDS] from the Copernicus Climate Change Service [C3S] on a daily basis and can be retrieved via Python scripts[82]. Further details can be found in each respective documentation [ECMWF, CDS, C3S].

ERA5 data of atmospheric and wave properties of $0.5° \times 0.5°$ resolution were used for forcing the numerical ocean- and wave-models ROMS and SWAN (section 4) and for validating model results. The data grid of size $29\,\text{km} \times 17\,\text{km}$ covers the whole research region and is illustrated for 2 m-air temperatures in Figure 16. A summary of every ERA5 variable which was used in the research project is shown in Table 1.

3.3.2. The BSH Circulation Prediction Model: Hydrodynamic Data

The BSHcmod [Dick et al., 2001] is a three-dimensional baroclinic circulation model, developed and operated by the Federal Maritime and Hydro-

---

[82]See section 8

Table 1: ERA5 variables, used for atmospheric forcing in the hydrodynamic and wave models ROMS and SWAN (see section 4).

Name	Resolution	Description	Usage
$t2m$	$(0.5° \times 0.5°)$, 1 h	2 m air temperature	ROMS
$u10$	$(0.5° \times 0.5°)$, 1 h	10 m zonal wind-velocity	ROMS
			SWAN
$v10$	$(0.5° \times 0.5°)$, 1 h	10 m meridional wind-velocity	ROMS
			SWAN
msl	$(0.5° \times 0.5°)$, 1 h	Air pressure at Sea Surface	ROMS
tp	$(0.5° \times 0.5°)$, 1 h	Total Precipitation	ROMS
$pair$	$(0.5° \times 0.5°)$, 1 h	Air pressure at Sea Surface	ROMS
tcc	$(0.5° \times 0.5°)$, 1 h	Total cloud cover	ROMS
ssr	$(0.5° \times 0.5°)$, 1 h	Surface net downward shortwave flux	ROMS
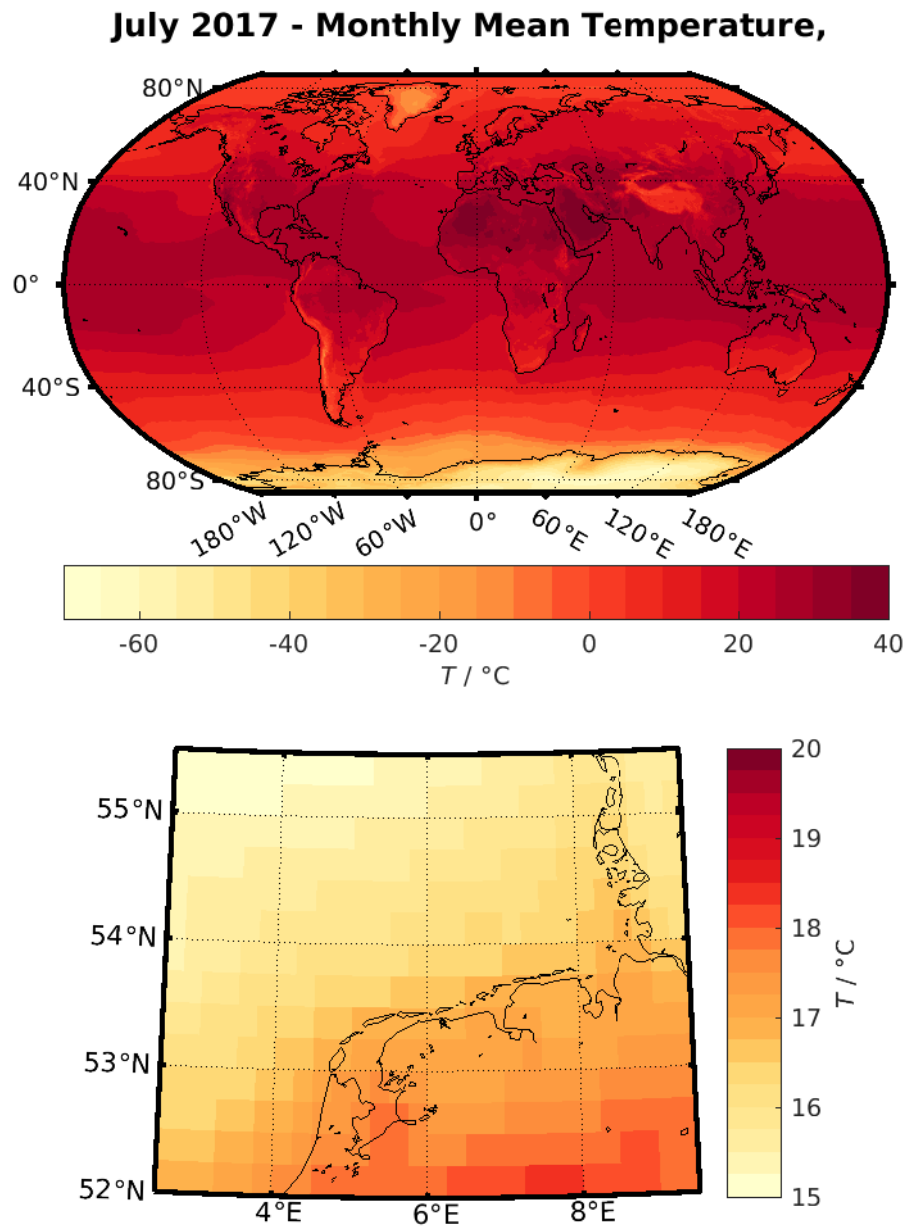
Figure 16: Top: Monthly mean $2\,\mathrm{m}$ temperatures for July 2017, taken from the ERA5 dataset. Bottom: $(29\,\mathrm{km} \times 17\,\mathrm{km})$-cropped data, covering the German Bight.

graphic Agency (BSH) of Germany. It covers the Northeastern Atlantic region, the North Sea and the Baltic Sea on different structured grid scales. These nested model-grids are used as daily operational model, for predicting oil spill distribution and for evaluating dispersion of pollutants. Vertical discretization is implemented via *s*-coordinates, developed by the BSH for

minimized numerical diffusion. Thus stratification of water masses, fronts and eddies are realistically represented[83]. Atmospheric forcing is provided by the German Weather Service (DWD) and river runoff is accounted for using data from the Swedish Meteorological and Hydrological Institute (SMHI) and the Federal Institute of Hydrology (BfG) in Germany.

Data from the 5 km-North Sea and Baltic Sea grid of the BSHcmod was kindly provided by the BSH[84] for the period of the macroplastics research project. Boundary- and initial-conditions for the developed hydrodynamic models, described in section 4, were based on BSHcmod datasets for sea surface elevation, baroclinic velocities, temperature and salinity. Details on boundary- and initial variables are given in respective sections for each model run. Spatial coverage of the BSHcmod is shown Figure 17: The top panel represents water depths whereas a regional crop of monthly mean surface currents for July 2017 is illustrated in the bottom plot.

3.3.3. Measurements

Additionally to the aforementioned datasets, model validation and forcing files were derived from measurements. Gauge data from the *Federal Waterways and Shipping Administration* [WSV], provided by the *Lower Saxony Water Management, Coastal Defence and Nature Conservation Agency (NLWKN)* and wave and meteorological data measured at research platforms FINO1 and FINO2 [FINO], which are operated by the BSH, were used for model validation. Additional data was accessed via the COSYNA data portal of the Helmholtz-Zentrum Geesthacht [Breitbach et al., 2016]: Measured temperatures and salinities at a research platform near Spiekeroog, operated by the ICBM, wave, temperature and conductivity data sampled at the Lightship German Bight and data from the wave rider [e.g. Datawell, 2020] buoy *Elbe*. River discharge data for the Elbe river was provided by the *River Basin Community* Elbe, data for the rivers Ems and Weser were provided by the NLWKN. Locations of measurements are shown in Figure 18, a list of data variables at each station is shown in Table 2. Figure 19 shows a combination of river data for the river Elbe at different gauge locations, which are the basis for prescribing runoff in the numerical models described in section 4. An overview for all major rivers within the modeling domain is given in Figure 78 to Figure 80 in Appendix B.

---

[83]A short description of this vertical discretization is given by Dick et al. [2008].

[84]Thanks to Dr. Thorger Brüning for kindly providing data and helpful feedback.
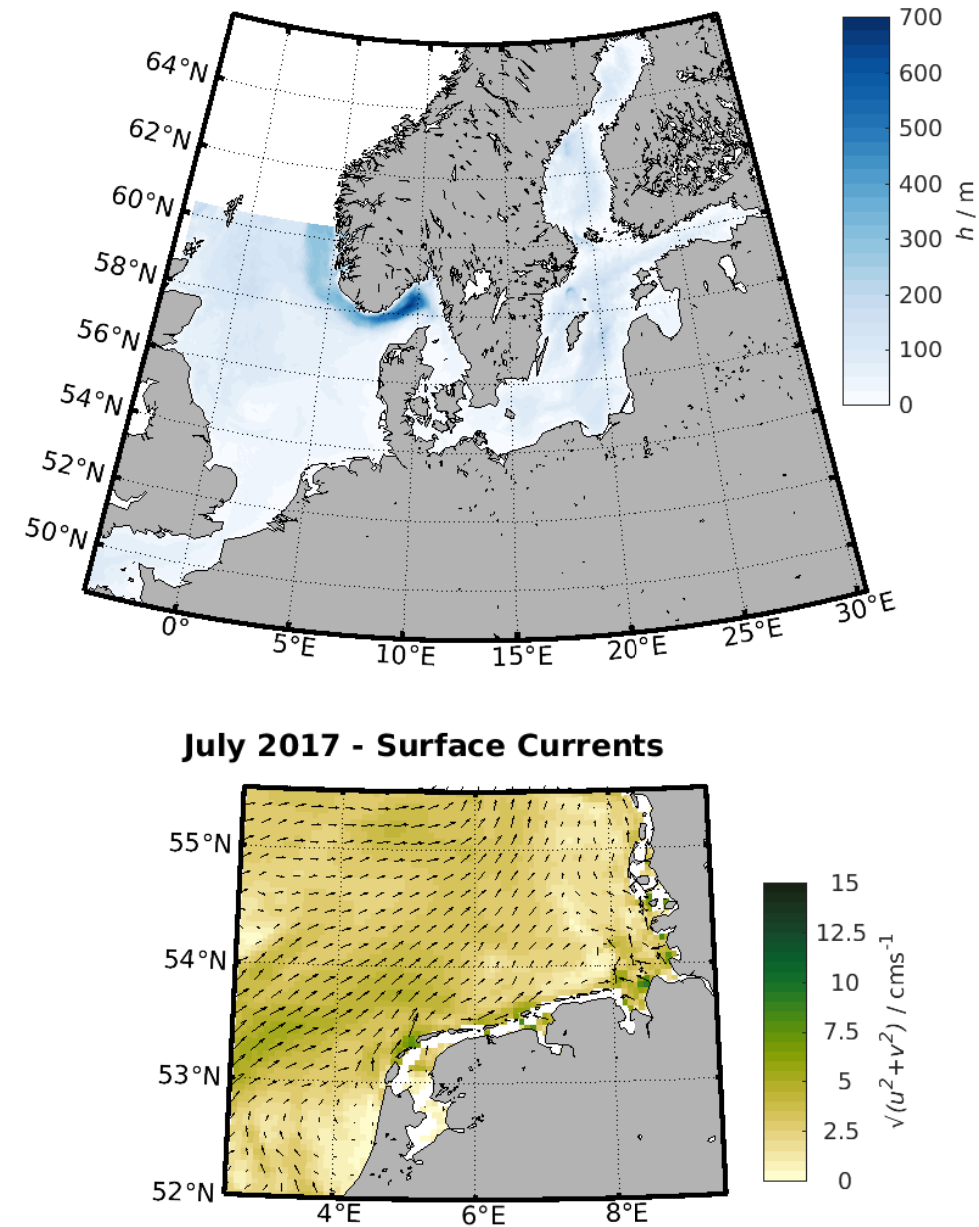
Figure 17: Illustration of the BSHcmod model. Shown data is based on the 1°-North Sea-Baltic Sea prediction model. Top: Bathymetry showing coverage of the complete modeling domain. Bottom: Monthly mean surface currents in the German Bight for July 2017. Color coding indicates absolute velocities, interpolated on v-grid points of the model. Current-directions on every 3rd grid point are indicated by arrows.
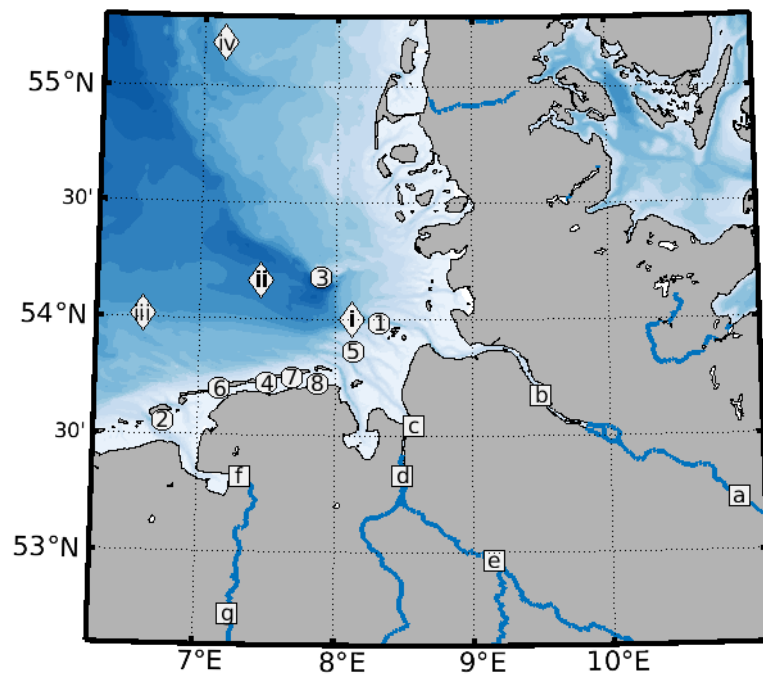
Figure 18: Location of measurement stations used for boundary forcing and model evaluation. Circles indicate gauge stations, squares measurement piles for river data and diamonds other measurement systems. Details are given in the text and in Table 2
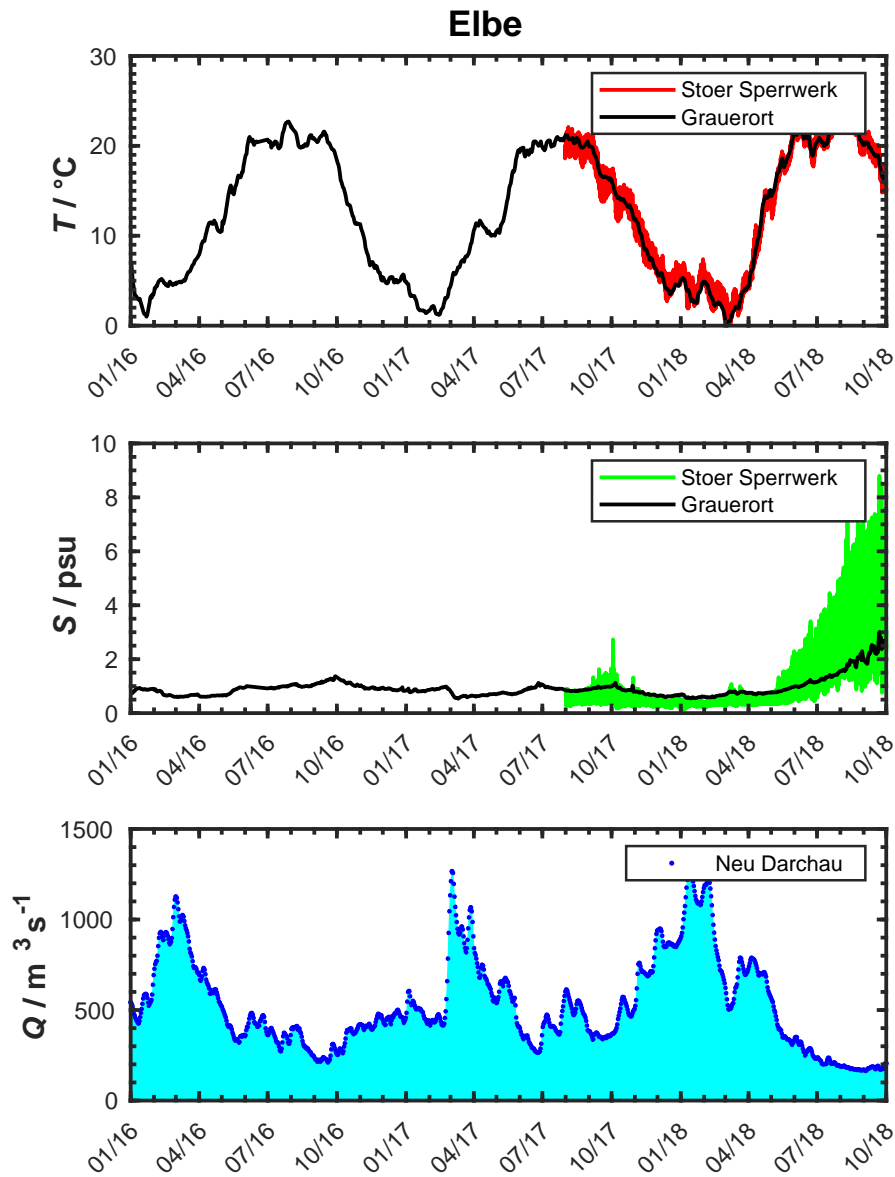
Figure 19: Data for the Elbe river from various pile stations. Solid red and green lines show temperature T and Salinity S at the pile *Stoer Sperrwerk* with 5 min temporal resolution, black lines show respective daily mean values measured at the pile *Grauerort*. Salinity values are derived from conductivity data. River discharge Q is depicted by blue dots in the bottom panel. Each dot represents a daily mean value at *Neu Darchau*. Gauge locations are visualized in Figure 18.

3. Research Region: The Southern North Sea

Installation and operation of a wave radar by working package 5 was integral part of the research project. Thus, an *Ocean Waves WaMoS II Wave and Surface Current Monitoring System* [WAMOS, 2012], in the following simply referred to as WAMOS, was installed on top of the *Evangelischer Jugendhof Spiekeroog* at $((E7°41'14'', N53°46'48'')$, Figure 20. WAMOS is an X-Band radar system, measuring *sea clutter*[85], with additional computing unit. 107×107 data points on a $4\,\mathrm{km}$ radius have been sampled, corresponding to a lateral resolution of about $75\mathrm{m} \times 75\mathrm{m}$ sized data points. Wave energy density spectra were calculated within 3 lateral data boxes on 64 equal sized bins on a frequency-interval $f \in [0.0055\mathrm{Hz}, 0.35\mathrm{Hz}]$. Data is calibrated using *ADCP* current data and pressure data measured by an *RBR* wave logger [RBR] at a fixed location $(E7°41'6'', N53°48'40'')$ at $10\,\mathrm{m}$ depth. Sampling box locations and the radar beam area are depicted in Figure 20. Further information on the WAMOS system and data, used for validating SP-Model data in subsubsection 4.3.4, is given by Wüllner [2018].

---

[85]I.e. backscattered microwaves from the sea surface.

Table 2: List of datasets used for model validation and forcing. Locations of each station are visualized in Figure 18. Details about temporal resolution and data quality are given in respective sections on model validation and forcing.

Index	Name	Location	Data	Data Source
1	Bake A	$(8°19', 53°59')$	ζ	[WSV]
2	Borkum Fischerbalje	$(6°45', 53°33')$	ζ	[WSV]
3	Helgoland Binnenhafen	$(7°53', 54°11')$	ζ	[WSV]
4	Langeoog	$(7°30', 53°43')$	ζ	[WSV]
5	Leuchtturm Alte Weser	$(8°8', 53°52')$	ζ, S, T	[WSV]
6	Norderney Riffgat	$(7°10', 53°42')$	ζ	[WSV]
7	Spiekeroog	$(7°41', 53°45')$	ζ, S, T	[WSV]
				[COSYNA]
8	Wangerooge West	$(7°52', 53°43')$	ζ	[WSV]
i	Wave Rider Elbe	$(8°7', 54°0')$	T, H_{sig}	[COSYNA]
ii	Lightship GB	$(7°27', 54°10')$	S, T	[COSYNA]
iii	FINO1	$(6°35', 54°1')$	H_{sig}, θ_w, T_p	[FINO]
			θ_{wind}, u_{wind}	
iv	FINO3	$(7°9', 55°11')$	H_{sig}, θ_w, T_p	[FINO]
			θ_{wind}, u_{wind}	
a	Neu Darchau	$(10°55', 53°14')$	Q	[WSV]
b	Grauerort	$(9°29', 53°41')$	S, T	[Elbe]
c	Bhv Alter Leuchtturm	$(8°34', 53°33')$	T	
d	Brake	$(8°29', 53°20')$	S, T	[NLWKN]
e	Intschede	$(9°9', 52°58')$	Q	[WSV]
f	Gandersum	$(7°19', 53°19')$	S, T	[NLWKN]
g	Versen	$(7°15', 52°44')$	Q	[WSV]
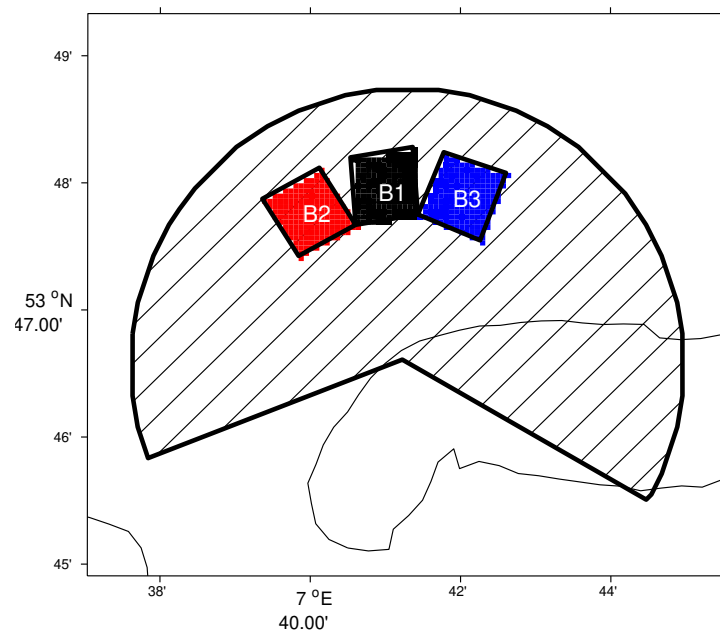
Figure 20: Location and sampling area (shaded cone) of the Wamos. The radar unit was installed at $(E7°41'14'', N53°46'48'')$ using a sampling radius of $4\,\mathrm{km}$. Time series of wave energy density were processed within the colored Boxes 1 to 3. (Figure from Wüllner [2018])

4. Hydrodynamic and Wave Model

A nested numerical model of the German Bight was developed using the hydrodynamic and wave models ROMS and SWAN within the COAWST-modeling system. Starting with a brief overview on these models in subsection 4.1, the geographical domain and approach to spatially discretizing the German Bight is discussed in subsection 4.2. This short compendium of the developed modeling framework is complemented by a validation of model results with measurements in subsection 3.3.

4.1. COAWST
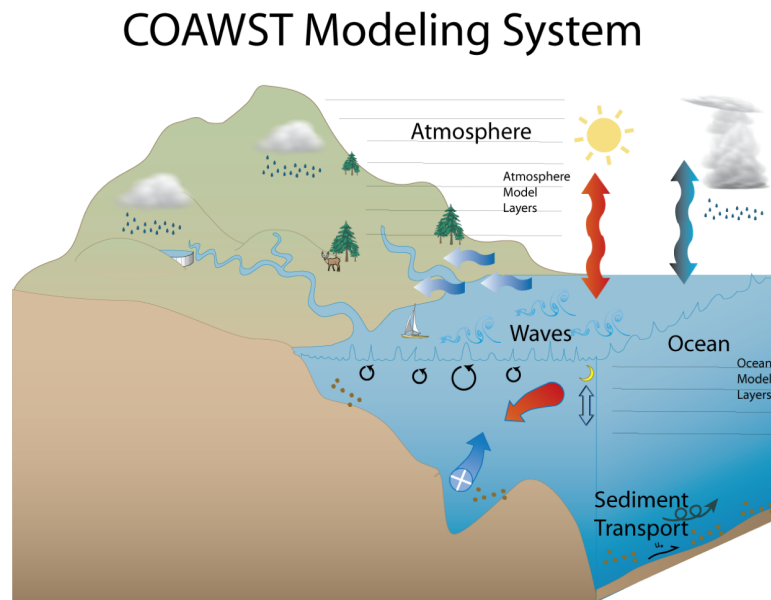
Figure 21: Schematic of the COAWST System. The hydrodynamic model ROMS, the wave model SWAN, the atmospheric model WRF and the Community Sediment Transport Modelling Project can be coupled via the Modelling Coupling Toolkit, allowing for realistic simulations of all physical processes in coastal systems. (Picture from Warner et al. [2010])

The numerical modeling system COAWST (Coupled Ocean-Atmosphere-Wave-Sediment Transport, Warner et al. [2008b] and Warner et al. [2010]) combines the hydrodynamic model ROMS [Shchepetkin and McWilliams, 2005], the atmospheric model WRF [Skamarock et al., 2005], the wave model SWAN [SWAN, 2015] and the Community Sediment Transport Model [Warner et al., 2008b]. Coupling of these models is achieved using the Model Coupling Toolkit (MCT, Larson et al. [2005], Warner et al. [2008a]), allowing for

realistic simulations of various physical and chemical properties on regional scale, as illustrated in Figure 21. Integral part of working package 1 of the macroplastics research project was development and operation of a coupled hydrodynamic-wave model for the German Bight using COAWST. Operation is based on atmospheric data provided by the DWD and ECMWF, hence WRF and the sediment model had been deactivated in all numerical experiments discussed in the present thesis. The following overview is based on Hahner [2016]. Further information can be found in the cited literature.

4.1.1. The Regional Ocean Modeling System (ROMS)

The Regional Ocean Modeling System (ROMS, Shchepetkin and McWilliams [2005]) is a three-dimensional hydrodynamic model, solving the primitive hydrostatic equations on an Arakawa-C-grid [Arakawa and Lamb, 1977] and terrain following vertical S-coordinates. The spatial discretization is illustrated in Figure 22. It accounts for horizontal and vertical diffusion of momentum and tracers via several user-defined parametrizations and the wetting and drying of grid cells in shallow regions. The following overview is based on the ROMS-documentations [Hedström, 2012] and ROMS.

(a) horizontal grid   (b) vertical grid
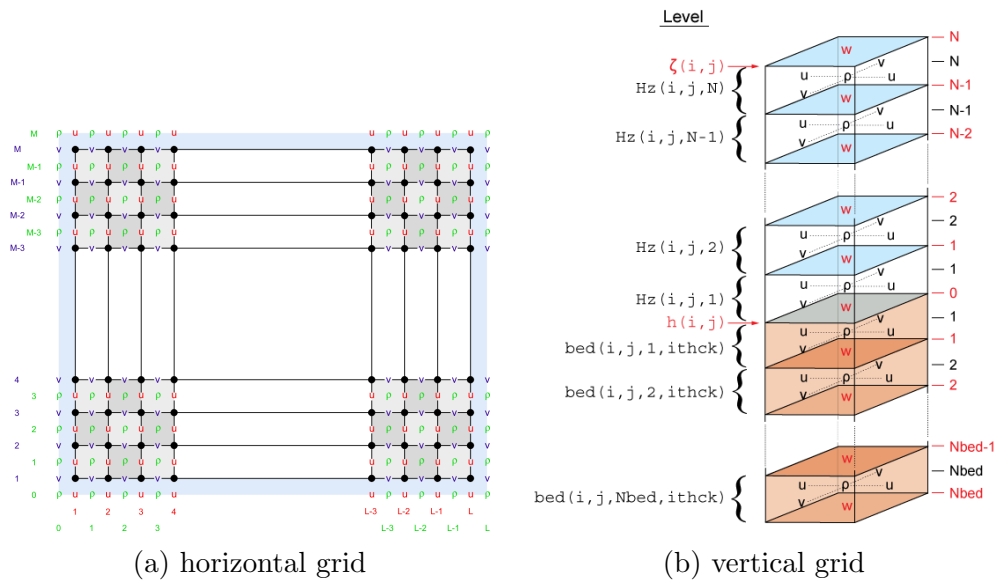
Figure 22: *Staggered Grids* and coordinates in ROMS. Taken from [ROMS].

The hydrostatic primitive equations (Table 10 in Appendix A) are solved using a split-explicit time scheme, i.e. depth-integrated two-dimensional momentum equations, solved on shorter time steps, are used as predictors for solving three-dimensional momentum equations with coarser time stepping.

The ratio of barotropic and baroclinic iterations can be set according to each application, usually ranging around ≈ 20.

In the vertical, two types of S-transformations can be used. Developed setups for the GB-Model, EI-Model and SI-Model (described below) are based on Transformation 2 [Hedström, 2012][86]:

$$
\begin{aligned}
\varsigma &= \varsigma(x, y, z) \\
z(x, y, \varsigma, t) &= \zeta(x, y, t) + S(x, y, \varsigma)\left(\zeta(x, y, t) + h(x, y)\right) \\
S(x, y, \varsigma) &= \frac{h_c \varsigma + h(x, y) C(\varsigma)}{h_c + h(x, y)}
\end{aligned}
\tag{41}
$$

$S(x, y, \varsigma)$ is the vertical transformation, $\zeta(x, y, t)$ the free surface, $h(x, y)$ the local water depth[87] and $\varsigma(x, y, z, t) \in [-1, 0]$ is a generalized vertical coordinate. $C(\varsigma) \in [-1, 0]$ is a customizable stretching function based on four arbitrary equations and two stretching parameters θ_s and θ_b, conditioning refined resolution near the surface and bottom layers if necessary. A thickness parameter h_c controls deactivation of vertical stretching at depths $h(x, y) \leq h_c$, avoiding numerical instabilities in such regions. Free surface and rigid bottom conditions are used at vertical boundaries as well as surface and bottom stresses[88]. A list of optional vertical transformation- and stretching functions is given in Table 9 in Appendix A.

Horizontal coordinates are based on a local orthogonal coordinate system with optional curvilinear description for spatial refinement in certain regions. However, a nesting approach on spherical coordinates was chosen in the following setups. As ROMS allows for horizontal refinement of nested grids by factors $3, 5$ or 7 in nested grids and *one-way*[89] or *two-way*[90] coupling scenarios, necessary high resolutions at the barrier islands and river regions for the present studies could be achieved. Unfortunately, both types of *online-nesting*[91] approaches revealed to be computationally expensive and prone to numerical instabilities in tidal flats. Thus an *offline-nesting*[92] approach

---

[86]Transformation 1 (see Appendix A, Table 9) was used in the SP-Model , developed by Wüllner [2018] (section 7).

[87]related to $z = 0$

[88]Defined as horizontal stresses (τ_x^s, τ_y^s) at the surface and (τ_x^b, τ_y^b) at the bottom.

[89]A coarse grid prescribes boundary data for a fine grid, hence momentum and tracers from the former are entering the later.

[90]Coarse and fine grids are permanently exchanging momentum and tracers.

[91]I.e. data is exchanged constantly between coarse and fine grids.

[92]A first run is performed, computing momentum and tracers solely on a coarse grid. Boundaries for a later run on a refined grid are then prescribed using the first run's data.

was chosen in some numerical experiments. For each model run, underlying nesting approaches are given in respective sections. Various horizontal boundary conditions are optional at open grid borders whereas an arbitrary *free-slip* or *no-slip* condition is applied at water-land interfaces.

In case of coupled ROMS-SWAN setups, wave-current interactions are described either by a vortex force or a radiations stress formulation [Kumar et al., 2011, 2012] of which the former formalism was chosen for all setups described in this thesis[93]. Vertical turbulence is described via four arbitrary turbulence closure models with tunable length scales [Warner et al., 2005]. As surface waves significantly enhance turbulence in upper water levels [Craig and Banner, 1994, Craig, 1996], wave effects can be regarded in these closure models [Carniel et al., 2009][94].

4.1.2. Simulating WAves Nearshore (SWAN)

Simulating WAves Nearshore (SWAN) is an open source third generation numerical wave model[95]. Solving the Wave Action Balance Equation

$$\partial_t N + \partial_x(c_{g_x} N) + \partial_y(c_{g_y} N) + \partial_\theta(c_\theta N) + \partial_\omega(c_\omega N) = \frac{S(\omega, \theta)}{\omega} \qquad (42)$$

SWAN calculates wave spectra and corresponding parameters like wave vector $\vec{k}$, significant wave height H_{sig} and wave period T on a structured spatial grid. In equation (42) $N(\omega, \theta) = E/\omega$ is the ratio of wave energy $E(\omega, \theta)$ and frequency ω, θ is the wave spectrum direction and S are source and sink terms for wave energy. Indices for wave celerity c denote dependencies on partial differentiation, e.g. $c_\omega = \partial_t \omega$[96]. Equation (42) is solved by a finite differences. Further information on numerical discretization and scheme is given by the technical manual [SWAN, 2015].

Wind input, wave breaking, bottom friction and whitecapping are treated in individual source and sink terms and are specified for each application by wind data, bottom grids and user defined physical parameters. A parameter study is given in Appendix G, descriptions of each parameter are given in [Holthuijsen, 2007, chap. 9] and SWAN [2015].

In coupled ROMS-SWAN setups, effects of currents on waves[97] are de-

---

[93]A comparative study is given by Hahner [2016] for the northern beach of Spiekeroog.
[94]Carniel et al. [2009] are also describing the impact of different closure models on Lagrangian drifters within the ROMS internal Lagrangian tracking module FLOATS.
[95][Holthuijsen, 2007, pp.194] give an overview of different wave models and generations.
[96]See [Holthuijsen, 2007, eqn. (7.3.31)-(7.3.33)] for various definitions of celerity.
[97]E.g. doppler shift and refraction.

rived from barotropic currents, computed inside ROMS.

4.1.3. The Model Coupling Toolkit MCT

Coupling of individual numerical models in COAWST is achieved by using the *Model Coupling Toolkit (MCT)* (Larson et al. [2005], Jacob et al. [2005]). Thus giving a comprehensive numerical suite for coastal applications, where physical properties can be activated and deactivated based on needs while keeping computations efficient. Each numerical model is running independently on different computational cores, while starting, pausing and exchanging variables between each model is handled by the MCT. Interpolation between different numerical grids is achieved using a *sparse matrix* with interpolation weights[98]. For the macroplastics research project, numerical models of the German Bight on various resolution grids are solely based on the hydrodynamic and wave models ROMS resp. SWAN. Atmospheric fields were prescribed by data allowing for advanced control of wind influences.

An iteration for one way coupling ROMS (blue time bar) and SWAN (green) is illustrated in Figure 23: Assuming time stepping of $1\,\mathrm{s}$ (SWAN), $0.5\,\mathrm{s}$ (ROMS) and $5\,\mathrm{s}$ (coupling for MCT) lengths, the MCT is halting SWAN after time step 5 (i.e. the coupling time $5\,\mathrm{s}$, red Stop arrow in Figure 23). While ROMS is still running, SWAN data is stored by the MCT (green send arrow). After additional 5 time steps, ROMS is also reaching coupling time, prompting the MCT to halt computations (red recieve arrow) and send wave data to the hydrodynamic model (red data arrow). A *continue* command from the MCT is then sending both models into the next iteration. Throughout this thesis, models were operating in two-way coupling setups with send and recieve prompts for both models. A list of exchanged variables in such applications is shown in Table 3.

Wave-current interactions are described via *Vortex Forces* throughout this thesis, accounting terms of equation (28) in the hydrostatic balance equation inside ROMS. ROMS is then calculating Stokes Drift internally via averaging equation (25) for each S-layer by using significant wave heights H_{sig} and wavelengths L computed by SWAN. Therefore, $A = H_{sig}/2$ and $k = \frac{2\pi}{L}$ are calculated on each vertical w-surface[99] and wave frequencies ω

---

[98]Details are given by Warner et al. [2008b].
[99]Differences of s- and w-layers are illustrated in Figure 22 (b).
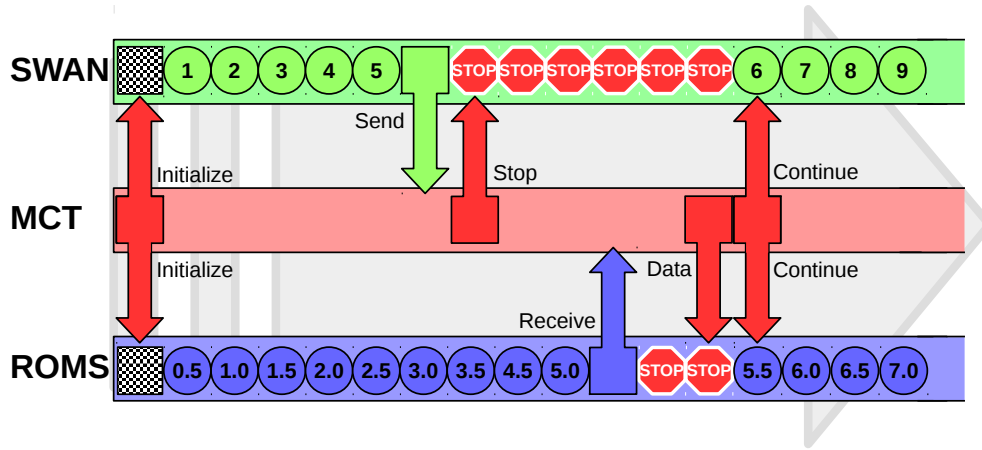
Figure 23: Schematic of a one way coupling application of ROMS and SWAN within the COAWST system. When the prescribed coupling time step of 5 s is reached by SWAN, the MCT pauses the wave model till ROMS reaches the corresponding time step- ROMS then recieves the sent variables by the MCT, which also handles the interpolation of the datafields from the SWAN- to the ROMS-grid. After completion of the data transfer, both models are continued by the MCT.

are derived from the dispersion relation [e.g. Malcherek, 2010]

$$\omega = \sqrt{gk \tanh{(kh)}} \qquad (43)$$

Here $g = 9.81 \, \mathrm{m \, s^{-1}}$ is the gravitational constant and h is local water depth.

4.1.4. Online Lagrangian Floats Module

ROMS allows for online tracking of Lagrangian particles in three-dimensional space within the water column via the implemented FLOATS module. Trajectories are integrated on each hydrodynamic time step using a fourth-order Milne predictor and fourth-order Hamming corrector. It is also accounting for optional vertical diffusion using random walks and different types of buoyancy. However, as implementation of additional drag terms for wind and Stokes Drift was beyond the time frame of the research project and large numbers of floats cause severe lengthening of computational times, the FLOATS module was just used for case studies in collaboration projects and for validating offline computations of Lagrangian particles.

Table 3: Exchange of variables in two-way coupled setups of the wave model SWAN and the hydrodynamic model ROMS. Arrows indicate the direction of data tarnsfer.

SWAN		ROMS	Description
DIR	→	Dwave	**Mean wave direction**
HSIGN	→	Hwave	**Significant wave height**
WLEN	→	Lwave	**Mean wave length**
TMBOT	→	Pwave_bot	**Bottom wave period**
TM01	→	Pwave_top	**Surface wave period**
QB	→	Wave_break	**Fraction of breaking waves**
DISSIP	→	Wave_dissip	**Dissipated wave energy**
X_VEL	←	ubar	**Depth intergrated u-currents**
Y_VEL	←	vbar	**Depth integrated v-currents**
SETUP	←	zeta	**Sea surface elevation**
BOT	←	h	**Bottom topography**

4.2. Geographical Domain and Spatial Discretization

Focus of this thesis is given on the distribution and accumulation of surface floating particles near the German coast and Eastfrisian barrier islands, thus needing high resolution numerical models with realistic meteorological data. Therefore, a hierarchy of numerical grids with increasing resolution near islands and coastal areas has been generated. Modeling domains of these nested grids are shown in Figure 24. At the coarse end of these grids is a SWAN-model containing the North-Atlantic, in the following labeled as NA-Model(Figure 24, top panel), containing 400×400 grid points and a horizontal resolution of approximately $8.48\,\mathrm{km} \times 4.20\,\mathrm{km}$. It is forced by 10m-winds from the ECMWF ERA5 dataset and is generating wave boundary conditions, which are used in higher resolution grids. The NA-Model was developed by Wüllner [2018] and slightly modified for purposes of the thesis at hand. The GB-Model (mid-left panel) resolves the German Bight area on a $1\,\mathrm{km} \times 1\,\mathrm{km}$ spatial grid. It is operational as coupled hydrodynamic-wave model or in sole ROMS or SWAN configurations. Boundary conditions are derived from BSHcmod data and the NA-Model, meteorological fields are based on ECMWF data. Using a refinement of three, the EI-Model (bottom panel) is next in the hierarchy, resolving $333\,\mathrm{m} \times 333\,\mathrm{m}$ near the Eastfrisian Islands. It can be nested online[100] into the GB-Model in arbitrary one-way or two-way configurations, but offline[101] nesting configurations

---

[100]Using nesting algorithms provided by COAWST.
[101]Boundary conditions for hydrodynamic and wave properties are derived from previous runs of the GB-Model .

yield improved numerical stability in tidal flats. Hydrodynamics and waves are computed in the vicinity of Spiekeroog on a $200\,\text{m} \times 200\,\text{m}$ grid[102]. This SI-Model (mid-right panel) is also operational in online- and offline-nesting scenarios using the GB-Model[103]. Vertical discretization is varying between 10 to 20 *S*-layers on each grid. Number of vertical levels was chosen depending on applications throughout this thesis[104]. Basic characteristics and possible configurations of each grid are summarized in Table 4. Additional information is given in respective sections of applications.

Additionally, the SP-Model developed by Wüllner [2018] yields high spatial resolution of $93\,\text{m} \times 50\,\text{m}$ near the Barrier Islands Langeroog, Spiekeroog and Wangerooge. It is operational in offline nesting configurations using hydrodynamic and wave boundary conditions derived from the GB-Model and was used in section 7 calculating barotropic currents and Stokes Drift on 15 vertical levels. Meteorological fields of this setup were based on 10m-winds from the *German Weather Service* DWD and meteorological data from the ERA5 model.

Table 4: Overview of numerical model grids shown in Figure 24. Albeit the NA-Model, hydrodynamics (ROMS) and waves (SWAN) are calculated calculated on each grid. Arrows indicate arbitrary nesting scenarios for each grid: standalone (absent arrow), online two-way nesting ($\leftrightarrow$), one-way nesting ($\rightarrow$).

Name	Resolution	Models	Nesting
NA	$(11.32 \times 10^{-2}, 3.77 \times 10^{-2})°$ $8.48\,\text{km} \times 4.20\,\text{km}$	SWAN	NA
GB	$(15.33 \times 10^{-3}, 8.99 \times 10^{-3})°$ $1\,\text{km} \times 1\,\text{km}$	ROMS + SWAN	GB $\quad$ GB $\leftrightarrow$ EI, GB $\leftrightarrow$ SI $\quad$ GB $\rightarrow$ EI, GB $\rightarrow$ SI
EI	$(5.11 \times 10^{-3}, 2.30 \times 10^{-3})°$ $0.33\,\text{km} \times 0.33\,\text{km}$	ROMS + SWAN	EI $\quad$ GB $\leftrightarrow$ EI $\quad$ GB $\rightarrow$ EI
SI	$(3.06 \times 10^{-3}, 1.80 \times 10^{-3})°$ $0.20\,\text{km} \times 0.20\,\text{km}$	ROMS + SWAN	SI $\quad$ GB $\leftrightarrow$ SI $\quad$ GB $\rightarrow$ SI
SP	$(1.02 \times 10^{-3}, 0.60 \times 10^{-3})°$ $93\,\text{m} \times 50\,\text{m}$	ROMS + SWAN	NA $\rightarrow$ GB $\quad$ GB $\rightarrow$ SP

---

[102]Refinement of 5 regarding the GB-Model .

[103]Nesting into the EI-Model is possible in offline scenarios.

[104]Using fewer vertical levels in nesting scenarios helps improving numerical stability and lowering computational costs. Smaller numbers of vertical layers are generally sufficient for refined grids (e.g. EI-Model and SI-Model), as water depths are shallow in these regions.
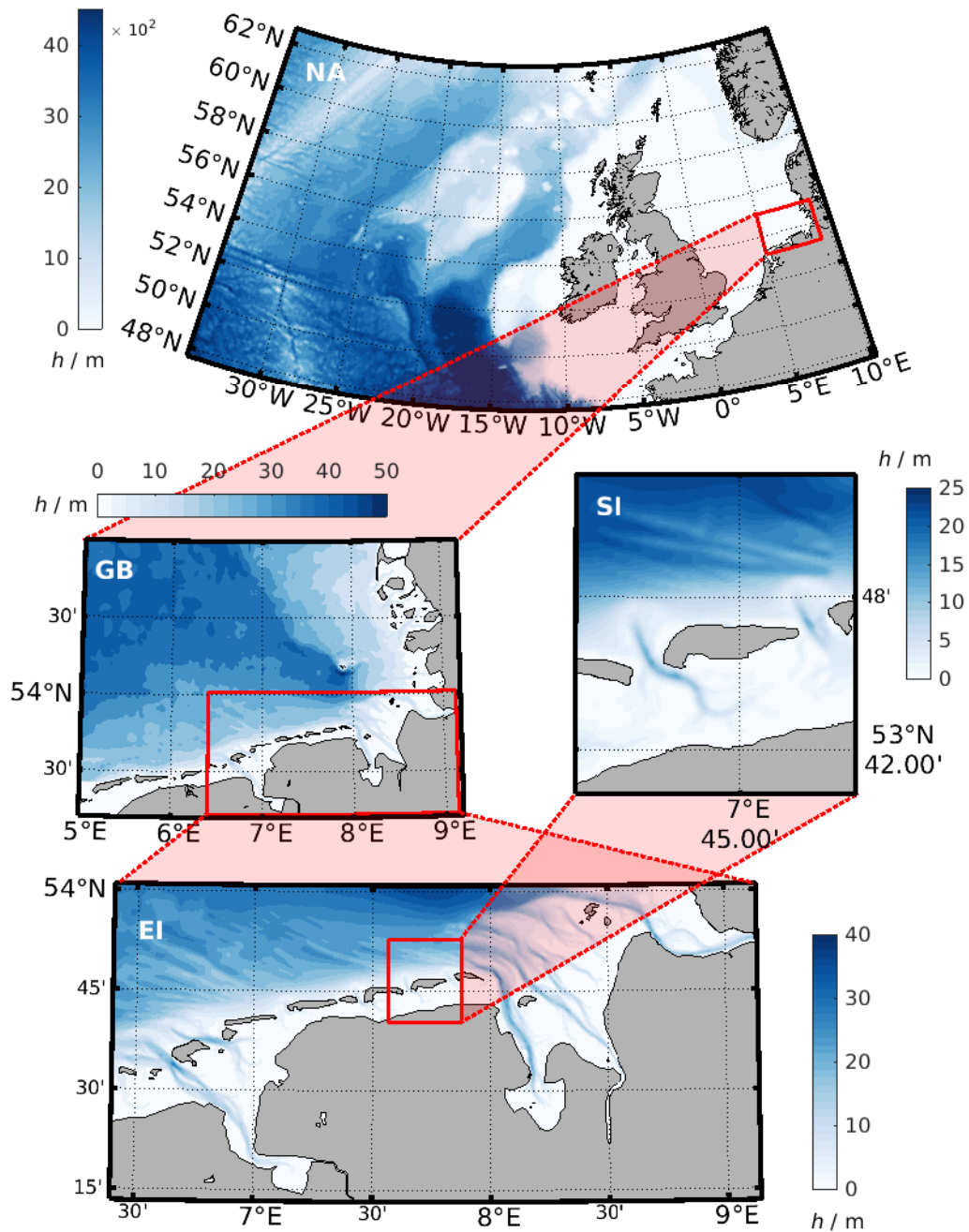
Figure 24: Refinement in the developed model framework: 1.) Bathymetry of the NA-Model with $(11.32 \times 10^{-2}, 3.77 \times 10^{-2})°$ spatial resolution. 2.) Water depths in the GB-Model, resolved on $(15.33 \times 10^{-3}, 8.99 \times 10^{-3})°$ grid points. 3.) The refined EI-Model with $(5.11 \times 10^{-3}, 2.30 \times 10^{-3})°$- sized grid cells. 4.) Spiekeroog as covered by the SI-Model on a $(3.06 \times 10^{-3}, 1.80 \times 10^{-3})°$ grid. Nesting locations of each grid are indicated by red borders. An overview of grid resolutions and possible nesting configurations is given in Table 4.

4.3. Model Validation

Models are validated in this section by comparing computations to measured data for selected periods, which are discussed in this thesis. Additionally, performance of the developed modeling framework is illustrated by comparing results to data from the BSHcmod.

4.3.1. NA Wave Model

Wave boundary conditions for each coupled setup, i.e. the GB-Model and grids of finer resolutions, are computed by the NA-Model. As boundaries of the GB-Model approximately coincide with the FINO 1 research platform, validation of the NA-Model is concentrating on data at this location. Model results for significant wave height H_{sig}, wave direction θ[105] and wave period T during a period from October 1st until November 7th in 2018 are shown in Figure 25 (red line). Measurements are represented by black dots. This period was characterized by intermediate to strong breezes, resulting in significant wave heights of up to $H_{sig} = 5\,\text{m}$ (top panel of Figure 25). Furthermore, a storm event[106], lasting from October 27th until October 30th, was generating maximum significant wave heights of almost $H_{sig} \approx 9\,\text{m}$. As shown in the upper panel of Figure 25, the NA-Model is representing significant wave heights fairly well during low to strong wind conditions. During the storm event in late October, the model is underestimating wave heights by almost $2\,\text{m}$. Computed mean wave directions θ, shown in the mid panel, are almost identical to measured data.

In the bottom panel, modeled mean absolute wave periods $TM01$[107] are compared to wave rider measurements at the research platform. Even though modeled results are showing the same trend as measurements, computed periods are persistently lower and lacking frequencies $T \geq 10\,\text{s}^{-1}$. This issue could not be solved by changing upper limits of discrete frequencies[108] in the model and might lead to underestimated Stokes Drift when calculations based on wave energy density (section 2) are used.

Strong gradients are absent in all computed parameters shown in Figure 25 causing model results to adopt a smoother appearance with less pronounced sharp peaks. This is possibly correlating with temporal resolution of the

---

[105]Wave directions are shown using nautical convention, i.e. decimal angle with respect to the northern axis and increasing in counterclockwise direction.
[106]Storm *Herwart* [e.g. Herold, 2018].
[107]See SWAN [2015] for various definitions of wave period inside SWAN.
[108]Parameter `fhigh` in SWAN.

ERA5 datasets, resulting in low pass filtered wind forcing of the model, and might be improved when high resolution wind data is used[109].
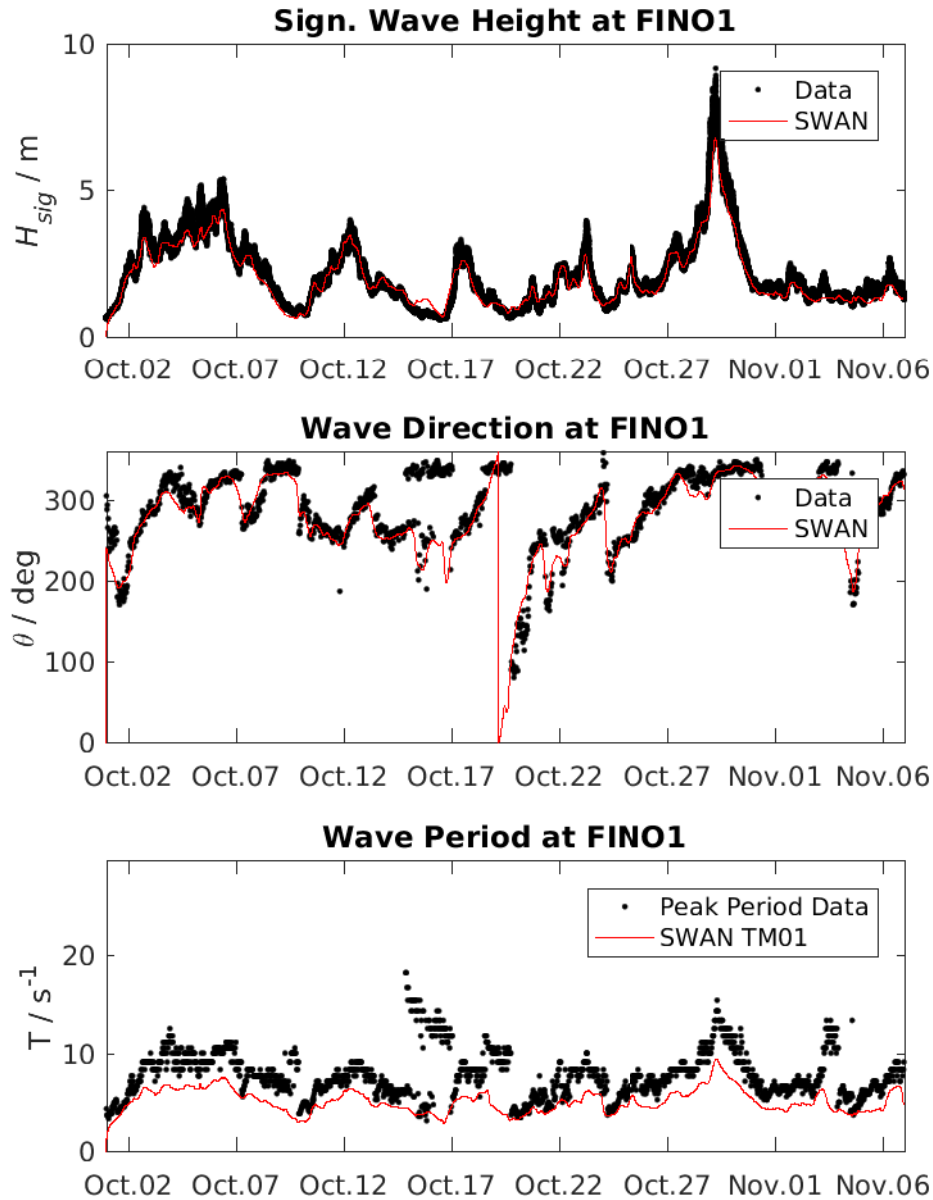

Figure 25: Comparison of computed (red) significant wave height H_{sign} (top), mean wave direction θ (mid) and mean absolute wave period $TM01$ (bottom) to measured data at FINO 1 (black dots). $TM01$ is compared to measured peak periods in the lower panel.

---

[109] One could also argue sharp peaks in measurement might be caused by high frequency noise.

4.3.2. GB Model

For validation runs, hydrodynamics of the GB-Model were forced by meteorological data derived from the ERA5 dataset. River discharges for the Ems, Weser and Elbe were prescribed by gauge data, shown in Figure 78 to Figure 80 in Appendix B. Data from the BSHcmod were providing boundaries and initial conditions of sea surface elevation, currents, salinity and temperature. Due to lacking data, freshwater runoff aside the main rivers was neglected. The SWAN part of the model was forced by wind inputs derived from the ERA5 dataset. Two runs were performed for periods from October 2016 until December 2017 resp. from December 2017 until December 2018[110]. Albeit just short periods during this long term runs are shown here for the sake of clarity, validation results are consistent throughout the aforementioned two-years period.

Sea Surface Elevation   Figure 26 is showing sea surface elevations (SSE) at the gauges *Leuchtturm Alte Weser* (top), Spiekeroog (mid) and *Bake A* (bottom). Computations of the GB-Model (red dotted line) are compared with pile measurements (solid black line). Albeit serving boundary and initial conditions, the blue dashed line is showing computed SSE from the BSHcmod (blue dashed line), serving as consistency check. The shown data corresponds to a one-year model run, initialized at December 20th 2017 by the regarding BSHcmod state. Results of the GB-Model are on par with the driving BSHcmod, but are showing finer spatial resolution. E.g. data at *Spiekeroog* is missing in BSHcmod data, as this area is masked out in this model due to coarser resolution. Both models are successfully representing measured gauge data. Similar plots for a period from October 2017 to November 2017 are shown in Figures 81 to 83 in Appendix B.

Waves   Modeled and measured wave parameters H_{sig}, θ and T at FINO1 are compared in Figure 84[111]. As in the NA-Model's case, a period from October 1st until November 7th, 2017 is shown. At this offshore location, the GB-Model is giving similar results as the NA-Model, i.e. showing good agreement with in-situ measurements for H_{sig} and θ. As in the later model, computed mean wave periods $T01$ are persistently lower than measured peak

---

[110]These periods coincide with deployments of wooden drifters by WP2 of the macroplastics project.

[111]Shown in Appendix B for clarity reasons.
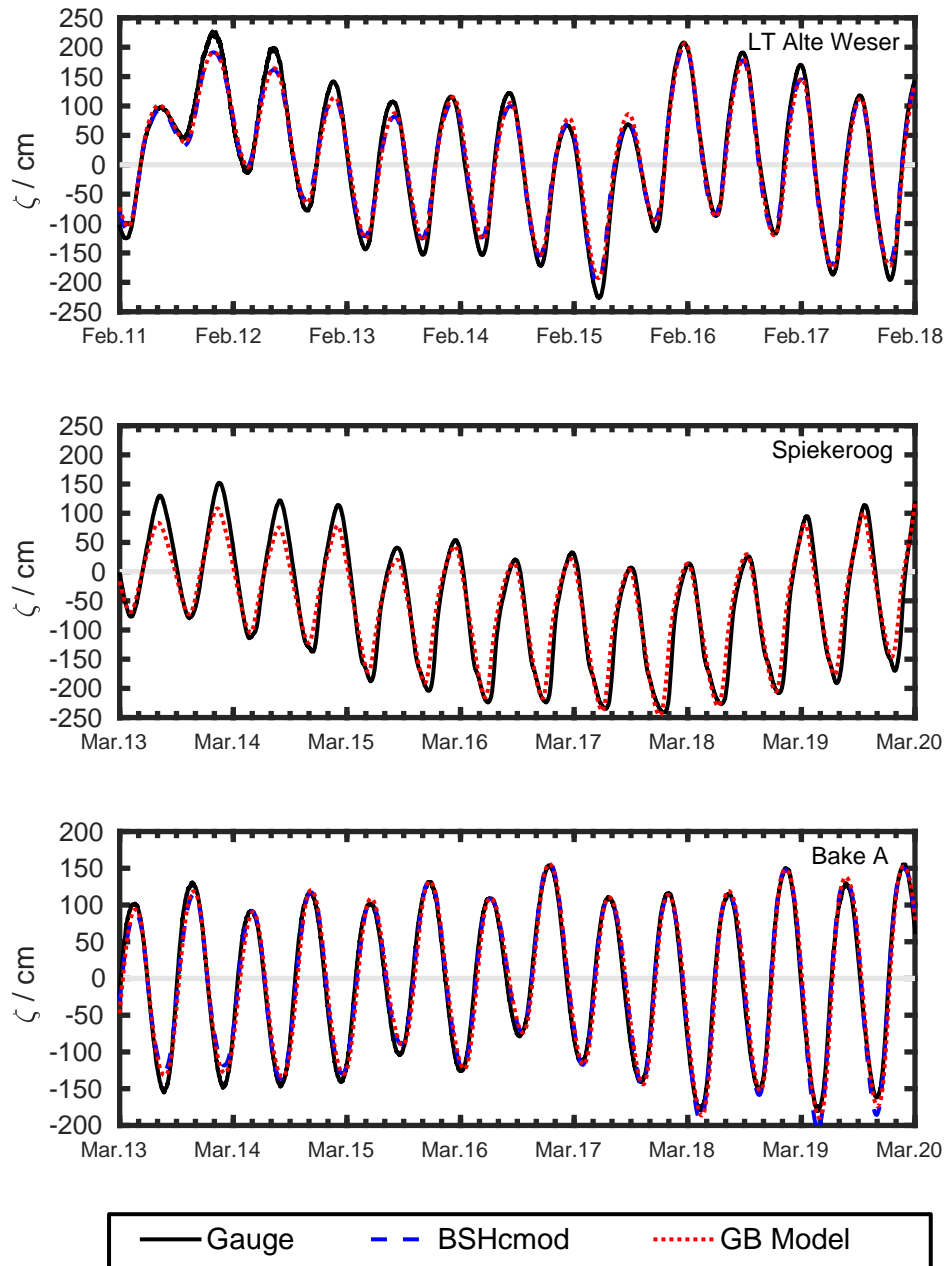
Figure 26: Comparison of sea surface elevation based on measured gauge data (black solid line), data from the BSHcmod (dashed blue line) and data from a one year run of the GB-Model (red dotted line), which was initialized and forced at the open boundaries by the BSHcmod data. At *Spiekeroog* (center panel), BSHcmod data is missing due to the coarse resolution in this region.

periods. In contrast to NA-Model results, significant wave heights during the storm event (peak at October 29th) are well resolved by the GB-Model.

4. Hydrodynamic and Wave Model

Comparing modeled significant wave heights to measurements at the wave rider buoy *Elbe*[112] in Figure 27) reveals that even wave heights during the storm event as well as local spikes of wave amplitudes are well resolved by the model.
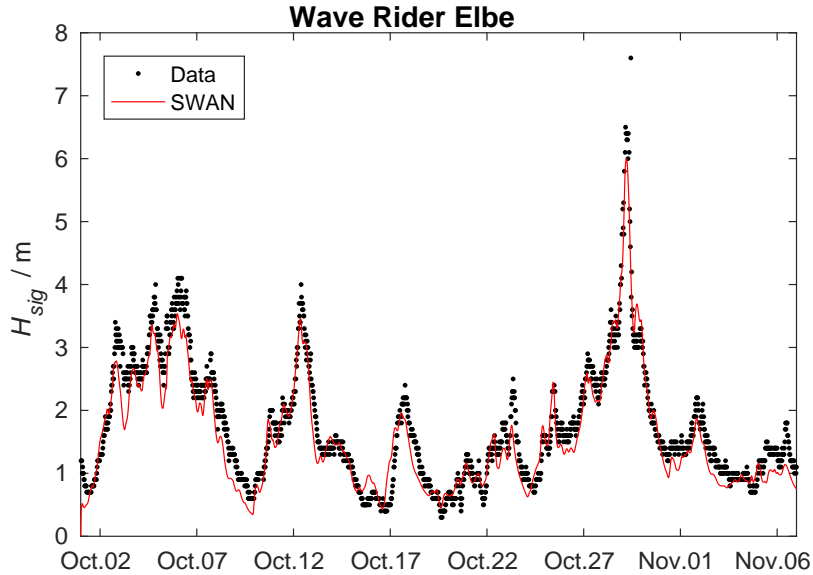
Figure 27: Comparison of significant wave heights H_{sig} to measurements at the wave rider Elbe $(8°7', 54°0')$. Measurements are depicted by black dots, a red line is indicating model results from the GB-Model.

During the BLEX experiment, discussed in section 7, an [RBR] wave logger was deployed at $(E7°41'6'', N53°48'40'')$, measuring significant wave heights and peak periods at the $10\,\mathrm{m}$ water line north of the island Spiekeroog. Measurements for a period from October 1st until November 7th, 2017 are shown in Figure 28 (black dots) and compared to model results (red line). Computed wave periods are again persistently lower than measured data whilst significant wave heights are slightly overestimated during calm periods, e.g. on October 21st. Parameter studies, shown in Appendix G, revealed that wave parameters are well described either for calm or windy periods and parameters have to be tuned accordingly.

4.3.3. EI Model

Meteorological and river discharges in the EI-Model are identical to the GB-Model. The model can either be used in one-way or two-way coupling

---

[112]Located at $(8°7', 54°0')$, see Figure 18.
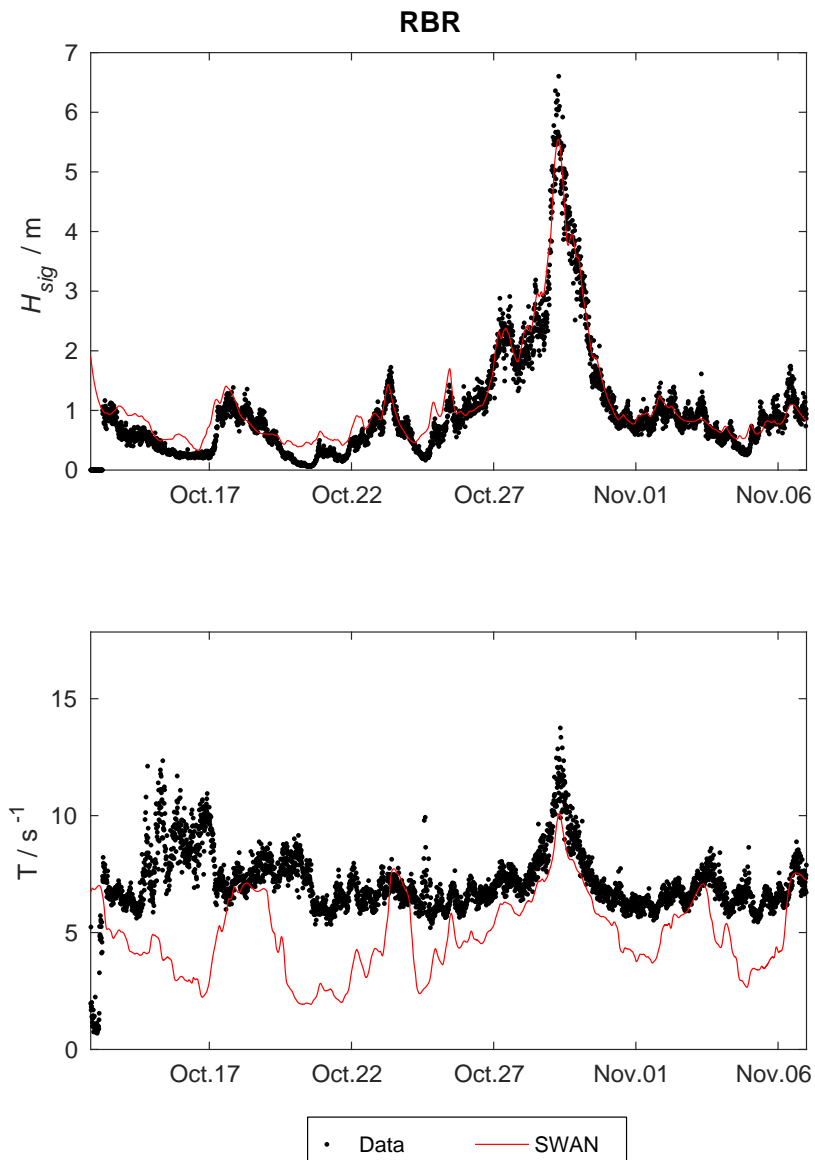
Figure 28: Comparison of computed significant wave heights H_{sig} and mean absolute wave period $TM01$ to the measured RBR data at $(E7°41'6'', N53°48'40'')$. Wave directions are shown using nautical convention.

applications. In this section, validation with measurements is shown for an offline one-way coupling application over the course of mid July 2018 until the end of September 2018. Hydrodynamic and wave boundaries were derived from a previous GB-Model simulation. Results of monthly mean submergence times, bottom stresses, salinities and temperatures were computed for a collaboration with Dr. Anja Singer[113]. Results based on two-way

---

[113]Senckenberg Joint Professorship *Benthos Ecology* at the ICBM.

coupled configurations are not shown, as these are prone to stability issues in long- to mid-term runs aside of principle studies.

Sea Surface Elevation   Comparisons of computed SSE, gauge measurements and BSHcmod data at *LT Alte Weser* (Figure 85), *Bake A* (Figure 86) and *Spiekeroog* (Figure 87) are shown in subsection B.3. At each gauge station, data of the EI-Model and the BSHcmod are almost indistinguishable and are consistent with measurements.

Salt and Temperature   As in the GB-Model's case, computed salinities at *Leuchturm Alte Weser* from the EI-Model deviate from measurements (not shown). Being located in the vicinity of the Weser and Elbe river mouths, this pile is exposed to constantly changing fronts. Thus reconstructing measurements exactly is almost impossible, when models are driven by too sparse datasets[114]. However, comparing model data from adjacent grid points to gauge data shows indeed satisfactory agreement. Figure 29 shows a comparison of monthly mean surface salinities (August 2018) computed by the EI-Model (top panel) with BSHcmod data (top-mid panel). Values of both models agree well, depicting fresh water inputs from the rivers and a front near the Weser and Elbe rivers in the eastern area. The EI-Model is better resolving small scale patterns due to its higher spatial and temporal resolution. However, the front is located slightly farther offshore in the BSHcmod, almost reaching the pile *LT Alte Weser* (diamond symbol). Salinity variations, depicted by standard variations for August 2018 in the lower-mid and bottom panels, reveal turbulence patterns in the EI-Model, which are absent in the BSHcmod, thus highlighting the finer spatial resolution of the EI-Model. These plots are also indicating noticeable salinity variations at the gauge location.

Top-bottom differences of monthly mean salinities for the same period, shown in Figure 88 (subsection B.3), also agree between both models, with the EI-Model better resolving vertical stratification in shallow coastal areas and near rivers. These differences are predominantly caused by the BSHcmod data lacking sufficient vertical resolution[115].

---

[114]In fact, datasets at hand are indeed high resolved for such hydrodynamic models.

[115]The BSHcmod is indeed capable of resolving these differences internally!
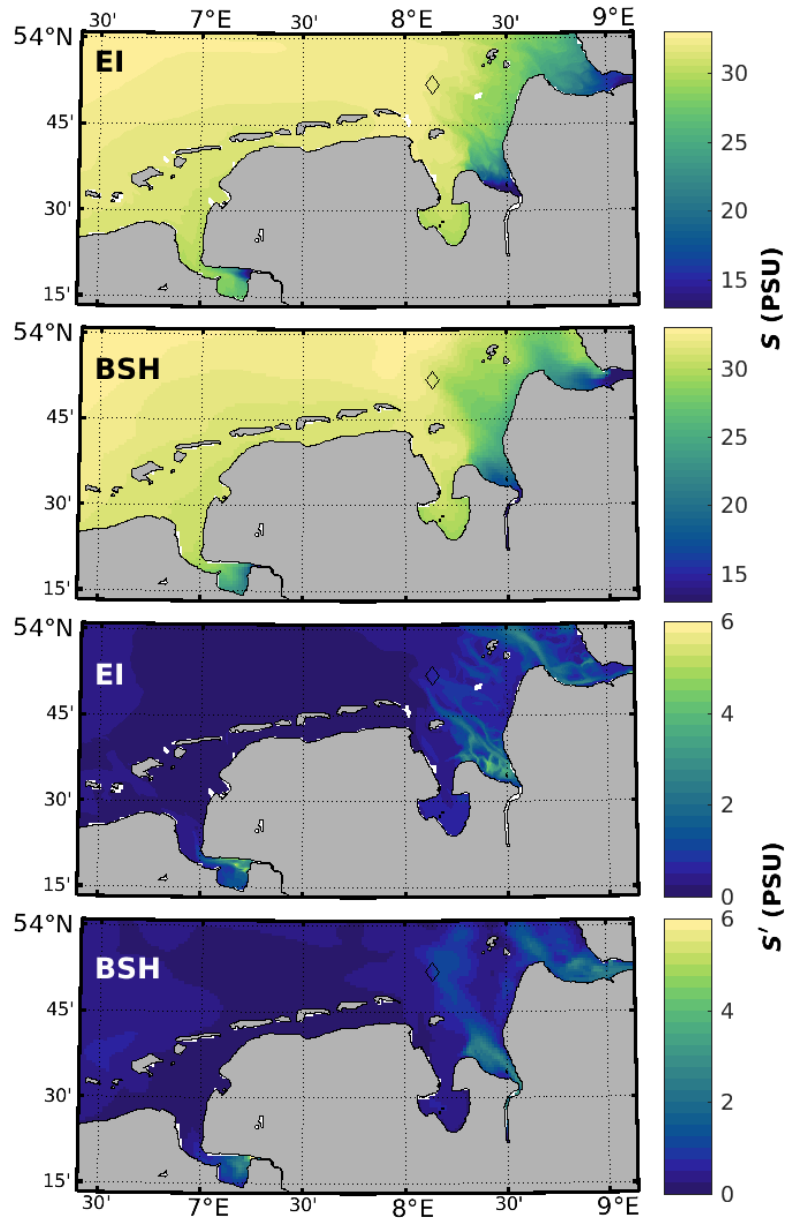
Figure 29: Comparison of monthly mean surface salinities for Aug. 2018 in the EI-Model (top) and the BSHcmod (mid-top) and corresponding standard deviations (mid-bottom and bottom). Location of the gauge station *Leuchtturm Alte Weser* is depicted by a diamond symbol.

4.3.4. SP Model

The SP-Model was developed by Wüllner [2018] and modified for evaluating combined influences of currents, Stokes Drift and wind drag on surface floats. In section 7, computed current and wave data for a period starting at October 17th 00:00:00 and ending on October 28th 00:00:00 is used in conjunction with trajectories measured by GPS-Drifters. Therefore, the SP-Model

was offline nested into the GB-Model and 10m-winds were prescribed by DWD data. Additional meteorological inputs[116] were derived from ERA5 dataset. Due to lacking measurements, validations in this section are limited to sea surface elevation and wave states. Wüllner [2018] compared simulated current velocities with measurements based on a moored ADCP[117] at the experimental site.

Sea Surface Elevation Computed sea surface elevations ζ are compared to measurements at the pile Spiekeroog in Figure 89 (subsection B.4). Computed SSE is resembling measurements during the 11 days period. Resulting tidal ranges in the model are also showing good agreement with gauge data, but are insignificantly underpredicting high waters on some days, e.g. on October 23rd, indicating marginal damping of the tidal signal in the model. After October 26th, the model starts predicting unrealistically high rising waters, but as this feature is beyond the temporal scope of the later experiments, this is considered negligible here.

Waves Modeled significant wave heights H_{sig} and wave periods $TM01$ are compared to RBR measurements at the $10\,\mathrm{m}$ water line north of Spiekeroog ($E7°41'6''$, $N53°48'40''$) in Figure 90 (subsection B.4). SWAN computations are well resolving peaks of wave heights (top panel) on October 18th, October 23rd and October 27th in height and duration. During calm states however, e.g. from October 19th until October 22nd, wave heights are slightly overestimated. Even excessive parameter studies could not lead to model configurations resembling both types of wave conditions, wherefore a compromise was chosen, accurately representing wave states for periods corresponding to drifter measurements in this area, which are presented in section 7. Peak wave periods (bottom panel) are significantly underestimated by the SWAN setup when compared to measured data. This might be caused by choosing too low cut-off frequencies in the model or by wind data lacking in temporal resolution[118] leading to inaccurately represented high frequency variations. As Stokes Drift values are calculated internally by ROMS via modeled significant wave heights and directions, inaccuracies in peak periods are assumed of minor relevance.

Modeled mean wave spectra (top left panel) are compared to WAMOS

---

[116]Solar radiation, cloud cover, air temperature, rel. humidity and precipitation.
[117]Acoustic Doppler Current Profiler, see [e.g. Thomson and Emery, 2014].
[118]In this case data on $1\,\mathrm{h}$ intervals was used.

radar measurements (top right) in Figure 30. In each panel, data spanning Box 1 of the radar cone (cf. Figure 20) were used. Shown spectra represent temporal and spacial medians of energy density for a period starting on October 21st 00:00:00 and ending on October 25th 08:30:00. The radial axis is indicating frequency values, angles are oriented in nautical convention. Computed directional distribution and the scaling of energy values in the model agree with measurements, but a modeled spreading of energies into northeastern directions (30°...60°) is absent in measurements. Computed absolute energies are slightly overestimated when compared to radar data.

Spacial medians of absolute Stokes Drift values for Box 1 are shown in the lower panel of Figure 30. Stokes Drift values were calculated using WAMOS data and equation (27) (black data) resp. derived from modeled wave heights and lengths inside ROMS (red line). Frequencies in the range $f \geq 0.35\,\mathrm{s}^{-1}$ were estimated using a high frequency tail $\propto f^{-3}$ [see e.g. Wüllner, 2018, SWAN, 2015][119]. Note also different cut-off frequencies in modeled $(1.46\,\mathrm{s}^{-1})$ and measured data $(0.35\,\mathrm{s}^{-1})$. Stokes Drift based on ROMS computations are overestimated for calm conditions during October 21st until October 23rd and during the second half of October 24th. For instances of strong wind conditions, i.e. big wave heights, however, Stokes Drift is significantly underestimated by ROMS. These differences cannot be explained by miscalculated wave heights, as computations of this parameter show good agreement with measurements at the wave logger's position (Figure 90) and hence must be caused by missing high frequencies or insufficient representation of bathymetries in the model: Installation of the radar was focused on resolving waves near a sand bank at the western tip of Spiekeroog. Wüllner [2018][120] found highly dynamic migration patterns of this sand bank when comparing measurements for the years 2016 and 2018. Even spacial resolution of the SP-Model is sufficient to resolving these patterns, they cannot be accurately represented in the model as bathymetry data on temporal basis of high resolutions is needed.

---

[119]Wüllner [2018] shows similar plots based on the same calculations and similar data. However, shown SWAN data therein differ from Figure 30, as nautical and mathematical angles were falsely translated.

[120]Personal communications, not shown therein.
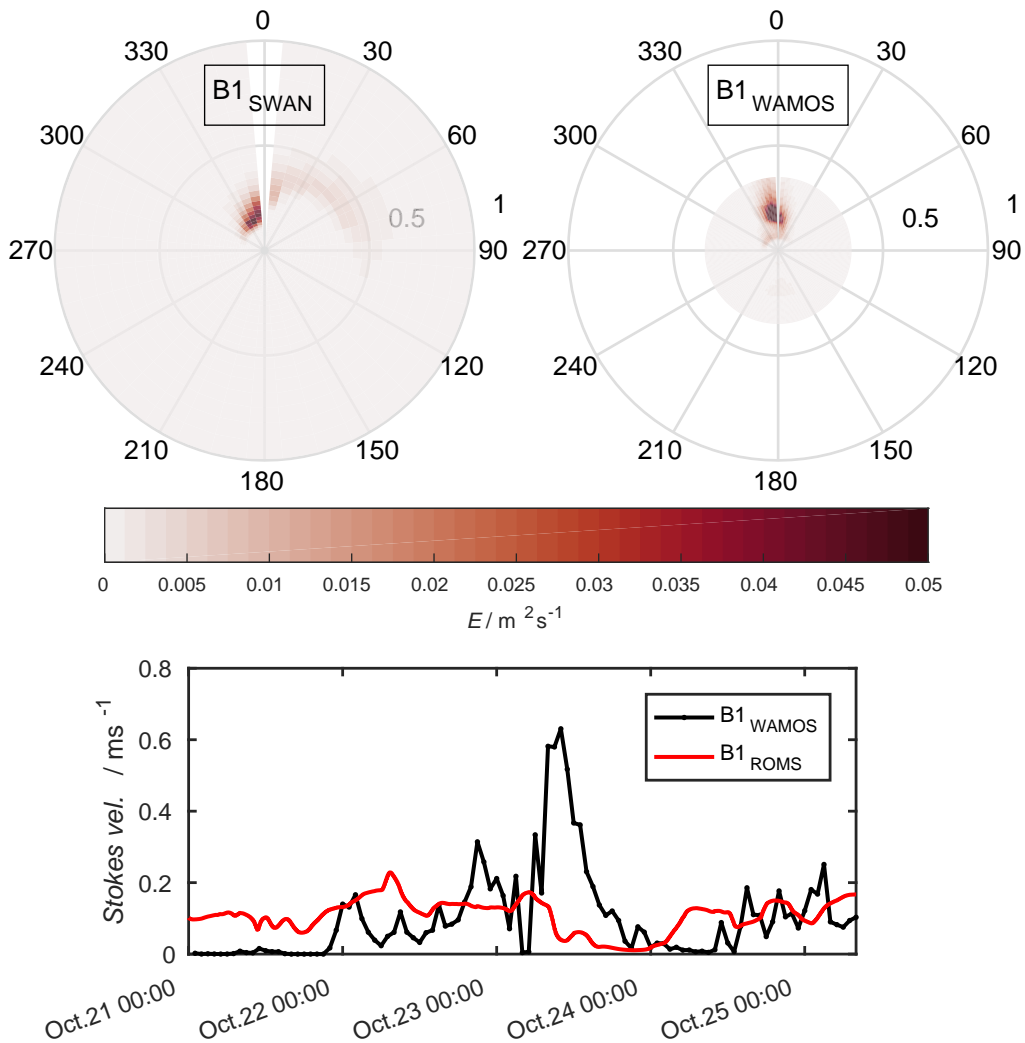
Figure 30: Comparison of modeled (top left) and measured (top right) wave spectra at the location of Box 1 (cf. subsection 3.3). Polar plots show the space-time median of the energy density from October 21st until October 25th. The radii denote frequencies and directions are shown in nautical degrees. Stokes Drifts in the lower are based on equation (25) for the ROMS case and equation (27) for the WAMOS data. Details are given n the text, calculations and representation of the plots are based on Wüllner [2018].

5. fLOPpSy: A Lagrangian Floats Matlab Model

A major focus of WP1[121] was developing an easy-to-use toolbox for calculating Lagrangian trajectories of surface litter, applying various physical properties. In contrast to the ROMS own floats module, the Floating Lagrangian Ocean Particles Prediction SYstem (fLOPpSy) allows for studying varying wind and wave drag parameters and even applying drag coefficients on surface currents. Modeled and measured data on different grids and spatiotemporal resolutions can easily be translated into matlab structs, which are then used for integrating Lagrangian trajectories using arbitrary numerical schemes (subsection 2.5) and allowing for switching between spatial grids in nesting applications. This section serves as brief description and validation of the toolbox, additional information on usage of fLOPpSy is given in Appendix C.

5.1. Basic Functionality

Computations are based on matlab structs storing gridded data of Eulerian currents $\vec{u}_e(t)$, wind velocities $\vec{u}_w(t)$ and Stokes Drift $\vec{u}_s(t)$. Velocity fields are then used in a rewritten form of conditional equation (18):

$$\vec{v}_p(t) = \underbrace{\vec{u}_e(t) + C_s\vec{u}_s(t) + \vec{u}'}_{\vec{u}_l(t)} + C_w'\boldsymbol{\alpha}\vec{u}_w(t) \tag{44}$$

giving Lagrangian trajectories $\vec{v}_p(t)$. A Stokes Drift coefficient C_s is introduced in (44) to account for additional forces of surface waves on particles. Setting $C_s = 1$ yields the term $\vec{u}_e + 1 \cdot \vec{u}_s$ to simply reflect Lagrangian current velocities $\vec{u}_l$. Wind velocities are multiplied by the rotational matrix $\boldsymbol{\alpha}$ (equation (14)) in the last term and a modified wind drag coefficient C_w', resembling the square root of equation (18), is introduced. Drag parameters can be set for each particle individually, allowing for parameter studies. Equation (44) is integrated using one arbitrary numerical scheme discussed in subsection 2.5. Choices of integration schemes and drag parameters within this thesis are given in respective sections. An overview about computational performance and accuracy of this toolbox in comparison to the ROMS floats module is given in the following subsections.

---

[121]And thus the thesis at hand.

5.2. Computational Performance

Computational efficiency is illustrated by mean values of total computation time t_{comp} in dependence of iteration numbers N_{it} for 5 individual runs of the swirl-current test described in subsubsection 2.5.4. Results of these calculations are shown in Figure 31. Time stepping lengths in seconds are denoted by small numbers for each marker. Computing times are exponentially increasing with numbers of iterations for each scheme. Using a simple Euler integration results in short computation times whereas using a Runge-Kutta scheme leads to slowest computations. However, considering accuracies of each integration method (Figure 12), Runge-Kutta integrations are most efficient in the sense of *computation time* to *accuracy* relations. Bilinear interpolations of velocity fields at each predictor and corrector time step using build-in MATLAB-interpolation methods are the bottleneck of this toolbox, resulting in memory-hungry applications. Errors when running FLOPPSY on computers with less than 16GB of RAM are likely. Thus, swapping out integrations to FORTRAN- or C-code should be taken into account in the future[122].

5.3. Handling of Nested Grids

Trajectories can be calculated using velocity fields of differing spatial and temporal resolutions. Checking actual particle positions at each iteration[123] ensures using available velocities of finest resolutions. An example for processing ROMS data to allow for this functionality is given in Appendix C.

Switching of particles between nested coarse and fine ROMS grids is illustrated by trajectories presented in section 6. Therein an online coupling applications of the GB-Model and SI-Model was used, investigating influences of surface currents, Stokes Drift and wind drag on surface drifting objects in nearshore regions at the barrier island *Spiekeroog*.

5.4. Comparison: ROMS vs. fLOPpSy

To illustrate the accuracy of integrated trajectories by FLOPPSY, Figure 32 shows a comparison of two trajectories calculated by the ROMS' internal

---

[122]Translating the PTRACK-function (see Appendix C) into mentioned programming languages and writing an interface for transferring floats and velocity structs with MATLAB is advised, as setting up applications and evaluation using the FLOPPSY-toolbox would remain fully functional.

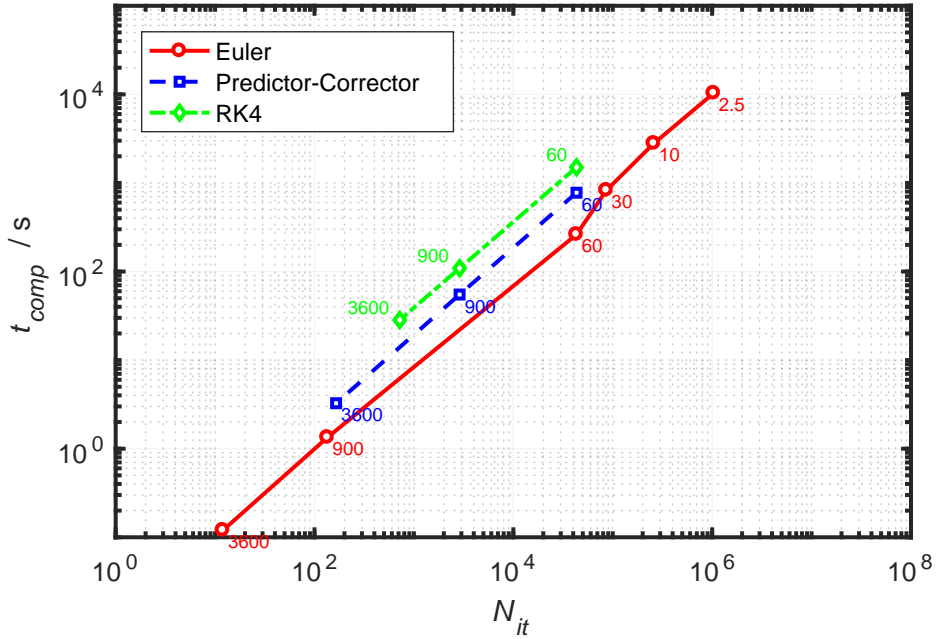[123]This is checked by the `Which_grid`-function of the toolbox.

Figure 31: Computational Performance of the Floppsy toolbox. Inside the `ptrack`-function total computational time t_{comp} for all itetations are calculated via MATLAB 's `tic` and `toc` function. Here, total computation times for different time steps of the rotational current test of subsubsection 2.5.4 are plotted versus the respective number of iterations N_{it}. For clarity, marks of each test are connected with lines. Small numbers at each mark denote corresponding time steps dt according to subsubsection 2.5.4.

FLOATS module (red trajectories) and FLOPPSY. FLOPPSY trajectories were calculated using RK4 integration with 5 min time stepping size and using ROMS surface currents of 10 min temporal resolution, corresponding to most "real" applications. FLOATS was using ROMS' surface currents at each time step of 5 s. Similar plots for various integration methods using time stepping lengths of 20 min resp. 5 min are shown in Appendix D.

Starting locations were based on GPS-drifter data from Meyerjürgens et al. [2019], current velocities were based on a one-year run from October 2016 until December 2017 using the GB-Model. Velocity values on masked landpoints were set to NaN inside FLOPPSY computations. Numerical handling of landpoints and its consequence on beaching parametrization is discussed in section 6.

Trajectories agree well over the course of 35 days (lower panel of Figure 32) with errors of less than 1 km (inlet graphs), corresponding to lateral resolutions of the current data. FLOATS are not penetrating water-land

interfaces at permanently masked landpoints[124]. In contrast, beaching occurs in all FLOPPSY calculations due to coarser temporal resolutions and longer time stepping sizes. However, beaching sites might be very possible for in-situ drifters, even though predictions are not coinciding with terminal locations of GPS-Drifters shown by Meyerjürgens et al. [2019], presumably a consequence of neglecting wind drag and Stokes Drift in these calculations.

Comparing various integration methods and time stepping lengths in Appendix D shows similar results when using improved Euler and RK4 integrations. Differences to FLOATS trajectories are significantly less when these methods are chosen over a simple Euler approach. Small differences between improved Euler and RK4 trajectories hint towards temporal resolutions of velocities as limiting factor.

---

[124]Normal currents at landmasks are vanishing due to *Nil*-boundary conditions inside ROMS.

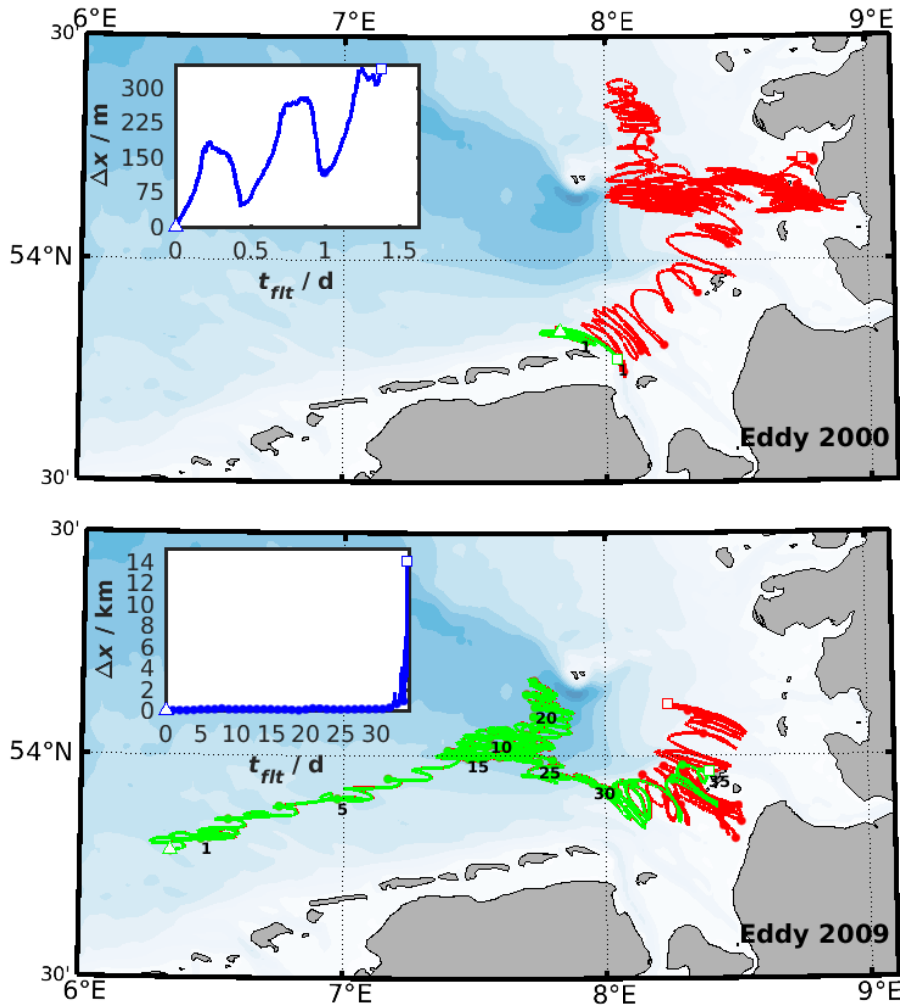Figure 32: Comparison of Lagrangian trajectories, calculated by FLOATS
(red trajectory) and FLOPPSY (green trajectory). Inlet graphs
show temporal evolution of distances between both models. 24 h
intervals are denotes by dots and numbers. FLOPPSY calcula-
tions were based on 10 min outputs of the GB-Model, FLOATS
trajectories were calculated inside ROMS using the model's time
stepping length $dt = 5\,\mathrm{s}$.

6. Wind, Waves and Surface Currents in Nearshore Regions

Even though physical processes for describing advection of Lagrangian particles in numerical models are well known, as described in section 2 and cited literature therein, the exact role of each quantity and its implementation into numerical models is still prospect of current research. For particles in offshore regions, wind and surface currents might be main drivers for particle distribution, whereas waves are of secondary importance. In deep waters, bathymetry is not affecting surface currents and surface waves significantly. Hence Stokes Drift, which is quadratically dependent on wave amplitudes (equation (25)) and parallel to local wind directions [e.g. Durgadoo et al., 2021], can be approximated by tuning wind drag in the absence of lateral boundaries like islands and coasts [Röhrs et al., 2012][125]. However, e.g. Röhrs et al. [2012] showed advection by Stokes Drift is excelling wind drag by a factor of two for drifters of iSPHERE type [MetOcean] and Carniel et al. [2009] found including dissipation processes due to wave breaking is improving long-term accuracies of trajectories in coupled ROMS-SWAN-applications.

Contributions of tidal currents, wind drag and Stokes Drift to particle advection and beaching processes in nearshore regions were investigated using the SI-Model and GB-Model in a two-way nesting application. Three different scenarios of varying wind and wave influences were considered and Lagrangian trajectories for each scenario were calculated using FLOPPSY. A detailed description of each scenario is given in subsection 6.2. Differences in beaching sites due to numerical handling as well as Lagrangian trajectories and diffusion patterns are shown in subsection 6.3 followed by a conclusion about the importance of each respective physical property in subsection 6.4. This academical test is expanded in section 7 using in-situ conditions for October 2017 and GPS-tracks of Box-drifters.

6.1. Methods

Hydrodynamics, winds and waves have been computed using the GB-Model and SI-Model in a two-way nesting application, considering three scenarios: (A) solely tidal forcing, (B) tidal and wind forcing, (C) tidal forcing and

---

[125]Describing wind drag via drag coefficients for Stokes Drift is also possible, see e.g. Durgadoo et al. [2021].

waves (see subsection 6.2). Particle trajectories were then calculated using the FLOPPSY toolbox and RK4-integration. Beaching of particles was not explicitly parametrized, just occuring due to numerics as described in sub-subsection 2.6.1. In theory, numerical beaching could be avoided by securing time stepping lengths dt satisfy the CFL-criterion.

Additionally, particles could not be advected by sole wind drag, thus sticking on *dry* model grid points until these were getting *wet* again[126]. This constraint is avoiding particles from 'flying' above landmasses, where no currents are present at all[127].

Numerical Beaching   Numerical grid points on German headlands and the Eastfrisian Islands are permanently masked as 'land' in both nested model grids. In Lagrangian computations surface velocities were set to *Nil* or *NaN*[128] at such land points (cf. subsection 2.6). These two options also affect potential beaching events and their location due to spatial interpolation of velocity values at such locations. Both approaches were tested in a first scenario, forcing the hydrodynamic model by tides and winds. The *Nan*-case was then used in the latter scenarios, supressing resuspension of beached particles.

Definition of Particle Clusters   Particle clusters $Clst_i(N, t, r_{max})$ are defined as sets of N particles with maximum distances of r_{max} to at least one particle of this respective set at time t:

$$Clst_i(N, t, r_{max}) := \{\vec{x}_j(t) \mid |\vec{x}_k(t) - \vec{x}_l(t)| \leq r_{max} \text{ for } k \neq l, N \geq N_{min}\}$$
(45)

Patches of at least two particles with maximum distances of $r_{max} = 600\,\text{m}$ were defined as clusters in each scenario by setting $r_{max} = 600\,\text{m}$[129] and minimal cardinal numbers $N_{min} = 2$. Note $|\vec{x}_k(t) - \vec{x}_l(t)|$ is a pairwise distance of two distinctive particles k and l, i.e. pairs of particles with distances $\geq r_{min}$ are generally found in clusters.

---

[126]ROMS allows for *drying* of grid cells, when an arbitrary critical water depth is reached. *Wetting* then occurs when critical water depth is exceeded again.

[127]Note this does not prevent particles from moving on and above landmasses, if a very long time step dt is chosen.

[128]*Not a Number*.

[129]Corresponding to spatial sizes of 3 adjacent grid cells in the finer model grid and $\frac{3}{5}$ grid cells in the coarser grid.

Cluster Statistics   As equation (45) incorporates degrees of freedom on the two-dimensional *lon-lat*-plane[130] for a fixed time t, description of cluster positions and spreading of particles is done via multidimensional statistics. A comprehensive overview on these statistical methods is given by Schönwiese [2013].

Cluster centers can either be defined by using the vectorial mean

$$S(t) = (\bar{x}, \bar{y}) = \frac{1}{N} \sum_{i=1}^{N} \vec{x}_i \tag{46}$$

or by the vectorial mode

$$Mod(t) = (x(t)_{i,max}, y(t)_{i,max}) \tag{47}$$

Here, $x_{i,max}$ and $y_{i,max}$ denote coordinate bins containing maximum particle counts. Both values are computed by counting numbers of particles within two-dimensional *lon-lat*-bins and are therefore depending on binning sizes. In the following, the term *cluster center* will refer to the vectorial mean of equation (46) if not stated otherwise. Note equation (46) is equivalent to the definition of a body's center of mass with homogeneous density distribution[131].

Spreading of particles within each cluster is quantified by the vectorial central moment

$$ZM_k(t) = \left(x'^k, y'^k\right) = \frac{1}{N} \sum_{i=1}^{N} (\vec{x}_i - S(t))^k \tag{48}$$

Here x' and y' denote deviations of each particle's coordinates from cluster centers. Using $k = 2$, the square root of equations (48) equals the standard deviation of particle coordinates within each cluster. The vectorial standard deviation SD is also used for measuring spreading of particles:

$$SD(t) = \sqrt{\frac{1}{N-1} \sum_{i=1}^{N} \left(x_i'^2 + y_i'^2\right)} \tag{49}$$

$x_i'^2 = (x_i - \bar{x})^2$ and $y_i'^2 = (y_i - \bar{y})^2$ are squared spatial deviations from cluster centers for each particle i. Note, in contrast to equation (48), the standard

---

[130]Or x-y-plane when regarded in a cartesian framework.
[131]Corresponding to identical types of litter items or GPS-Drifters in each ensemble.

deviation SD is not regarding x- and y-deviations separately, but can be interpreted as *mass inertia*, used in classical mechanics.

6.2. Model Scenarios

Distinctive effects of *tidal currents*, *wind drag* and *Stokes Drift* on Lagrangian trajectories at the surface layer are evaluated using the GB-Model and SI-Model in a nested-grid application. Three configurations of these hydrodynamic models were evaluated by varying forcing conditions. In each model scenario, ensembles of $7 \times 7 = 49$ particles were released inside a rectangular area near the island *Spiekeroog*, located in the SI-Model's grid. Ensemble centers were located in a distance of $2.5\,\mathrm{km}$ from the island's northern shoreline. Particles were initially separated by $200\,\mathrm{m}$, corresponding to coordinate spacings of the hydrodynamic grid, hence releasing one particle at each ρ-point inside this area. A total number of 4 ensembles was set for each scenario at varying states of the tidal cycle: ① released at low tides, ② and ④ released at zero-crossings of the rising resp. falling tidal elevations, ③ released at high tides. Release locations and temporal placing of each ensemble are illustrated in Figure 33. Lagrangian trajectories were computed for a 14 days period using the FLOPPSY toolbox and regarding a spin-up time of one day in the hydrodynamic model[132]. Lagrangian computations were terminated after reaching the end of this 14 days period resp. considering all particles as beached.

Influence of Numerics on Beaching   In a first test, effects of time stepping and handling of land points (*Nil* or *NaN*) on *numerical beaching* (subsubsection 2.6.1) were tested. Therefore, terminal particle locations of computed trajectories based on surface currents and direct windage were compared. Thus a constant wind drag coefficient $C_w = 1.4 \times 10^{-2}$ was used in two different integration schemes (Simple Euler and RK4). Potential differences between *Nil*- and *NaN*-cases on coastal distributions of beached particles were then evaluated by comparing results based on time stepping lengths of $dt = \{25\,\mathrm{s}, 5\,\mathrm{min}, 10\,\mathrm{min}, 20\,\mathrm{min}, 60\,\mathrm{min}\}$. These time steps were chosen with respect to the CFL-criterion and temporal resolution of the modeled

---

[132]I.e. releasing ensembles at respective tidal cycles of the second day after model initialization.
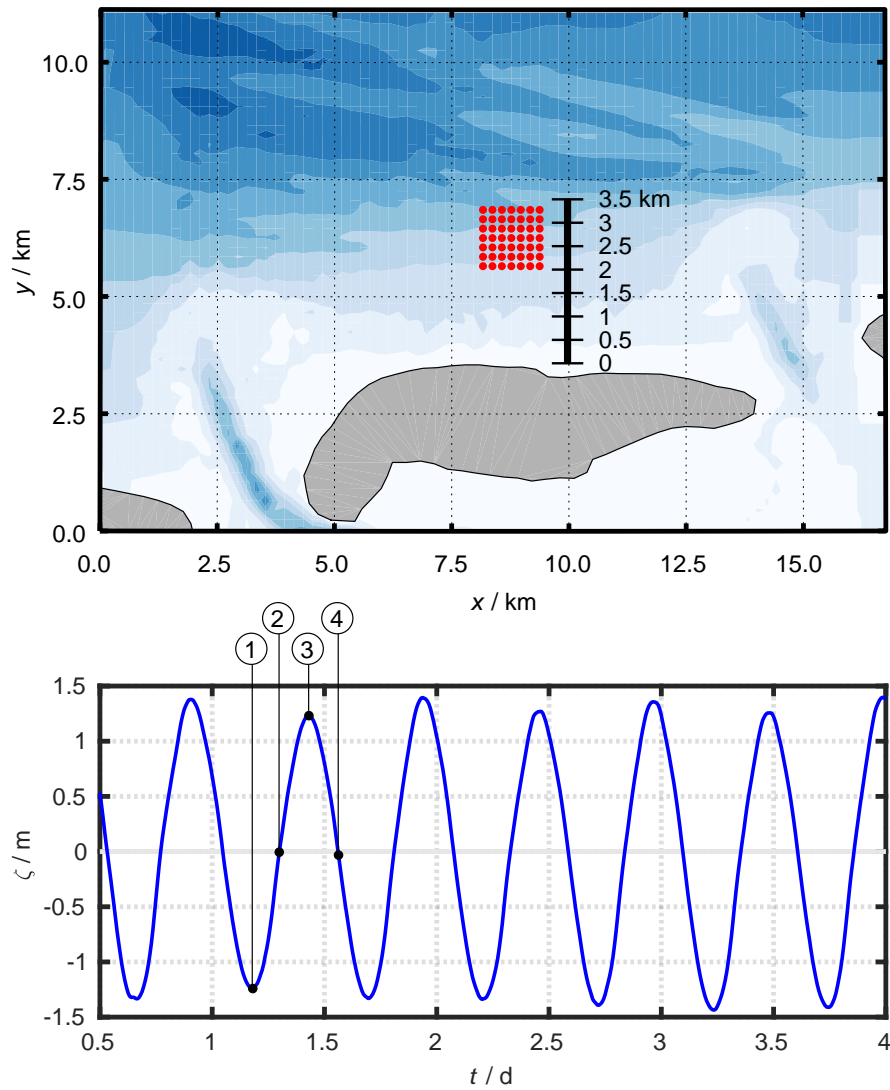
Figure 33: Starting positions (top panel) and times (bottom panel) of La-
grangian particles. Top: Red dots indicate individual particle
locations, bottom depths are shown by contours of $2.5\,\mathrm{m}$ spac-
ing. Bottom: Temporal evolution of sea surface elevation ζ at
the center position of the release area. Release times, denoted by
circled numbers, are placed during the first flood and ebb cycle
of the hydrodynamic model after a spin-up time of one day.

surface currents[133]. Courant numbers (C_u, C_v) for each time step are[134]

$$
\begin{aligned}
C_u = \frac{u_{max} \cdot dt}{\Delta x} &= \{0.29, 3.42, 6.85, 13.69, 41.07\} \\
C_v = \frac{v_{max} \cdot dt}{\Delta y} &= \{0.84, 10.72, 21.43, 42.87, 128.61\}
\end{aligned}
\tag{50}
$$

where $\Delta x = \Delta y = 200\,\text{m}$ is the horizontal spacing of the nested SI-Model-grid and u_{max} and v_{max} are maximum advecting velocities[135] within modeling period. Each time stepping lengths, except $dt = 25\,\text{s}$, is exceeding $C_{u,v} = 1$. Note the CFL-criterion is less strict when using an RK4 integration scheme.

Additionally, a location based beaching algorithm (cf. subsection 2.6) was tested. Here particles were discarded from integrations when passing grid cells neighbouring land points.

Scenario A Forcing of the GB-Model was solely derived from surface elevation data and baroclinic velocities from the BSHcmod with initialization on October 1st, 2016 at 00:00:00 (UTC). Atmospheric forcings (i.e. winds) and waves were neglected. Comparing modeled surface elevations of Scenario A (Figure 33) with measurements from the pile near Spiekeroog (Figure 87) show similar magnitudes of tidal elevations and periods. Hence tidal currents are realistically represented by this scenario. Lagrangian trajectories were then calculated using these tidal driven surface currents. Additionally, the influence of particle diffusion via a Random Walk, using (32) in equation (44), on beaching was evaluated in this scenario.

Scenario B Based on Scenario A, analytical winds of $6\,\text{m}\,\text{s}^{-1}$ amplitude were added, using constant wind directions of $280°$[136]. Thus resulting in constant onshore directed winds of $10°$ inclination towards the German coast. Wind stress was calculated by the drag formula of Yelland and Taylor [1996] using a constant drag coefficient of 2.6×10^{-3}. In the Lagrangian model, three wind drag coefficients of $C'_w = \{0.0, 0.7, 1.4\} \times 10^{-2}$ were applied[137]. Deflection of Leeway drift was neglected in this scenario, i.e. $\alpha = 0$ in equation (44).

---

[133]Corresponding to fractionals or multiples of the velocity data's temporal spacing of $dt_{data} = 10\,\text{min}$

[134]Given in ascending order according to dt.

[135]I.e. the sum of surface current velocity and direct windage $C_w \cdot u_w$.

[136]In mathematical degrees.

[137]The latter corresponding to best fit values for GPS-drifter data by Heinrich [2018], whereas $C'_w = 0.0$ is corresponding to submerged particles in the surface water column.

Table 5: Overview of Scenarios A to C.

Scenario	Hydrodynamic Model	Lagrangian Model
A	Tidal Forcing:	Surface Currents $\vec{u}$
	SSE and Currents from BSHcmod	
B	Tidal Forcing (Scenario A)	Surface Currents $\vec{u}$
	Surface Momentum Flux:	Wind Drag $C_w \cdot \vec{u}_w$
	Analytical Winds, $u_w = 6\,\mathrm{m\,s^{-1}}$	$C_w = \{0, 7, 14\} \times 10^{-3}$
C	Tidal Forcing (Scenario A)	Surface Currents $\vec{u}$
	Surface Waves (SWAN):	Stokes Drift $C_{St} \cdot \vec{u}_w$
	JONSWAP-spectrum, $H_{sig} = 2\,\mathrm{m}$	$C_{St} = \{1.00, 0.50, 0.25\}$

Scenario C   Again starting from Scenario A, additional waves were computed using a JONSWAP-Spectrum at open boundaries of the GB-Model. Therein a significant wave height of $H_{sig} = 2\,\mathrm{m}$ and mean wave directions parallel to winds of Scenario B were prescribed. Inside the modeling grid, wave parameters were computed by coupling of ROMS and SWAN, regarding current-wave interactions via Vortex Forces. Stokes Drift was then added to surface currents using three drag parameters $C_{St_i} = \{1.00, 0.50, 0.25\}$ in the Lagrangian model, resulting in $\vec{u}_l = \vec{u}_e + C_{St}\vec{u}_{St}$ in conditional equation (44). A short overview on each scenario is given in Table 5.

6.3. Results

6.3.1. Numerical Beaching

Figure 34 shows beaching locations, i.e. terminal positions of each Lagrangian trajectory, when grid points on the model's landmask are handled as *Nil*. In each panel, beaching locations for an Euler (orange squares) and RK4 integration (cyan dots) are shown. Clusters have been identified regarding maximum particle distances of $r_{max} = 3 \cdot \Delta x = 600\,\mathrm{m}$, with Δx being the model grid's spatial resolution, and a minimum number of $N_{clust} = 2$ particles per cluster. Cluster centers and respective particle numbers are denoted by red (Simple Euler) and blue (RK4) crosses and numbers. Irrespective of integration steps dt, all particles beached after at least 14 days. Two main beaching locations can be identified at the northern coast of the island Spiekeroog resp. the German coastline between $E7°45'0''$ and $E7°52'50''$. In case of RK4 integrations, varying time stepping length dt resulted in almost absent differences of cluster locations, sizes and numbers.

Satisfying the CFL-criterion by using Euler integrations with $dt = 25\,\mathrm{s}$

resembled Cluster Centers and respective particle counts of RK4 results. However, results of both integration schemes quickly differ with raising dt. Hence, growing numbers of particles are reaching the German coast with increasing time stepping lengths in the Euler case, shifting overall distributions into southeastern directions. Using $dt = 60$ min, particles were quickly beaching at the coasts of Spiekeroog and Langeoog (located at the eastern border). This effect is less prominent when using an RK4 integration scheme due to each successive predictor and corrector steps. Note time stepping lengths beyond 10 min might be unreasonable choices in such dynamic regions of fine spatiotemporal geographical and velocity features.

Similar plots for handling landpoints as *NaN* are shown in Figure 35. In this case, reduced numbers of particles reached the German coast when RK4 integrations were used. Satisfying the CFL-criterion in Simple Euler integrations showed similar results. Main beaching locations are located at the northern beach of Spiekeroog, but are showing a more evenly distribution when compared to the *Nil* case, forming one big cluster at this location. In each case, the barrier island prevented a majority of particles from reaching the southern located German coast.

Lagrangian trajectories for *Nil* and *NaN* cases, shown in Figure 36 resp. Figure 37, reveal underlying beaching processes. Setting masked grid points to zero velocities, particles approaching meridional shorelines[138] enter regions of vanishing v-velocities, which are directed normal to shorelines, while non-vanishing u-velocities are still present. This effect is a direct consequence of using data on an Arakawa-C-grid (cf. Figure 22) with u- and v-velocities defined on particular coordinates. Thus, parallel directed transport to shorelines occurs in regions of vanishing v-velocities, as u-velocities are still present. Resulting alongshore trajectories are specifically apparent for ensemble ② using $dt = 10$ min, shown in the bottom right panel of Figure 36. Similar numerical mechanisms are present at zonal directed shorelines, where u- but not v-velocities vanish[139]. In contrast, *NaN*-landpoints induce *NaN*-velocities[140] at adjacent particle locations (cf. subsection 2.6), terminating integrations of such trajectories. Particles then are beached indefinitely.

---

[138]I.e. landmask perimeters parallel to longitudes.

[139]This indeed is physically reasonable in hydrodynamic models, as boundary conditions prescribe vanishing normal velocities, not allowing currents to penetrate solid borders ('Wall-condition').

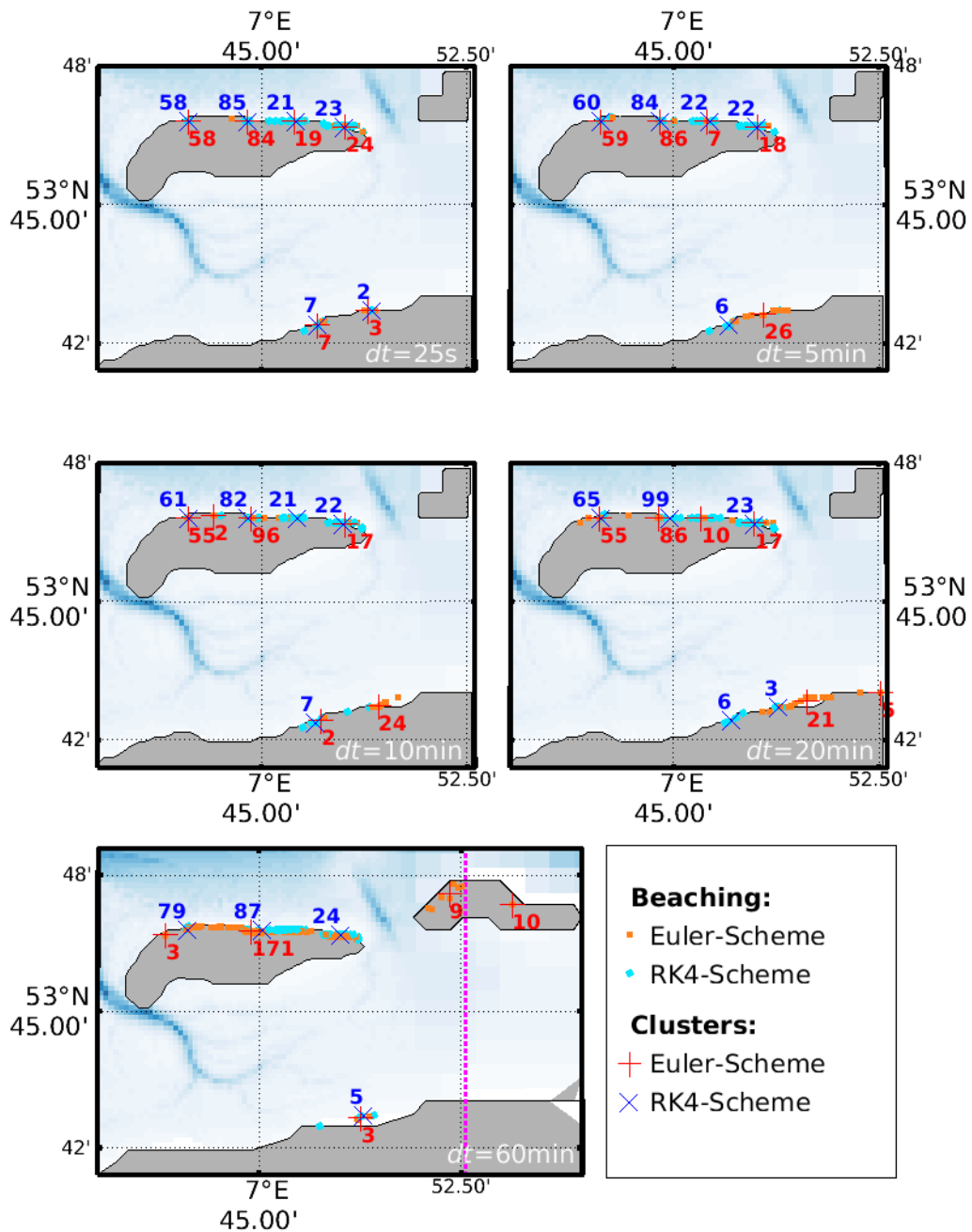[140]And hence *NaN* position vectors due to numerical integration of trajectories.

Figure 34: Beaching locations after 14 days integration time using different time stepping sizes *dt*. Orange squares and red plus-signs denote resulting beaching locations resp. cluster centers when using Euler integration, cyan dots and blue crosses denote respective parameters for RK4 integrations. Differing time stepping lengths *dt* are mentioned in each panel. In this case, landpoints were handled as *Nil*.

Using a location based parametrization of particle beaching leads to similar distribution patterns, with a majority of Lagrangian particles ending up
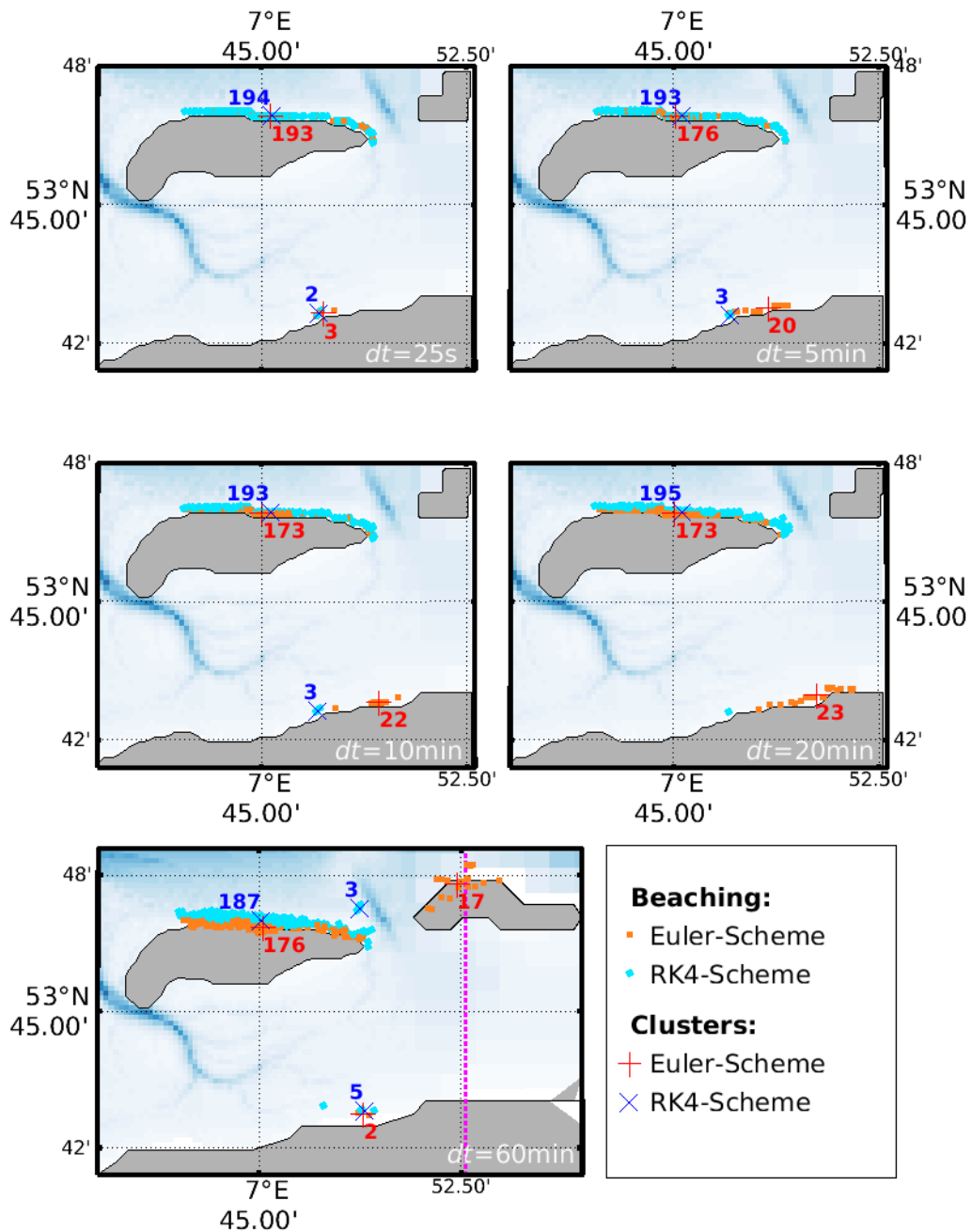
Figure 35: Beaching locations after 14 days integration time using different time stepping sizes *dt*. Orange squares and red plus-signs denote resulting beaching locations resp. cluster centers when using Euler integration, cyan dots and blue crosses denote respective parameters for RK4 integrations. Differing time stepping lengths *dt* are mentioned in each panel. In this case, landpoints were handled as *NaN*.

at the barrier island's beaches (shown in Appendix E, Figure 102). Particle distributions are less clustered when compared to the *Nil*-case without
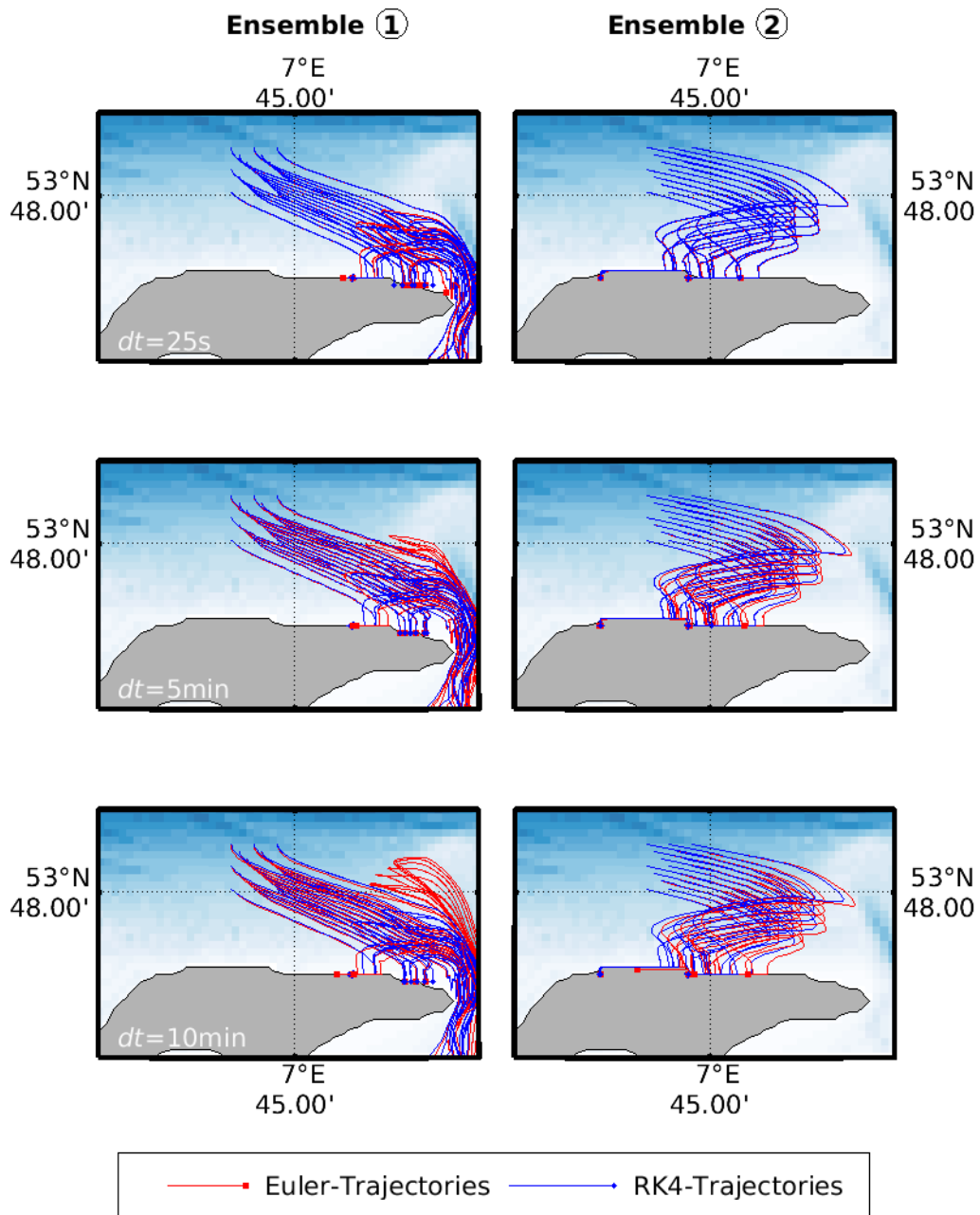
Figure 36: Lagrangian trajectories for Simple Euler (red lines) and RK4 integration schemes (blue lines) using time stepping lengths $dt = 25\,\mathrm{s}$ (top panels), $dt = 5\,\mathrm{min}$ (center panels) and $dt = 10\,\mathrm{min}$ (bottom panels). Terminal locations are indicated by squares (Euler) and dots (RK4). Landpoints were handled as *Nil* in all panels.

parametrization and time stepping lengths are impacting results to a lesser degree. In contrast to *NaN*-results, two distinguished Clusters formed at the northern beach of Spiekeroog. Extending "beaching perimeters" around
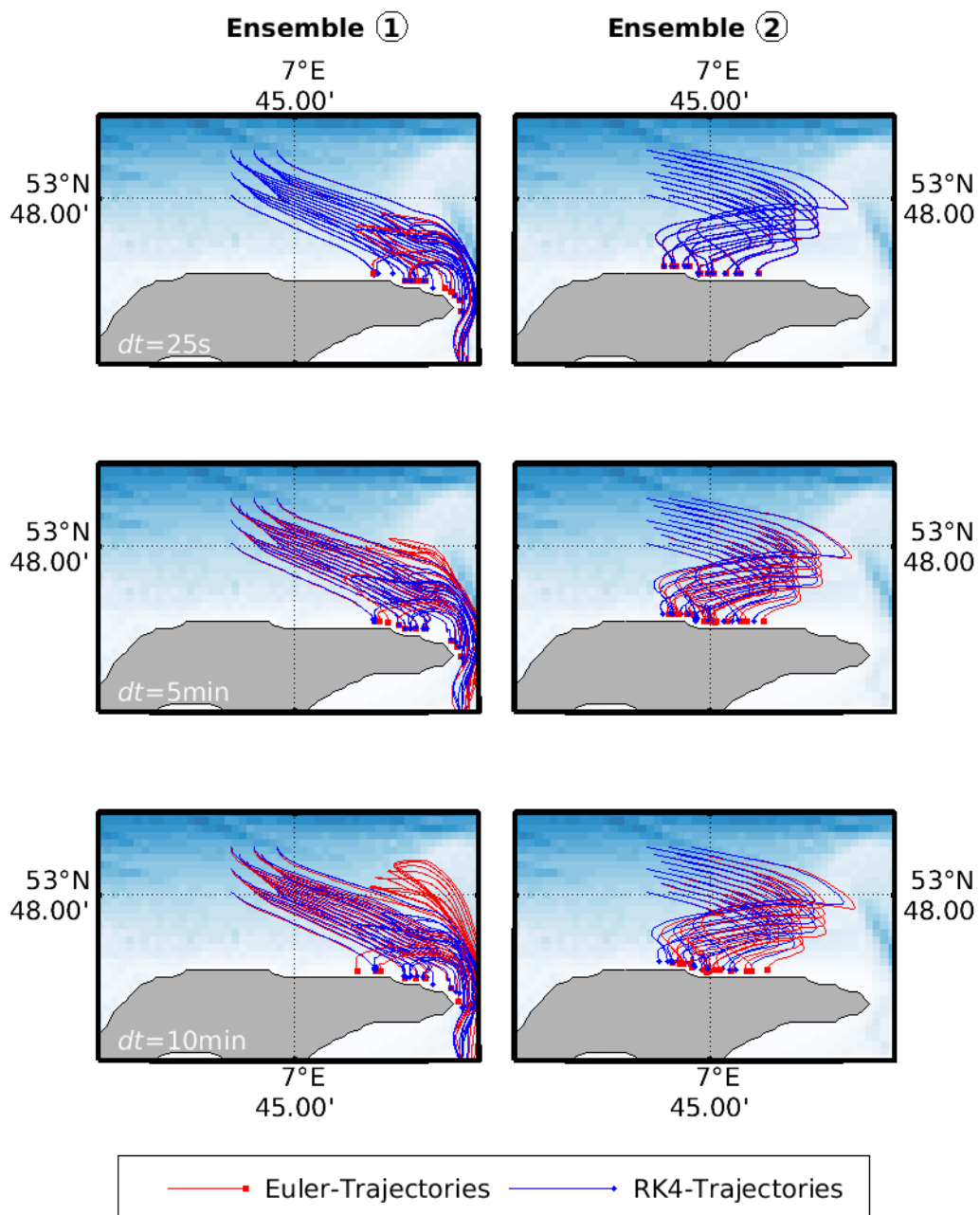
Figure 37: Lagrangian trajectories for Simple Euler (red lines) and RK4 integration schemes (blue lines) using time stepping lengths $dt = 25\,\text{s}$ (top panels), $dt = 5\,\text{min}$ (center panels) and $dt = 10\,\text{min}$ (bottom panels). Terminal locations are indicated by squares (Euler) and dots (RK4). Landpoints were handled as *NaN* in all panels.

each landmask, e.g. by one grid cell[141], is resulting in more evenly distributions of individual beaching locations at the modeling site. Note particles

---

[141]Not shown here

leaving the nested grid were not included in Figure 102.

In the following subsections, beaching of particles solely resulted by *NaN*-velocities, thus neglecting resuspension and artificial alongshore trajectories. Additionally, RK4 integrations with $dt = 5\,\text{min}$ were used in all Lagrangian computations.

6.3.2. Scenario A

Temporal Evolution of Ensembles   Temporal evolution of ensembles is illustrated in Figure 38 and Figure 39, showing trajectories for ensemble centers S calculated by equation (46) using $N_{min} = 49$ and $r_{max} = \infty$. Discrete S-locations are plotted over the course of several tidal stages. Corresponding $ZM2$-ellipses (equation (48)) for each center are shown in respective colors. Color coding and ID-numbers are illustrated by inserts in each panel using time stamps with respect to the model's reference time (x-axis) and modeled SSE, denoted as z in these plots, at the modeling domain (y-axis). Locations of individual particles are also shown by small dots of brighter colors. Time stamps correspond to increasing index times, helping identifying ensemble centers[142]. S_1 coincides with ensemble release times in each panel, ensemble-IDs ① to ④ are referenced in Figure 33.

Ensembles ① (ebb release, Figure 38 top), ② (rising Nil-release, Figure 38 top) and ④ (dropping Nil-release, Figure 39 bottom) are showing an overall drift in eastern direction with overlapping terminal S-locations within error-bounds[143] at the northern beach of the island Langeoog. However, temporal evolution of ensemble ① deviates significantly, as corresponding particles entered the tidal channel, separating Spiekeroog and Langeoog, during the first two rising tidal cycles after release. Particles were then rapidly traversing the vicinity of Langeoog, causing significantly smaller $ZM2$-values due to relatively short traveling times. The resulting S-trajectory in this case is showing tidal induced oscillating patterns with pronounced meridional-extension. This extension is caused by narrowing currents within the channel and bathymetrical features in this region. Contrary, suspension periods of ensembles ② and ④ were generally longer, resulting in progressively growing $ZM2$-ellipses, i.e. stronger diffusion. Additionally, oscillation patterns of these ensembles are pronounced in zonal-direction, even though S-trajectories are passing the tidal channel several times.

---

[142]For example S_1 denoting the center corresponding to time stamp 1.
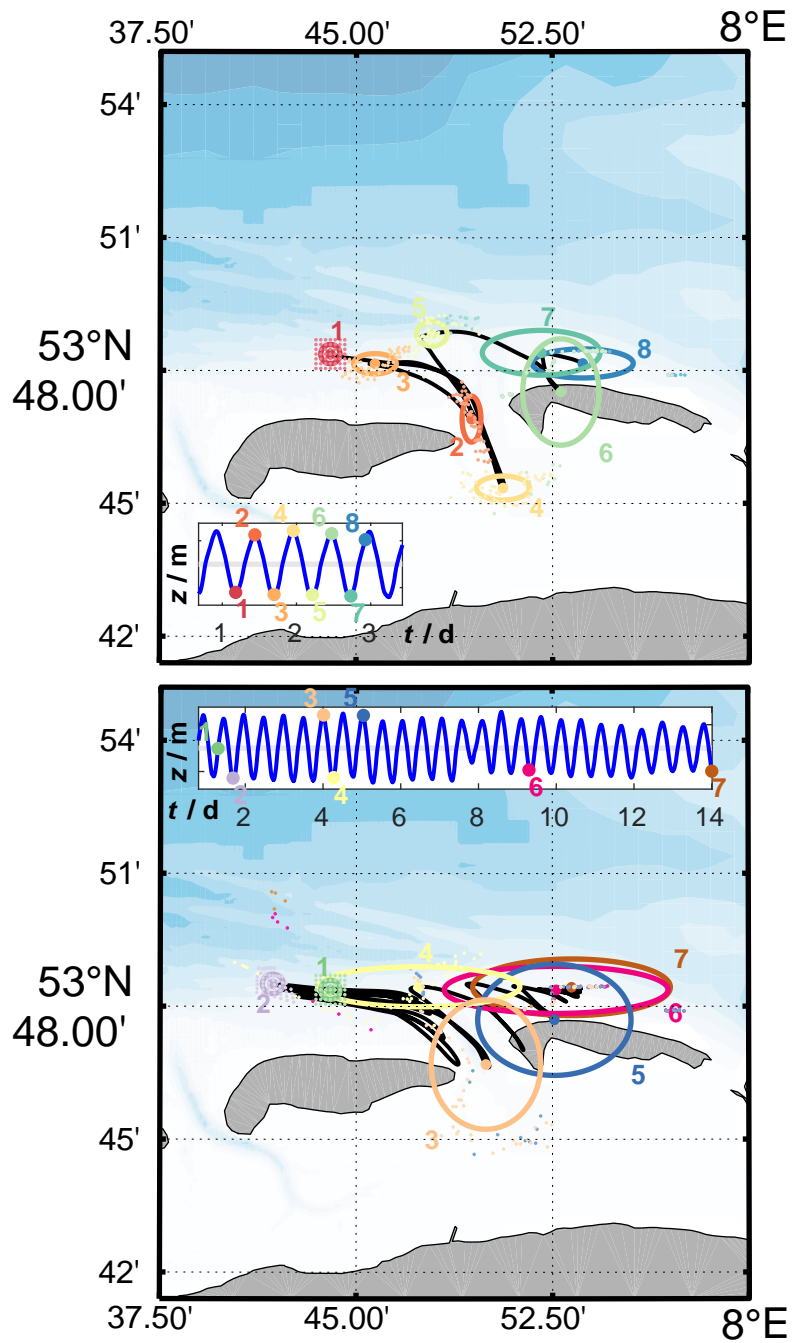[143]Defined by ZM-ellipses.

Figure 38: Trajectories of ensemble centers S for releases ① (top panel) and ② (bottom panel). Centers at discrete time steps and respective $ZM2$-ellipses are shown by bold dots and ellipses. Small, brighter dots are indicating individual particle positions. Color coding is illustrated in the inserts, showing temporal evolution of surface elevation (here z) at the modeling site. Details are given in the text.
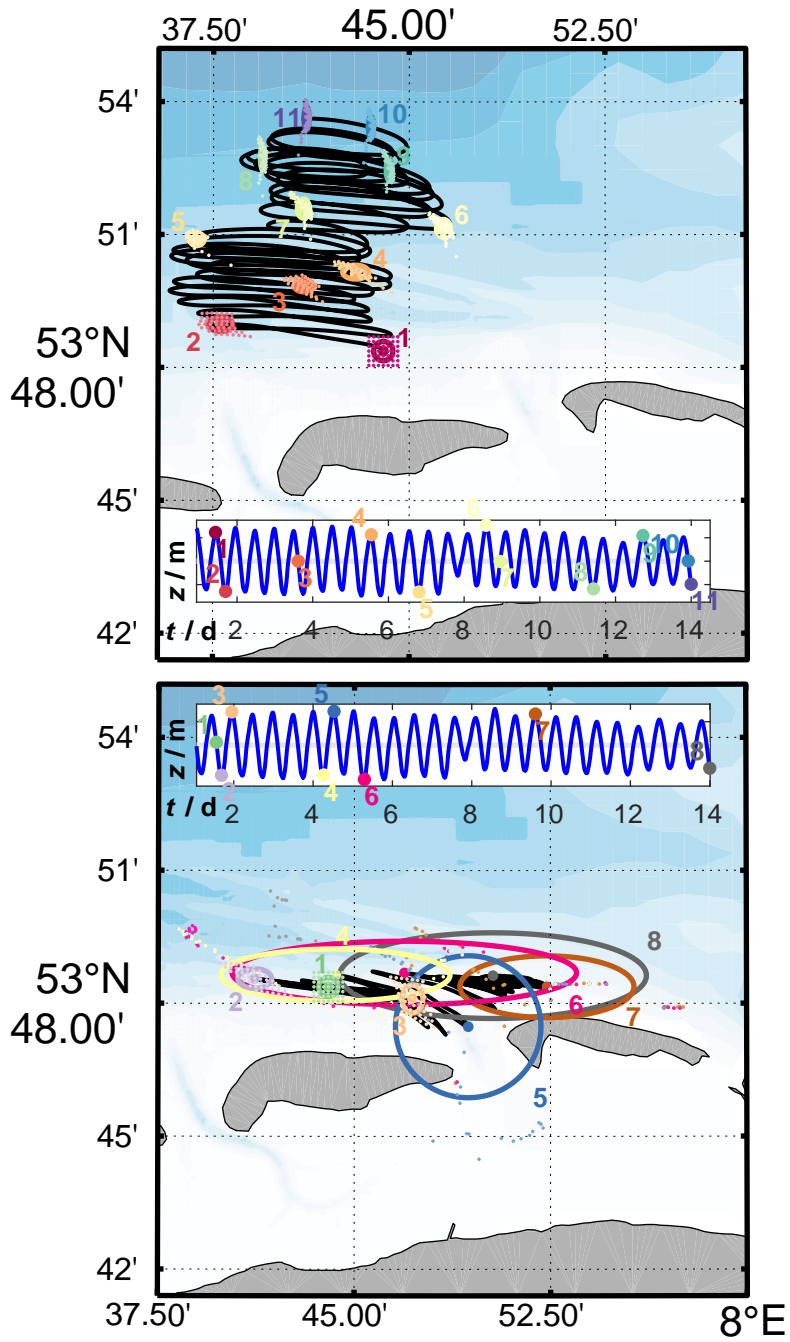
Figure 39: Trajectories of ensemble centers S for releases ③ (top panel) and ④ (bottom panel). Centers at discrete time steps and respective $ZM2$-ellipses are shown by bold dots and ellipses. Small, brighter dots are indicating individual particle positions. Color coding is illustrated in the inserts, showing temporal evolution of surface elevation (here z) at the modeling site. Details are given in the text.

Looking at ensemble ③ (flood release, Figure 39 bottom), the resulting S-trajectory is gradually moving into offshore waters. Even though suspension periods were longest for this ensemble, particle diffusion was significantly reduced. As bathymetrical features are showing minor effects on surface currents in deeper waters and particles were traveling distant from spacial boundaries, diffusion was solely caused by initial separations of particles in this case.

Cluster Formation   Further evaluation of diffusion and accumulation patterns is given by cluster formations using equation (45) with $N_{min} = 2$, $r_{max} = 600\,\text{m}$ and $t = 14\,\text{d}$. S-Trajectories and corresponding $ZM2$-ellipses of such clusters are shown in Figure 40 to Figure 43. Starting and terminal locations of individual particles are again denoted by small dots of lighter color, clusters are defined by ID and color coding. In each plot, inserted tables are showing particle numbers N, standard deviations SD for release (start) and terminal (end) cluster locations (equation (49)) as well as minimum and maximum traveling times of individual particles for reaching respective clusters (t_{min} resp. t_{max}). Thus $t_{max} - t_{min}$ is giving time intervals of beaching events in each cluster[144].

In case of ensemble ① (Figure 40), 4 clusters were forming at the northern beach of Wangerooge. Note Clusters 1 and 3 appear in about $1\,\text{km}$ distance from coastlines as these are located on the landmask of the coarse grid of the hydrodynamic model. Cluster 1 is formed by significantly larger particle numbers ($N_1 = 31$) when compared to Clusters 2 to 4. It is also showing highest SD-values, i.e. highest amounts of particle spreading. Clusters 2 and 4, located at the northwestern edge of the island, are containing same amounts of particles ($N_2 = N_4 = 5$) with minimum standard deviations. These small SD values might be caused by locating inside the finer nested grid but also by small amounts of particles in these clusters. Beaching periods for Cluster 4 are standing out as particles beached within a short period of $1.16\,\text{h}$. As located at the northwestern head of Wangerooge, this short beaching period might be caused by high velocities in the tidal channel, transporting particles over relatively long distances within short times. Tidal oscillations are visible in cluster trajectories, causing clusters to form ellipsoidal shapes. Trajectory eccentricities are oriented into zonal directions in nearshore regions north of the islands, and into meridional di-

---

[144]Note $t_{min} = t_{max} \approx 13\,\text{d}$ for offshore clusters, as no individual beaching events occur for such clusters.

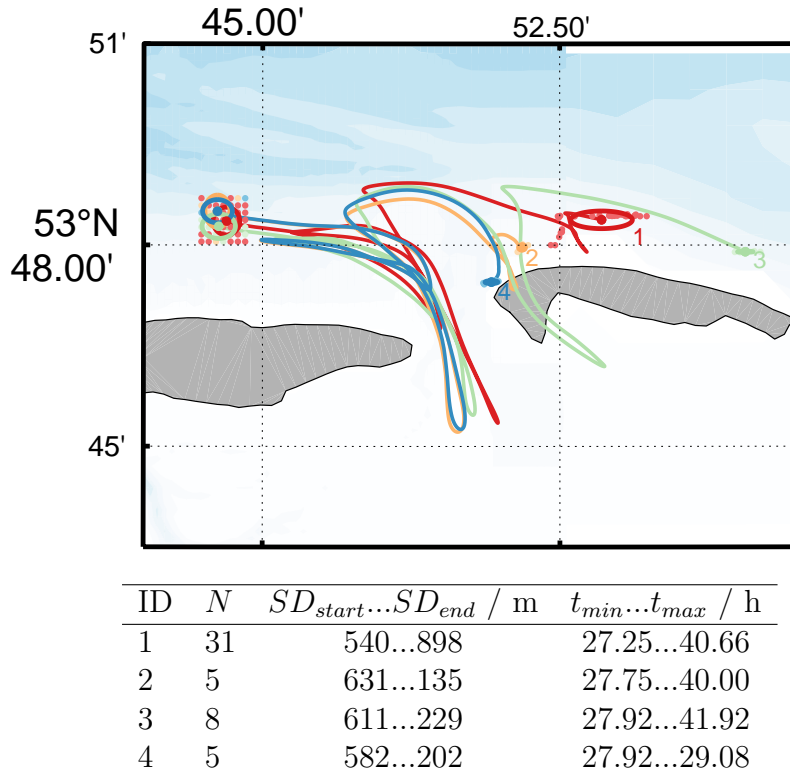| ID	N	$SD_{start}...SD_{end}$ / m	$t_{min}...t_{max}$ / h
1	31	540...898	27.25...40.66
2	5	631...135	27.75...40.00
3	8	611...229	27.92...41.92
4	5	582...202	27.92...29.08

Figure 40: Terminal cluster locations for ensemble ① as defined by (46) using $N = 2$ and $r_{max} = 600$ m. Ellipses depict vectorial central moments, path of cluster centers are shown as solid lines. Details on each cluster are given in the table.

rections within the tidal channel, resembling prevailing current directions. Thus geographical features in these shallow regions are significantly influencing tidal transport. Particles of Cluster 3 were traveling farthest, finally beaching at the eastern edge of Wangerooge.

Particles of ensemble ② (Figure 41) were released during rising tides. Strongly varying SD values and widespread beaching periods in the range of 170 hours for Clusters 1 to 3 indicate particles were subject to stronger mixing as in the case of ensemble ①. However, terminal locations of these clusters are comparable to findings for ensemble ①. Clusters are again located at the northern beach of Wangerooge with cluster trajectories showing several passages through the tidal channel[145]. Contrarily, 5 particles were seemingly converging ($SD_{start} = 434$ m vs. $SD_{end} = 415$ m) and forming Cluster 4 in the offshore region. Note this cluster was not solely formed by particles starting farthest north of the release area but is also contain-

---

[145]Note trajectories are plotted for cluster centers with $r_{max} = 600$ m, possibly crossing coasts and landmasks, as can be seen e.g. by Cluster 2's trajectory in Figure 41.

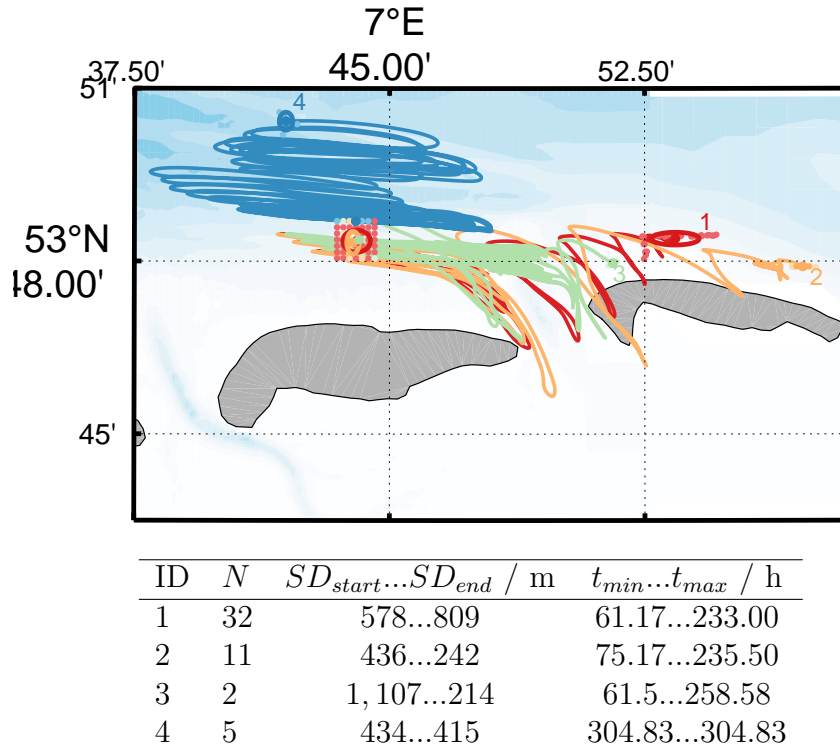| ID	N	$SD_{start}...SD_{end}$ / m	$t_{min}...t_{max}$ / h
1	32	578...809	61.17...233.00
2	11	436...242	75.17...235.50
3	2	$1,107...214$	61.5...258.58
4	5	434...415	304.83...304.83

Figure 41: Terminal cluster locations for ensemble ② as defined by (46) using $N = 2$ and $r_{max} = 600$ m. Ellipses depict vectorial central moments, path of cluster centers are shown as solid lines. Details on each cluster are given in the table.

ing one particle originating at the center. Overall, particle trajectories are again indicating transport patterns into eastern directions with beaching sites located at the northern beach of Wangerooge.

Figure 42 shows cluster formation of ensemble ③, which was released at maximum tidal elevation. In this case, all particles were transported into offshore direction, staying closely packed for a period of 14 days. Trajectory of this 49 particles cluster north of Spiekeroog shows oscillation patterns with zonal eccentricity but almost absent net zonal transport.

Ensemble ④ (Figure 43) showed highest spatial and temporal diffusion, leading to formation of 6 distinct clusters: three at the northern beach of Wangerooge (IDs 1, 2 and 3), two in offshore regions north of Spiekeroog (IDs 5 and 6) and one cluster consisting of 2 particles at the eastern tip of Spiekeroog (ID 4), the latter being formed by particles passing the tidal channel. Even though formation of Cluster 4 seems realistic, it might be interpreted as artifact of the beaching parametrization as particles can stick to shores when crossing in short distances to landmasks. Ignoring Cluster 4, 30 particles beached at the island Wangerooge whereas 16 particles were
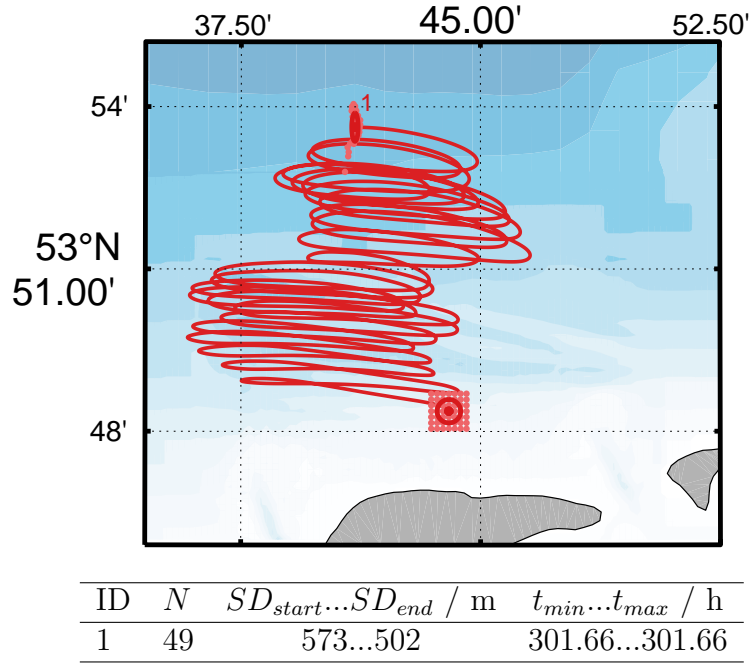
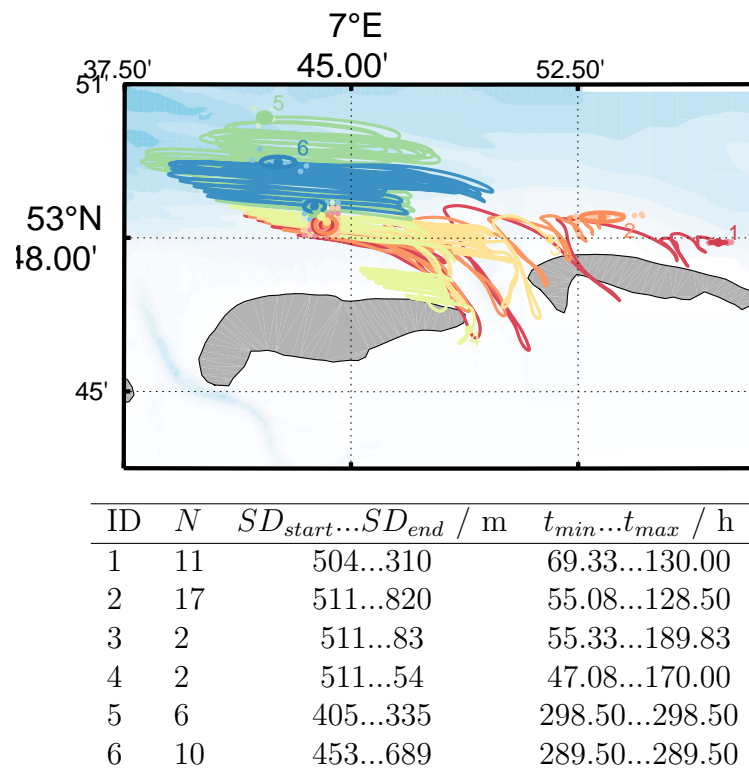| ID	N	$SD_{start}...SD_{end}$ / m	$t_{min}...t_{max}$ / h
1	49	573...502	301.66...301.66

Figure 42: Terminal cluster locations for ensemble ③ as defined by (46) using $N = 2$ and $r_{max} = 600\,$m. Ellipses depict vectorial central moments, path of cluster centers are shown as solid lines. Details on each cluster are given in the table.

transported into offshore regions.

Beaching Terminal particle locations for each ensemble at the end of simulations, i.e. after 13 days of floating times, are shown in the top panel of Figure 44. Open symbols depict free floating particles at the end of these 13 days. Coastlines are derived from landmasks in this plot for a better representation of the latter. Amounts and terminal locations of beached particles seem qualitatively tied to temporal releases during tidal cycles.

When released during rising tides (ensembles ①, orange squares and ②, cyan circles), particles were transported by onshore directed[146] tidal currents, eventually beaching southeast of their release location at the island Wangerooge. In case of ensemble ① (orange squares), a majority of particles was staying inside the fine computational grid, which is denoted by the dotted border in Figure 44. As seen by cluster formations, these particles were then flushed at the eastern edge resp. northern coast of Wangerooge during the first tidal cycle. This is further represented by histograms of beached particles in the lower panels of Figure 44 (orange bars). Note beaching is

---

[146]I.e. southeastward.

ID	N	$SD_{start}...SD_{end}$ / m	$t_{min}...t_{max}$ / h
1	11	504...310	69.33...130.00
2	17	511...820	55.08...128.50
3	2	511...83	55.33...189.83
4	2	511...54	47.08...170.00
5	6	405...335	298.50...298.50
6	10	453...689	289.50...289.50

Figure 43: Terminal cluster locations for ensemble ④ as defined by (46) using $N = 2$ and $r_{max} = 600\,\text{m}$. Ellipses depict vectorial central moments, path of cluster centers are shown as solid lines. Details on each cluster are given in the table.

defined by NaN-position vectors of particles, thus individual particles not moving after certain periods but are still able to refloat are not considered in these histograms[147].

Cumulated numbers of beaching particles for ensemble ② are slightly lower (cyan bars in the cumulated histogram, Figure 44), but temporal trends differ significantly. Beaching events were absent for two days after release and then suddenly rising to 39 over the course of two days. Further beaching events were distributed until the end of simulations, leading to total numbers of 45 beached particles. Main beaching areas are again located at the northern coast of Wangerooge, showing a slight shift towards the East. Remaining 4 particles formed a small cluster north of the release area.

A similar trend is shown by ensemble ④ (magenta) with beached particles forming patches at the northern coastline of Wangerooge. Total amounts are slightly lower (33 beached particles in total), but temporal evolution of beaching events is almost identical. As already seen by ensemble ②, remaining particles were forming two clusters north of the starting area. In contrast to other ensembles, 2 particles were beaching at the eastern edge of Spiekeroog.

Beaching events were absent in the case of ensemble ③ (yellow diamonds), released at high tides.

Adding a diffusion term according to equation (32) did not significantly change cluster formations and locations on such small space-time-scales considered here. This is shown in Figure 103 of Appendix E, where some individual particles are redistributed between closley neighbouring clusters but cluster locations and temporal spacing of beaching events agree with results presented above.

6.3.3. Scenario B

Trajectories for this scenario have been calculated using three different wind drag values, i.e. $C_1 = 0.000$, $C_2 = 0.007$ and $C_3 = 0.014$, with the former resembling completely submerged particles floating in the uppermost water column. $C_3 = 1.4 \times 10^{-2}$ was chosen according to best fit values for GPS-Drifters found by Heinrich [2018]. Numerical diffusion terms or wind

---

[147]One might argue these particles should be defined as beached without adopting NaN-positions. However, as they are numerically able to move after flushing events in later time steps, the mathematical definition by NaN values will be used throughout this thesis.
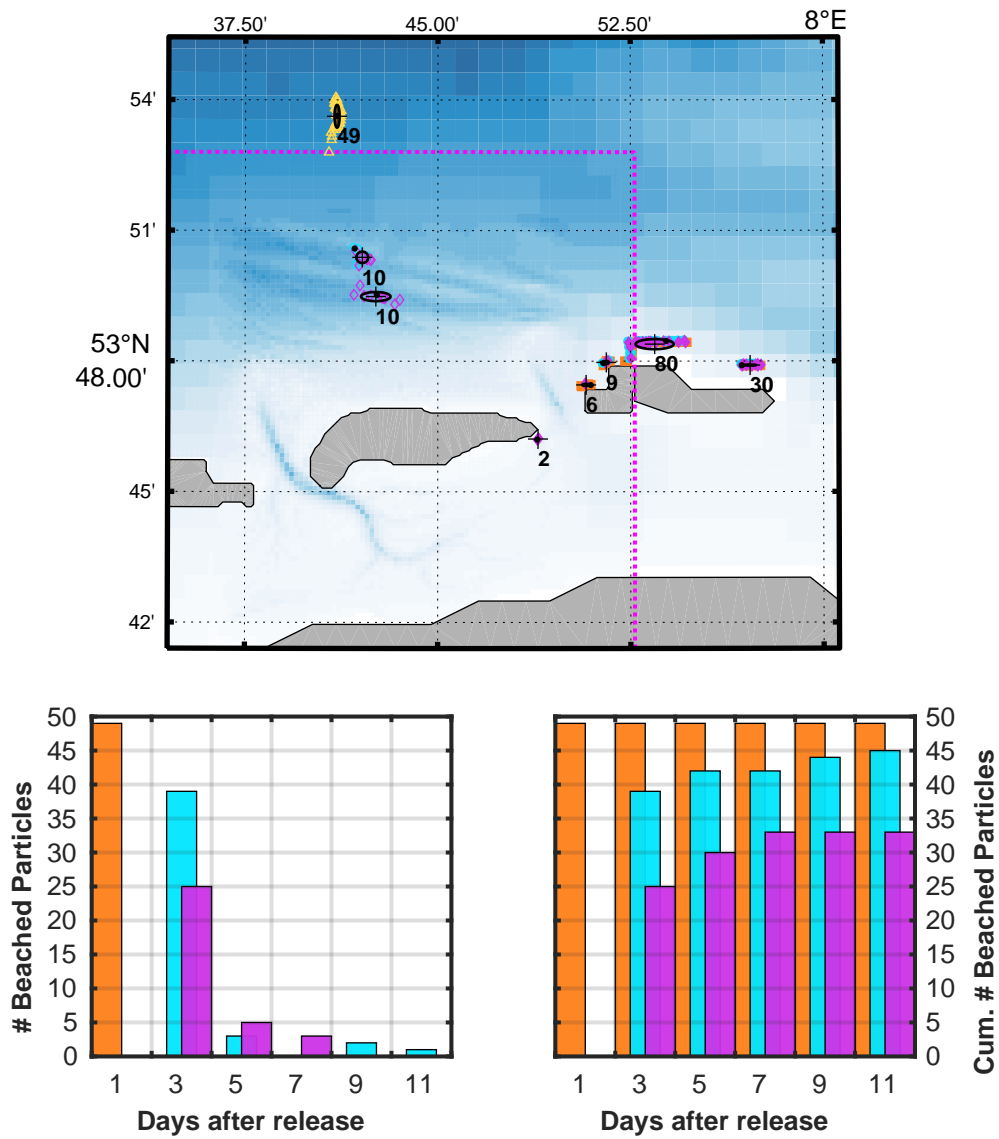
Figure 44: Distribution of Lagrangian floats after 14 days of simulations. Terminal locations of individual particles are shown in the top panel: ① orange squares, ② cyan circles, ③ yellow triangles and ④ magenta diamonds (cf. Figure 33). Non-beaching particles are indicated by open symbols. Temporal histograms of beaching events for each ensemble are shown in the bottom panels: absolute numbers on the left and cumulated numbers on the right. Labels on the abscissa indicate class centers, binning sizes were set to 2 d. Time values are referenced to individual ensemble release times.

deflection were neglected in these computations.

Temporal Evolution of Ensembles Temporal evolution of each ensemble for absent wind drag is shown in Figure 45 to Figure 46. Plots for wind drag coefficients $C_2 = 7 \times 10^{-3}$ and $C_3 = 14 \times 10^{-3}$ are shown in Figure 104 to Figure 107 in Appendix E.

For particles of ensemble ① (Figure 45, top), released at low tides, similar eastern transport as seen for sole tidal currents is evident. The ensemble trajectory, however, is showing more tidal oscillations before reaching the cluster's terminal location at Wangerooge. Surprisingly, as wind induced currents are assumed to strengthen coastal directed transport, floating periods are longer than seen for Scenario A. Additionally, the trajectory is traveling further distances through the tidal channel into backbarrier regions. Applying direct wind drag of $C_2 = 7 \times 10^{-3}$ (Figure 104 in Appendix E) further hindered eastern, but strengthened southern transports through the tidal channel, leading particles to beach at the eastern edge of Spiekeroog and at the German coast. Further raising wind drag to $C_3 = 14 \times 10^{-3}$ (Figure 106 in Appendix E) caused the whole ensemble ① washing up at the northeastern beach of Spiekeroog during the first tidal cycle.

In case of ensemble ② (Figure 45, bottom), onshore directed transport by wind induced currents was adding up to rising tides, leading the ensemble center ending up at the northeastern beach of Spiekeroog. Onshore directed transport was further enhanced by applying wind drags C_2 and C_3, causing beaching of the whole ensemble at the northern beach of Spiekeroog within one tidal period (Figure 104 and Figure 106 in Appendix E).

Contrary to ebb releases, flood released ensemble ③ was ending up at the northern beach of Spiekeroog. Eastern directed tidal transports, thus into the vicinity of strong currents at the tidal channel, were averted by the offshore directed tidal currents, counteracting wind induced currents. Applying intermediate wind drag C_2 on particles (top panel of Figure 105 in Appendix E), tidal currents were still causing zonal oscillations but no net transport. As meridional wind induced currents were then exceeding counter-directed tidal transports, particles were quickly washed up at Spiekeroog. Increasing wind drag (C_3, shown in the top panel of Figure 107, Appendix E) further enhanced onshore directed transport, restraining particles to beach at the northern coast of Spiekeroog. Due to significantly shortened floating times, particle diffusion due to tidal oscillations and bathymetrical features
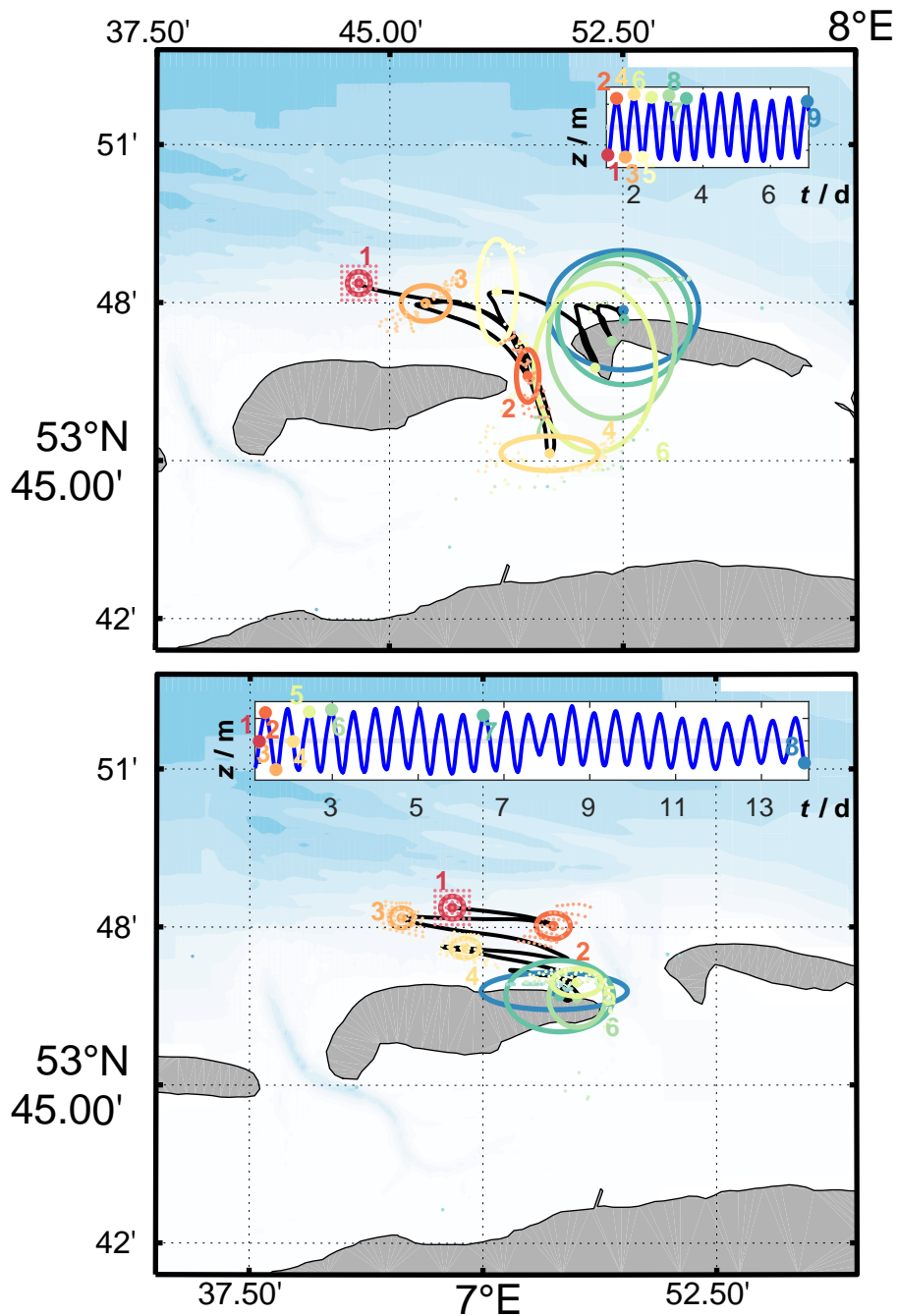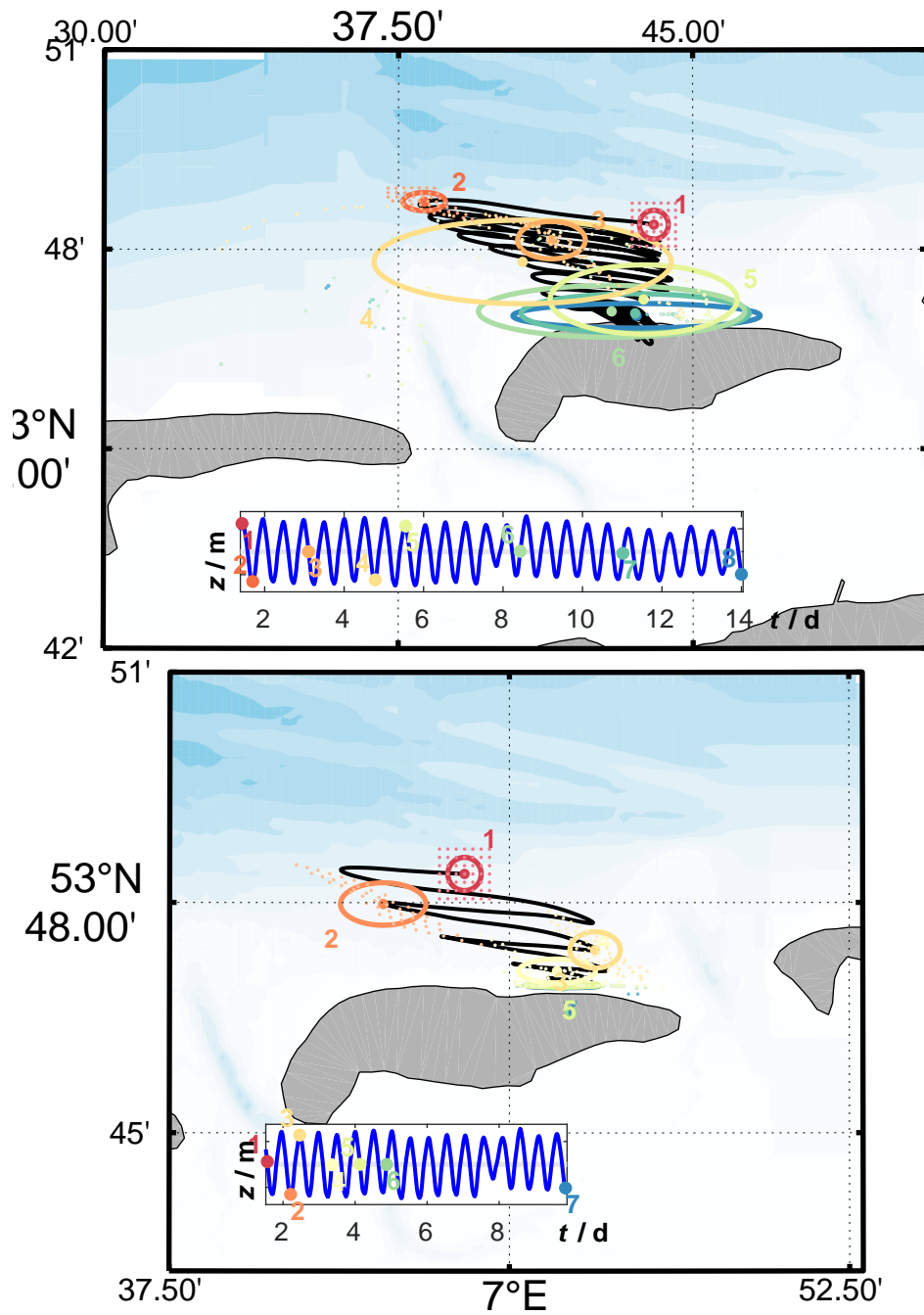
Figure 45: Trajectories of ensemble centers S for releases ① (top panel) and ② (bottom panel), when wind induced currents are regarded. Centers at discrete time steps and respective $ZM2$-ellipses are shown by bold dots and ellipses. Small, brighter dots are indicating individual particle positions. Color coding is illustrated in the inserts, showing temporal evolution of surface elevation (here z) at the modeling site. No direct wind drag on particles was applied.

Figure 46: Trajectories of ensemble centers S for releases ③ (top panel) and ④ (bottom panel), when wind induced currents are regarded. Centers at discrete time steps and respective $ZM2$-ellipses are shown by bold dots and ellipses. Small, brighter dots are indicating individual particle positions. Color coding is illustrated in the inserts, showing temporal evolution of surface elevation (here z) at the modeling site. No direct wind drag on particles was applied.

is significantly lowered with increasing wind drag.

Trajectories of ensemble ④ (bottom panels of Figures 46, 105 and 107) qualitatively replicated findings for ensemble ②. Thus onshore directed currents and direct wind drag seem significantly hindering differences for particle releases at rising resp. falling tides when timed at zero-crossings.

Cluster Formation Formation and trajectories of clusters are shown in Figures 47 to 50 (no wind drag on drifters) and Figures 108 to 115 in Appendix E (wind drags C_2 resp. C_3 on drifters).

In case of ensemble ①, wind induced currents were accelerating transport into eastern direction and the vicinity of the tidal channel. Formation of two clusters (IDs 2 and 3) at the northwestern beach of Wangerooge can be identified, where particles washed up during a temporal period of 36.58 h (Cluster 2) resp. 48.41 h, yielding significantly longer time intervals than in Scenario A's case. Although counterintuitive at first glance, this result is caused by wind driven southward directed surface currents, elongating retention times at the tidal channel and forcing meridional oscillations of particles. Formation periods of clusters at the beach of Wangerooge are extended by the channel acting as "particle trap", occasionally allowing individual particles to escape its catchment. A third cluster at the eastern tip of Spiekeroog near the tidal channel, which was absent for solely tidal driven transports, contains significant particle counts in this scenario. Looking at the grey trajectory[148] of one individual particle, eventually washing up at the German coast, highlights the importance of the channel in this scenario: Being trapped within the channel for 4 tidal cycles, i.e. at least two days, the particle beached at the German coast.

Adding wind drag of $C_2 = 7 \times 10^{-3}$ (Figure 108, Appendix E) further enhanced southern directed transport, yielding a main cluster at the northeastern beach of Spiekeroog (Cluster 1) and two smaller clusters at the German coast south of Spiekeroog. Particles were again performing meridional oscillations at the channel, but wind drag enhanced escape probabilities at the channel's southern outlet. Further increasing wind drag to $C_3 = 14 \times 10^{-3}$ (Figure 112, Appendix E) yielded beaching of the whole ensemble at the northeastern beach of Spiekeroog.

Particles of Ensemble ② (Figure 48), released during onshore directed tidal inflow, were clustering at the northeastern beach (Cluster 1) and east-

---

[148]In the following, grey trajectories indicate paths of individual particles which are not part of any cluster with $N \geq 2$.

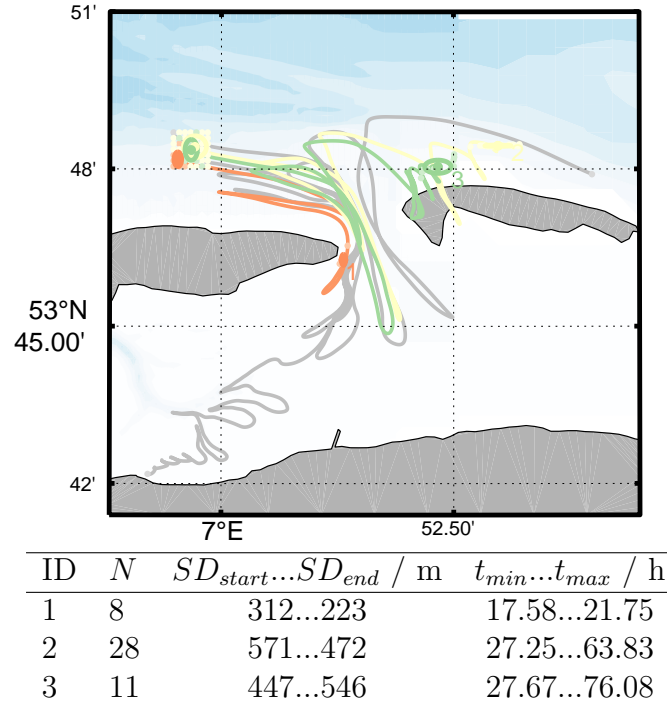| ID	N	$SD_{start}...SD_{end}$ / m	$t_{min}...t_{max}$ / h
1	8	312...223	17.58...21.75
2	28	571...472	27.25...63.83
3	11	447...546	27.67...76.08

Figure 47: Terminal cluster locations for ensemble ① as defined by (46) using $N = 2$, $r_{max} = 600$ m and neglecting wind drag on drifters. Ellipses depict vectorial central moments, path of cluster centers are indicated by solid lines. Individual trajectories for particles outlying any cluster are colored grey. Details on each cluster are given in the table.

ern tip (Cluster 2) of Spiekeroog and at the northwestern head of Wangerooge, with the latter being of significantly smaller size (2 particles). Two individual transects (grey) were passing the eastern tidal channel, separating Spiekeroog and Wangerooge, entering backbarrier regions south of Spiekeroog. One particle beached at the southwestern head of the island, whilst the other left the tidal flats via the western channel. This indicates wind induced currents are not hindering exchange of surface waters through tidal channels for moderate winds[149]. Applying wind drag led particles to quickly beach at the northern beach of Spiekeroog within intervals of 10 h...16 h for $C_2 = 7 \times 10^{-3}$ (Figure 109) resp. 5 h...13 h for $C_3 = 14 \times 10^{-3}$ (Figure 113) after release, i.e. approximately one M2-tidal period.

Results for ensemble ③, shown in Figure 49, are showing totally contrary patterns to Scenario A, as 88% of particles washed onshore the northern beach of Spiekeroog (Cluster 1) and few particles were traveling in west-

---

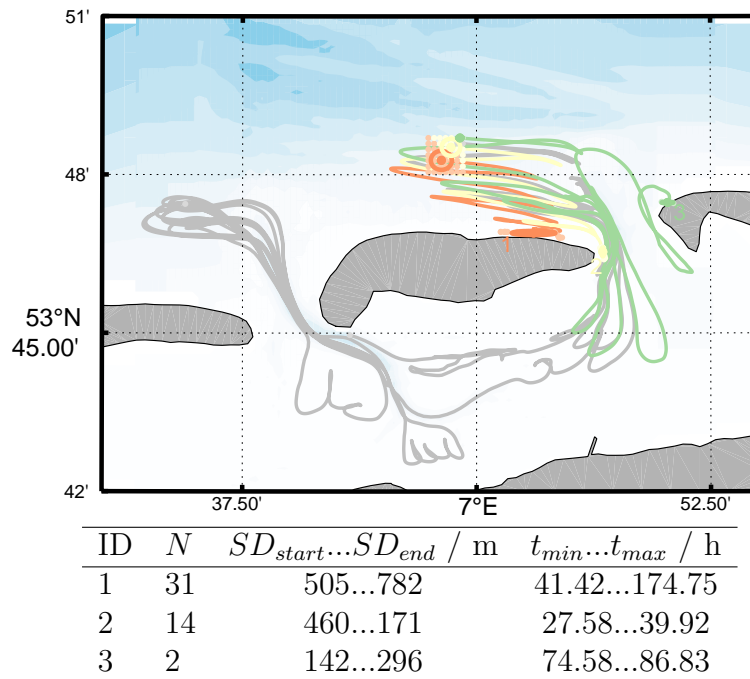[149]Note $u_{wind} = 6 \, \text{m s}^{-1}$ was fixed.

ID	N	$SD_{start}...SD_{end}$ / m	$t_{min}...t_{max}$ / h
1	31	505...782	41.42...174.75
2	14	460...171	27.58...39.92
3	2	142...296	74.58...86.83

Figure 48: Particle Clusters of ensemble ② at the end of simulation time. Cluster parameters were set to $N = 2$ and $r_{max} = 600\,\text{m}$, wind drag on particles was not considered. Details are given in the table and text.

ern directions, almost orthogonal to wind directions. Particles of Cluster 2 (yellow trajectory) were performing several oscillations in the eastern tidal channel, whereas one individual particle (grey) traveled into the vicinity of Langeoog, possibly washing up if computations continued after 14 days. Again, oscillations show zonal eccentricity in nearshore regions north of the islands. Adding direct wind drag led to beaching of whole ensembles within a few hours after release (Figure 110 and Figure 114 in Appendix E).

In case of Ensemble ④, one single cluster formed at the northeastern beach of Spiekeroog with beaching events occuring over periods of 1.8 days to 7.0 days after release, relating to about 4 to 14 M2-tidal cycles. Adding wind drag (Appendix E) shortened beaching periods to a maximum of two M2-tidal cycles for $C_2 = 7 \times 10^{-3}$ (Figure 111) and even less for $C_3 = 14 \times 10^{-3}$ (Figure 115).

Beaching   As seen by cluster formations, regarding wind driven surface currents significantly altered spatiotemporal patterns of beaching events, thus increasing total amounts of beached particles. Figure 51, respectively Figure 116 and Figure 117 in Appendix E, show beaching locations and

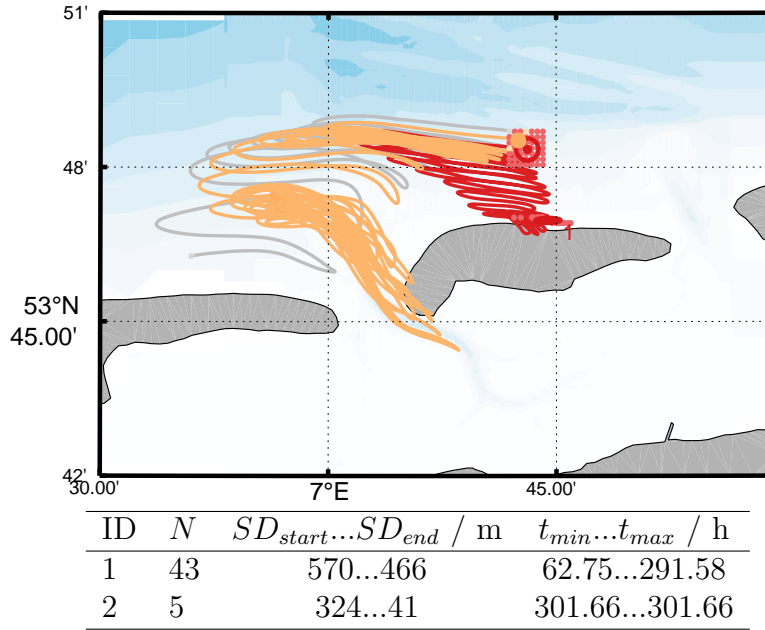| ID	N	$SD_{start}...SD_{end}$ / m	$t_{min}...t_{max}$ / h
1	43	570...466	62.75...291.58
2	5	324...41	301.66...301.66

Figure 49: Particle Clusters of ensemble ③ at the end of the simulations. Minimal cardinal number for each cluster was set to $N = 2$ and maximum distances $r_{max} = 600\,\text{m}$. Wind drag on particles was not considered, cluster details are given by the table.

ID	N	$SD_{start}...SD_{end}$ / m	$t_{min}...t_{max}$ / h
1	49	573...859	44.08...168.25
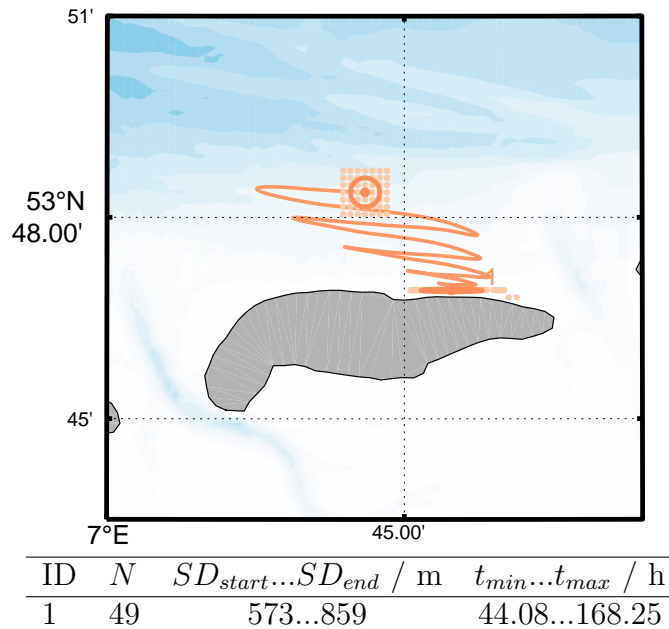
Figure 50: Particle Clusters of ensemble ④ at the end of the simulations. Minimal cardinal number for each cluster was $N = 2$ and maximum distance $r_{max} = 600\,\text{m}$. No direct windage was applied in these simulations. Details are given in the table and text.

temporal histograms of particles with and without applied wind drag.

Neglecting wind drag on particles ($C_1 = 0.00$, Figure 51) caused northern coasts of Spiekeroog and Wangerooge as major sinks of particles. Beached particle numbers at the former island are about three times higher with 145 at Spiekeroog vs. 42 at Wangerooge. Accumulation areas at both islands are located near the tidal channel. In contrast to sole tidal transports (Scenario A), Langeoog can be identified as potential accumulation site, acting as beaching location for an individual particle originating from ensemble ③ (yellow triangle) and having an offshore cluster of 6 particles in its northern vicinity. In the long term, the later might end up at Langeroog due to wind driven currents. Additionally, another individual drifter beached at the German coast.

Adding wind drag of $C_2 = 7 \times 10^{-3}$ (Figure 116 in Appendix E) further shifted beaching locations towards Spiekeroog and the German coast as winds amplified southward directed transports, preventing particles from reaching other islands. Further increasing wind drag ($C_3 = 14 \times 10^{-3}$, Figure 117) caused particles of each ensemble beaching at the northern coast of Spiekeroog within two days.

Temporal evolutions of beaching events are illustrated by histograms of Figures 51, 116 and 117. Ignoring wind drag, 39 particles of ensemble ① (orange) beached within two days, followed by 9 particles during days 2 to 4 after release. One last particle finally washed ashore until day 6. This is contrasting ensemble histograms for Scenario A, where all 49 particles beached during the first two days after release. Particles of ensembles ② (cyan) and ④ (magenta) showed similar temporal evolutions with maximum beaching counts during the period 2 to 4 days after ensemble releases. When compared to Scenario A's histograms, free floating periods are shortened and total amounts of beaching events are increased. Ensemble ④ was beaching at the northern coast of Spiekeroog as a whole, whilst a small fractions of ensemble ② beached at the eastern resp. western heads of Spiekeroog resp. Wangerooge near the tidal channel. 42 particles of Ensemble ③ (yellow) beached at Spiekeroog with maximum numbers in the 5 d interval. In contrast to Scenario A, where wind driven currents were absent, just 6 particles belonging to Ensemble ③ stayed afloat until the end of the modeling period.

Increasing wind drag caused all particles to wash up at coast within less than 4 ($C_2 = 7 \times 10^{-3}$, Figure 116) resp. 2 days ($C_3 = 14 \times 10^{-3}$, Figure 117). In both cases, Spiekeroog acts as major sink, attracting 177 particles for C_2
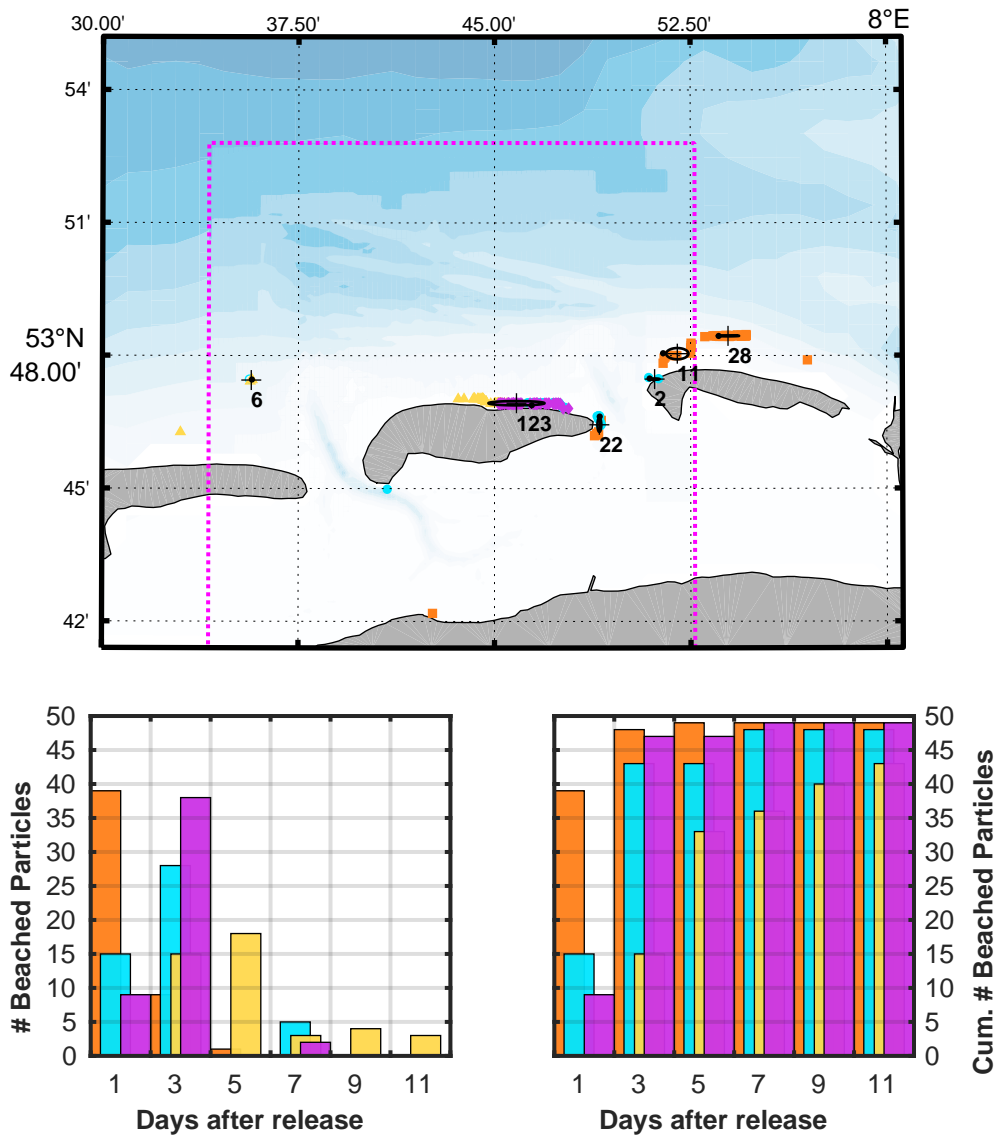
Figure 51: Distribution of Lagrangian floats after 14 days of simulations, when wind driven surface due to Northwestern winds are regarded. Terminal locations of individual particles are shown in the top panel: ① orange squares, ② cyan circles, ③ yellow triangles and ④ magenta diamonds (cf. Figure 33). Non-beaching particles are indicated by open symbols. Temporal histograms of beaching events for each ensemble are shown in the bottom panels: absolute numbers on the left and cumulated numbers on the right. Labels on the abscissa indicate class centers, binning sizes were set to 2 d. Time values are referenced to individual ensemble release times. Wind drag on particles was neglected in these computations.

and all 196 particles for C_3. For the latter, shoreward directed transports are drastically increased, even preventing particles from entering the tidal channels and reaching the German coast, which acted as minor sink for moderate wind drag C_2.

6.3.4. Scenario C

Starting from Scenario A, Stokes Drift based on a JONSWAP wave spectrum was added to tidal forcings of the hydrodynamic model. Mean wave directions were set parallel to winds of Scenario B[150], i.e. 10° inclined to normal directions of the islands' northern coasts. Drag coefficients for Stokes Drift $C_{St_i} = \{1.00, 0.50, 0.25\}$ were applied to Stokes Drift, plots for drag values C_{St_2} and C_{St_3} are shown in Appendix E.

Temporal Evolution of Ensembles Figure 52 and Figure 53 show temporal evolutions of ensemble centers ① to ④ for $C_{St_1} = 1.00$. South-southeast oriented wave directions and depth induced wave refraction were adding up to incoming waves onto the northern beach of Spiekeroog, causing strong southward directed wave transports at the surface layer. When regarding Stokes Drift velocities with $C_{St_1} = 1.00$ in the Lagrangian model, wave transports caused by Stokes Drift were of similar order as seen for highest wind drag values in Scenario B, causing particles of each ensemble to quickly beach at Spiekeroog. Results for Ensemble ① are standing out, as several particles passed the eastern tidal channel, entering backbarrier tidal flats. Here, wave refraction towards the island's coast was causing particles to finally washing up at the southern beach of Spiekeroog. Depth induced wave breaking occurs north of the islands, causing decreasing wave heights and thus smaller Stokes Drift values within the tidal channel. As wave generations at the tidal flats are fetch limited and because of shallow waters, transports by Stokes Drift are significantly lowered when compared to open beaches north of the islands.

Decreasing drag coefficients to $C_{St_2} = 0.50$ (Figure 118 and Figure 119 in Appendix E) and $C_{St_3} = 0.25$ (Figure 120 and Figure 121 in Appendix E) significantly lowered shoreward transports of particles, causing ensembles ①, ② and ④ qualitatively representing patterns found in Scenario B for absent wind drag. For ensemble ③, no beaching occured when using lowered drag

---

[150]Note, for the purpose of showing distinct influences of wind driven currents and waves, wind forcing was neglected in this Scenario C.
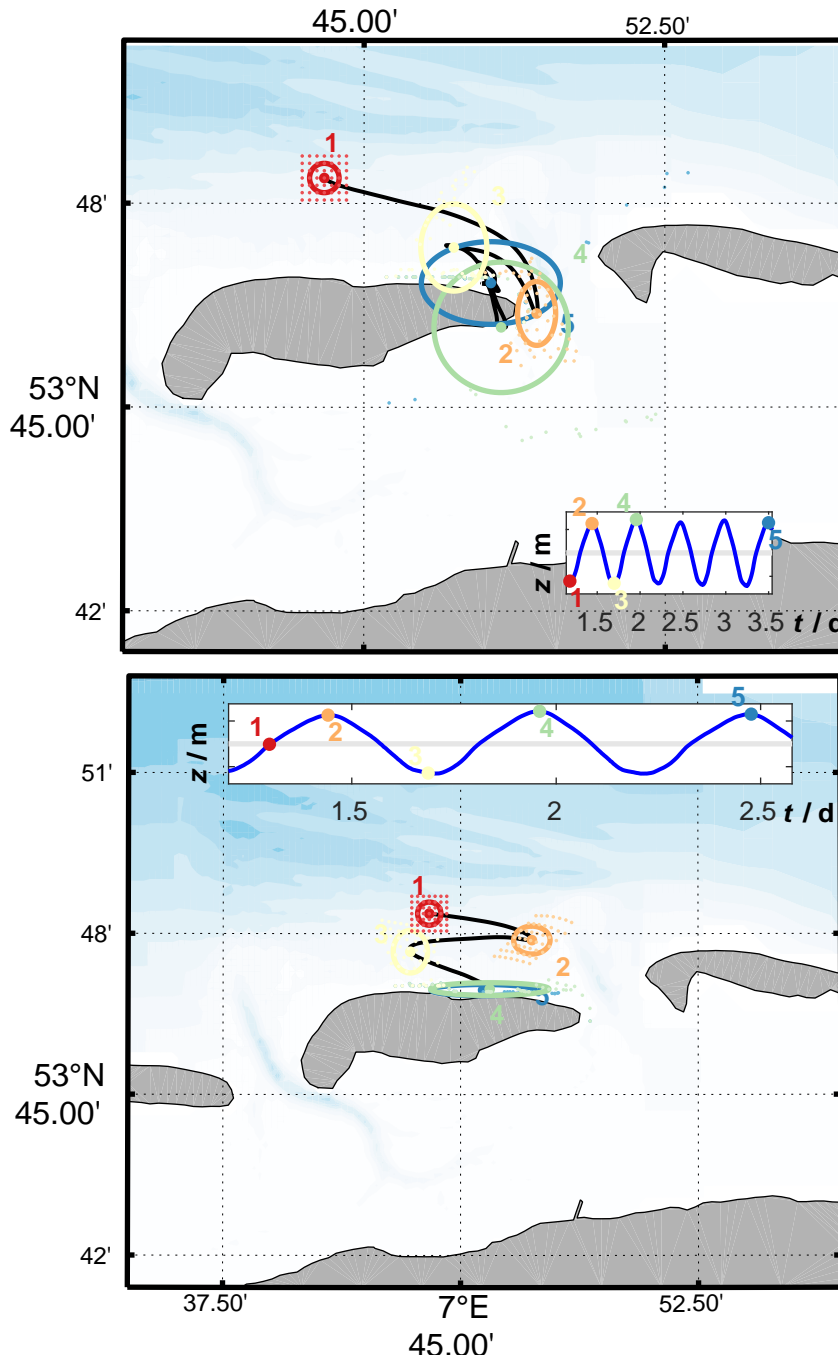
Figure 52: Trajectory of ensemble centers S for ensembles ① (top panel) and ② (bottom panel). Centers at discrete time steps and the respective $ZM2$-ellipses are shown by dots and ellipses. Individual particles for corresponding time steps are shown by smaller and lighter dots. Color coding is illustrated by the insert, where surface elevation at the modeling region is shown. Full Stokes Drift, i.e. $C_{St} = 1.00$ was regarded in trajectory integrations. Details are given in the text.
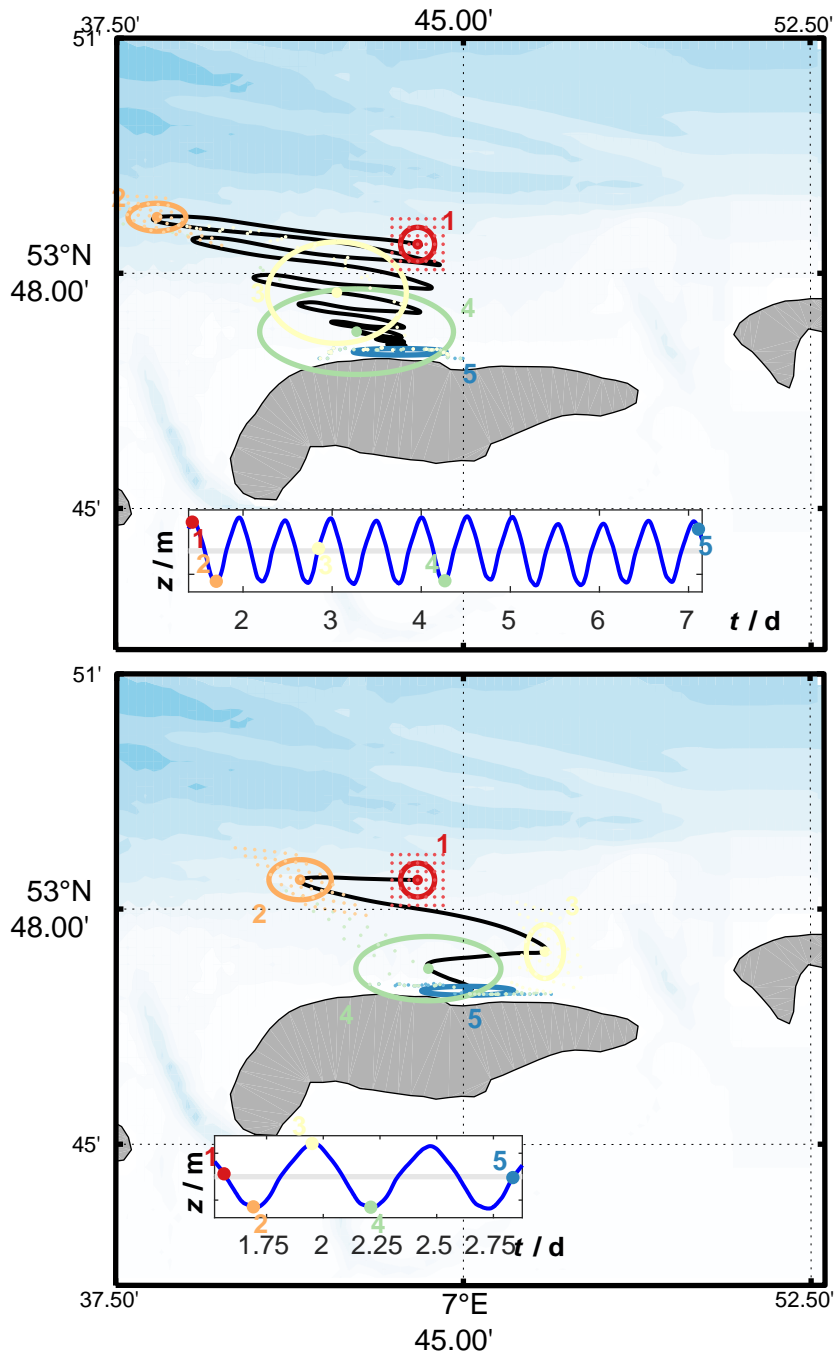
Figure 53: Trajectory of ensemble centers S for ensembles ③ (top panel) and ④ (bottom panel). Centers at discrete time steps and the respective $ZM2$-ellipses are shown by dots and ellipses. Individual particles for corresponding time steps are shown by smaller and lighter dots. Color coding is illustrated by the insert, where surface elevation at the modeling region is shown. Full Stokes Drift, i.e. $C_{St} = 1.00$ was regarded in trajectory integrations. Details are given in the text.

values C_{St_2} and C_{St_3}.

Cluster Formation   Cluster formations for ensemble ① and $C_{St_1} = 1.00$ are shown in Figure 54, plots for $C_{St_2} = 0.50$ and $C_{St_3} = 0.25$ are shown in Figures 122 and 126 in Appendix E. Contrary to results of Scenarios A and B, terminal particle locations are showing patterns of stronger diffusion, creating individual clusters at the northeastern beach of Spiekeroog (Cluster 1), the eastern edge of Spiekeroog near the tidal channel (Cluster 2), and two clusters at the northwestern beach of Wangerooge (Clusters 4 and 5, and one individually beached particle). Cluster 3, located at the southwestern head of Spiekeroog, was absent in previous scenarios and was formed by 2 particles, passing the tidal channel between Spiekeroog and Wangerooge. As mentioned above, clusters oriented antiparallel to wind directions are caused by depth induced refraction of waves and thus Stokes Drift. Even though covering large areas, clusters were formed by initially closely packed particles. Time spans of cluster formations differed significantly, with Clusters 4 and 5 being formed shortly after one day and in the latter case over short periods of less than 30 min and Clusters 1 and 2 showing significantly larger formation periods. Cluster 3 started forming approx. 3 days after release, as particles had longest traveling distances and were passing regions of small Stokes Drift values until reaching the southern coast of Spiekeroog.

Decreasing drag coefficients for Stokes Drift (Figure 122 and Figure 126) marginally lowered spatial distribution between individual clusters and were still resulting in significant wave transports, causing beaching at the southern coast (cf. Cluster in Figure 126, for $C_{St_3} = 0.25$) and the eastern tip of Spiekeroog near the tidal channel ($C_{St_2} = 0.50$, Figure 122, Cluster 2). In contrast to Scenarios A and B, clusters at the eastern tip were formed by significantly higher particle counts, even though tidal driven surface currents are parallel directed to beaches at the channels. Thus depth induced wave refraction is considered as important transport mechanism.

Clusters of ensemble ② are shown in Figure 55 resp. Figures 123 and 127. Fully accounting for Stokes Drift, i.e. using $C_{St_1} = 1.00$ (Figure 55), each particle except one was rapidly washed ashore at the northern beach of Spiekeroog, forming two distinct clusters. Cluster 1 (orange) was forming over the course of one M2-tidal cycle by particles starting nearest to the island's coastline. Particles of Cluster 2, originating further offshore, started beaching afterwards during rising tides. Some particles, forming the latter,
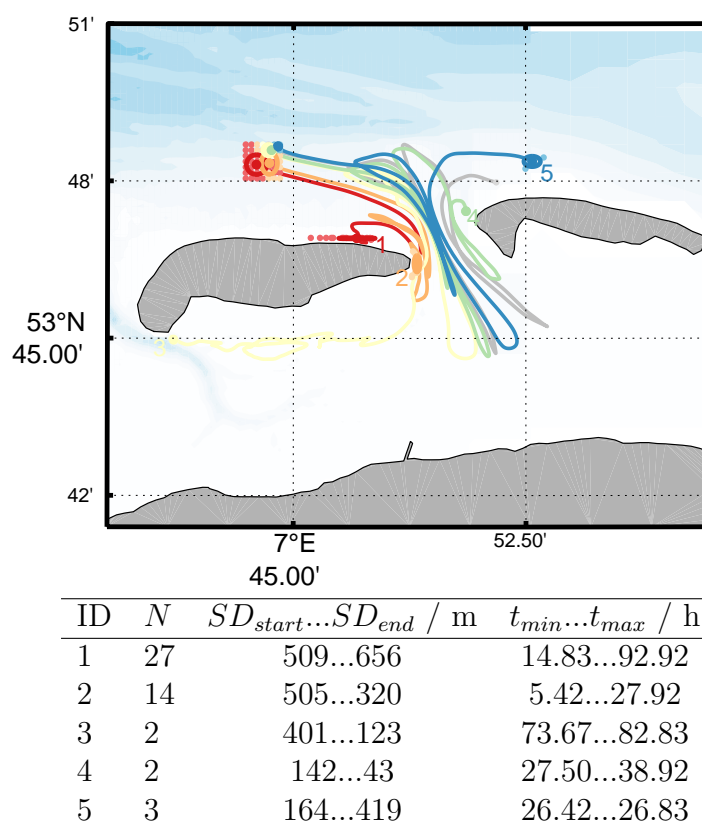
| ID	N	$SD_{start}...SD_{end}$ / m	$t_{min}...t_{max}$ / h
1	27	509...656	14.83...92.92
2	14	505...320	5.42...27.92
3	2	401...123	73.67...82.83
4	2	142...43	27.50...38.92
5	3	164...419	26.42...26.83

Figure 54: Particle Clusters of ensemble ①. Clusters were calculated using $N = 2$ and $r_{max} = 600$ m. A drag value $C_{St} = 1.00$ was applied to Stokes Drift. Cluster properties are given in the table.

were floating for nearly 3 days, i.e. 5 to 6 M2-tidal cycles[151], until eventually beaching. Again, an individual particle beached at the eastern tip of Spiekeroog in the vicinity of the tidal channel.

Decreasing Stokes Drift transports by setting $C_{St_2} = 0.50$ (Figure 123 in Appendix E) was increasing floating periods, shifting cluster locations in eastern directions due to the residual circulation of the North Sea. In this case, beaching locations are evenly distributed at the northern coastline of Spiekeroog. Two particles, originating from the northeastern edge of the release area, washed up at the tidal channel. Further decreasing Stokes Drift influences ($C_{St_3} = 0.25$, Figure 127 in Appendix E) led particles passing the tidal channel and ending up at the northern beach of Wangerooge (on individual, grey trajectory) and the southern beach of Spiekeroog (three particles, Cluster 3).

In case of ensemble ③, released at high tide, particles were beaching at

---

[151]Note trajectories are depicting cluster centers, thus possibly showing fewer tidal cycles than individual particles.

ID	N	$SD_{start}...SD_{end}$ / m	$t_{min}...t_{max}$ / h
1	21	445...605	7.83...13.08
2	27	459...718	14.50...65.25
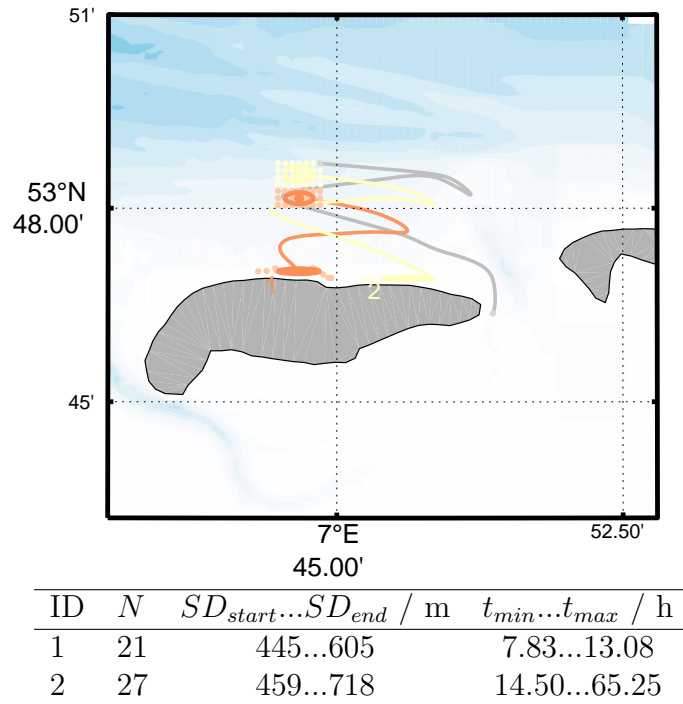
Figure 55: Particle Clusters of ensemble ②. Clusters were calculated using $N = 2$ and $r_{max} = 600\,\text{m}$. A drag value $C_{St} = 1.00$ was applied to Stokes Drift. Cluster properties are given in the table.

the northern beach of Spiekeroog over a period of 1.5 to 11 tidal cycles, i.e. approximately 6 days (Figure 56). Even though beaching occured for a long period, formation of one single cluster is similar to findings in Scenario B using wind drag.

Lowering drag values for Stokes Drift ($C_{St_2} = 0.50$, Figure 124 in Appendix E) yielded 5 particles washing up at the northern beach of Spiekeroog, whilst 44 remaining particles were transported northward into offshore waters. Applying just a fourth of Stokes Drift to particles ($C_{St_3} = 0.25$, Figure 128 in Appendix E) balanced offshore directed transport by tidal currents (Scenario A), resulting in no meridional net transport and almost absent diffusion of particles ($SD_{start} = 573\,\text{m}$ vs. $SD_{end} = 847\,\text{m}$.)

Results for Ensemble ④ (Figure 57) show similar patterns of beaching locations, but floating times were significantly lowered as particles were influenced by offshore directed tidal currents for shorter periods.

Decreasing drag values for Stokes Drift (Figures 125 and Figure 129 in Appendix E) extended floating times and increased spreading of beaching locations at the northern beach of Spiekeroog. Irrespective of drag value choices C_{St_i}, all particles beached at the northern beach of Spiekeroog for

ID	N	$SD_{start}...SD_{end}$ / m	$t_{min}...t_{max}$ / h
1	49	573...1112	18.00...136.33
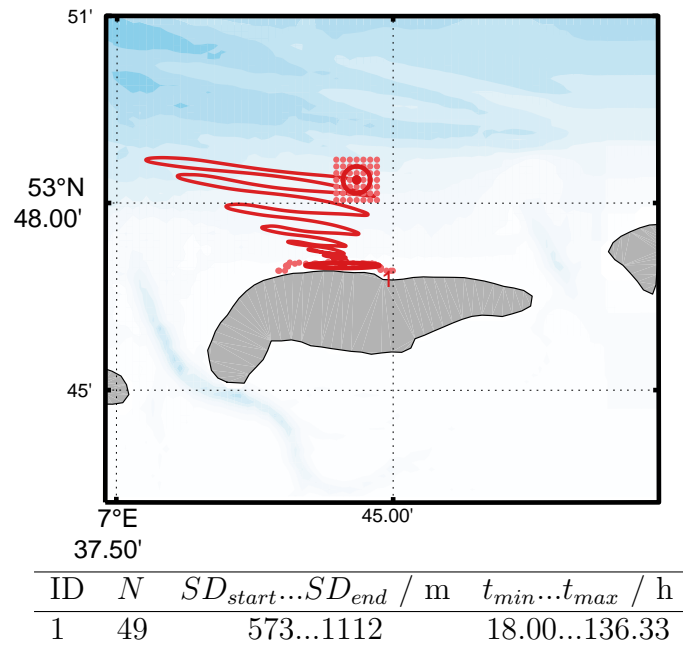
Figure 56: Particle Clusters of ensemble ③. Clusters were calculated using $N = 2$ and $r_{max} = 600\,$m. A drag value $C_{St} = 1.00$ was applied to Stokes Drift. Cluster properties are given in the table.

ID	N	$SD_{start}...SD_{end}$ / m	$t_{min}...t_{max}$ / h
1	49	573...1106	11.58...30.66
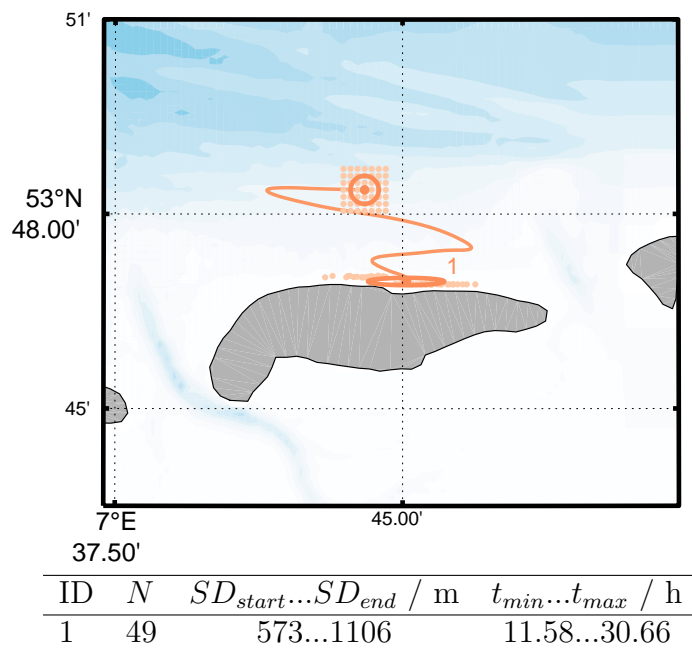
Figure 57: Particle Clusters of ensemble ④. Clusters were calculated using $N = 2$ and $r_{max} = 600\,$m. A drag value $C_{St} = 1.00$ was applied to Stokes Drift. Cluster properties are given in the table.

ensemble ④.

Beaching   Similar to Scenario B, addition of Stokes Drag to the Lagrangian advection equation (44) shortened floating periods, accelerating onshore directed transport and beaching periods.

Using full Stokes Drift ($C_{St_1} = 1.00$, Figure 58) resulted in Spiekeroog as main beaching location, as 173 out of 196 particles ended up at the island's northern coastline. Further beaching locations were solely formed by particles of ensemble ①, released during rising tides, thus forming clusters at the northwestern beach of Wangerooge (6 particles in total), the eastern tip of Spiekeroog near the tidal channel (15 particles) and the southwestern head of Spiekeroog (2 particles). In total, Stokes Drift led to beaching of every Lagrangian float.

Lowering drag coefficients for Stokes Drift ($C_{St_2} = 0.50$ and $C_{St_3} = 0.25$ in Figures 130 resp. 131, Appendix E) shifted beaching locations towards eastern directions, increasing numbers of beached particles at Wangerooge. Hence 23 resp. 37 particles were beaching at the eastern island for $C_{St_2} = 0.50$ (Figure 130) resp. $C_{St_3} = 0.25$ (Figure 131). Even for lowering Stokes Drift drag values, each particle of ensembles ①, ② and ④ was beaching within 6 days. In case of ensemble ③, released at maximum tidal elevations, lowered drag values significantly decreased beaching numbers, as only 4 particles ended up at Spiekeroog for $C_{St_2} = 0.50$ and transports by tides and Stokes Drift even balanced each other for $C_{St_3} = 0.25$, resulting in no beaching events.

6.4. Conclusion

Lagrangian trajectories and thus formation of clusters are influenced by choice of numerical models, i.e. integration schemes, time stepping, beaching parametrization and considering a variety of physical parameters like wind drag and Stokes Drift. Using short time stepping lengths in trajectory integrations as well as high temporal and spatial resolutions is necessary for accurately simulating small scale, nearshore scenarios.

In general, tides are causing eastern directed transport of surface drifting objects, parallel to general North Sea circulation patterns, i.e. counter-clockwise along the barrier islands. However, transport of surface drifting particles is strongly dependent on release times according to tidal cycles, yielding significant differences in distribution patterns. E.g. tidal currents
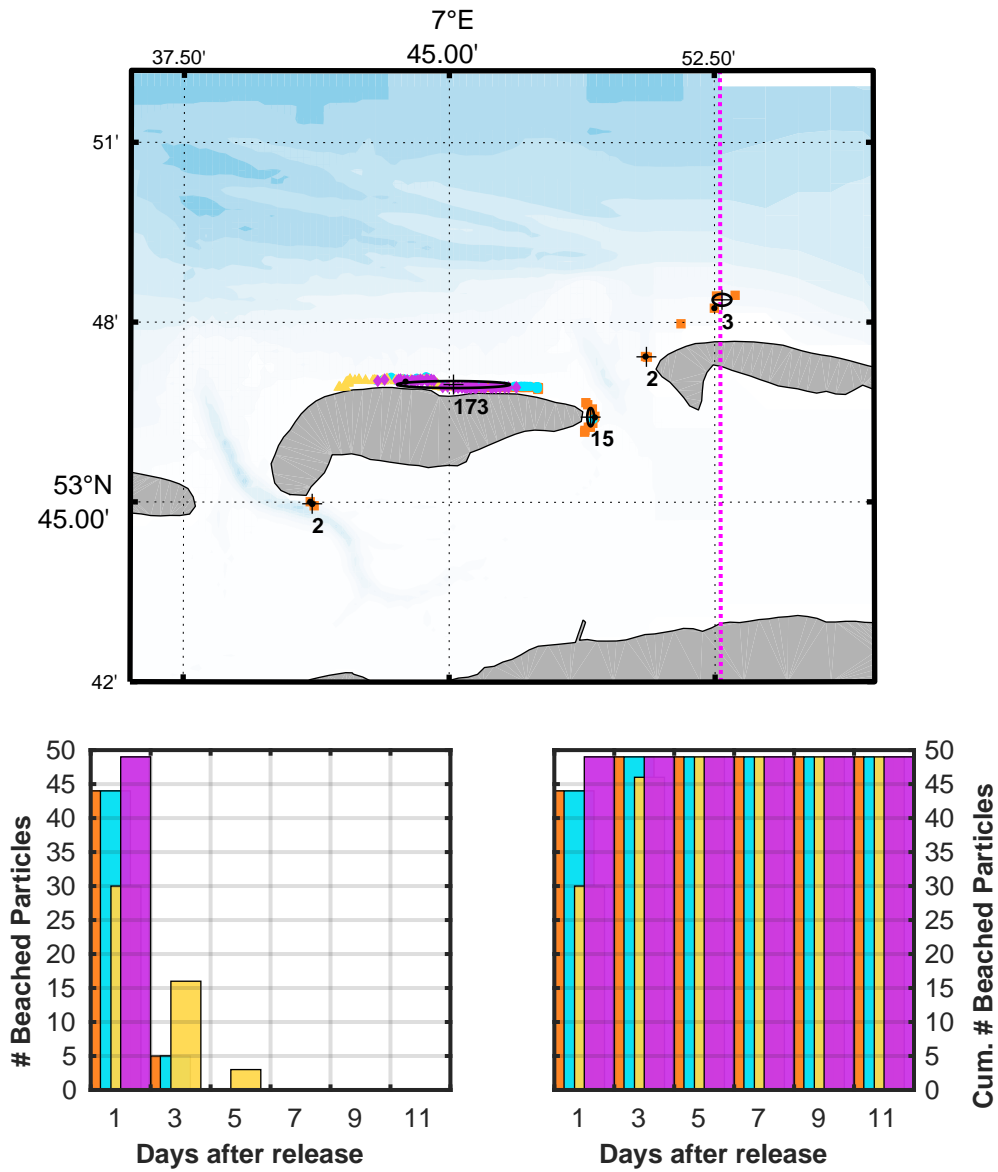
Figure 58: Distribution of Lagrangian floats after 14 days of simulation, when Stokes Drift with $C_{St_1} = 1.00$ is applied to particles. Terminal locations of ensembles are shown in the top panel: ① orange squares, ② cyan circles, ③ yellow triangles and ④ magenta diamonds (cf. Figure 33). Histograms in the bottom panels are showing temporal distributions of beaching events (left) and respective cumulated frequencies (right). Binning sizes were set to 2 days and values are referenced to ensemble releases.

are initially transporting ebb-released particles from offshore waters towards the islands and the German coast and flood-released particles in opposite directions. Even when calculating transports for short periods of less than 14 days, small temporal differences of particle releases resulted in significantly differing distributions within a few days.

Tidal oscillations are causing ellipsoidal patterns in trajectories with varying eccentricities in zonal and meridional directions due to geographical features of the modeling region, thus showing pronounced zonal oscillations north of the barrier islands and pronounced meridional oscillations within tidal channels. Maximum surface velocities occur in these channels, which are somehow acting as temporary traps for floating objects, causing several meridional oscillations before leaving at one end of the channel. This mechanism is causing exchange of surface waters, and thus surface drifting objects, and enhancing mixing, thus particle diffusion.

Wind induced currents by onshore directed winds are increasing beaching probabilities for surface drifting particles to small degrees, thus lessening differences for releases at different tidal stages. However, addition of wind drag to particles is needed for significantly increasing onshore directed transports and beaching probabilities.

Adding Stokes Drift to Eulerian currents is similarly increasing onshore directed transports and beaching probabilities. In contrast to wind driven currents and wind drag, Stokes Drift velocities are generally oriented normal to coastlines, thus increasing beaching probabilities at each open coast and possibly creating clusters at wind sheltered locations, e.g. at southern coastlines of the islands. Wind drag, on the other hand, might even hinder particles from beaching at such locations, depending on wind direction.

In Conclusion, wind drag and Stokes Drift are considered essential for adequately modeling nearshore distributions of Lagrangian particles at the surface layer.

7. BLEX: Beaching Litter EXperiment

In October 2017, the experimental campaign BLEX (Beaching Litter EXperiment) was performed by WPs 1 and 5, evaluating beaching processes at the northern beach of Spiekeroog. The WAMOS wave radar was installed on top of the *Evangelischer Jugendhof Spiekeroog*, observing incoming waves near the tidal channel, separating Langeroog and Spiekeroog, and the northwestern coastline of Spiekeroog (see subsection 3.3). Two ensembles of GPS-drifters were deployed inside the radar cone, simulating surface drifting debris, advected by currents, winds and waves. Drifter trajectories, tracked on 10 min-intervals, were compared to modeled currents and Stoke Drifts, based on a high resolution, coupled ROMS-SWAN-model (SP-Model , see section 4). By comparing drifter velocities, derived from GPS-tracks, with DWD wind data and simulated currents and waves, influences of each physical property was investigated.

In subsection 7.1, drifter designs by WP5 are shown and data collections are described. Additionally, regression models for calculating drag parameters via drifter data and computed currents and Stokes Drift are explained in this section. Measured tracks and model results are presented in subsection 7.2, followed by evaluations of drag parameters based on modeled hydrodynamic states and measured drifter velocities. This section is closed by numerical reconstructions of drifter velocities using estimated drag parameters and modeled hydrodynamics in the Lagrangian toolbox FLOPPSY. Results are checked for consistency in subsection 7.3, using same methods data from the GB-Model.

7.1. Methods

7.1.1. GPS Drifters

GPS-Drifters were deployed on a transect at the surf zone north of the island Spiekeroog on two consecutive dates in October 2017. A first set of 8 GPS-Drifters was released on October 18th, followed by a second set of 9 drifters on Oktober 24th, release locations and measured trajectories are shown in Figure 61. Each set was consisting of two different drifter types: One *Type A* drifter, equipped with submerged drag wings and described by Meyerjürgens et al. [2019], and 7 resp. 8 *Type B* drifters, made of food containers equipped with GPS-Trackers and sand ballasts [Breitbach, 2018]. Both drifter designs are shown in Figures 59 and 60 respectively.
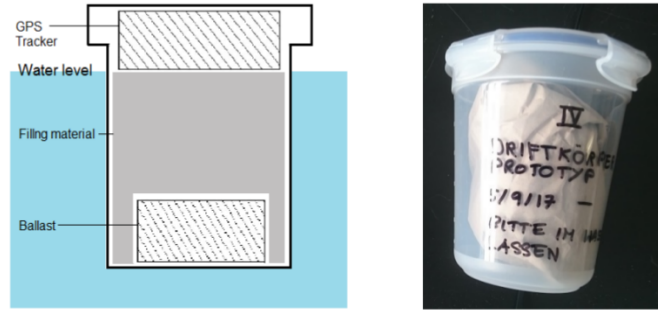
Figure 59: Box-Drifters of Type B. These drifters were made from common PP-food containers of cylindrical shape, measuring a volume of 760 ml. Containers were equipped with GPS-trackers and ballast weights, securing vertical orientation in the upper water column. Total mass of these drifters was 346.5 g. Details are given by Breitbach [2018]. (Image taken from Breitbach [2018])

Wind induced Leeway velocities u_{leeway} can be estimated according to Suara et al. [2015]

$$u_{leeway} = \frac{A}{R} u_w \tag{51}$$

with $A = 0.07$ [Niiler and Paduan, 1995] and the drag area ratio R, defined as

$$R = \frac{c_o A_o}{c_w A_w} \tag{52}$$

$c_{o,w}$ and $A_{o,w}$ are drag coefficients and areas exposed to water (o) resp. wind (w). Note, u_w in equation (51) is the downwind velocity and u_{leeway} are resulting wind induced drifter velocities, hence $\frac{A}{R}$ equals wind drag C'_w in conditional equation (44) for vanishing deflection angles α. Thus, using $R = 25.6$ for Type A drifters [Meyerjürgens et al., 2019] and $R = 4$ for Type B drifters [Breitbach, 2018], theoretical estimates for C'_w are:

$$
\begin{aligned}
C'_{w_A} &= 2.73 \times 10^{-3} \\
C'_{w_B} &= 1.75 \times 10^{-2}
\end{aligned}
\tag{53}
$$

Note deeper drafting depths for Type A drifters ($\approx 50\,\text{cm}$, depth of drag wings) than for Type B drifters (around 10 cm). Hence deflections $\angle\,(\vec{v}_p, \vec{u}_w)$ between drifter and wind velocities $\vec{v}_p$ resp. $\vec{u}_w$ are expected bigger for the former type due to stronger Ekman deflection[152]. Due to symmetrical

---

[152]Note $\angle\,(\vec{v}_p, \vec{u}_w)$ does not equal α from equation (44), with the latter describing deflection of wind induced drag velocities.
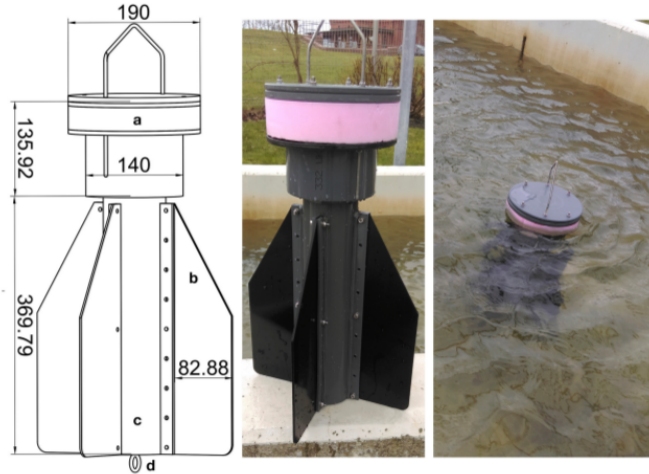
Figure 60: GPS-Drifters of Type A. Measurements in the left plot are given in millimeters, showing (a) buoyant parts, containing an GPS-tracker; (b) drag wings; (c) cylindrical shaped housing, containing battery packs and ballast weights; (d) mount for optional drogue. Details are given by Meyerjürgens et al. [2019]. (Image taken from Meyerjürgens et al. [2019])

shapings and compact sizes, deflection angles $\alpha \approx \pm 0$[153] for wind induced drift velocities are assumed for both drifter types [Allen and Plourde, 1999].

GPS Tracks A first set of Drifters (*Set* ①, drifter indices 1 to 8) was released at the location of the RBR and ADCP within the radar's sampling area in the morning of October 18th at 6:40am (UTC). A second set (*Set* ②, drifter indices 9 to 17) was released at the morning of October 24th on a transect perpendicular to Spiekeroog's coastline. On this transect, drifters of type B were deployed pairwise on 500 m intervals, resulting in varying starting times of each drifter for the period 07:40am to 08:00am. Positions of each drifter were locked on 10 min-intervals. Table 6 and Figure 61 show release coordinates and trajectories.

Drifter velocities Velocities $\vec{v}_p^{t_i}$ for each tracked time stamp t_i and drifter p were calculated using three locations $\vec{x}_p^{t_k}$ for t_{i-1}, t_i and t_{i+1}, leading[154]

$$\vec{v}_p^{t_i} = \frac{1}{2} \left(\frac{\vec{x}_p^{t_i} - \vec{x}_p^{t_{i-1}}}{t_i - t_{i-1}} + \frac{\vec{x}_p^{t_{i+1}} - \vec{x}_p^{t_i}}{t_{i+1} - t_i} \right) \tag{54}$$

---

[153]I.e. small values, evenly distributed to the left and right hand side.
[154]Following the notation of section 2.

7. BLEX: Beaching Litter EXperiment

Using these velocities as response vectors, drag coefficients and deflection angles were estimated via multidimensional linear regression. This is described in the following sections.

7.1.2. Numerical Model

Using meteorological data from the DWD (winds) and ERA5 datasets, waves and hydrodynamics were computed using the NA-Model, GB-Model and the SP-Model in one-way nesting configurations.

Wave parameters for a period starting on October 1st, 00:00:00, 2017 until November 7th, 00:00:00 were computed by the NA-Model using ERA5 winds. Time stepping was set to 5 min, directional and a frequency spaces were discretized by 72 meshes resp. 58 bins in the interval 0.02Hz ... 5.00Hz. Computations were serving wave boundaries for the GB-Model on 15 min intervals.

The GB-Model was operating in a coupled ROMS-SWAN configuration. 20 vertical layers and time stepping lengths of 2 s were used in the hydrodynamic part to secure stability in shallow areas. Atmospheric forcings were derived from ERA5 data and boundary resp. initial conditions were taken from the BSHcmod. Numerics in SWAN were accordingly set to the NA-Model run, using wave boundary conditions computed by the latter and ERA5 wind data. Coupling intervals for ROMS and SWAN were set to 10 min. Computed wave and hydrodynamic data was written on 15 min intervals, serving boundaries for the SP-Model.

Computations of the SP-Model were performed using boundary and initial conditions from the GB-Model. ROMS was operating on 15 vertical levels using time steps of 0.5 s length. The model was forced by DWD wind data and meteorological fields from the ECMWF dataset. Coupling intervals with SWAN were set to five minutes, using same numerical parameters for wave predictions as described above. Computations of waves and hydrodynamics were stored on 5 min intervals. Minimizing computational costs, the SP-Model was operated for an eleven day period, starting on October 17th 00:00:00 and covering floating periods of GPS-Drifters at the experimental site and securing sufficient spin-up times of one day.

Validations in section 4 are showing good agreement with measurements. Even though wave heights near Spiekeroog for strong winds on October 23rd and October 27th are underestimated, these errors can be neglected as no drifter measurements were performed for these wind events.

Estimation of Wind Drag and Influence of Stokes Drift   Using data[155] of Eulerian surface currents $\vec{u}_e^{t_i}$, Stokes Drift $\vec{u}_{St}^{t_i}$ and wind velocities $\vec{u}_w^{t_i}$ in equation (44) and combining with (54) yields $2N_t$ linear equations for time steps t_i[156]:

$$
\begin{aligned}
\vec{v}_p^{t_1} &= \vec{u}_e^{t_1} + \vec{u}_{St}^{t_1} + \boldsymbol{\alpha} C_w \vec{u}_w^{t_1} \\
\vdots &= \vdots \\
\vec{v}_p^{t_{N_t}} &= \vec{u}_e^{t_{N_t}} + \vec{u}_{St}^{t_{N_t}} + \boldsymbol{\alpha} C_w \vec{u}_w^{t_{N_t}}
\end{aligned}
\tag{55}
$$

Writing components (u, v) for time steps t_i and using $a := C_w \cos(\alpha)$ and $b := C_w \sin(\alpha)$, equation (55) can be written as[157]

$$
\begin{aligned}
u_p^{t_i} &= u_l^{t_i} + a u_w^{t_i} - b v_w^{t_i} \\
v_p^{t_i} &= u_l^{t_i} + a v_w^{t_i} + b u_w^{t_i}
\end{aligned}
\tag{56}
$$

Thus, all $2N_t$ linear equations in (55) can be written in compact matrix notation:

$$
\underbrace{\begin{pmatrix} u_p^{t_1} - u_l^{t_1} \\ \vdots \\ u_p^{t_{N_t}} - u_l^{t_{N_t}} \\ v_p^{t_1} - v_l^{t_1} \\ \vdots \\ v_p^{t_{N_t}} - v_l^{t_{N_t}} \end{pmatrix}}_{:=\vec{y}} = \underbrace{\begin{pmatrix} u_w^{t_1} & -v_w^{t_1} & 1 & 0 \\ \vdots & \vdots & \vdots & \vdots \\ u_w^{t_{N_t}} & -v_w^{t_{N_t}} & 1 & 0 \\ v_w^{t_1} & u_w^{t_1} & 0 & 1 \\ \vdots & \vdots & \vdots & \vdots \\ v_w^{t_1} & u_w^{t_{N_t}} & 0 & 1 \end{pmatrix}}_{:=A} \cdot \underbrace{\begin{pmatrix} a \\ b \\ u_{err} \\ v_{err} \end{pmatrix}}_{:=\vec{x}}
\tag{57}
$$

where (u_{err}, v_{err}) describe optional constant error terms, possibly present in modeled or measured data[158]. $u_l^{t_i} = u_e^{t_i} + u_{St}^{t_i}$ in the *response vector* $\vec{y}$ as well as $u_w^{t_i}$ in the *observation matrix* A were obtained by linear interpolation of modeled velocities onto drifter's GPS-positions $\vec{x}_p^{t_i}$ in space and time. *Predictors* $\vec{x}$ were calculated by solving equation (57) with a Least Means Squares (LMS) method using MATLAB's *multiple linear regression* function `regress` [Chatterjee and Hadi, 1986]. Wind drag C_w and deflection angle α

---

[155]In this case from numerical models.
[156]For a clearer view, primes in drag coefficients of equations (44) and (54) are neglected.
[157]Only written for index i for clarity reasons.
[158]Allen and Plourde [1999] are also using y-intercepts for Leeway estimations in their linear model.

were then determined by

$$
\begin{aligned}
C_w &= \sqrt{a^2 + b^2} \\
\alpha &= \arctan\left(\frac{b}{a}\right)
\end{aligned}
\tag{58}
$$

In the following, error ranges for drag parameters (58) are given via Gaussian error propagation [BPIM, 2008] using 95%-confidence intervals for a and b.

Lagrangian Modeling Trajectories for each GPS-Drifter were calculated using the FLOPPSY toolbox and ensembles of Lagrangian particles with varying drag parameters α and C_w within respective error bounds. Diffusion effects are parametrized by varying temporal releases of particles in the interval $t_{1,p} \pm 1\,\mathrm{h}$. Here $t_{1,p}$ are GPS-recorded releases for drifters p. Spacing in these intervals was set to 5 min and trajectories were computed using RK4 integrations with 2.5 s time stepping lengths.

7.2. Results

7.2.1. Stokes Drift and Wind

Temporal mean ratios of computed Stoke Drift velocities and data for 10m wind speeds on each numerical grid point of the SP-Model are shown in Figure 61. Each panel corresponds to retention periods of Drifter Ensembles ① and ② at the modeling site (cf. Table 6).

During retention times of drifter Set ① at the experimental site, i.e. October 18th, 6am until October 19th, 24pm, winds were exhibiting directional shifts (left polarplot of Figure 61, note the nautical convention). Starting with about $5\,\mathrm{m\,s}^{-1}$ amplitude at angles around 210°, i.e. incoming from Southwestern directions, winds were shifting towards SE directions during a 10 h period after drifter releases[159]. In contrast, Stokes Drift directions were evenly distributed, showing maximum velocity values in ranges of $20\,\mathrm{cm\,s}^{-1}...30\,\mathrm{cm\,s}^{-1}$, incoming from northwestern directions, i.e. around 330°. Wave refraction towards Southern located shallow waters and wave steepening due to decreasing water depths were causing increasing Stokes Drift velocities near beaches (cf. equation (25)), eventually vanishing in close distances to shorelines as waves broke. Being exposed to larger waves and sheltering backbarrier tidal flats, the islands' Northern beaches were

---

[159]See also interpolated velocities on drifter locations in Figure 62.
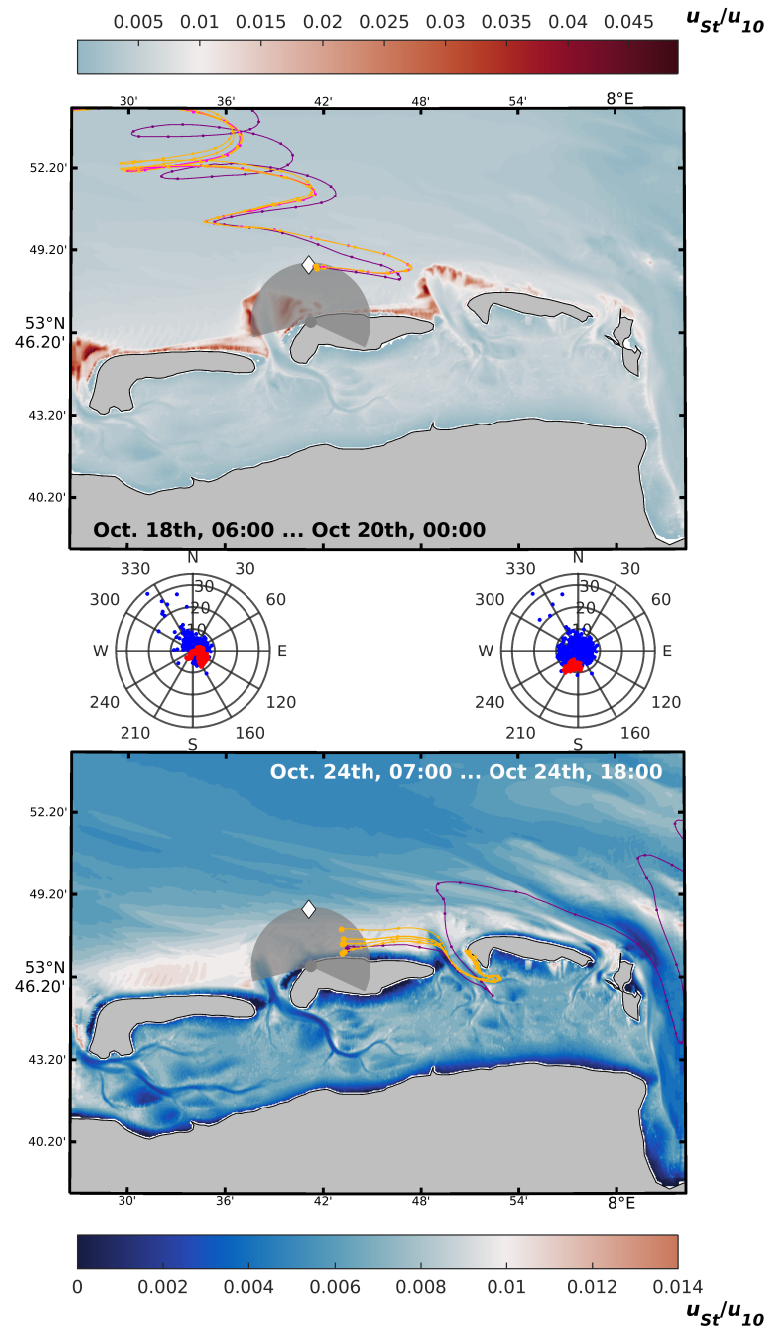
Figure 61: Ratio of computed Stokes Drift and 10m wind data, u_{St}/u_{10}, for retention periods of Drifter ensembles ① (top) and ② (bottom). Polar plots are showing corresponding velocity distributions (red: u_{10} in $\mathrm{m\,s^{-1}}$, blue: u_{St} in $\mathrm{cm\,s^{-1}}$, left: Set ①, right: Set ②). Dots in trajectories for Drifter Types A (purple) and Type B (orange) are indicating 1 h intervals. Sampling area and position of the WAMOS radar and RBR are indicated by a cone shape resp. diamond symbol.

affected by larger waves and thus stronger Stokes Drift. Hence Stokes Drift values are balancing or even exceeding values of $0.01 \cdot u_w$ (top panel of Figure 61). Note $u_{St} \approx 0.01 \cdot u_w$ equals ranges of assumed wind induced drift velocities for Lagrangian drifters.

For retention periods of drifter Set ②, depicted by the bottom panel and right polarplot of Figure 61, incoming Stokes Drift velocities from Northwestern directions were less prominent, yielding smaller u_{St}/u_{10} ratios at the experimental site. Maximum ratios of 0.01 were again present near northern beaches of the islands, thus balancing Stokes Drift and assumed wind induced drifter velocities. Persistent winds, blowing in Northnortheastern directions were possibly decreasing incoming wave energies from open North Sea regions.

7.2.2. GPS Tracks

GPS-Trajectories for drifter ensembles ① (top) and ② (bottom) are shown in Figure 61, spatiotemporal start and end locations as well as retention times within the modeling area are shown in Table 6. Trajectories of Type B drifters (orange) were closely bound in both sets. In case of Set ①, these drifters left the experimental site after mean retention times of (31.53 ± 0.45)h. Set ② beached as whole ensemble after mean floating times of (8.50 ± 0.40)h, eventually forming a closely packed cluster at the western edge of Wangerooge. Center location resp. SD-value for this cluster are $(7°51'1'', 53°47'7'') \pm 210$ m (cf. equations (46) and (49)).

Trajectories of Type A drifters (purple) were clearly deviating. In case of Set ①, retention time exceeded values for Type B drifters by almost 11 h. Contrary to other designs, drifter Type A of Set ② left the modeling site after 26.33 h, reentering at the eastern boundary for a short period until eventually leaving (cf. Figure 61, bottom panel).

Wind data and modeled Eulerian surface currents and Stokes Drift from the SP-Model were interpolated[160] onto tracked GPS-positions in space and time. These velocities are compared with drifter velocities for IDs 1 (Type A) and 2 (Type B), derived from GPS-data of Ensemble ①, in Figure 62. Velocities for IDs 12 (Type A) and 17 (Type B) of ensemble ② are shown in Figure 63. An overview for each drifter is given in Figures 132 and 133 in Appendix F. Note currents are depicted in nautical convention, i.e. indicating incoming directions, whilst drifter velocities (black) are representing

---

[160]Linear interpolation using MATLAB's `interp1`- (time) and `interp2` (space) functions.

Table 6: Individual date and locations for each drifter's journey. Time stamps for leaving the experimental site resp. beaching are shown in the third column. Drifters 1 and 12 were of type A.

ID	Start	End	Left/Beached	Res. Time
1	18-Oct 06:40:00	20-Nov 02:00:00	20-Oct 00:50:00	42:20
	(7.6919,53.8101)	(8.6240,54.0890)	**left**	
2	18-Oct 06:40:00	27-Oct 03:00:00	19-Oct 13:20:00	30:40
	(7.6925,53.8104)	(8.2806,54.7507)	**left**	
3	18-Oct 06:40:00	29-Oct 02:30:00	19-Oct 14:30:00	31:50
	(7.6925,53.8104)	(8.8791,54.4081)	**left**	
4	18-Oct 06:40:00	27-Oct 10:30:00	19-Oct 14:30:00	31:50
	(7.6927,53.8103)	(8.4146,54.7480)	**left**	
5	18-Oct 06:40:00	27-Oct 17:10:00	19-Oct 14:30:00	31:50
	(7.6924,53.8103)	(8.4174,54.7407)	**left**	
6	18-Oct 06:50:00	28-Oct 01:40:00	19-Oct 14:30:00	31:40
	(7.7001,53.81)	(8.5842,54.3138)	**left**	
7	18-Oct 06:40:00	28-Oct 03:10:00	19-Oct 14:20:00	31:40
	(7.6924,53.8103)	(8.4692,54.5770)	**left**	
8	18-Oct 06:40:00	26-Oct 19:30:00	19-Oct 13:50:00	31:10
	(7.6935,53.8089)	(8.2820,54.8482)	**left**	
9	24-Oct 07:40:00	24-Oct 16:10:00	24-Oct 16:10:00	8:30
	(7.7193,53.7844)	(7.8512,53.7846)	**beached**	
10	24-Oct 08:00:00	24-Oct 16:40:00	24-Oct 16:40:00	8:40
	(7.721,53.7904)	(7.8507,53.7849)	**beached**	
11	24-Oct 07:40:00	24-Oct 16:40:00	24-Oct 16:40:00	9:00
	(7.7191,53.7845)	(7.8497,53.7856)	**beached**	
12	24-Oct 07:40:00	29-Oct 05:50:00	25-Oct 21:20:00	26:20
	(7.7243,53.787)	(7.7243,53.787)	**left**	
13	24-Oct 08:00:00	24-Oct 16:40:00	24-Oct 16:40:00	8:40
	(7.7205,53.7932)	(7.8472,53.7872)	**beached**	
14	24-Oct 08:00:00	24-Oct 15:40:00	24-Oct 15:40:00	7:40
	(7.7183,53.7991)	(7.8556,53.7833)	**beached**	
15	24-Oct 08:00:00	24-Oct 16:20:00	24-Oct 16:20:00	8:20
	(7.7202,53.7931)	(7.8486,53.7862)	**beached**	
16	24-Oct 08:00:00	24-Oct 16:20:00	24-Oct 16:20:00	8:20
	(7.7217,53.7855)	(7.8491,53.7860)	**beached**	
17	24-Oct 07:50:00	24-Oct 16:40:00	24-Oct 16:40:00	8:50
	(7.7193,53.7901)	(7.8507,53.7849)	**beached**	

Figure 62: Phase diagrams for Type A drifter 1 and Type B drifter 2 of Ensemble ①. Currents (blue), Stokes Drift (red) and wind velocities (green) are in nautical convention, drifter velocities (black) are pointing into traveling directions. Note different scalings of velocity components. Dots indicate 1 h intervals, numbers represent time stamps in hours.

traveling directions.

Velocities of both drifter types (black lines in Figure 62) are highly correlated with surface currents (blue line) in case of ensemble ①. Tidal ellipses in these velocity components are clearly visible. Wind velocities (green)[161] are almost identical for both drifters, indicating lacking small scale features in wind data[162]. Wind speeds were initially North-Northeast directed, showing ceasing amplitudes for a 4 hours period after drifter releases. Winds were subsequently changing into western directions, showing increasing amplitudes for an 6 hour interval, and finally adopting northwestern directions and rising amplitudes. Wind drag is reflected by pronounced eccentricities to northwestern directions of drifter velocities (black lines). This effect is less apparent for Type A drifter 1. Largely southern directed Stokes Drift velocities (red lines) were counteracting wind directions, reflecting depth induced wave refraction towards the islands' shores. As drifters were moving

---

[161]Note different units!

[162]This is of second importance in offshore regions, where wind patterns are not influenced by obstacles and thus homogeneous on large scales.
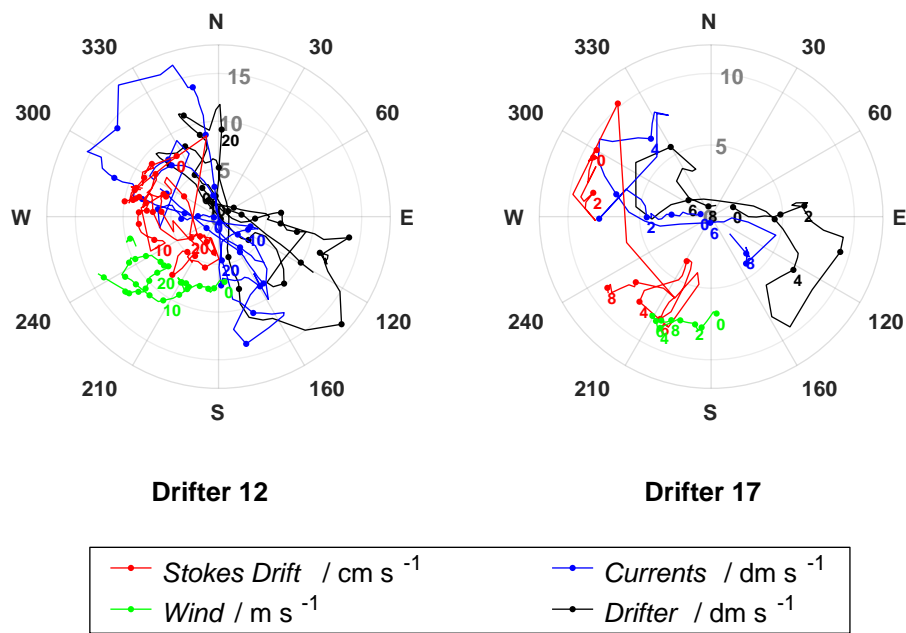
Figure 63: Phase diagrams for Type A drifter 12 and Type B drifter 17 of Ensemble ②. Currents (blue), Stokes Drift (red) and wind velocities (green) are in nautical convention, drifter velocities (black) are pointing traveling directions.

into deeper waters, Stokes Drift directions gradually adopted northwestern directions during the last 4 h interval of drifter 1 (Type A), thus acting parallel to prevailing winds as drifter 1 was traveling deeper waters and depth induced wave refraction became negligible.

Phase diagrams of the second ensemble's drifters 12 (Type A) and 17 (Type B) are shown in Figure 63. Transitions of velocities adopt more chaotic patterns, as drifters were traveling nearshore waters with rapidly changing bathymetry and wave breaking, increasing small scale fluctuations in currents. Both drifters were initially exposed to prevailing winds from south-southwestern directions for a 10 h period, coinciding with overall retention times for each Type B drifter. Incoming Stokes Drift from northwestern directions during the first 3 h interval was balancing northern directed components of wind drag and adding to eastern directed components of the latter. Hence resulting eastern transports due to wind and waves were adding to zonal tidal components of surface currents (blue) and resulting in eastward drifter velocities (black). After 3 h (Drifter 17, Type B) resp. 5 h (Drifter 12, Type A) of floating time, strong surface currents from Northeast (blue) were affecting both drifters, reflecting strong zonal currents at

the tidal channel, separating Spiekeroog and Wangerooge. After performing one-half oscillation, Drifter 12 eventually left the channel at the northern outlet. In contrast, Type B drifters of Set ② were eventually beaching at the eastern tip of Wangerooge as a whole ensemble (c.f. Figure 61). Stokes Drift was adding up to wind drag, counteracting Eulerian surface currents and resulting in beaching of each drifter (cf. left panel of Figure 63). Assuming $C_w \approx 0.01$, Stokes Drift values were of same orders as wind drag for majorities of floating times.

7.2.3. Drag Coefficients

Drag coefficients were estimated using equation (57) for three linear drag models, i.e. *(a)* setting $u_l^{t_i} = u_e^{t_i} + u_{St}^{t_i}$ with modeled surface currents and Stokes Drift, *(b)* setting $u_l^{t_i} = u_e^{t_i}$, i.e. neglecting Stokes Drift[163] and *(c)* setting $u_l^{t_i} = u_e^{t_i}$ but using modeled Stokes Drift in the observation matrix A to predict a second set of drift parameters α_{St} and C_{St}. Results for each linear drag model, based on individual velocity data of each drifter for neglecting error terms, i.e. $u_{err} = v_{err} = 0$, are shown in Figure 64. Mean drag values for different drifter types and ensembles are depicted by shaded areas and solid lines in Figure 64 and summarized in Table 7. Results for regarding error terms are shown in Figure 134 and Table 11 in Appendix F.

Drag Model a Estimated wind drag parameters C_w and deflection angles α_w are shown in the top line of Figure 64 for each drifter. Results for drifter Set ① are shown in magenta coloring, results for Set ② in cyan. Drifter types can be differed by shapes of symbols: Squares indicating Type A and circles indicating Type B drifters. Shaded areas denote estimates and 95%-confidence intervals based on combined velocity data of all Type B drifters of each set.

   Set ①: Estimated drag coefficients for Type B drifters (magenta circles) are homogeneously distributed at $C_w = (2.69 \pm 0.28) \times 10^{-2}$, thus exceeding theoretical values of equation (53). Estimates $C_w = (1.20 \pm 0.40) \times 10^{-2}$ for drifter Type A (magenta square) are significantly lower but also deviating from theoretical values given by equation (53).

   Estimated deflection angles (right panel) are evenly distributed around $\alpha_w = (-24 \pm 2)°$ for Type B drifters and unexpectedly high ($\alpha_w = -48 \pm 9$)

---

[163]The "classical" approach commonly used in literature, see cites in section 2.
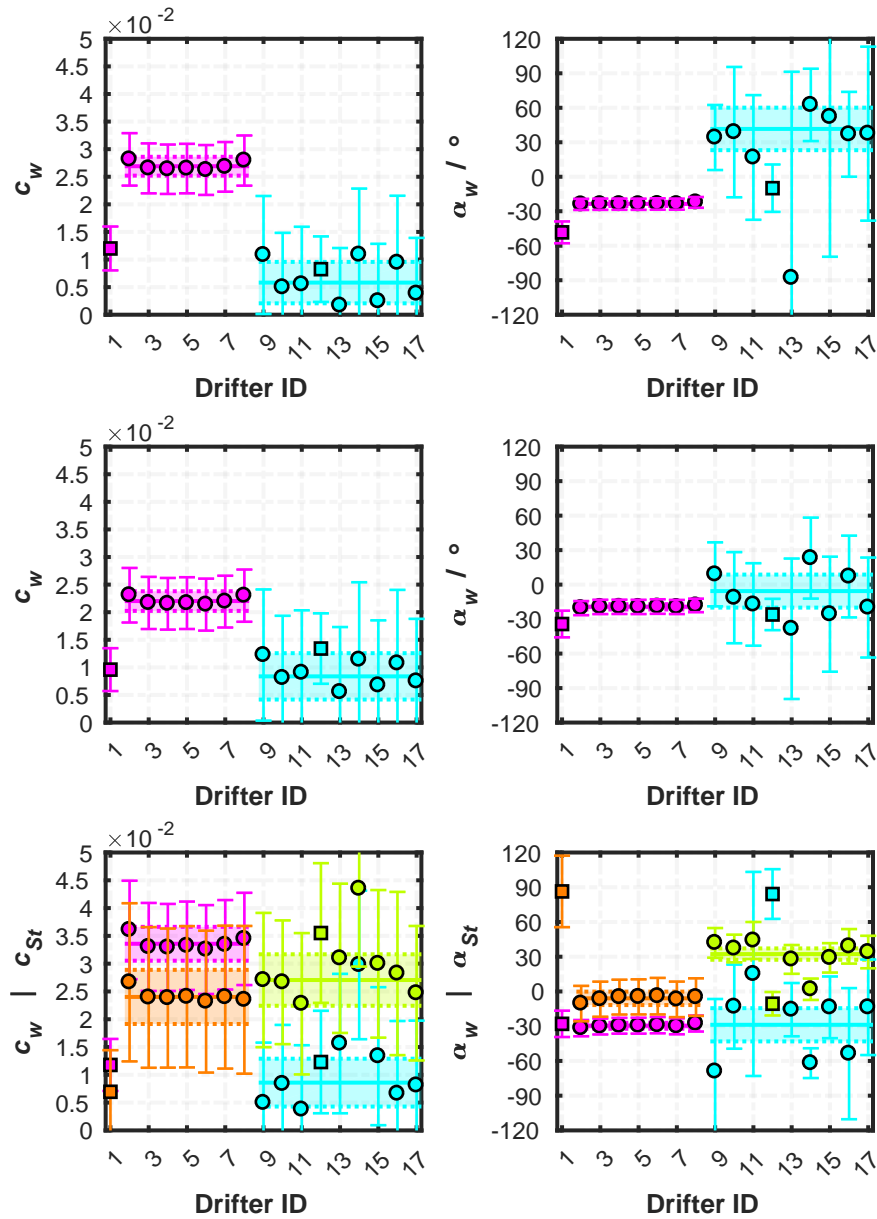
Figure 64: Estimated values of drag coefficients C_i and deflection angles α_i using equation (57). Squares indicate Type A, circles indicate Type B drifters. The top line provides estimates for constant Stokes Drift and current velocities, the second line for neglecting Stokes Drift. Estimates in the bottom line are based on assuming Stokes Drift as additional observation variable. Error terms in equation (57) were neglected for all estimates shown. Note the scaling of drag parameters in the bottom panel, where $\times 10^{-2}$ is valid for wind drag c_w but not Stokes drag c_{St}.

Table 7: Estimated drag coefficients, if constant error terms are neglected, i.e. $u_{err} = v_{err} := 0$.

ID	$\alpha_w/°$	$C_w \times 10^{-2}$	$\alpha_{St}/°$	C_{St}
Model a				
1	-48 ± 9	1.20 ± 0.40	0	1.00
2-8	-24 ± 2	2.69 ± 0.28	0	1.00
12	-10 ± 21	0.83 ± 0.59	0	1.00
9-17	42 ± 18	0.58 ± 0.38	0	1.00
Model b				
1	-34 ± 12	0.96 ± 0.39	$-$	$-$
2-8	-19 ± 2	2.20 ± 0.18	$-$	$-$
12	-26 ± 14	1.34 ± 0.64	$-$	$-$
9-17	-6 ± 14	0.84 ± 0.42	$-$	$-$
Model c				
1	-28 ± 11	1.18 ± 0.47	86 ± 31	0.69 ± 0.75
2-8	-30 ± 3	3.36 ± 0.30	-6 ± 6	2.40 ± 0.49
12	84 ± 21	1.23 ± 0.92	44 ± 16	3.55 ± 1.25
9-17	-29 ± 14	0.86 ± 0.43	32 ± 5	2.71 ± 0.46

for Type A. In both cases, deflection angles are pointing right hand side of wind directions[164], possibly hinting at underestimated Ekman currents or Coriolis Stokes effect by the hydrodynamic resp. wave models. As Stokes Drift was fixed in Regression Model a, lacking Coriolis Stokes effects might be falsely comprised by wind deflection angles. As wind drag is lower for drifter Type A, Stokes Drift is affecting drag of these drifters to higher degrees, making errors therein more severe.

Set ②: Estimated wind drag drag coefficient for Type B drifters significantly surpass estimates for ensemble ①, yielding $C_w = (0.58 \pm 0.38) \times 10^{-2}$. Values based on velocity data of individual drifters show strong variations around this value, likely caused by small deviations in individual release locations in space and time. These variations are likely caused by small scale variations of currents and Stokes Drift due to bathymetrical changes and wave breaking. Being even lower than the theoretical values in equation (53) ($C'_{w_B} = 1.75 \times 10^{-2}$), Stokes Drift is dominating transports of these drifters. The estimated drag coefficient $C_w = (0.83 \pm 0.59) \times 10^{-2}$ for drifter Type A matches its respective theoretical value within error bounds and does not significantly deviate from drag coefficients for drifters of Type B. Differences in estimates for Sets ① and ② might be caused by differing res-

---

[164]Angles are given in mathematical convention throughout this section, i.e. positive values indicating counterclockwise rotations.

idence areas as Stokes Drift is considered a main transport mechanism in shallow regions, even exceeding wind drag. Furthermore, thinner vertical layers in shallow regions of the hydrodynamic model are better representing wind driven surface currents[165].

Deflection angles are $\alpha = (-10\pm21)°$ for drifter Type A and $\alpha = (42\pm18)°$ for Type B. The upper bound interval for the former, i.e. $-10°...11°$, represents moderate values, evenly distributed to left and right hand directions of winds. Lower bound values, i.e. $-31°... -10°$ are again indicating shortcomings in either hydrodynamic or wave data. Deflection angles for Type B drifters are significantly scattered around $\alpha_w = (42 \pm 18)°$, representing deflection to the left hand sides of wind directions. Drifters of Set ② were traveling parallel to Spiekeroog's coastline for about a third of absolute floating times. On these transects, adjusting wind drag to the left is balancing Stokes Drift, refracted towards beaches, i.e. pointing right hand side of drifter paths. C_w estimates for these drifters are significantly surpassing estimates for Set ①, hinting at the model overestimating Stokes Drift in these areas. Integrating Stokes Drift over multiple layers could improve results, as Stokes Drift rapidly decreases with depth (c.f. equation (25)).

Drag Model b C_w and α_w estimates using Regression Model b, are shown in mid panels of Figure 64 and in Table 7.

Set ①: Drag values $C_w = (0.96 \pm 0.39) \times 10^{-2}$ (Type A) and $C_w = (2.20\pm0.18)\times 10^{-2}$ (Type B) are smaller than estimated by Model a. This is a direct consequence of neglecting Stokes Drift, as wind direction and Stokes Drift are counter directed in prevailing paths of Set ① (e.g. Figure 62). Drag values for drifter Type A (ID1), however, agree within error ranges in both Regression Models a and b.

Deflection angles $\alpha_w = (-34 \pm 12)°$ for drifter Type A resp. $\alpha_w = (-19 \pm 2)$ for Type B drifters are smaller than computed by Model a, but within comparable ranges. Eventually, Models a and b are resulting in insignificant differences for drifters of Set ①, traveling into offshore directions.

Set ②: Estimated drag values are $C_w = (1.34 \pm 0.64) \times 10^{-2}$ (Type A) and $C_w = 0.84 \pm 0.42$ (Type B), resembling estimates of Drag Model a within error ranges. However, best fit values for both drifter types are showing positive offsets, possibly accounting for lacking eastern components

---

[165]Possibly causing overestimated surface currents, as drogues of in-situ drifters might span several vertical layers, necessitating integrations of multiple layers.

in drift velocities in comparison to Model a[166]. Unlike Model a, individual drag values (cyan circles and square) are lying within error bounds of ensemble means (shaded area) and are showing smaller error bounds, possibly indicating lacking small scale variations due to depth induced wave breaking. In conclusion, individual drag estimates of Models a and b agree within error bounds.

Contrary to Set ①, estimated deflection angles for Type B drifters are clearly differing from Model a estimates, yielding $\alpha_w = (-6 \pm 14)°$. Again indicating overestimates in wave refraction towards beaches resp. in Stokes Drift values, differences for Models a and b could possibly vanish when tuning depth induced wave breaking in SWAN[167]. Estimated deflection angle $\alpha_w = (-26 \pm 14)°$ for drifter Type A is again resembling findings of Model a within error ranges. These minor differences might be caused by longer floating periods of Drifter 12 in deeper offshore waters. Stokes Drift values are smaller in these areas and adopt approximately parallel directions to winds as depth induced refraction becomes less important.

Drag Model c Drag values and deflection angles for wind drag, C_w resp. α_w (magenta and cyan), and Stokes Drift, C_{St} resp. α_{St} (orange and lime), are shown in the bottom panels of Figure 64 and in Table 7. Note differences in magnitudes of respective drag coefficients on the ordinate of Figure 64.

Set ①: Stokes Drag for the Type A drifter was estimated to $C_{St} = 0.69 \pm 0.75$, yielding about three-fourth of absolute Stokes Drift velocities. Estimated wind drag $C_w = (1.18 \pm 0.47) \times 10^{-2}$ is resembling estimates by Regression Model a within error ranges. Thus, applying drag parameters to Stokes Drift is insignificantly affecting wind drag estimates for Drifter 1. Drag coefficients for Type B drifters were estimated to $C_{St} = 2.40 \pm 0.49$ resp. $C_w = (3.36 \pm 0.30) \times 10^{-2}$. Comparing to Regression Models a and b, drag values are estimated significantly higher. As winds and waves were predominantly antiparallel directed for these drifters (cf. Figure 62), higher C_{St} values imply increasing wind drag C_w.

Deflection angles for drifter Types B were estimated to $\alpha_{St} = (-6 \pm 6)°$ resp. $\alpha_w = (-30 \pm 3)°$. Wind deflection is lying outside uncertainty bounds of Models a and b but of comparable magnitudes and indicating same

---

[166]As previously mentioned, Stokes Drift and wind directions were resulting overall eastern directed transport in nearshore regions of Spiekeroog.

[167]Note breaking parameters were based on validations with measurements, shown in subsection 4.3

directions. Deflection angles $\alpha_{St} = -12°...0°$ for Stokes Drift are small and contradicting missing Coriolis Stokes effects in the model, as wind deflection angles were estimated to even higher degrees in this drag model. Estimates of Stokes Drift deflection for drifter Type A are unreasonably high, yielding $\alpha_w = (86 \pm 31)°$, i.e. perpendicular to modeled wave directions. Wind deflection $\alpha_w = (28 \pm 11)°$ is lowest of all drag models, but again agrees with Models a and b within error ranges.

Set ②: Stokes Drift drag coefficients were estimated to $C_{St} = 3.55 \pm 1.25$ (Type A) resp. $C_{St} = 2.71 \pm 0.46$ (Type B), indicating overestimated depth induced wave breaking in shallow areas by the wave model. Wind drag values were estimated to $C_w = (1.23 \pm 0.92) \times 10^{-2}$ for Type A resp. $C_w = (0.86 \pm 0.43) \times 10^{-2})$ for Type B. Hence, estimated wind drag values agree within error ranges in each drag model.

Wind deflection angles for both drifter types significantly differ from previous estimates, yielding $\alpha_w = (84 \pm 21)°$ (Type A) and $\alpha_w = (-29 \pm 14)°$ (Type B). Stokes deflection angles for both drifter Types agree within error ranges, yielding $\alpha_{St} = (44 \pm 16)°$ for Type A and $\alpha_{St} = (32 \pm 5)°$ for Type B. These values are pointing to the left hand side of Stokes Drift directions and thus towards alongshore traveling directions of Type B drifters (cf. Figure 61). In combination with high C_{St} values, these estimates are indicating overestimated wave breaking by the model.

7.2.4. Reconstruction of Velocities

Drifter velocities were reconstructed using equation (56). Therefore interpolated model velocities (e.g. Figure 132) and estimated drift parameters (Figure 64 and Figure 134) have been used. Results for Drifters 1, 2 (Ensemble ①) and Drifters 12, 14 (Ensemble ②) are shown in Figures 65 resp. 66. Shaded areas are indicating ranges for varying drift parameters within respective error bounds. $u_{err}-$ and $v_{err}-$terms were neglected in these plots[168] Measured drifter velocities, shown by black dots in each plot, are based on logged GPS-data using equation (54).

Zonal velocities of drifter 1 (Type A, Set ①, top panels of Figure 65) are adequately represented by each regression model, whereas meridional velocities significantly differ from measured velocities based on GPS-data (black dots): At the beginning of simulations, Models a and b show good agreement

---

[168]Reconstructions for additional drifters as well for models retaining u_{err} and v_{err} (parameters of Table 11) are shown in Appendix F.
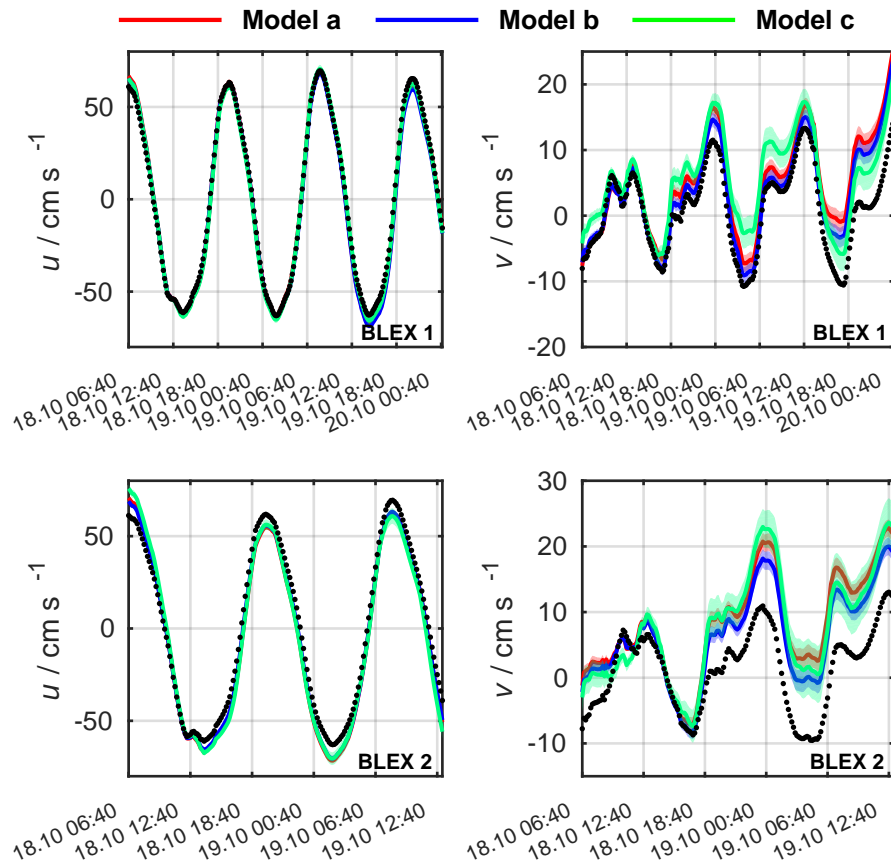
Figure 65: Reconstruction of drifter velocities using equation(56) and individual drag estimates (cf. Figure 64). Gaussian error bounds are shown by shaded areas, drifter velocities based on GPS-data are shown by black dots.

within error ranges over a period of the first 12 hours of floating time, but are overestimating v-velocities afterward. Differences between both models are minor. In contrast, v-velocities are initially overestimated by Model c, then well predicted for a six hours period starting on Oct. 18th, 10:00 until quickly adopting offsets towards positive v-velocities. Note decreasing importances of Stokes Drift for drifters entering deeper waters. Thus using C_{St} does not improve accuracies for periods after Oct. 18th, 16:00[169]. Each model is resulting in similar zonal velocities for drifter 2 (Type B, ensemble ①, bottom panels of Figure 65), differing from GPS-data at local velocity extrema but agreeing within error ranges for intermediate velocities. As seen for drifter 1, modeled meridional velocities are significantly differing from measurements, showing positive offsets for almost entire modeling periods. Again, Model b (solely winds) is giving most accurate results for floating periods in deeper waters after Oct. 18th, around 14:00. Retaining Stokes Drift using drag parameters C_{St} yields well represented v-velocities in shallow to intermediate waters, i.e. for periods around 10:00 until 18:40 of Oct. 18th. Significant offsets in meridional velocities for each drifter of ensemble ①[170] are present for each drag model, yielding overestimated velocities in northern directions.

Fitted u- and v-velocities for Drifter 12 (Type A, ensemble ②, top panels of Figure 66) are well representing variations of measured data, but are offset towards positive values when compared to the latter. These offsets are more significant for zonal velocities, depicted on the left panel, and again increasing at local extrema. During the drifters' journey parallel to the beach of Spiekeroog, i.e. first 4 hours in Figure 66 (cf. Figure 61), absolute velocities are especially overestimated by Model c (green), possibly causing drifters washing up at the beach of Spiekeroog, when using this drag model[171]. In case of Drifter 14 (Type B, ensemble ②) drag parameters based on Models a and b are resulting in equivalent zonal velocities within error bounds. In contrast, Model c is significantly overestimating u-velocities, as measured data are lying outside respective error bounds most of the time. In contrast, meridional velocities during the first 3 h interval are well represented within error ranges by Model c, but not Models a and b. When entering the tidal channel region, easily recognized by a sharp dip in v-velocities in the sec-

---

[169] Also spatial varying vertical layer thicknesses due to S-coordinates in the hydrodynamic model might impact accuracies.

[170] See Appendix F for drifters 3 to 8.

[171] Note negative v-velocities are southern directed.
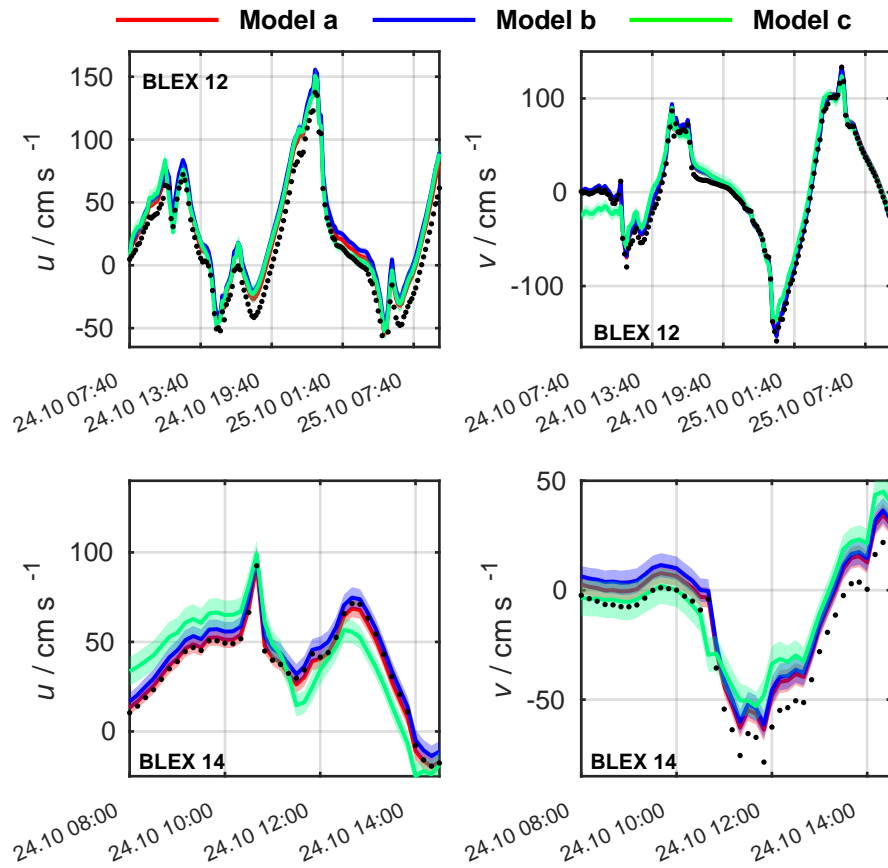
Figure 66: Reconstruction of drifter velocities using equation(56) and individual drag estimates (cf. Figure 64). Gaussian error bounds are shown by shaded areas, drifter velocities based on GPS-data are shown by black dots.

ond 2 h interval, each drag model fails reproducing meridional velocities. As Type B drifters are showing similar velocity profiles throughout ensemble ② but individual drift parameters significantly differ in Drag Models a to c (Figure 64), accuracies and error ranges of reconstructed velocities, shown in Figures 138 to 139 in Appendix F, are varying for drifters 9 to 18 (see Appendix F).

Retaining constant error terms u_{err} and v_{err} in equation (57) increases error ranges for each model, as these parameters are of magnitudes of surface currents (u_l, v_l) (cf. Table 11). Hence velocities for drifters of Ensemble ① are reproduced within error ranges by each model. However, reconstructed velocities for drifters of ensemble ② still significantly differ from measurements (Figures 140 to 146 in Appendix F).

7.2.5. Lagrangian Modeling

Trajectories for individual drifters were computed by the Lagrangian modeling toolbox FLOPPSY using RK4 integrations with $dt = 5\,\mathrm{min}$[172] and SP-Model data on 5 min intervals. Ensemble mean drag parameters for Models a to c, depicted by shaded areas resp. solid lines in Figure 64[173], were used in these calculations. As differences in computed trajectories for individual Type B drifters were minor for both ensembles, discussions are limited to IDs 1 (Type A, Set ①), 2 (Type B, Set ①), 10 (Type B, Set ②) and 12 (Type A, Set ②) in this section. Results are shown in Figures 67 to 70. Red trajectories are representing drifter paths for using drag parameters of Model a. Deviations for changing deflection angles α_w (green) and drag coefficients C_w (yellow) within respective error intervals are indicated by shaded areas[174]. Zonal and meridional drifter velocities computed by the Lagrangian model are shown in the mid and bottom panels of each plot. Velocities based on GPS-measurements are shown by black dots. Time intervals on the abscissa are coinciding with trajectory segments denoted by dots in the upper panels. Segments are generally representing 6 h (Set ①) resp. 2 h intervals (Set ②). Lagrangian trajectories for drifters using Drag Models b and c are shown in Appendix F, Figures 147 to 158. In case of the latter model, varying drag parameters α_{St} resp. C_{St} were used while keeping

---

[172]Using $dt = 1\,\mathrm{min}$ resulted in almost identical trajectories for Drifter 1 (not shown).
[173]Cf. Table 7.
[174]The yellow area in Figure 67 is e.g. indicating envelopes of two trajectories for fixed deflection angle $\alpha_w = -48°$ but varying drag coefficients in the range $C_w = (1.20 - 0.40...1.20 + 0.40) \times 10^{-2}$, c.f. Table 7.

7. BLEX: Beaching Litter EXperiment

fixed 'best fit values' for α_w and C_w.

Lagrangian trajectories of Drifter 1 using Drag Model a are shown by red trajectories in the top panel of Figure 67). Computations are significantly deviating from GPS-tracks (black), resulting in underestimated net movement in meridional directions. Computed v-velocities, shown in the bottom panel, are rarely exceeding $10\,\mathrm{cm\,s^{-1}}$ in the initial $18\,\mathrm{h}$ interval. Using upper bounds of estimated drag coefficients, i.e. $c_w = 1.60 \times 10^{-2}$, was not significantly increasing meridional velocities for this time interval[175]. Even though underestimating absolute v-velocities, temporal locations of maxima and minima are represented by the Lagrangian model. Thus tidal ellipses were replicated but lacking North-South semi-axes. However, the local maximum near Oct. 19th, 00:00 is delayed within the model. Measurements and simulations are offset towards positive values, indicating prevailing winds into northern directions (cf. Figure 62). Wind gusts are represented by sharp peaks and dips in velocities. Zonal u-velocities were predominantly tidal driven during floating periods of Ensemble ①. Lagrangian computations are representing temporal evolutions and maxima of measurements, but underestimating minima. Note offsets in v-velocities are indicating errors in wind driven surface currents or over- resp. underestimated drag coefficients C_w. However, inaccuracies in local extrema of velocities are hinting at errors in tidal components of the hydrodynamic model.

Altering C_w and α_w (green and yellow shaded regions) within error bounds did not improve accuracies of modeled trajectories. Neglecting Stokes Drift (Model b, Figure 148 in Appendix F) barely increased northward velocities in shallow waters due to smaller C_w values. Hence offshore directed transport, particularly in the initial $12\,\mathrm{h}$ interval, is significantly underestimated. Choice of drag parameters was resulting in minor differences in this interval. Altering wind drag C_w within error bounds was stronger impacting velocities and trajectories than altering α_w. Choosing drag parametrization based on Regression Model c (Figure 149) was neither improving Lagrangian trajectories.

Calculations for Type B drifters of Ensemble ① (exemplary BLEX 2, Figure 68) are also underestimating v-velocities, but resulted in increased net transports towards offshore regions. Maxima of meridional velocities in deeper waters (approx. Oct. 18th, 18:40 and later periods) are showing same

---

[175]Note meridional v-velocities are denoting North-South directed velocity components with positive values indicating northern directions. Hence zonal u-velocities are indicating West-East directed velocities pointing into eastern directions for positive values.
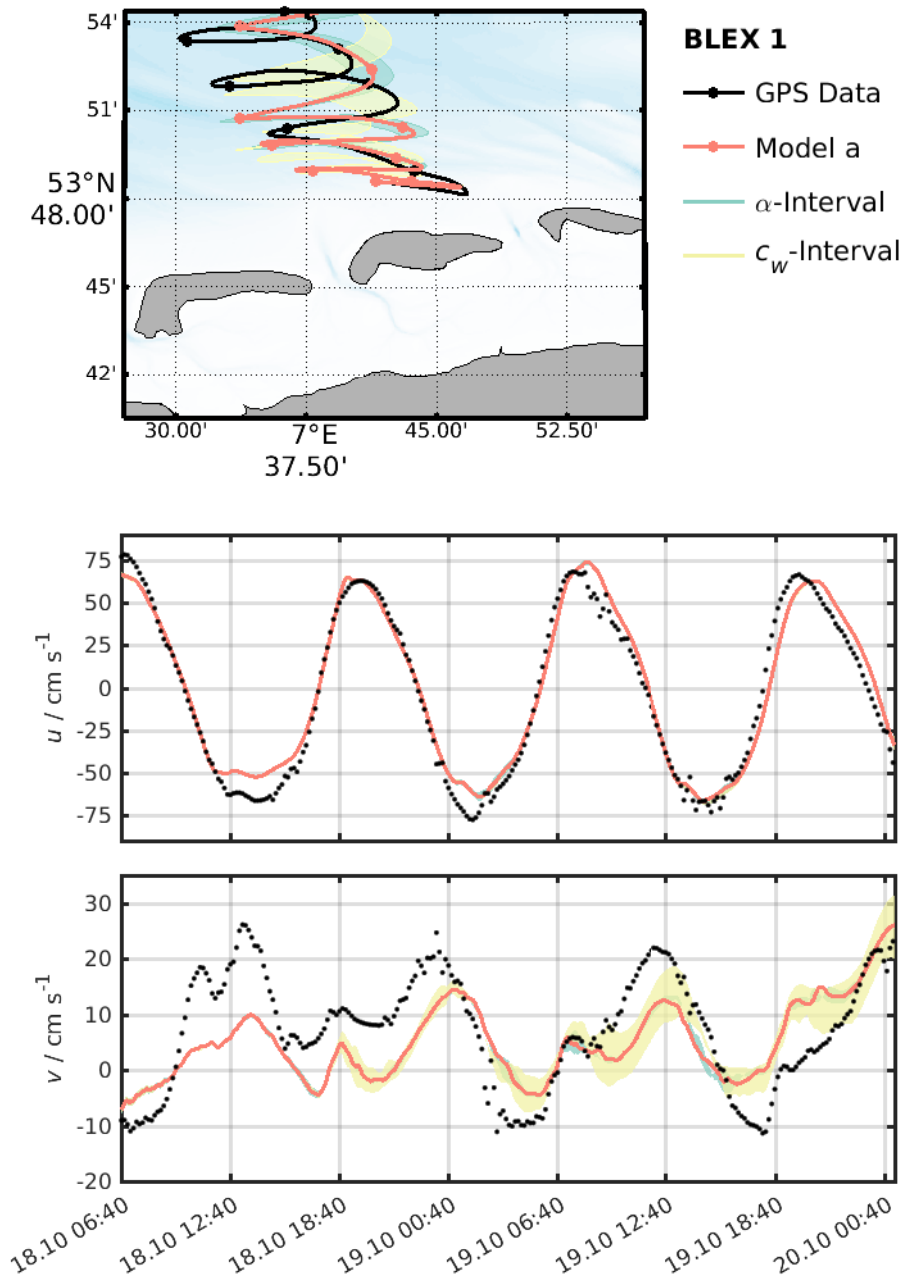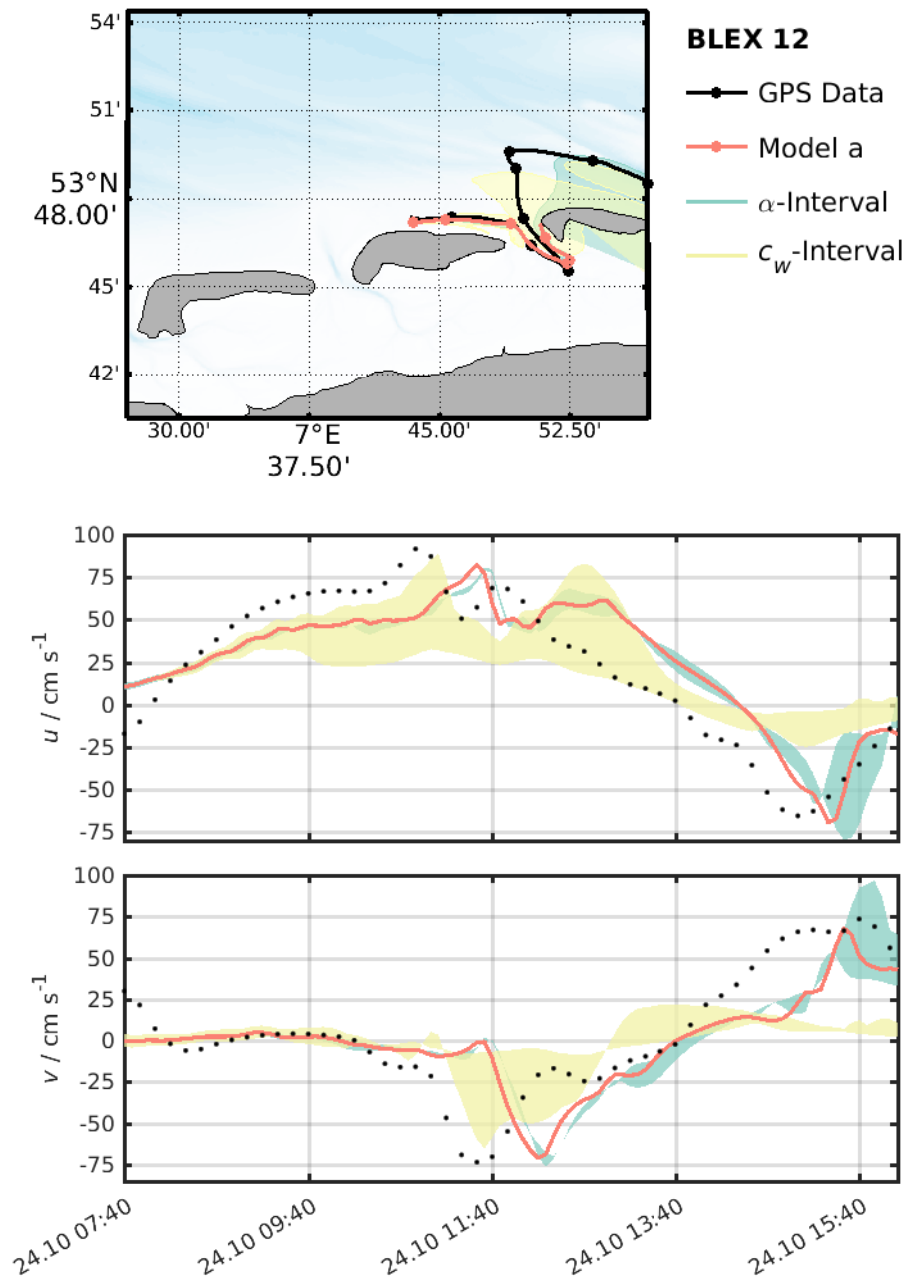
Figure 67: Computed trajectories for Drifter 1 (Type A), using drag parameters for Model a without error term and Runge-Kutha intergartion. The lower panels show corresponding drifter velocities. Dots indicate 6 h-intervals, shaded areas denote ranges for varying drag values (yellow) and rotation angles (green) within error ranges of the regression.

amplitudes by Lagrangian estimates and measurements. As in case of Drifter 1, zonal velocities are well represented by the model. Varying deflection angles within error bounds ($\pm 5°$, green shaded area) was not significantly altering Lagrangian trajectories due to small error intervals. Varying C_w, however, affected trajectories to similar degrees as seen for Drifter 1. Using Regression Models b and c (Figures 151 and 152 in Appendix F) did not improve Lagrangian calculations. Accuracies even decreased when using Drag Model c, as $C_{St} = 2.40 \pm 0.49$ increased shoreward directed Stokes Drift, hampering northward movement of Lagrangian particles.

Drifters 10 (Type B) and 12 (Type A) are exemplarily shown for Set ② in Figures 69 resp. 70. Contrary to measured tracks, Lagrangian computations for drifter Type A (ID 12, Figure 70) predicted beaching at the western edge of Wangerooge when using best fit parameters (red trajectory), whilst modeled drifter 10 (Type B, Figure 69) was leaving at the eastern boundary of the modeling site. Varying drag parameters significantly altered Lagrangian trajectories of both drifters, averting beaching when using C_w values in lower error bounds for drifter 12 resp. causing beaching of drifter 10 for certain combinations of drag parameters. Thus, the model is qualitatively reproducing drifter paths within error ranges. Lagrangian computations for drifters 11 to 17 of Type B were resulting in similar paths and are not shown here. Lagrangian velocities are lacking measurements by approx. 1 hour. Possible one hour shifts of measured and modeled data were checked several times and are negated[176].

Using drag parameters based on Regression Model b led to similar results for drifter 10 (Type B, Figure 154). Eastern directed zonal velocities were underestimated in both cases, resulting in a late arrival at the tidal channel. In this area, currents are varying with tidal cycles, resulting in large differences between Lagrangian trajectories and measurements due to differing residence periods of modeled and measured drifters. Using Regression Model c resulted in coinciding beaching locations of Lagrangian and measured trajectories, independent of choices for C_{St} and α_{St} within error intervals. However, the model was underestimating floating periods due to absent transits of the tidal channel.

For drifter 12 (Type A), Lagrangian velocities based on Regression Model b are almost resembling measurements, but are showing large error bounds

---

[176]One hour time shifts in North Sea data are common mistakes, as data are referenced to various time zones depending on sources: e.g. UTC, CET or CEST. Note CEST = CET+1 h=UTC+2 h.
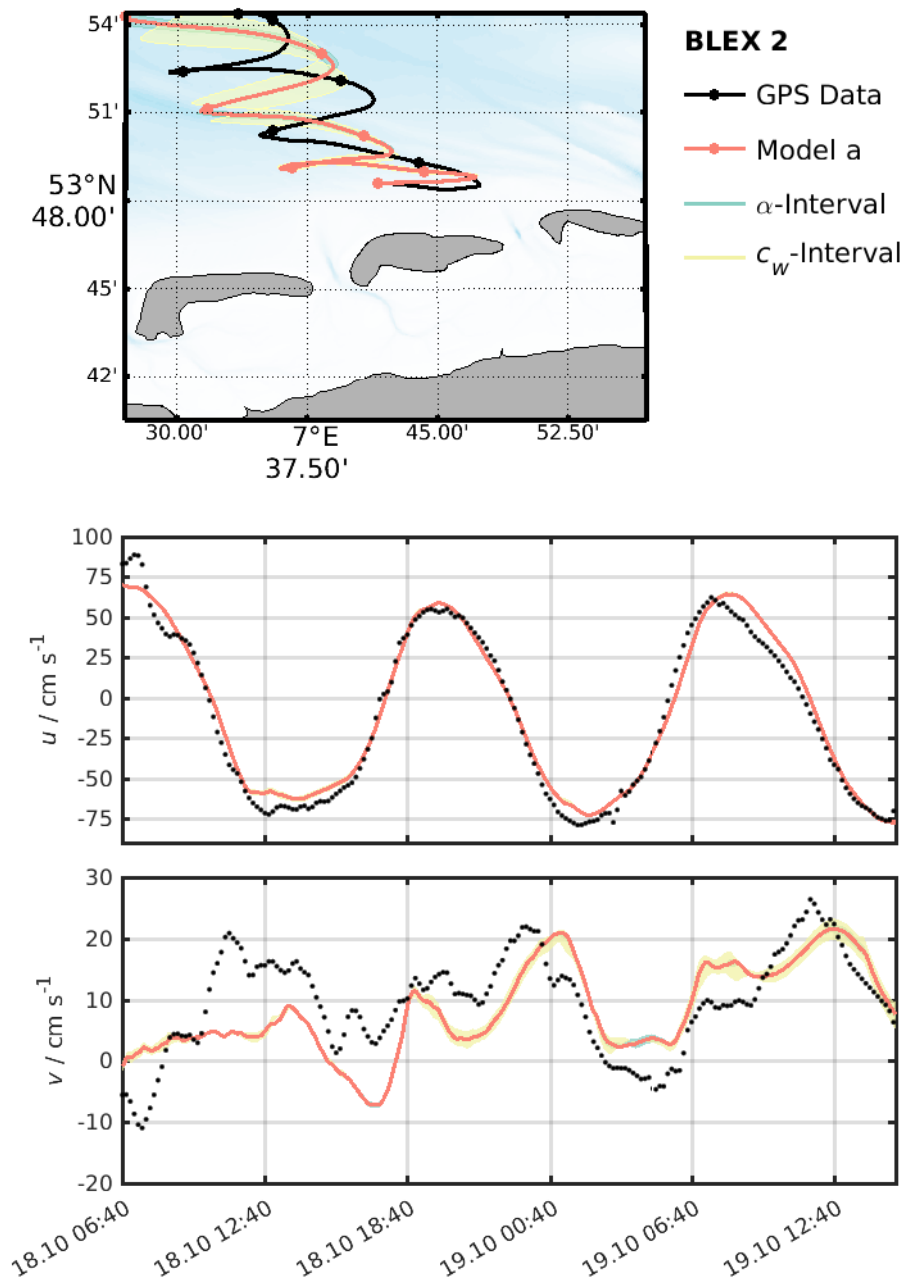
Figure 68: Computed trajectories for Drifter 2 (Type B) using drag parameters for Model a without error term and Runge-Kutha integration. The lower panels show corresponding drifter velocities. Dots indicate 6 h-intervals, shaded areas denote ranges for varying drag values (yellow) and rotation angles (green) within error ranges of the regression.
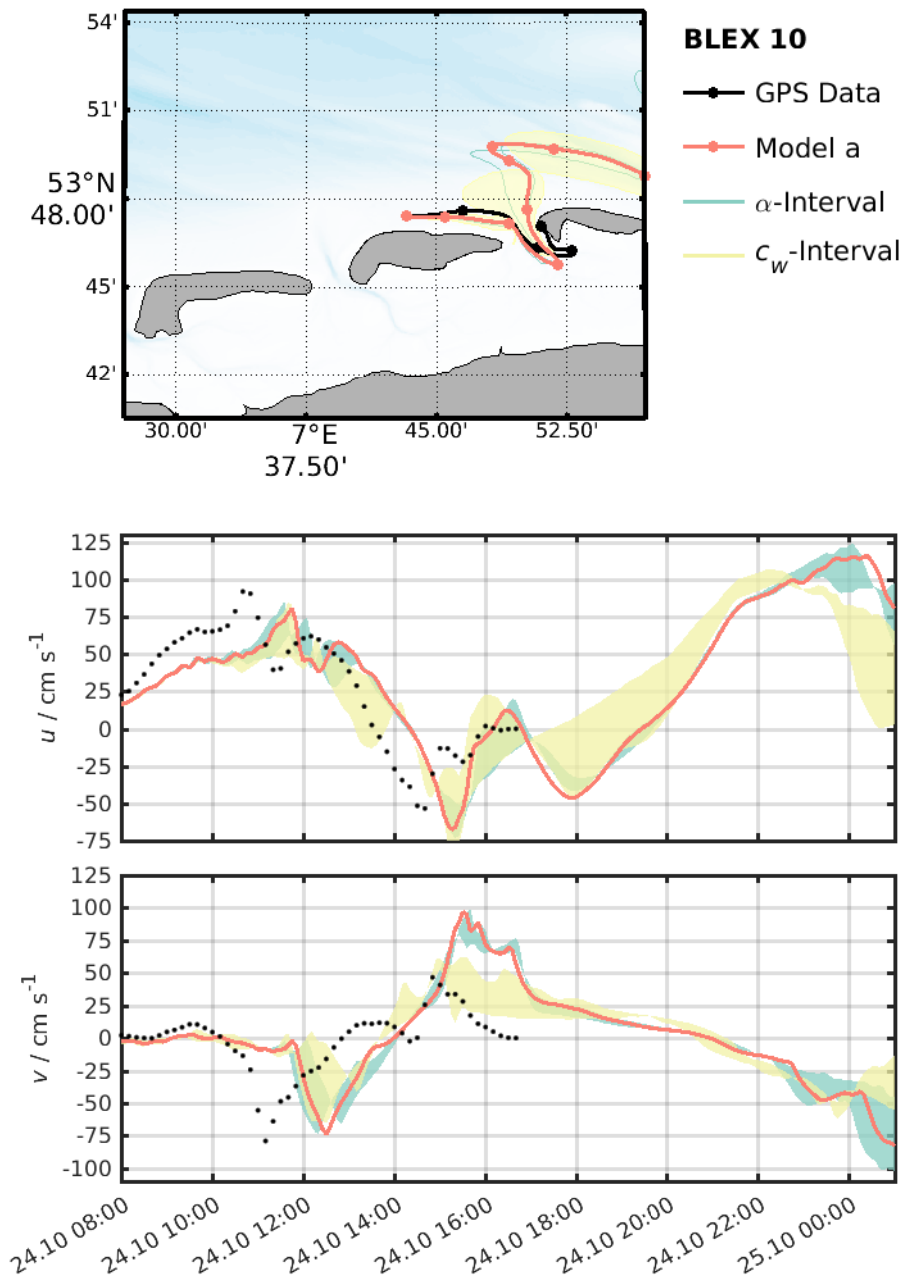
Figure 69: Computed trajectories for Drifter 12 (Type A) using drag parameters for Model *a* without error term and Runge-Kutha integration. The lower panels show corresponding drifter velocities. Dots indicate 6 h-intervals, shaded areas denote ranges for varying drag values (yellow) and rotation angles (green) within error ranges of the regression.

(Figure 157 in Appendix F). Leaving sites at the eastern boundary are well represented by Lagrangian trajectories. Varying wind drag C_w showed strong impact on Lagrangian trajectories. Using e.g. C_w in upper bounds of confidence intervals resulted in Lagrangian computations almost redrawing measured tracks (northern yellow perimeter in Figure 157). On the other hand, setting C_w to lower bounds of estimations resulted in Lagrangian trajectories traveling south of Wangerooge. Adding drag parameters C_{St} and α_{St} based on Regression Model c represented measured longshore transit of Drifter 10 at the beach of Spiekeroog (red trajectory in Figure 158) over the course of approx. 9 hours. Strong western directed zonal currents at the channel's northern outlet, seen in the mid panel of Figure 158, were then causing simulations to diverge from measurements. Albeit small error bounds for α_{St} ($\pm 5°$, cf. Table 7), varying deflection angles significantly impacted trajectories. Choosing lower bound $\alpha_{St} = 27°$ led to wash up at the northern beach of Spiekeroog after approx. three hours, whereas choosing upper bound value $\alpha_{St} = 37°$ caused trajectories leaving at the northern boundary of the modeling site.

7.3. Consistency Check: GB-Model

Although Lagrangian velocities represented magnitudes and temporal evolutions of measured drifter velocities when choosing arbitrary drag parameters within confidence intervals for Set ②, Lagrangian trajectories significantly differed from measurements for Ensemble ①. Drag parameters and Lagrangian trajectories have been estimated using modeled velocity data, possibly biased by shortcomings of the SP-Model. Thus, regression models and Lagrangian computations were estimated again using data from the GB-Model, featuring better vertical resolution on a coarse spatial grid. Validations for this model also showed good agreement with the BSHcmod and measurements.

Temporal mean surface velocities of both models for drifters' floating periods are compared in Figure 71. Black arrows are representing SP-Model velocities, red arrows data from the GB-Model. For both models, velocities have been bilinearly interpolated onto ρ-points of the fine grid and are plotted for every 10th grid point.

Surface velocities qualitatively agree near islands, with the SP-Model better resolving small scale features[177]. However, the SP-Model seems under-

---

[177]Also caused by the coarser landmasks in the GB-Model .

Figure 70: Computed trajectories for Drifter 14 (Type B) using drag parameters for Model a without error term and Runge-Kutha integration. The lower panels show corresponding drifter velocities. Dots indicate 6 h-intervals, shaded areas denote ranges for varying drag values (yellow) and rotation angles (green) within error ranges of the regression.
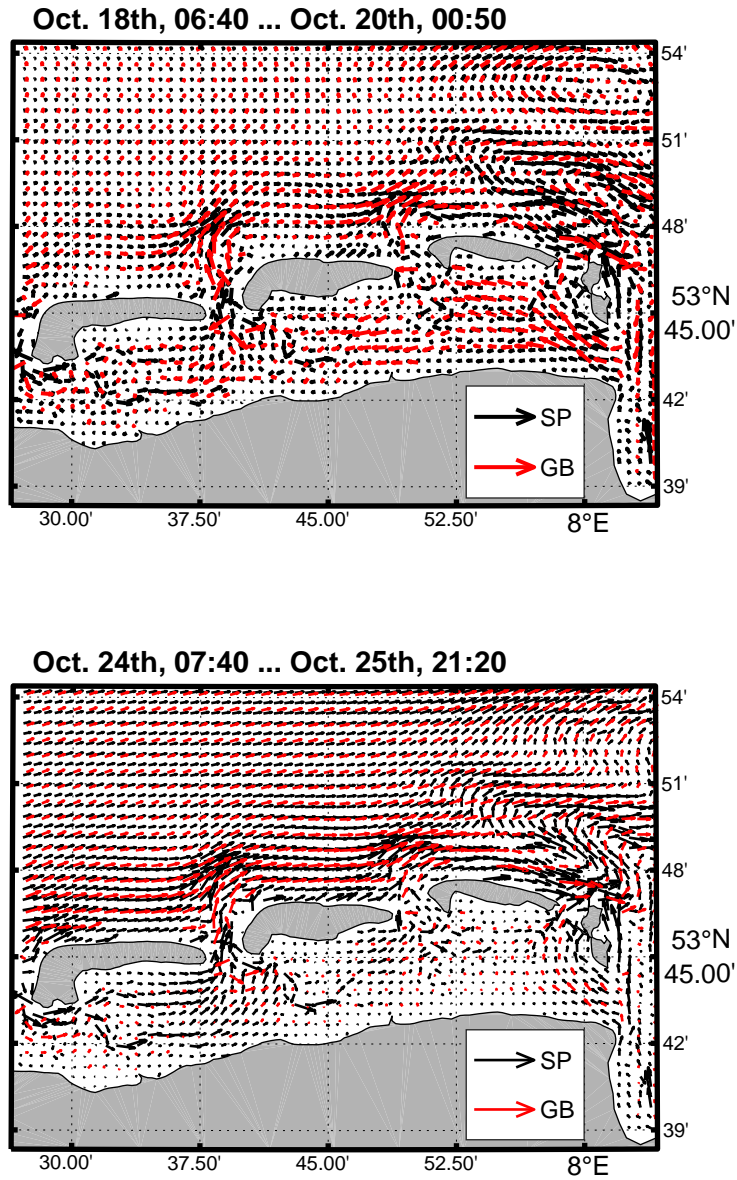
Figure 71: Temporal mean surface velocities for floating periods of drifter Sets ① (top) and ② (bottom). SP-Model data (black) and GB-Model data (red) were bilinearly interpolated on ρ-points of the former grid and plotted for every 10th cell.

estimating meridional velocities caused by southern winds in the top panel, which were main drivers for advecting drifters of Set ①. This is illustrated by Figure 159 in Appendix F, showing mean differences of both models in zonal and meridional velocities. For drifting periods of Ensemble ② (Figure 159, bottom panels) zonal velocities are significantly smaller in the SP-Model. Differences in meridional (Set ①) and zonal (Set ②) velocities can be caused by differing thicknesses of vertical layers, as these are representing wind driven layers[178]. Velocities of both models are especially differing in components correlating with prevailing wind directions for each period.

Velocity vectors of both models are significantly differing at the northern boundary of the SP-Model, which is seemingly underestimating northward components of v-velocities[179].

7.3.1. Drag Parameters

Drag parameters were again estimated using surface velocities from the GB-Model. Results for each drag model are shown in Figure 72[180]. As Type B drifters of ensemble ② were initially traveling in shallow waters near Spiekeroog, parameters of these drifters have been discarded due to insufficient spatial resolution of the GB-Model.

Estimated drag parameters for drifter Type A of Ensemble ① (ID 1) are $C_w = (0.39 \pm 0.12) \times 10^{-2}$ (Model a), $C_w = (0.71 \pm 0.13) \times 10^{-2}$ (Model b) and $C_w = (0.24 \pm 0.27) \times 10^{-2}$ resp. $C_{St} = 0.49 \pm 0.25$ (Model c). Deflections were estimated to $\alpha_w = (-46 \pm 9)°$ (Model a), $\alpha_w = (17 \pm 5)°$ (Model b) and $\alpha_w = (22 \pm 32)°$ resp. $\alpha_{St} = (18 \pm 15)°$ (Model c).

Regression Model a is resembling theoretical values (0.273×10^{-2}, equation (53)) within error ranges. Deflection $\alpha_w = (-46 \pm 9)°$ is pointing right hand side of wind directions and resembles magnitudes of wind induced currents in surface layers, discussed in subsection 2.2 and e.g. Yoshikawa and Masuda [2009] and Huang [1979]. Neglecting Stokes Drift in Model b resulted in counterclockwise deflections $\alpha_w = 12°...23°$, i.e. to the left. Discrepancies might be caused by neglecting Coriolis-Stokes forces when coupling ROMS

---

[178]Large numbers of vertical levels, thus thin surface layers, are better representing wind driven currents, cf. subsubsection 2.2.1. The importance of vertical layers in Lagrangian models is e.g. discussed by Callies et al. [2011].

[179]Tuning of nudging parameters in the SP-Model did not improve results, thus recommending two-way-nesting of both grids. This approach, however, did not turn out practicable due to instabilities and computational costs.

[180]Results regarding error terms in equation (57) are not shown here, as using constant velocity offsets did not improve Lagrangian trajectories.
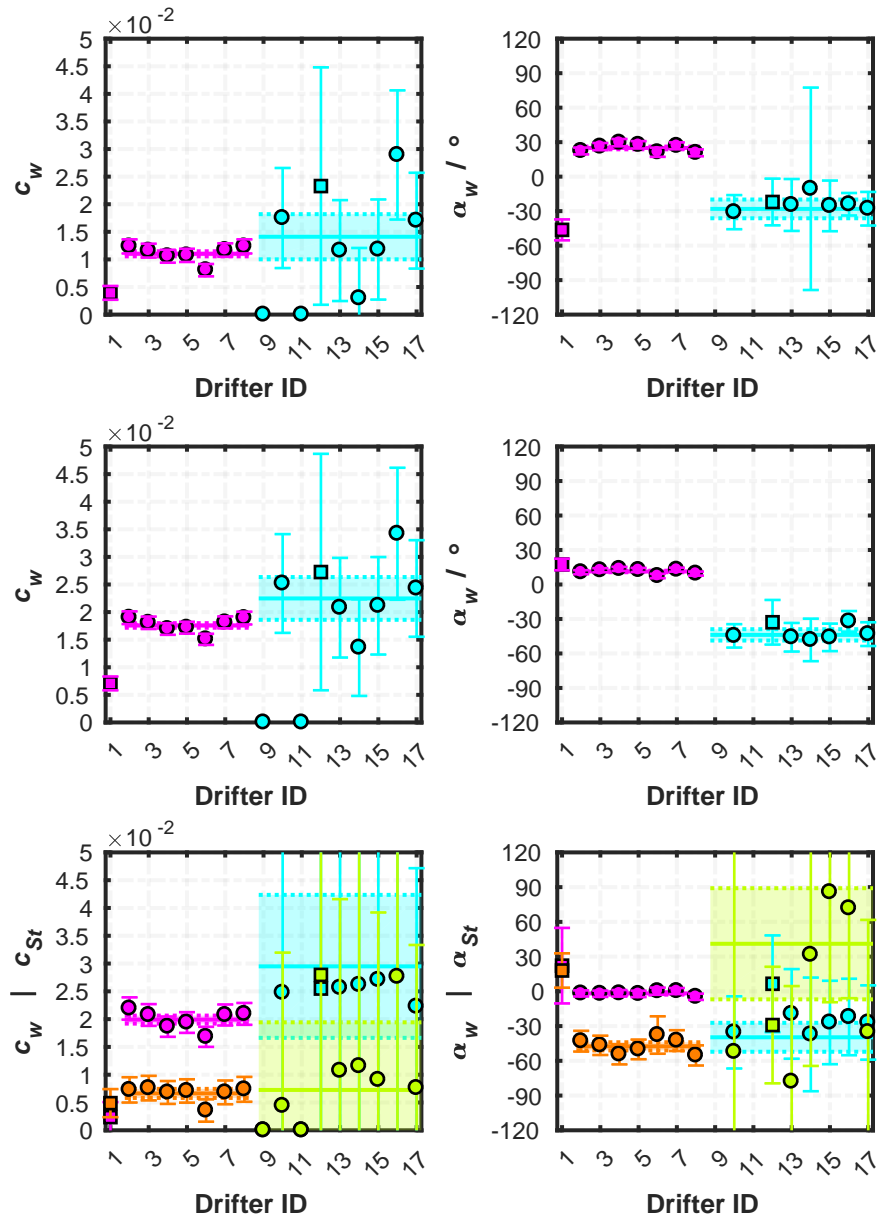
Figure 72: Estimated drag coefficients and deflection angles using response data from the GB-Model and neglecting error terms.

Table 8: Comparison of drag parameters for Drifter Types B of ensemble ①,
when either data of the GB-Model or SP-Model are used. Constant
error terms are neglected in these estimations.

ID	$\alpha_w/°$	$C_w \times 10^{-2}$	$\alpha_{St}/°$	C_{St}
Model a				
GB-Model	25 ± 1	1.10 ± 0.05	0	1.00
SP-Model	-24 ± 2	2.69 ± 0.28	0	1.00
Model b				
GB-Model	11 ± 1	1.46 ± 0.04	$-$	$-$
SP-Model	-19 ± 2	2.20 ± 0.18	$-$	$-$
Model c				
GB-Model	-2 ± 1	1.99 ± 0.07	-47 ± 9	0.66 ± 0.08
SP-Model	-30 ± 3	3.36 ± 0.30	-6 ± 6	2.40 ± 0.49

and SWAN, causing Regression Model a compensating lacking Stokes Drift deflection by increasing wind deflection angles. Positive α_w values in Model b are potentially caused by model data, overestimating deflection of wind driven surface currents, thus compensated by adjusting wind directions via α_w[181]. Regression Model c was estimating significantly lower drag values C_w and C_{St} than remaining models and resulting in moderate counterclockwise oriented deflection angles for Stokes Drift and wind drag.

Mean drag parameters for Type B drifters are listed in Table 8, comparing results for using GB-Model and SP-Model data. Deflection angles α_w for Regression Models a and b are of same magnitudes, but counterdirected. Using different numbers of vertical layers, i.e. $N_{SP} = 15$ resp. $N_{GB} = 20$, is possibly affecting these differences to some degree. Additionally, spatial resolutions of wind data and surface currents of both models are significantly differing[182]. Wind drag estimates C_w based on SP-Model data are twice of GB-Model estimates for Regression Models a and b, also indicating influences of differing surface layers, as winds induce larger surface currents in shallower top layers.

Comparing drag estimates by Regression Model c shows significantly differing results. Using GB-Model data resulted in highest wind drags C_w, almost doubling estimates by Model a. Wind deflection angles were estimated almost absent, yielding $\alpha_w = -2° \pm 1°$. Drag values $C_{St} = 0.66 \pm 0.08$

---

[181]Using insufficient numbers of vertical layers is generally causing overestimated Ekman deflection, as the surface layer is "too deep". Using too many layers, i.e. "too shallow" surface layers, is causing opposite effects. The latter can easily be solved by integrating currents in multiple layers.

[182]Note forcing of the SP-Model by high resolution wind data from the BSH (cf. Wüllner [2018]) and horizontal resolutions of both grids given in Table 4.

are of similar magnitudes as in case of drifter Type A. However, estimated deflection $\alpha_{St} = -47°$ seems unreasonably high, likely caused by lacking resolutions of bottom topography in the GB-Model, impacting wave breaking in the numerical model.

In conclusion, winds were estimated influencing Type B drifters to higher degrees in each Regression Model, thus confirming theoretical estimates in equation (53).

7.3.2. Lagrangian Trajectories

Discussion of Lagrangian trajectories will be limited to drifters 1 (Type A) and 2 (Type B), as coarse spatial resolutions of the GB-Model were causing minor differences of individual trajectories for ensemble ①. Trajectories for varying ranges of drag parameters were again computed using the FLOPPSY toolbox. Results for both drifters, using drag paramaters based on Regression Model a, are shown in Figures 73 resp. 74. Results using Drag Models b and c are shown in Figures 160 to 165 in Appendix F.

Using Drag Model a, meridional velocities of drifter 1 were again underestimated in nearshore regions, i.e. in the initial $26\,\text{h}$ interval (Figure 73, bottom panel), roughly corresponding to the drifter's retention period at the SP-Model grid. Zonal velocities are largely well represented by the Lagrangian model. Although underestimating meridional drift, Lagrangian and measured trajectories qualitatively agree, resulting in north-northeastern directed advection. After reaching the peninsula Eiderstedt in northeastern parts of Figure 73, Lagrangian trajectories significantly differed from measured tracks, likely caused by coarse spatial resolutions of the model grid. Varying wind drag C_w (yellow shades) altered trajectories to higher degrees than varying deflection angles α_w.

Lagrangian trajectories based on Model b are shown in Figure 161 in Appendix F. Computations were predicting overall drift directions fairly well, but resulted in beaching at Helgoland for best fit drag parameters and varying C_w values. Using lower limits of deflection angles α_w avoided beaching at the island. Meridional velocities were again underestimated for the initial $24\,\text{h}$ period.

Using drift parameters C_{St} and α_{St}, shown in Figure 162, resulted in initially similar Lagrangian trajectories. However, as modeled drifters were entering nearshore regions, varying drag parameters significantly impacted drifter paths. Hence terminal locations of Lagrangian simulations are largely
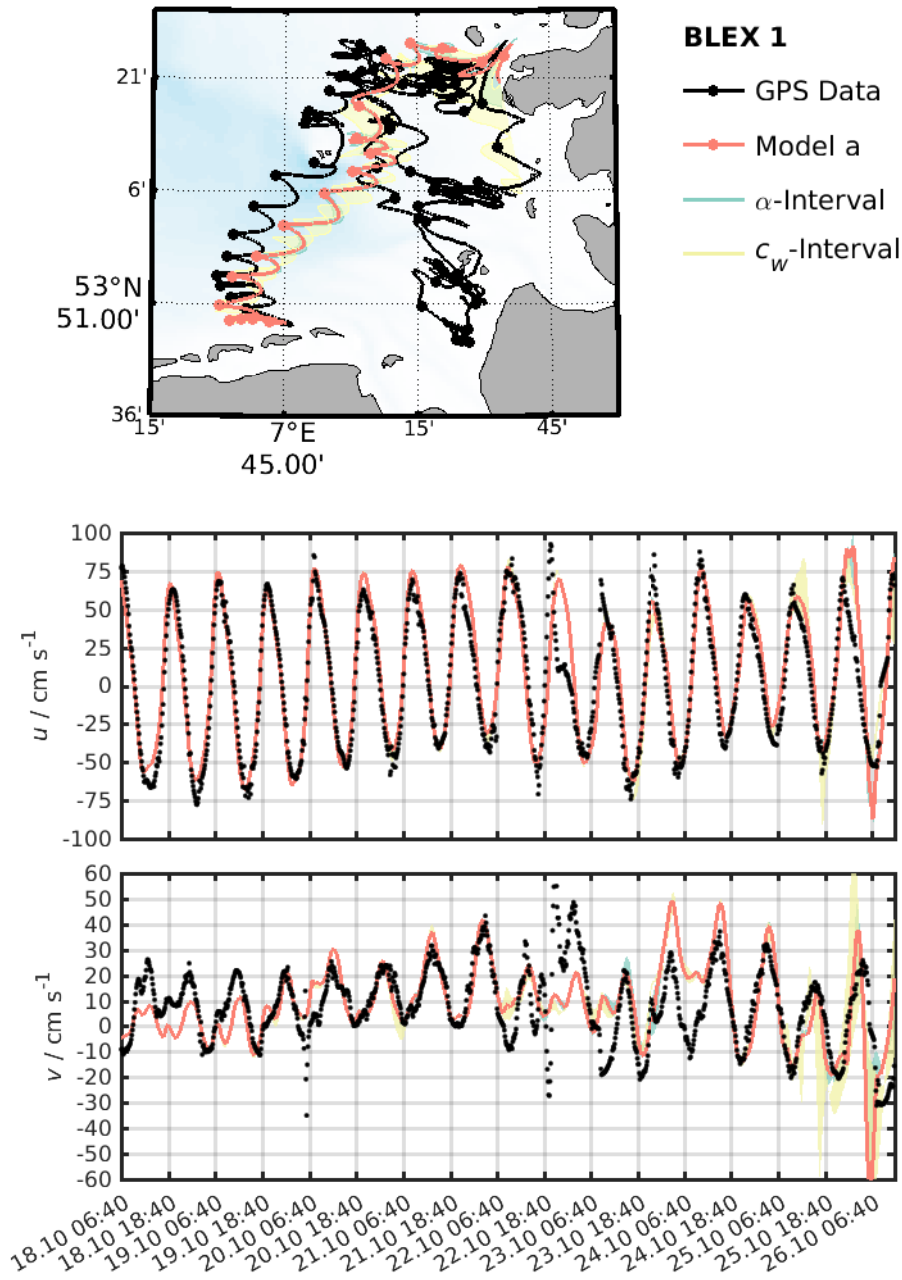
Figure 73: Computed trajectories for Drifter 1 (Type A) using drag parameters for Model a without error term and Runge-Kutha integration. The lower panels show corresponding drifter velocities. Dots indicate 6 h-intervals, shaded areas denote ranges for varying drag values (yellow) and rotation angles (green) within error ranges of the regression.

scattered, but overall drift directions are qualitatively replicating measurements.

Figure 74 shows measured (black) and Lagrangian (Model a, red) trajectories for Type B drifter 2. Meridional velocities were again significantly underestimated, but of higher magnitudes than in Type A drifter's case due to higher C_w values. Lagrangian v-velocities were lacking for initial periods of 60 hours[183]. Directories of Lagrangian trajectories, however, were initially qualitatively resembling measurements. Measured and modeled trajectories split north of Helgoland, leading Lagrangian trajectories turning East and thus beaching at the North Frisian Island Süderoogsand within two days. Measured GPS-tracks were breaking into northwestern directions near Helgoland and then turning East until beaching occured at Sylt. Changes into eastern directions of both trajectories were caused by strong winds, influencing GPS-drifters further North due to higher v-velocities. Using Regression Model b improved accuracies of Lagrangian trajectories until passing Helgoland, but resulted in identical beaching locations. Using drag parameters for Stokes Drift and winds based on Model c resulted in Lagrangian trajectories, representing GPS-tracks fairly well until reaching Helgoland. North of Helgoland, the westward "dodge" at approx. $(E7.75°, N54.1°)$ is less prominent in computed drifter paths. Beaching location of the GPS-drifter at Sylt was reproduced by Lagrangian trajectories using this drag model.

7.4. Conclusion

Drag coefficients of GPS-drifters, traveling near the Eastfrisian Islands were estimated using surface currents from the GB-Model, the SP-Model and DWD wind data. Estimates significantly differed when using different Drag Models and using data computed on different scales. Drift parameters are clearly deviating from theoretical estimates based on Niiler and Paduan [1995][184] (equation (53)) in each regression model and are significantly varying between SP-Model and GB-Model data, confirming finding by e.g. Stanev et al. [2019], Carson et al. [2013], Callies et al. [2011][185]. Although boundaries might reduce accuracies of tidal and surface currents

---

[183]Note 12 h intervals in Figure 74.

[184]Note theoretical estimates (53) are neglecting Stokes Drift and are assumed for smooth water surfaces.

[185]Callies et al. [2011] compared three numerical models of varying vertical and spatial resolutions, concluding significantly differing long term drift, even for validated models. Appropriately adjusting drag parameters even allows for using barotropic velocities.
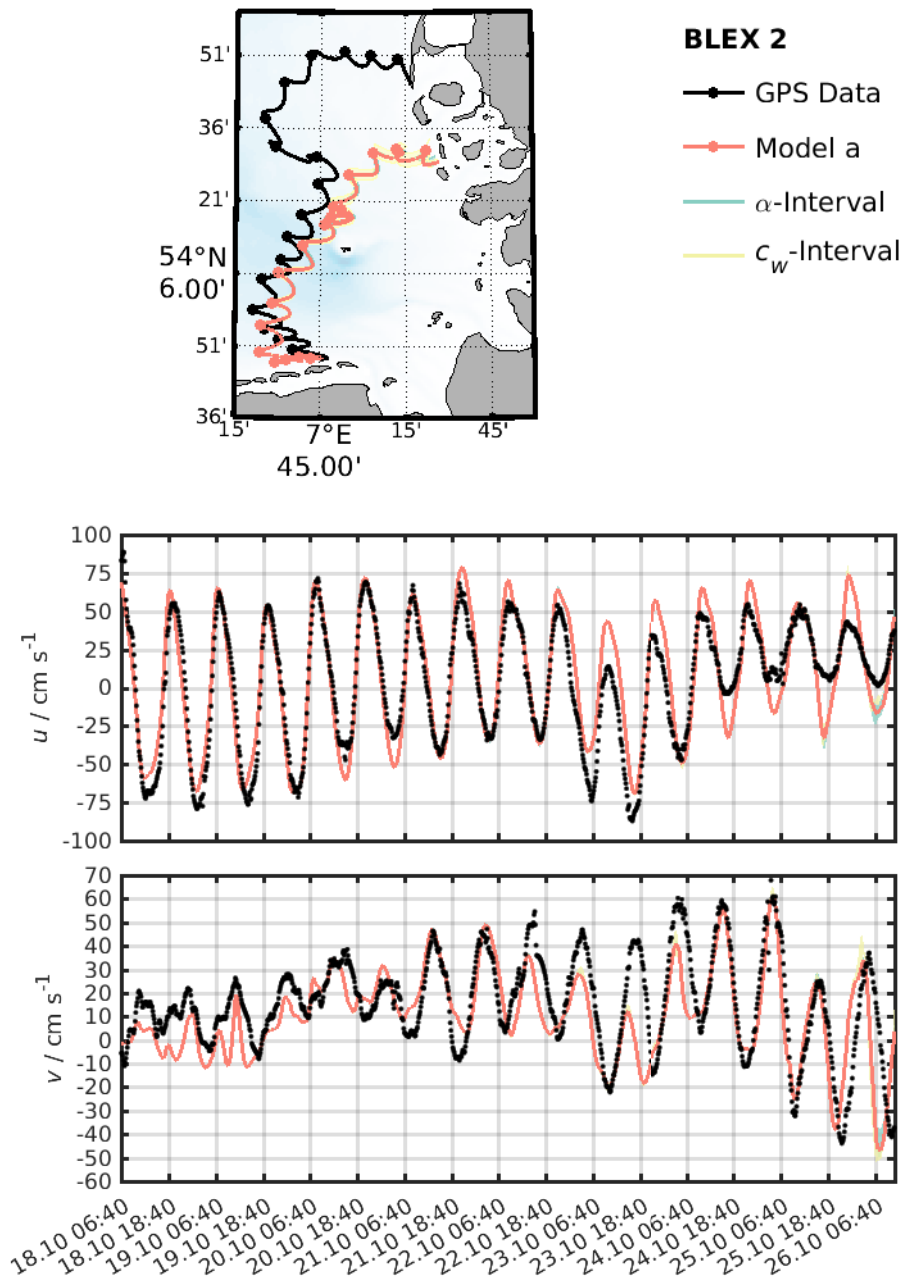
Figure 74: Computed trajectories for Drifter 2 (Type B) using drag parameters for Model a without error term and Runge-Kutha integration. The lower panels show corresponding drifter velocities. Dots indicate 6 h-intervals, shaded areas denote ranges for varying drag values (yellow) and rotation angles (green) within error ranges of the regression.

in the SP-Model, differing drag parameters for using either intermediate- or high-resolution data are indicting small scale variations and vertical layering significantly influencing estimated parameters and thus Lagrangian simulations. Vertical layering in hydrodynamic models is significantly influencing computed wind induced currents and Stokes Drift velocities, as both are decreasing in amplitudes and changing directions for increasing depths. Layer thickness is varying in both models due to S-coordinates, possibly necessitating drag parameters varying with water depths. In summary, drag parameters for Lagrangian modeling have to be specifically estimated for individual numerical models and modeling regions.

Allen and Plourde [1999] and Anderson et al. [1998] note linear drag models might not be applicable over broad ranges of wind velocities, suggesting fit-polynoms. Binning of wind velocities using absolute values $\sqrt{u_w^2 + v_w^2}$ might also improve parameter estimations. Additionally, higher leeway velocities are achieved during rising winds [Allen and Plourde, 1999], suggesting binning of rising and ceasing winds for regressions[186].

Regression model c was predicting large α_{St} values, possibly caused by absent Coriolis-Stokes effects in the coupled hydrodynamic-wave model. Implementing and testing this effect in COAWST is suggested [e.g. Deng et al., 2012][187].

Lagrangian trajectories were qualitatively representing measured drift directions for certain combinations of drag parameters in deeper waters. Although beaching locations of Set ② could be replicated, individual drag parameters and resulting trajectories for these drifters were significantly differing. Small changes of deflection angles or drag coefficients were resulting significantly differing Lagrangian trajectories. This reveals the highly dynamical nature even on short temporal scales in nearshore regions. Coastal topography and bathymetrical features are influencing wave characteristics and surface currents in coastal areas, causing strong variations of individual drag estimates and trajectories redrawing isobaths. Wave directions and Stokes Drift velocities are strongly influenced by bottom topography due to refraction, wave set-up and depth induced wave breaking. Hence, high resolution of topographical features such as coastlines and bathymetry is

---

[186]Allen and Plourde [1999] assume energy transfers from atmosphere to waves for rising winds are causing these differences. Hence, this effect might be accounted for when regarding Stokes Drift.

[187]Depth dependent Stokes drift is calculated in COAWST in lines 208 ff. of `wec_stokes.F`.

crucial. Although using high resolution topography data at the modeling site, tidal action and seasonal storms are creating dynamic topographies on short time scales, which cannot be represented in numerical models[188]. Island's shadowing effects on winds, not represented by wind data and the numerical model, are also likely affecting surface drift in these areas.

Stokes Drift was shown significantly differing from local wind directions in shallow waters and at beaches due to refraction and underlying strong varying magnitudes, caused by depth induced wave breaking. Regarding Stokes Drift in Lagrangian modeling even resulted in drifters beaching on locations normal oriented to seaward winds in section 6. Hence, parametrization of Stokes Drift by increasing wind drag seems not applicable in nearshore areas and coastal models of high spatial resolutions.

In conclusion, quantitatively forecasting drift of floating particles (e.g. marine debris) in nearshore areas seems impossible, even on short time scales. However, qualitative behavior and overall distributions can be estimated when using drifter ensembles of varying drag parameters in Lagrangian models. Drag models and parameters should be chosen carefully in numerical models, as e.g. using Regression Model c resulted in "overparametrization" for certain drifters, i.e. unreasonable values for C_{St} and α_{St}. Additionally, Even small changes in drag angle α and drag paramater c lead to large differences in computed trajectories. This reveals the highly dynamical nature even on short temporal scales in nearshore regions. Trajectories also show parallel flow of surface currents to bathymetry lines, necessitating accurate representations of topography data.

---

[188]Wüllner [2018] compared satellite data for 2016, provided by the NLWKN, to survey data from late 2017 and found a sandbank North of Spiekeroog migrating several hundreds of meters on time scales of less than two years (personal communication).

8. Collaborations and Disposal

Collaborations associated to modeling and methodical efforts of the Macroplastics research project are summarized in this section. Methods for investigating particle exchange between tidal flats and offshore areas at the Eastfrisian Islands and distributions at these areas are proposed in subsection 8.1, source locations of passive drifting larvae in the upper water column are discussed in subsection 8.2 and implementation of decay processes for Lagrangian particles is shown in subsection 8.3. Parts of these subsections have been or will be published on scientific journals and conferences. Majorities of this section were not finalized until the research project expired, thus it is serving as disposal for the work group *Physical Oceanography (Theory)* at the ICBM in Oldenburg.

8.1. Particle Distribution and exchange at the Eastfrisian Islands

Parts of this subsection and figures were submitted as Meyerjürgens et al. [2021][189].

As the Eastfrisian Islands are major touristic attractors and important ecosystems for marine animals and sea birds, these islands are hugely affected by beached and nearshore floating litter. General oceanographic and geographic features of the barrier islands are described in subsection 3.2. Most beach cleanups in this region are restricted to touristic spots whilst large areas are nature reserves with little to no human activities. Hence, roles of individual islands and even distinct beachlines differ: Touristic hot spots might be seen as litter sources whereas preserves are supposed sinks, possibly re-emitting litter due to lacking or absent clean ups.

To help identifying potential sources and sinks of plastics, scripts for generating connectivity maps [see e.g. van der Molen et al., 2018] have been developed as part of the FLOPPSY toolbox. Connectivity maps were generated for the German Bight using velocities and wave parameters computed by the nested EI-Model (section 4). Maps were based on arbitrary start locations of Lagrangian trajectories at the island's coasts, interpreted as sources of debris. Potential litter sources for specific areas were identified by trajectory crossings and weighted by numbers of crossings. Thus trajectories are connecting source and target areas and numbers of such trajectories are

---

[189]Currently in major revision.

giving measurements of significance.

Figure 75 (taken from Meyerjürgens et al. [2021]) shows connectivity maps for the barrier islands Norderney, Spiekeroog and Mellum over the course of 31 days during October 2016. Continuous seeding locations at u- and v-points, neighbouring landmasks of islands and the German coast were used[190]. Histograms for trajectory numbers, connecting respective locations, were calculated using 3×3[191] grid cells for spatial binning. Probability densities were calculated by dividing counts by total amounts of particle releases. These can be interpreted as likeliness for each source location polluting areas of interest.

8.2. Particle Distribution at the Backside of the Island Spiekeroog

Potential source pools for migrating species at artificial islands in backbarrier regions at Spiekeroog were evaluated using the SI-Model and GB-Model in a two-way nesting application. Sea surface elevations were prescribed at open boundaries of the GB-Model using extrapolated WSV gauge data [WSV], corrected in phase and amplitude using a FVCOM [Chen et al., 2003] North Sea model reference run, operated by our work group. Velocities at open boundaries were calculated via barotropic pressure gradients, boundaries for salt and temperatures were derived from the BSHcmod using a nudging relation. Initial states of the model have also been derived from the BSHcmod. Validations for October 2016 showed good agreement with gauge data and the time series station near Spiekeroog (cf. subsection 3.3).

Distributions of passively drifting larvae were estimated using the online Lagrangian floats module inside ROMS, computing advection of neutrally buoyant particles via a fourth-order Milne predictor and fourth-order Hamming corrector at each time step of hydrodynamic computations (online particle tracking). Start locations were uniformly distributed on each grid cell of the SP-Model within the surface layer, continuously releasing particles over 11 ebb and flood cycles for 2 modeling scenarios: Scenario a, solely using tidal forcings, i.e. deactivating winds and Scenario b, using constant analytical northwesterly winds of $6\,\mathrm{m\,s^{-1}}$ magnitudes. The latter corresponding to mean wind conditions at the study site[192]. Wind stress was calculated using

---

[190]Note spatial resolutions of $333\,\mathrm{m} \times 333\,\mathrm{m}$ in the EI-Model.
[191]I. e. $1000\,\mathrm{m} \times 1000\,\mathrm{m}$.
[192]Based on measurements in backbarrier tidal flats at Spiekeroog during the Befmate
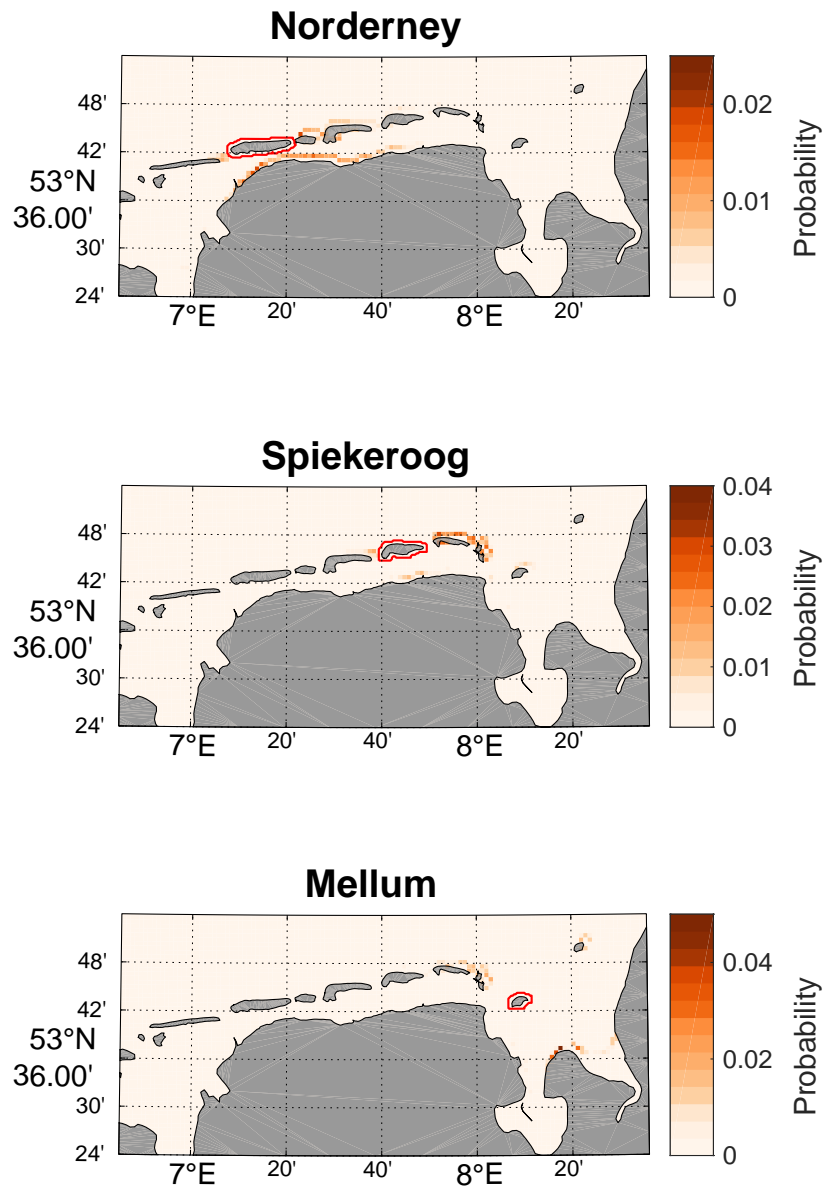
Figure 75: Connectivity maps for three barrier islands: Norderney (top), Spiekeroog (center) and Mellum (bottom) for October 2016. Probabilities for each $1000\,\text{m} \times 1000\,\text{m}$ bin are based on total amounts of particles reaching respective target areas, thus resulting in differing populations throughout subplots. Note differing color limits in each plot.

the drag formula by Yelland and Taylor [1996] with constant drag of 0.0026. Waves were neglected in both model scenarios.

Connectivity maps were generated for 29 d simulation periods using 500m × 500m horizontal bins and a 1000m × 1000m target area, bordering locations of artificial islands, shown by the red area in Figure 76.

Connectivity maps are shown in Figure 76, indicating 500m × 500m bins of sources for particles crossing the target area, i.e. numbers of "settling particles". Influences of release periods during tidal cycles and of wind driven surface currents are indicated by differences of respective conditions ("No Wind" vs. "Wind" resp. "Ebb Release" vs "Flood Release") in the bottom plots resp. right column plots of Figure 76.

In scenario *(a)* particles originating at the tidal flats, South of Spiekeroog, were reaching the target area regardless of variations in release times. Particles originating from offshore areas North of Spiekeroog were just reaching the target area when released during low tides ("Ebb", top left panel). Contrary, particles originating Southwest of the island were reaching the target area when released during high tides ("Flood", center left panel). Difference of both cases ("Ebb" minus "Flood"), shown in the bottom left panel, are indicating increased numbers of particles originating from offshore regions during "Flood" releases and increased numbers of particles originating from tidal flats during "Ebb" releases. Thus, tidal currents are transporting particles towards the tidal flats during rising tides, increasing settling probabilities at the study site. Vice versa, particles from backbarrier regions are transported towards the target area during falling tides.

In scenario *(b)* settling particles originating from offshore regions were absent, regardless of release periods, as wind driven currents hindered Southern transports. Increased numbers of settling particles, originating near the western tidal channel, for "Ebb" Releases also hint starting times as important factors for settling probabilities (panels in the center column).

Comparing Scenarios *a* and *b* for Ebb releases (top right plot) indicates southwesterly winds preventing particle inflow from offshore areas and locations East of Spiekeroog. Numbers of settling particles originating west and southwest of the island, however, were increased by wind driven currents. Same plots for Flood releases (center right panel) indicate southwesterly winds strengthen particle settling, when originating from upwind directions. Hence, wind driven currents are significantly influencing transports in tidal

---

research project, personal communication.
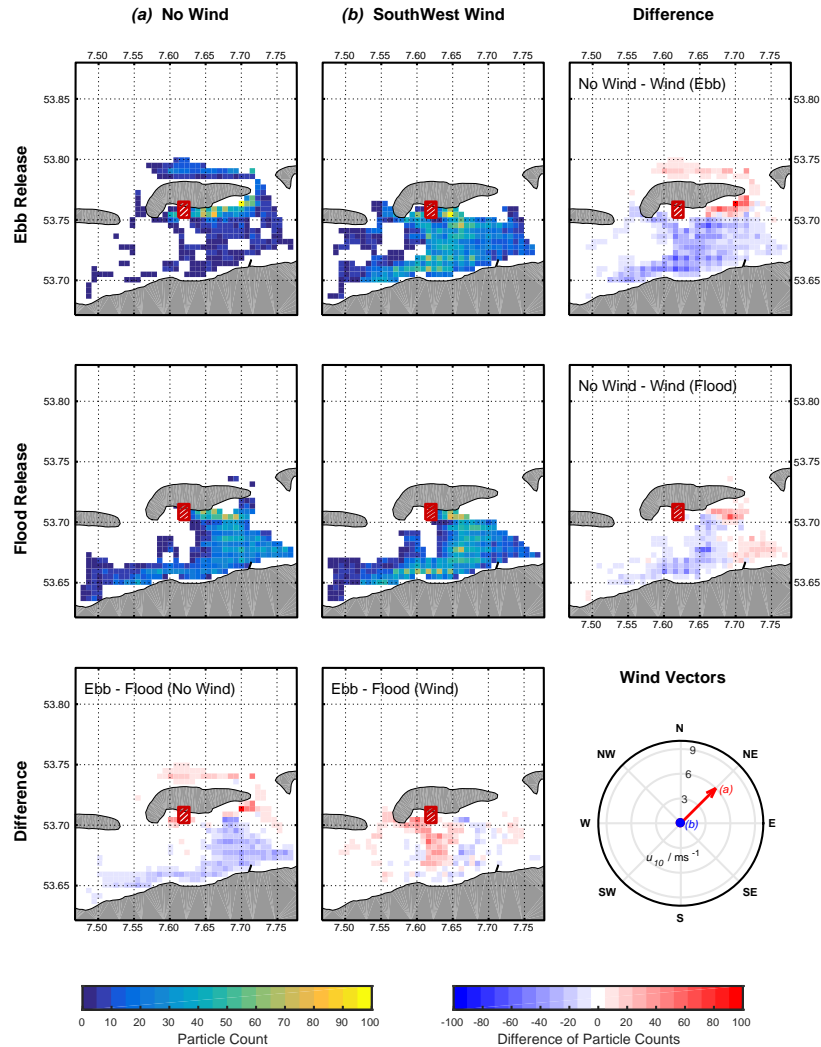
Figure 76: Connectivity maps for the red target area. Histograms of particle counts, passing the target area, are shown in each panel. Bins of origin are sized 500m × 500m. Results when solely using tidal currents are shown in the left column, the mid column shows results for regarding wind driven currents. "Ebb Release" and "Flood Release" are refering to release periods of Lagrangian particles. Differences of shown histograms are indicated by the right column resp. bottom line plots. Wind vectors for both scenarios are shown in the lower right panel.

flats, likely hindering or strengthen exchange of backbarrier waters with off-shore waters and thus drifting particles resp. species.

8.3. Decaying Lagrangian Particles

Distribution of environmental DNA (eDNA) was simulated using the EI-Model and GB-Model in a two-way nesting. The vertical was discretized by 30 S-layers and the model was forced by tides and uniform winds of constant $6\,\mathrm{m\,s^{-1}}$ amplitudes from Southeastern directions. Lagrangian trajectories were computed by ROMS' online FLOATS-module, using 12 point sources within an area locating the Dornum Oyster Reef, Southeast of Langeroog. The area is shown by its red perimeter in Figure 77. Particle sources were placed in bottom layers 1, 2 and 5 of each grid cell within the area, releasing 984996 particles in total over a 19 days period. Time dependent concentration values $N(t)$, exponentially decaying with an arbitrary constant k, have been applied to each particle using matlab, after Lagrangian computations ended. Initially starting at $N_0 = N(t_0)$, concentrations ware decreasing in time:

$$N(t) = \begin{cases} 0 & t < t_0 \\ N_0 \exp\left(-k(t - t_0)\right) & t \geq t_0 \end{cases} \tag{59}$$

Lagrangian particles are representing fluid parcels carrying time dependent eDNA-concentrations $N(t)$ in this frame. Vertically integrated concentrations in 333m $\times$ 333m bins at the end of simulations are shown in Figure 77. A decay constant of $k = 0.029\,\mathrm{h^{-1}}$, reminiscing crabs in inshore areas[193], was used in these plots. Due to lacking sampling data, starting concentrations were set to an arbitrary value of $N_0 = 1000$ (w/o unit). Results were normalized to maximum total concentrations of individual grid cells[194].

8.4. Numerical Models, Toolbox and Datasets

Datasets discussed in section 3, numerical models described in section 4, the Lagrangian toolbox fLOPpSy and MatLab scripts for generating boundary resp. initial conditions and evaluating model results were disposed to the work group *Physical Oceanography (Theory)* at the ICBM. Additionally, all results shown in this thesis are stored at the work group on storages provided and operated by the University of Oldenburg. Thus providing a

---

[193]Cf. table 1 of Collins et al. [2018].
[194]Resulting in maximum concentration values of $N(t) = 1.0$ within each cell
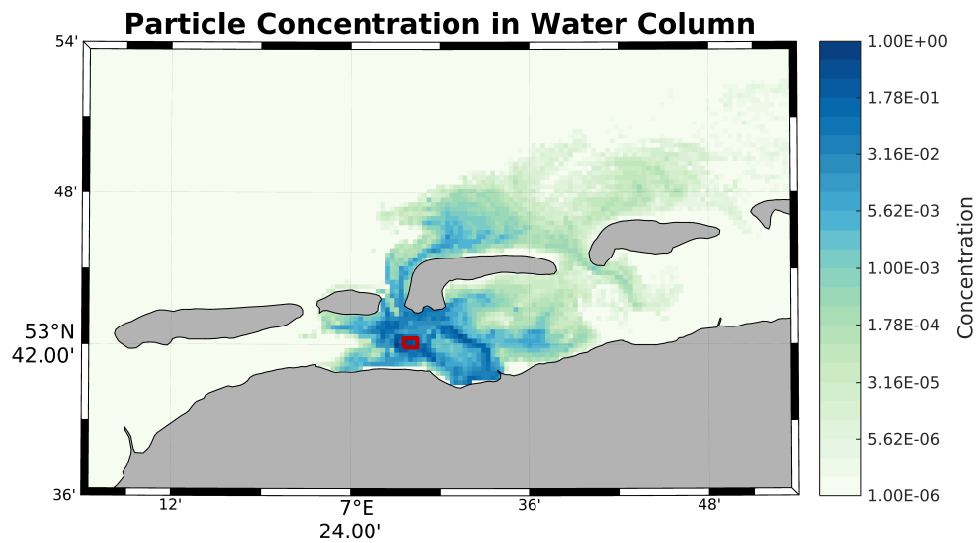
Figure 77: Normalized eDNA concentrations for Crabs. Colorcoding indicates vertical integrated values for individual grid cells of the hydrodynamic model. Logarithmic color spacing was used. Taken from Schadewell et al. [2019].

fully operational modeling framework of hydrodynamic states and especially Lagrangian computations in the German Bight. This thesis, in conjunction with master's theses by Heinrich [2018], Wüllner [2018], Schönung [2018] and Hahner [2016], is giving an overview and short manual for future studies.

9. Acknowledgement

References

A. A. Allen and J. V. Plourde. Review of Leeway: Field Experiments and Implementation. Final Report CG-D-08-99, U.S. Coast Guard Research and Development Center, 1999.

A. Anderson, A. Odulo, and M. Spaulding. Modelling of Leeway Drift. Final Report CG-D-06-99, U.S. Coast Guard Research and Development Center, 1998.

A. Arakawa and V. R. Lamb. Computational Design of the Basic Dynamical Processes of the UCLA General Circulation Model. *Methods of Computational Physics*, 17, 1977.

F. Ardhuin, A. D. Jenkins, and K. A. Belibassakis. Comments on "The Three-Dimensional Current and Surface Wave Equations". *Journal of Physical Oceanography*, 38(6), 2008.

M. Bakhoday-Paskyabi. Particle Motions Beneath Irrotational Water Waves. *Ocean Dynamics*, 65, 2015.

B. Bell, H. Hersbach, P. Berrisford, P. Dahlgren, A. Horányi, J. Muñoz Sabater, J. Nicolas, R. Radu, D. Schepers, A. Simmons, C. Soci, and J-N. Thépaut. ERA5 Hourly Data on Single Levels from 1950 to 1978 (Preliminary Version). *Copernicus Climate Change Service (C3S) Climate Data Store (CDS)*, July 2020. URL https://cds.climate.copernicus.eu/cdsapp#!/dataset/reanalysis-era5-single-levels?tab=overview. Accessed on July 10th, 2020.

A.-C. Bennis and F. Ardhuin. Comments on "The Depth-Dependent Current and Wave Interaction Equations: A Revision". *Journal of Physical Oceanography*, 41, 2011.

T. G. Benton. From Castaways to Throwaways: Marine Litter in the Pitcairn Islands. *Biological Journal of the Linnean Society*, 56, 1995.

BPIM. Evaluation of Measurement Data — Guide to the Expression of Uncertainty in Measurement. Technical Report CGM 100:2008, Bureau International des Poids et Mesures, 2008.

References

G. Breitbach, H. Krasemann, D. Behr, S. Beringer, U. Lange, N. Vo, and F. Schroeder. Accessing Diverse Data Comprehensively –CODM, the COSYNA Data Portal. *Ocean Science*, 12, 2016.

M. Breitbach. Predominant Distribution Pattern of simulated Macroplastic in the German Bight. Master's thesis, Carl von Ossietzky Universität Oldenburg, 2018.

O. Breivik and A. A. Allen. An Operational Search and Rescue Model for the Norwegian Sea and the North Sea. *Journal of Marine Systems*, 69, 2008.

O. Breivik, P. A. E. Janssen, and J.-R. Bidlot. Approximate Stokes Drift Profiles in Deep Water. *Journal of Physical Oceanography*, 44, 2014.

C3S. *The Copernicus Climate Change Service*. URL `https://climate.copernicus.eu/`. Last retrieved on March 7th, 2016.

U. Callies, A. Plüß, J. Kappenberg, and H. Kapitza. Particle Tracking in the Vicinity of Helgoland, North Sea: a Model Comparison. *Ocean Dynamics*, 61, 2011.

S. Carniel, J. C. Warner, J. Chiggiato, and M. Sclavo. Investigating the Impact of Surface Wave Breaking on Modeling the Trajectories of Drifters in the Northern Adriatic Sea during a Wind-Storm Event. *Ocean Modelling*, 30, 2009.

H. S. Carson, M. R. Lamson, D. Nakashima, D. Toloumi, J. Hafner, N. Maximenko, and K. J. McDermid. Tracking the Sources and Sinks of Local Marine Debris in Hawai'i. *Marine Environmental Research*, 84, 2013.

L. Cavaleri and P. M. Rizzoli. Wind Wave Prediction in Shallow Water: Theory and Applications. *Journal of Geophysical Research: Oceans*, 86 (C11), 1981.

CDS. *Climate Data Store (CDS) Documentation*. Climate Data Store (CDS). URL `https://confluence.ecmwf.int/display/CKB/Climate+Data+Store+%28CDS%29+documentationhttps://confluence.ecmwf.int/display/CKB/Climate+Data+Store+%28CDS%29+documentation`. Last retrieved on March 7th, 2020.

H. Charnock. *Understanding the North Sea System*. Chapman & Hall for the Royal Society, 1994.

S. Chatterjee and A.S. Hadi. Influential Observations, High Leverage Points, and Outliers in Linear Regression. *Statistical Science*, 1, 1986.

C. Chen, H. Liu, and R. C. Beardsley. An Unstructured Grid, Finite-Volume, Three-Dimensional, Primitive Equations Ocean Model: Application to Coastal Ocean and Estuaries. *Journal of Atmospheric and Oceanic Technology*, 20, 2003.

R. A. Collins, O. S. Wangensteen, E. J. O'Gorman, S. Mariani, D. W. Sims, and M. J. Genner. Persistence of Environmental DNA in Marine Systems. *Communications Biology*, 1, 2018.

COSYNA. *COSYNA data web portal (CODM)*. Helmholtz-Zentrum Geesthacht (HZG). URL `http://codm.hzg.de/codm/`. Last retrieved on March 7th, 2016.

P. Craig. Velocity Profiles and Surface Roughness under Breaking Waves. *Journal of Geophysical Research*, 101, 1996.

P. Craig and M. Banner. Modelling Wave-Enhanced Turbulence in the Ocean Surface Layer. *Journal of Phyical Oceanography*, 24, 1994.

K. Critchell and J. Lambrechts. Modelling Accumulation of Marine Plastics in the Coastal Zone; What are the Dominant Physical Processes? *Estuarine, Coastal and Shelf Science*, 171, 2016.

K. Critchell, A. Grech, J. Schlaefer, F. P. Andutta, J. Lambrechts, E. Wolanski, and M. Hamann. Modelling the Fate of Marine Debris Along a Complex Shoreline: Lessons from the Great Barrier Reef. *Estuarine, Coastal and Shelf Science*, 167(Part B), 2015.

B. Cushman-Roisin and J.-M. Beckers. *Introduction to Geophysical Fluid Dynamics*, volume 101 of *International Geophysics Series*. Academic Press, 2nd edition, 2011.

Datawell. *Waverider Manual*. Datawell BV oceanographic instruments, 2020. URL `https://www.datawell.nl/Portals/0/Documents/Manuals/datawell_manual_dwr-mk3_dwr-g_wr-sg_2020-02-01.pdf`. Last tretrieved on March2021.

Z. Deng, L. Xie, G. Han, X. Zhang, and K. Wu. The Effect of Coriolis-Stokes Forcing on Upper Ocean Circulation in a Two-Way Coupled Wave-Current Model. *Chinese Journal of Oceanology and Limnology*, 2012.

References

C. Dibke, M. Fischer, and B. M. Scholz-Böttcher. Microplastic Mass Concentrations and Distribution in German Bight Waters by Pyrolysis–Gas Chromatography–Mass Spectrometry/Thermochemolysis Reveal Potential Impact of Marine Coatings: Do Ships Leave Skid Marks? *Environmental Science & Technology*, 55, 2021.

S. Dick, E. Kleine, and F. Janssen. A New Operational Circulation Model for the North Sea and the Baltic Using a Novel Vertical Co-ordinate - Setup and First Results. In *Proceedings of the Fifth International Conference on EuroGOOS. Exeter, UK*, May 2008.

S.E. Dick, E. Kleine, S. H. Müller-Navarra, H. Klein, and H. Komo. The Operational Circulation Model of BSH (BSHcmod) - Model Description and Validation. *Berichte des Bundesamtes für Seeschifffahrt und Hydrographie*, 29, 2001.

K. Döös, J. Kjellsson, and B. Jönsson. TRACMASS—A Lagrangian Trajectory Model. In *Preventive Methods for Coastal Protection*, pages 225–249. Springer International Publishing, 2013.

J. V. Durgadoo, A. Biastoch, A. L. New, S. Rühs, A. J.G. Nurser, Y. Drillet, and J.-R. Bidlot. Strategies for Simulating the Drift of Marine Debris. *Journal of Operational Oceanography*, 14, 2021.

K. Döös, B. Jönsson, and J. Kjellsson. *TRACMASS - Lagrangian Trajectory Code Documentation and Manual*. Stockholms Universitet, 2016.

ECMWF. *ERA5*. European Center for Medium-Range Weather Forecasts (ECMWF). URL `https://confluence.ecmwf.int/display/CKB/ERA5%3A+data+documentation#ERA5:datadocumentation-HowtociteERA5`. Last retrieved on November 11th, 2020.

V. W. Ekman. On the Influence of the Earth's Rotation on Ocean Currents. *Archives of Mathematics, Astronomy and Physics*, 2, 1905.

FGG Elbe. *Elbe Datenportal*. Flussgebietsgemeinschaft (FGG) Elbe, Otto-v.-Guericke Straße 5, 39104 Magdeburg, GERMANY. URL `https://www.elbe-datenportal.de/FisFggElbe/content/auswertung/UntersuchungsbereichHydro_notFilter_gewaesser`. Last retrieved on February 17th, 2020.

C. Eriksson and H. Burton. Origins and Biological Accumulation of Small Plastic Particles in Fur Seals from Macquarie Island. *AMBIO A Journal of the Human Environment*, 32, 2003.

N. Fabbroni. *Numerical Simulation of Passive Tracers Dispersion in the Sea*. PhD thesis, Universita di Bologna, 2009.

FINO. *FINO Datenbank*. Bundesanstalt für Seeschiffahrt und Hydrographie (BSH). URL `http://fino.bsh.de`. Last retrieved on December 3rd, 2019.

J. Fredsoe and R. Deigaard. *Mechanics of Coastal Sediment Transport*. Advanced Series on Ocean Engineering. World Scientific Publishing, 1992.

G. Gerdts, K. Thomas, D. Herzke, M. Haeckel, B. Scholz-Böttcher, C. Laforsch, F. Lagarde, A. M. Mahon, M. L. Pedrotti, G. de Lucia, P. Sobral, J. Gago, S. Muniategui Lorenzo, F. Norén, M. Hassellöv, T. Kögel, V. Tirelli, M. Caetano, A. Collignon, and P. Licandro. *Defining the Baselines and Standards for Microplastics Analyses in European Waters (JPI-O BASEMAN)*, pages 120–122. 2017.

M. C. Goldstein and D. S. Goodwin. Gooseneck Barnacles (*Lepas* spp.) Ingest Microplastic Debris in the North Pacific Subtropical Gyre. *PeerJ*, 1, 2013.

S. Grashorn, K. A. Lettmann, J.-O. Wolff, T. H. Badewien, and E. Stanev. East-Frisian Wadden Sea Hydrodynamics and Wave Propagation in an Unstructured-Grid Model. *Ocean Dynamics*, 65, 2015.

L. Gutow, M. Ricker, J. M. Holstein, J. Dannheim, E. V. Stanev, and J. Wolff. Distribution and trajectories of floating and benthic marine macrolitter in the south-eastern North Sea. *Marine Pollution Bulletin*, 131(Part A), 2018.

F. Hahner. Interaktion von Wellen und Strömungen am Nordstrand von Spiekeroog. Untersuchung mit dem gekoppelten Strömungs-Wellenmodell COAWST. Master's thesis, Car von Ossietzky Universität Oldenburg, 2016.

K. S. Hedström. *DRAFT Technical Manual for a Coupled Sea-Ice/Ocean Circulation Model (Version 4)*. U.S. Department of the Interior, Bureau of Ocean Energy Management, Herndon Virgina, March 2012.

References

P. Heinrich. Particle Tracking und Finite-Time Lyapunov-Exponenten in der Deutschen Bucht. Master's thesis, Carl von Ossietzky Universität Oldenburg, 2018.

C. Herold. *Rückblick Sturmsaison 2017/2018*. Wetterdienst.de - Wetter- und Klimaberatung, 2018. URL `https://www.wetterdienst.de/Deutschlandwetter/Thema_des_Tages/3346/rueckblick-sturmsaison-20172018`. Last retrieved on March 2021.

D. O. Hodgins and S. L. M. Hodgins. Leeway Dynamic Study Phase I Development and Verification of a Mathematical Drift Model for Four-person Liferafts. Technical Report TP 12309E, Transport Canada, Transort Development Centre, 1995.

D. O. Hodgins and S. L. M. Hodgins. Phase II Leeway Dynamics Program: Development and Verification of a Mathematical Drift Model for Liferafts and Small Boats. Technical report, Canadian Coast Guard, Nova Scotia, Canada, 1998.

L. H. Holthuijsen. *Waves in Oceanic and Coastal Waters*. Cambridge University Press, 2007.

M.J. Howarth. North Sea Circulation. *Encyclopedia of Ocean Sciences*, 4, 2001.

N. E. Huang. On Surface Drift Currents in the Ocean. *Journal of Fluid Mechanics*, 91, 1979.

R. Jacob, J. Larson, and E. Ong. M × N Communication and Parallel Interpolation in Community Climate System Model Version 3 Using the Model Coupling Toolkit. *International Journal of High Performance Computing Applications*, 19, 2005.

J. R. Jambeck, R. Geyer, C. Wilcox, T. R. Siegler, M. Perryman, A. Andrady, R. Narayan, and K. L. Law. Plastic Waste Inputs from Land into the Ocean. *Science*, 347, 2015.

Kenneth I. Joy. Numerical Methods for Particle Tracing in Vector Fileds. *online course*, 2007. URL `http://graphics.cs.ucdavis.edu/~joy/ecs277/other-notes/Numerical-Methods-for-Particle-Tracing-in-Vector-Fields.pdf`. Last retrieved on February 12th, 2019.

S. Kaza, L. C. Yao, P. Bhada-Tata, and F. Van Woerden. *What a Waste 2.0: A Global Snapshot of Solid Waste Management to 2050.* Washington, DC: World Bank, 2018.

K.E. Kenyon. Stokes Drift for Random Gravity Waves. *Journal of Geophysical Research*, 74, 1969.

G. J. Komen, S. Hasselmann, and K. Hasselmann. On the Existence of a Fully Developed Wind-Sea Spectrum. *Journal of Physical Oceanography*, 14(8), 1984.

N Kumar, G. Voulgaris, and J. C. Warner. Implementation and Modification of a Three-Dimensional Radiation Stress Formulation for Surf Zone and Rip-Current Applications. *Coastal Engineering*, 58, 2011.

N. Kumar, G. Voulgaris, J. C. Warner, and M. Olabarrieta. Implementation of the Vortex Force Formalism in the Coupled Ocean-Atmosphere-Wave-Sediment Transport (COAWST) Modeling System for Inner Shelf and Surf Zone Applications. *Ocean Modelling*, 47, 2012.

J. Larson, R. Jacob, and E. Ong. The Model Coupling Toolkit: A New Fortran90 Toolkit for Building Multiphysics Parallel Coupled Models. *International Journal of High Performance Computing Applications*, 19, 2005.

K. L. Law, S. E. Moret-Ferguson, D. S. Goodwin, E. R. Zettler, E. DeForce, T. Kukulka, and G Proskurowski. Distribution of Surface Plastic Devbris in the Eastern Pacific Ocean from an 11-Year Data Set. *Environmental Science and Technology*, 48, 2014.

K. A. Lettmann, J.-O. Wolff, and T. H. Badewien. Modeling the Impact of Wind and Waves on Suspended Particulate Matter Fluxes in the East Frisian Wadden Sea (southern North Sea). *Ocean Dynamics Special Issue FG Watt*, 2009.

S. Liubartseva, G. Coppini, R. Lecci, and E. Clementi. Tracking Plastics in the Mediterranean: 2D Lagrangian Model. *Marine Pollution Bulletin*, 129, 2018.

M. S. Longuet-Higgins and R. W. Stewart. Radiation Stresses in Water Waves: A Physical Discussion with Applications. *Deep Sea Research and Oceanographic Abstracts*, 11, 1964.

References

Macroplastics North Sea. *The Macroplastics Research Project Portal*. Institute for Chemistry and Biology of the Marine Environment (ICBM), University Oldenburg. URL `www.macroplastics.de`. Last retrieved on August 20th, 2020.

A Malcherek. *Gezeiten und Wellen: Die Hydromechanik der Küstengewässer*. Vieweg + Teubner, 2010.

N. Maximenko, J. Hafner, and P. Niiler. Pathways of Marine Debris Derived from Trajectories of Lagrangian Drifters. *Marine Pollution Bulletin*, 65, 2012.

J. C. McWilliams, J. M. Restrepo, and E. M. Lane. An Asymptotic Theory for the Interaction of Waves and Currents in Coastal Waters. *Journal of Fluid Mechanics*, 511, 2004.

C. C. Mei, M. Sitiasnie, and D. K.-P. Yue. *Theory and Application of Ocean Surface Waves. (Advanced Series on Ocean Engineering: Volume 23)*. World Scientific Publishing, 2005.

G. L. Mellor. The Three-Dimensional Current and Surface Wave Equations. *Journal of Physical Oceanography*, 33, 2003.

G. L. Mellor. Corrigendum. *Journal of Physical Oceanography*, 35, 2005.

G. L. Mellor. The Depth-Dependent Current and Wave Interaction Equations: A Revision. *Journal of Physical Oceanography*, 38(11), 2008.

G. L. Mellor. Corrigendum. *Journal of Physical Oceanography*, 41, 2011.

MetOcean. *iSPHERE Brochure*. MetOcean Telematics, 21 Thornhill Drive, Dartmouth, Nova Scotia, Canada. URL `https://metocean.com/wp-content/uploads/2017/09/iSPHERE-3.pdf`. Last retrieved on August 31st, 2018.

J. Meyerjürgens, T. Badewien, S. Garaba, J.-O. Wolff, and O. Zielinski. A State-of-the-Art Compact Surface Drifter Reveals Pathways of Floating Marine Litter in the German Bight. *Frontiers in Marine Science*, 6, 2019.

J. Meyerjürgens, M. Ricker, C. Aden, T. Badewien, J. Barrelet, H. Freund, F. Hahner, K. Lettmann, I. Mose, P. Schaal, R. Schöneich-Argent, E. Stanev, J.-O. Wolff, and O. Zielinski. Sources, Pathways and Abatement Strategies of Macroplastic Pollution: An Interdisciplinary Approach

for the Southern North Sea. *Environmental Research Letters*, 2021. in review.

D. Neumann, U. Callies, and M. Matthies. Marine Litter Ensemble Transport Simulation in the Southern North Sea. *Marine Pollution Bulletin*, 86, 2014.

P.-P. Niiler and J. D. Paduan. Wind-Driven Motions in the Northeast Pacific as Measured by Lagrangian Drifters. *Journal of Physical Oceanography*, 25, 1995.

NLWKN. *Niedersächsischen Landesdatenbank für wasserwirtschaftliche Daten*. Niedersächsischer Landesbetrieb für Wasserwirtschaft, Küsten- und Naturschutz (NLWKN), Am Sportplatz 23, 26506 Norden, GERMANY. URL `http://www.wasserdaten.niedersachsen.de/`. Last retrieved on 20th, 2020.

R. Pawlowicz. *M_Map: A Mapping Package for MATLAB, version 1.4m*, 2020. URL `www.eoas.ubc.ca/~rich/map.html`.

J. Pedlosky. *Geophysical Fluid Dynamics*. Springer New York, 2 edition, 1987.

O. M. Phillips. *The Dynamics of the Upper Ocean*. Cambridge Monographs on Mechanics and Applied Mathematics. Cambridge University Press, 2 edition, 1977.

RBR. *RBR solo3 RBR duet3 Instrument Guide*. RBR Ltd., 359 Terry Fox Drive, Ottawa, Canada. URL `https://rbr-global.com/wp-content/uploads/2022/03/RBR-Compact-Instrument-Guide-0008814revB-1.pdf#%5B%7B%22num%22%3A123%2C%22gen%22%3A0%7D%2C%7B%22name%22%3A%22XYZ%22%7D%2C50.69%2C465.52%2C0%5D`. Last retrieved on April 20th, 2021.

P. L. Richardson. Drifting in the Wind: Leeway Error in Shipdrift Data. *Deep-Sea Research I*, 44, 1997.

ROMS. *MyROMS website*, November . URL `www.myroms.org`. Last retrieved on March 7th, 2019.

J. Röhrs, K. H. Christensen, L. R. Hole, G. Broström, M. Drivdal, and S. Sundby. Observation-Based Evaluation of Surface Wave Effects on

References

Currents and Trajectory Forecasts. *Ocean Dynamics*, 62, 2012. ISSN 1616-7228.

Y. Schadewell, F. Hahner, K. Lettmann, T. Janzen, R. Collins, S. Mariani, M. Genner, J.-O. Wolff, and G. Gerlach. Evaluating Spatial Distribution of Aquatic Animals by Modelling Water-Borne environmental DNA, 06 2019.

R. Schöneich-Argent, K. Stephan, M. Ricker, F. Hahner, and J. Meyerjürgens. Plastik - Rohstoff, Wertstoff, Abfallprodukt und glglobal Problem. Wissenschaftler-Team der Carl von Ossietzky Universität Oldenburg erforscht die Wege das Plastikmülls in der Nordsee. *Natur- und Umweltschutz. Zeitschrift der Naturschutz- und Forschungsgemeinschaft Der Mellumrat e.V.*, 15, 2016.

R. Schöneich-Argent, M. Ricker, J. Meyerjürgens, F. Hahner, and K. Stephan. Projekt Makroplastik in der südlichen Nordsee - Ein Zwischenbericht. *Natur- und Umweltschutz. Zeitschrift der Naturschutz- und Forschungsgemeinschaft Der Mellumrat e.V.*, 16, 2017.

W. Schönfeld. Numerical Simulation of the Dispersion of Artificial Radionuclides in the English Channel and the North Sea. *Journal of Marine Systems*, 6, 1995.

M. Schönung. Modellierung der Verdriftung von Makroplastik in der Unterweser mit FVCOM. Master's thesis, Carl von Ossietzky Universität Oldenburg, 2018.

C.-D. Schönwiese. *Praktische Statistik für Meteorologen und Geowissenschaftler*. Gebr. Borntraeger Verlagsbuchhandlung, 5 edition, 2013.

E. Y. Shchekinova, Y. Kumkar, and G. Coppini. Numerical Reconstruction of Trajectory of Small-Size Surface Drifter in the Mediterranean Sea Reconstruction of Surface Drift in the Mediterranean Sea. *Ocean Dynamics*, 66, 2016.

A. F. Shchepetkin and J. C. McWilliams. The Regional Ocean Modeling System (ROMS): A Split-Explicit, Free-Surface, Topography-Following-Coordinate Ocean Model. *Ocean Modelling*, 9, 2005.

W. C. Skamarock, J. B. Klemp, D. O. Gill, D. M. Barker, and J. G. Powers. A Description of the Advanced Research WRF Version 2. Technical Report NCAR/TN–468+STR, National Center for Atmospheric Research, Boulder, Colorado, USA, 2005.

Y. Song and D. B. Haidvogel. A Semi-Implicit Ocean Circulation Model Using a Generalized Topography-Following Coordinate System. *Journal of Computational Physics*, 115, 1994.

E. Stanev, G. Flöser, and J.-O. Wolff. Dynamic Control on Water Exchanges between Tidal Basins and the Open Ocean. A Case Study for the East Frisian Wadden Sea. *Ocean Dynamics*, 53, 2003a.

E. Stanev, J.-O. Wolff, K. Bolding, and G. Flöser. On the Circulation in the East Frisian Wadden Sea: Numerical modeling and data analysis. *Ocean Dynamics*, 53, 2003b.

E.V. Stanev, T.H. Badewien, H. Freund, S. Grayek, F. Hahner, J. Meyerjürgens, M. Ricker, R.I. Schöneich-Argent, J.-O. Wolff, and O. Zielinski. Extreme Westward Surface Drift in the North Sea: Public Reports of Stranded Drifters and Lagrangian Tracking. *Continental Shelf Research*, 177, 2019.

J. Staneva, E.V. Stanev, J.-O. Wolff, T. H. Badewien, R. Reuter, B. Flemming, A. Bartholoma, and K. Bolding. Hydrodynamics and Sediment Dynamics in the German Bight. A Focus on Observations and Numerical Modelling in the East Frisian Wadden Sea. *Continental Shelf Research*, 29, 2009.

K. Suara, C. Wang, Y. Feng, R. J. Brown, H. Chanson, and M. Borgas. High-Resolution GNSS-Tracked Drifter for Studying Surface Dispersion in Shallow Water. *Journal of Atmospheric and Oceanic Technology*, 32, 2015.

I. A. Svendsen. *Introduction to Nearshore Hydrodynamics*. Advanced Series on Ocean Engineering. World Scientific Publishing, 2006.

SWAN. *SWAN User Manual; SWAN Scientific and Technical Documentation (SWAN Cycle III, V.41.01A)*. Delft University of Technology, Faculty of Civil Engineering and Geosciences, Environmental Fluid Mechanics Section., Delft, Netherlands, 2015. URL `www.swan.tudelft.nl`.

References

M. Thiel, I. A. Hinojosa, L. Miranda, J. F. Pnoja, M. M. Rivadeneira, and N. Vasquez. Anthropogenic Marine Debris in the Coastal Environment: A Multi-Year Comparison Between Coastal Waters and Local Shores. *Marine Pollution Bulletin*, 71, 2013.

R. C. Thompson, C. J. Moore, F. S. vom Saal, and S. H. Swan. Plastics, the Environment and Human Health: Current Consensus and Future Trends. *Philosophical Transactions of the Royal Society of London*, 364, 2009.

R. E. Thomson and W. J. Emery. *Data Analysis Methods in Physical Oceanography*. Elsevier Science Publishers B. V., 2014.

W. R. Turrell. A simple Model of Wind-Blown Tidal Strandlines: How Marine Litter is Deposited on a Mid-Latitude, Macro-Tidal Shelf Sea Beach. *Marine Pollution Bulletin*, 137, 2018.

J. van der Molen, L. M. García-García, P. Whomersley, A. Callaway, P. E. Posen, and K. Hyder. Connectivity of Larval Stages of Sedentary Marine Communities between Hard Substrates and Offshore Structures in the North Sea. *Scientific Reports*, 8, 2018.

J.A. van Franeker. Plastic Ingestion in the North Atlantic Fulmar. *Marine Pollution Bulletin*, 16, 1985.

E. van Sebille, C. Wilcox, L. Lebreton, N. Maximenko, B. D. Hardesty, J. van Franeker, M. Eriksen, D. Siegel, F. Galgani, and K. L. Law. A Global Inventory of Small Floating Plastic Debris. *Environmental Research Letters*, 15, 2015.

M. K. Viršek, M. N. Lovšin, Š. Koren, A. Kržan, and M. Peterlin. Microplastics as a Vector for the Transport of the Bacterial Fish Pathogen Species Aeromonas Salmonicida. *Marine Pollution Bulletin*, 125, 2017.

WAMOS. *WaMoS II Wave and Surface Current Monitoring System Operating Manual, Version 4.0*. Ocean WaveS GmbH, Vor dem Bardowicker Tore 6b, 21339 Lüneburg, Germany, 2012.

J. C. Warner, C. R. Sherwood, H. G. Arango, and R. P. Signell. Performance of Four Turbulence Closure Models Implemented Using a Generic Length Scale Method. *Ocean Modelling*, 8, 2005.

J. C. Warner, N. Perlin, and E. D. Skyllingstad. Using the Model Coupling Toolkit to Couple Earth System Models. *Environmental Modelling & Software*, 23, 2008a.

J. C. Warner, C. R. Sherwood, R. P. Signell, C. K. Harris, and H. G. Arango. Development of a Three-Dimensional, Regional, Coupled Wave, Current, and Sediment-Transport Model. *Computers & Geosciences*, 34, 2008b.

J. C. Warner, B. Armstrong, R. He, and J. B. Zambon. Development of a Coupled Ocean–Atmosphere–Wave–Sediment Transport (COAWST) Modeling System. *Ocean Modelling*, 35, 2010.

P. Wessel and W. H. F. Smith. A Global, Self-Consistent, Hierarchical, High-Resolution Shoreline Database. *Journal of Geophysical Research*, 101, 1996.

WSV. *Pegel-Online*. Wasserstraßen- und Schifffahrtsverwaltung des Bundes (WSV). URL `www.pegelonline.wsv.de`. Last retrieved on March 7th, 2019.

T. Wüllner. Stokes Drift in der Deutschen Bucht - Eine Analyse mithilfe des gekoppelten Wellen-Strömungsmodells COAWST. Master's thesis, Carl von Ossietzky University Oldenburg, 2018.

M. Yelland and . K. Taylor. Wind Stress Measurements from the Open Ocean. *Journal of Physical Oceanography*, 26, 1996.

Y. Yoshikawa and A. Masuda. Seasonal Variations in the Speed Factor and Deflection Angle of the Wind-Driven Surface Flow in the Tsushima Strait. *Journal of Geophysical Research*, 114, 2009.

A. ROMS : HPE and Vertical Coordinate Transformations

Table 9: Vertical Transformation functions of ROMS.

Transformation 1	$z(x, y, \varsigma, t) = S(x, y, \varsigma) + \zeta(x, y, t) \left(1 + \frac{S(x,y,\varsigma)}{h(x,y)} \right)$
	$S(x, y, \varsigma) = h_c\varsigma + (h(x, y) - h_c)C(\varsigma)$
Transformation 2	$z(x, y, \varsigma, t) = \zeta(x, y, t) + S(x, y, \varsigma)(\zeta(x, y, t) + h(x, y))$
	$S(x, y, \varsigma) = \frac{h_c\varsigma + h(x,y)C(\varsigma)}{h_c + h(x,y)}$
Stretching 1	$C(\varsigma) = (1 - \theta_b)\frac{\sinh(\theta_s\varsigma)}{\sinh(\theta_s)} + \theta_b \left(\frac{\tanh(\theta_s(\varsigma+0.5))}{2\tanh(\theta_s/2)} - \frac{1}{2} \right)$
[Song and Haidvogel, 1994]	
Stretching 4	$C_s(\varsigma) = \begin{cases} \frac{1-\cosh(\theta_s\varsigma)}{\cosh(\theta_s)-1} & \text{, for } \theta_s > 0 \\ -\varsigma^2 & \text{, for } \theta_s \leq 0 \end{cases}$
	$C(\varsigma) = \frac{\exp(\theta_b C_s(\varsigma))-1}{1-\exp(-\theta_b)}$

174

Table 10: Hydrostatic primitive equations and diffusion equation for scalar tracers C in cartesian coordinates. [ROMS]

Hor. Momentum	$D_t \vec{u} - f\hat{z} \times \vec{u} = -\nabla_X \phi - \partial_z \left(\overline{\vec{u}'w'} - \nu\partial_z\vec{u} \right) + \mathcal{F} + \mathcal{D}$
Vert. Momentum	$\partial_z \phi = -\frac{\rho g}{\rho_0}$
Continuity	$\nabla \cdot \vec{v} = 0$
Diffusion	$\partial_t \vec{v} \cdot (\nabla C) = -\partial_z \left(\overline{C'w'} - \nu_\theta \partial_z C \right) + \mathcal{F}_C + \mathcal{D}_C$
Velocity	$\vec{v} = (\vec{u}, w) = (u, v, w)$
Turbulent Velocity	$\vec{v}' = (\vec{u}', w') = (u', v', w')$
Reynolds Stresses	$\overline{u_i'w'} = -K_M \partial_z u_i$
Turbulent Adv. of Tracers	$\overline{C'w'} = -K_C \partial_z C$
Diffusion Terms	$\mathcal{D}$
External Forces	$\mathcal{F}$
Turbulent Viscosity	K_M
Turbulent Diffusivity	K_C
Coriolis Parameter	$f(x, y)$
Molecular Viskosity	ν

B. Research Region

B.1. River Runoff
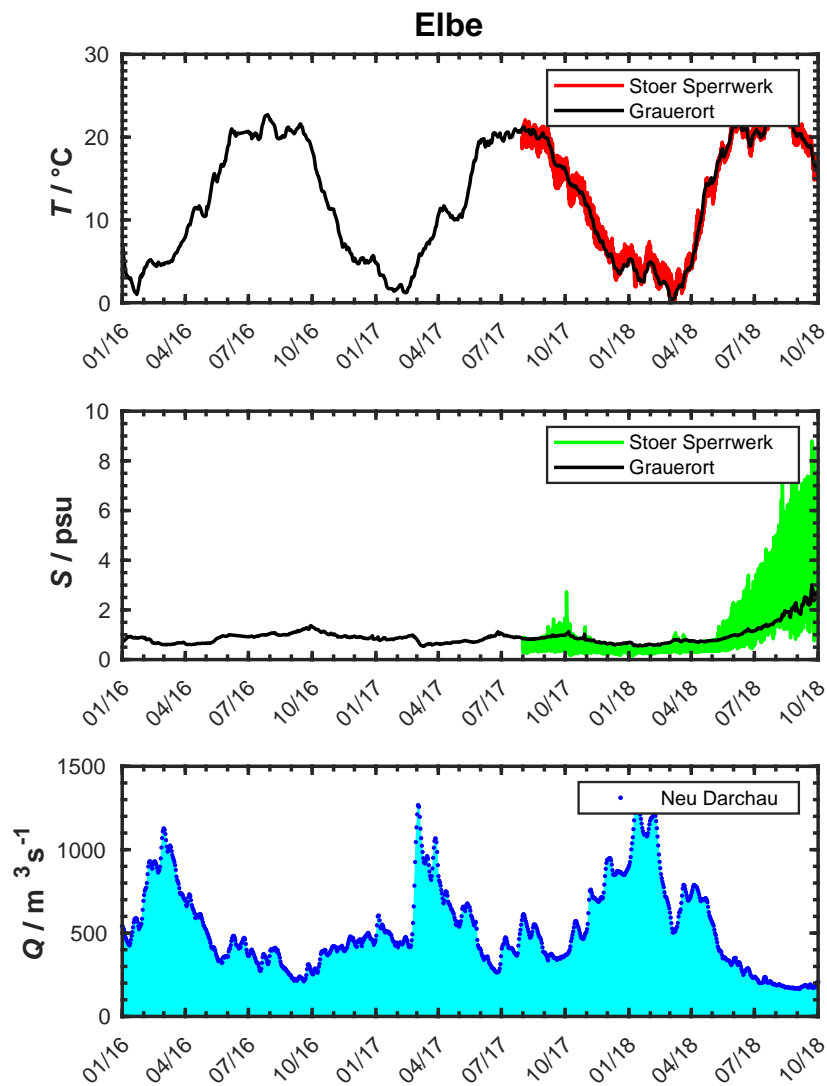
Figure 78: Elbe river data from various pile stations. Solid red and green lines show temperature T and Salinity S at the pile *Stoer Sperrwerk* with 5 min temporal resolution, black lines show respective daily mean values measured at the pile *Grauerort*. Salinity values are derived from conductivity data. River discharge Q is depicted by blue dots in the bottom panel. Each dot represents a daily mean value at *Neu Darchau*. Gauge locations are visualized in Figure 18.
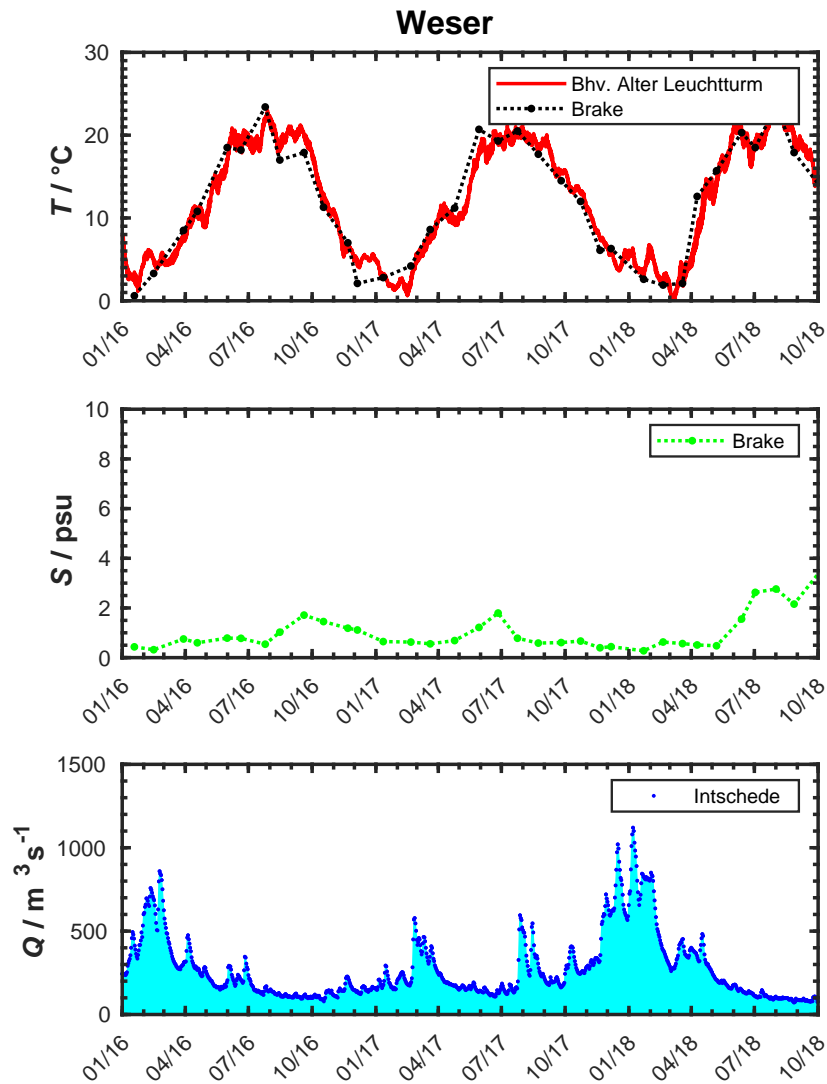
Figure 79: Weser river data at various pile stations. Temperatures T on 5 min intervals from the pile *Bremerhaven Alter Leuchtturm* are denoted ba a solid red line. Black dots indicate point measurements at the pile *Brake*. Salinity values S at the pile *Brake* (green dots) were derived from point measurements of conductivity. Daily mean river discharges Q were taken from the pile at *Intschede*. Dashed lines illustrate interpolated values for visualizing temporal trends.
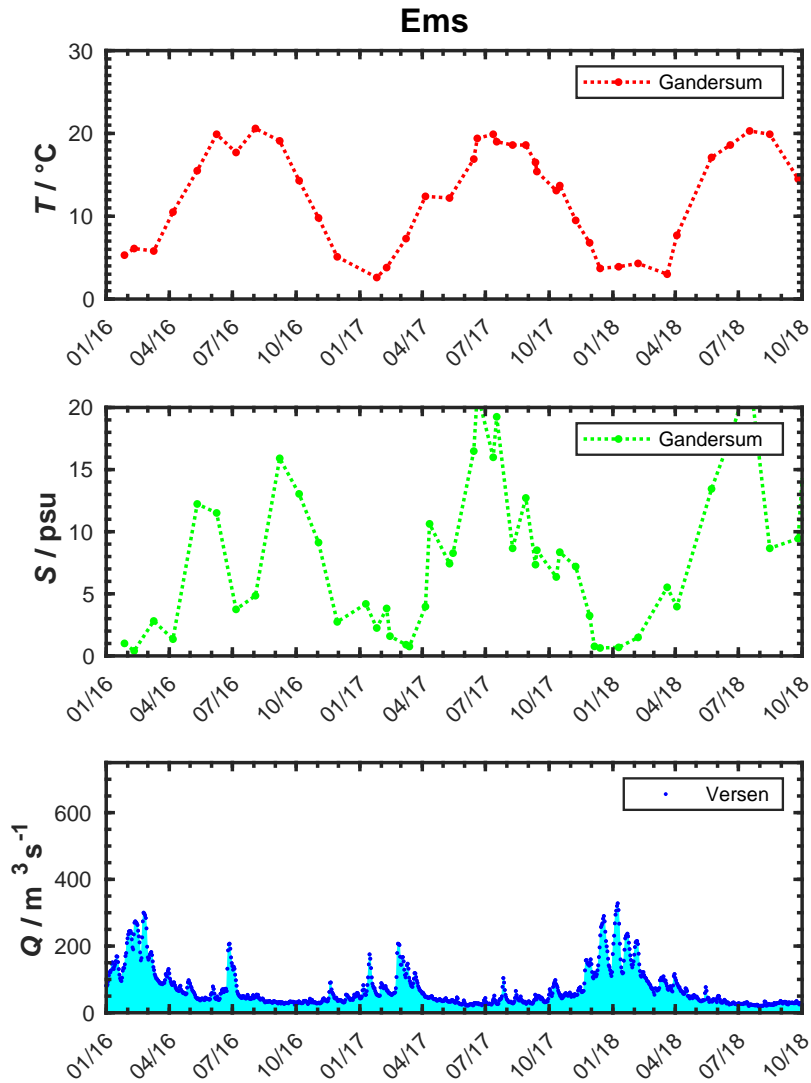
Figure 80: River data of the Ems. Temperature T (red dots, upper panel) and salinity S (green dots, middle panel) values are taken from point measurements at the pile in *Gandersum*. Dashed lines indicate temporal trends. Daily mean values of river discharge at *Versen* are illustrated by blue dots in the lower panel. Salinity values were derived from conductivity data.

B.2. GB-Model
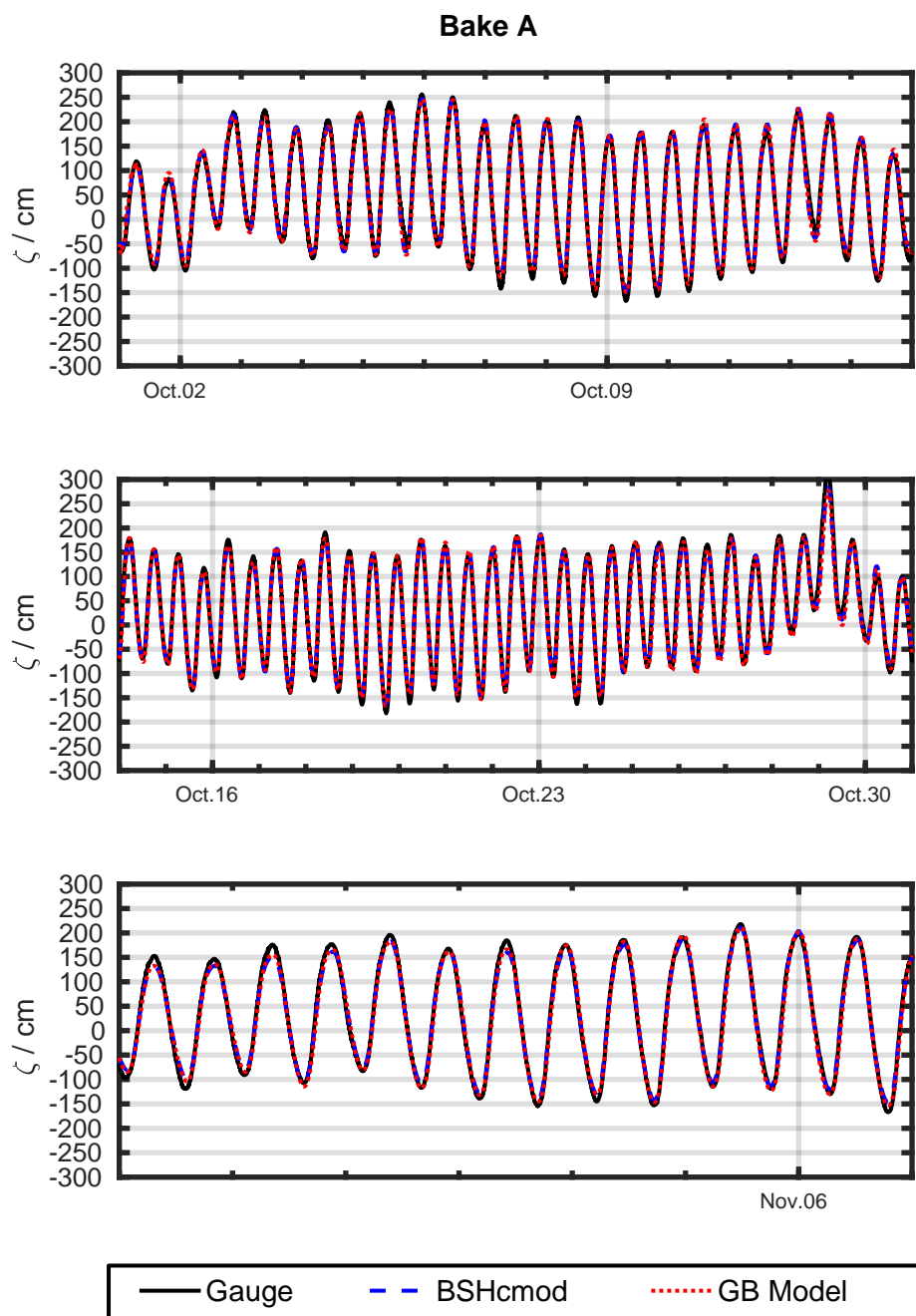
Bake A

Figure 81: Comparison of modelled Sea Surface Elevation in the GB-Model (red) with measured values at the gauge *Bake A* (black) and data from the BSHcmod. Labels on the abscissa indicate dates for mondays, tick spacings are 1 day.
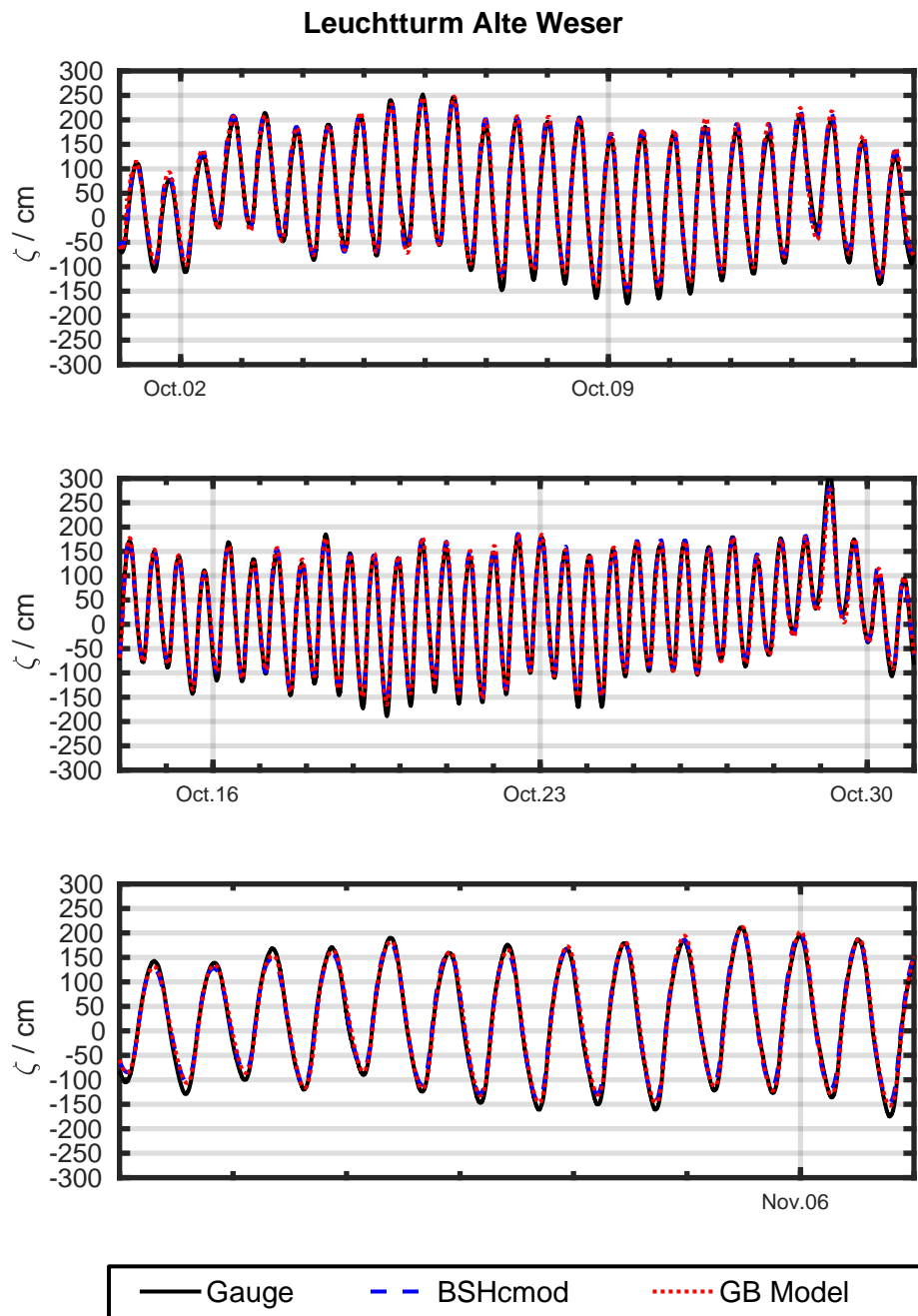
Figure 82: Comparison of modelled Sea Surface Elevation in the GB-Model with measured values at the gauge *LT Alte Weser* and data from the driving BSHcmod . Labels on the abscissa indicate dates for each monday, spacing of ticks is 1 day.

Messpfahl Spiekeroog
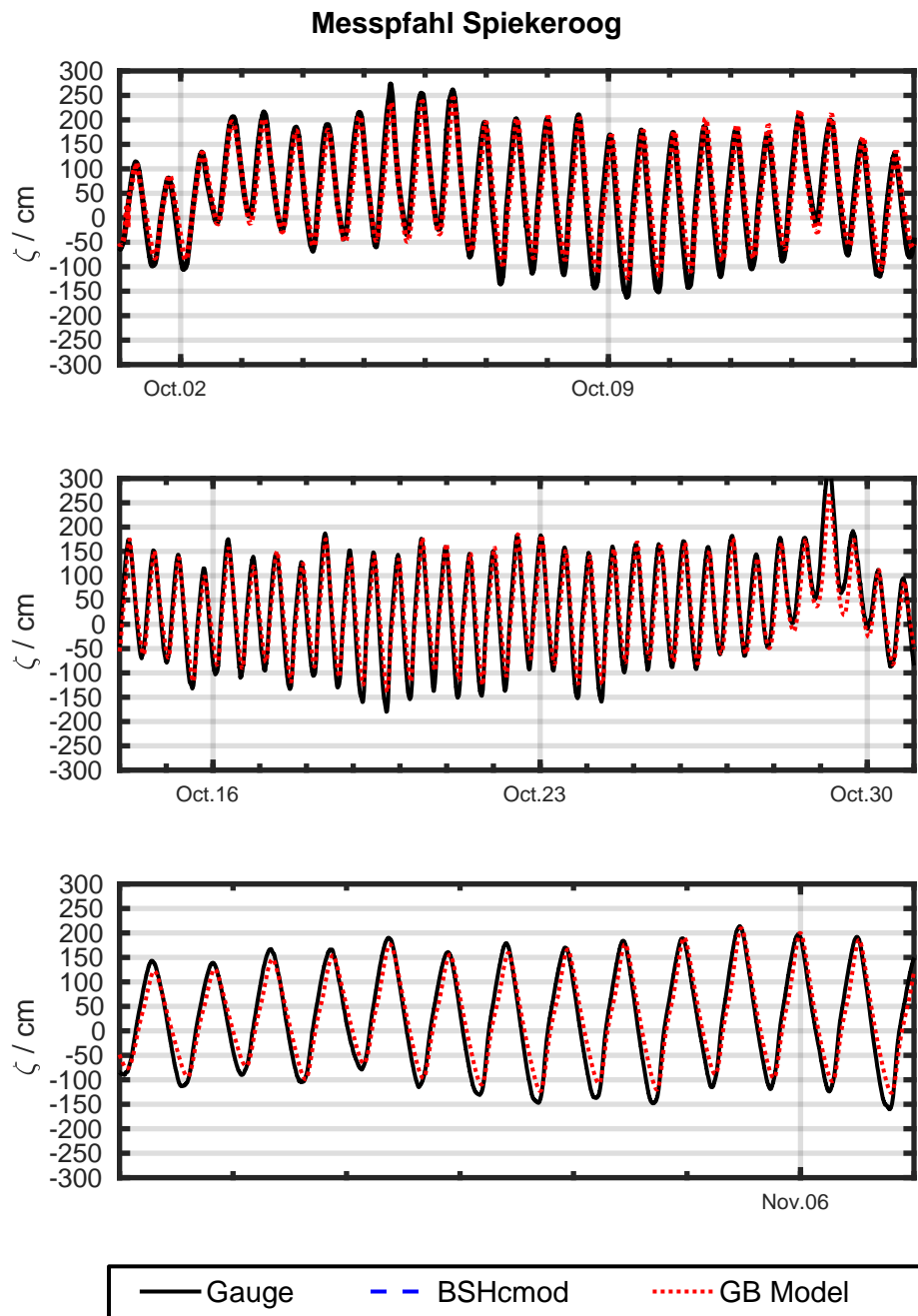
Figure 83: Comparison of modelled Sea Surface Elevation in the GB-Model with measured values at the gauge *Spiekeroog* and data from the driving BSHcmod . Labels on the abscissa indicate dates for each monday, spacing of ticks is 1 day.
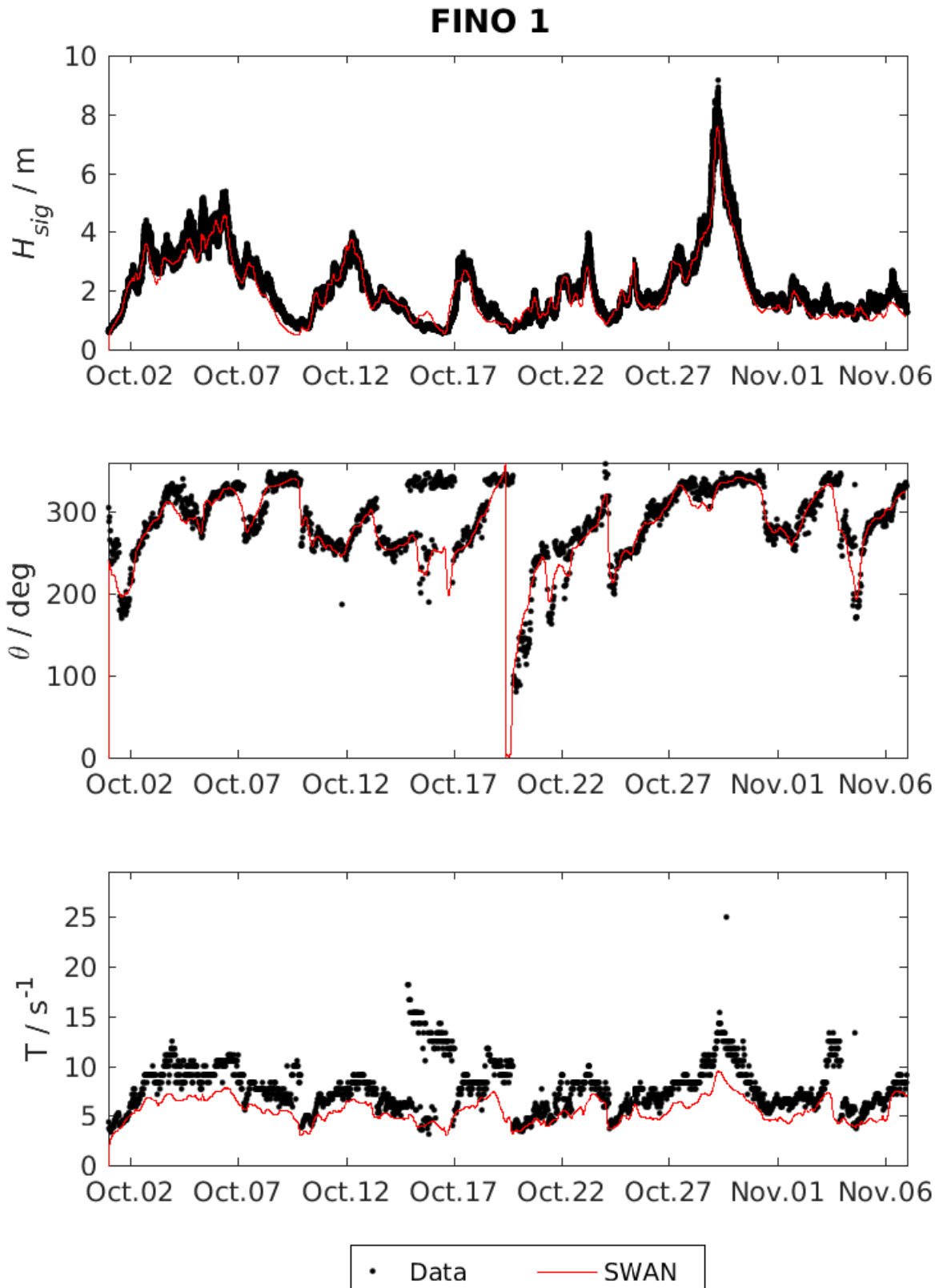
Figure 84: Comparison of computed wave data for significant wave height H_{sign}, mean wave direction θ and mean absolute wave period $TM01$ (red) with the measurements (black). Measured t values are indicating peak periods. Wave directions are defined in nautical convention.

B.3. EI-Model

Leuchtturm Alte Weser
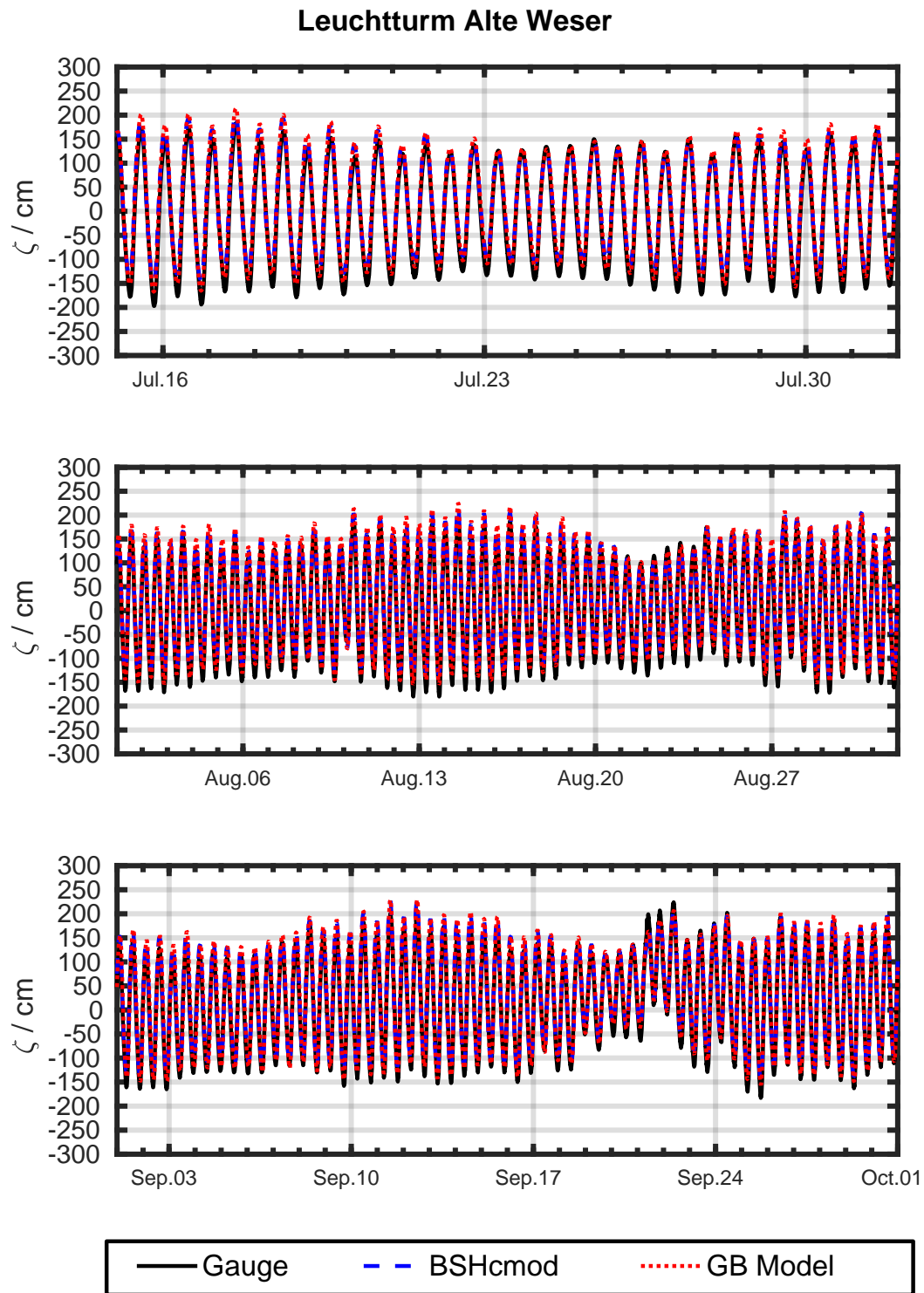
Figure 85: Comparison of sea surface elevation based on measured gauge data (black solid line), data from the BSHcmod (dashed blue line) and computations by the EI-Model (red dotted line). The latter was running in an offline one-way coupling scenario with data from the GB-Model. Initializing for July 14th, 2018, simulations ended on October 5th, 2018. Data location is $(8°8', 53°52')$.
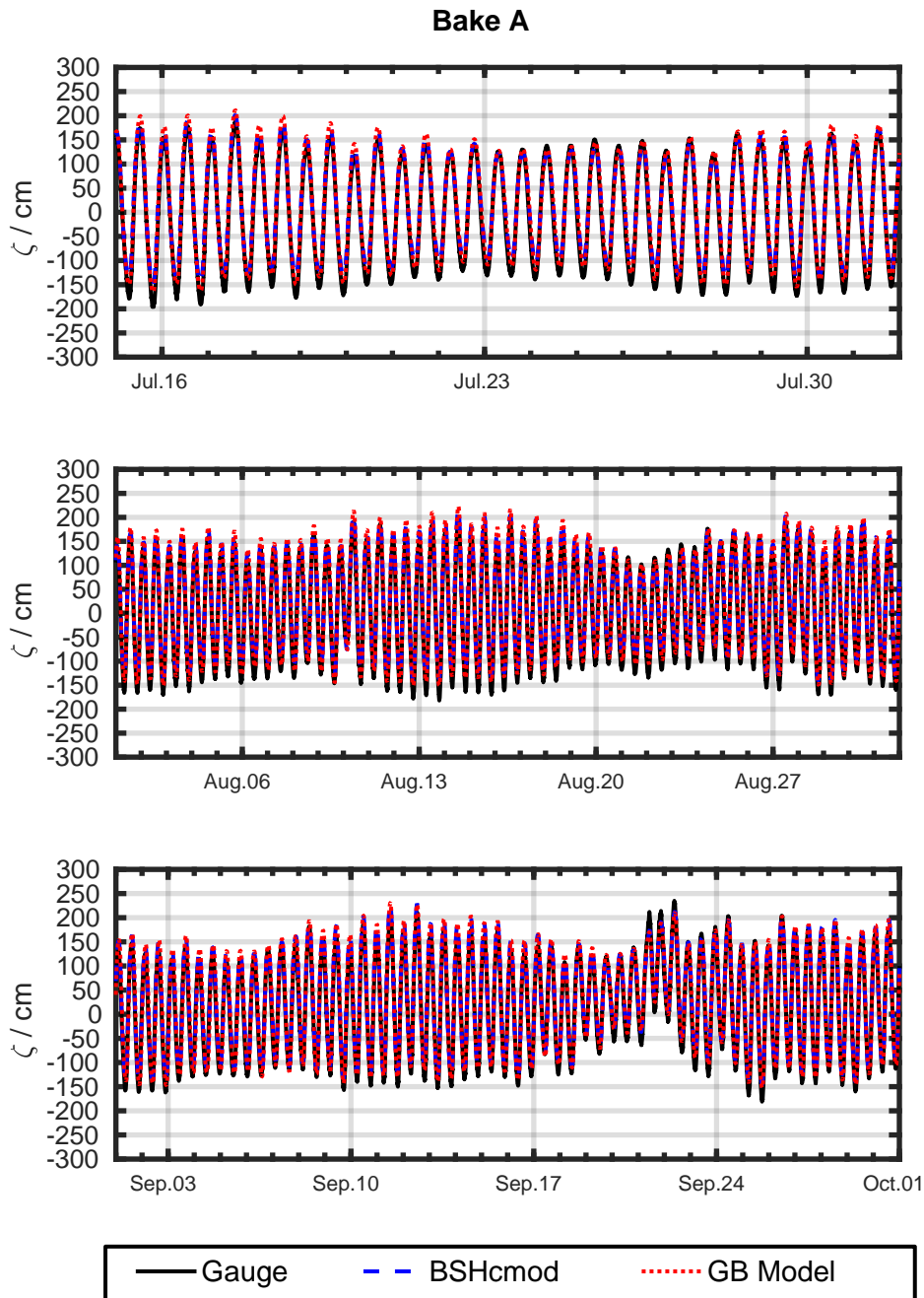
Figure 86: Comparison of sea surface elevation based on measured gauge data (black solid line), data from the BSHcmod (dashed blue line) and computations by the EI-Model (red dotted line). The latter was running in an offline one-way coupling scenario with data from the GB-Model. Initializing for July 14th, 2018, simulations ended on October 5th, 2018. Data location is $(8°19', 53°59')$.

Messpfahl Spiekeroog
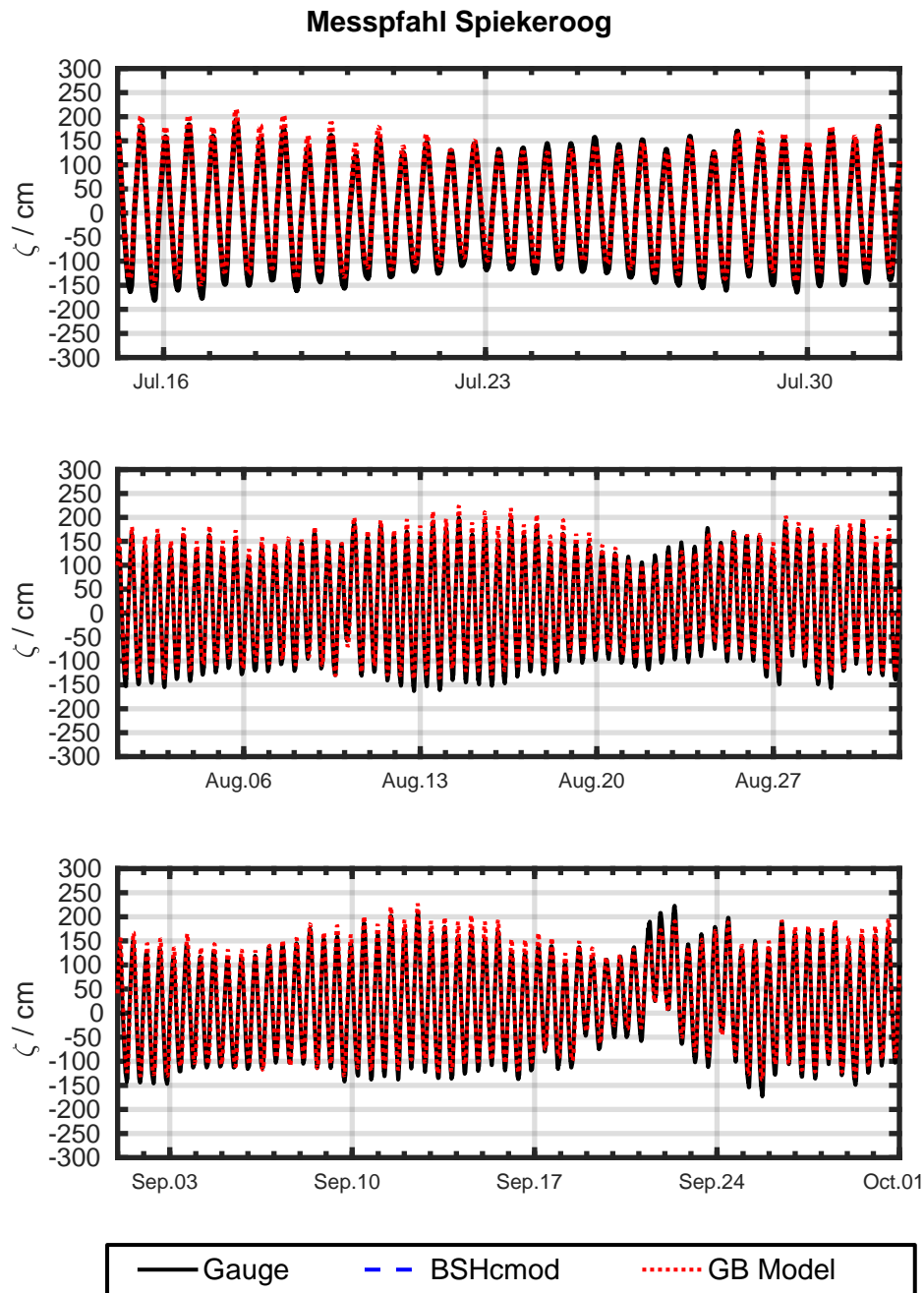
Figure 87: Comparison of sea surface elevation based on measured gauge data (black solid line) and computations by the EI-Model (red dotted line). The latter was running in an offline one-way coupling scenario with data from the GB-Model. Initializing for July 14th, 2018, simulations ended on October 5th, 2018. Data location is $(7°41', 53°45')$
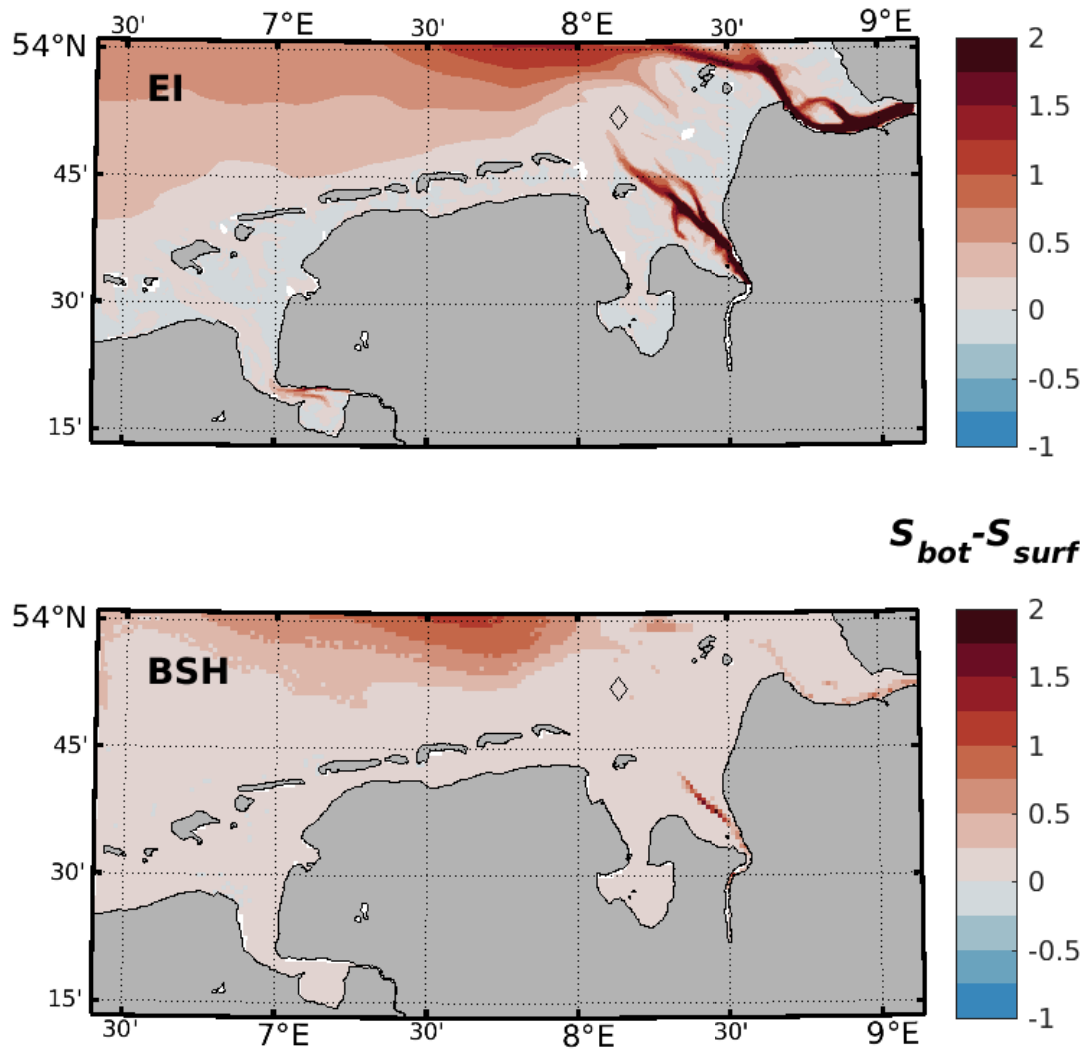
Figure 88: Comparison of monthly mean bottom-top salinity differences for Aug. 2018 in the EI-Model (top) and the BSHcmod (bottom). Location of the gauge station *Leuchtturm Alte Weser* is depicted by an diamond symbol.

B.4. SP-Model
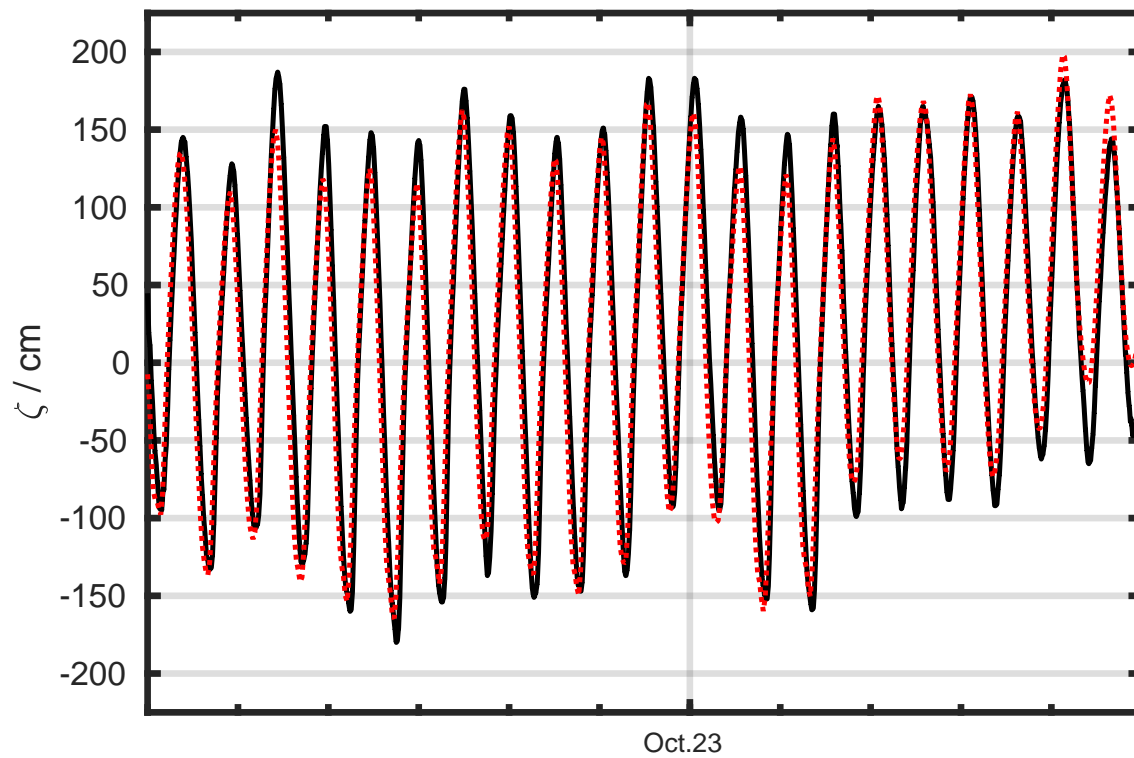
Figure 89: Comparison of sea surface elevation based on measured gauge data (black solid line) and model results from the SP-Model (red dotted line), which was initialized and forced by data from the GB-Model. Modeling period was corresponding to a 11 days period starting at Tuesday, October 17th 2017, 00:00:00 and ending at Saturday, October 28th 2017, 01:00:00.
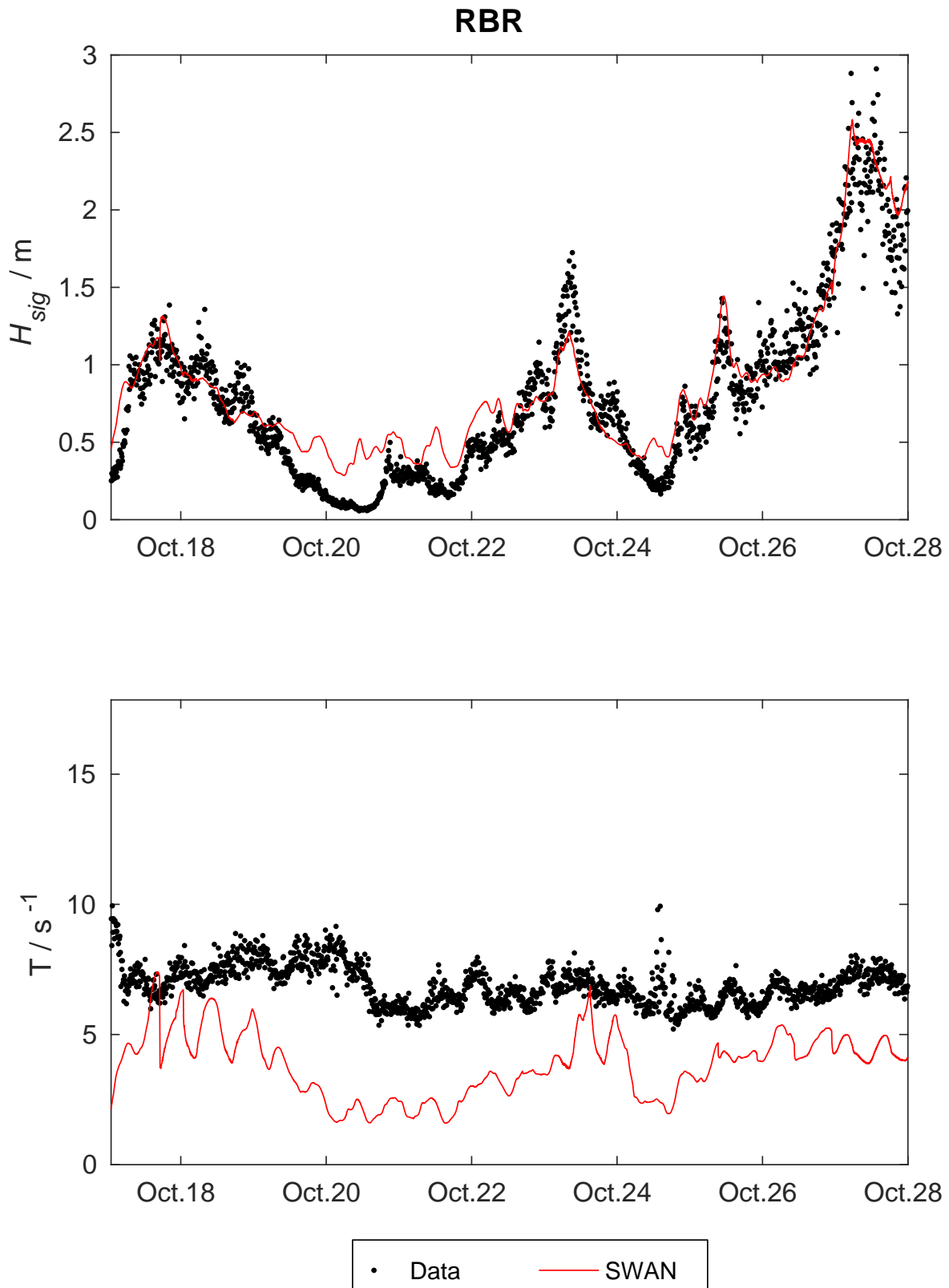
Figure 90: Comparison of modeled significant wave heights H_{sig} (top) and wave periods T (bottom) with RBR wave logger measurements at $(E7°41'6'', N53°48'40'')$. The red line is showing computations, measurements are indicated by black dots.

C. The MatLab floats toolbox: Short Documentation / Manual

This short description gives an overview of the basic functionality of the MATLAB toolbox described in section 5. This description follows the usage based on data from a ROMS-run and follows the workflow of setting up all necessary structures and computations after the ROMS-run was performed. Here, an example based on the numerical experiment of section 6 is used: A ROMS simulation of the two-way coupled GB-Model and SI-Model was performed with boundary forcing from the BSHcmod and constant analytical winds of $6\,\mathrm{m\,s^{-1}}$ velocity and $\theta_{wind} = 280°$ direction in mathematical sense, i.e. wind coming from North-NorthWest. 30 vertical layers were used and current velocities were stored seperately in history files for each day and model grid[195]. For this basic example, advection of two particles over the course of two days was computed using a wind drag coefficient of 1.4×10^{-2}.

C.1. Folder Structure

The Toolbox has a basic folder structure which assures easy use if it remains unaltered.[196]

C.2. Building ocean-, wind- and waves structs

The toolbox calculates horizontal advection of particles based on current, wind and wave data[197] which can be present on different numerical grids but all have to be converted to have consistent units, e.g. even though spherical and cartesian coordinates can be used, these units are not allowed to change between two datasets. Same holds true for velocity units, i.e. if surface currents are given in $\mathrm{m\,s^{-1}}$ on a cartesian grid, wind and Stokes Drift velocities must also be converted to $\mathrm{m\,s^{-1}}$ on a cartesian grid. Velocity units and grid coordinates have to consistent also, meaning in the case of spherical coordinates, velocities must be converted to degrees per second. Each field has to be present as a MATLAB-Struct with the fields `grd` for each numerical grid, e.g. in this case `grd(1)` for a coarse grid and `grd(2)` for a finer nested grid, in which velocity values, grid- and time-coordinates are stored. Due to the interpolation algorithms used in the tracking code, spatial coordinates have to be present on a structured grid[198]. Example code to generate such struct from a nested roms-simulation is given in the script `A_build_structs_from_roms.m`. First, a Project name must be defined in line 9. This name is used for naming subfolders within the toolbox folder for storing intermediate data and thus should not contain spaces or special characters. In line 12, the folder containing the

---

[195]E.g. `ocean_his_00001.nc` containing velocity values of the first 24 hours on the GB-Model grid and `ocean_his_spiekeroog_00001.nc` containing the respective values on the SI-Model grid.

[196]`/home/flo/floppsy/`. Schaubild über Ordnerstruktur einfügen.

[197]Stokes Drift

[198]i.e. unstructured data has to be interpolated on a structured grid before stored in these structs.

velocity data is set and in line 15 to 17 file names of the ROMS-history netcdf-files[199] for the coarse grid are set.

```matlab
8   %% ===== Set name of Project =====
9   pname = 'si_wind_tides';
10
11  %% ===== set folder of files =====
12  folder = '/media/flo/Elements/spiekeroog_ma/wind_tides/';
13
14  %% ===== set number and name of coarse files =====
15  his_pre = [folder 'ocean_his'];
16  nstart = 2; %if multiple history files: set index of first file
        to read in
17  nend = 3;   %index of last file to read in
```

A char with the names of each file is then generated in lines 19 to 30 and no changes need to be made here by the user.

In lines 32 and 33 variable names of horizontal velocities are set, e.g. u and v for horizontal baroclinic currents or *u_wind* and *v_wind* for driving winds[200], and the index of the respective vertical layers are set[201]. a matlab-struct containing the chosen variables is then created by the MATLAB function his2struct, which is written for ROMS-history netcdf files but can be used as blueprint for generating structs from other numerical models. This struct is stored as field grd(1) of the struct ocn in line 38.

```matlab
31  %% ===== build struct =====
32  vars = {'u','v'};
33  layer = 30;
34
35  tic
36  ocean_struct = his2struct(hisfile,vars,layer);
37  toc
38  ocn.grd(1)=ocean_struct;
```

The same procedure is done for the fine grid in lines 42 to 66 and the data of the fine grid is stored as field grd(2).

```matlab
42  %% ===== set number and name of fine files =====
```

---

[199]Containing the data for currents, grid etc.

[200]Not in this example.

[201]Currently just one layer is needed here as the current revision of the toolbox just uses horizontal currents within one layer for calculating trajectories. In the case of an ROMS dataset with 30 vertical layers, *layer=30* corresponds to the surface and *layer=1* to the bottom layer.

```matlab
43  his_pre = [folder 'ocean_his_spiekeroog'];
44  nstart = 2;
45  nend = 3;
46
47  %% ===== Build his character =====
48  for ii = nstart:nend
49      if ii<10
50          hisfile{ii-nstart+1} = [his_pre '_0000' int2str(ii) '.nc'];
51      elseif ii<100
52          hisfile{ii-nstart+1} = [his_pre '_000' int2str(ii) '.nc'];
53      else
54          hisfile{ii-nstart+1} = [his_pre '_00' int2str(ii) '.nc'];
55      end
56  end
57
58  clear nfiles his_pre i
59  %% ===== build struct =====
60  vars = {'u','v'};
61  layer = 30;
62
63  tic
64  ocean_struct = his2struct(hisfile,vars,layer);
65  toc
66  ocn.grd(2)=ocean_struct;
```

_____

As mentioned above, coordinte and velocity values need to be consistent. In this case, a spherical grid and velocity values in meters per seconds are given, thus velocity values are converted to degrees per seconds in lines 76 to 81. In lines 83 to 99 coordinate and data arrays are permuted to match MATLAB's meshgrid notation and finally in lines 102 to 105, the struct containing the ocean currents is saved as

tt ocn.mat within the subfolder vel_structs/[pname]. This struct is later used for computing particle advection. In this example, [pname]=si_wind_tides

```matlab
68  %% ===== unit conversions and permute lateral grid =====
69  %velocity and coordinate units have to be consistent, i.e. if
       spherical
70  %coordinates are used, velocities have to be described in deg/
       seconds.
71  %Also, all gridded data have to be present in mtalb meshgrid
       format,
```

```matlab
72  %otherwise interpolation errors might occur.
73
74  disp('--- conversion of ocean struct ---');
75  for i=1:length(ocn.grd)
76      % convert velocities to rad/s:
77      [ocn.grd(i).u,ocn.grd(i).v] =...
78          uv2spheric(ocn.grd(i).u,ocn.grd(i).v,ocn.grd(i).y_u);
79      %convert to deg/s:
80      ocn.grd(i).u = ocn.grd(i).u .*(180./pi);
81      ocn.grd(i).v = ocn.grd(i).v .*(180./pi);
82
83      %meshgrid arrays:
84      [x,y] = meshgrid(ocn.grd(i).x_u(:,1),ocn.grd(i).y_u(1,:));
85              %permute(x_u,[2 1]) also possible for structured
                   grids
86      ocn.grd(i).x_u = x;
87      ocn.grd(i).y_u = y;
88      [x,y] = meshgrid(ocn.grd(i).x_v(:,1),ocn.grd(i).y_v(1,:));
89      ocn.grd(i).x_v = x;
90      ocn.grd(i).y_v = y;
91      [x,y] = meshgrid(ocn.grd(i).x_rho(:,1),ocn.grd(i).y_rho(1,:))
              ;
92      ocn.grd(i).x_rho = x;
93      ocn.grd(i).y_rho = y;
94      [x,y] = meshgrid(ocn.grd(i).x_psi(:,1),ocn.grd(i).y_psi(1,:))
              ;
95      ocn.grd(i).x_psi = x;
96      ocn.grd(i).y_psi = y;
97      %ocn.grd(i).y_psi = ocn.grd(i).y_psi';
98      ocn.grd(i).u = permute(ocn.grd(i).u,[2 1 3 4]);
99      ocn.grd(i).v = permute(ocn.grd(i).v,[2 1 3 4]);
100 end
101
102 %% ===== save ocn-struct =====
103 mkdir(['./vel_structs/' pname]);     %create subfolder for project
104
105 save(['./vel_structs/' pname '/ocn.mat'],'ocn','-v7.3')
```

As analytical wind forcing was used in this example by defining a constant wind using the

drag formulae by Yelland and Taylor [1996], no wind velocities are stored in the ROMS history files. Thus, the wind struct is defined by prescribing the same parameter as in the simulation's analytical surface momentum flux[202]. This is done in the shown example code in lines 107 to 112 by definition of the wind speed amplitude and the wind direction angle. This analytical wind speeds are then interpolated on the same grid and time coordinates as the ocean currents, converted to units of degrees per seconds and stored as `wind_struct` in lines 107 to 149 and then saved as matlab struct `wind.mat` in the project's subfolder.

```matlab
107  %% ===== build u,v-wind struct =====
108  windamp = 6.0;        %m/s
109  winddir = 280.0;         %wind direction in deg (mathematical sense)
110
111  Uwind = windamp.*cos(winddir.*pi./180);      %u-component in m/s
112  Vwind = windamp.*sin(winddir.*pi./180);      %v-component in m/s
113  %% ===== grid to coarse-grid =====
114  wind_struct = struct('ocean_time',[],'spherical',[],'x_rho'
         ,[],...
115      'y_rho',[],'Uwind',[],'Vwind',[]);
116              %ROMS wind velocities are given on rho-gridpoints
117
118  wind_struct.ocean_time = ocn.grd(1).ocean_time;
119  wind_struct.spherical = ocn.grd(1).spherical;
120  wind_struct.x_rho = ocn.grd(1).x_rho;
121  wind_struct.y_rho = ocn.grd(1).y_rho;
122  wind_struct.Uwind = Uwind.*...
123      ones(size(wind_struct.x_rho,1),size(wind_struct.x_rho,2),...
124      size(ocn.grd(1).u,3),size(ocn.grd(1).u,4));
125  wind_struct.Vwind = Vwind.*ones(size(wind_struct.Uwind));
126  %convert from m/s to ded/s:
127  [wind_struct.Uwind,wind_struct.Vwind] =...
128          uv2spheric(wind_struct.Uwind,wind_struct.Vwind,
               wind_struct.y_rho);
129
130  wind.grd(1) = wind_struct;
131  %% ===== grid to fine-grid =====
132  wind_struct = struct('ocean_time',[],'spherical',[],'x_rho'
         ,[],...
133      'y_rho',[],'Uwind',[],'Vwind',[]);
134
```

---

[202]These are set in the ROMS analytical `ana_smflux.h` file.

```matlab
135   wind_struct.ocean_time = ocn.grd(2).ocean_time;
136   wind_struct.spherical = ocn.grd(2).spherical;
137   wind_struct.x_rho = ocn.grd(2).x_rho;
138   wind_struct.y_rho = ocn.grd(2).y_rho;
139   wind_struct.Uwind = Uwind.*...
140        ones(size(wind_struct.x_rho,1),size(wind_struct.x_rho,2),...
141        size(ocn.grd(2).u,3),size(ocn.grd(2).u,4));
142   wind_struct.Vwind = Vwind.*ones(size(wind_struct.Uwind));
143   %convert from m/s to ded/s:
144   [wind_struct.Uwind,wind_struct.Vwind] =...
145        uv2spheric(wind_struct.Uwind,wind_struct.Vwind,
                wind_struct.y_rho);
146
147   wind.grd(2) = wind_struct;
148   %% ===== save ocn-struct =====
149   save(['./vel_structs/' pname  '/wind.mat'],'wind','-v7.3')
```

For this example, no wave parameters are used but the respective struct can easily be computed by copying lines 31 to 105, setting `vars = {u_stokes,v_stokes}` and saving these values as `wav.mat` in the project's subfolder.

C.3. Initializing the floats struct

Calculated trajectories are stored in a *floats-struct*, which is a matlab struct. This struct contains data of each float with fields for x- and y-position at each time step, a time-vector t, an index number which helps to identify each float within this struct and a flag for identifying the smallest grid, that contains the respective float. An example script for generating a floats-struct is given as `B_initialize_floats.m`. Here the project's name can be defined in line 8, which should be the same as for the velocity-structs.

```matlab
7   %% ===== Project Name =====
8   pname = 'si_wind_tides';
```

Lines 10 to 34 show an example to graphically place floats location within a model grid using the helping function `set_floats_graphically`, but in this example a manual definition of two floats' starting locations is given in lines 36 to 38. The starting time of each float is given in line 41. Note that this starting time has to be defined in units of the velocity data in respect to the data's reference time, i.e. in this case seconds with reference time 0 s. The `spherical` switch in line 44 indicates the units of floats coordinates x and y and has to be the same as for velocity structs, in this case `spherical=1`.

```matlab
36  %% ===== or set release location manually =====
37  x_f = [7.73,7.74];        %longitude
38  y_f = [53.81,53.82];      %latitude
39
40  %% ===== set release time for each float =====
41  t = [90000,93600];    %seconds after reference time of velocity
       data
42
43  %% ===== spherical or cartesian coordinates? =====
44  spherical = 1;   %switch, 0=cartesian (m), 1=spherical (deglon,
       deglat)
```

The struct is initialized in lines 46 to 64 and saved in the projects subfolder in lines 66 to 69.

```matlab
46  %% ===== determine number of floats =====
47  Nfloats = length(t);
48
49  %% ===== build floats struct =====
50  disp('--- build floats struct ---');
51
52  %initalize floats_struct with staring location and time:
53  floats = struct('index',[],'t',[],'x',[],'y',...
54      [],'grd',[],'spherical',[]);
55
56  for n=1:Nfloats
57      floats(n).index = n;    %float indexing number
58      floats(n).t(1) = t(n);  %time vector
59      floats(n).x(1) = x_f(n);  %x-coordinate
60      floats(n).y(1) = y_f(n);  %y-coordinate
61      floats(n).spherical = spherical;
62      floats(n).grd(1) = 0;   %index of smallest,
63                              %float containing grid,
64                              %initialized with zero
65  end
66  disp('  ... done');
67  %% ===== Save floats-struct in project subfolder =====
68  mkdir(['./flt_structs/' pname]);    %create subfolder for project
69  save(['./flt_structs/' pname '/flt.mat'],'floats','-v7.3')
```

C.4. Computation of floats trajectories

After creating the velocity- and floats-structures with each particle's starting point, trajectories ca be computed by using either the function `ptrack` or `ptrack2`,which can be found in the `helping_functions` subfolder. The difference between these two functions is that velocity fields have to be summed up before passing it as one struct to the `ptrack` function, whereas each struct for ocean, wind and Stokes Drift velocities are passed individually to the `ptrack2` function and drag coefficients for wind velocities are applied individually to each particle of the floats struct. Both approaches are shown in the example code `C_calculate_trajectories.m`, but just usage of `ptrack` is discuussed here, as each velocity field has to be interpolated individually to the particles position for each iteration in the

tt ptrack2-function and thus computation become numerically expensive and slow[203].

In lines 7 to 15 of the example code, the project's name and the name and path of the respective velocity structs is given by the user. In this example, no Stakes Drift velocities are taken into account, thus the waves-struct is defined as empty `char`. The floats struct, which havs been initailized in the previous section, is laoded to the MATLAB's workspace in line 18.

```matlab
7   %% ===== Project Name =====
8   pname = 'si_wind_tides';
9
10  %% ===== load ocean, wind and waves struct =====
11  %Load ocen, wind and waves velocity structures. Use blank char if
        one
12  %struct does not exist, e.g. wav = {}.
13  load(['./vel_structs/' pname '/ocn.mat']);    %surface currents
14  load(['./vel_structs/' pname '/wind.mat']);  %wind speed
15  waves = {};                                   %Stokes Drift
        velocity
16
17  %% ===== load floats struct =====
18  load(['./flt_structs/' pname '/flt.mat']);
```

As mentioned above, usage of

tt ptrack2 with individual wind drag parameters for each particle is cumbersum. Therefore, C'_w and α from equations (44) are given in lines 29 and 30 and the velocity fields then are summed up the function `sum_up`, which interpolates all velocity fields to the currents space-time and then uses equation (44) to create on velocity structure.

```matlab
28  %Set wind drag and deflection:
```

---

[203]Thus, for parameter studies of different drag coefficients, it is adviced to perform multiple computations of trajectories with different C'_w and *alpha* values and storing resulting values as individual MATLAB-structs.

```
29  Cw = 0.014;         %wind drag coefficient
30  alpha = 0.00;           %deflection angle of floats and wind
        direction
31
32  %sum up velocity struct:
33  ocean = sum_up(ocn,waves,wind,Cw,alpha);
```

Finally, the integration method and time stepping size and the layer, in which particles should be advected are defined in lines 39 to 42 and the trajectories are then calculated in line 50 using the `ptrack`-function. In this case, just surface velocities are present in the currents-struct, thus `layer=1`, and a simple Euler method with time step of $dt = 5\,\mathrm{min}$ is used. The floats-structure containing all computed trajectories is then stored in the floats-subfolder in line 82[204].

```
38  %% ===== Set integration method, time step and layer of
        velocities =====
39  layer = 1;  %vertical layer of 3D-velocities
40  dt = 5*60;  %integration time step in s,
41              %generally time units of velocity structs
42  method = 'euler';   %integration method

50  [floats imax] = ptrack(floats,ocean,layer,dt,method);

81  %% ===== Save calculated floats-struct in project subfolder =====
82  save(['./flt_structs/' pname '/flt.mat'],'floats','-v7.3')
```

---

[204]Note some lines of the example code are omitted here.

D. Comparison: ROMS FLOATS vs. fLOPpSy
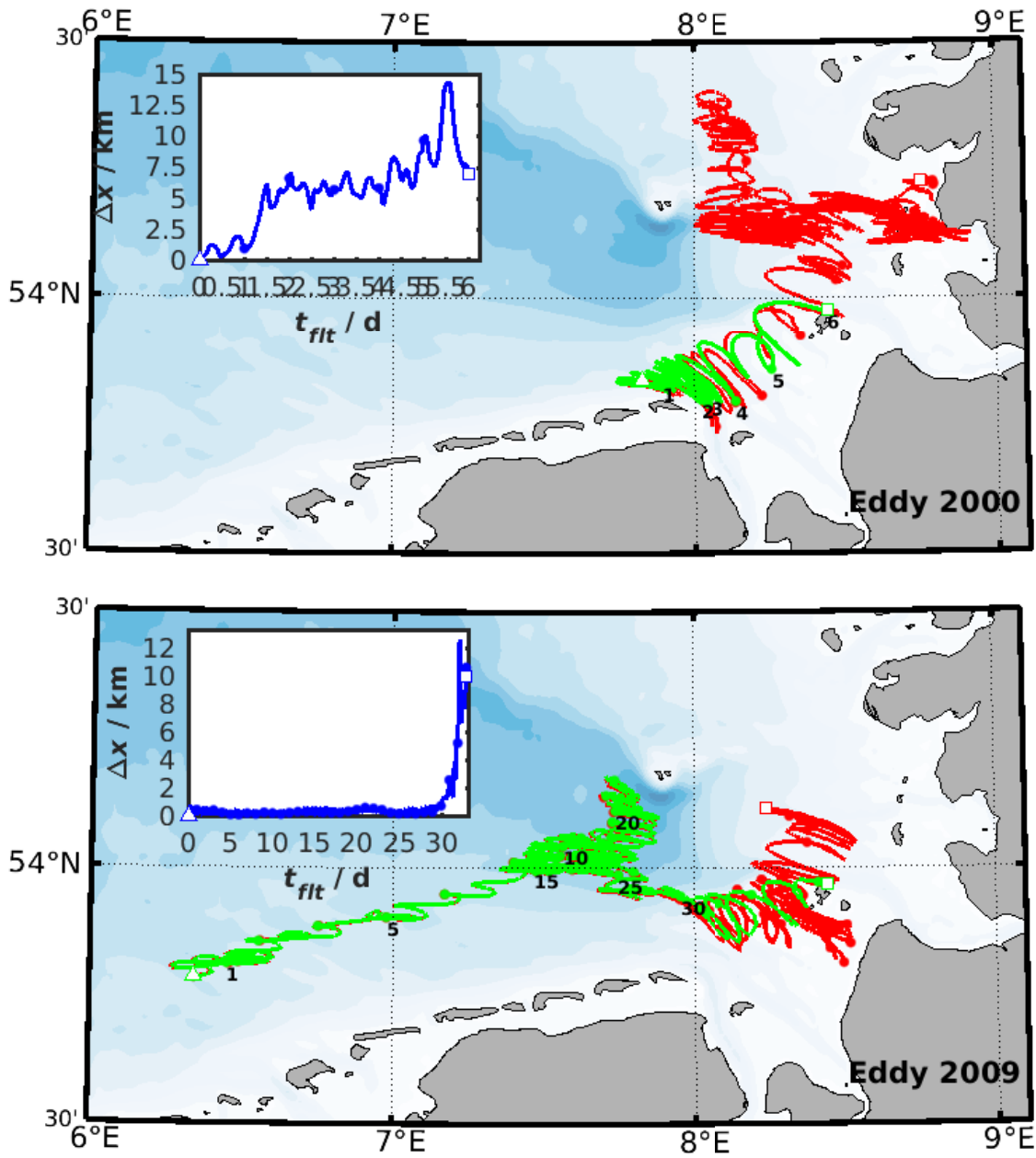
Figure 91: Trajectories calculated by the ROMS online floats module (red trajectory) and the FLOPPSY toolbox (green trajectory) using Euler integration with $dt = 20\,\text{min}$. Inlet graphs show temporal evolutions of differences. Dots and numbers denote particle locations on 24 h intervals. Details are given in section 5.
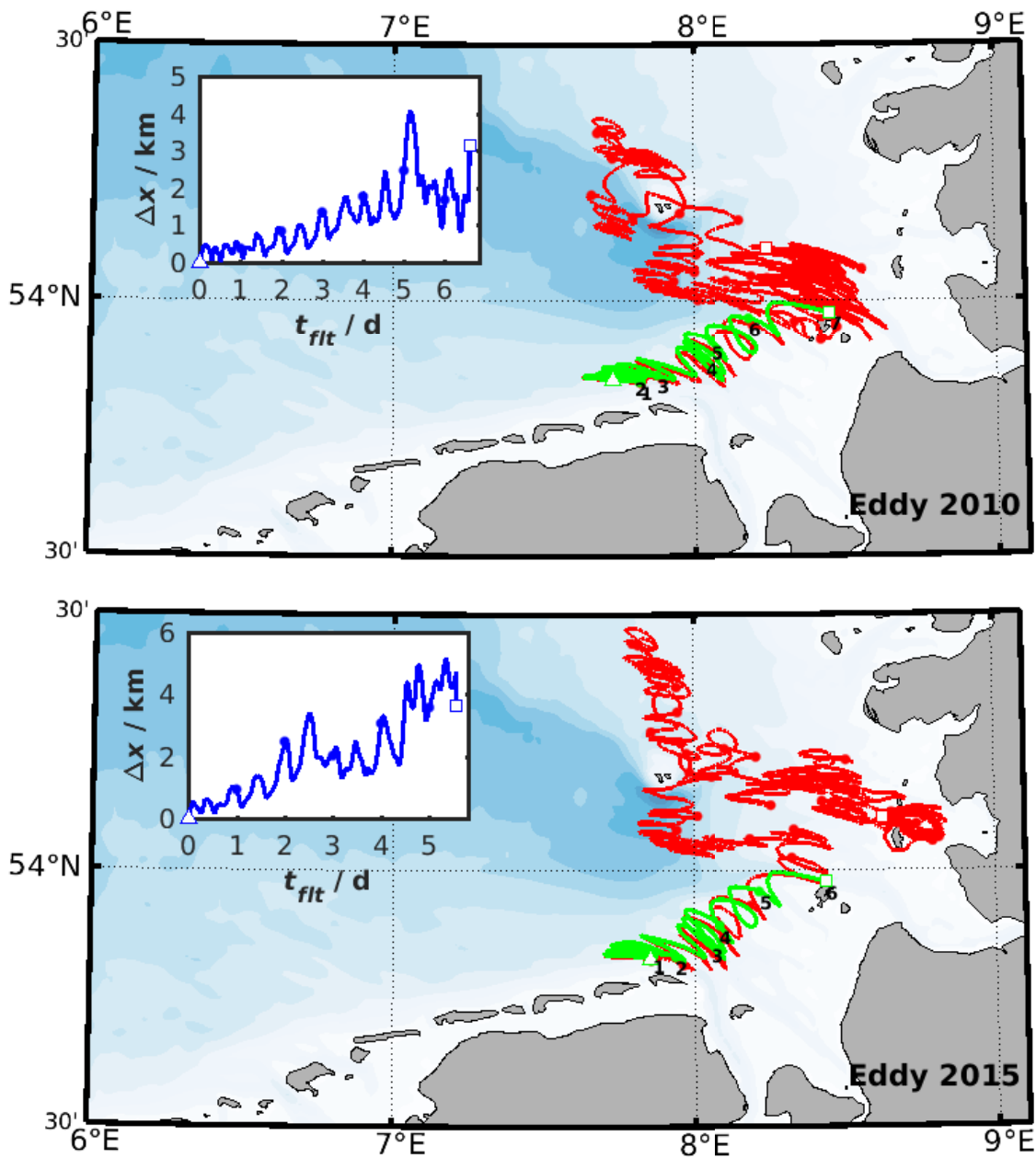
Figure 92: Trajectories calculated by the ROMS online floats module (red trajectory) and the FLOPPSY toolbox (green trajectory) using Euler integration with $dt = 20\,\mathrm{min}$. Inlet graphs show temporal evolutions of differences. Dots and numbers denote particle locations on 24 h intervals. Details are given in section 5.
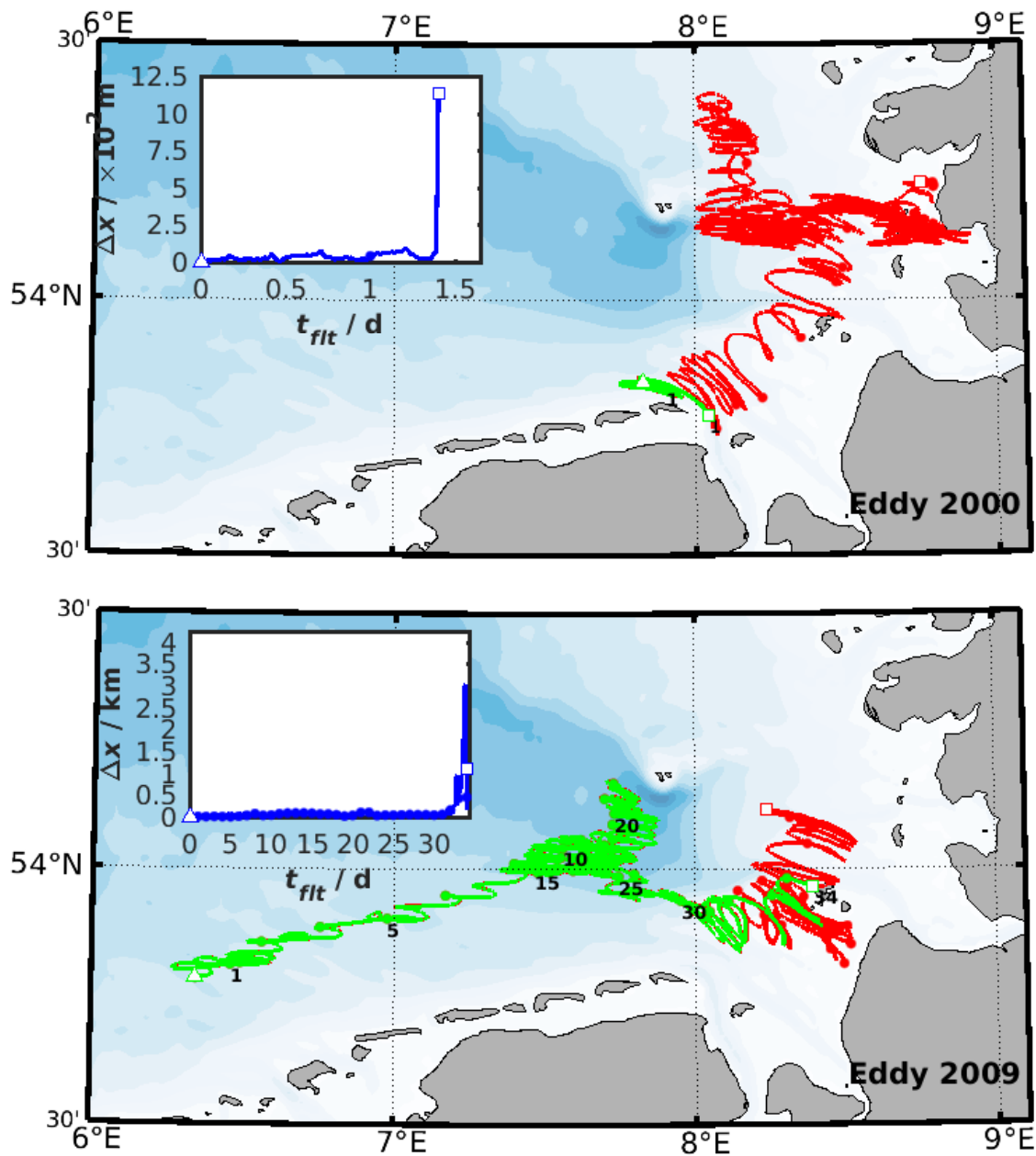
Figure 93: Trajectories calculated by the ROMS online floats module (red trajectory) and the FLOPPSY toolbox (green trajectory) using Improved Euler integrations with $dt = 20$ min. Inlet graphs show temporal evolutions of differences. Dots and numbers denote particle locations on 24 h intervals. Details are given in section 5.
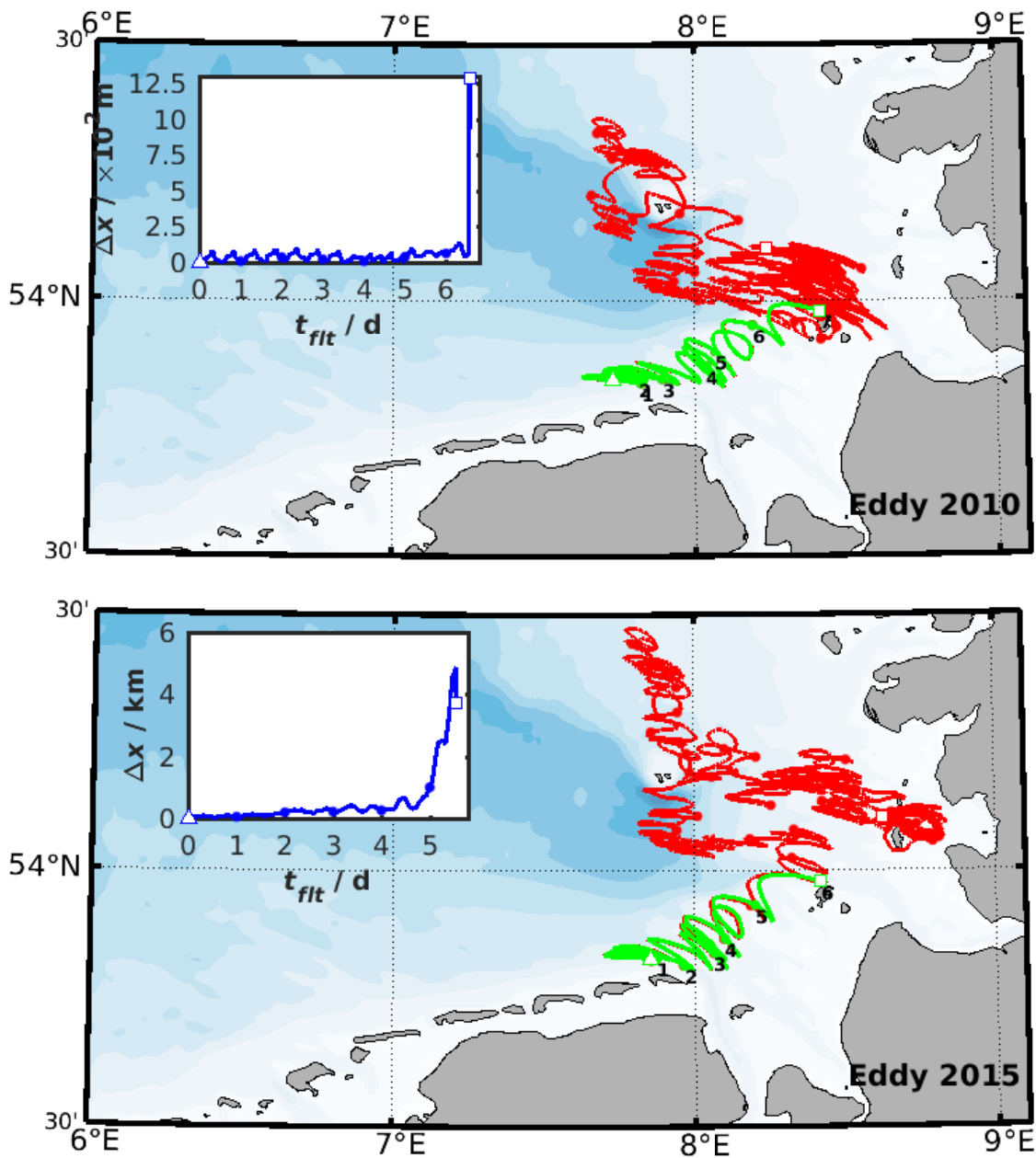
Figure 94: Trajectories calculated by the ROMS online floats module (red trajectory) and the FLOPPSY toolbox (green trajectory) using Improved Euler integrations with $dt = 20\,\text{min}$. Inlet graphs show temporal evolutions of differences. Dots and numbers denote particle locations on 24 h intervals. Details are given in section 5.
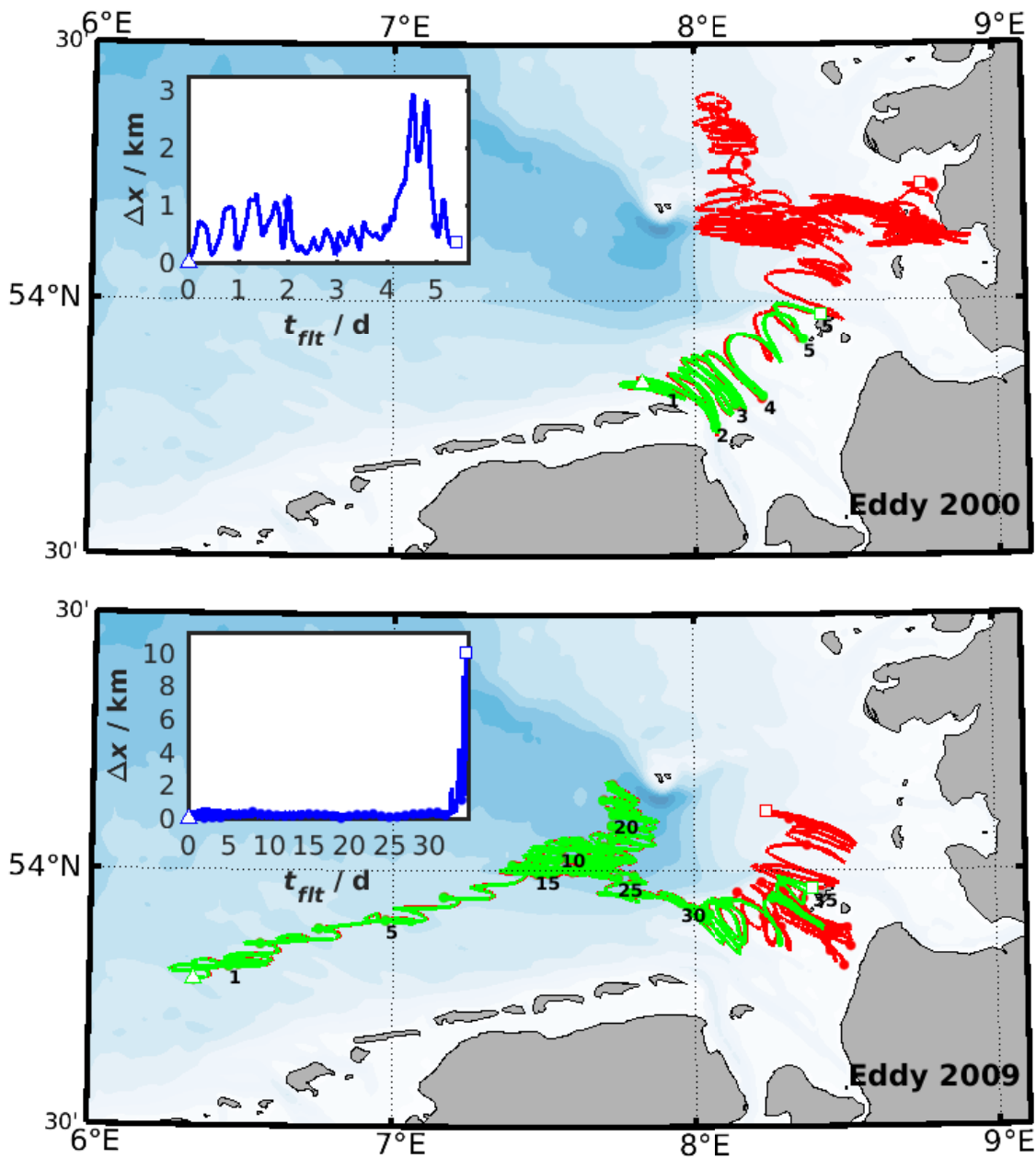
Figure 95: Trajectories calculated by the ROMS online floats module (red trajectory) and the ꜰLOPᴘSʏ toolbox (green trajectory) using RK4 integration with $dt = 20\,\text{min}$. Inlet graphs show temporal evolutions of differences. Dots and numbers denote particle locations on $24\,\text{h}$ intervals. Details are given in section 5.
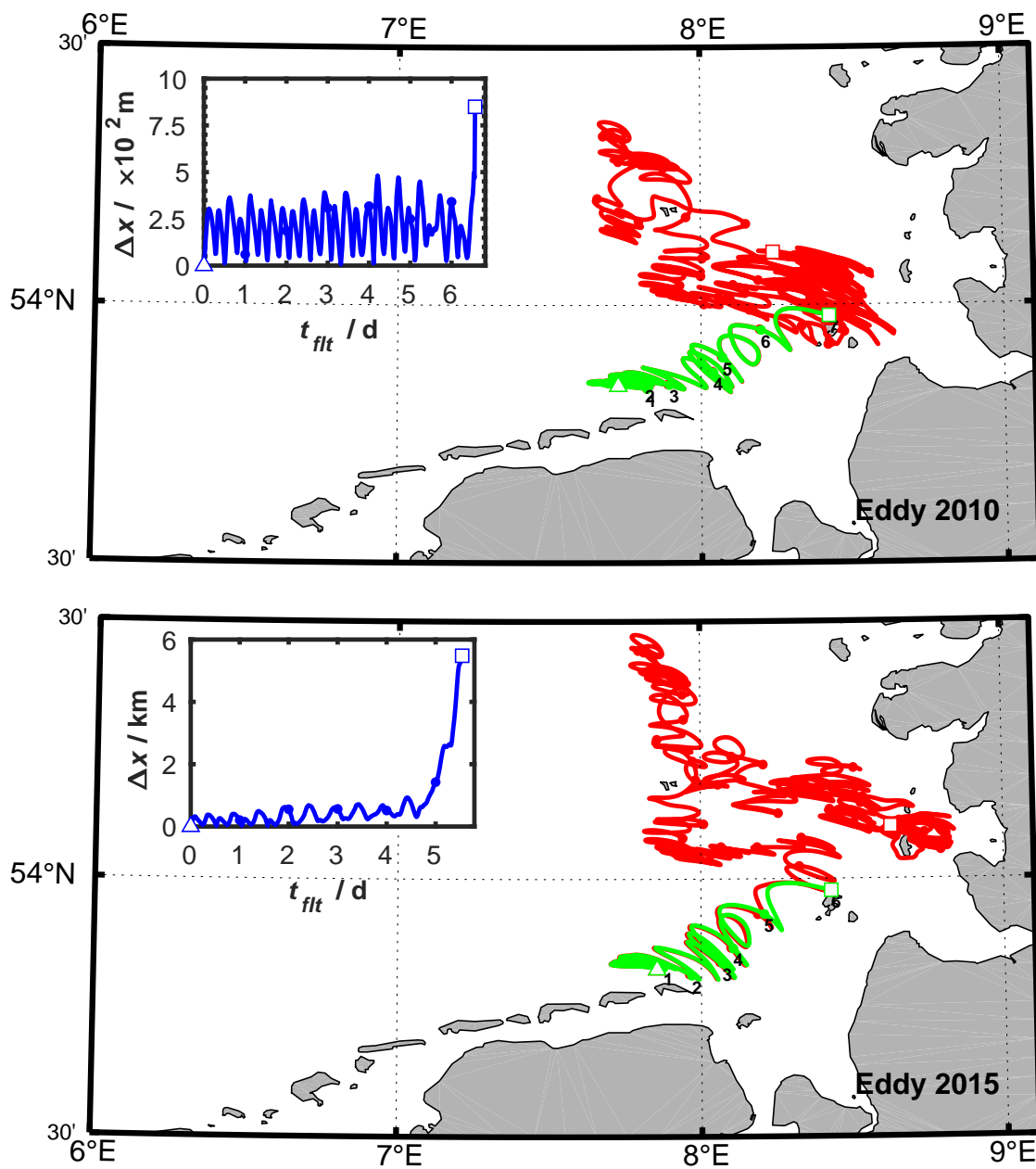
Figure 96: Trajectories calculated by the ROMS online floats module (red trajectory) and the ꜰLOPꜱꜱʏ toolbox (green trajectory) using RK4 integration with $dt = 20 \, \mathrm{min}$. Inlet graphs show temporal evolutions of differences. Dots and numbers denote particle locations on 24 h intervals. Details are given in section 5.
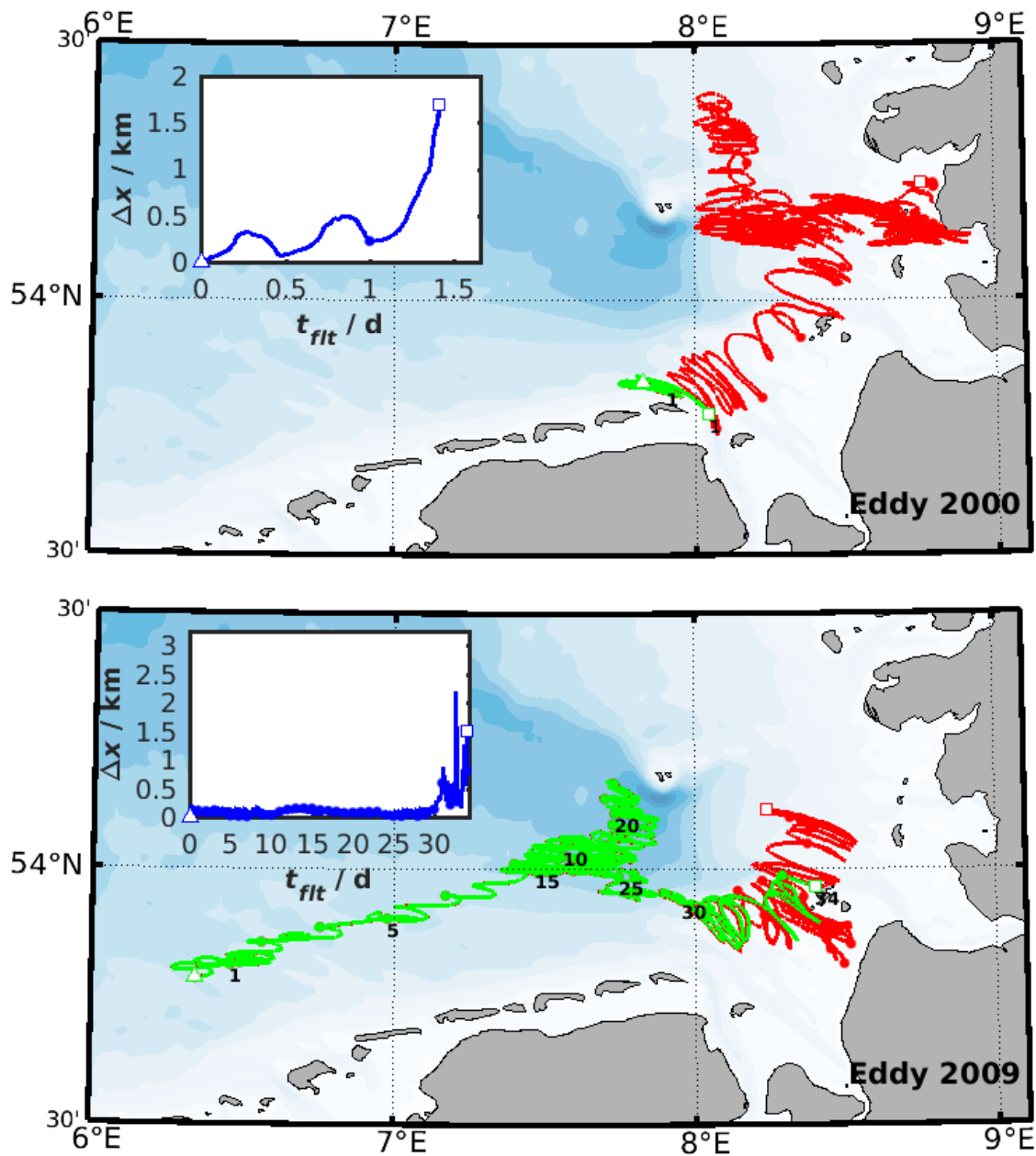
Figure 97: Trajectories calculated by the ROMS online floats module (red trajectory) and the ғLOPᴘSʏ toolbox (green trajectory) using Euler integration with $dt = 5\,\mathrm{min}$. Inlet graphs show temporal evolutions of differences. Dots and numbers denote particle locations on 24 h intervals. Details are given in section 5.
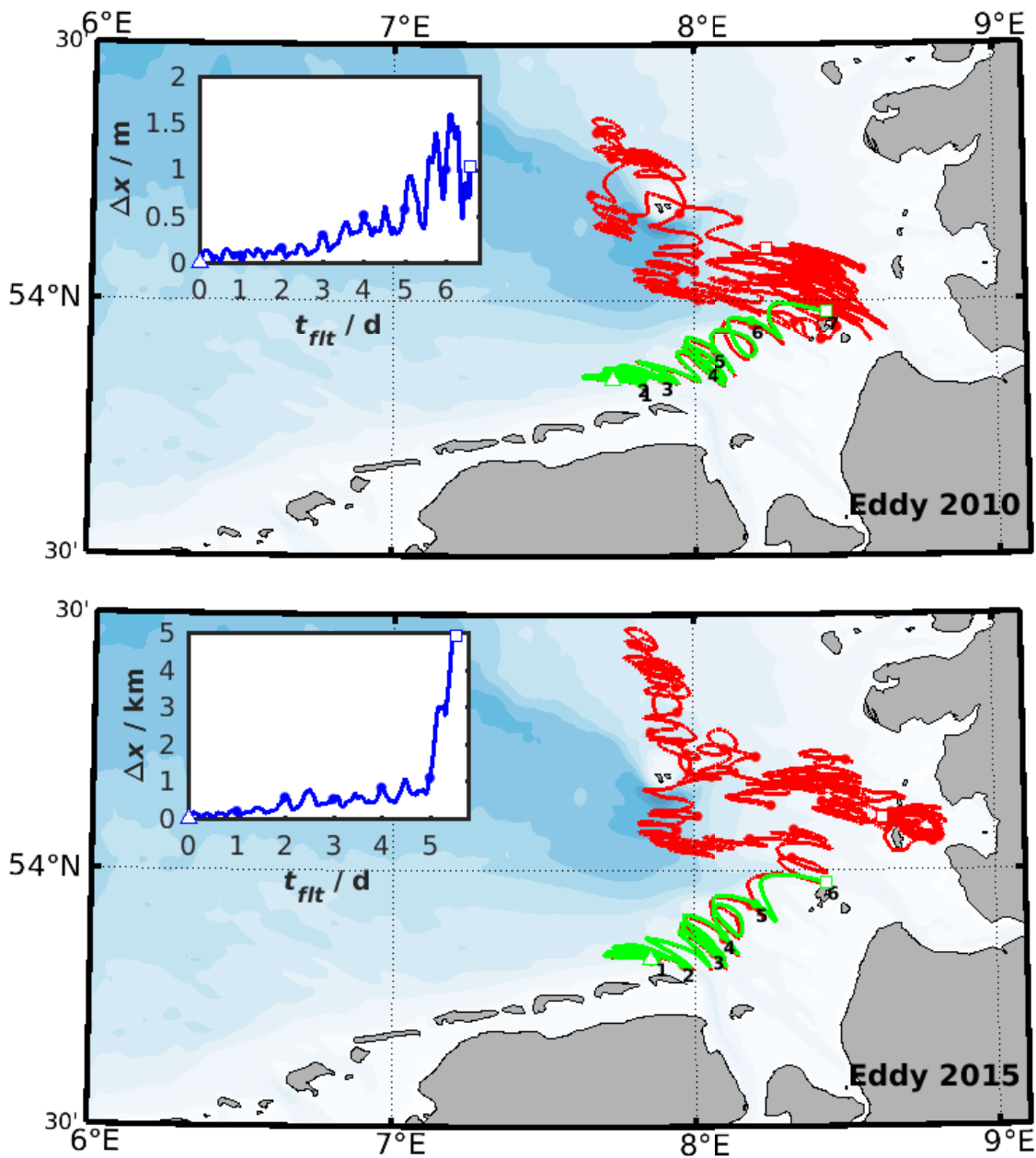
Figure 98: Trajectories calculated by the ROMS online floats module (red trajectory) and the FLOPPSY toolbox (green trajectory) using Euler integration with $dt = 5\,\mathrm{min}$. Inlet graphs show temporal evolutions of differences. Dots and numbers denote particle locations on 24 h intervals. Details are given in section 5.
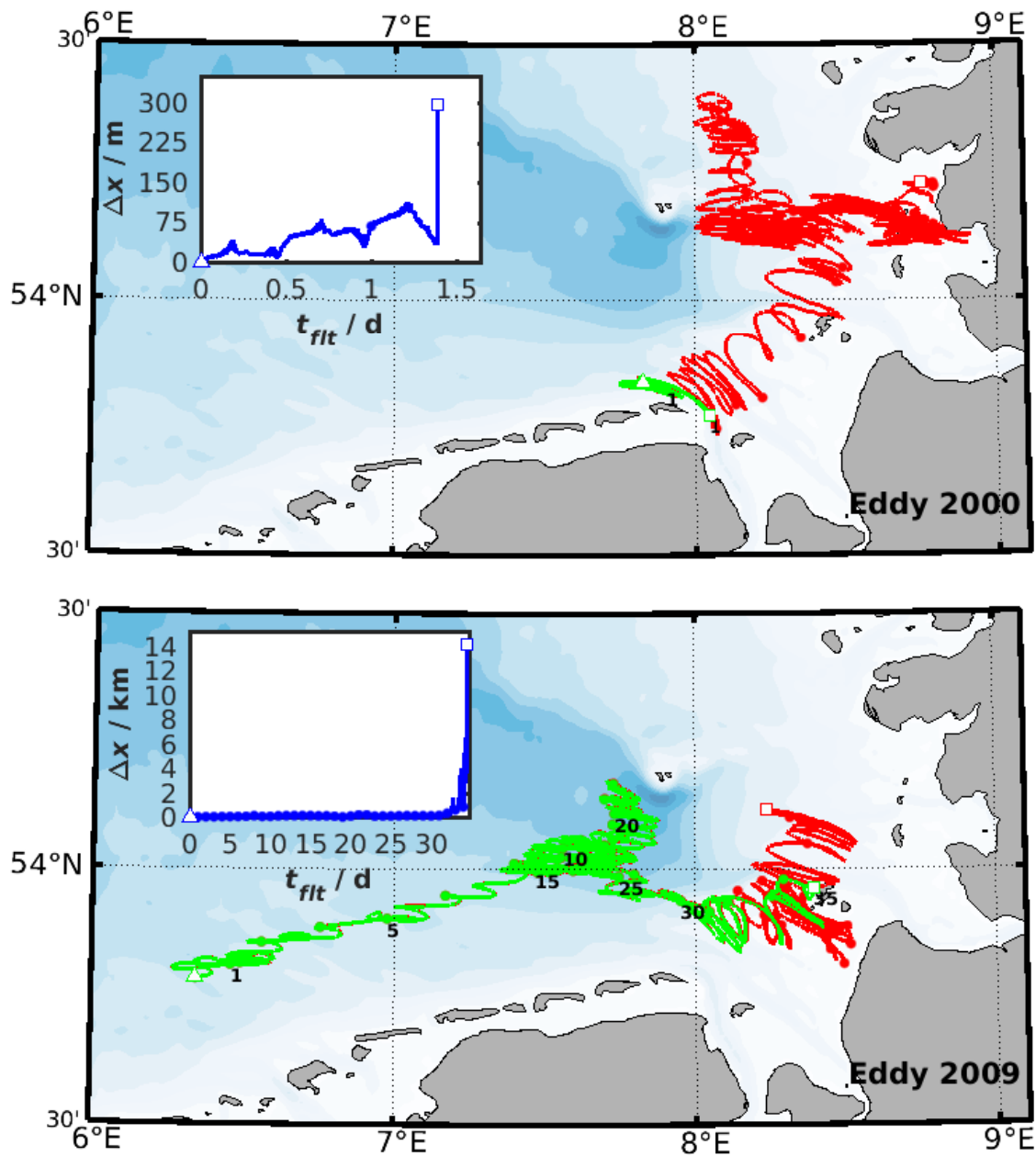
Figure 99: Trajectories calculated by the ROMS online floats module (red trajectory) and the ꜰLOPᴘSʏ toolbox (green trajectory) using Improved Euler integration with $dt = 5$ min. Inlet graphs show temporal evolutions of differences. Dots and numbers denote particle locations on 24 h intervals. Details are given in section 5.
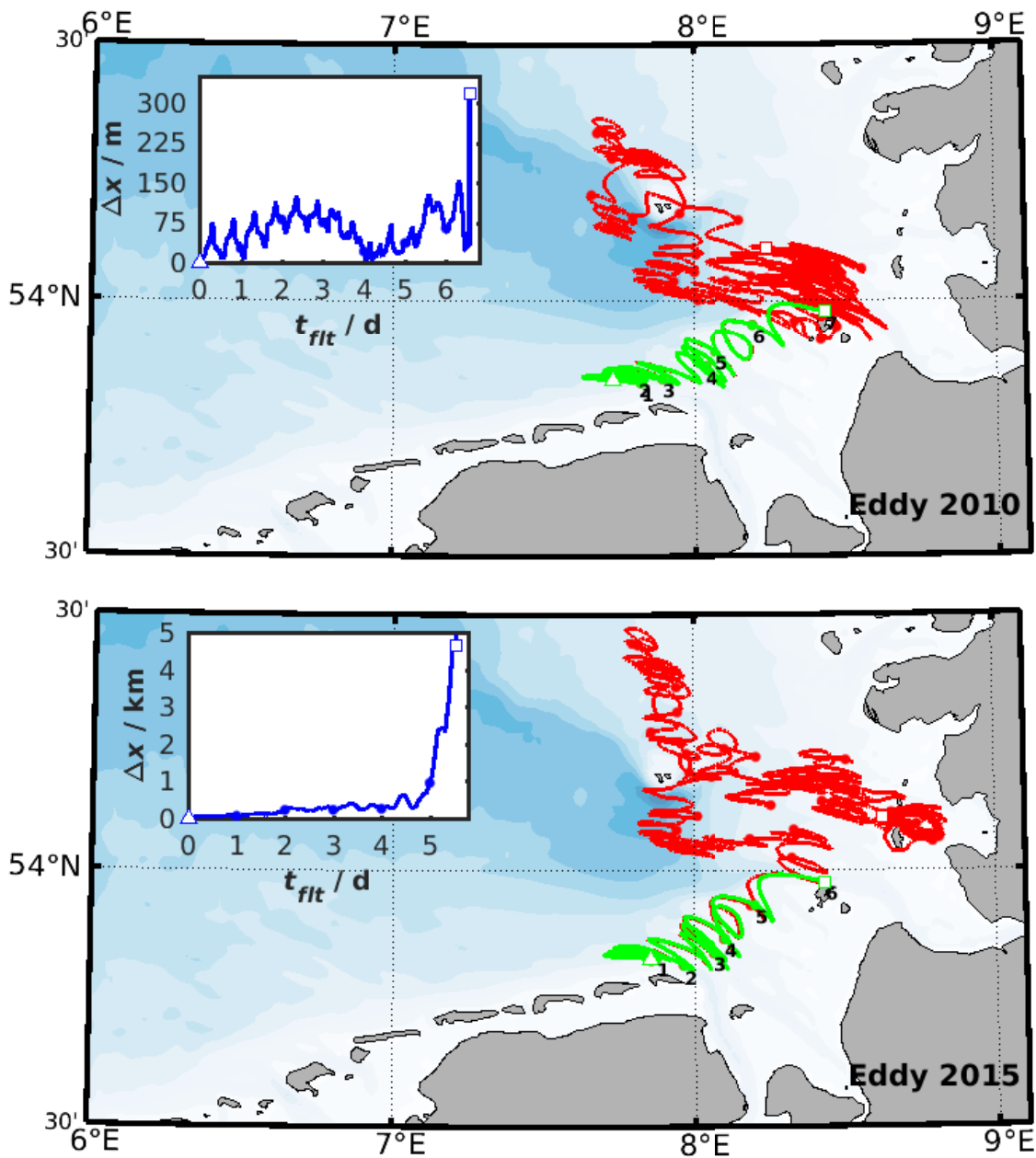
Figure 100: Trajectories calculated by the ROMS online floats module (red trajectory) and the FLOPPSY toolbox (green trajectory) using Improved Euler integration with $dt = 5\,\mathrm{min}$. Inlet graphs show temporal evolutions of differences. Dots and numbers denote particle locations on 24 h intervals. Details are given in section 5.
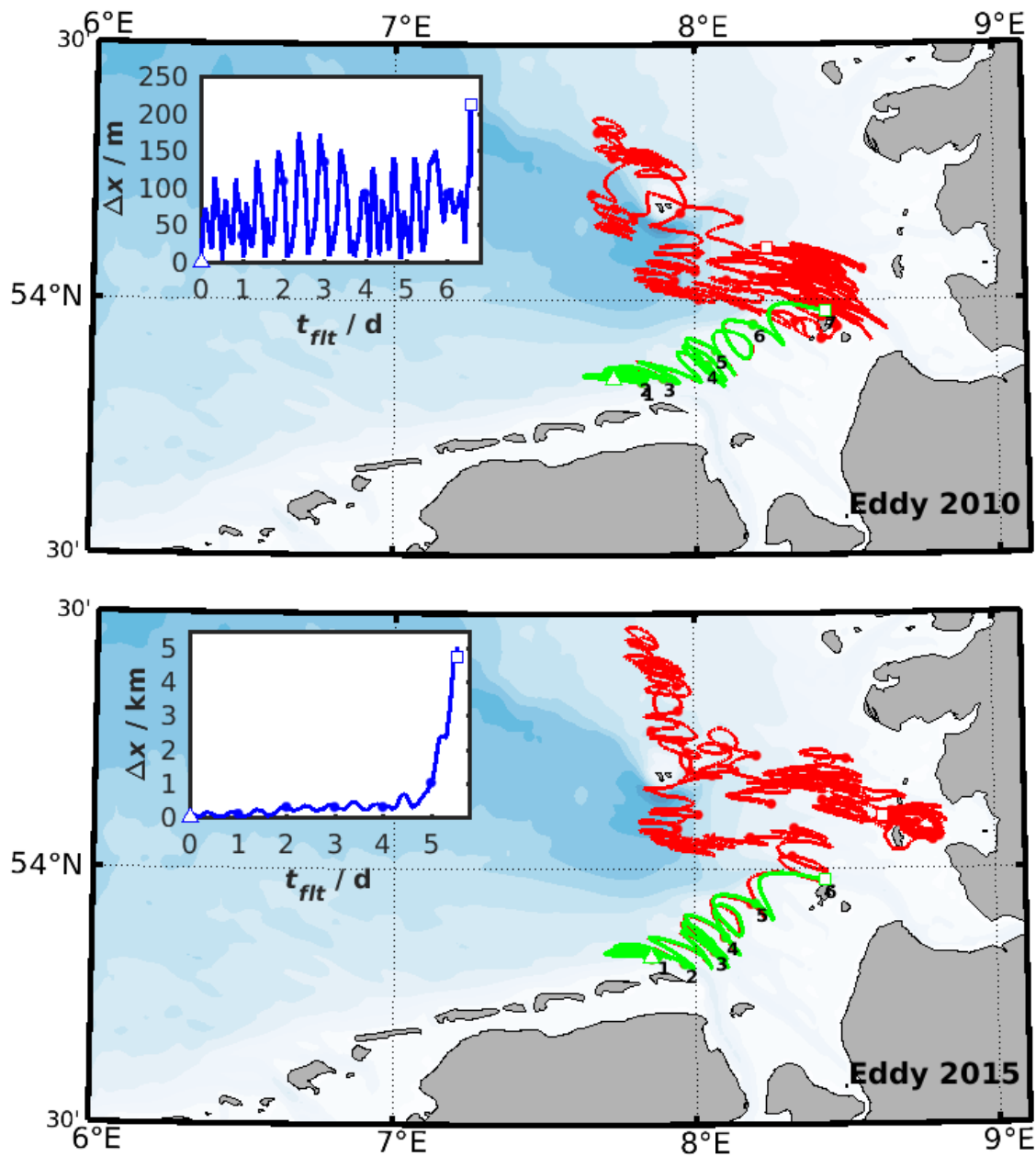
Figure 101: Trajectories calculated by the ROMS online floats module (red trajectory) and the FLOPPSY toolbox (green trajectory) using RK4 integration with $dt = 5\,\mathrm{min}$. Inlet graphs show temporal evolutions of differences. Dots and numbers denote particle locations on 24 h intervals. Details are given in section 5.

E. Wind, Waves and Currents in Nearshore Regions

E.1. Handling of Land Points
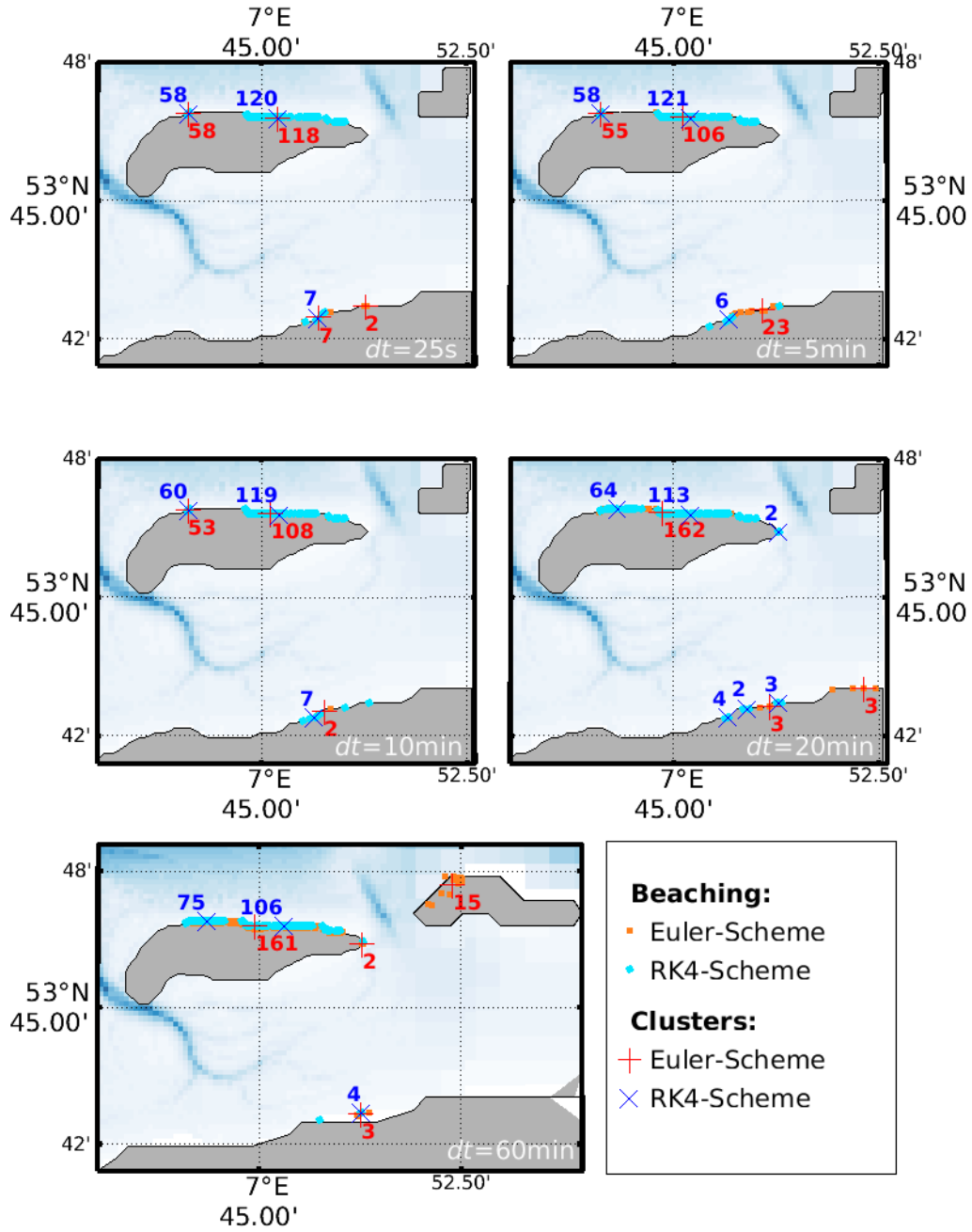
Figure 102: Beaching Locations after 14 days integration time using different time stepping lengths dt. Orange squares and red plus-signs denote resulting beaching locations resp. cluster centers when using Euler integration, cyan dots and blue crosses denote respective parameters for RK4 integrations. Differing time stepping lengths dt are mentioned in each panel. Landpoints were handled as *Nil*, but location based parametrization was used.

E.2. Scenario A
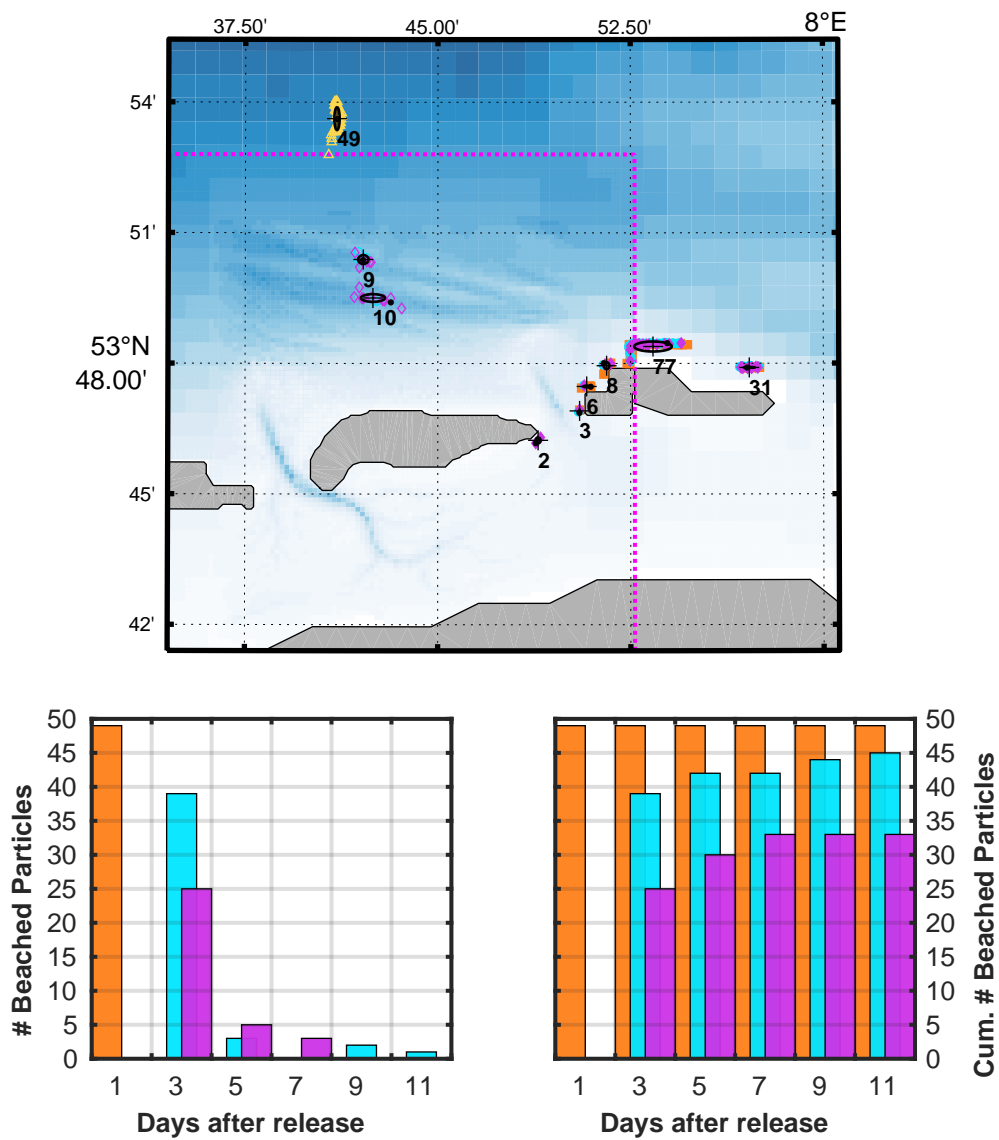
Figure 103: Same as Figure 44, but regarding diffusion terms according to equation (32): Distribution of Lagrangian floats for 4 ensembles of 49 particles after 14 days of simulation. Temporal spacing between releases is shown in Figure 33.

E.3. Scenario B
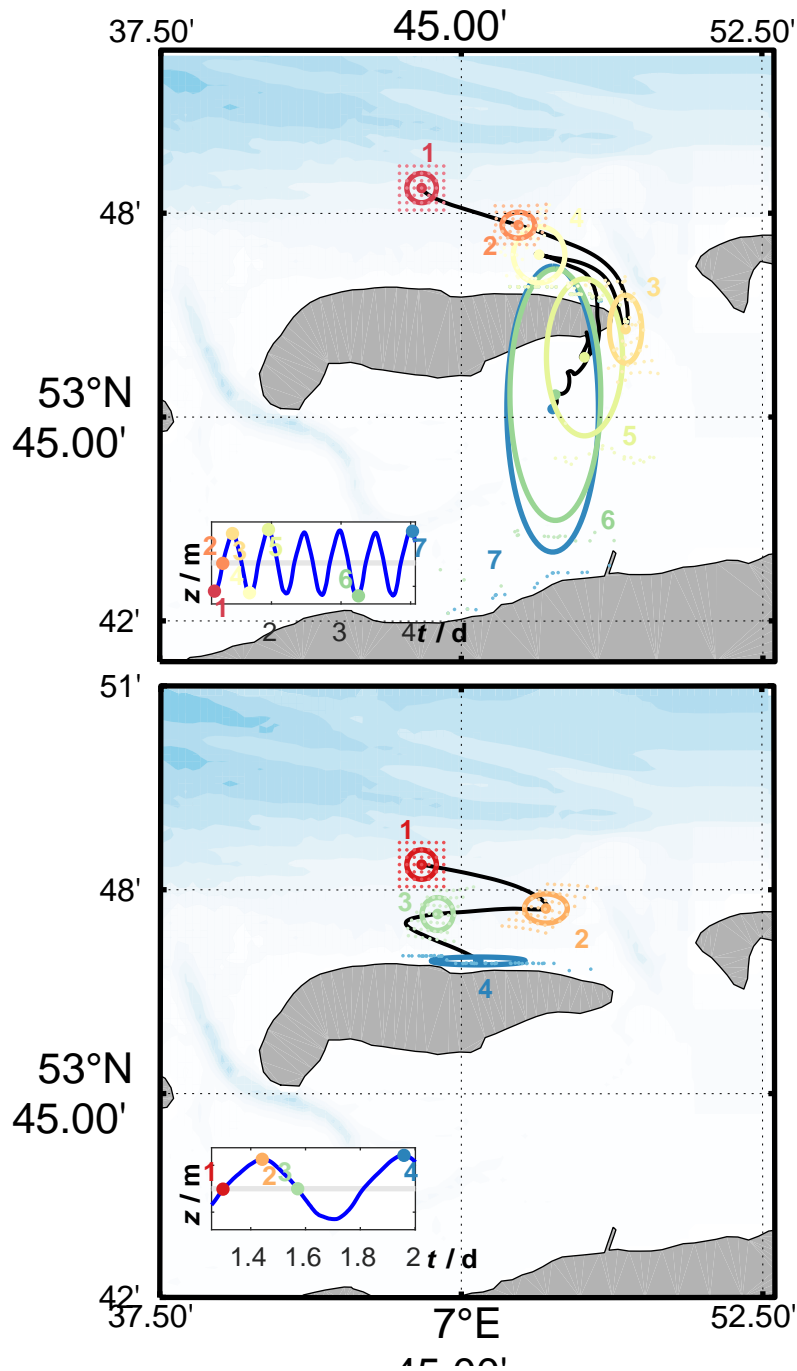
Figure 104: Trajectories of ensemble centers S for releases ① (top panel) and ② (bottom panel), when wind induced currents are regarded. Centers at discrete time steps and respective $ZM2$-ellipses are shown by bold dots and ellipses. Small, brighter dots are indicating individual particle positions. Color coding is illustrated in inserts, showing temporal evolution of surface elevation (here z) at the modeling site. Wind drag of $C_2 = 7 \times 10^{-3}$ was applied on particles.
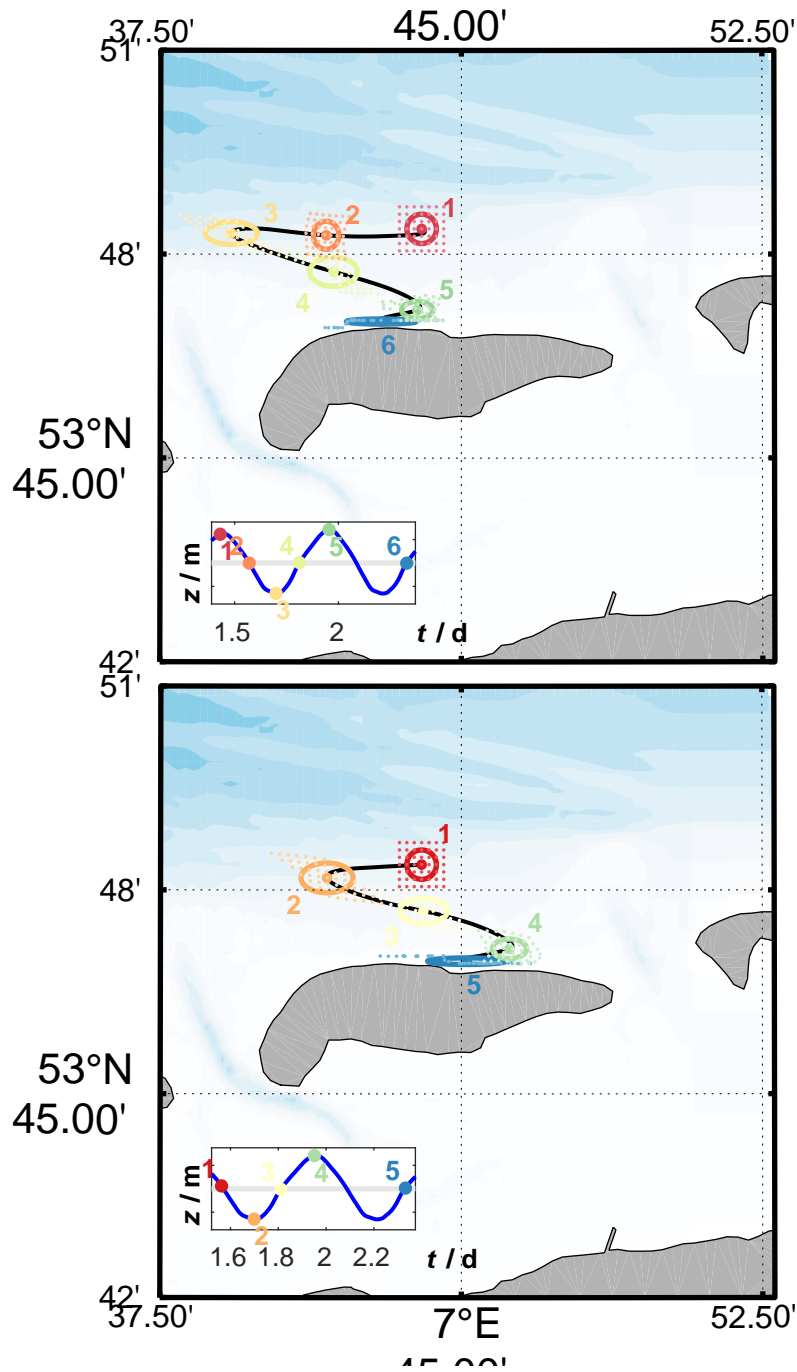
Figure 105: Trajectories of ensemble centers S for releases ③ (top panel) and ④ (bottom panel), when wind induced currents are regarded. Centers at discrete time steps and respective $ZM2$-ellipses are shown by bold dots and ellipses. Small, brighter dots are indicating individual particle positions. Color coding is illustrated in inserts, showing temporal evolution of surface elevation (here z) at the modeling site. Wind drag of $C_2 = 7 \times 10^{-3}$ was applied on particles.
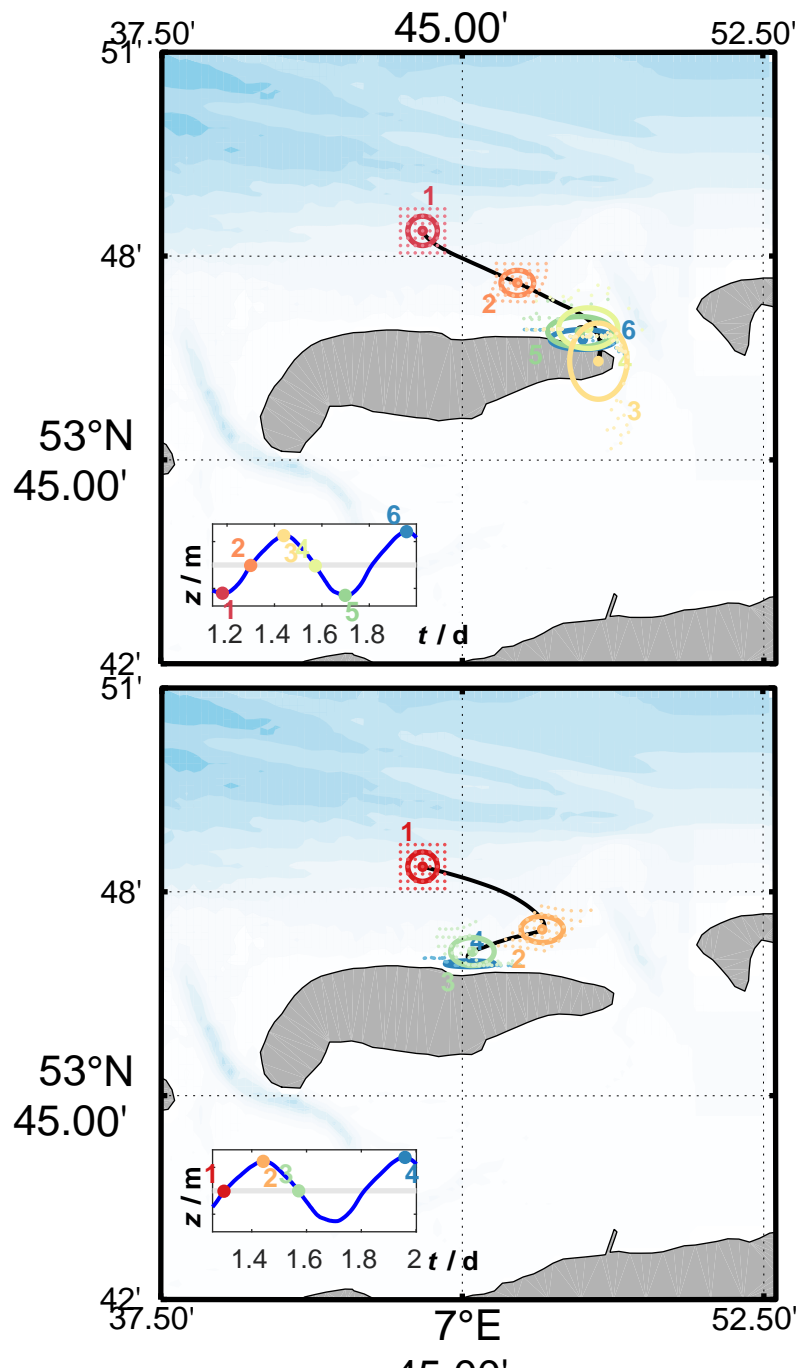
Figure 106: Trajectories of ensemble centers S for releases ① (top panel) and ② (bottom panel), when wind induced currents are regarded. Centers at discrete time steps and respective $ZM2$-ellipses are shown by bold dots and ellipses. Small, brighter dots are indicating individual particle positions. Color coding is illustrated in inserts, showing temporal evolution of surface elevation (here z) at the modeling site. Wind drag of $C_3 = 14 \times 10^{-3}$ was applied on particles.
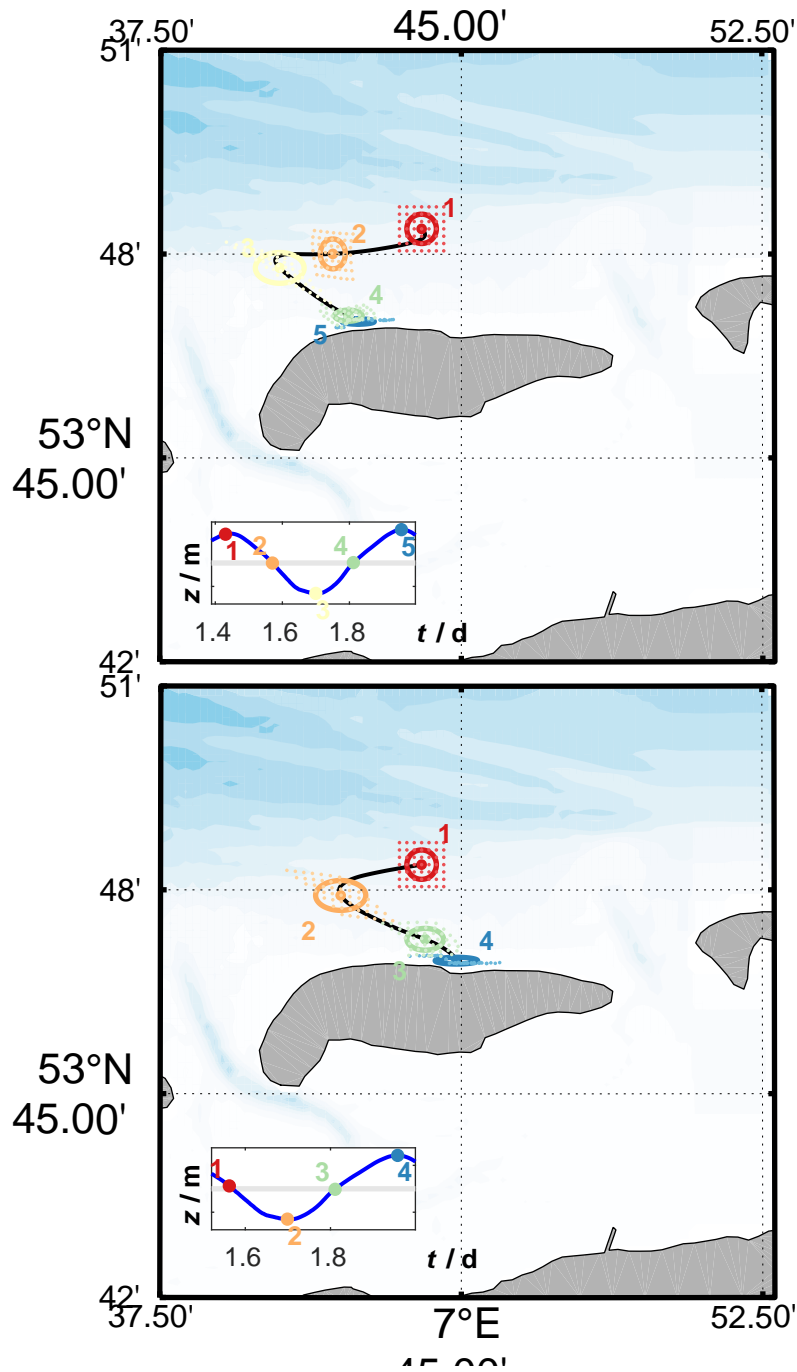
Figure 107: Trajectories of ensemble centers S for releases ③ (top panel) and ④ (bottom panel), when wind induced currents are regarded. Centers at discrete time steps and respective $ZM2$-ellipses are shown by bold dots and ellipses. Small, brighter dots are indicating individual particle positions. Color coding is illustrated in inserts, showing temporal evolution of surface elevation (here z) at the modeling site. Wind drag of $C_3 = 14 \times 10^{-3}$ was applied on particles.

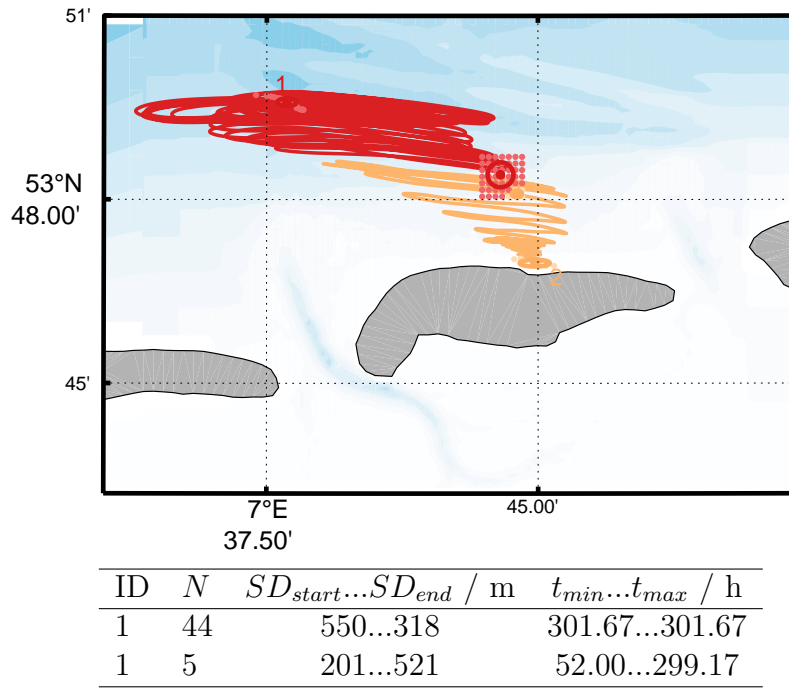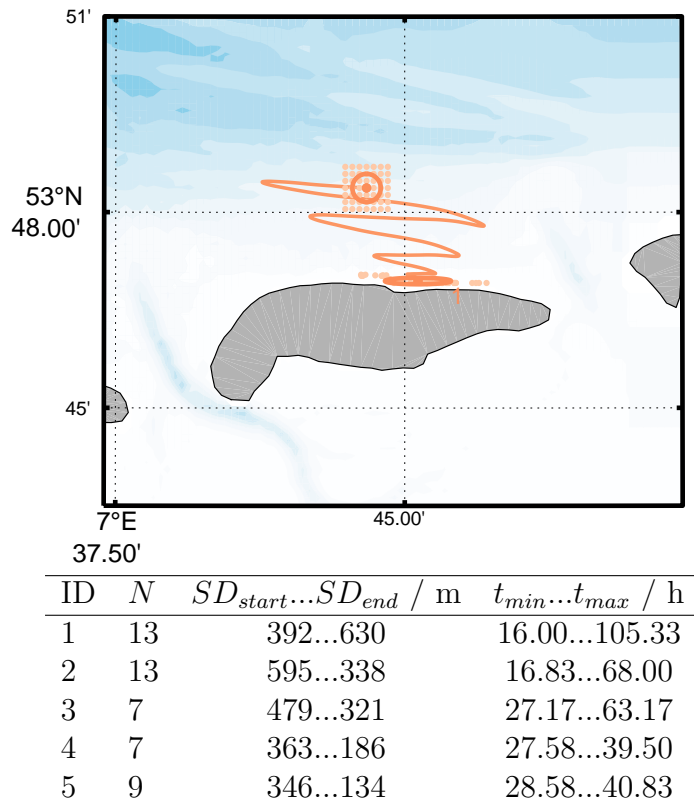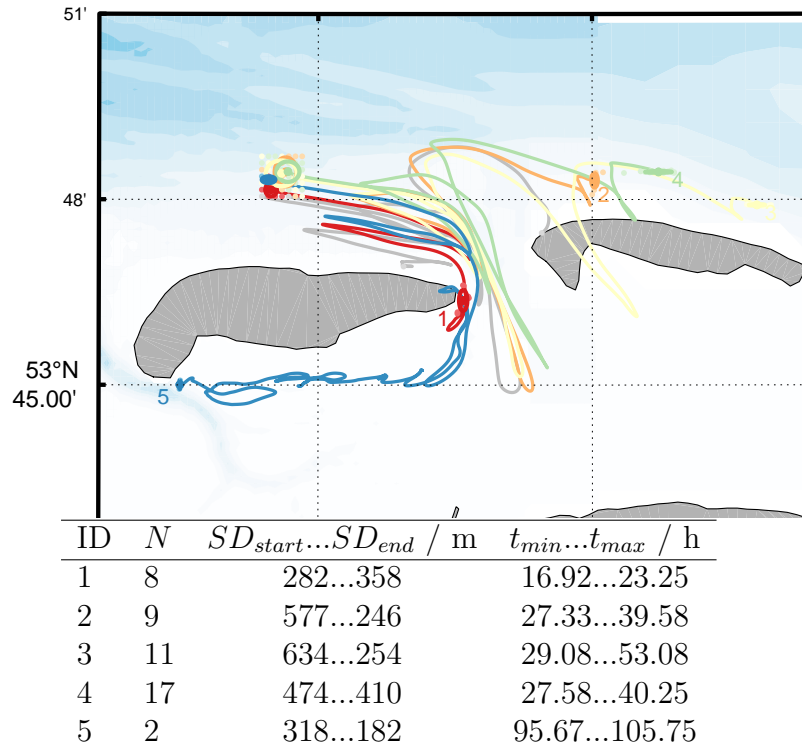| ID	N	$SD_{start}...SD_{end}$ / m	$t_{min}...t_{max}$ / h
1	30	529...1025	5.83...307.67
2	9	344...599	43.50...67.25
3	9	270...523	55.58...67.33
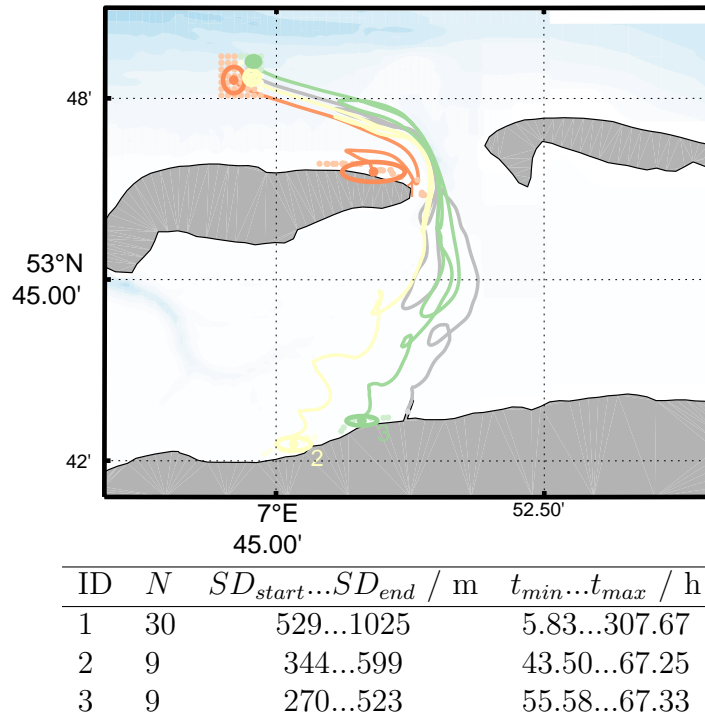
Figure 108: Terminal clusters locations for Ensemble ①. Minimal cardinal numbers were $N = 2$ and max. particle distances $r_{max} = 600\,\text{m}$. Wind drag using $C_2 = 7 \times 10^{-3}$ was regarded.

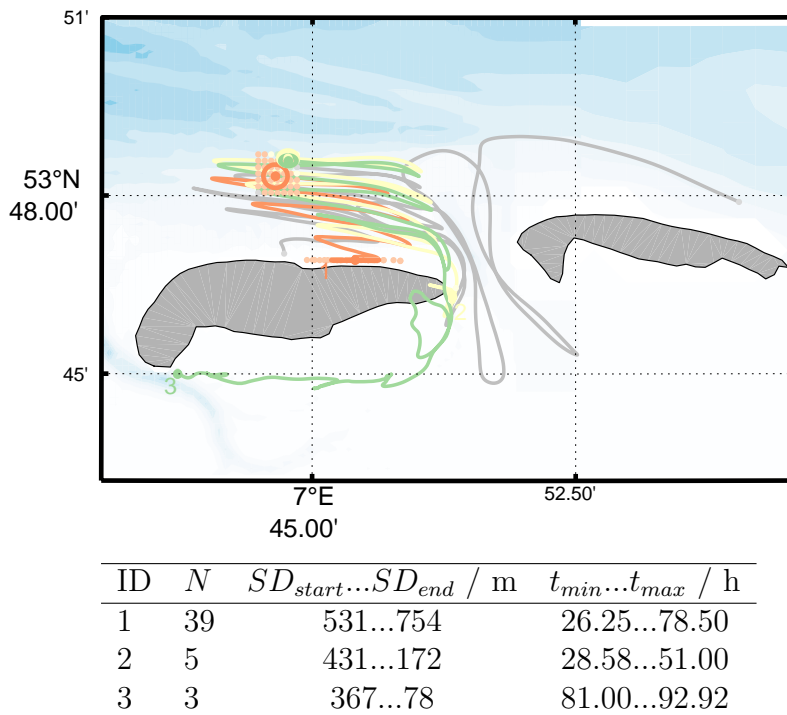| ID	N	$SD_{start}...SD_{end}$ / m	$t_{min}...t_{max}$ / h
1	49	573...1296	10.17...16.17
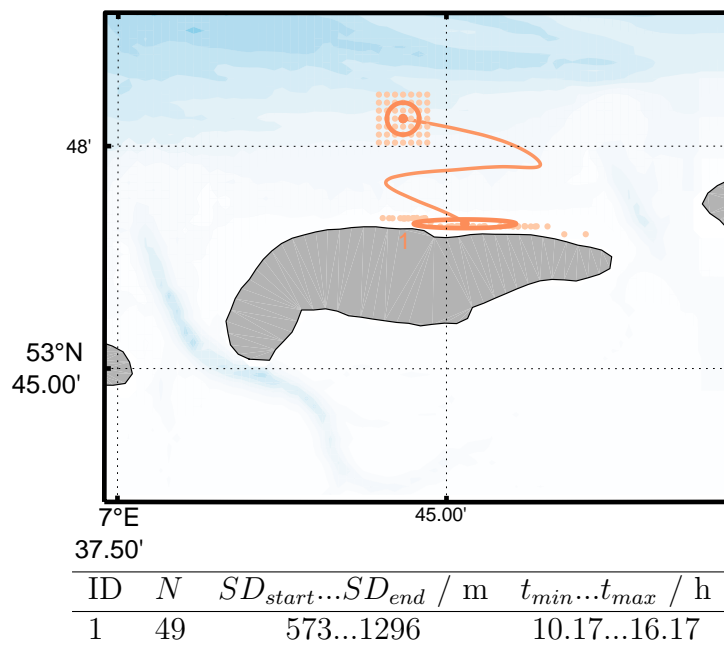
Figure 109: Terminal clusters locations for Ensemble ②. Minimal cardinal numbers were $N = 2$ and max. particle distances $r_{max} = 600\,\text{m}$. Wind drag using $C_2 = 7 \times 10^{-3}$ was regarded.

ID	N	$SD_{start}...SD_{end}$ / m	$t_{min}...t_{max}$ / h
1	49	573...962	11.83...20.75
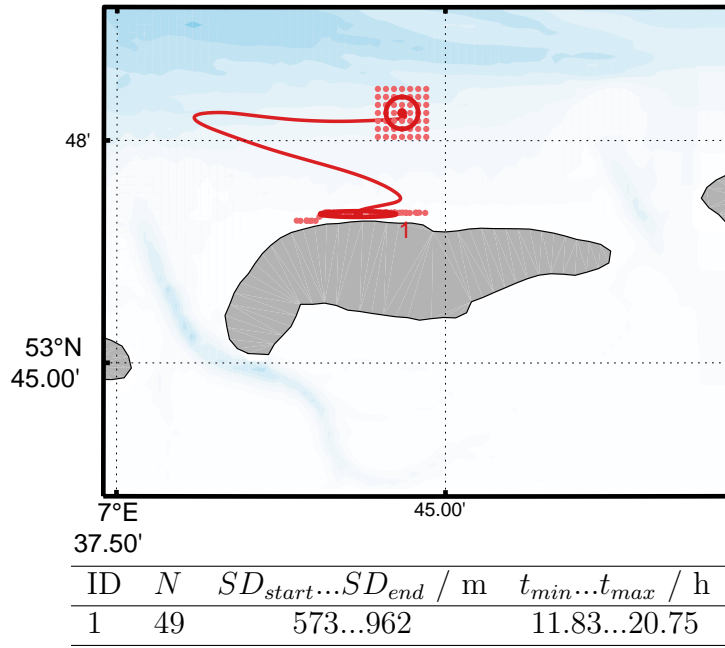
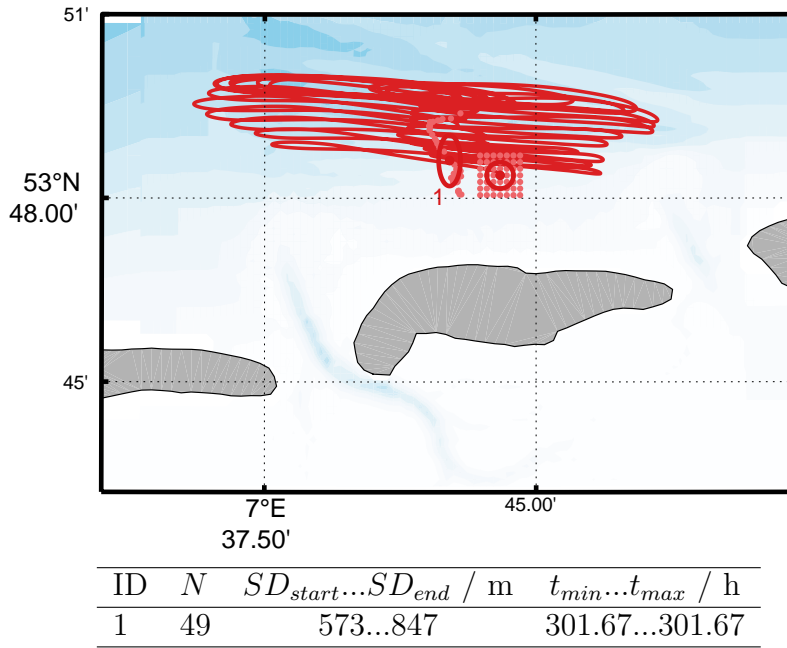Figure 110: Terminal clusters locations for Ensemble ③. Minimal cardinal numbers were $N = 2$ and max. particle distances $r_{max} = 600\,\mathrm{m}$. Wind drag using $C_2 = 7 \times 10^{-3}$ was regarded.

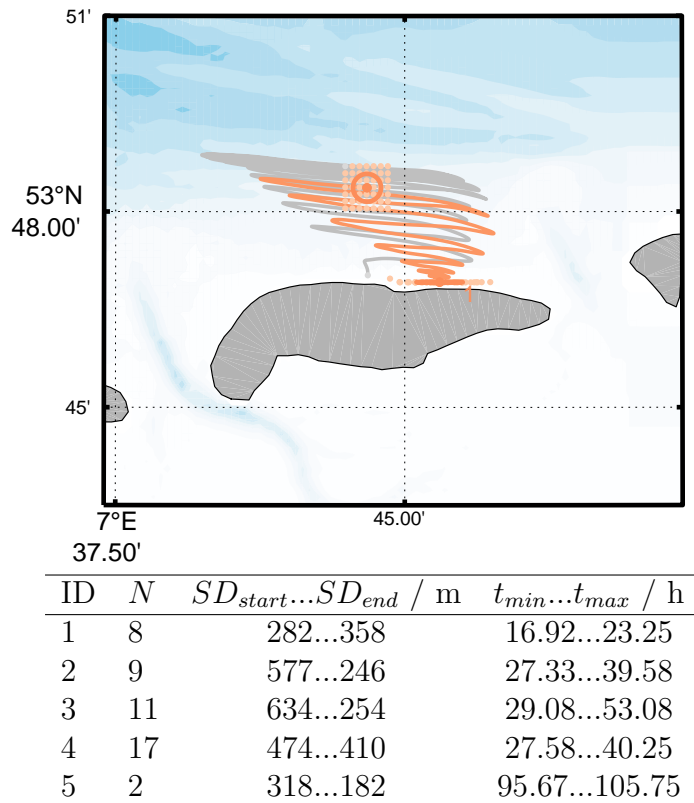| ID	N	$SD_{start}...SD_{end}$ / m	$t_{min}...t_{max}$ / h
1	49	573...1082	9.08...19.42
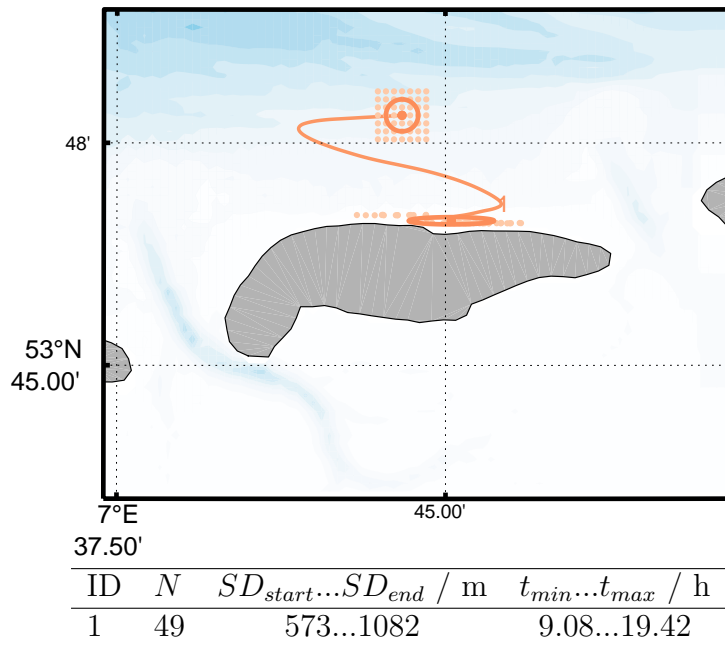
Figure 111: Terminal clusters locations for Ensemble ④. Minimal cardinal numbers were $N = 2$ and max. particle distances $r_{max} = 600\,\mathrm{m}$. Wind drag using $C_2 = 7 \times 10^{-3}$ was regarded.

ID	N	$SD_{start}...SD_{end}$ / m	$t_{min}...t_{max}$ / h
1	49	573...938	4.67...307.67
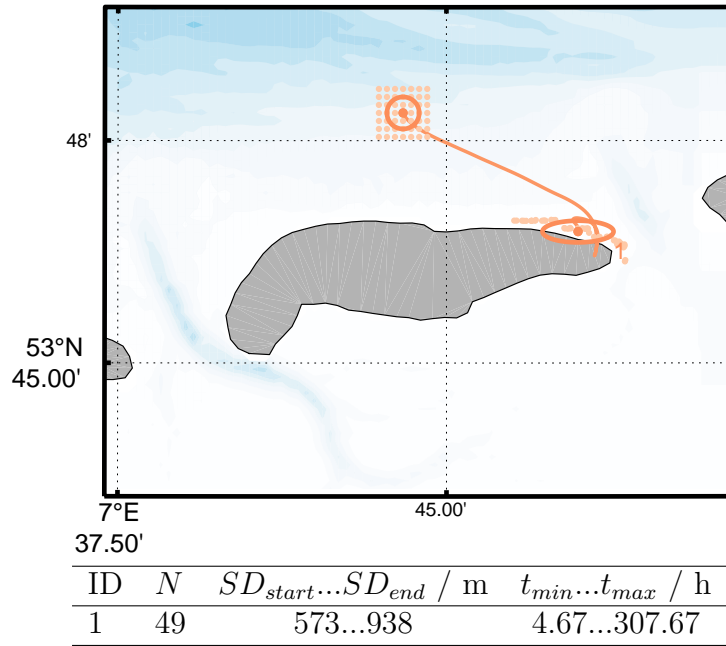
Figure 112: Terminal clusters locations for Ensemble ①. Minimal cardinal numbers were $N = 2$ and max. particle distances $r_{max} = 600$ m. Wind drag using $C_3 = 14 \times 10^{-3}$ was regarded.

ID	N	$SD_{start}...SD_{end}$ / m	$t_{min}...t_{max}$ / h
1	49	573...682	5.00...13.00
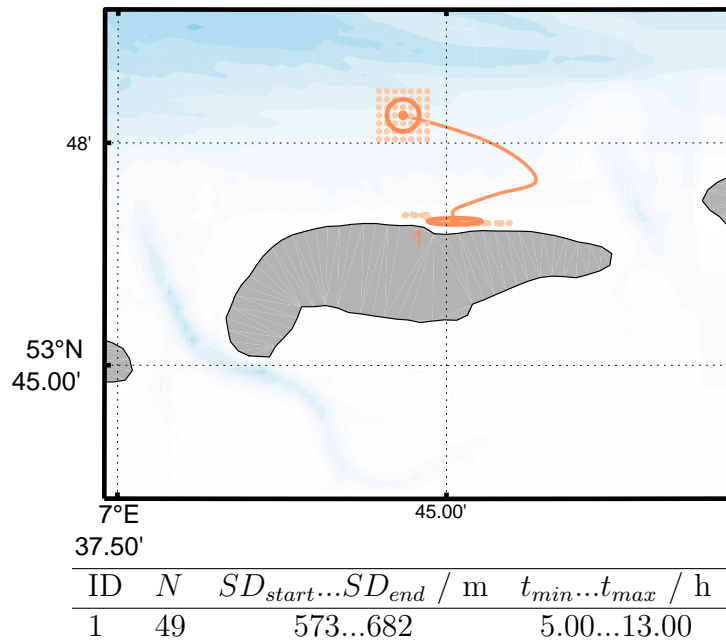
Figure 113: Terminal clusters locations for Ensemble ②. Minimal cardinal numbers were $N = 2$ and max. particle distances $r_{max} = 600$ m. Wind drag using $C_3 = 14 \times 10^{-3}$ was regarded.

ID	N	$SD_{start}...SD_{end}$ / m	$t_{min}...t_{max}$ / h
1	49	573...450	7.83...10.42
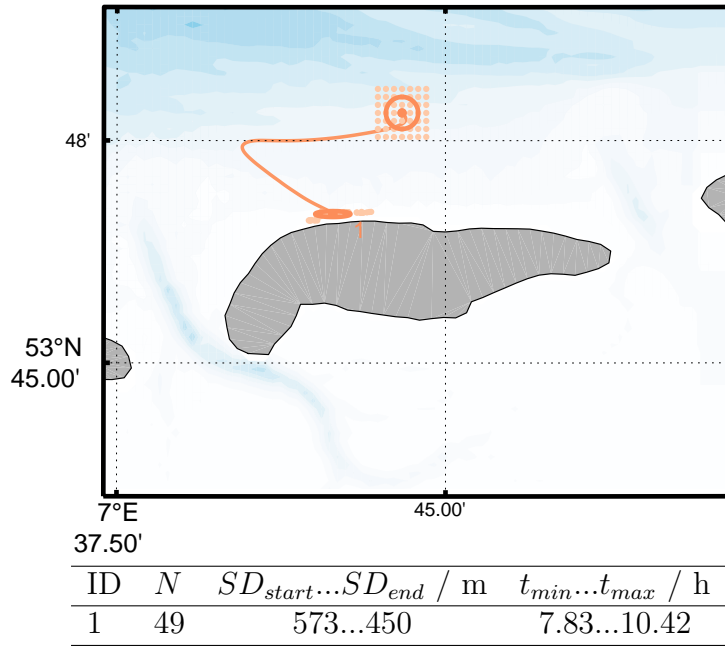
Figure 114: Terminal clusters locations for Ensemble ③. Minimal cardinal numbers were $N = 2$ and max. particle distances $r_{max} = 600$ m. Wind drag using $C_3 = 14 \times 10^{-3}$ was regarded.

ID	N	$SD_{start}...SD_{end}$ / m	$t_{min}...t_{max}$ / h
1	49	573...592	5.92...8.67
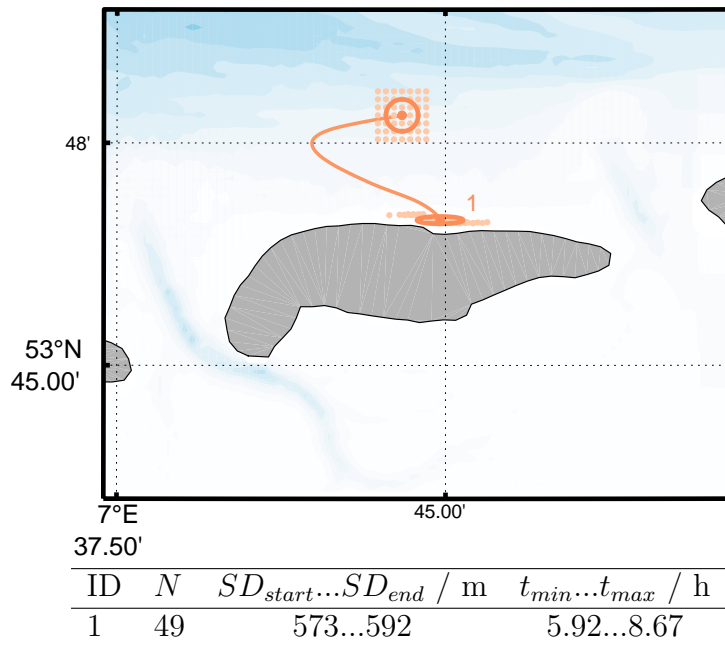
Figure 115: Terminal clusters locations for Ensemble ①. Minimal cardinal numbers were $N = 2$ and max. particle distances $r_{max} = 600$ m. Wind drag using $C_3 = 14 \times 10^{-3}$ was regarded.
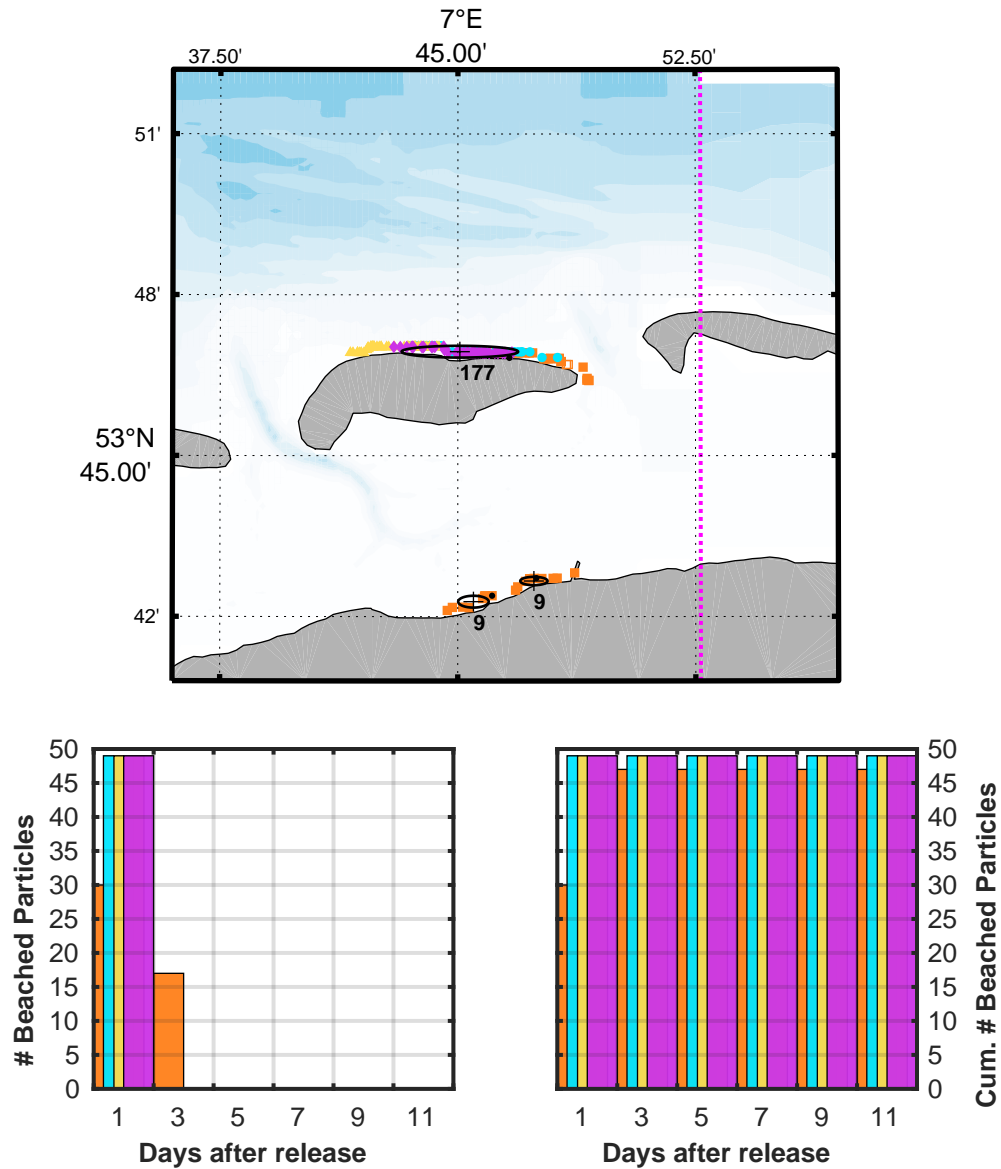
Figure 116: Same as Figure 51, but regarding wind drag using $C_2 = 7 \times 10^{-3}$: Distribution of Lagrangian floats for 4 ensembles of 49 particles after 14 days of simulation. Temporal spacing between releases is shown in Figure 33.
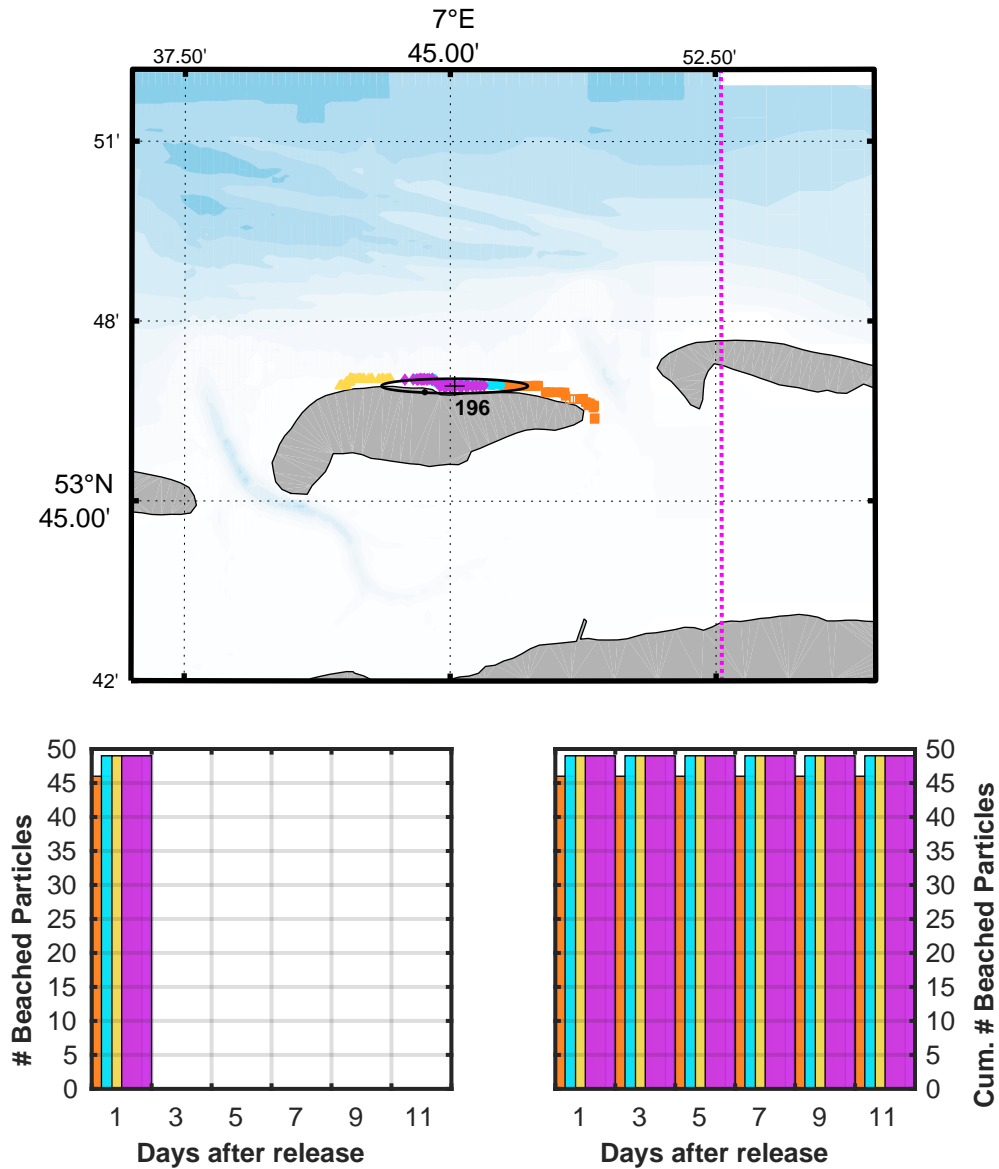
Figure 117: Same as Figure 51, but but regarding wind drag using $C_3 = 14 \times 10^{-3}$: Distribution of Lagrangian floats for 4 ensembles of 49 particles after 14 days of simulation. Temporal spacing between releases is shown in Figure 33.

E.4. Scenario C
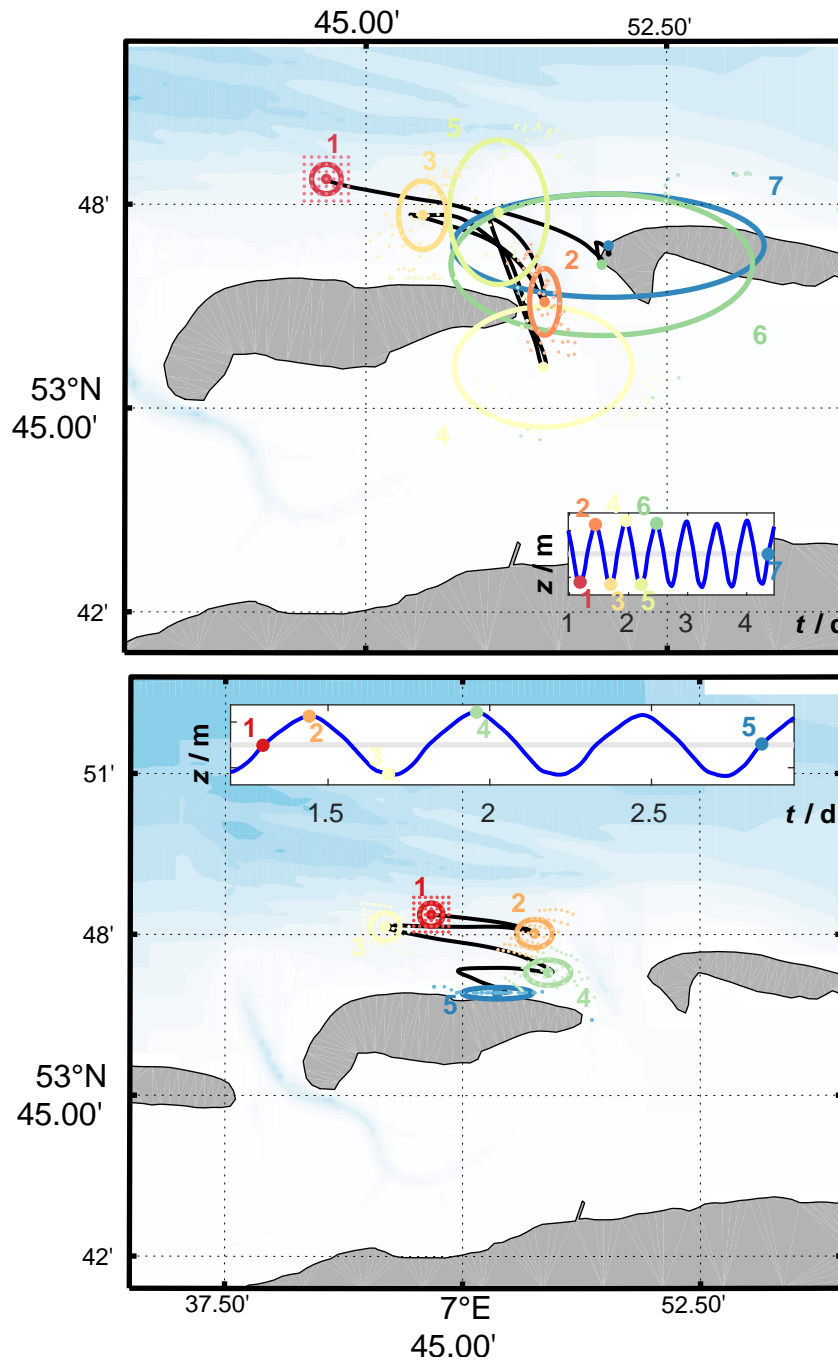
Figure 118: Ensembles ① (top panel) and ② centers S trajectories. Centers at discrete time steps and respective $ZM2$-ellipses are shown by dots and ellipses. Individual particles for corresponding time steps are shown by smaller and lighter dots. Color coding is illustrated in inserts, showing temporal evolution of surface elevation (here z) at the modeling site. Stokes Drift was regarded using $C_{St} = 0.50$.
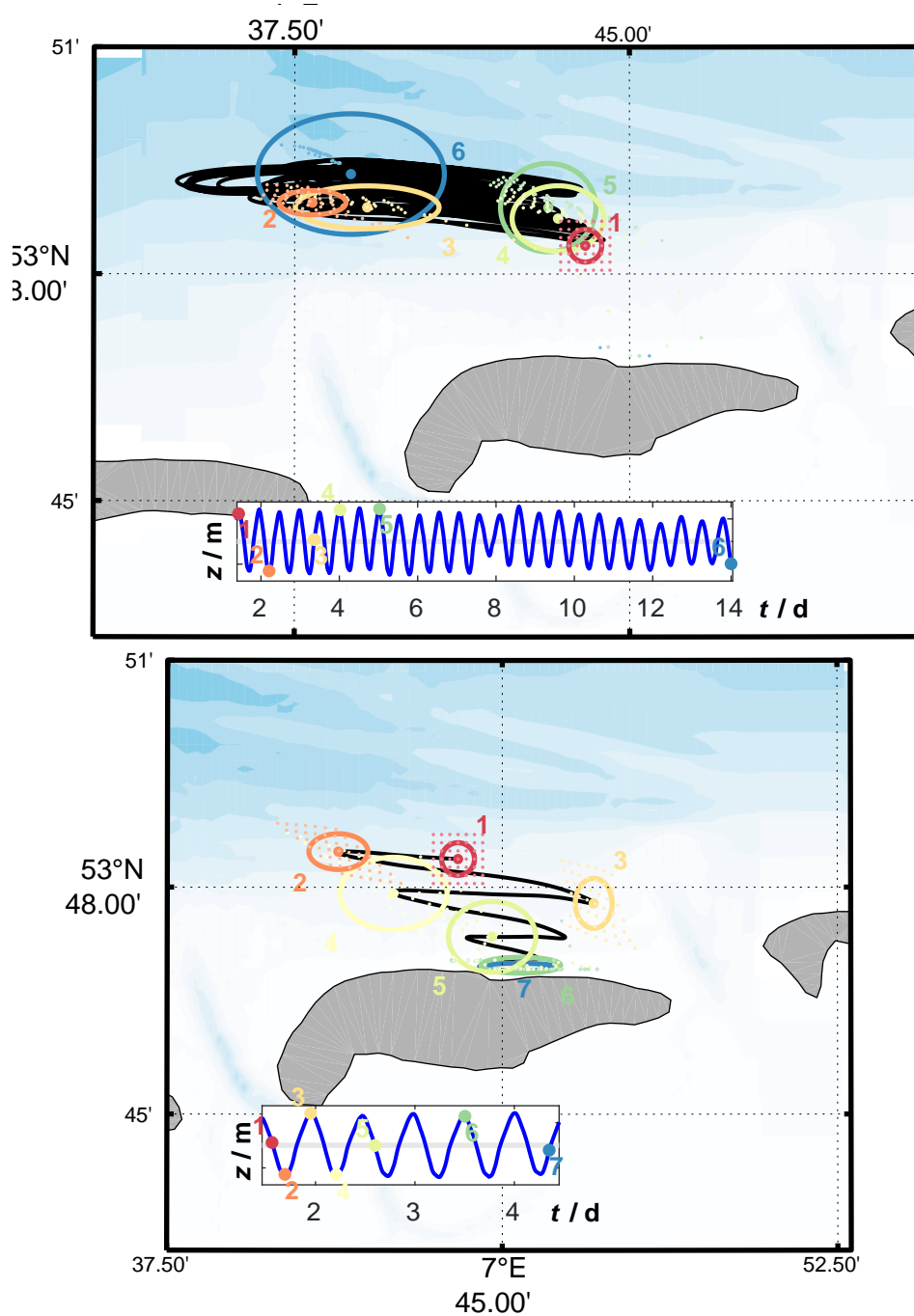
Figure 119: Ensembles ③ (top panel) and ④ centers S trajectories. Centers at discrete time steps and respective $ZM2$-ellipses are shown by dots and ellipses. Individual particles for corresponding time steps are shown by smaller and lighter dots. Color coding is illustrated in inserts, showing temporal evolution of surface elevation (here z) at the modeling site. Stokes Drift was regarded using $C_{St} = 0.50$.
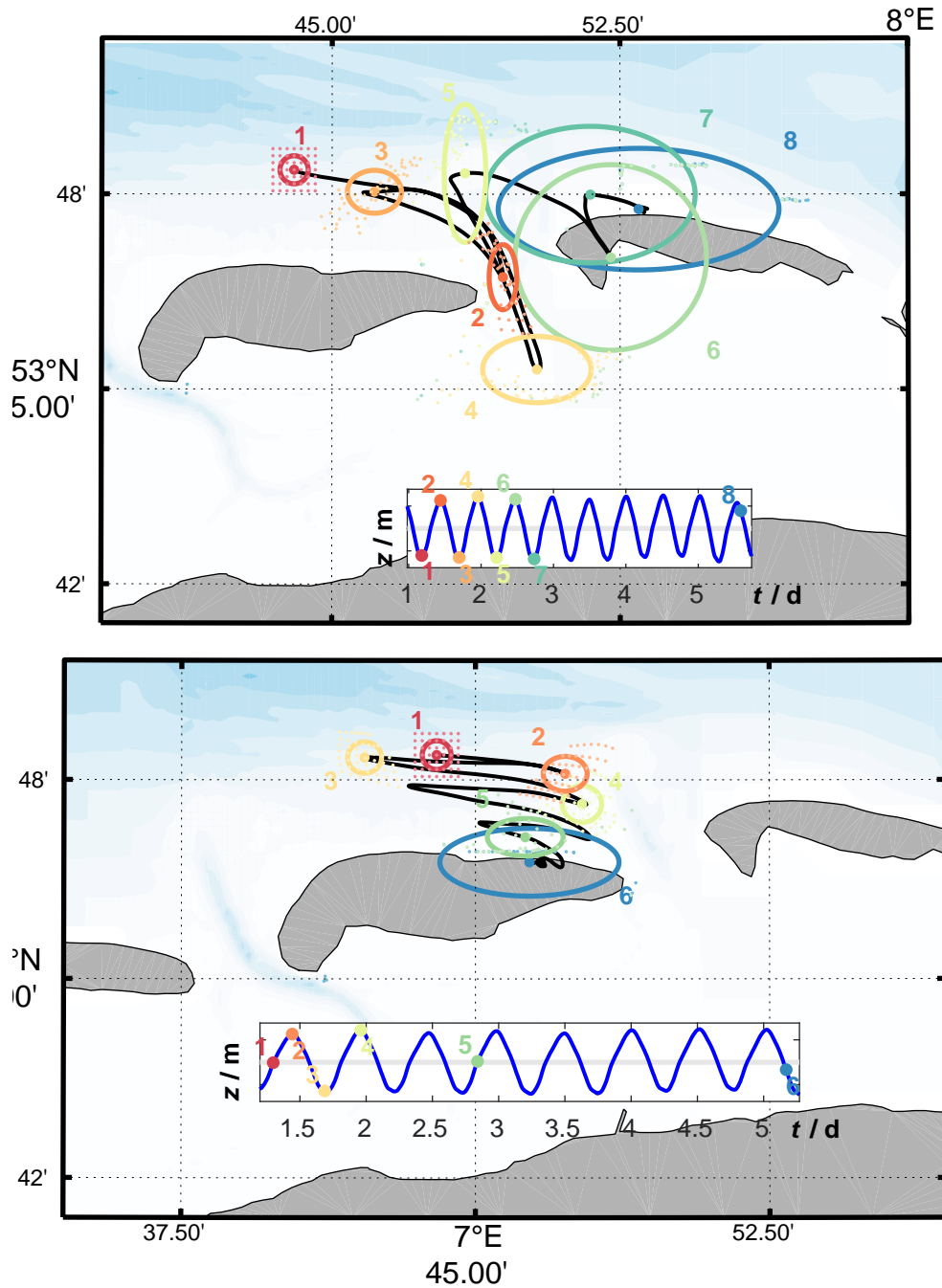
Figure 120: Ensembles ① (top panel) and ② centers S trajectories. Centers at discrete time
steps and respective $ZM2$-ellipses are shown by dots and ellipses. Individual par-
ticles for corresponding time steps are shown by smaller and lighter dots. Color
coding is illustrated in inserts, showing temporal evolution of surface elevation (here
z) at the modeling site. Stokes Drift was regarded using $C_{St} = 0.25$.
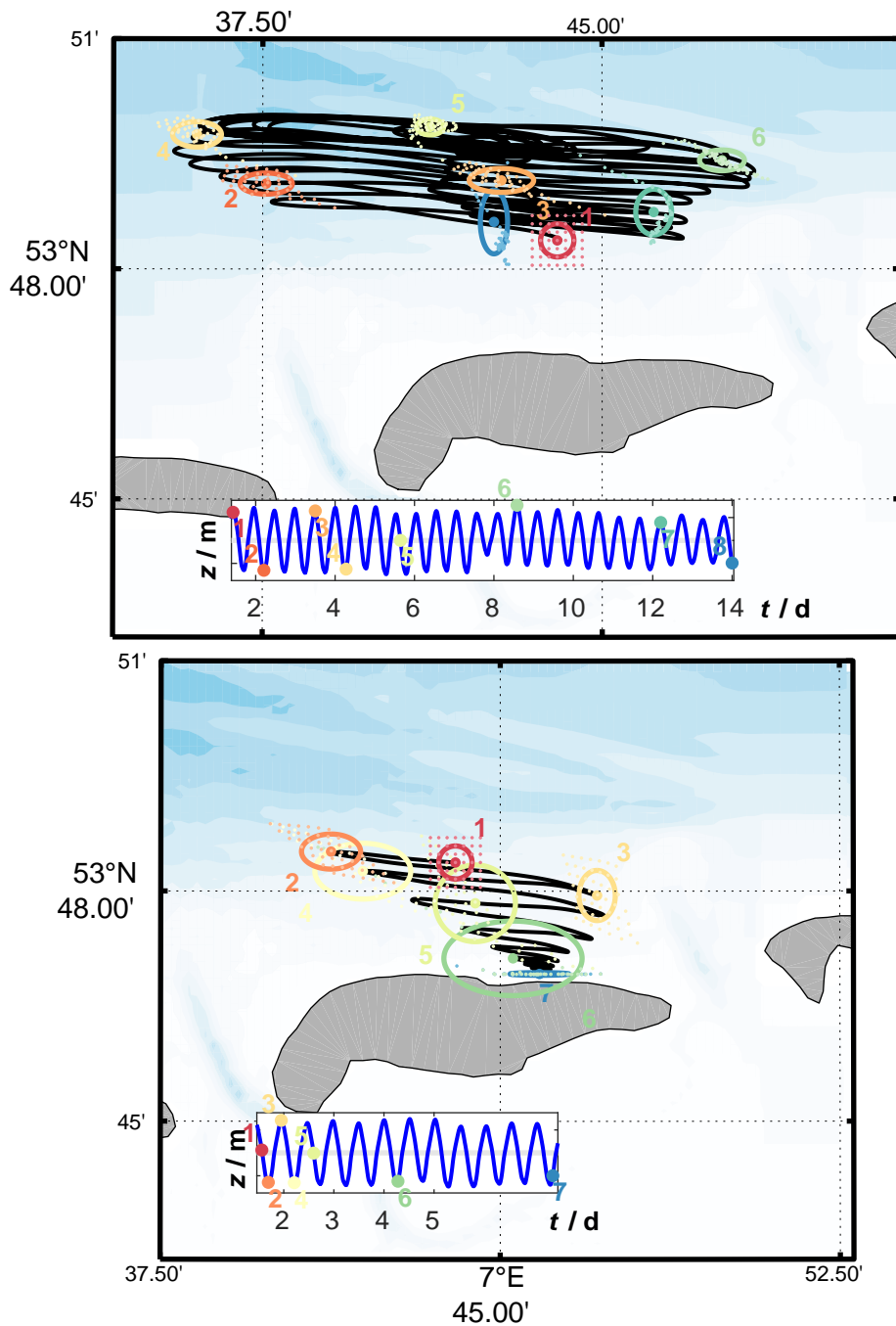
Figure 121: Ensembles ③ (top panel) and ④ centers S trajectories. Centers at discrete time steps and respective $ZM2$-ellipses are shown by dots and ellipses. Individual particles for corresponding time steps are shown by smaller and lighter dots. Color coding is illustrated in inserts, showing temporal evolution of surface elevation (here z) at the modeling site. Stokes Drift was regarded using $C_{St} = 0.25$.

ID	N	$SD_{start}...SD_{end}$ / m	$t_{min}...t_{max}$ / h
1	13	392...630	16.00...105.33
2	13	595...338	16.83...68.00
3	7	479...321	27.17...63.17
4	7	363...186	27.58...39.50
5	9	346...134	28.58...40.83
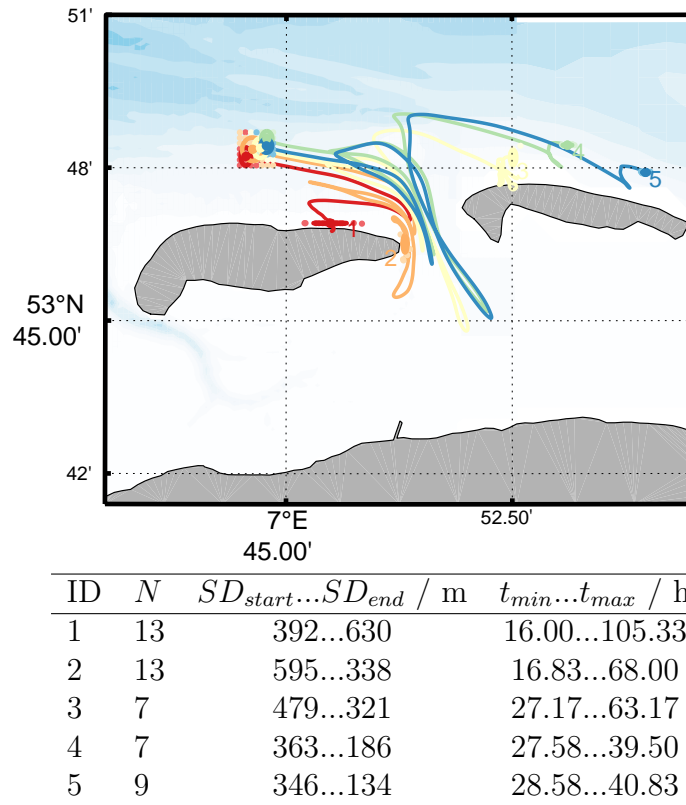
Figure 122: Terminal clusters locations for Ensemble ①. Minimal cardinal numbers were $N = 2$ and max. particle distances $r_{max} = 600$ m. Stokes Drift using $C_{St} = 0.50$ was regarded.

ID	N	$SD_{start}...SD_{end}$ / m	$t_{min}...t_{max}$ / h
1	47	561...1071	20.92...41.08
1	2	142...9	27.17...27.67
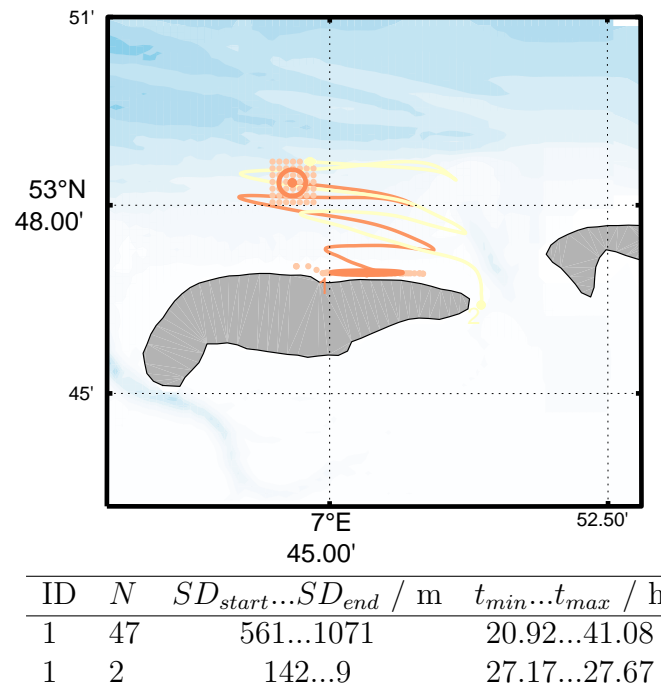
Figure 123: Terminal clusters locations for Ensemble ②. Minimal cardinal numbers were $N = 2$ and max. particle distances $r_{max} = 600$ m. Stokes Drift using $C_{St} = 0.50$ was regarded.

ID	N	$SD_{start}...SD_{end}$ / m	$t_{min}...t_{max}$ / h
1	44	550...318	301.67...301.67
1	5	201...521	52.00...299.17

Figure 124: Terminal clusters locations for Ensemble ③. Minimal cardinal numbers were $N = 2$ and max. particle distances $r_{max} = 600$ m. Stokes Drift using $C_{St} = 0.50$ was regarded.

ID	N	$SD_{start}...SD_{end}$ / m	$t_{min}...t_{max}$ / h
1	13	392...630	16.00...105.33
2	13	595...338	16.83...68.00
3	7	479...321	27.17...63.17
4	7	363...186	27.58...39.50
5	9	346...134	28.58...40.83

Figure 125: Terminal clusters locations for Ensemble ④. Minimal cardinal numbers were $N = 2$ and max. particle distances $r_{max} = 600$ m. Stokes Drift using $C_{St} = 0.50$ was regarded.

ID	N	$SD_{start}...SD_{end}$ / m	$t_{min}...t_{max}$ / h
1	8	282...358	16.92...23.25
2	9	577...246	27.33...39.58
3	11	634...254	29.08...53.08
4	17	474...410	27.58...40.25
5	2	318...182	95.67...105.75

Figure 126: Terminal clusters locations for Ensemble ①. Minimal cardinal numbers were $N = 2$ and max. particle distances $r_{max} = 600$ m. Stokes Drift using $C_{St} = 0.25$ was regarded.

ID	N	$SD_{start}...SD_{end}$ / m	$t_{min}...t_{max}$ / h
1	39	531...754	26.25...78.50
2	5	431...172	28.58...51.00
3	3	367...78	81.00...92.92

Figure 127: Terminal clusters locations for Ensemble ②. Minimal cardinal numbers were $N = 2$ and max. particle distances $r_{max} = 600$ m. Stokes Drift using $C_{St} = 0.25$ was regarded.

ID	N	$SD_{start}...SD_{end}$ / m	$t_{min}...t_{max}$ / h
1	49	573...847	301.67...301.67

Figure 128: Terminal clusters locations for Ensemble ③. Minimal cardinal numbers were $N = 2$ and max. particle distances $r_{max} = 600\,\text{m}$. Stokes Drift using $C_{St} = 0.25$ was regarded.

ID	N	$SD_{start}...SD_{end}$ / m	$t_{min}...t_{max}$ / h
1	8	282...358	16.92...23.25
2	9	577...246	27.33...39.58
3	11	634...254	29.08...53.08
4	17	474...410	27.58...40.25
5	2	318...182	95.67...105.75

Figure 129: Terminal clusters locations for Ensemble ④. Minimal cardinal numbers were $N = 2$ and max. particle distances $r_{max} = 600\,\text{m}$. Stokes Drift using $C_{St} = 0.25$ was regarded.
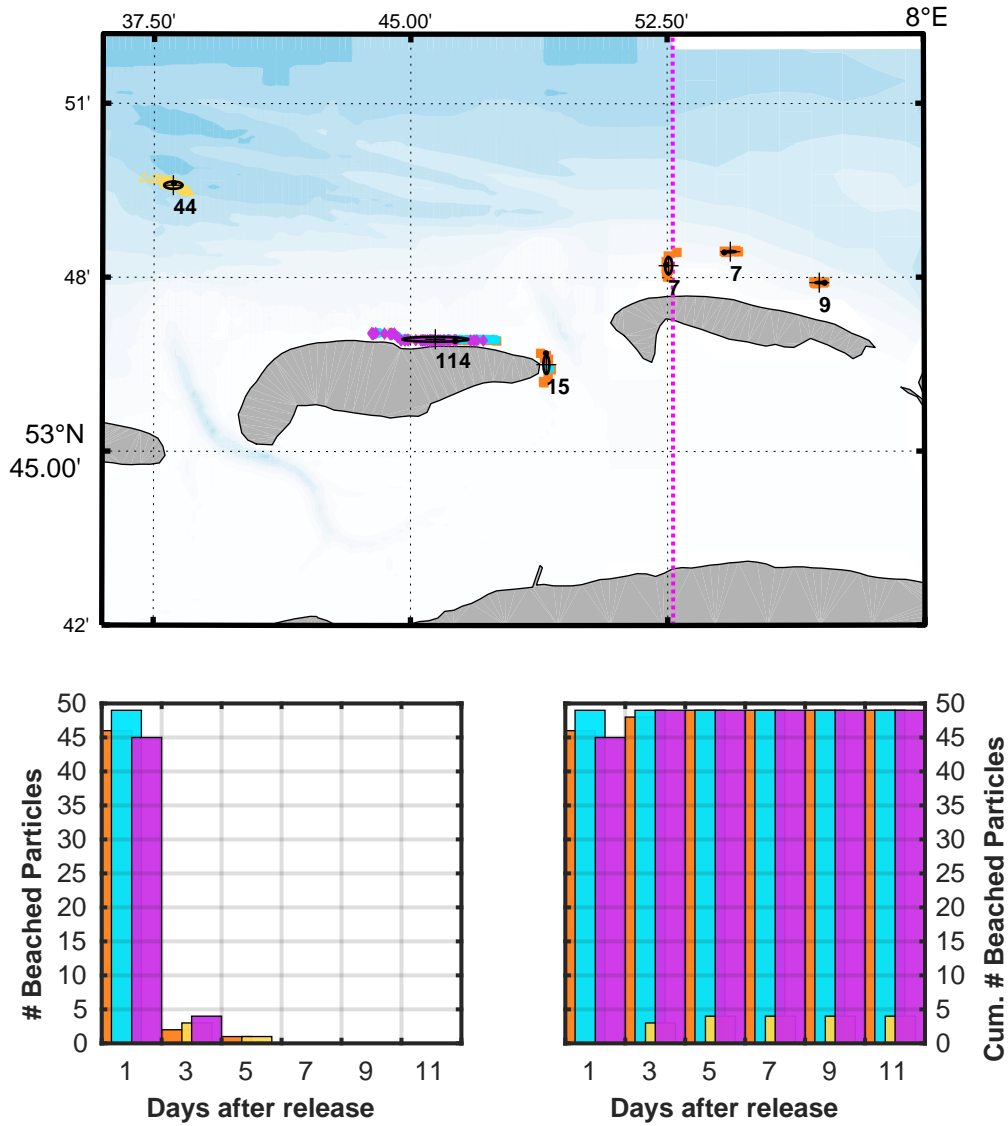
Figure 130: Terminal locations of ensembles, when Stokes Drift is regarded using $C_{St} = 0.50$: Ensembles ① orange squares, ② cyan circles, ③ yellow triangles and ④ magenta diamonds (cf. Figure 33). Histograms depict temporal distributions of beaching events (left) and respective cumulated frequencies (right). Binning sizes were set to 2 days, values are referenced to ensembles releases.
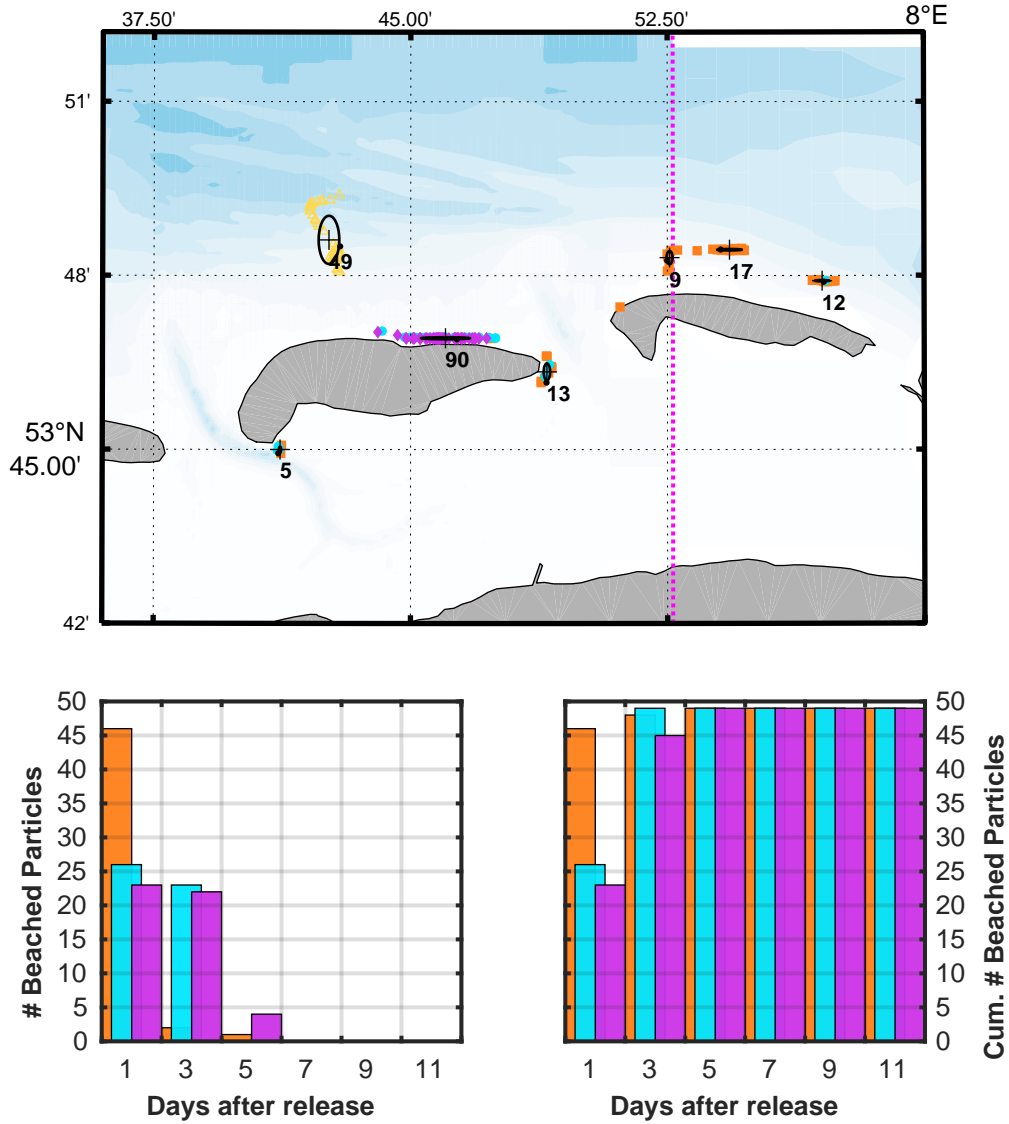
Figure 131: Terminal locations of ensembles, when Stokes Drift is regarded using $C_{St} = 0.25$: Ensembles ① orange squares, ② cyan circles, ③ yellow triangles and ④ magenta diamonds (cf. Figure 33). Histograms depict temporal distributions of beaching events (left) and respective cumulated frequencies (right). Binning sizes were set to 2 days, values are referenced to ensembles releases.

F. BLEX

F.1. Phase Diagrams
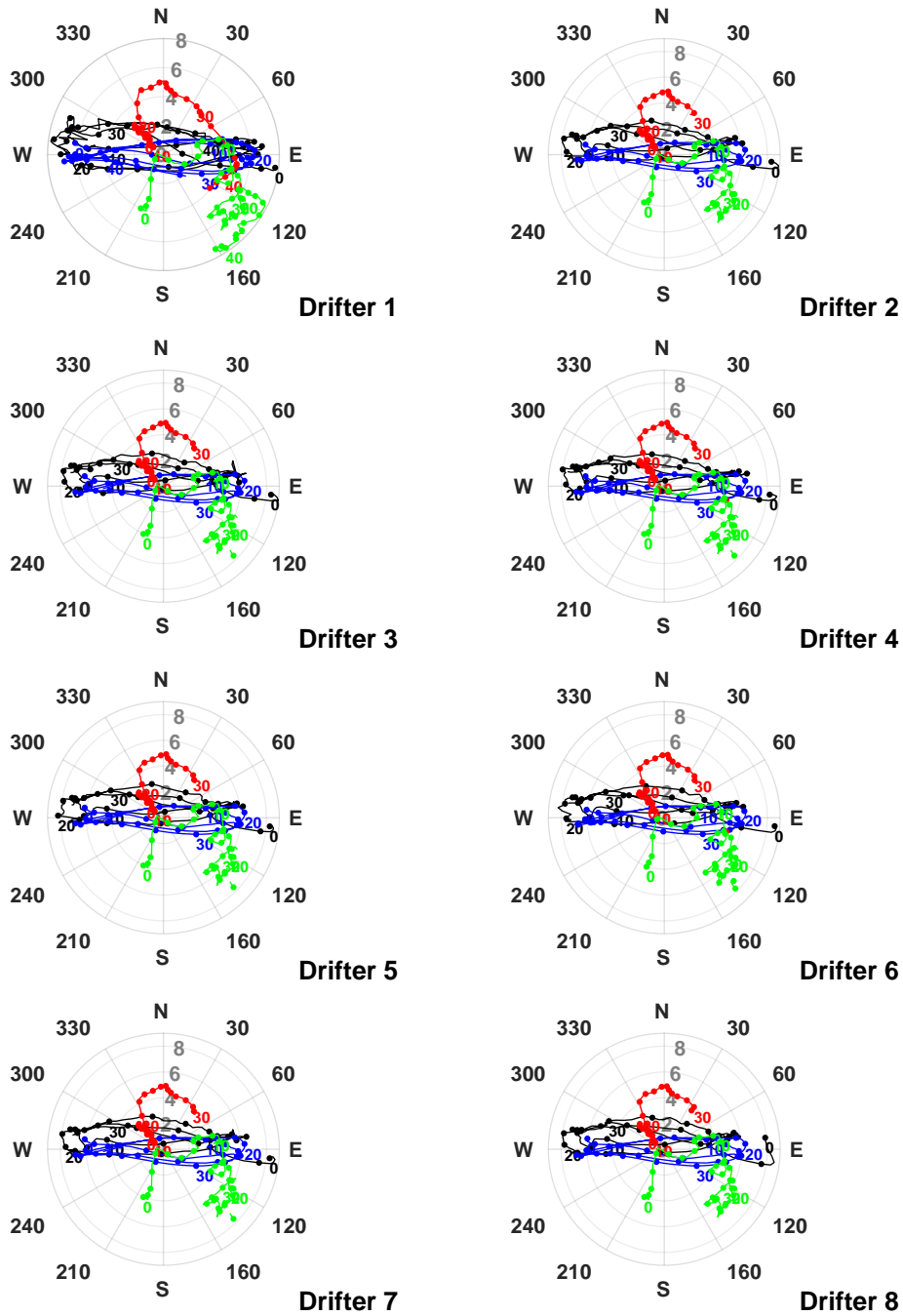
Figure 132: Phase diagrams for individual GPS-drifters of Ensemble ①. Currents (blue, in dm s^{-1}), Stokes Drift (red, in cm s^{-1}) and wind velocities (green, in m s^{-1}) are depicted in nautical convention, drifter velocities (black, in dm s^{-1}) are pointing in traveling direction. Dots denote 10 h-intervals.
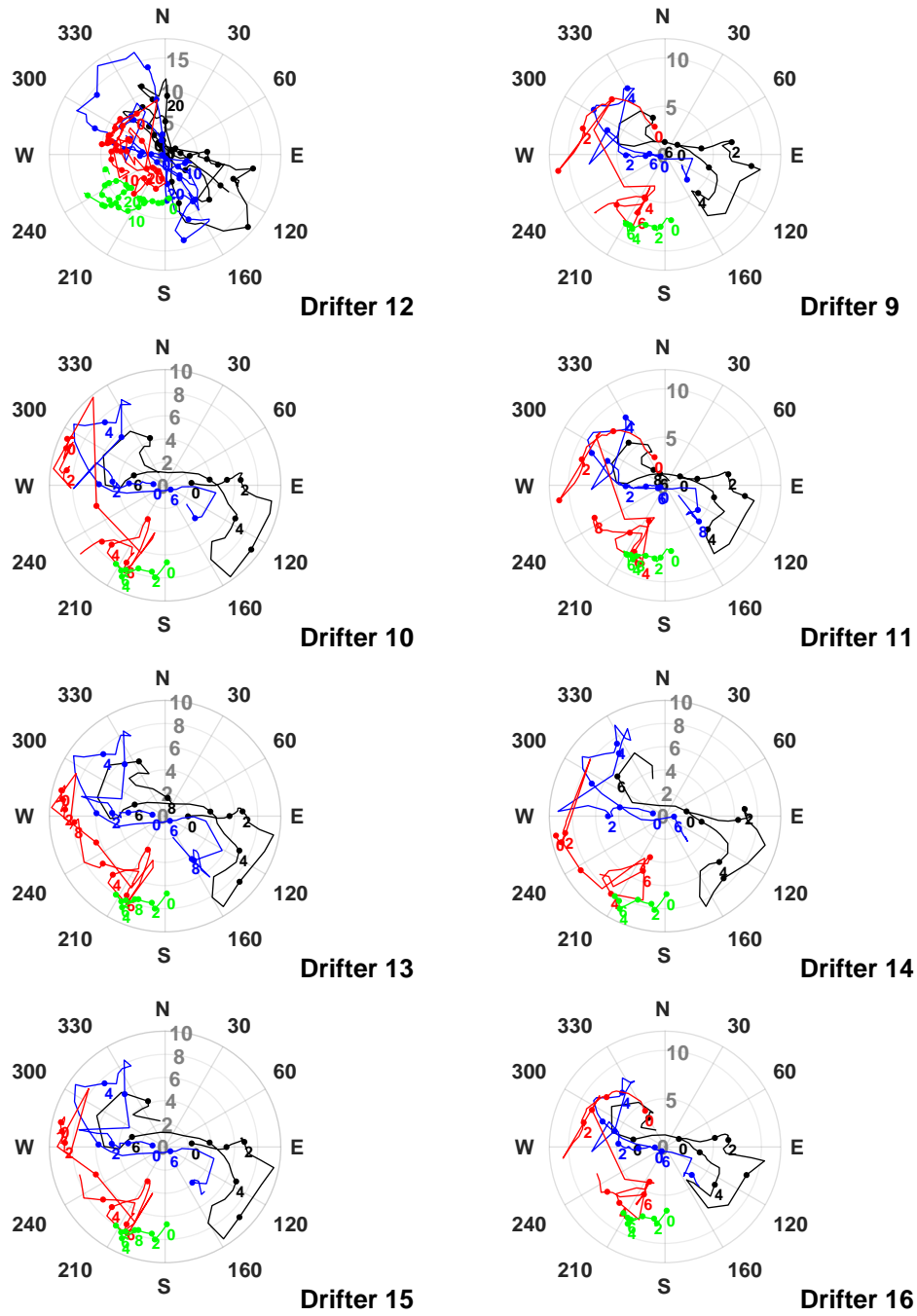
Figure 133: Phase diagrams for individual GPS-drifters of Ensemble ②. Currents (blue, in $\mathrm{dm\,s^{-1}}$), Stokes Drift (red, in $\mathrm{cm\,s^{-1}}$) and wind velocities (green, in $\mathrm{m\,s^{-1}}$) are depicted in nautical convention, drifter velocities (black, in $\mathrm{dm\,s^{-1}}$) are pointing in traveling direction. Dots denote 10 h-intervals.

F.2. Drag Parameters, Regarding Error Terms
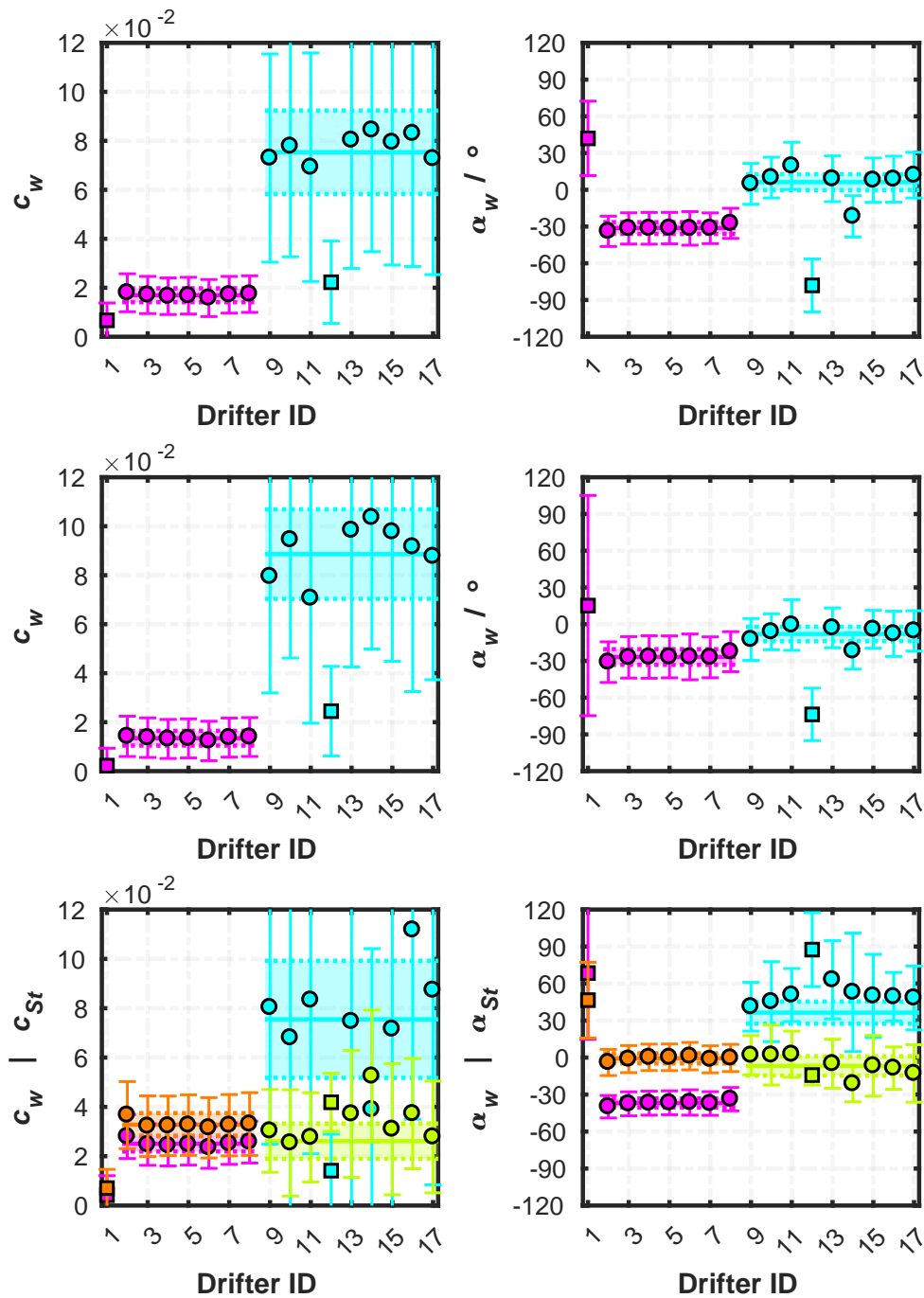
Figure 134: Estimated values of drag coefficients C_i and deflection angles α_i, using equation (57). Squares indicate Type A, circles indicate Type B drifters. All parameters were calculated by retaining constant error terms in equation (57), details on each model are given in subsection 7.2. Note the scaling of drag values in the bottom line: $\times 10^{-2}$ for wind drag C_w but not for Stokes drag C_{St}.

Table 11: Estimated drag coefficients, if constant error terms are regarded.

ID	$\alpha_w/°$	$C_w \times 10^{-2}$	α_{St}	$C_{St}/°$	$u_{err}/\mathrm{cm\,s^{-1}}$	$v_{err}/\mathrm{cm\,s^{-1}}$
Model a						
1	42 ± 30	0.67 ± 0.71	0	1.00	-5.03 ± 1.98	7.41 ± 1.98
2-8	-31 ± 5	1.69 ± 0.28	0	1.00	-4.31 ± 0.68	4.25 ± 0.68
12	-78 ± 22	2.23 ± 1.68	0	1.00	-13.16 ± 8.05	16.40 ± 8.05
9-17	6 ± 6	7.53 ± 1.70	0	1.00	11.59 ± 6.74	63.48 ± 6.74
Model b						
1	15 ± 90	0.23 ± 0.71	$-$	$-$	-3.42 ± 1.98	6.47 ± 1.98
2-8	-27 ± 6	1.35 ± 0.30	$-$	$-$	-3.88 ± 0.72	3.42 ± 0.72
12	-74 ± 21	2.45 ± 1.83	$-$	$-$	-9.98 ± 8.77	15.82 ± 8.77
9-17	-8 ± 6	8.86 ± 1.83	$-$	$-$	35.18 ± 7.23	69.70 ± 7.23
Model c						
1	68 ± 54	0.42 ± 0.79	47 ± 31	0.71 ± 0.76	-4.96 ± 2.08	6.10 ± 2.08
2-8	-37 ± 4	2.51 ± 0.32	-1 ± 4	3.28 ± 0.47	-5.26 ± 0.67	6.17 ± 0.67
12	88 ± 30	1.41 ± 1.48	-14 ± 8	4.19 ± 1.18	-22.30 ± 7.15	21.46 ± 7.15
9-17	36 ± 9	7.55 ± 2.37	-7 ± 8	2.61 ± 0.72	-27.88 ± 10.84	60.86 ± 10.84

F.3. Reconstruction of Velocities
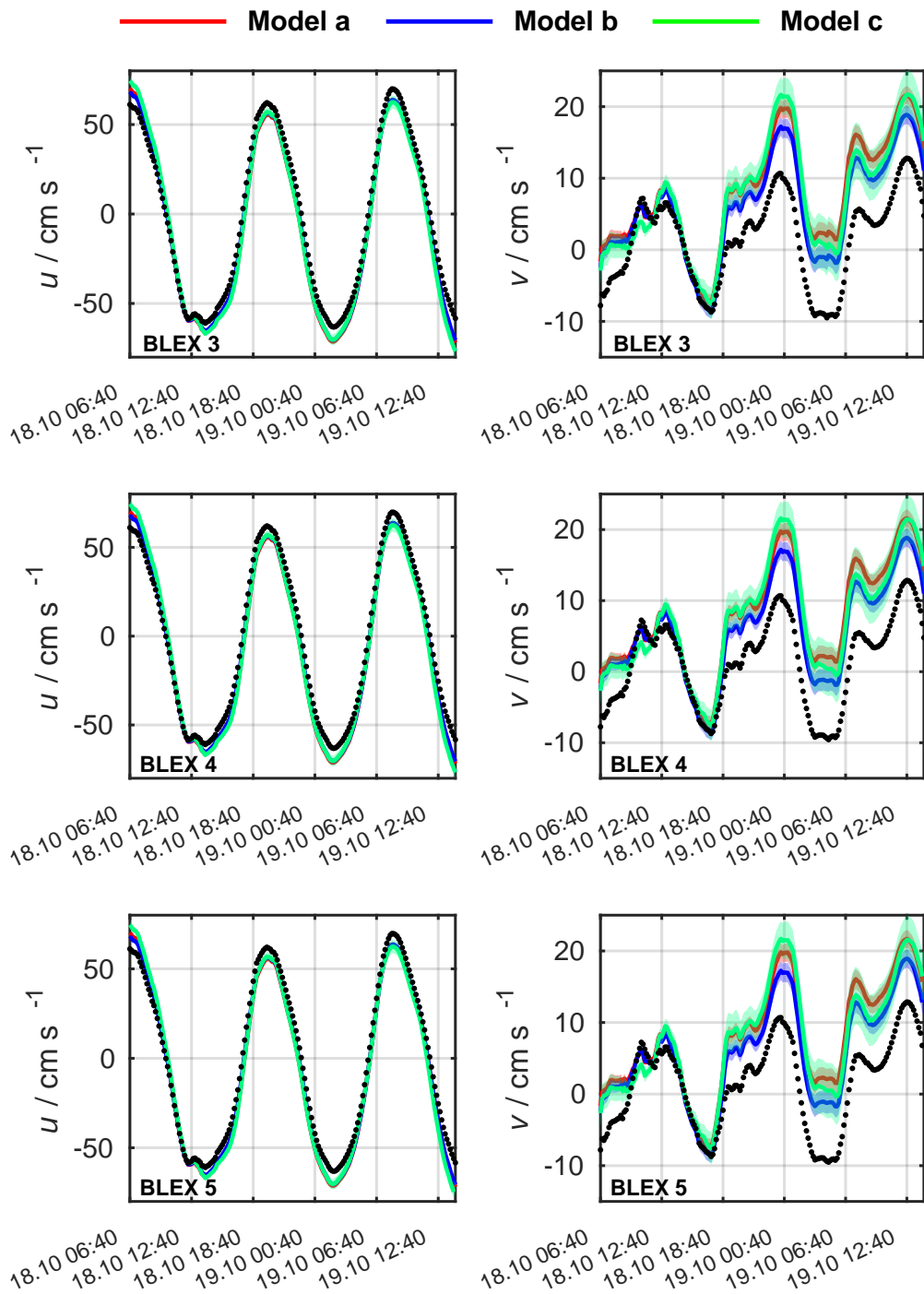
Figure 135: Reconstructed drifter velocities for Type B drifters of ensemble ① if error terms are neglected. Details are given in subsection 7.2.
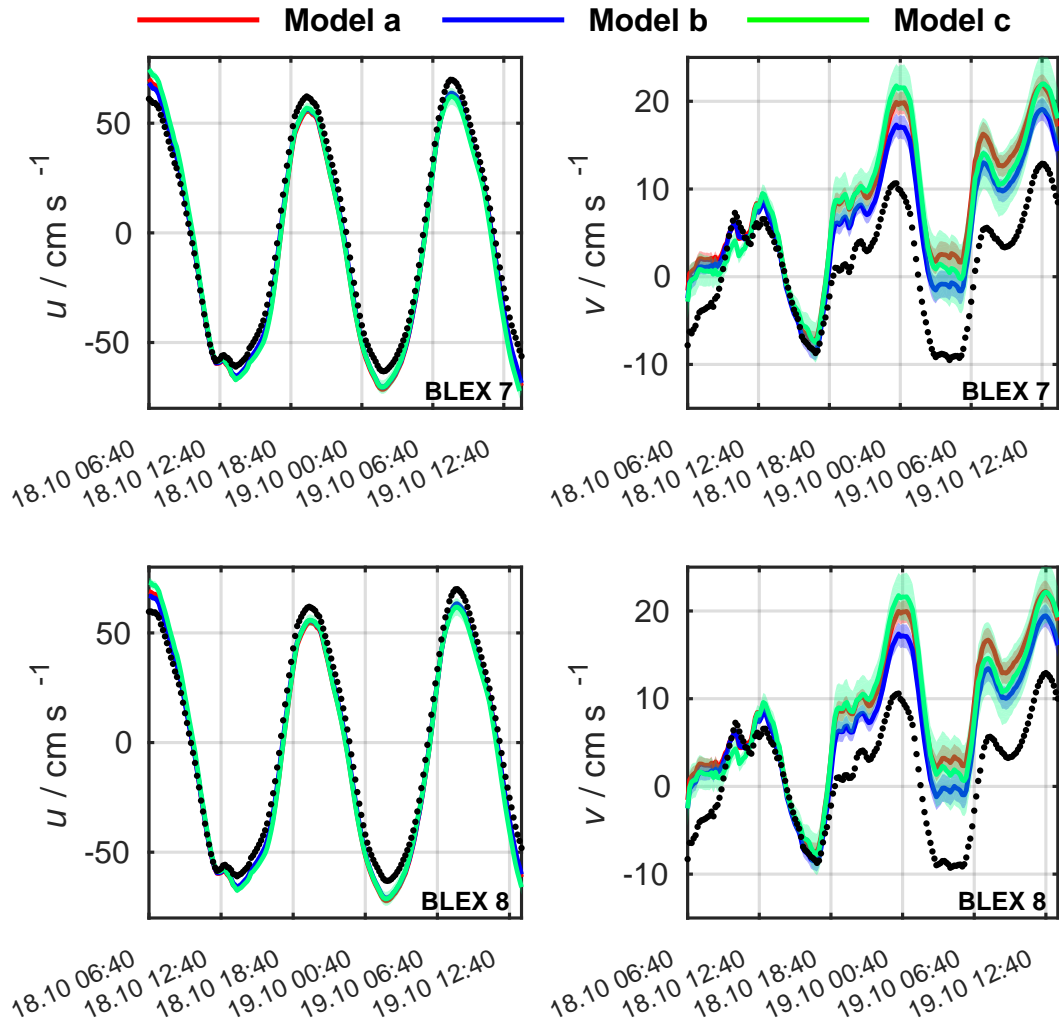
Figure 136: Reconstructed drifter velocities for Type B drifters of ensemble ① if error terms are neglected. Details are given in subsection 7.2.
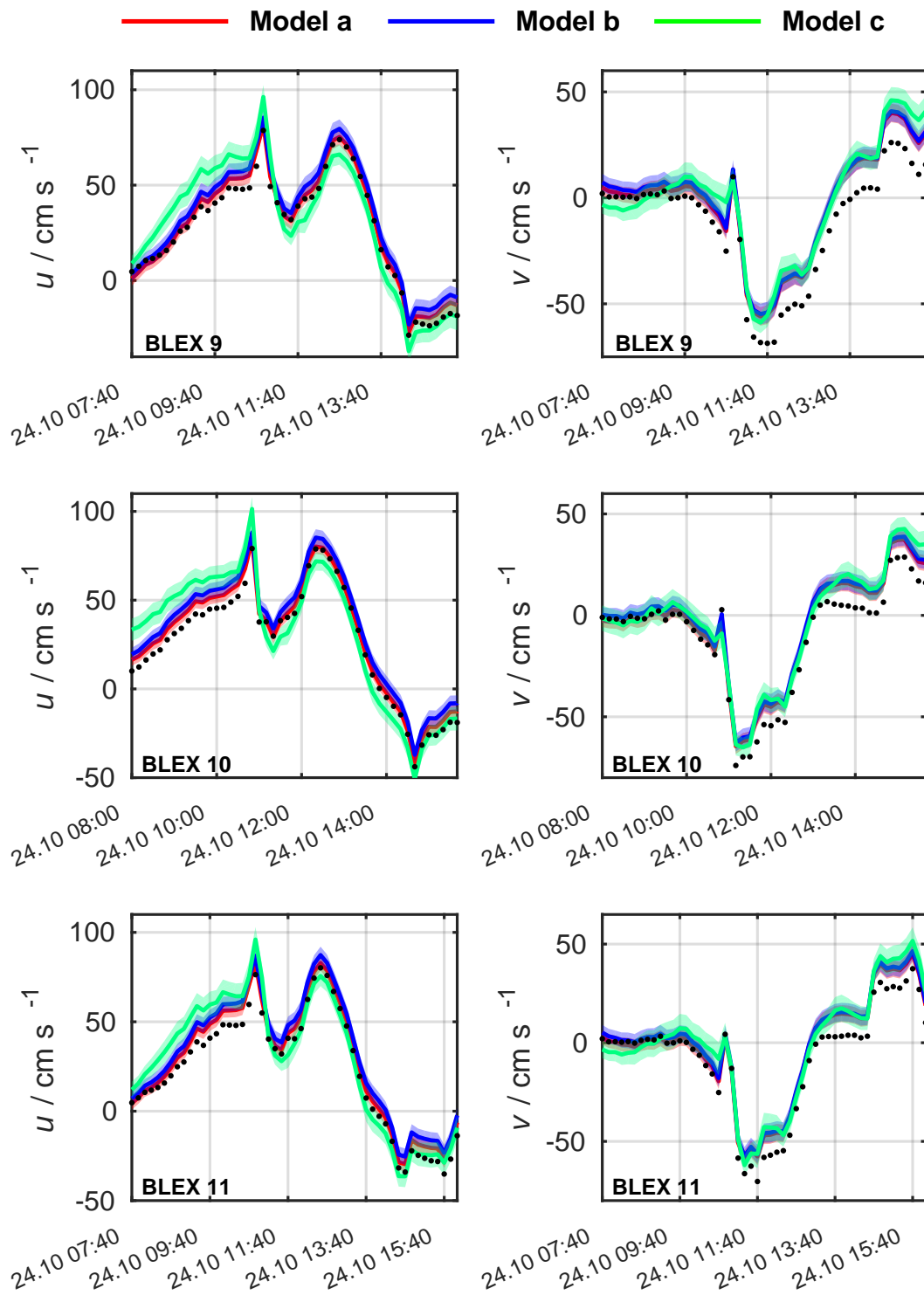
Figure 137: Reconstructed drifter velocities for Type B drifters of ensemble ② if error terms are neglected. Details are given in subsection 7.2.
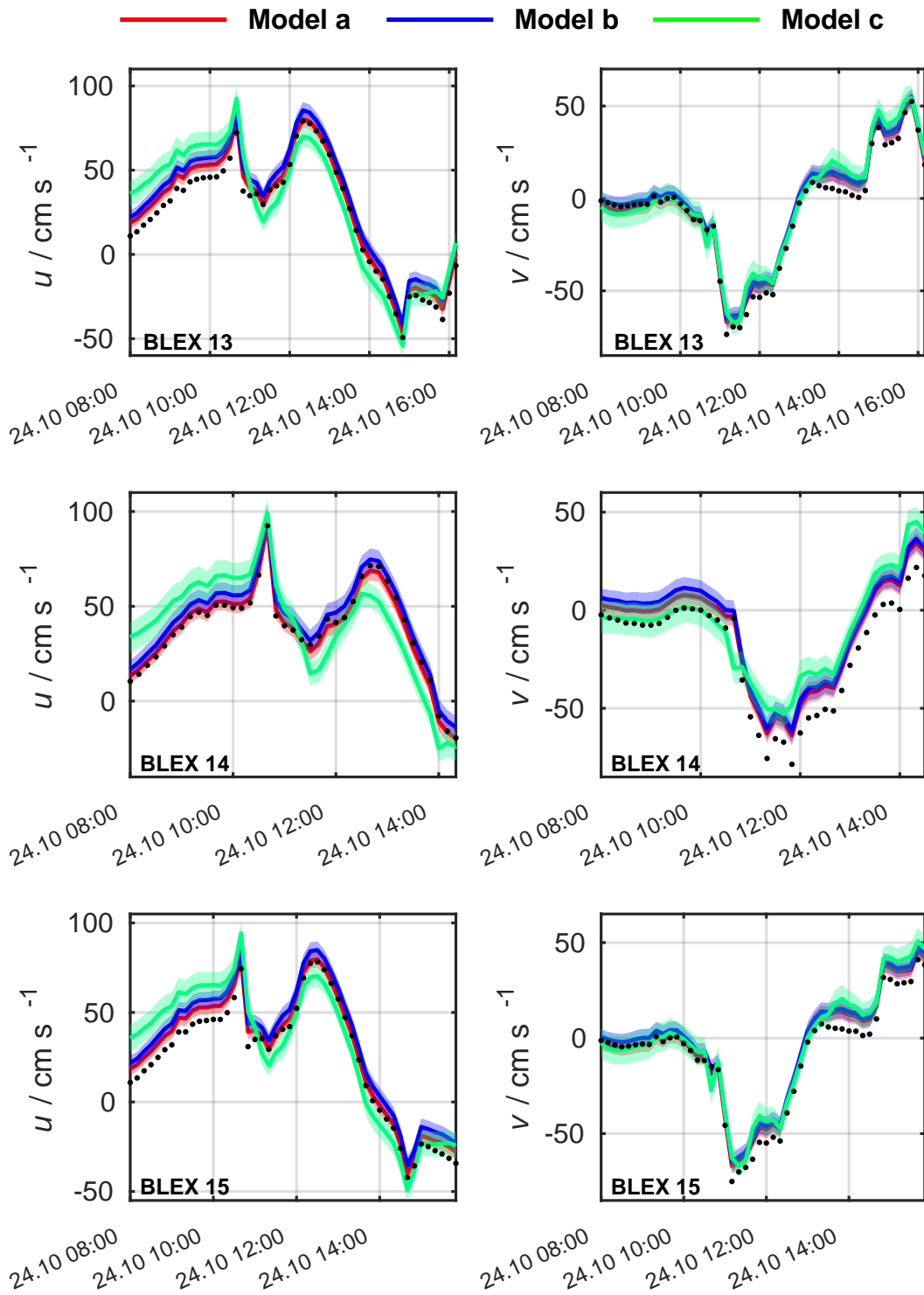
Figure 138: Reconstructed drifter velocities for Type B drifters of ensemble ② if error terms are neglected. Details are given in subsection 7.2.
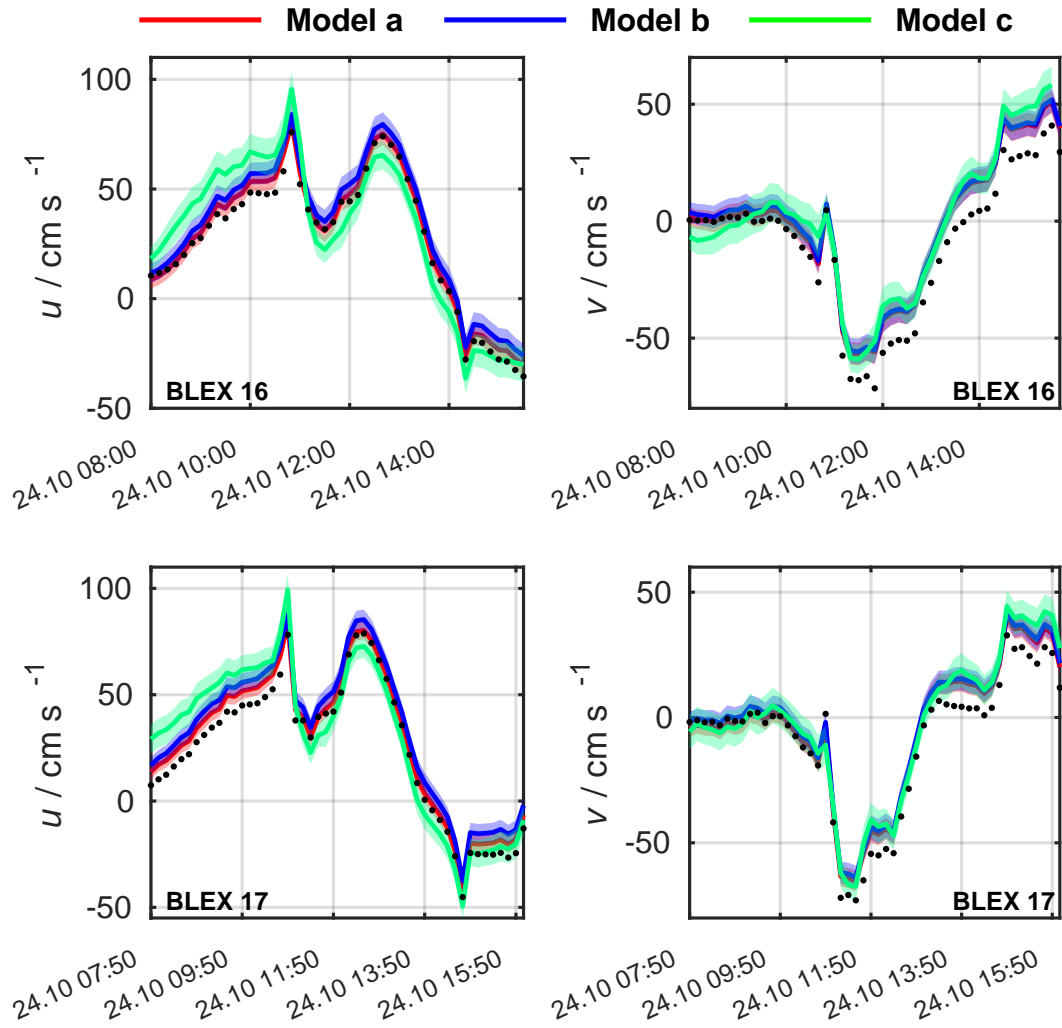
Figure 139: Reconstructed drifter velocities for Type B drifters of ensemble ② if error terms are neglected. Details are given in subsection 7.2.
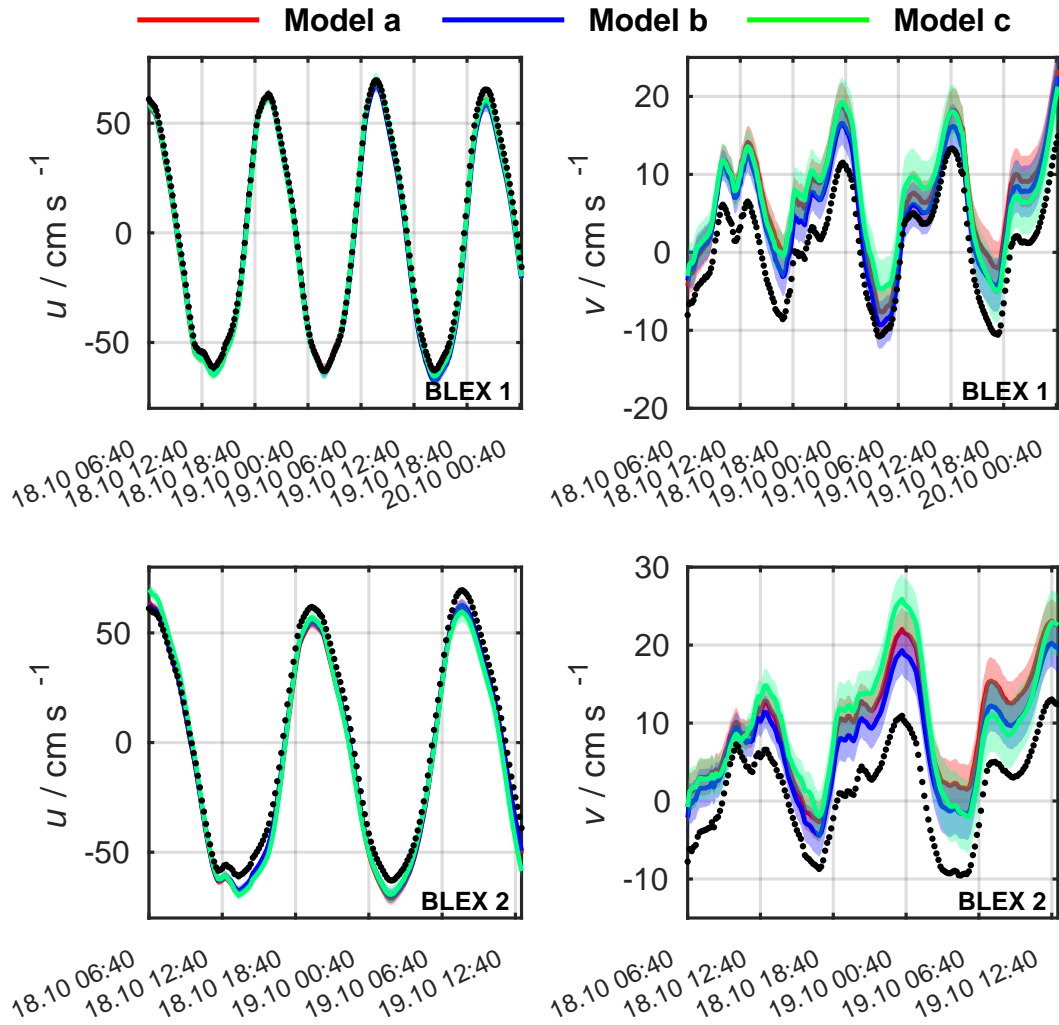
Figure 140: Reconstructed drifter velocities for drifters 1 (Type A) and 2 (Type B) of ensemble ①, if constant error terms are regarded. Details are given in subsection 7.2.
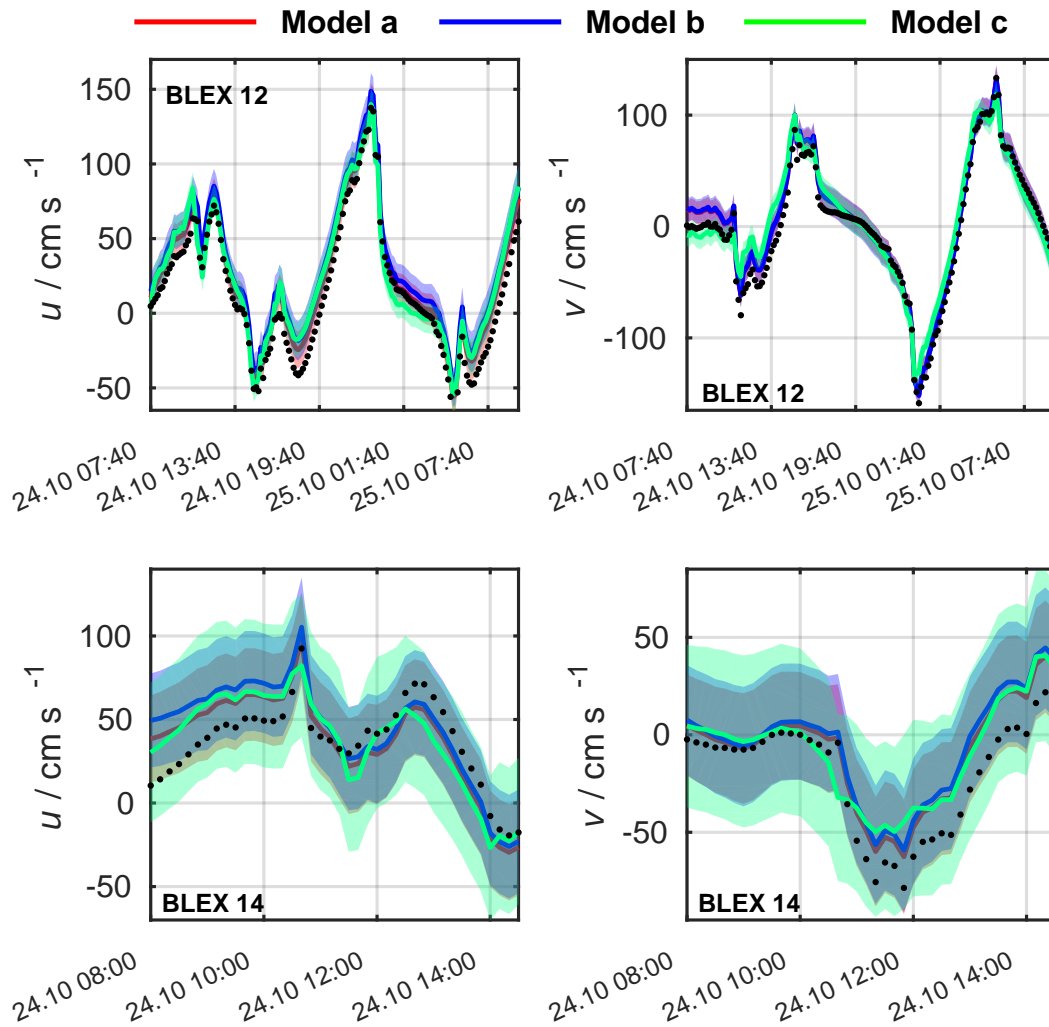
Figure 141: Reconstructed drifter velocities for drifters 12 (Type A) and 14 (Type B) of ensemble ②, if constant error terms are regarded. Details are given in subsection 7.2.
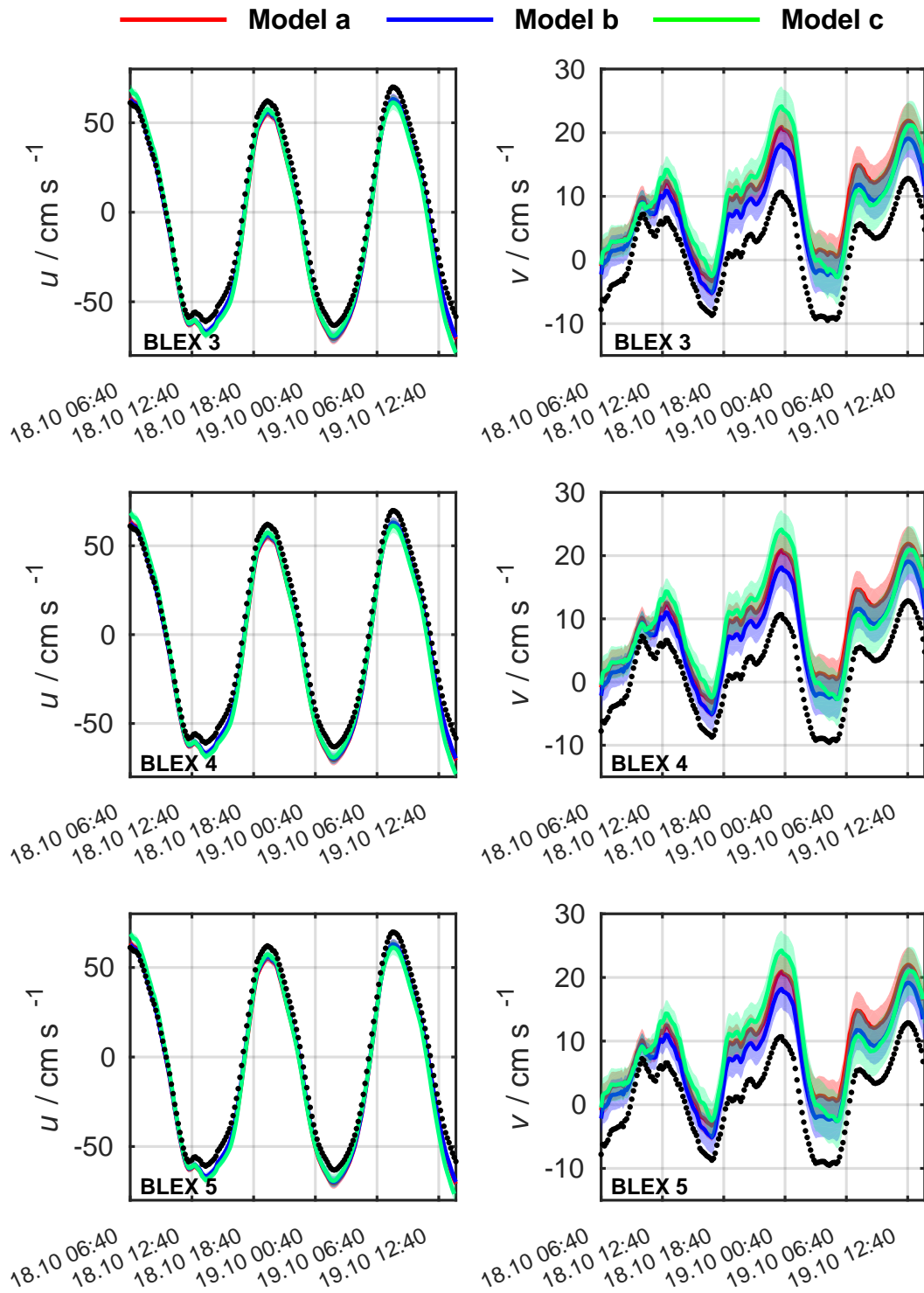
Figure 142: Reconstructed drifter velocities for Type B drifters of ensemble ① if error terms are regarded. Details are given in subsection 7.2.
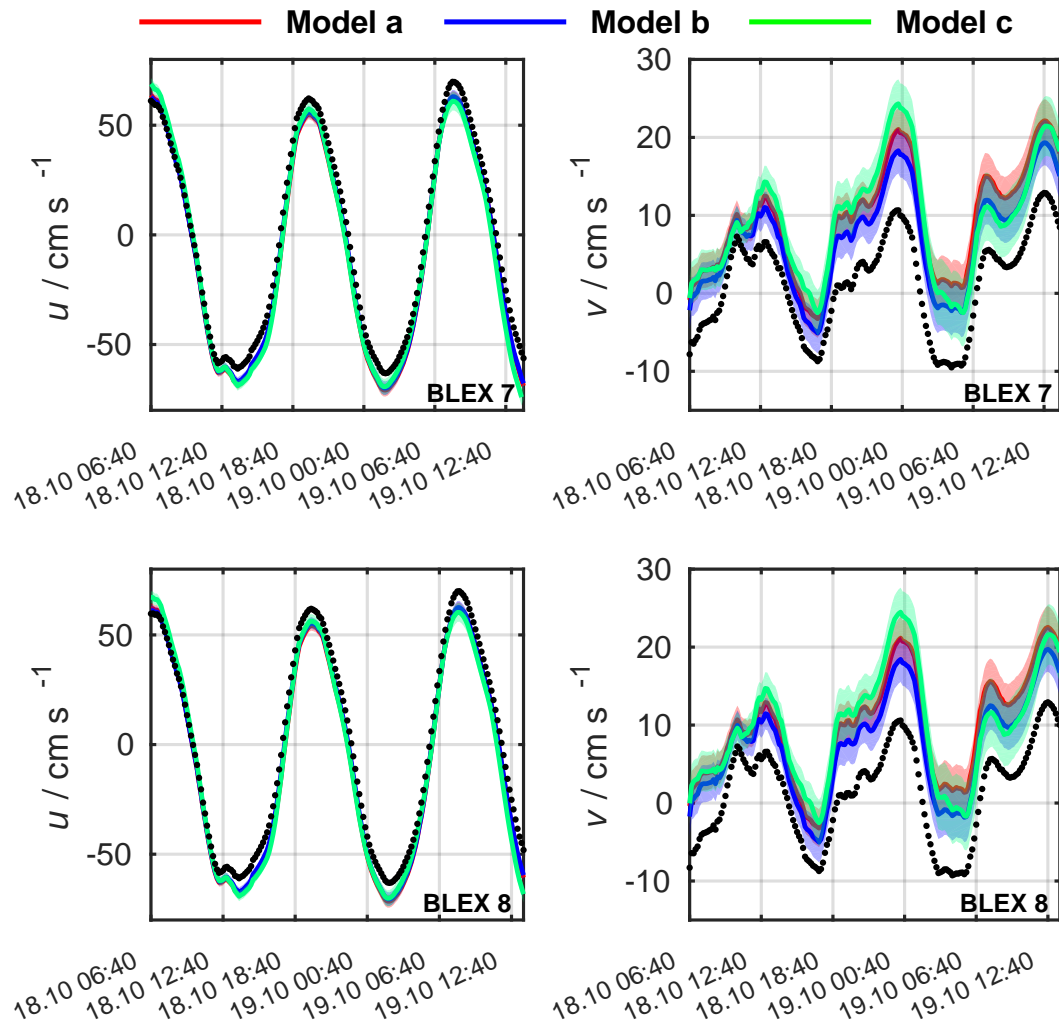
Figure 143: Reconstructed drifter velocities for Type B drifters of ensemble ① if error terms are regarded. Details are given in subsection 7.2.
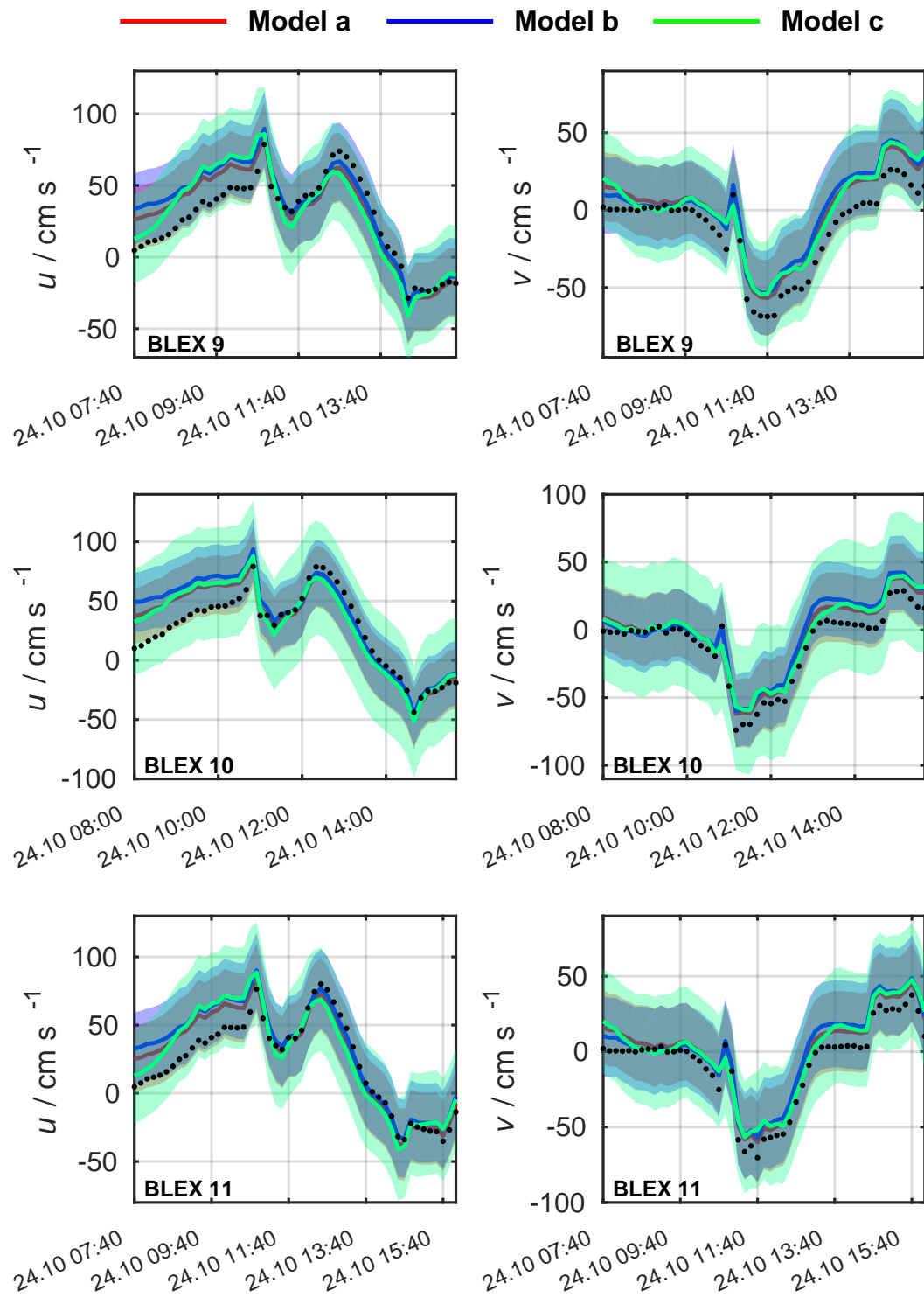
Figure 144: Reconstructed drifter velocities for Type B drifters of ensemble ② if error terms are regarded. Details are given in subsection 7.2.
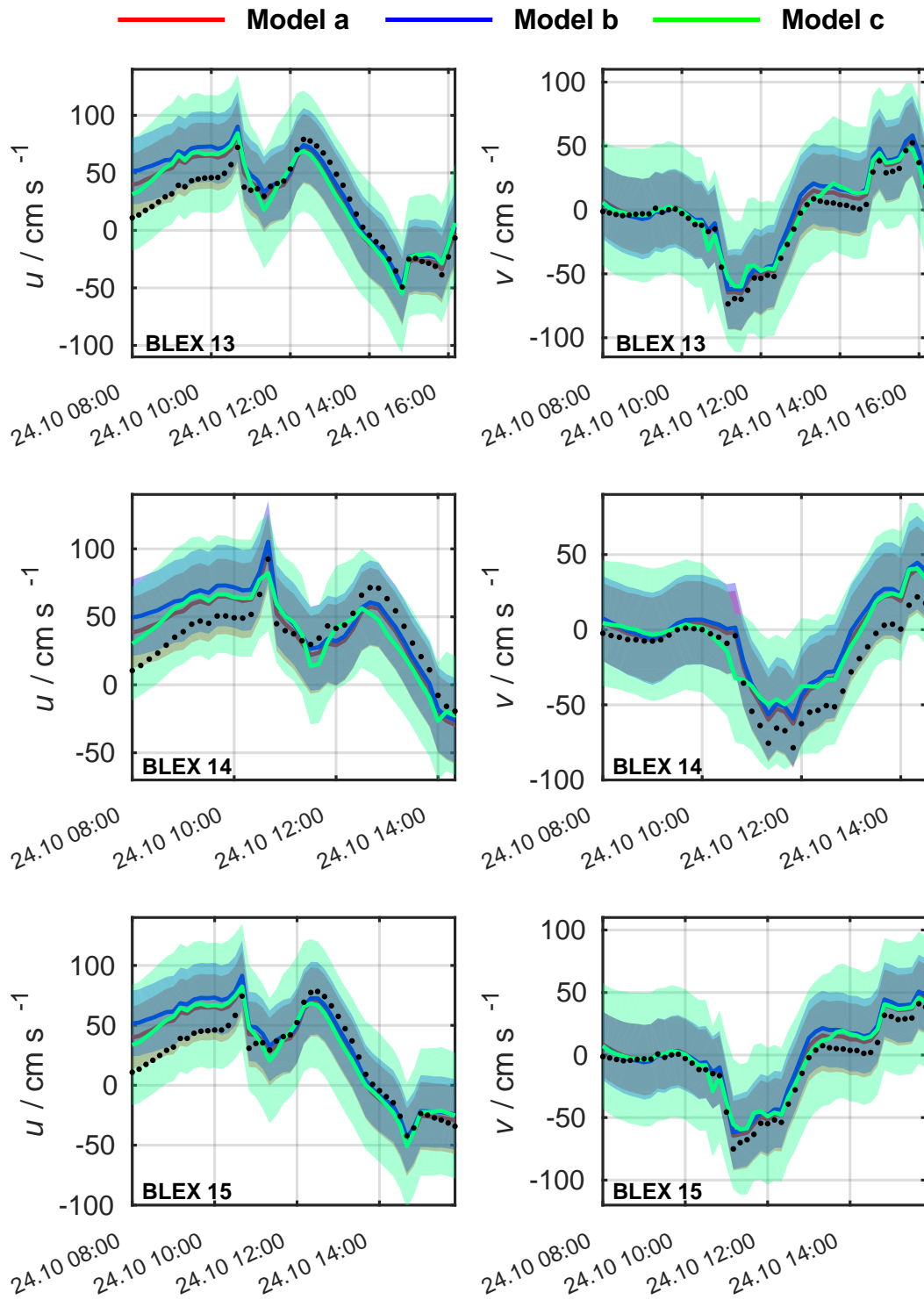
Figure 145: Reconstructed drifter velocities for Type B drifters of ensemble ② if error terms are regarded. Details are given in subsection 7.2.
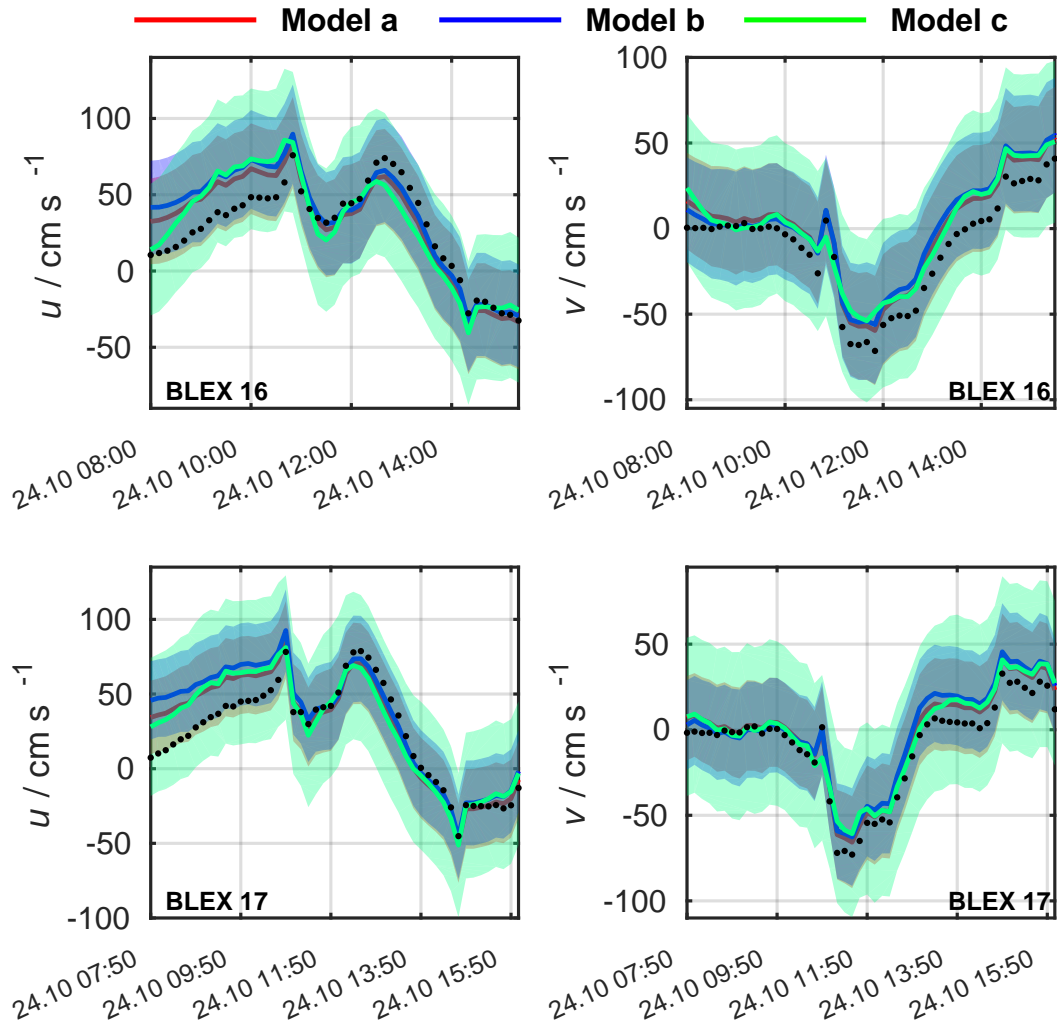
Figure 146: Reconstructed drifter velocities for Type B drifters of ensemble ② if error terms are regarded. Details are given in subsection 7.2.

F.4. Lagrangian Modeling, SP-Model, neglecting error terms
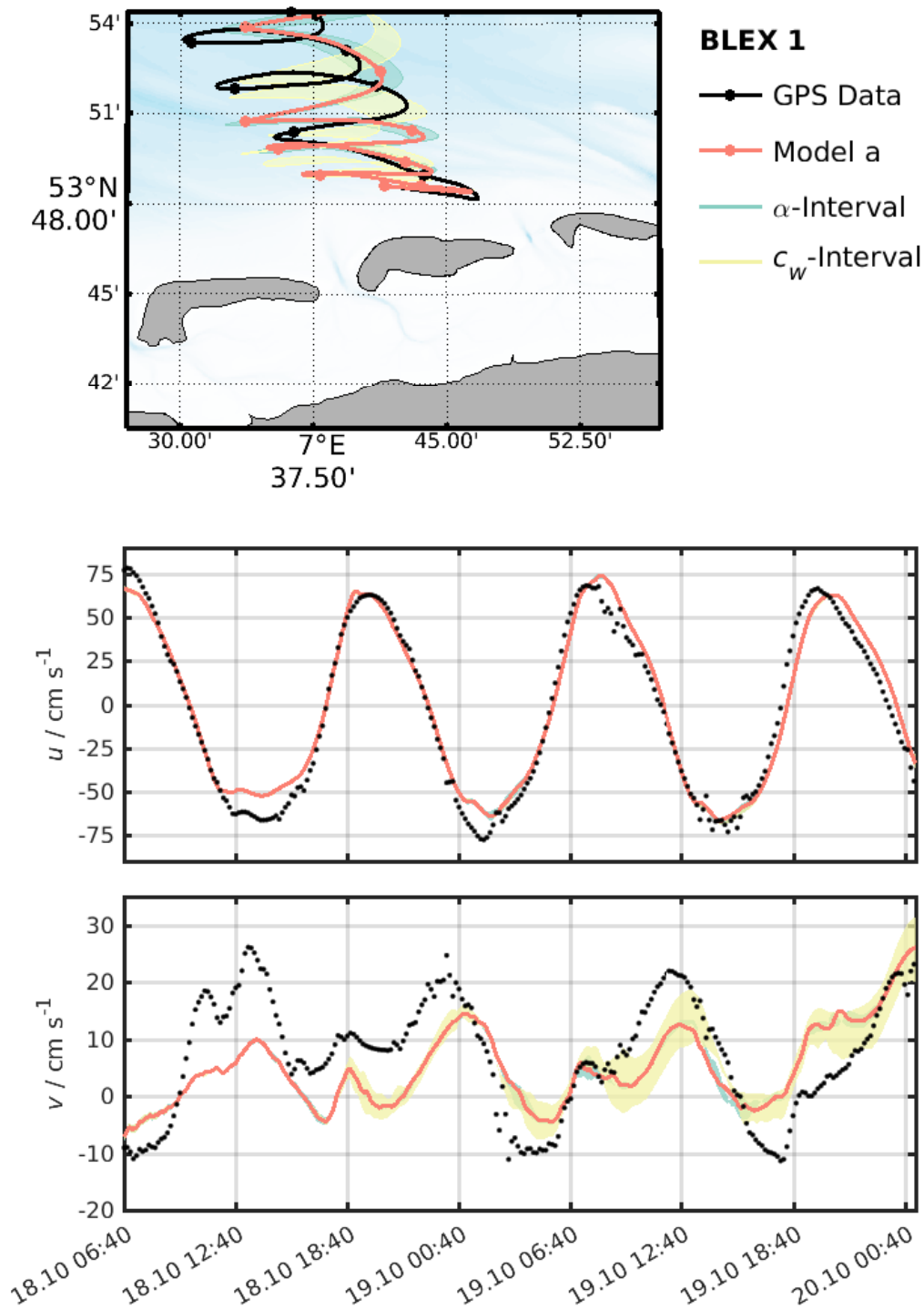
Figure 147: Computed trajectories for Drifter 3 (Type B) using drag parameters for Model a without error term and Runge-Kutha integration. Details are given in subsection 7.2.
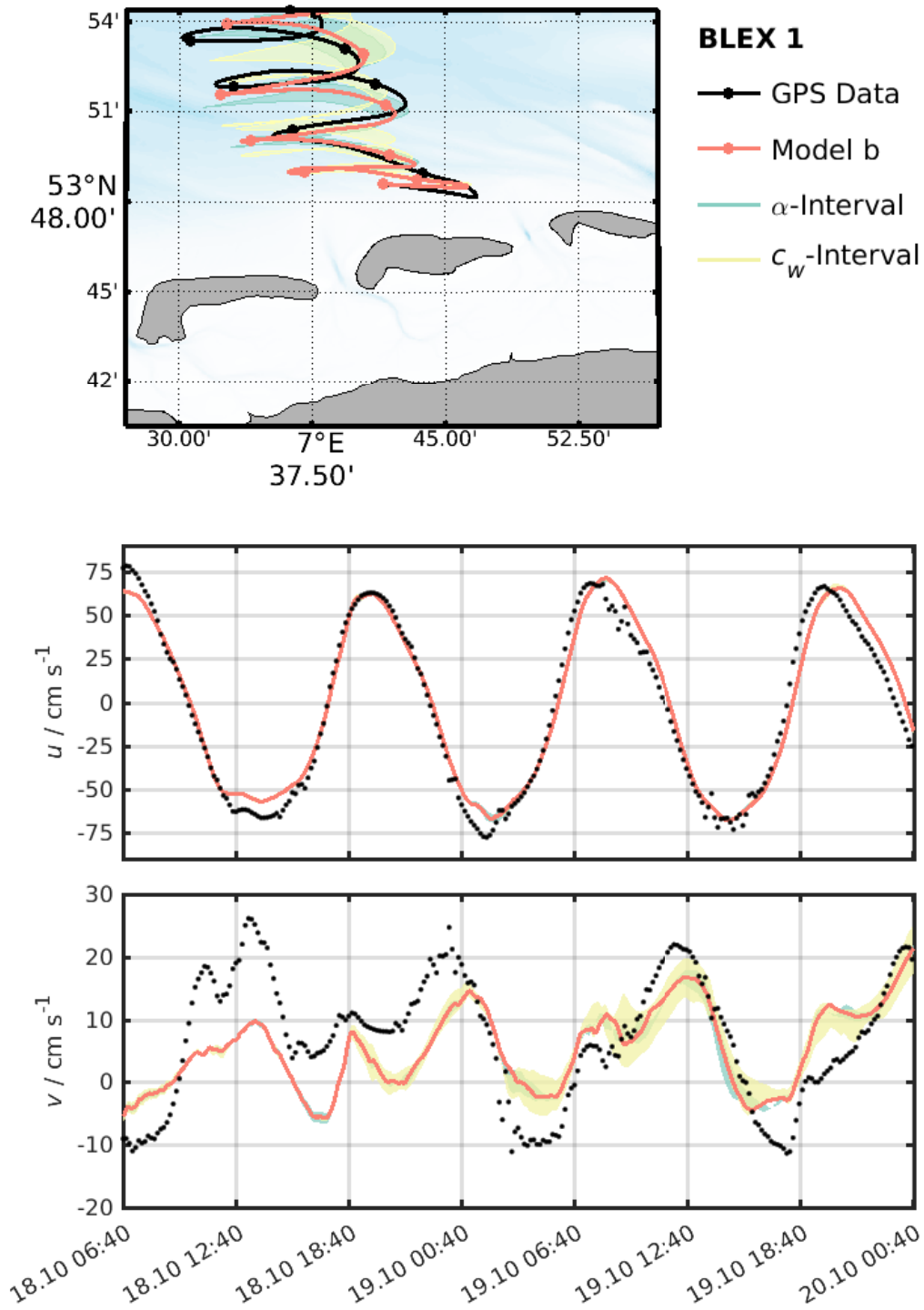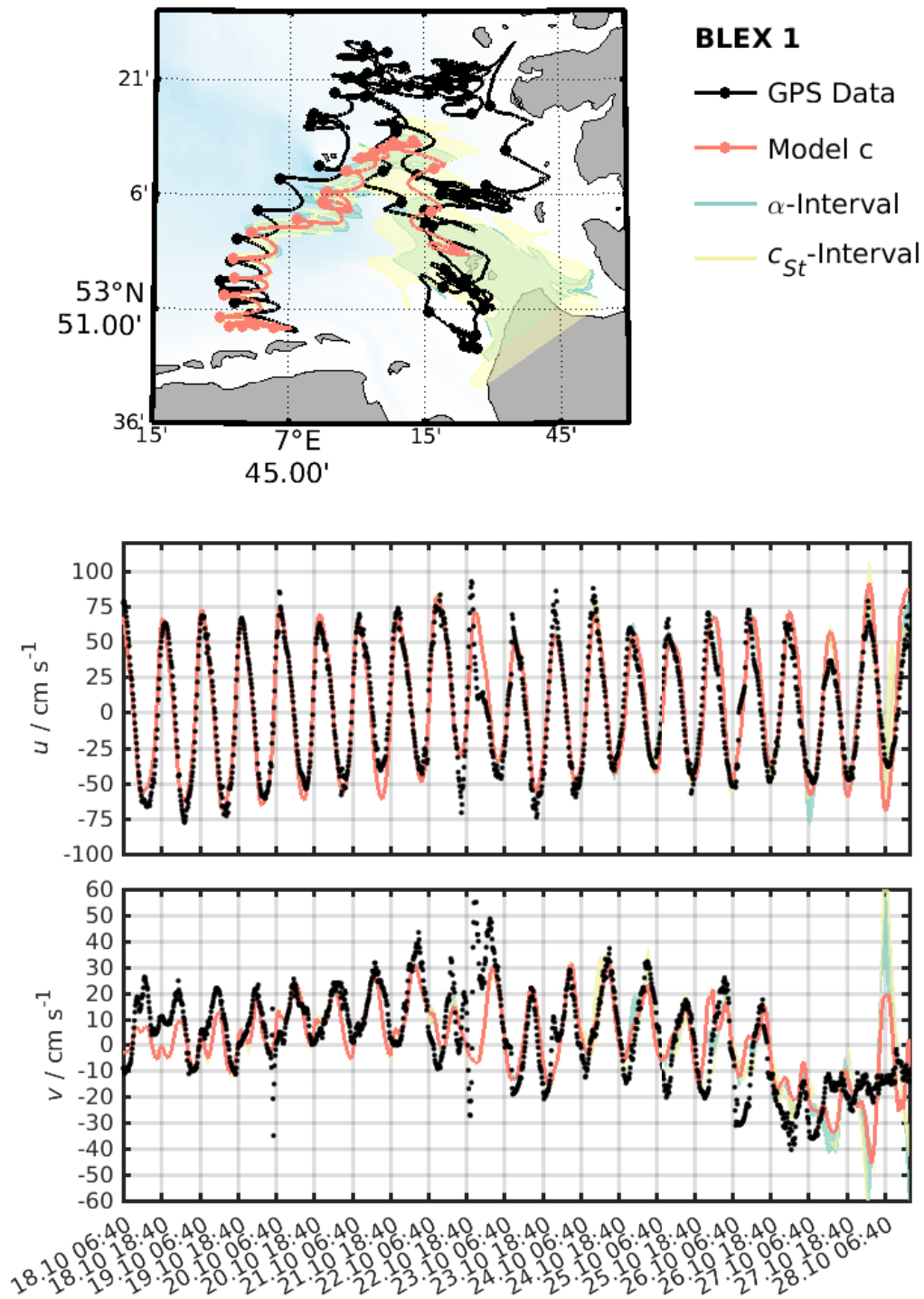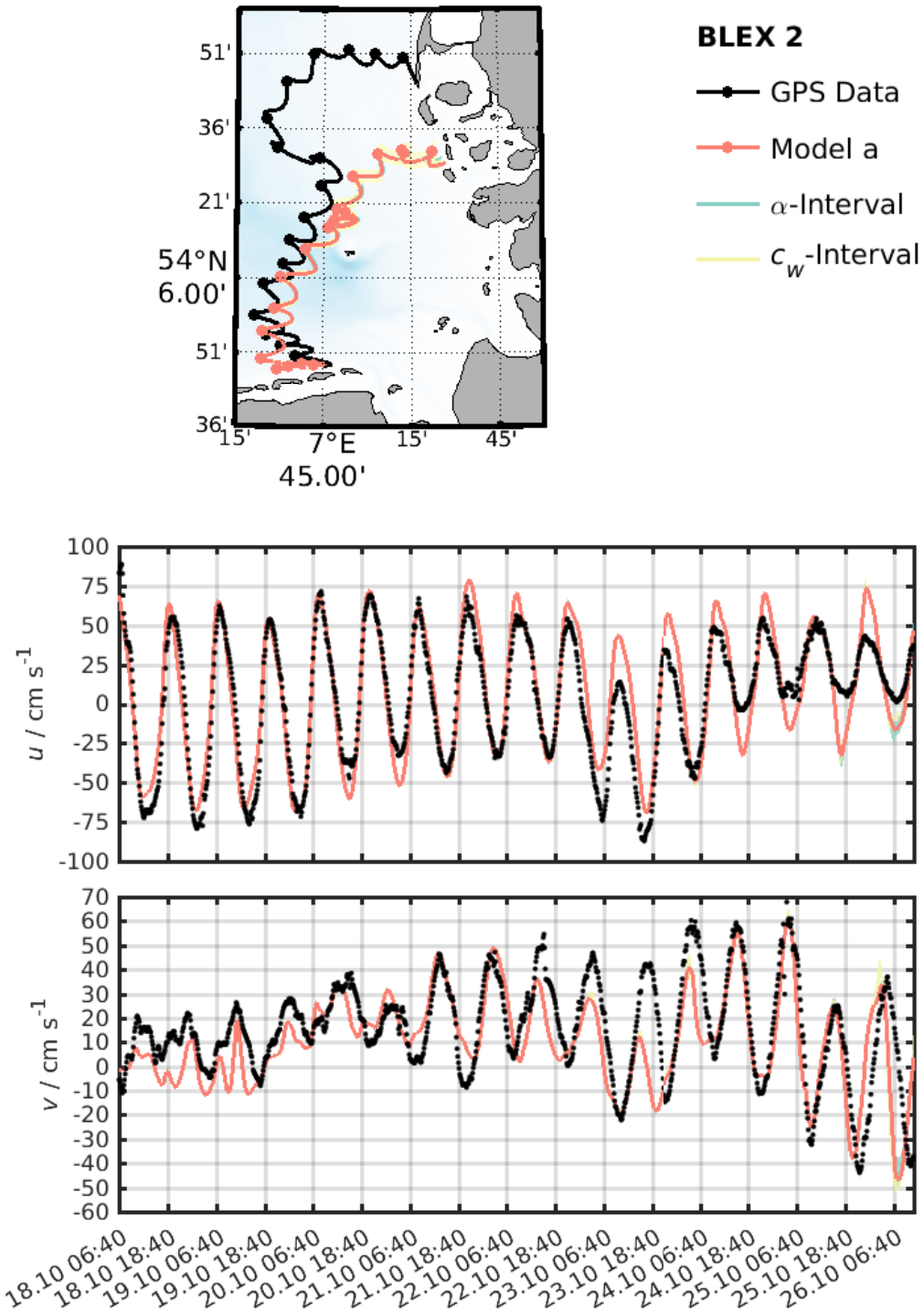
Figure 148: Computed trajectories for Drifter 3 (Type B) using drag parameters for Model a without error term and Runge-Kutha integration. Details are given in subsection 7.2.
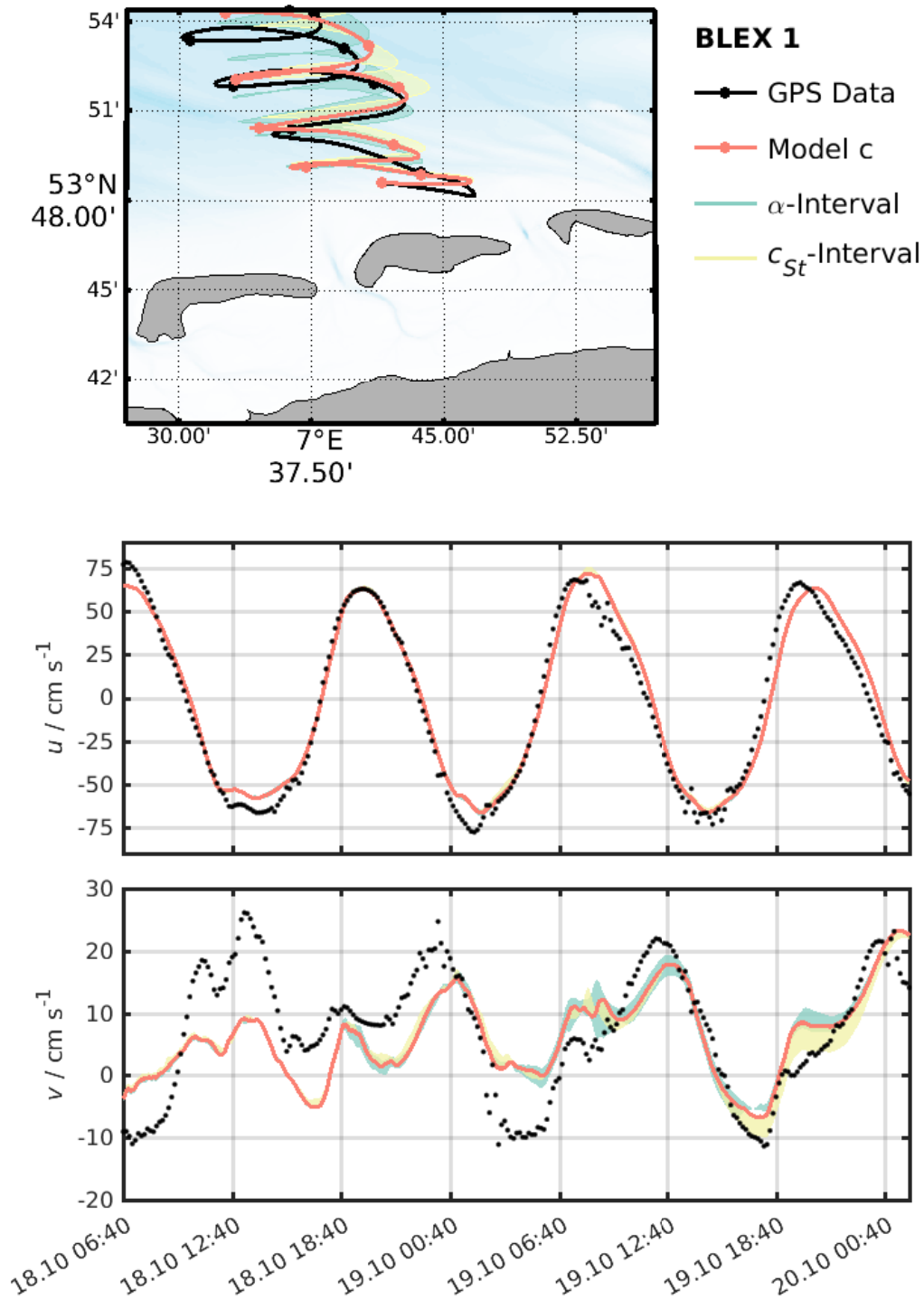
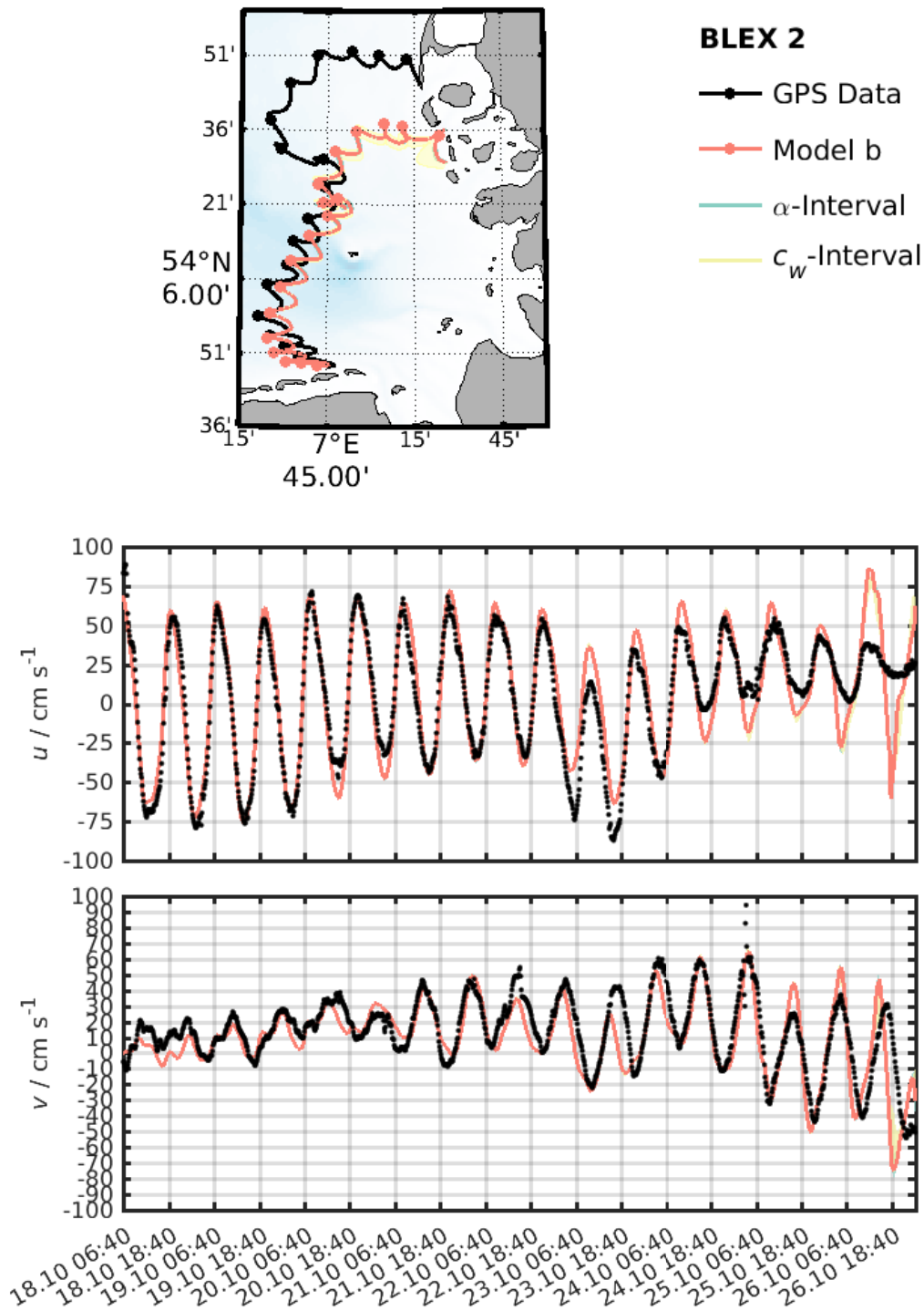Figure 149: Computed trajectories for Drifter 3 (Type B) using drag parameters for Model a without error term and Runge-Kutha integration. Details are given in subsection 7.2.
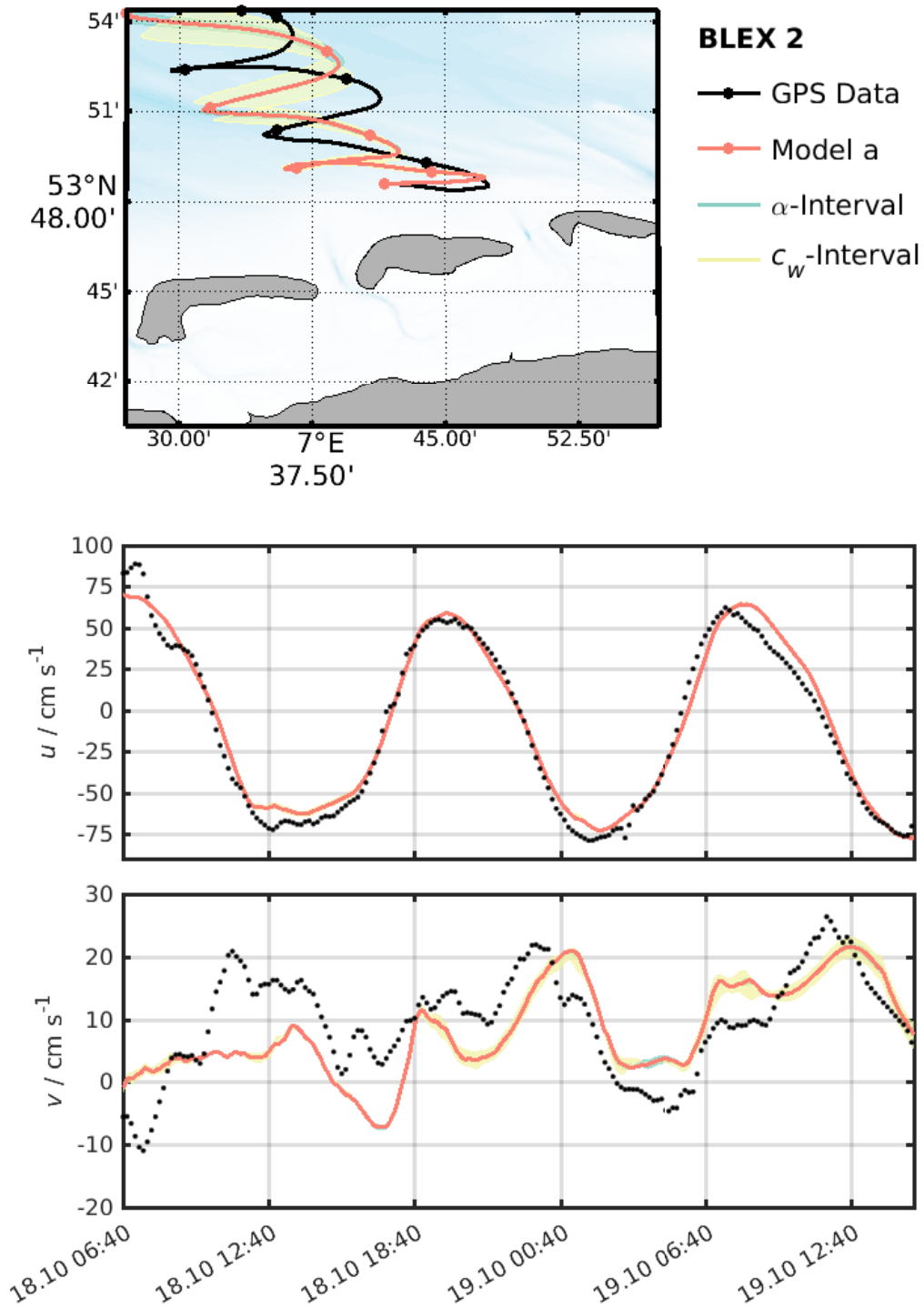
Figure 150: Computed trajectories for Drifter 3 (Type B) using drag parameters for Model a without error term and Runge-Kutha integration. Details are given in subsection 7.2.
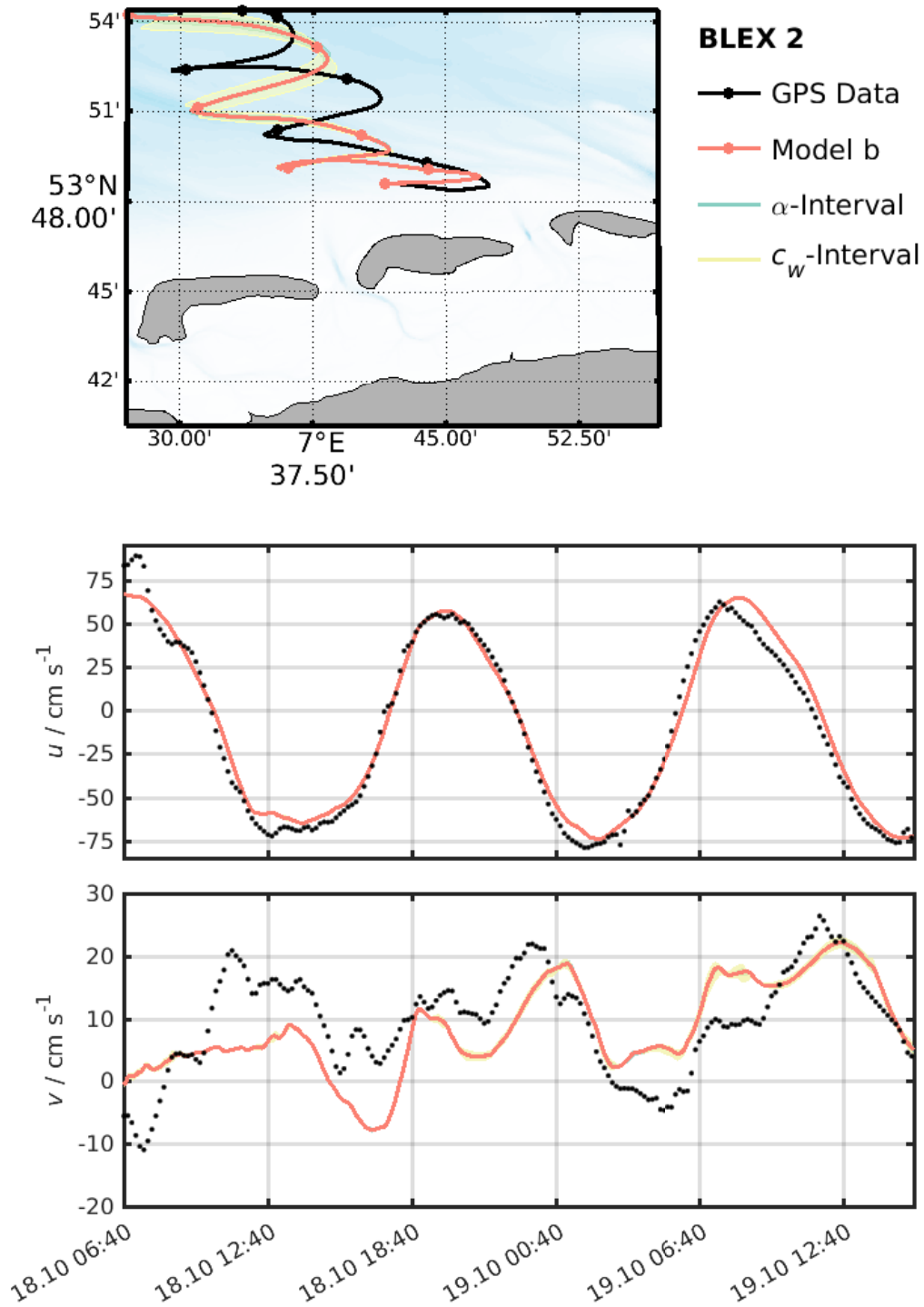
Figure 151: Computed trajectories for Drifter 3 (Type B) using drag parameters for Model a without error term and Runge-Kutha integration. Details are given in subsection 7.2.
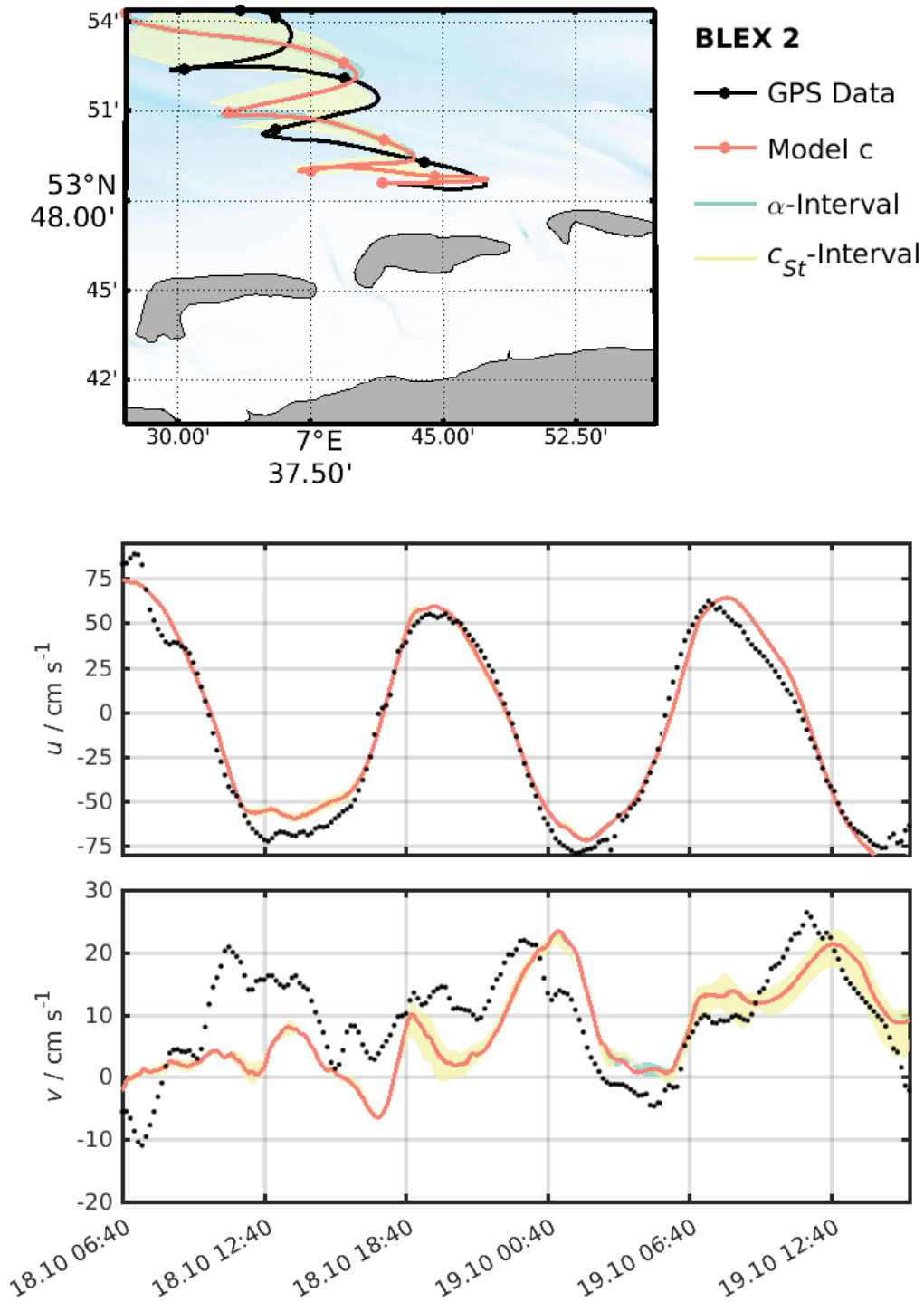
Figure 152: Computed trajectories for Drifter 3 (Type B) using drag parameters for Model a without error term and Runge-Kutha integration. Details are given in subsection 7.2.
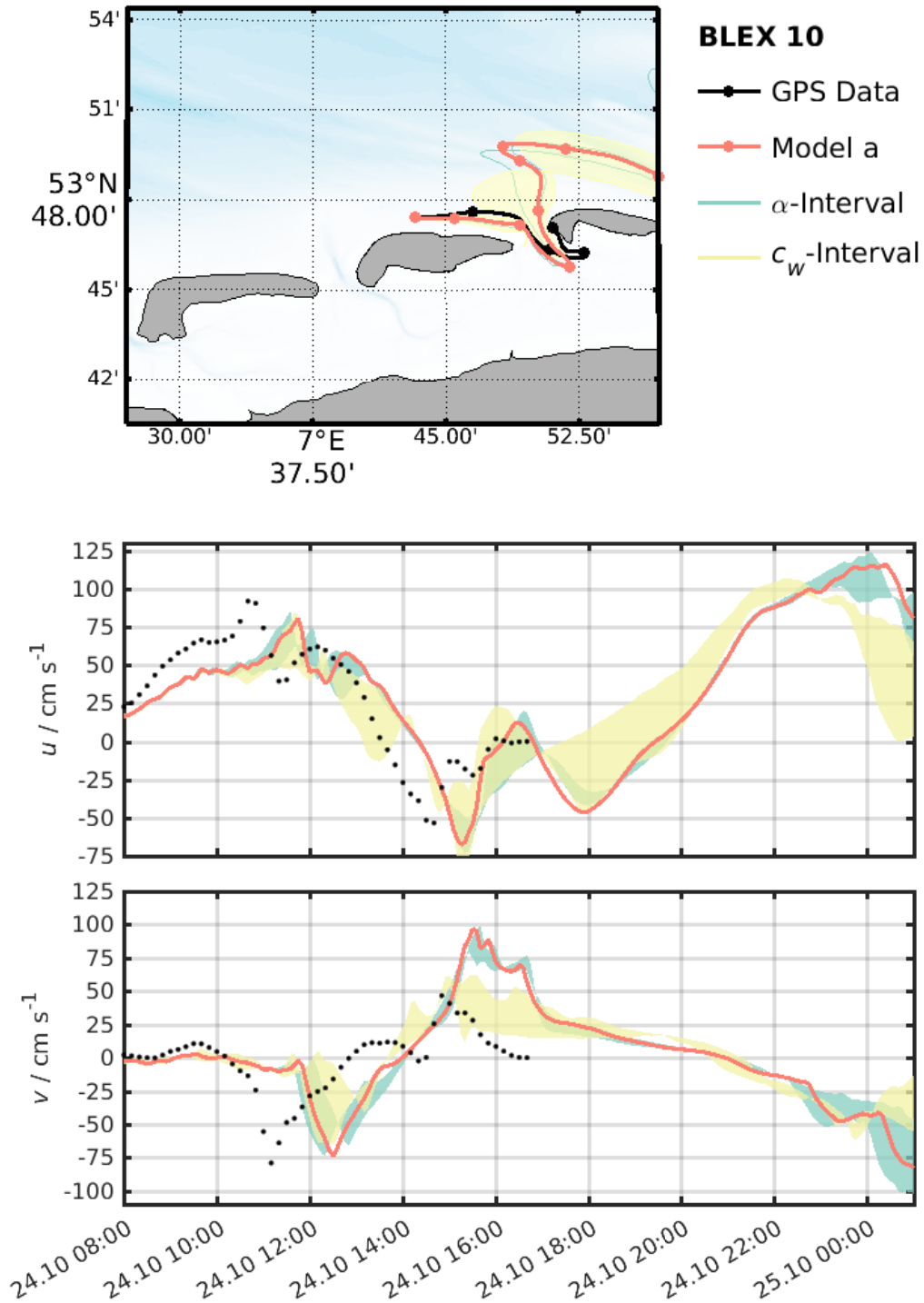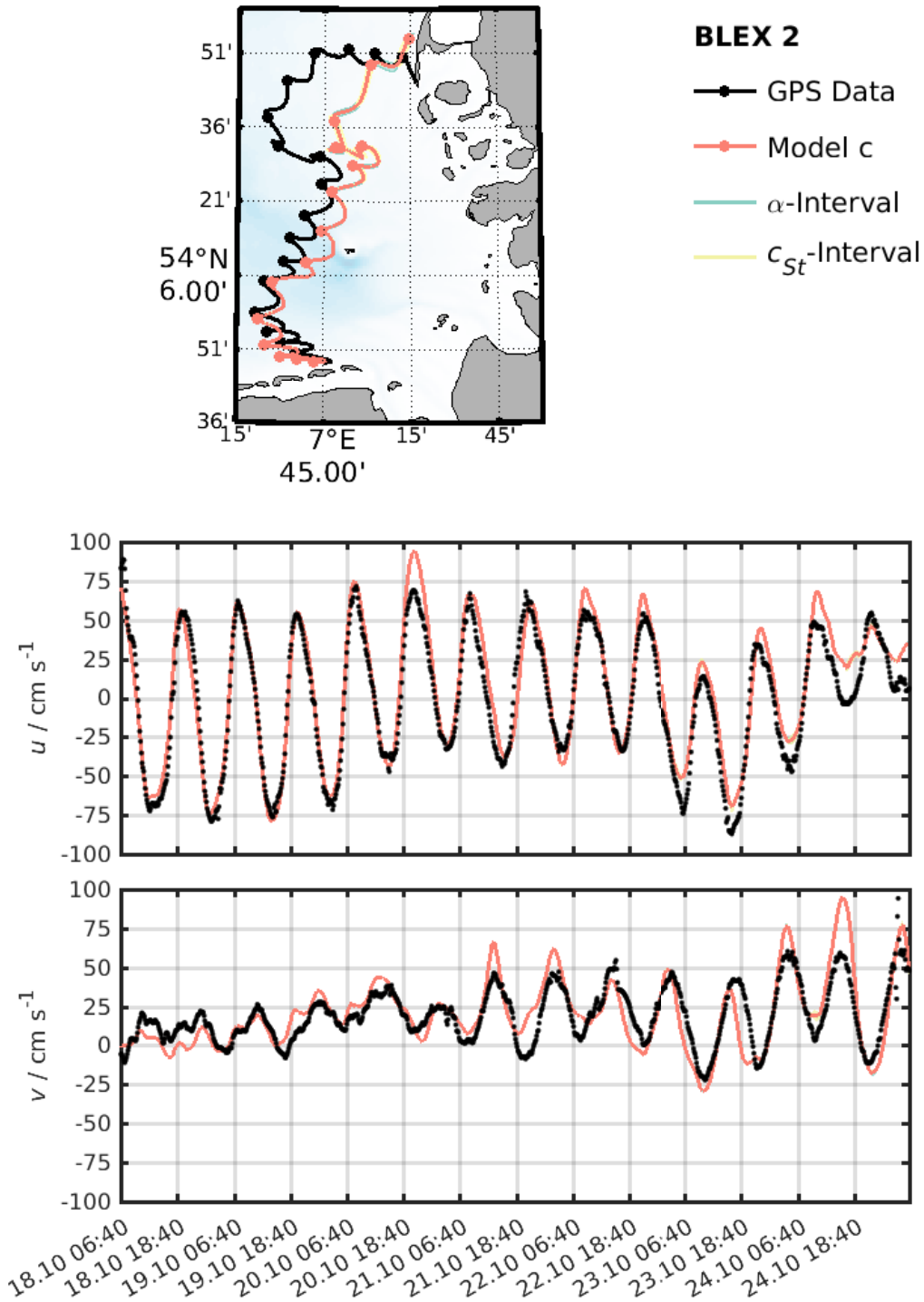
Figure 153: Computed trajectories for Drifter 3 (Type B) using drag parameters for Model a without error term and Runge-Kutha integration. Details are given in subsection 7.2.
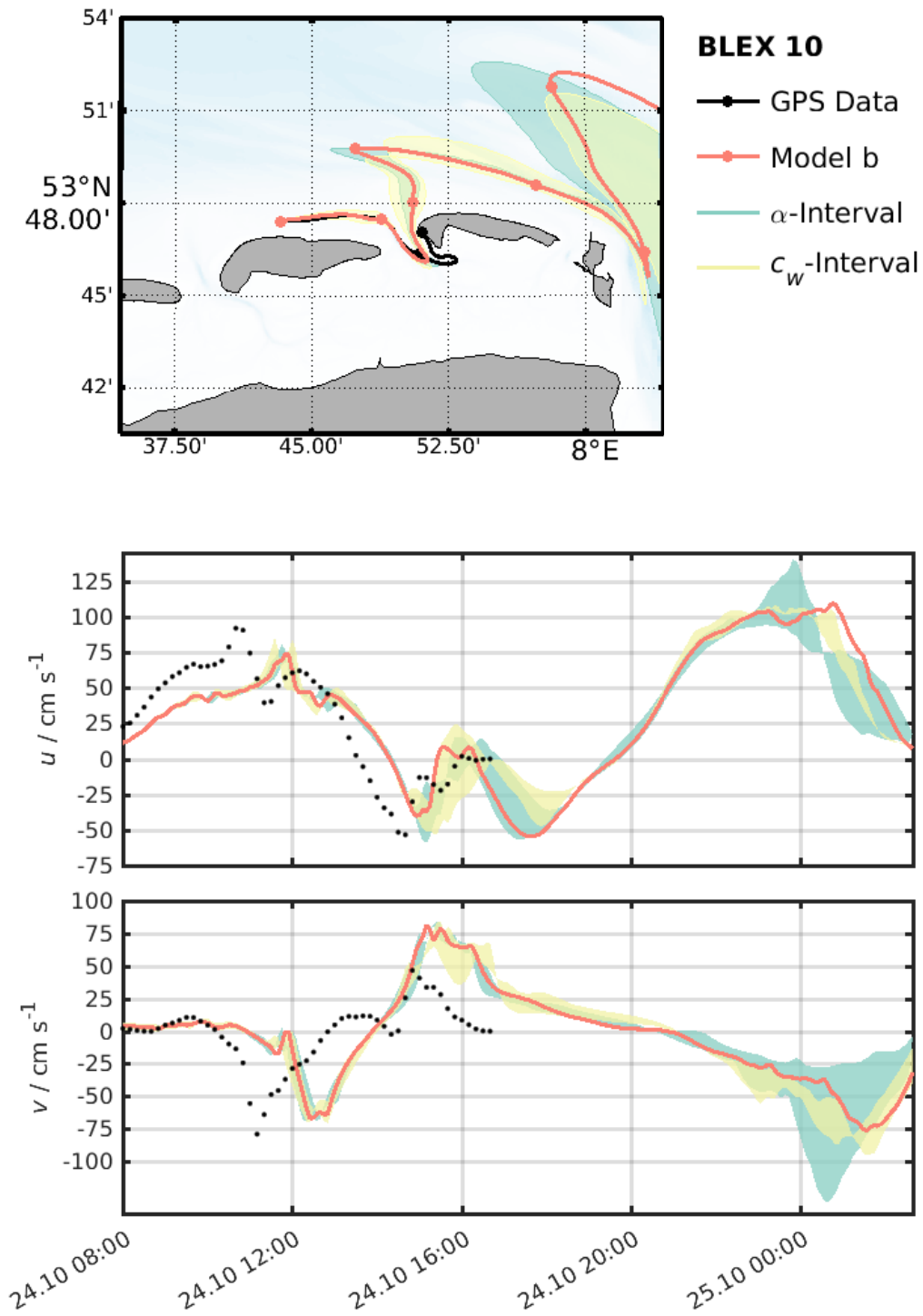
Figure 154: Computed trajectories for Drifter 3 (Type B) using drag parameters for Model a without error term and Runge-Kutha integration. Details are given in subsection 7.2.
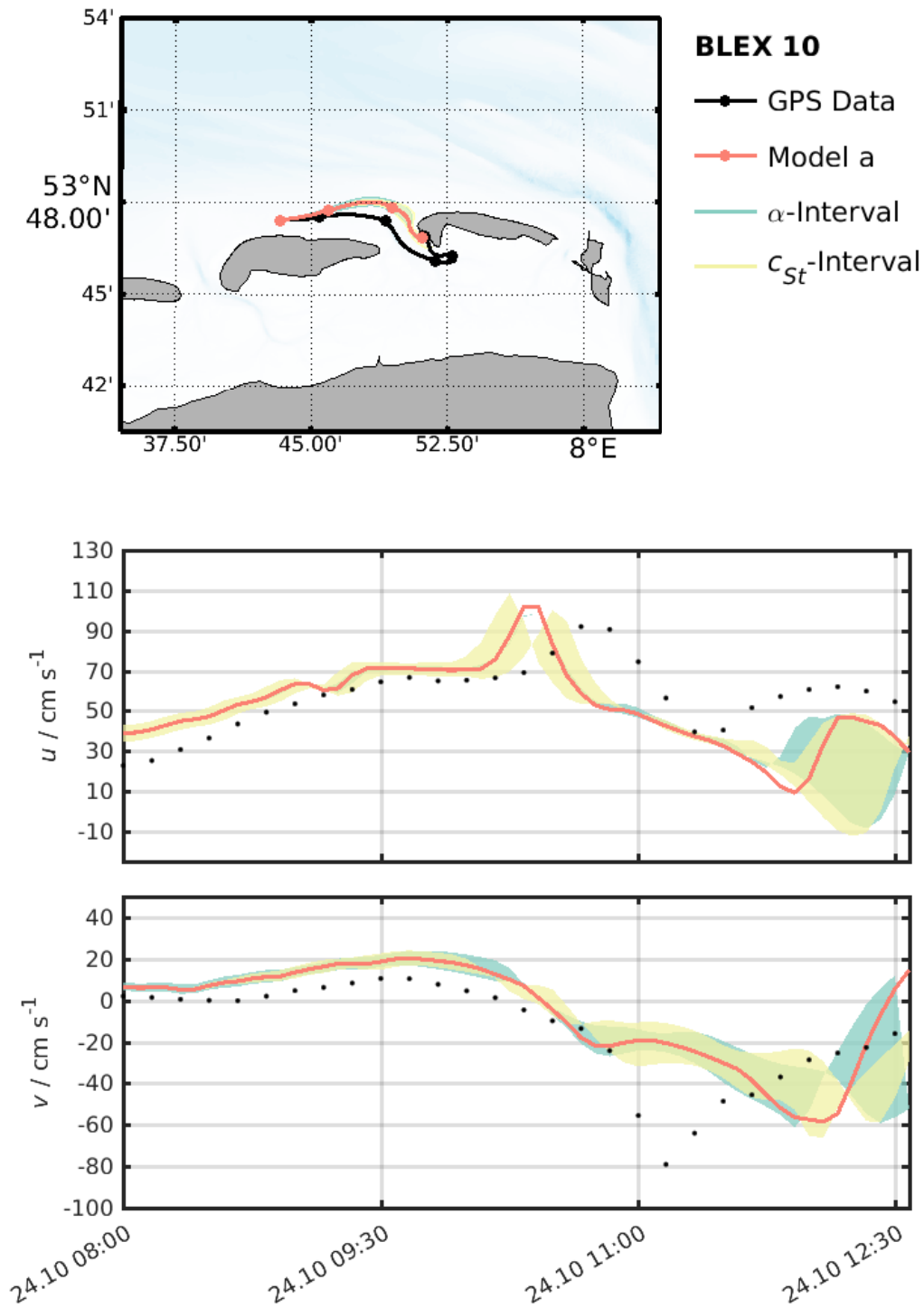
Figure 155: Computed trajectories for Drifter 3 (Type B) using drag parameters for Model a without error term and Runge-Kutha integration. Details are given in subsection 7.2.
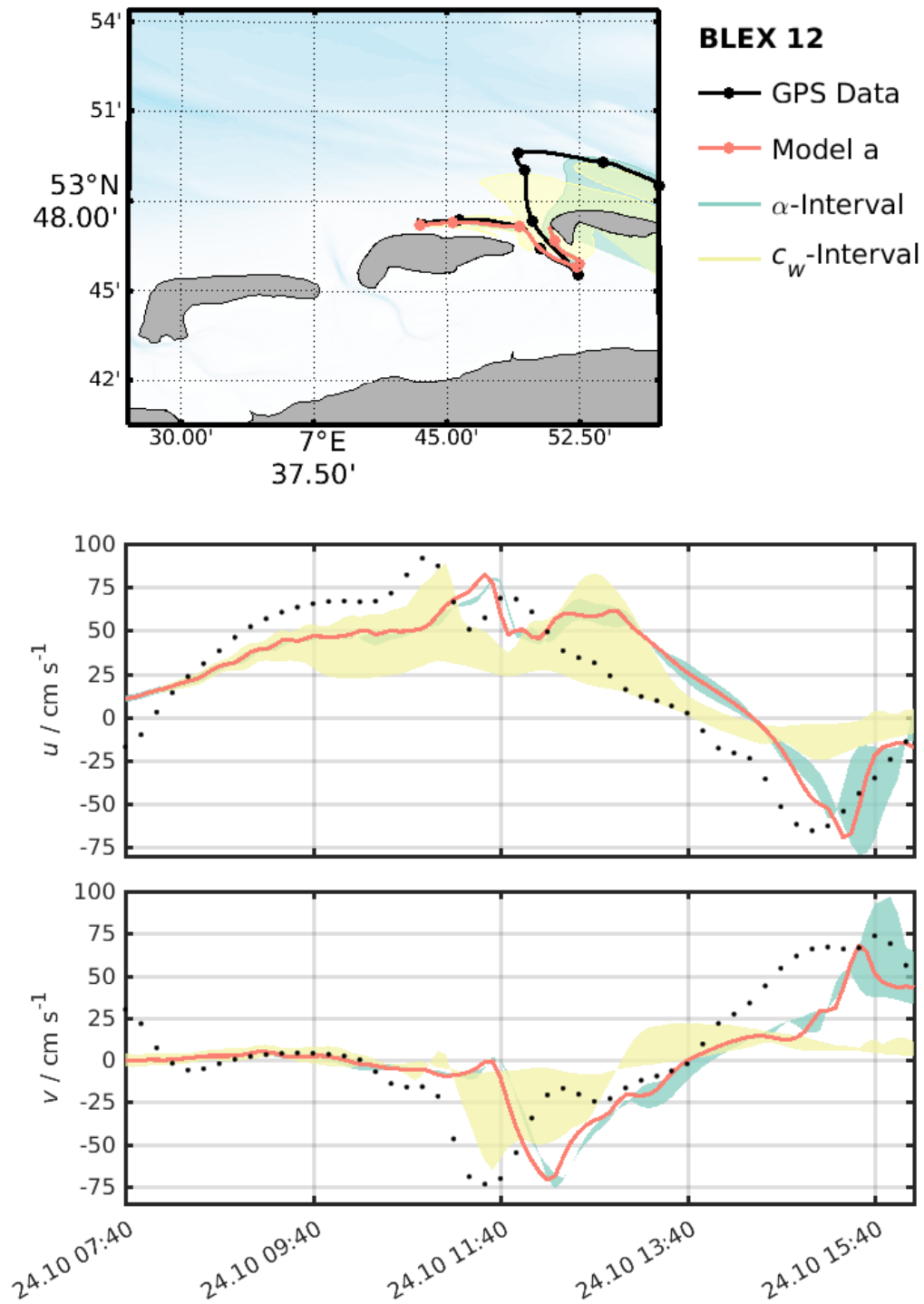
Figure 156: Computed trajectories for Drifter 3 (Type B) using drag parameters for Model a without error term and Runge-Kutha integration. Details are given in subsection 7.2.
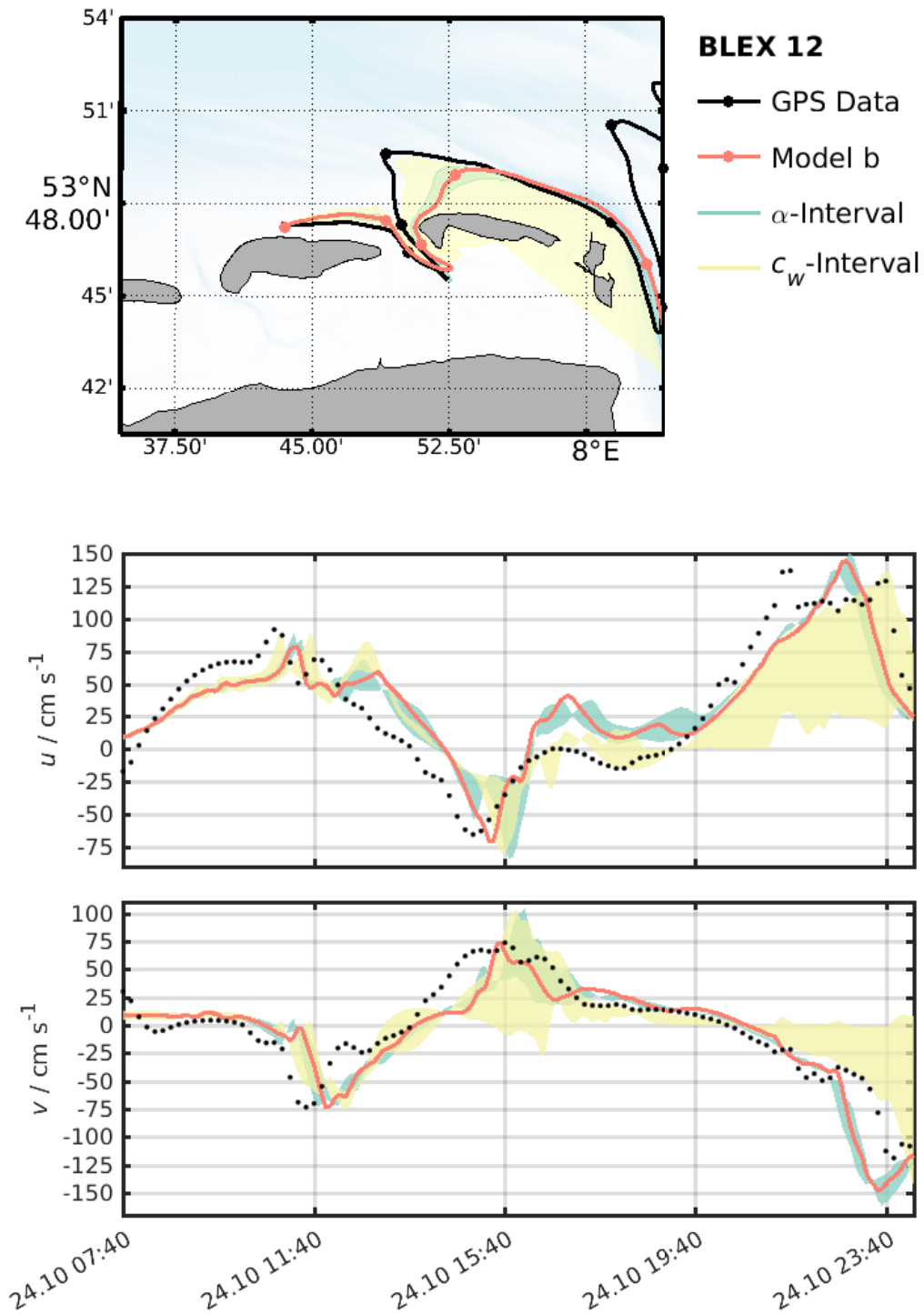
Figure 157: Computed trajectories for Drifter 3 (Type B) using drag parameters for Model a without error term and Runge-Kutha integration. Details are given in subsection 7.2.
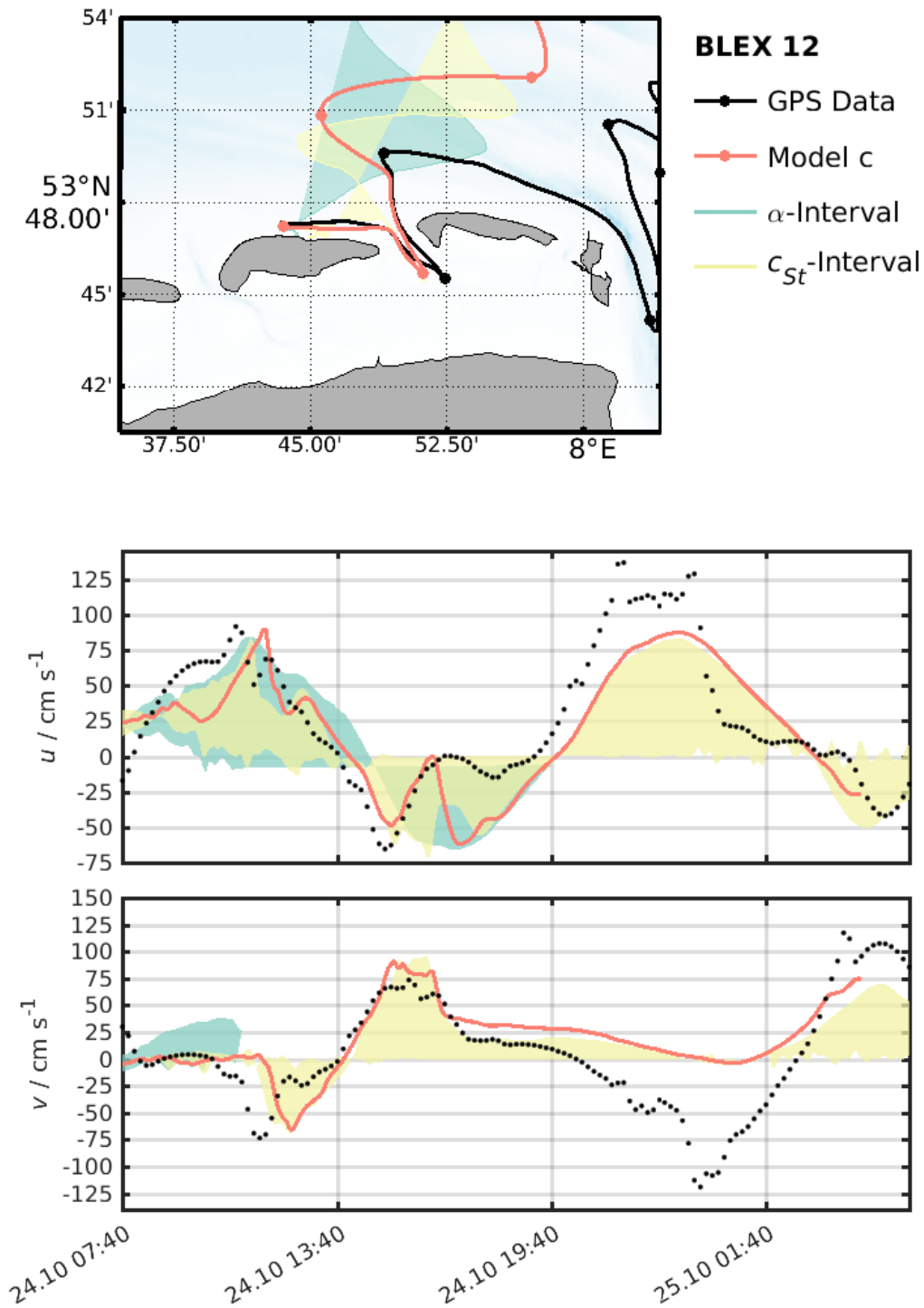
Figure 158: Computed trajectories for Drifter 3 (Type B) using drag parameters for Model a without error term and Runge-Kutha integration. Details are given in subsection 7.2.

F.5. GB-Model vs. SP-Model
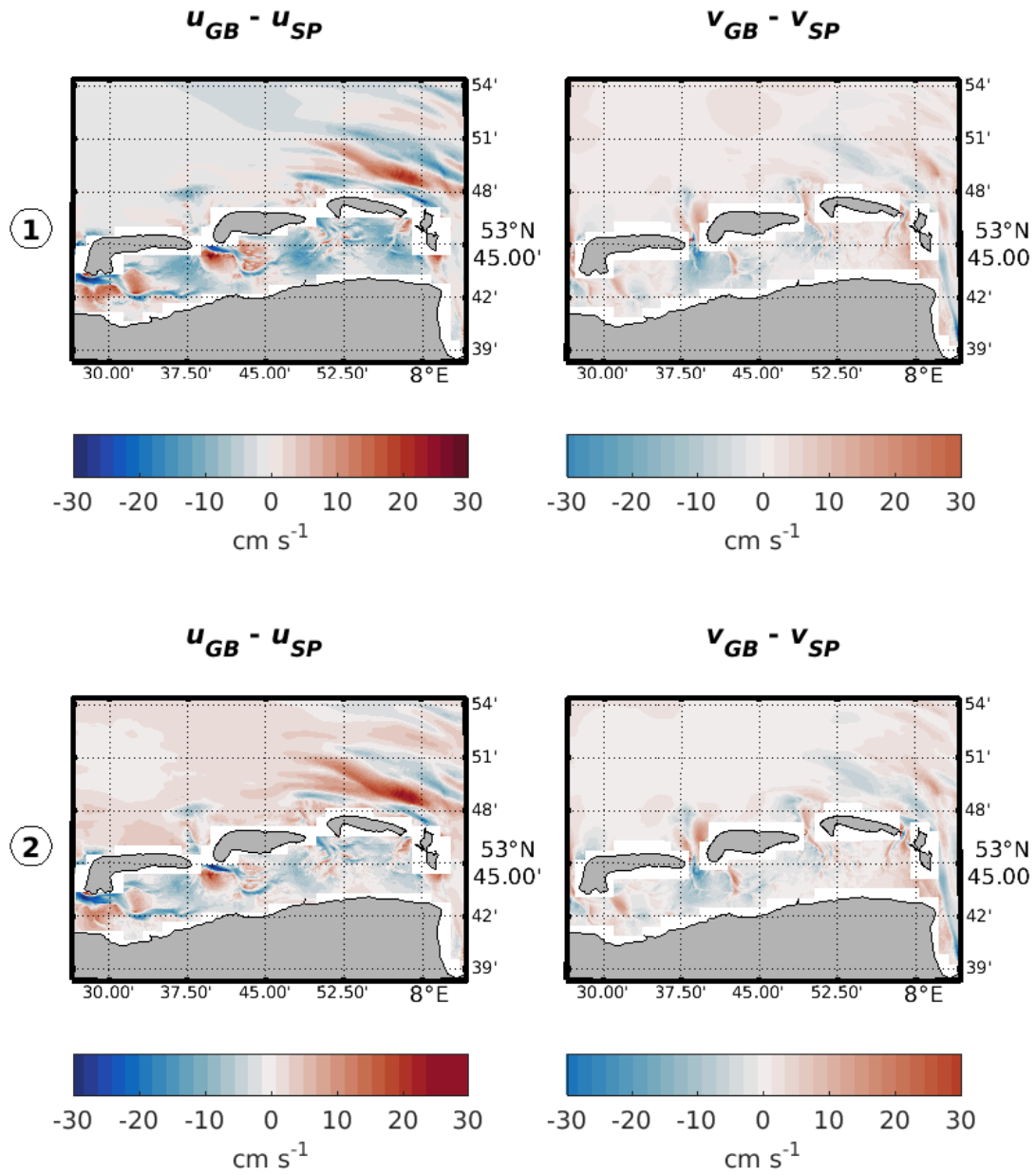
Figure 159: Differences of mean zonal and meridional velocities of the GB-Model and SP-Model. Colors show temporal means for floating periods of GPS-drifters within the SP-Model-grid. Plots in the upper line depict floating period of ensemble ①, floating period of ensemble ② are shown in the bottom line. Velocitiy data of both models were linearly interpolated onto the SP-Model's ρ-grid, all values show subtracts of the SP-Model from the GB-Model , i.e. positive values indcicate higher velocities in the GB-Model.

F.6. Lagrangian Trajectories: GB-Model
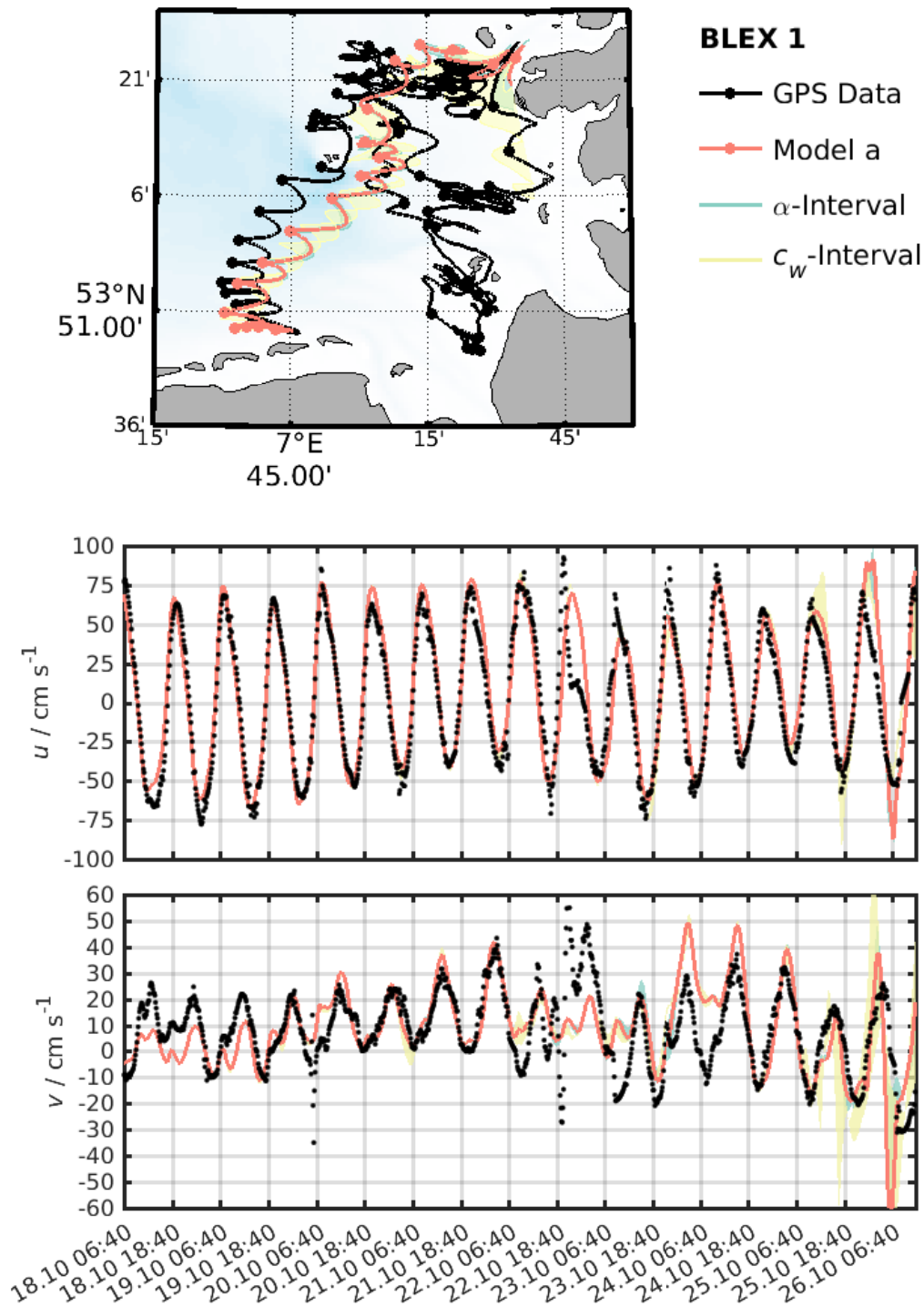
Figure 160: Computed trajectories for Drifter 1 (Type A) using drag parameters for Model *a* without error term and Runge-Kutha integration. Details are given in subsection 7.2.
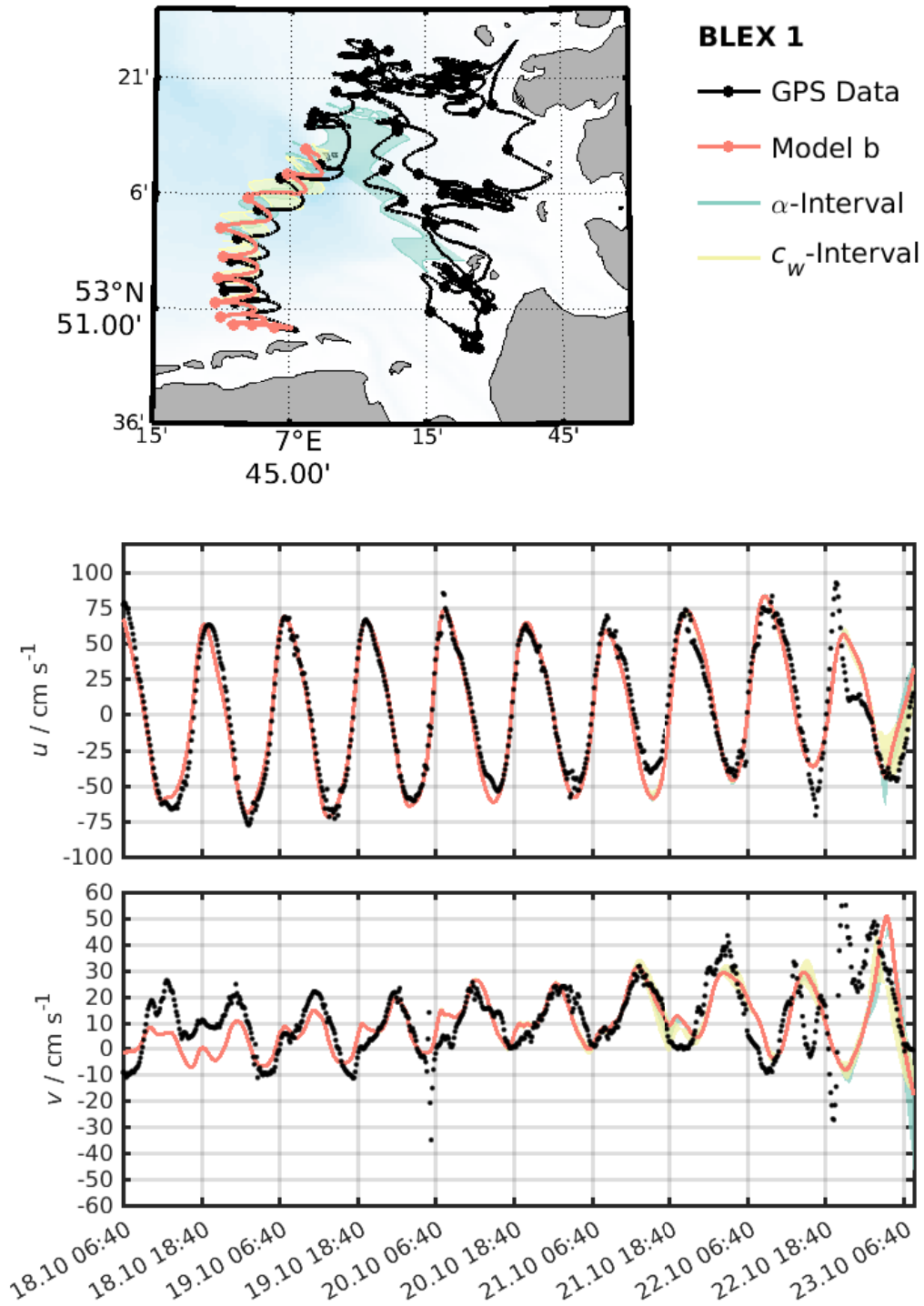
Figure 161: Computed trajectories for Drifter 1 (Type A) using drag parameters for Model *b* without error term and Runge-Kutha integration. Details are given in subsection 7.2.

Figure 162: Computed trajectories for Drifter 1 (Type A) using drag parameters for Model *c* without error term and Runge-Kutha integration. Details are given in subsection 7.2.

Figure 163: Computed trajectories for Drifter 2 (Type B) using drag parameters for Model *a* without error term and Runge-Kutha integration. Details are given in subsection 7.2.

Figure 164: Computed trajectories for Drifter 2 (Type B) using drag parameters for Model *b* without error term and Runge-Kutha integration. Details are given in subsection 7.2.

Figure 165: Computed trajectories for Drifter 2 (Type B) using drag parameters for Model *c* without error term and Runge-Kutha integration. Details are given in subsection 7.2.

G. SWAN Parameter Tests

To resolve Stokes Drift properties in realistic applications, a good agreement of computed significant wave height and wave direction with in-situ data is crucial. This section shows a comparison of these properties for different sets of parameters in SWANcomputations of the GB-Model with measured data at FINO 1, Wave Rider Elbe and wave buoy data at the island Spiekeroog over the course of the BLEX experiment described in section 7. Based on reference settings described below, SWAN parameters for wind growth, depth induced wave breaking and whitecapping were changed. For each test, just one of each parameters was altered while keeping all others in their reference state. The following settings have been altered [SWAN, 2015][205],[206]

- The **wave growth** term by Cavaleri and Rizzoli [1981]: `AGROW [a]`. a is the proportionality coefficient with a default value of `a=0.0015`.[207]

- **Depth induced wave breaking**: `BREaking CONstant [alpha] [gamma]`. A constant breaker index `gamma` ($\gamma = \frac{A_{max}}{h}$), which is the ratio of maximum wave amplitude A_{max} and local bottom depth h [Holthuijsen, 2007], was used in these simulations, `alpha` (α) is the proportionality coefficient of dissipation. Default values are `alpha=1.0` and `gamma=0.73`. A fixed value $\alpha = 1.0$ was used in all computations and $\gamma = (0.5, 0.73, 0.9, 1.5, 2.0)$ was tested.

- **Whitecapping**: `KOMen [cds2] [stpm] [powst] [delta] [powk]`. This command applies a formulation for whitecapping by Komen et al. [1984] where `cds2` (C_{ds}) determines the rate of whitecapping dissipation, `stpm` ($\tilde{s}^2_{PM}$) is the wave steepness of a Pearson-Mosskowitz spectrum, `powst` is the power of steepness normalized with the Pearson-Moskowitz wave steepness, `delta` (δ) is a coefficient which determines the whitecapping's dependency on wave number and `powk` is the wave number-normalized power of the wave number.

The reference settings are:

```
GEN3 KOMen 1.5e-5 3.02e-3 AGROW 0.004
BREaking  CONstant 1.0  1.5
WCAP KOM 2.36e-5 3.02e-3 2 1 1
```

Figure 166 to Figure 186 show the influence of each parameter on significant wave height, mean wave direction and wave period in comparison to measured data. Tested values for each parameter are given in these plots. Note that all other parameters were kept in thier reference

---

[205] This list shows the corresponding command-line of the SWAN input files in the format `KEYWORD [parameter 1] [parameter 2] ...` and a short description of each parameter and it's respective default value. Details about each option can be founf in SWAN [2015] and the cited literature.

[206] Plots: /home/flo/check_waves_blex/BLEX_GB/compare_waves.m

[207] agrow tests neu mit gamma=15 machen!

state, e.g. in Figure 166 just the breaker index γ was altered. These plots are also meant as guidance for future simulations.
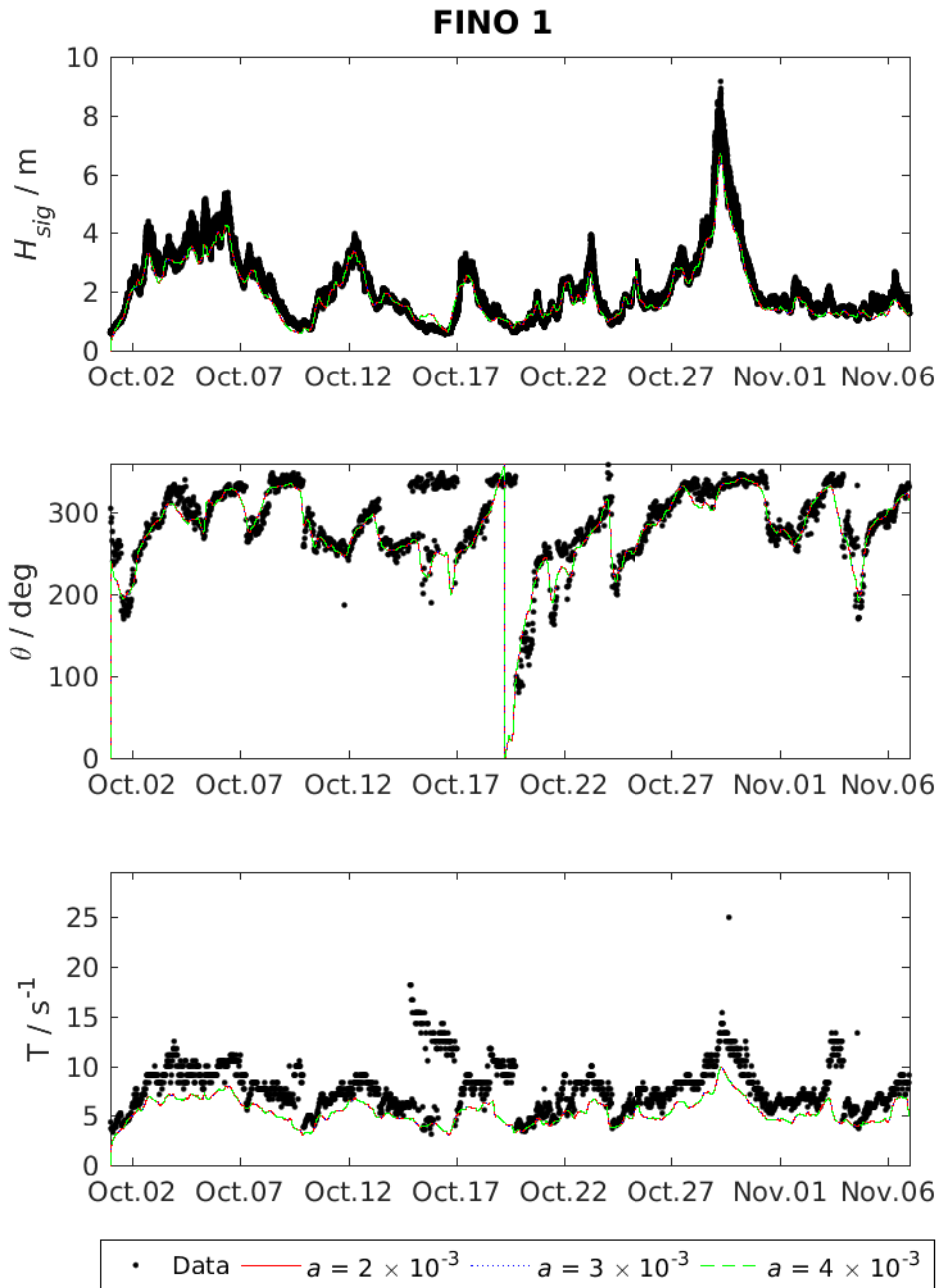
Figure 166: Influence of the proportionality coefficient a in the wave growth term `AGROW` on significant wave height H_{sig}, mean wave direction θ and mean period T in comparison with measured data at FINO 1 (dots). SWAN data of T show the mean period `TM01`, measured T-data were labeled as peak period. All other parameters were kept in their reference state, details are given in the text.
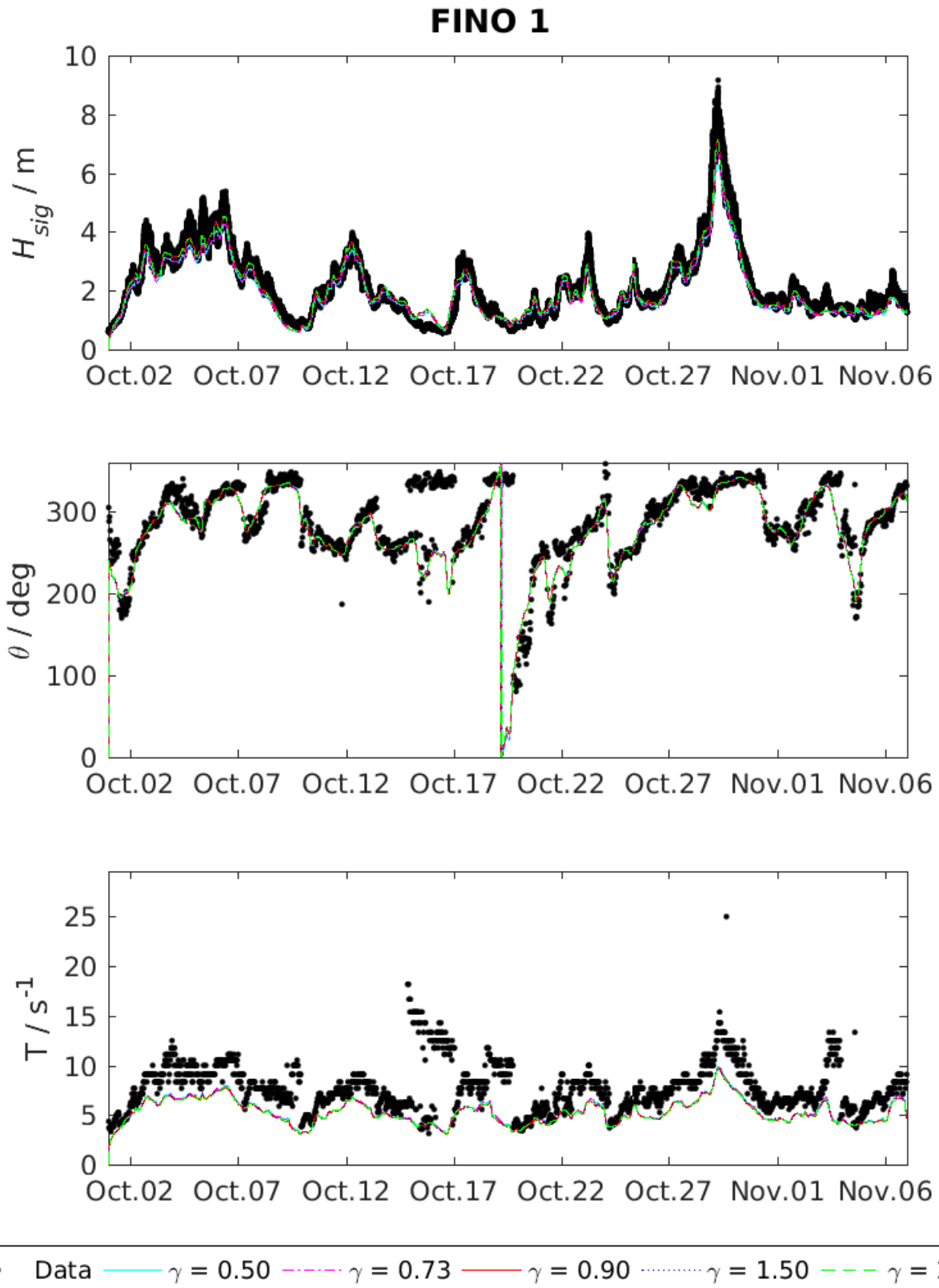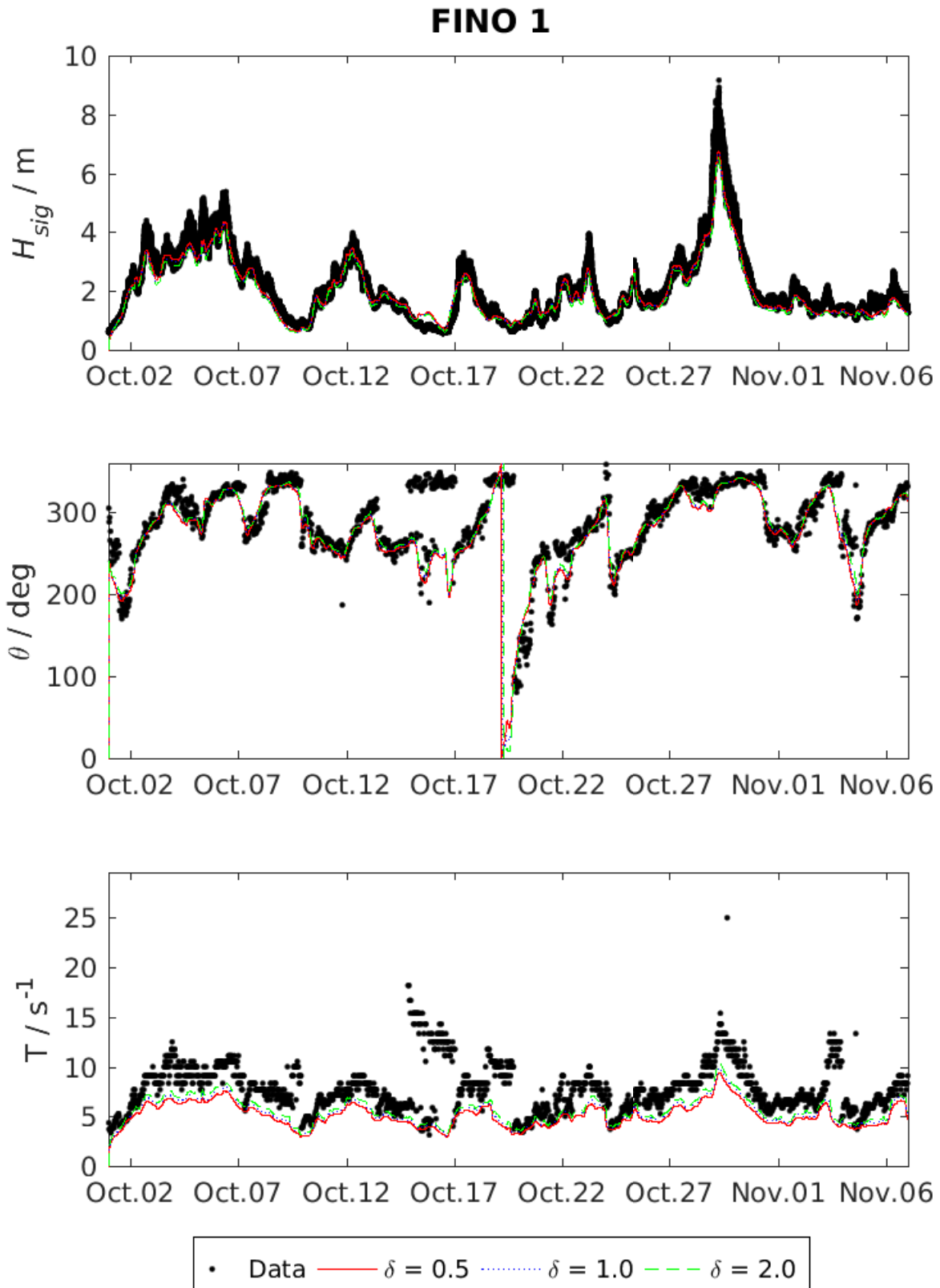
Figure 167: Influence of the Breaker Index γ on significant wave height H_{sig}, mean wave direction θ and mean period T in comparison with measured data at FINO 1 (dots). SWAN data of T show the mean period `TM01`, measured T-data were labeled as peak period. All other parameters were kept in their reference state, details are given in the text.
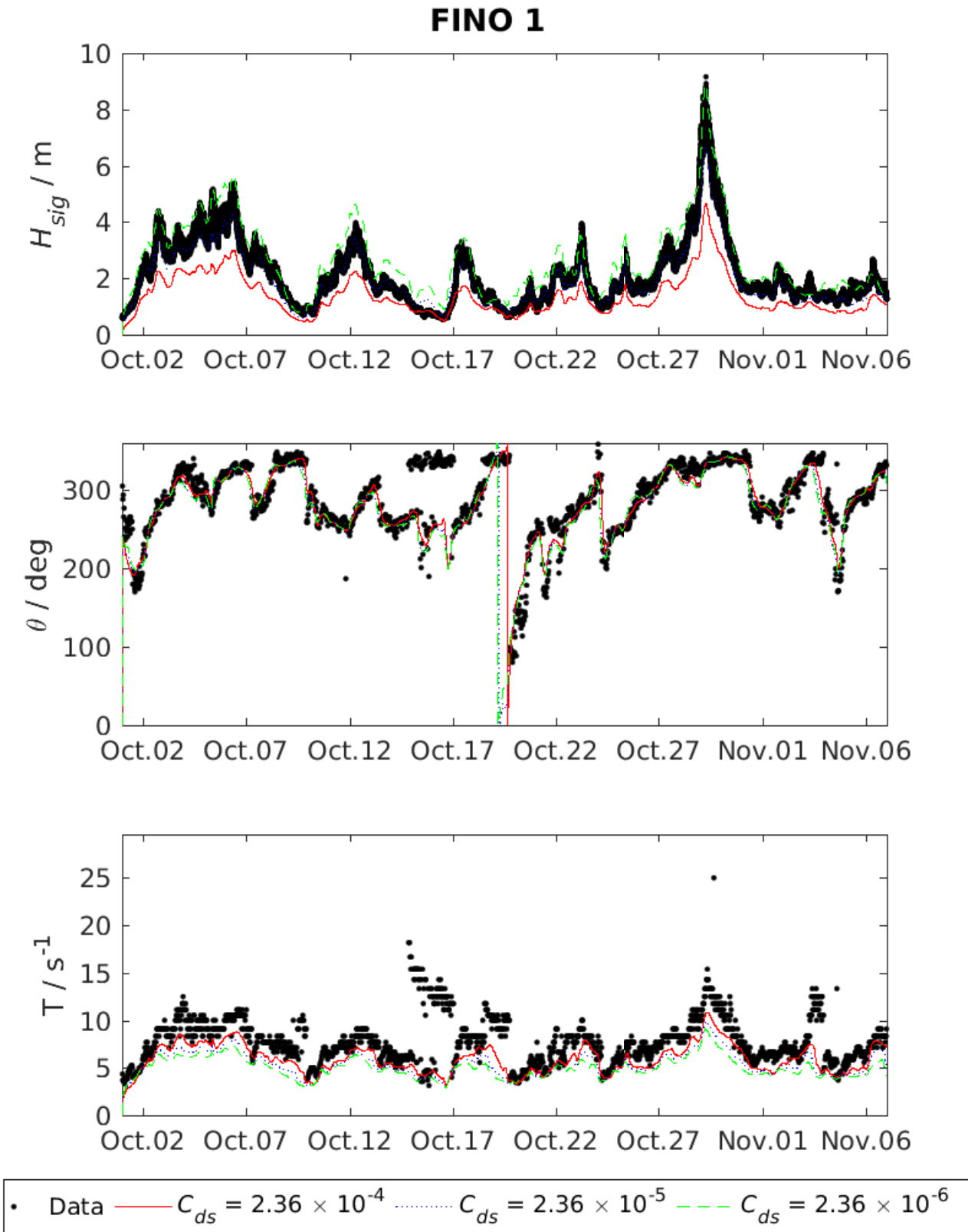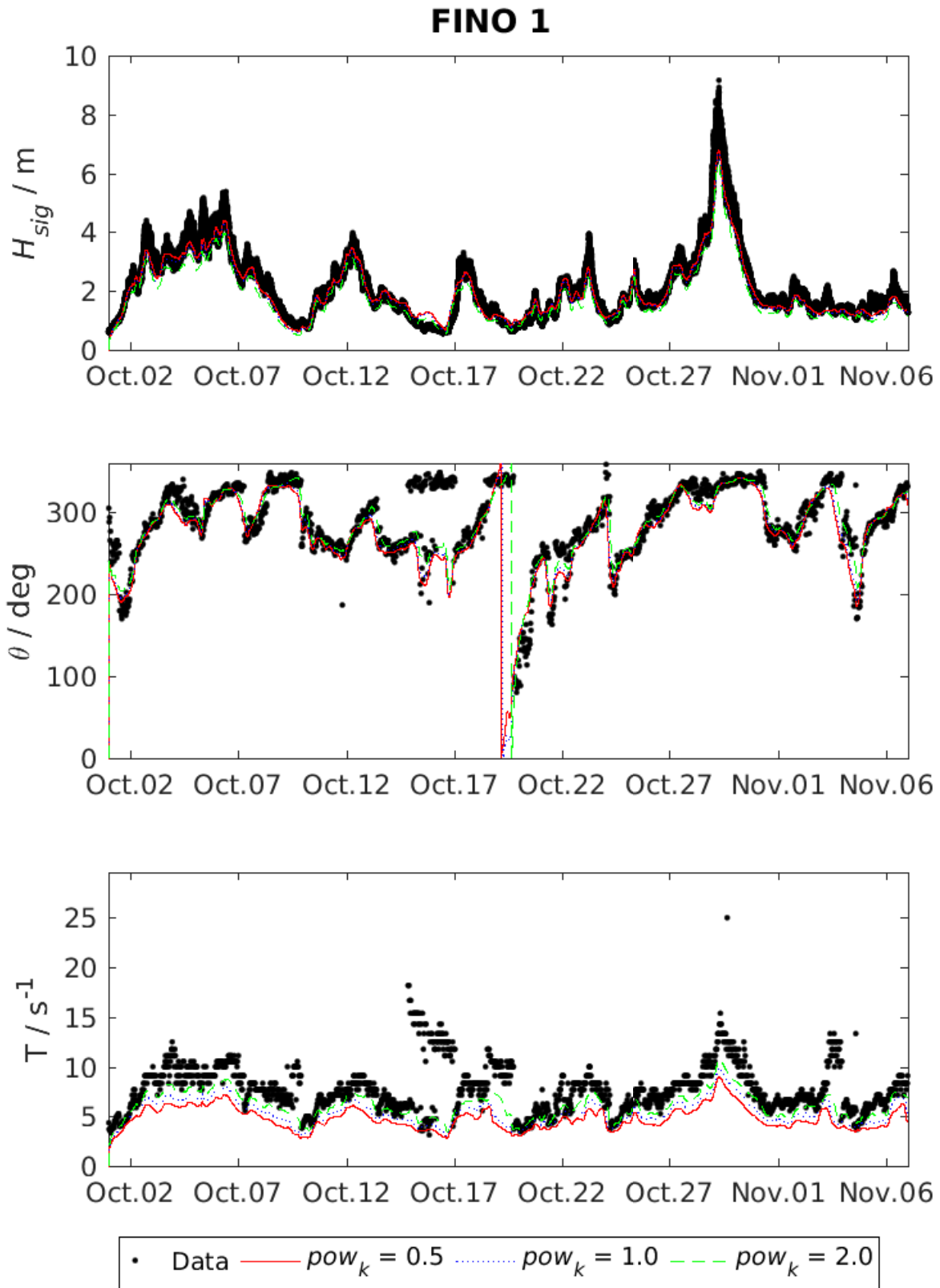
Figure 168: Influence of the dissipation rate of whitecapping C_{dc} on significant wave height H_{sig}, mean wave direction θ and mean period T in comparison with measured data at FINO 1 (dots). SWAN data of T show the mean period TM01, measured T-data were labeled as peak period. All other parameters were kept in their reference state, details are given in the text.

FINO 1
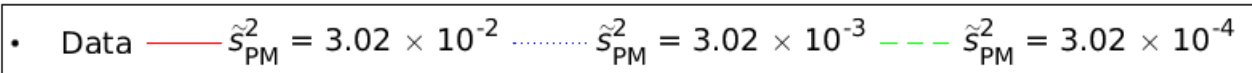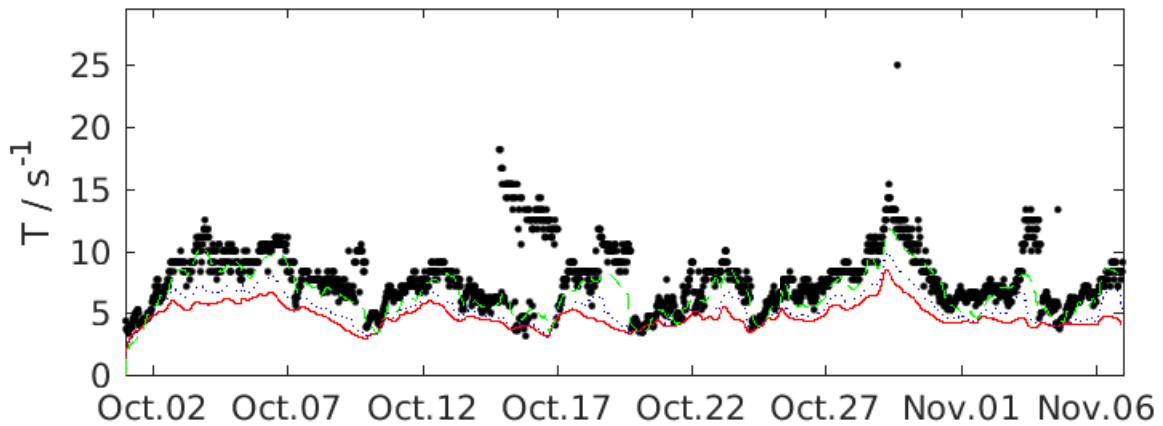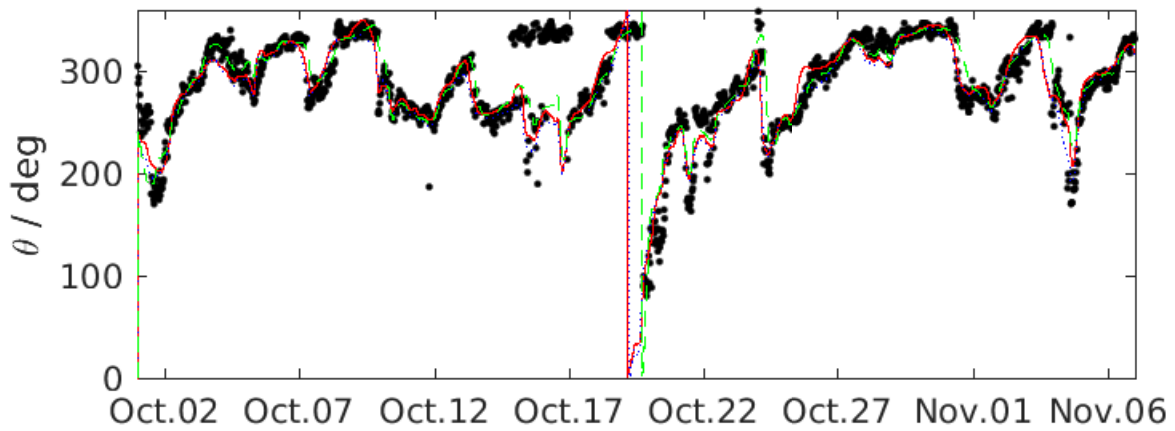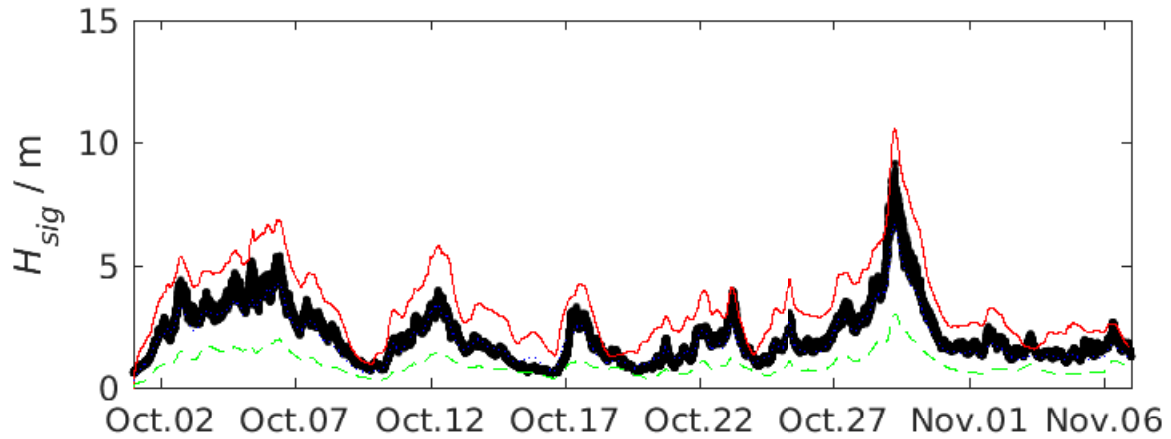
Figure 169: Influence of the wave steepness *stpm* on significant wave height H_{sig}, mean wave direction θ and mean period T in comparison with measured data at FINO 1 (dots). SWAN data of T show the mean period `TM01`, measured T-data were labeled as peak period. All other parameters were kept in their reference state, details are given in the text.
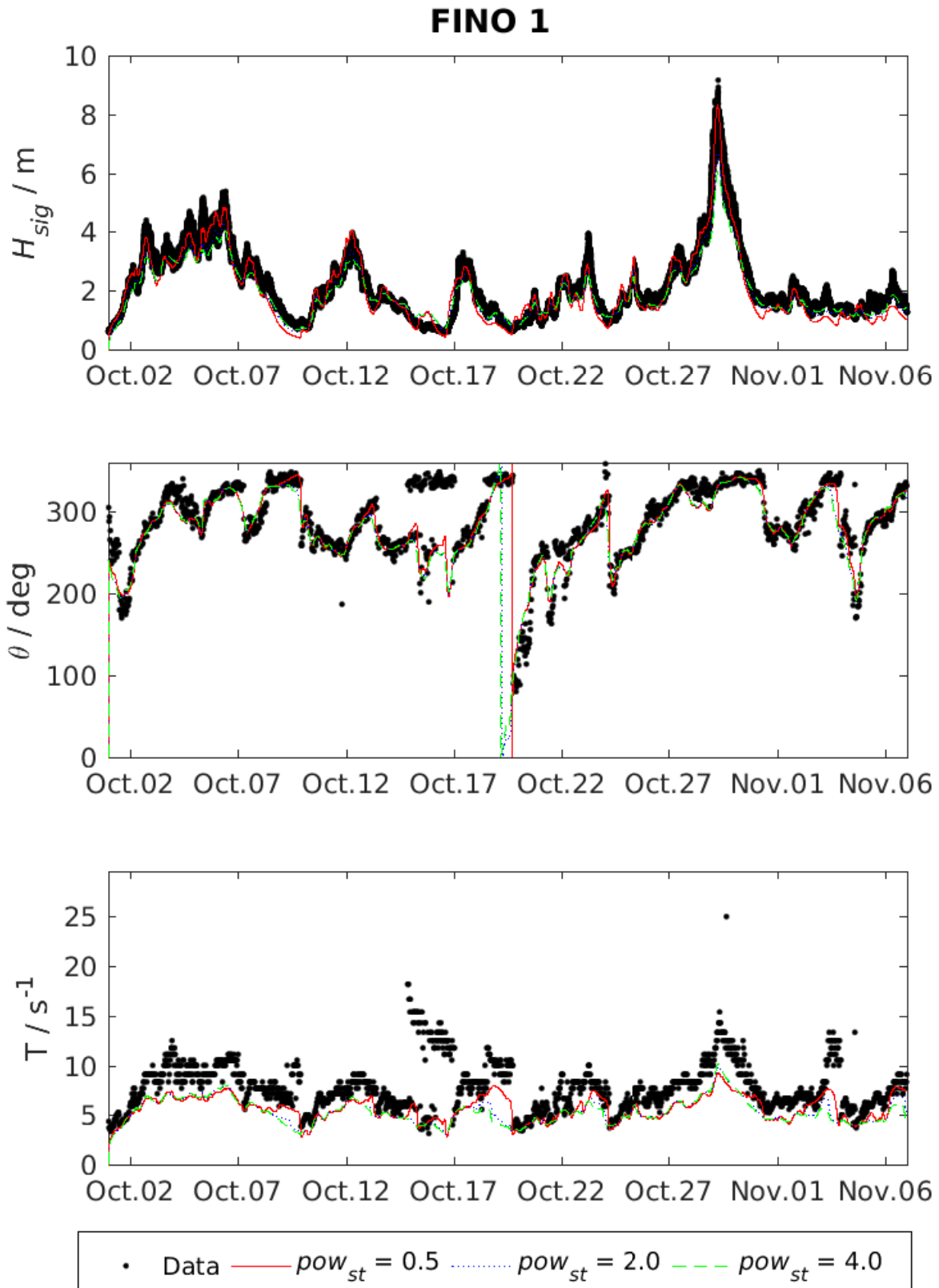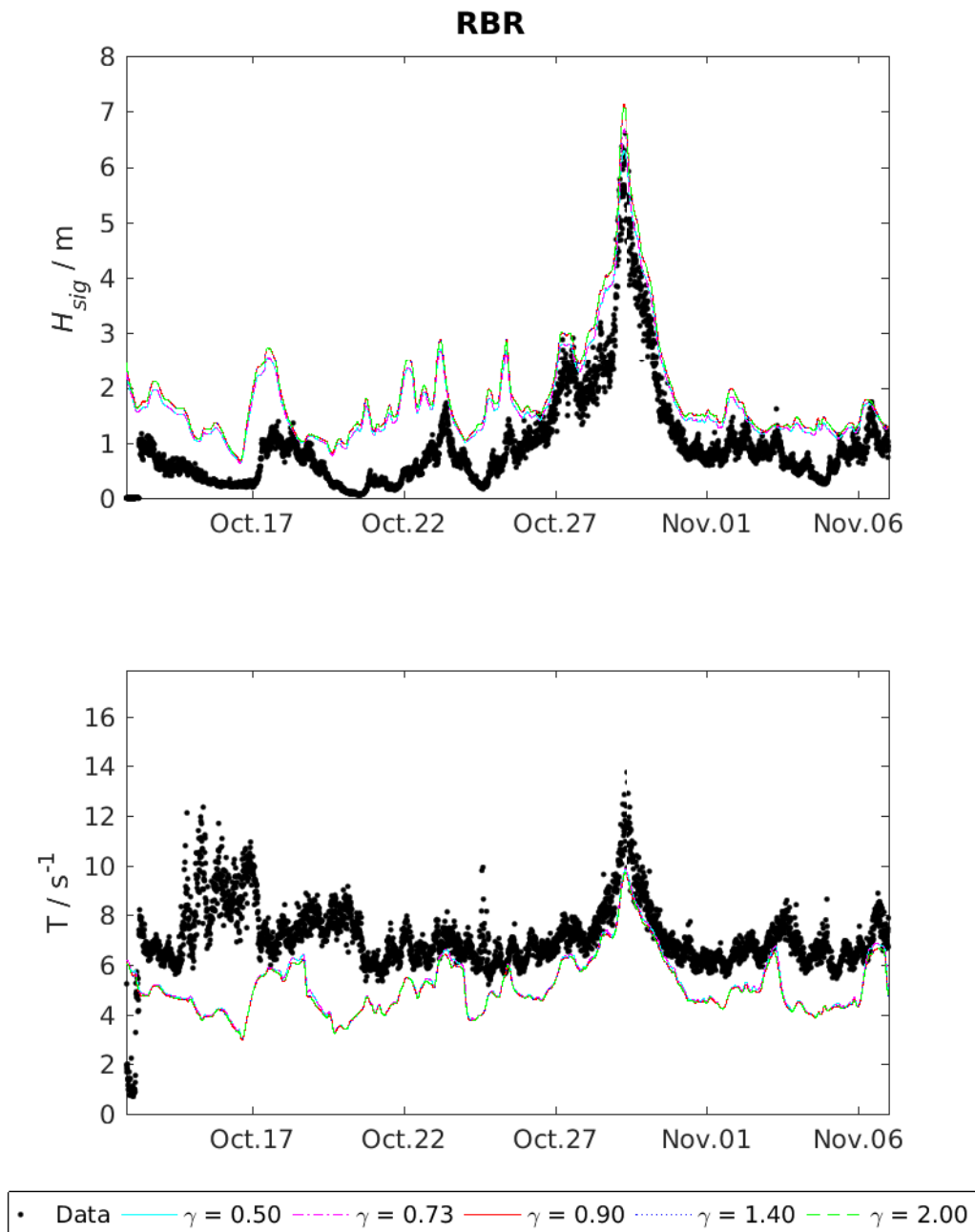
Figure 170: Influence of the power of steepness pow_{st} on significant wave height H_{sig}, mean wave direction θ and mean period T in comparison with measured data at FINO 1 (dots). SWAN data of T show the mean period `TM01`, measured T-data were labeled as peak period. All other parameters were kept in their reference state, details are given in the text.

Figure 171: Influence of wave number dependency of whitecapping δ on significant wave height H_{sig}, mean wave direction θ and mean period T in comparison with measured data at FINO 1 (dots). SWAN data of T show the mean period TM01, measured T-data were labeled as peak period. All other parameters were kept in their reference state, details are given in the text.

Figure 172: Influence of wave number normalized power pow_k on significant wave height H_{sig}, mean wave direction θ and mean period T in comparison with measured data at FINO 1 (dots). SWAN data of T show the mean period TM01, measured T-data were labeled as peak period. All other parameters were kept in their reference state, details are given in the text.
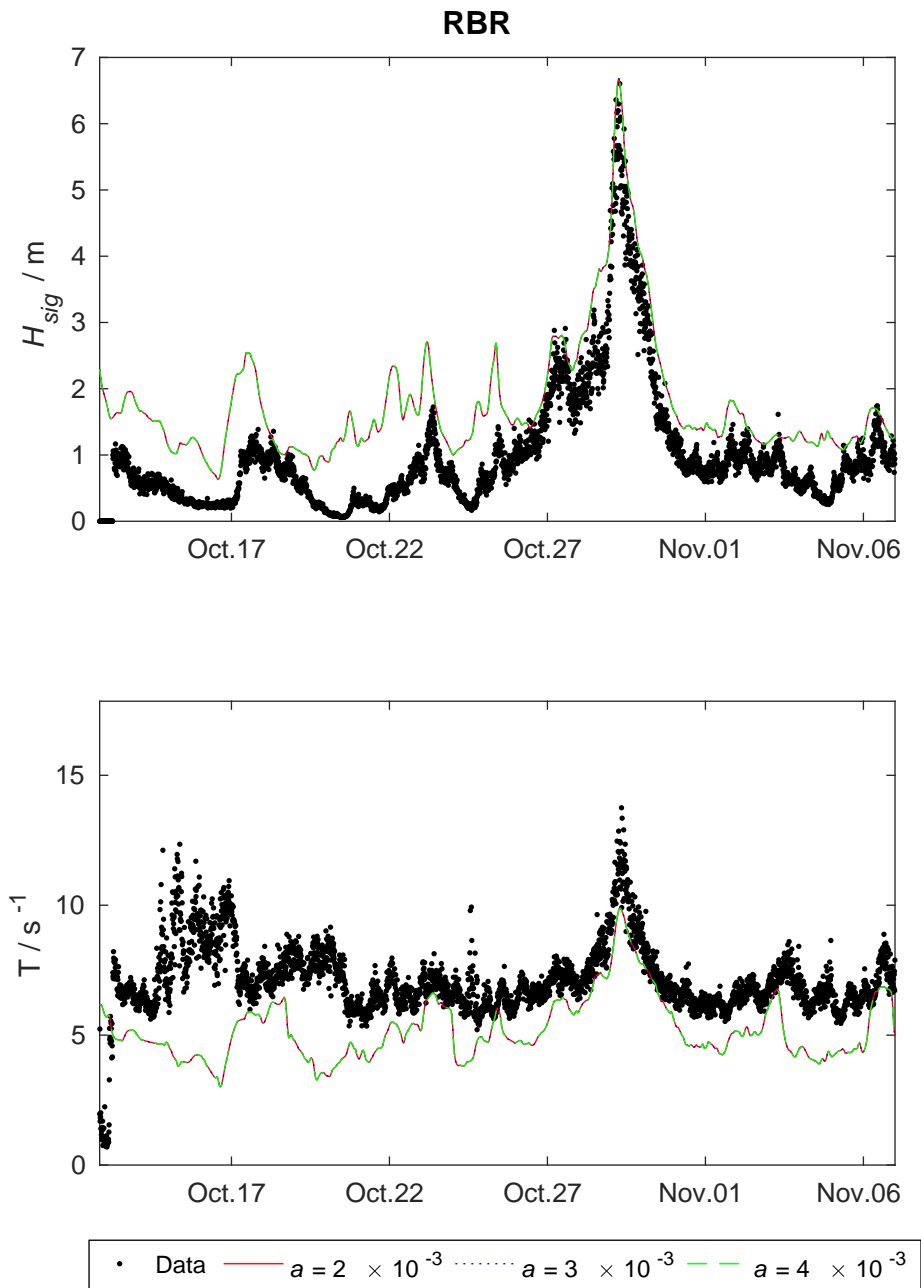
Figure 173: Influence of the proportionality coefficient a in the wave growth term `AGROW` on significant wave height H_{sig} and mean period T in comparison with measured data at rbr 1 (dots). SWAN data of T show the mean period `TM01`, measured T-data were labeled as peak period. All other parameters were kept in their reference state, details are given in the text.
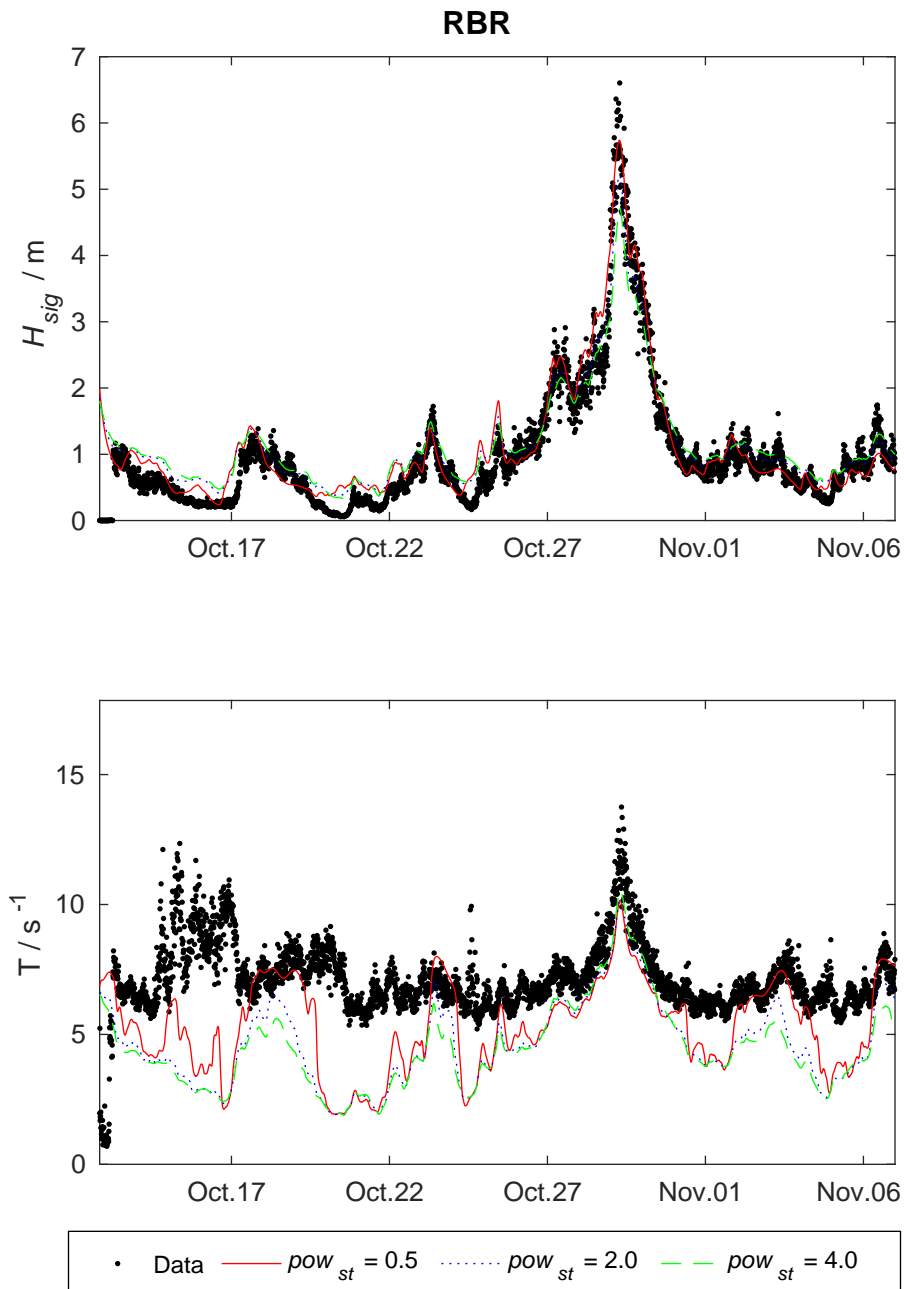
Figure 174: Influence of the Breaker Index γ on significant wave height H_{sig} and mean period T in comparison with measured data at rbr 1 (dots). SWAN data of T show the mean period `TM01`, measured T-data were labeled as peak period. All other parameters were kept in their reference state, details are given in the text.
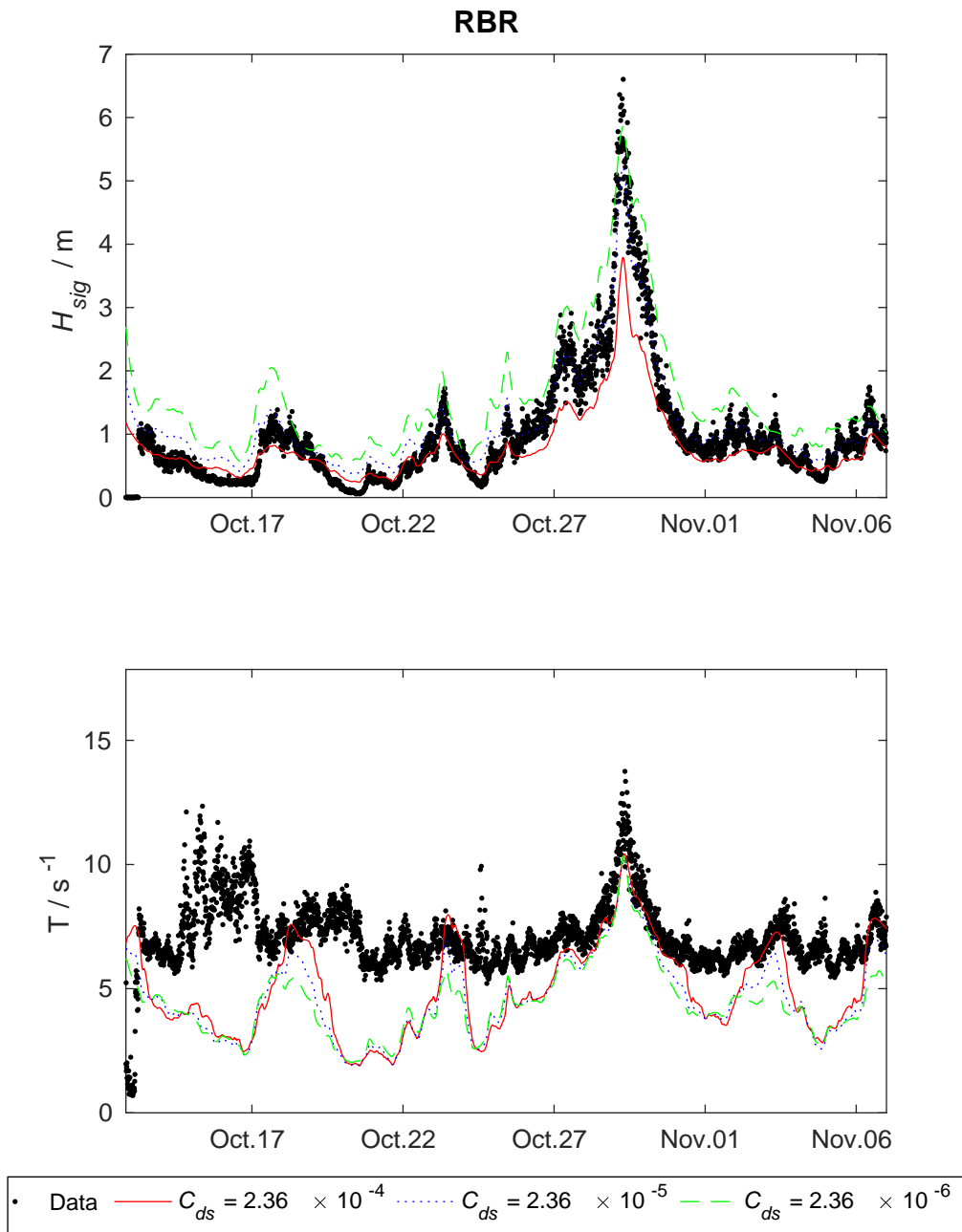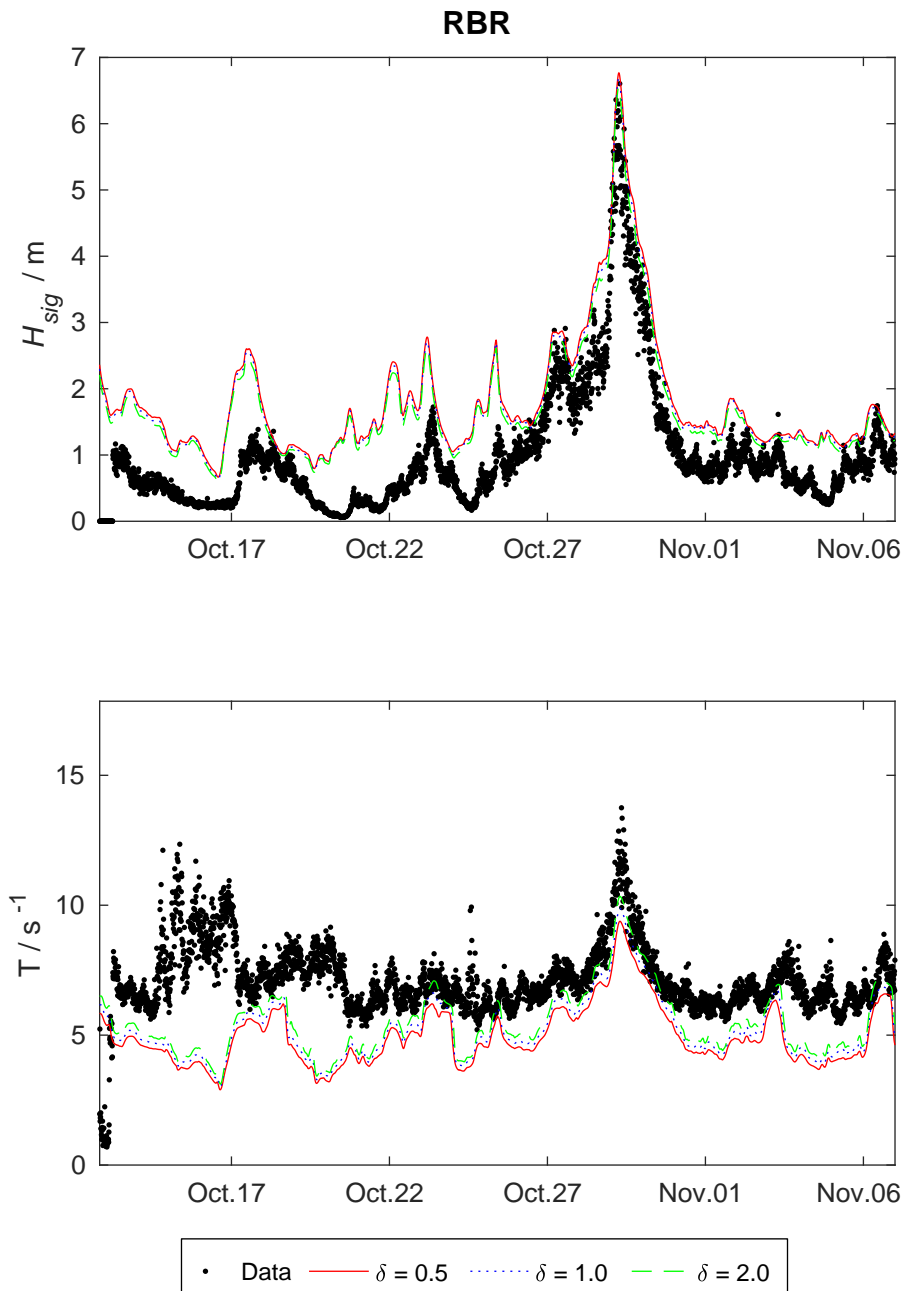
Figure 175: Influence of the dissipation rate of whitecapping C_{dc} on significant wave height H_{sig} and mean period T in comparison with measured data at RBR (dots). SWAN data of T show the mean period `TM01`, measured T-data were labeled as peak period. All other parameters were kept in their reference state, details are given in the text.
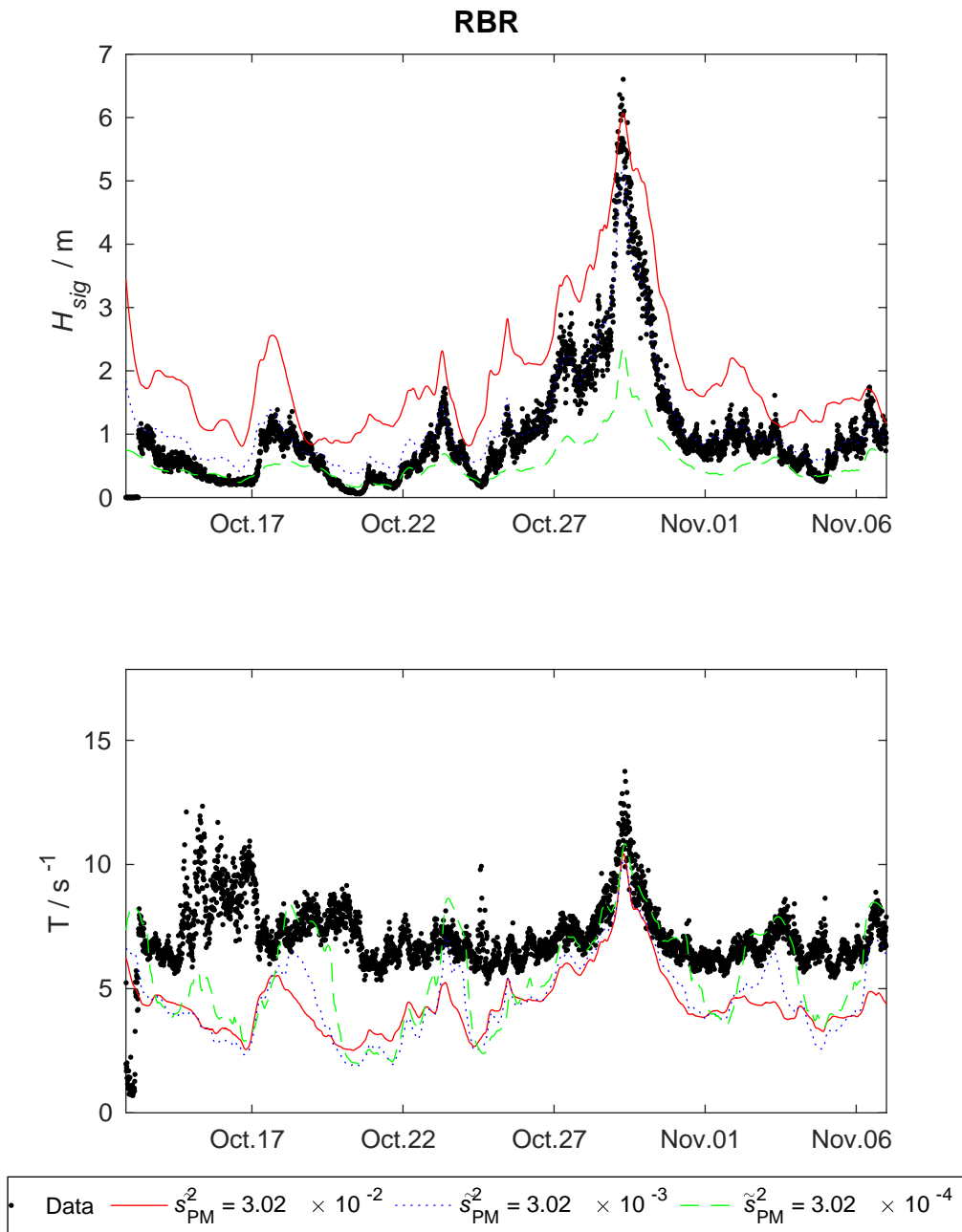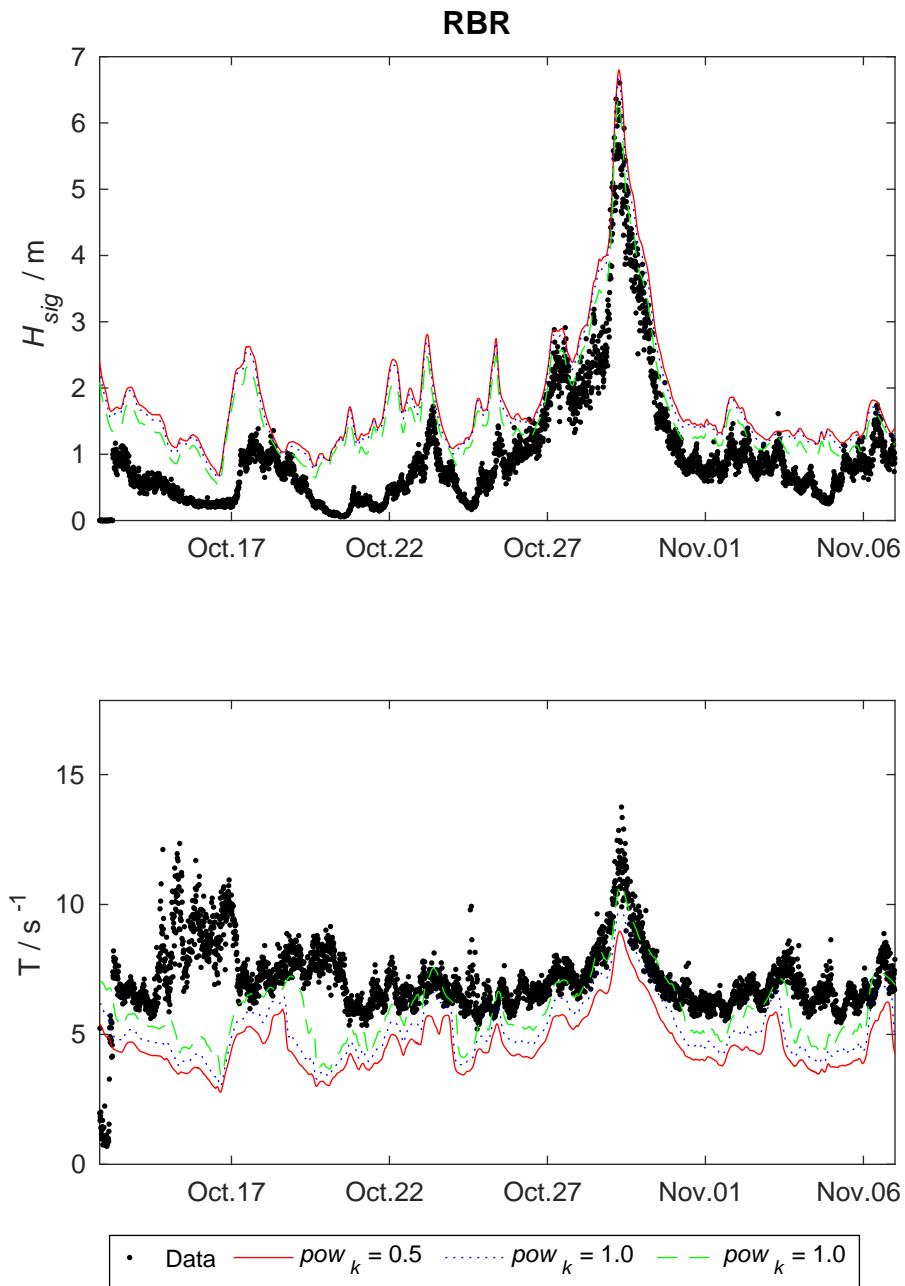
Figure 176: Influence of the wave steepness *stpm* on significant wave height H_{sig} and wave period T in comparison with measured data at RBR (dots). SWAN data of T show the mean period TM01, measured T-data were labeled as peak period. All other parameters were kept in their reference state, details are given in the text.

Figure 177: Influence of the power of steepness pow_{st} on significant wave height H_{sig} and wave period T in comparison with measured data at RBR (dots). SWAN data of T show the mean period TM01, measured T-data were labeled as peak period. All other parameters were kept in their reference state, details are given in the text.

Figure 178: Influence of wave number dependency of whitecapping δ on significant wave height H_{sig} and wave period T in comparison with measured data at RBR (dots). SWAN data of T show the mean period `TM01`, measured T-data were labeled as peak period. All other parameters were kept in their reference state, details are given in the text.

Figure 179: Influence of wave number normalized power pow_k on significant wave height H_{sig} and wave period T in comparison with measured data at RBR (dots). SWAN data of T show the mean period `TM01`, measured T-data were labeled as peak period. All other parameters were kept in their reference state, details are given in the text.
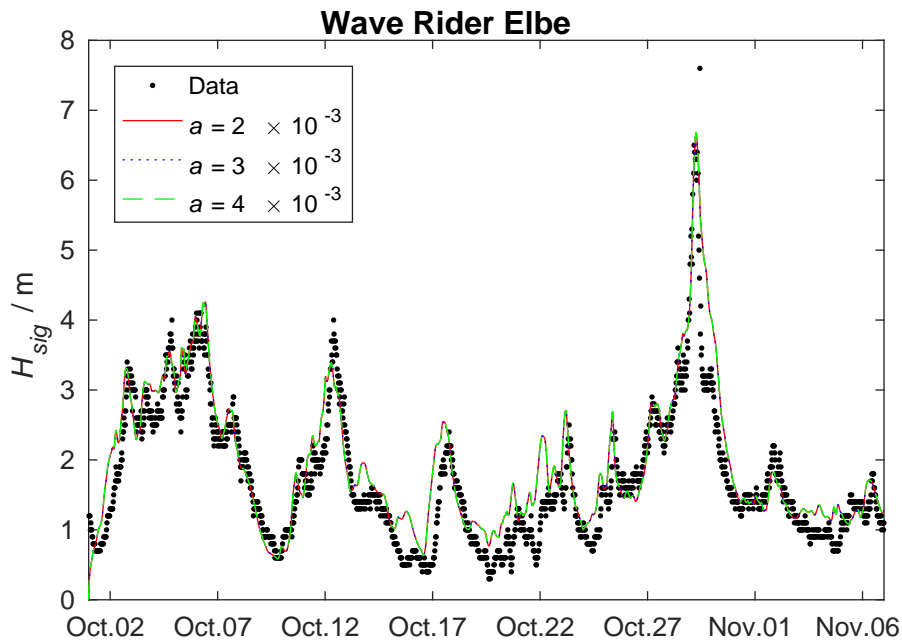
Figure 180: Influence of the proportionality coefficient a in the wave growth term `AGROW` on significant wave height H_{sig} in comparison with measured data at Wave Rider Elbe 1 (dots). All other parameters were kept in their reference state, details are given in the text.
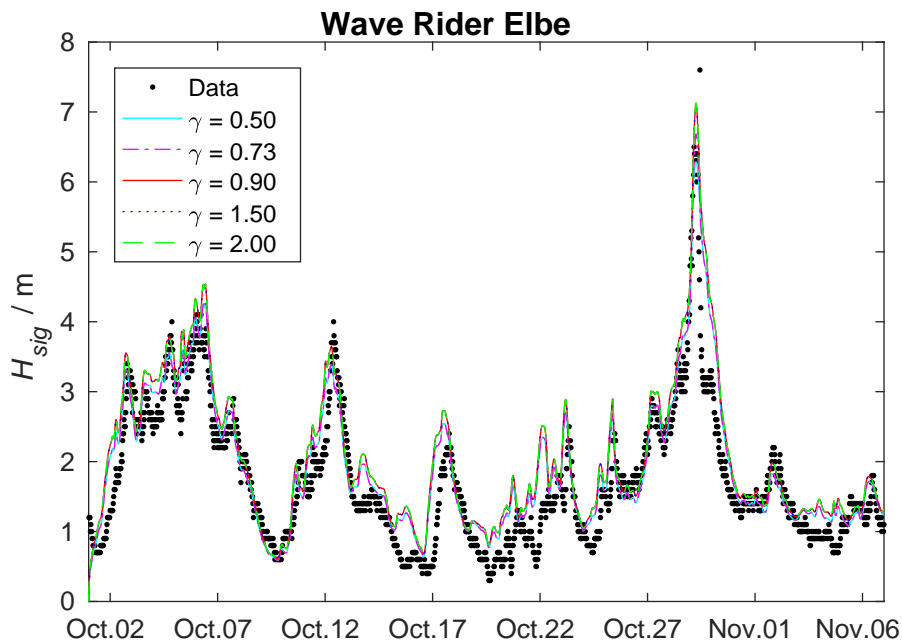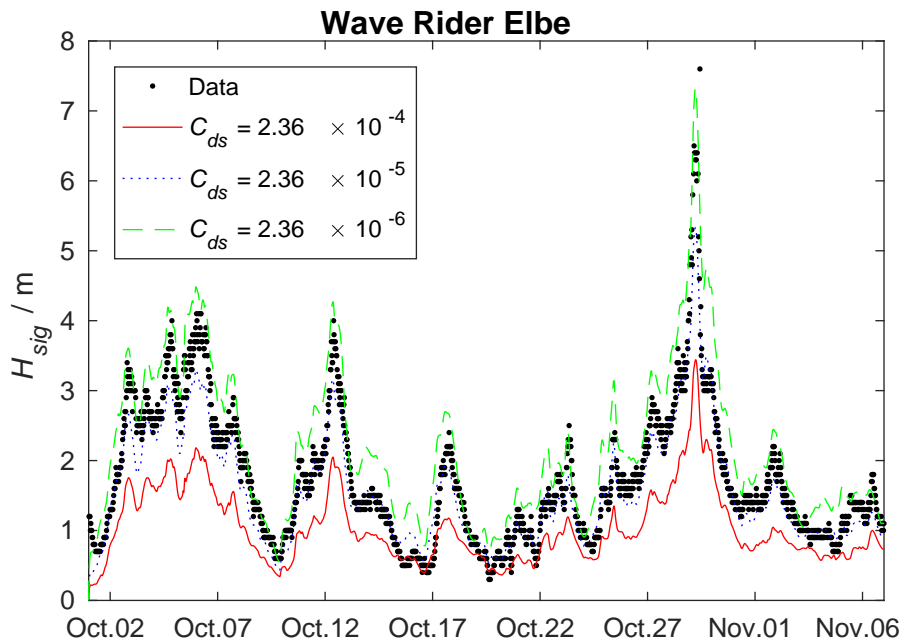

Figure 181: Influence of the Breaker Index γ on significant wave height H_{sig} in comparison with measured data at Wave Rider Elbe 1 (dots). All other parameters were kept in their reference state, details are given in the text.
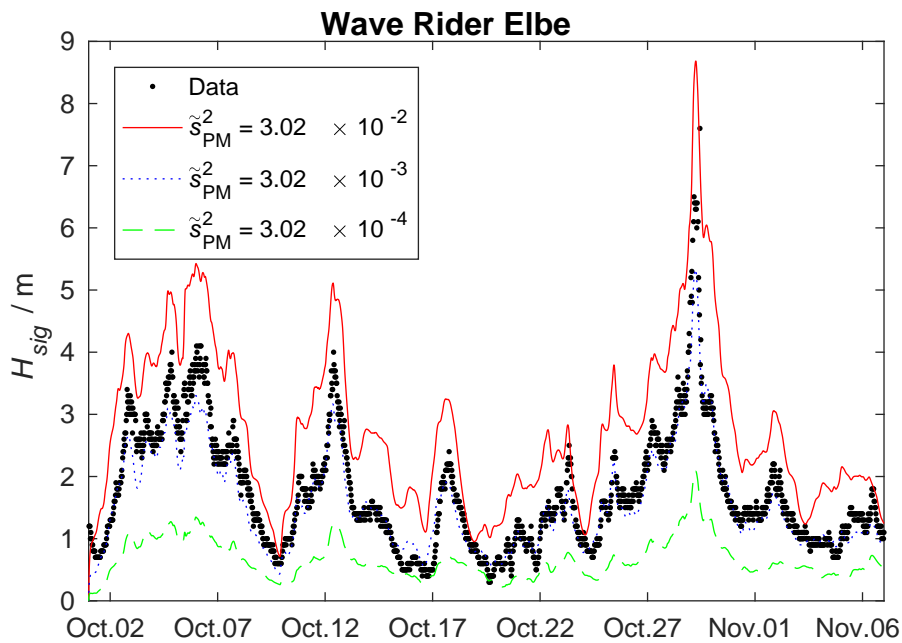
Figure 182: Influence of the dissipation rate of whitecapping C_{dc} on significant wave height H_{sig} in comparison with measured data at Wave Rider Elbe (dots). All other parameters were kept in their reference state, details are given in the text.
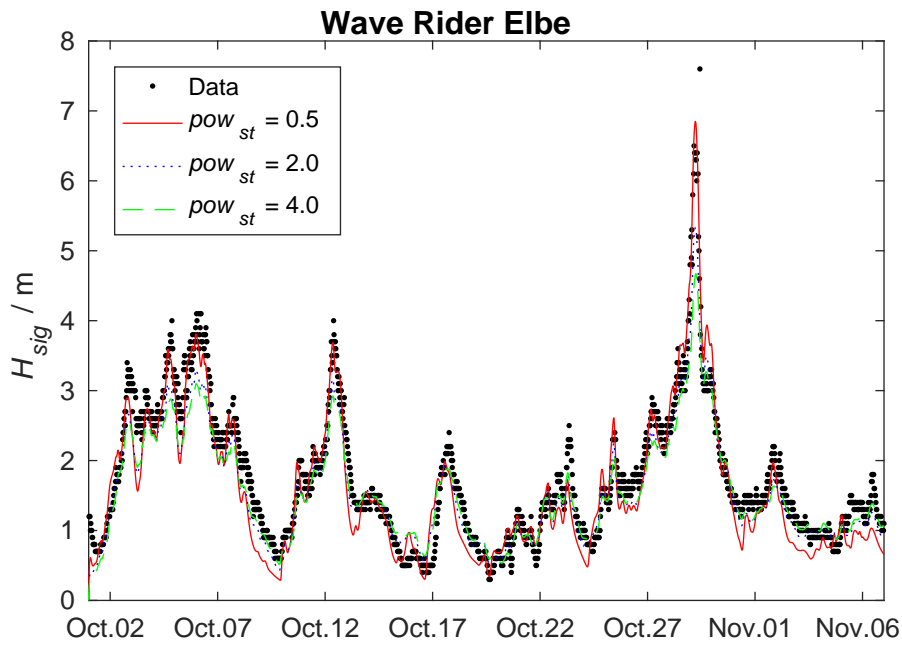

Figure 183: Influence of the wave steepness $stpm$ on significant wave height H_{sig} in comparison with measured data at Wave Rider Elbe (dots). All other parameters were kept in their reference state, details are given in the text.

Figure 184: Influence of the power of steepness pow_{st} on significant wave height H_{sig} in comparison with measured data at Wave Rider Elbe (dots). All other parameters were kept in their reference state, details are given in the text.
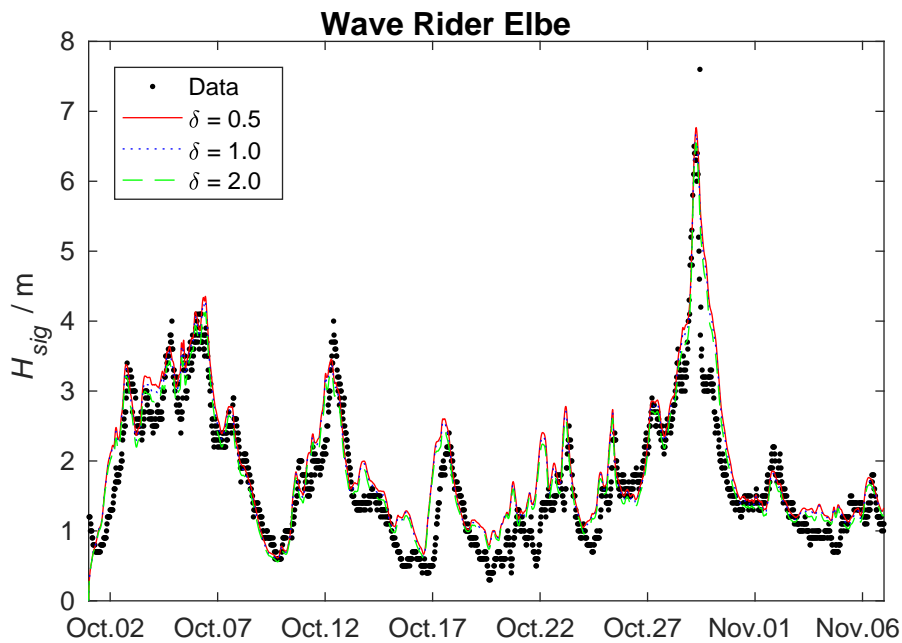

Figure 185: Influence of wave number dependency of whitecapping δ on significant wave height H_{sig} in comparison with measured data at Wave Rider Elbe (dots). All other parameters were kept in their reference state, details are given in the text.
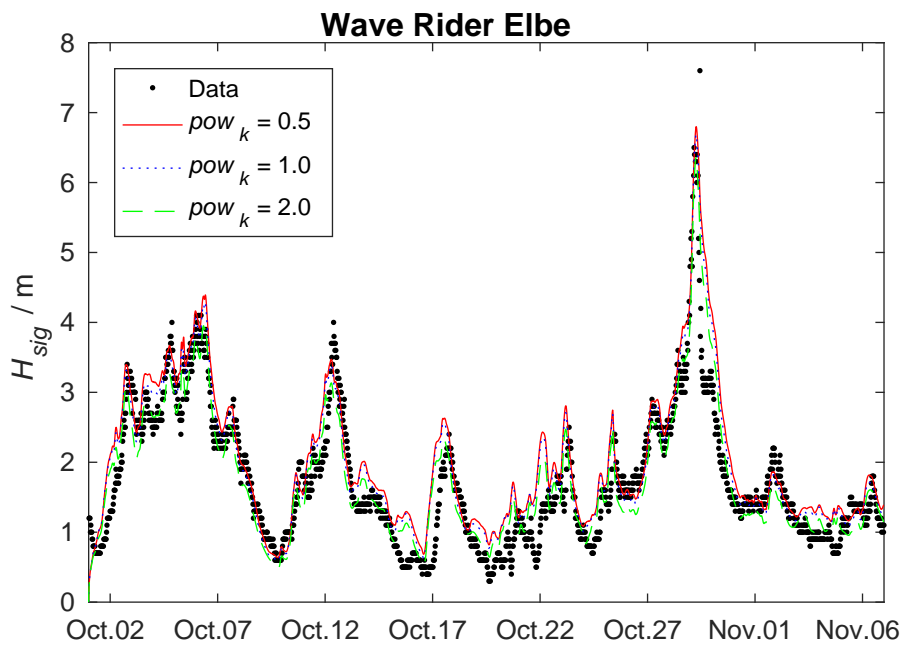
Figure 186: Influence of wave number normalized power pow_k on significant wave height H_{sig} in comparison with measured data at Wave Rider Elbe (dots). All other parameters were kept in their reference state, details are given in the text.